UNIVERSIDADE DE LISBOA

FACULDADE DE CIÊNCIAS

Boulder deposits related to extreme marine events in the western coast of Portugal

Doutoramento em Geologia

Especialidade em Geologia Económica e do Ambiente

Maria Alexandra Soares Gomes Cardoso de Oliveira

Tese orientada por:

Prof. Doutor César Augusto Canêlhas Freire de Andrade

Prof. Doutor Ramiro Neves

Documento especialmente elaborado para a obtenção do grau de doutor

2017

UNIVERSIDADE DE LISBOA

FACULDADE DE CIÊNCIAS

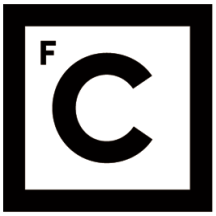

Ciências
ULisboa

Boulder deposits related to extreme marine events in the western coast of Portugal

Doutoramento em Geologia
Especialidade em Geologia Económica e do Ambiente

Maria Alexandra Soares Gomes Cardoso de Oliveira

Tese orientada por:
Prof. Doutor César Augusto Canêlhas Freire de Andrade
Prof. Doutor Ramiro Neves

Júri:
Presidente:
- Doutora Maria da Conceição Pombo de Freitas

Vogais:
- Doutor Alastair G. Dawson
- Doutor Pedro Manuel Rodrigues Roque Proença e Cunha
- Doutor César Augusto Canêlhas Freire de Andrade
- Doutor Rui Pires de Matos Taborda

Documento especialmente elaborado para a obtenção do grau de doutor

Com o apoio da Fundação para a Ciência e Tecnologia (SFRH/BD/66017/2009)

2017

Ouve, o mar veste a inquietude da terra.

Oliverio Macías Álvarez

Acknowledgments

The work developed during the past seven years has been demanding (in more ways than one) and it would not have been possible without the support and guidance given by many people and institutions.

Foremost, I am grateful to Professor César Freire de Andrade, for the fundamental advice, the encouragement and the humane character. It has been a privilege.

My thanks also go to Professor Ramiro Neves and Professor Maria da Conceição Freitas for text revision, enthusiasm and motivation.

I am grateful to Alastair Dawson for the availability, the suggestions and publications provided.

A genuine thank you to Cristina Branquinho, Pedro Pinho and Esteve Llop Vallverdú, for the contagious enthusiasm, for the motivational conversations and for the precious help in the development and application of the lichen growth curve and in lichen species identification.

I also would like to aknowledge José Madeira and Rui Taborda for their on-occasion but precious inputs, crucial in the resolution of specific questions that aided the development of this work.

My thanks to Susana Barbosa, for the advice and support given in the statistical modelling of extreme values and for text revision.

I would also like to thank the following people:

- Ronald Goble of the Department of Earth & Atmospheric Sciences of the University of Nebraska-Lincoln, for age estimation of samples;
- Paulo Henriques, geologist in the Portuguese National Authority for Civil Protection, for information and photographic record of rock-falls in the Ericeira region;
- João Pedro Henriques Gil from the Portuguese charity Santa Casa da Misericórdia for information about the history of Ericeira and for suggesting reading material essential to a better comprehension of the study area;

- Joaquim Meireles from the Museu Municipal de Peniche for information about the effects of the 1st November 1755 tsunami in the Peniche region;
- Paula Marques Figueiredo for the constant exchange of data regarding boulders transported during specific storms, historical records of earthquakes and tsunami events and age estimation techniques;
- Ana Paula Gomes for the suggestions and support;
- Vera Lopes for all the help in the laboratory;
- Instituto Dom Luiz and Centro de Geologia da Universidade de Lisboa, specially to Célia Lee, for the logistic and technical support provided;
- Rita González-Villanueva, Alexandra Amorim, Tania Ferreira and Vera Lopes, for partial or complete revision of this document.

I would like to acknowledge the following friends, colleagues and family members for field work assistance: Alexandra Amorim, Ana Mafalda Carapuço, Anthony Kitchin, Catarina Lavinas, Diogo Carreira, João Nuno Silva, Mariana Ramos, Paula Marques Figueiredo, Pedro Costa, Raquel Martins, Rita González-Villanueva, Sandra Moreira, Sónia Queiroz, Tanya Silveira, Tiago Silva and Vera Paio Lopes.

Also, my thanks go to Ana Mafalda Carapuço, Ana Nobre Silva, Bárbara Proença, Mónica Ribeiro and Tanya Silveira, for their help in the task of numerical modelling of waves using SWAN, through the time-consuming preparation and implementation of workshops and on-occasion much needed clarifications.

On a personal note, I would like to thank Catarina, Mónica and Sandra, for the precious encounters, for sharing and for understanding, and, when everything else failed, for ginjinha!

I am grateful to my office colleagues (and friends) Ana Mesquita Rocha and Rita González-Villanueva for the shared time, experiences, laughs and motivational talks.

I would like to acknowledge an awesome group of women, with whom I had the privilege to work with. They are Alexandra Amorim, Ana Mafalda Carapuço, Anabela Cruces, Tania Ferreira, Tanya Silveira and Vera Lopes. Thank you for your help, your friendship, your motivation and for believing that I could do and be better. You have

been an inspiration and have made this endeavour into an endearing and enriching personal and professional experience.

To my volleyball friends, companions and coaches, in both the AEFCL and Clube Oriental de Lisboa teams, for the moral support throughout this project, in particular to Andreia Maia, Carolina Costa, Guida Mendes Bernardo, Inês Fragata, Joana Lupi Caetano, Leonor Mira Godinho, Marisa Magalhães, Pedro Henriques Gonçalves, Sara Dias Narciso and Sofia Freire.

To my (many) closest friends who have been present in the past 7 years. I would especially like to acknowledge Catarina Guerreiro, Catarina Lavinas, Diogo Carreira, Helga Garcia, João Leitão, Margarida Rodrigues, Mariana Ramos, Raquel Martins, Rita Pimenta, Rita Teixeira, Rute Durão and Vasco Fonseca. Thank you for pushing me forward, for the shoulder, for the long talks, for listening and being patient, for the drinks and laughs and for being the spectacular friends that you are.

My heartfelt thanks to my family. To my dearest parents, sister, nephew, uncles, and cousins, thank you for being here, for worrying, for listening and for waiting. I would like to particularly acknowledge Ana Cardoso Oliveira for the help in establishing goals and how to better organize my work, which was fundamental in these last and decisive months.

Finally, to João, for always being here and for the selfless time and care (and infinite patience). There are no words to express my gratitude.

The work undertaken was partially funded by FCT (Fundação para a Ciência e Tecnologia) through a PhD scholarship (SFRH/BD/66017/2009) and supported by IDL through UID/GEO/50019/2013 program, also financed by FCT.

This study uses data collected under project GETS (PTDC/CTE-GEX/65948/2006) financed by the FCT, the European NEAREST project (EU-Contract 037110) and the Faculdade de Ciências da Universidade de Lisboa/Instituto Dom Luiz/Agência Portuguesa do Ambiente, I.P. project "Creation and implementation of a Costal Monitoring System for the jurisdiction area of Administração da Região Hidrográfica do Tejo IP").

Resumo

Este trabalho descreve um extenso e complexo depósito de mais de 1600 blocos transportados por evento(s) marinho(s) extremo(s), sobre plataformas estruturais e arribas baixas, entre 2 m e 13 m acima do nível médio do mar (anmm), localizadas na costa O portuguesa, a N da Ericeira. Este depósito inclui cristas e aglomerados de blocos, onde por vezes é visível imbricação, e blocos isolados, frequentemente localizados junto ao bordo da escarpa das arribas e dos degraus das plataformas.

Os principais objetivos deste trabalho incluíram: (1) identificação, (2) datação e (3) cálculo do intervalo de recorrência associado aos eventos responsáveis pelo transporte e deposição dos blocos. Foi também testada a aplicabilidade de métodos de análise de palaeocorrentes, frequentemente utilizados em estudos de depósitos fluviais, a este depósito de blocos costeiro. Um outro objetivo foi o desenvolvimento e aplicação de métodos de datação baseados no crescimento de líquenes, método este frequentemente utilizado no estudo de depósitos glaciares.

Existiram algumas questões associadas ao estudo deste depósito de blocos. A questão principal diz respeito à determinação dos processos que deram origem ao depósito (de natureza tsunamigénica ou tempestítica). Outra, não menos importante, foi a determinação das características do depósito herdadas das ondas que originaram o seu transporte e deposição, independentemente da geomorfologia enquadrante. Existiram outras questões mais específicas relacionadas com o estudo destes depósitos: como e quais as aproximações numéricas a aplicar de forma a inferir características das ondas, baseadas exclusivamente nas características dos blocos; como proceder à datação do transporte dos blocos.

Neste trabalho foram usados vários indicadores para descortinar os processos envolvidos na origem do depósito de blocos em análise, tais como: (1) análise das diferentes acumulações que constituem o depósito, diferenciadas com base na morfologia, na posição e nas características de blocos individuais; (2) monitorização de transporte de blocos por tempestades atuais, modelação de propagação de ondas na área de estudo e análise estatística de valores extremos de agitação marinha; (3) aplicação de soluções numéricas de transporte de blocos; (4) datação baseada em

análise comparativa de fotografias aéreas, em liquenometria, em taxas de erosão e em luminescência oticamente estimulada.

A análise da morfologia das acumulações de blocos e da sua distribuição espacial foi baseada em premissas utilizadas no estudo de palaeocorrentes com o objetivo de inferir a direção do escoamento responsável pelo transporte e deposição dos blocos. O estudo de depósitos análogos atuais sugere que as cristas de blocos e a presença de imbricação estão associadas ao trabalho repetitivo de ondas de tempestade. Esta organização contrasta com a ausência de estrutura interna que caracteriza os depósitos de blocos resultantes de tsunamis atuais. Além disso, a distribuição da camada fonte, da massa e das propriedades direcionais dos blocos imbricados indicam transporte por curtas distâncias principalmente seguindo uma direção do quadrante O-NO, compatível com o regime de agitação atual e contrário à localização da principal fonte tsunamigénica que afeta a área de estudo, a SO de Portugal Continental.

O movimento de blocos resultante de tempestades atuais, com características conhecidas, evidencia percursos de transporte, disposição dos blocos e local de deposição semelhantes aos observados no depósito inicialmente estudado. O movimento dos blocos sobre as plataformas estruturais sugere que a direção de transporte é parcialmente controlada pela direção do espraio e da ressaca das ondas, que por sua vez é parcialmente controlado pela maré que influencia o alcance das ondas rebentadas. De uma forma geral, a moda direcional dominante observada no depósito é herdada do rumo das ondas (essencialmente de O) em frente à área de estudo e as restantes assinaturas direcionais observadas no depósito correspondem a um controle geomorfológico do escoamento e a uma herança topográfica. Esta herança é observada em alterações locais das propriedades direcionais de blocos, que mimetizam a configuração da linha de costa, com ênfase nas zonas da plataforma estrutural onde se desenvolvem entalhes alinhadas NO-SE.

O transporte de blocos é mais frequente nos sectores da área de estudo que apresentam uma elevada exposição ao regime de agitação dominante de O-NO. Esta frequência fica expressa em cristas de blocos bem desenvolvidas alinhadas transversalmente ao escoamento dominante, que por sua vez é também

parcialmente controlado pelos entalhes nas plataformas estruturais, que funcionam como canais naturais que geram afunilamento do escoamento e consequente aumento de velocidade e do potencial de remoção e transporte de blocos. Os sectores expostos a OSO apresentam inundações menos frequentes, refletidas em acumulações constituídas por cristas de blocos mal desenvolvidas ou incipientes (alinhamentos de blocos).

A análise estatística de valores extremos feita com base no regime de agitação desde 1953 a 2009 indica um intervalo de recorrência de 2 a 5 anos para tempestades com capacidade de gerar transporte e deposição de blocos em segmentos da linha de costa expostos a O e NO, e de mais de 20 anos em segmentos da linha costa expostos a OSO.

Finalmente, e apesar das fragilidades inerentes a estas aproximações, a aplicação de soluções numéricas que simulam o transporte de blocos indica períodos de onda e alturas de onda significativa compatíveis com ondas de tempestade e com o regime de agitação atual que afeta a costa O portuguesa.

A datação do depósito baseada em comparação de fotografias aéreas e em liquenometria indicam que o transporte de blocos sobre as plataformas estruturais é frequente, implicando uma origem tempestítica de parte do depósito. Adicionalmente, os resultados da aplicação de liquenometria mostram uma idade recente do depósito, com blocos mais antigos depositados por volta dos séculos XIV-XV, a grande maioria dos blocos tendo sido depositada desde ~1875 até à data. Apesar de, neste local, o arranque e transporte de blocos ser um fenómeno frequente, foi detetado um hiato de blocos depositados entre 1875 e 1740, sendo os blocos anteriores à última idade raros. A escassez de partículas mais antigas que 1740 sugere: um elevado dinamismo destes depósitos, nos quais a adição e remoção blocos é frequente, acabando estes por ter um período de residência tipicamente inferior a 200 anos; aliado à existência de um evento erosivo que terá parcialmente obliterado uma acumulação de blocos pré-existente. Dado a coincidência entre a idade do hiato de deposição de blocos e o tsunami de *AD* 1755, considera-se que este evento terá uma assinatura essencialmente erosiva, atingindo uma cota mínima de 9 m anmm. Estes resultados são apoiados por datações de areias marinhas com

fonte provável nos fundos submarinos proximais, encontradas debaixo de alguns blocos, de 230±20 a 290±50 anos.

Os conjuntos de blocos com idade anterior a *AD* 1755, que corresponderão a um depósito remanescente, encontram-se preferencialmente localizados em troços costeiros expostos a OSO. A idade, posição e elevada energia necessárias para transportar estes blocos sugere que os mesmos correspondem a deposição em períodos de elevada tempestuosidade, possivelmente associados a períodos com índices negativos de Oscilação do Atlântico Norte (North Atlantic Oscillation - NAO).

Este trabalho contribui para a discussão da interpretação de depósitos de blocos no que diz respeito à assinatura deposicional/erosiva associada a tempestades e tsunamis em contexto rochoso. Para além disso contribui para a discussão sobre o controle geomorfológico dos processos físicos que ocorrem neste mesmo contexto. A análise de palaeocorrentes frequentemente aplicada a depósitos fluviais revelou-se assim uma ferramenta valiosa na interpretação de processos físicos complexos que ocorrem no sector costeiro em análise. No entanto, e especialmente em locais com linhas de costa irregulares, é essencial ter uma aproximação integrada de diversos indicadores de forma a descrever e validar, de forma mais completa, modelos conceptuais de transporte de blocos.

Outra contribuição relevante deste trabalho corresponde a um modelo de crescimento de líquenes da espécie *Opegrapha durieui* Mont. (Roux and Egea, 1992) que permite datar até 500 anos a exposição de superfícies de calcário parcialmente cobertas por esta espécie.

Palavras-chave:

Geomorfologia; costa rochosa; Tsunami de *AD* 1755; liquenometria; tempestuosidade

Abstract

This work describes a complex boulder accumulation found in the Portuguese western coastline, N of Ericeira, containing over 1600 boulders sitting on a structural platform and low cliffs at 2-13 m above mean sea level (amsl). The main objective of this work consisted in the identification (storm *vs* tsunami), age estimation and the computation of recurrence intervals of extreme events responsible for the transport and deposition of this boulder accumulation.

Several proxies were used to interpret the origin of the deposit under analysis, such as: morphological characteristics of the boulder accumulation and of individual boulder positions and arrangement; monitoring boulder movement by storms, numerical modelling of storm wave propagation and with statistical analysis of extreme values applied to the wave regime; application of numerical approximations describing boulder movement; age estimation based on aerial photographs, lichenometry, erosion rates and optically stimulated luminesce (OSL) of finer sediments of marine origin.

Distribution of source layer, mass and directional properties indicate short-lived boulder transport following a flow directed from the W-NW, compatible with the modern-day wave regime rather than the major tsunamigenic source, located SW of Portugal. Statistical modelling of extreme values applied to the wave regime and comparison with storm wave parameters which generated observed boulder movement, indicate 2-5-years recurrence interval for the occurrence of storms capable to generate boulder transport and deposition in the W-NW facing segments, and a higher than 20 years in the WSW-facing segments of the study area. Moreover, the application of numerical solutions to the boulder dataset indicate wave periods and significant wave heights compatible with a storm origin and with the wave regime affecting the western Portuguese coastline.

A strong geomorphological signature is observed in the morphological characteristics of the boulder accumulations. This is reflected in local changes of directional properties of boulders which mimic the coastline configuration, with emphasis in areas of the structural platforms where NW-SE aligned indentations

exist. These indentations function as natural channels and generate a funnelling effect increasing the potential to detach and transport boulder-size particles.

Age estimation results based on the comparison of aerial photographs and lichenometry indicate that boulder transport frequently occurs, thus implying a storm origin to at least part of the deposit. Additionally, it indicates an extremely recent age for the boulder accumulation from around the 14th-15th centuries. Moreover, age estimation results obtained for lichenometry show that this boulder accumulation mainly comprises boulders recently deposited (past ~140 years), which is confirmed with results from OSL age estimation of marine sand patches found within a boulder cluster, of 230-290 years. The fact that older boulders are scarce and that boulder transport and deposition frequently occurs suggests that: the boulder deposit under analysis is highly dynamic and that particles typically present a residence period lower than 200 years; the *AD* 1755 tsunami, which reached a minimum height of 9 m amsl, partly obliterated a previously existing boulder accumulation, having mostly generated an essentially erosive signature. The presence of older and sometimes heavier boulders located higher up and further inland in WSW facing segments of the coastline indicates boulder deposition on these locations during higher storminess periods, probably associated with periods of negative NAO index.

This work contributes to the discussion regarding sedimentological/erosional signatures of boulder-size accumulations associated with storms and tsunamis in rocky coastlines and to a better understanding of the geomorphological controls and physical processes occurring within this context. Another relevant contribution was the development of a lichen growth model for the species *Opegrapha durieui* Mont. (Roux and Egea, 1992), which allows estimating the age of limestone surface exposure of up to ~500 years.

Keywords:

Geomorphology; rocky coastline; *AD* 1755 tsunami; lichenometry; storminess

Table of contents

List of figures

List of tables

1

Introduction

The study of extreme marine events and their effects is of paramount importance in coastal management, especially when assessing hazards and risks associated with marine inundations. Coastal deposits related to inundations by extreme marine events, such as storms and tsunamis, contribute with information relative to the effects of past events, some of which may have not been observed nor otherwise recorded, and this greatly benefits any holistic approach to coastal risk assessment. Inland extent of inundations, maximum run-up, flow velocity necessary to generate the deposit and flow direction may be extracted from sedimentological characteristics of deposits associated with extreme marine events (*e.g.* Hindson *et al*., 1996; Gelfenbaum and Jaffe, 2003; Jaffe and Gelfenbaum, 2007; Costa *et al*., 2012). In this regard, coastal boulder accumulations are particularly important as they reflect upward and inland transport of large particles and thus, represent maximum flow capability in sedimentological terms and destruction potential.

Coastal boulder deposits other than marine terraces exist and have been previously identified in several locations along the western coast of Portugal. However, some have not been investigated in detail, namely in what concerns sources, transport mechanisms, origin (storm *vs* tsunami) and post- emplacement dynamics and chronology. In this respect, the discovery of a complex coastal boulder accumulation

N and S of Coxos beach, near Ericeira, 40 km NW of Lisbon, has provided a unique opportunity to study and monitor the development of these deposits and to investigate the forcing factors modulating their present-day aspect.

I first found this deposit in September 2010, while conducting a visit to the field site, in search of one boulder allegedly transported inland during a swell event in 2003. Given that this location is a surfing spot, surfers had noticed the appearance of this boulder and tagged the date of transport in a cement inscription. This presented a rare opportunity to study the transport of a boulder associated with a known recent event for which oceanographic data were available.

When I arrived at the location, the boulder transported in 2003 was missing (it was returned to the ocean in a later inundation). Instead, I found a large accumulation of heterometric boulders sitting on a structural rocky platform and reaching 13 m above mean seal level (amsl). Given the substantial number of boulders and their proximity to a sea cliff developing inland, my first instinct was to assume that the accumulation was the result of rock-fall, or, alternatively, that it represented remnants of an *in situ* dismantled limestone layer. However, an intensive and unsuccessful search for a compatible source layer outcropping inland of and/or higher than the deposit and the strong similarities found between the layers outcropping below the boulders, led to the acknowledgment that this deposit was in fact the result of upward and landward transport and deposition by unknown extreme marine event(s).

The discussion and identification of the type of wave(s) (storm wave and/or tsunami wave) responsible for this accumulation makes the central topic of the research addressed in this work. The proximity of the Portuguese coast to a seismic tsunami source, where the *AD* 1755 tsunami was generated, and the high elevation of the boulder accumulation (well above the reach of ordinary storms) were both indicative of a tsunami origin. However, a report of boulder transport by a storm along the same platforms, though at lower elevations, did exist and thus extremest storms could not be disregarded as a possible origin for the whole or part of this deposit. Another particularly interesting challenge was the age estimation of the

boulder deposit, which was addressed in this work using lichenometry, and validated by other techniques.

The understanding of the processes involved in the origin of this boulder accumulation provides insights to the origin of similar deposits along the Portuguese west coast and elsewhere. The rich information associated with its complexity led to the decision to concentrate efforts in reconstructing the geological history hidden in this occurrence, rather than dispersing alongshore and study several accumulations.

The specific objectives of this work are:

1. To identify the type of wave(s) (storm and/or tsunami) responsible for the boulder accumulation identified N of Ericeira and to constrain the wave parameters;
2. To constrain the age(s) of the deposit;
3. To estimate recurrence of extreme events responsible for accumulating and reworking this boulder deposit.

Rocky coasts are the most common type of coastline and form about 50-75% of the world's coastline (Emery and Kuhn, 1982; Kusky, 2010). In contrast, most of the research addressing coastal sediment entrainment, transport and deposition has been developed in sand-rich environments, the dynamics of sandy and larger particle sediments, and of contexts in which they occur, being substantially different. The investigation of the mechanisms that controlled the accumulation and attributes of the boulder deposit herein addressed was considered an opportunity to further the present-day knowledge on both coastal dynamics within rocky coastline contexts and on coastal boulder deposits.

∴

In addition to this introductory chapter, this dissertation is subdivided in 9 more chapters.

The related work is contained in three chapters: 2-Extreme marine events in Portugal, 3-Coarse deposits related with extreme marine events and 4-Numerical solutions of boulder movement. The second chapter is dedicated to the definition and description of extreme marine events having affected the Portuguese coastline. Its first section comprises a critical analysis of information reported in tsunami catalogues encompassing the Portuguese coastline and a comparison with original descriptions of tsunami inundations retrieved from historical documentary records. Additionally, a comparative analysis of the effects of the *AD* 1755 tsunami in various locations and geomorphological contexts along the Portuguese coastline is presented. The second section contains a brief presentation about changes in storminess trends, both recently and throughout the mid to late Holocene, in the W coast of Portugal, focusing on an alternative justification for boulder transport and deposition, other than a tsunami or a higher sea level. The third chapter is focused on coastal boulder accumulations associated with extreme marine events. In this chapter a review of boulder deposits' classification, their occurrence worldwide, with emphasis in Portugal, and issues regarding their interpretation, are presented. In the fourth chapter a critical review of numerical solutions used to simulate boulder transport by ocean waves is undertaken. Approximations available in the literature are presented, analysed and corrected when necessary/possible. To evaluate their applicability within different contexts, these approximations were further applied to an extensive dataset of boulder deposits with known origin.

The study area is described in the fifth chapter, which contains a lithostratigraphic and geomorphological characterization. Moreover, the oceanographic forcing affecting the western coast of Portugal and the study area specifically is also presented.

Methods used in this work are described in chapter six and address criteria used in the identification of boulder deposits, methods of data acquisition during field and laboratory work, data processing methods and age estimation techniques.

Results and interpretations are presented in chapter seven and are organized in four sections. The first section comprises the detailed description of the Coxos boulder deposit, boulder characteristics and spatial variation of boulders' attributes. The

second section is dedicated to the description of observed boulder movements, of the events responsible for that movement, of numerical modelling of storm wave propagation and of their recurrence using statistical modelling of extreme values. Results regarding the application of selected numerical solutions for boulder transport, reviewed in chapter 4, are presented in the third section. Finally, in the fourth section, results obtained from age estimation techniques are presented.

The eighth chapter contains the integration of interpretations presented in the previous chapter and overall discussion. Conclusions are presented in the ninth chapter.

Additional supplementary material supporting and/or extending the information presented in the various chapters was structured in appendices. The appendix A contains transcribed and/or translated historical records of tsunami inundation affecting the Portuguese coastline, commented in chapter 2 (Extreme marine events in Portugal). The appendix B contains a list of variables used and corresponding symbols. The appendices C through H encompass derivation of numerical approximations and data used when comparing them, presented in chapter 4 (Numerical solutions of boulder movement). The appendix I comprises the script used in the statistical modelling of extreme significant wave heights, periods and wave power, further described in section 6.4.2 (Statistical modelling of extreme events). Mass density values of samples collected from outcropping layers in which boulders were sourced, measured in the laboratory, are presented in appendix J. Appendix K contains information regarding the recently observed boulder movement described in section 7.2.1 (Observations of boulder movement). Relevant data used in the age estimation based on lichenometry, erosion rates measured with a micro-erosion-meter and optically stimulated luminescence (OSL) and presented in section 7.4 (Age estimation) are organized in appendices L through P.

2

Extreme marine events in Portugal

Extreme events of coastal flooding are, by nature, infrequent, their frequency decreasing with increasing magnitude of the driving ocean surface disturbance, usually a storm or tsunami. In practice, the wording "extreme" usually refers to events rarer than the 90th percentile of the observed probability density function of a describing variable, such as wave height, and having severe impacts on society and biophysical systems (Sillmann, 2009). Other ways to define an extreme event are: (1) occurrences with intensity above an absolute impact-related threshold, which will vary from place to place; and (2) occurrences that surpass a specific duration (hours, days, *etc.*) above an absolute or percentile threshold (IPCC, 2012).

In this work, extreme marine events are defined as atypical inrushes of the sea caused either by storms or tsunamis, capable of generating one or several of the following consequences: morphological changes, coastline retreat, intense flooding of low-lying areas, destruction of structures and more specifically, dislodgment, transport and deposition of boulder-sized or larger particles (see chapter 3 for

definitions) landward of the coastline and above the spring high tide water level (~2 m amsl) in the studied area.

This chapter comprises an analysis of extreme events which have affected the Portuguese coastline and could have played a key role in the development of the boulder deposit of Coxos beach. Given the differences in the frequency and energy associated with tsunamis and storms, and the type of information available for consultation, the occurrence and characterization of these dissimilar events are presented in different sections addressed in this chapter.

Known tsunamis affecting the Portuguese coastline are related to seismic activity and its effects have been extensively described by historians, scholars and witnesses since historical times. In the first section of this chapter (2.1 Tsunamis), an analysis of tsunamis affecting the Portuguese coastline, primarily based on the Portuguese tsunami catalogue by Baptista and Miranda (2009), is presented. The information in this database was cross-checked with the well-known catalogues of Moreira de Mendonça (in this work referred as Mendonça, 1758), of Galbis Rodriguez (in this work referred as Rodriguez, 1932-40), Perrey (1847) and many others. The main objective was the identification of tsunamis capable of generating boulder transport and deposition inland. Furthermore, the effects of the *AD* 1755 tsunami in various locations along the Portuguese coastline and their relationship with geomorphological contexts is also addressed.

Similarly, storm events occurring before the installation of scalar buoys are described in written documents, such as newspapers. However, the analysis of the storm wave regime is better achieved based on hindcasts elaborated by meteorological models or inferred from the geological record. In the second section of this chapter (2.2 Sea storms), storm events will be addressed mainly in what respects storminess trends inferred from both the analysis of hindcast time series and from evidences of periods of increased storminess occurring during the mid- to late Holocene, detected in the geological record. It is argued that boulder transport and deposition at elevations incompatible with the current storm wave regime could be attributed to periods of increased storminess, rather than a tsunami inundation, or even a higher mean sea level.

2.1 Tsunamis

The nomenclature more frequently used in tsunami research includes terms such as tsunami arrival time, inundation distance and run-up. Following indications from the Intergovernmental Oceanographic Commission (2013), these terms can be defined as: (1) arrival time - the time of arrival of the first tsunami wave in a specific location; (2) inundation distance - the horizontal distance inland of an inundation, generally measured perpendicularly to the shoreline; (3) run-up – local maximum elevation reached by seawater measured relative to mean sea level, ideally at the local maximum of the horizontal inundation. Where the elevation is not measured at the maximum of the horizontal inundation, it is often referred to as inundation height.

Historical and instrumental records of tsunami occurrence in mainland Portugal have been extensively used to identify seismic sources, wave parameters (height, length, inundation height) and effects of tsunami inundation. These data-sets are of extreme importance in risk/hazard assessments of coastal populated areas, in the calibration of tsunami propagation models and in the identification of evacuation and safe zones, fostering a better comprehension of tsunami deposits as evidences of tsunami events preserved in the geological record. In turn, these are essential to the definition of recurrence intervals of tsunami inundation, particularly when the length of the data-set exceeds the time covered by the documentary records.

The systematic collection of original eyewitness descriptions of tsunami inundations in Portugal started with the inquiry of the Marquis of Pombal, launched in the aftermath of the well-known *AD* 1755 Lisbon earthquake and tsunami, and continued with several compilations by other authors (*e.g.* Mendonça, 1758; Lopes, 1841; Perrey, 1847; Sousa, 1919; Rodriguez, 1932-40; Campos, 1991; Baptista and Miranda, 2009).

A compilation of historical tsunami occurrences that reached mainland Portugal based on the tsunami catalogue by Baptista and Miranda (2009) is presented in Table I and epicenters proposed therein are represented in Figure 1.

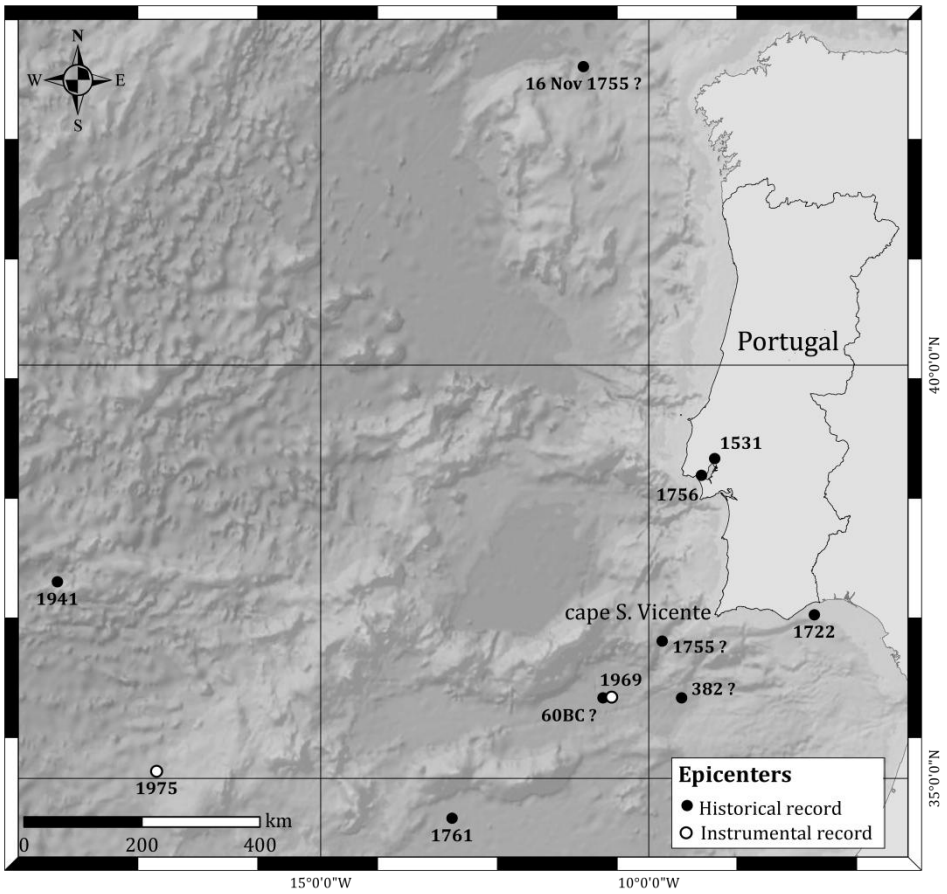

Figure 1: Location of the epicenters of earthquakes responsible for tsunamis that affected the Portuguese mainland. Location of epicenters extracted from Baptista and Miranda (2009). World Ocean Basemap from Esri®ArcMap™

Table I: Tsunami occurrences that reached the Portuguese mainland. Tsunami intensities based on the Papadopoulos and Imamura (2001) scale. * Instrumental records according to the catalogues mentioned in text

DATE	OBSERVED IN	OBSERVATIONS	REFERENCES
~60 BC	Portugal and Galicia	Vague description; Tsunami intensity VII.	Brito (1595); Sousa (1678-80); Mendonça (1758); Moreira (1988); Campos (1991)
AD 382	Portugal and Spain	Vague descriptions of the effects; The sea covered some islands and stripped them of soil, possibly near cape S. Vincente; Tsunami intensity VI;	Brito (1607); Mendonça (1758); Rodriguez (1932-40); Moreira (1988); Campos (1991)
26 Jan. 1531	Portugal, mainly in Lisbon, Santarém, Almeirim, Azambuja	The earthquake occurred at dawn lasting app 20 sec; It generated a tsunami in Tagus estuary that caused the destruction of ships; There are no reports of inundation; Tsunami intensity V.	Resende (1554); Sandoval (1560-1620); Garibay (1628); Maria (1744); Couto (1778); Perrey (1847); Babinet (1861); Mendonça (1758); Rodriguez (1932-40); Campos (1991); Justo and Salwa (1998)

DATE	OBSERVED IN	OBSERVATIONS	REFERENCES
27 Dec. 1722	Algarve (Portugal)	The earthquake occurred at 5/6h *P.M.* lasting for a "hail Mary" (8-15 sec); Possibly generated a local tsunami that affected only part of the Algarve coast; Ships were left dry in rivers; Tsunami intensity IV.	Mascarenhas (1723); Maria (1744), Belem (1750); Mendonça (1758); Lopes (1841); Perrey (1847); Sousa (1916); Rodriguez (1932-40); Campos (1991); Baptista *et al.* (2007)
1 Nov. 1755	Portugal, Spain, Morocco, France, Azores; Madeira, UK, Caribbean	The earthquake occurred at 9h30 and lasted for 6 -7 min; Generated a tsunami with inundation height of: 15 m in Cadiz; 10 m in cape S. Vincente; 5 m in Lisbon and 1.2 m in Oporto; Tsunami intensity XI.	Mascarenhas (1756); Mendonça (1758); Lopes (1841); Leal (1874); Sousa (1919); Sousa (1928); Campos (1991); Baptista *et al.* (1998a); Muir-Wood and Mignan (2009)
16 Nov. 1755	Galicia and Lisbon	The earthquake occurred at 15h30; There is only mention of great destruction caused by the earthquake and the tsunami; Tsunami intensity V.	Sanches (1757); Mendonça (1758); Perrey (1847); Rodriguez (1932-40); Campos (1991);
29 Mar. 1756	Lisbon	There is only a mention to a violent shock and movement of the waters in the Tagus estuary; Tsunami intensity III.	Perrey (1847); Rodriguez (1932-40); Campos (1991)
31 Mar. 1761	Portugal, Spain, Ireland, UK	The earthquake occurred at 12h00 and lasted for 5 min; Generated a tsunami with inundation height of 2.4 m in Lisbon; Tsunami intensity IV.	Molloy (1761); Unknown (1761); Perrey (1847); Campos (1991); Baptista *et al.* (2006)
18 Nov. 1929*	Portugal, Eastern coast of USA	Wave amplitude of 0.19 m measured in Leixões tide gauge; Tsunami intensity II.	Baptista and Miranda (2009)
25 Nov. 1941*	Portugal, Morocco, UK	Wave amplitude of 0.10 m measured in Lagos tide gauge; Tsunami intensity II.	Campos (1991); Baptista and Miranda (2009)
28 Feb. 1969*	Mainland Portugal, Azores, Spain and Morocco	The earthquake occurred at 2h40; Wave amplitude of 0.30 m Portuguese tide gauges; Tsunami intensity III.	Campos (1991); Baptista and Miranda (2009)
26 May 1975*	Mainland Portugal, Spain, N. Africa	Wave amplitude of 0.30 m measured in Lagos tide gauge; Tsunami intensity II.	Campos (1991); Baptista and Miranda (2009)

In the following pages, details about these events are presented in chronological order. Most of the original references cited in the catalogues consulted were pursued and relevant information was translated and is presented in Appendix A to minimize (mis)interpretations by subsequent authors ("who tells a tale adds a tail").

2.1.1 ~60 BC

The ~60 BC tsunami is the oldest event mentioned in the catalogues as having affected the Portuguese coastline, from which there are only vague descriptions by Brito (1595), Sousa (1678-80) and Mendonça (1758) (further details in Appendix A1). The similarity of the event's description by all three authors is indicative of the same bibliographical source.

Pereira *et al.* (1986) and Moreira (1988) attribute this earthquake with epicenter at the same general location as that of *AD* 1755, SW of offshore Portugal and within the Portuguese Margin, where tectonic structures responsible for high magnitude earthquakes are located (*e.g*. Zitellini *et al*., 2009). Baptista and Miranda (2009) attribute a tsunami intensity of VII, classifying it as a damaging tsunami.

2.1.2 AD 382

There is only vague information regarding specific effects of the *AD* 382 earthquake and tsunami. Besides Brito (1607), other authors (*e.g.* Mendonça, 1758; Rodriguez, 1932-40) describe this event citing the former author, with more condensed but similar descriptions, focusing on the destruction of the islands near cape S. Vincente and not presenting additional information (see Appendix A2 for further details).

Pereira *et al.* (1986) and Moreira (1988) attribute an epicenter at the same general location as that of *AD* 1755, SW of Portugal mainland. Baptista and Miranda (2009) classified this event as a slightly damaging tsunami, with an intensity of VI.

In review of tsunamis and their sedimentological imprints in the Algarve coast, Andrade *et al.* (2016) dismiss the 60 BC and *AD* 238 tsunamis, arguing that Brito (1595; 1607), the original author describing the occurrence and effects of these earthquakes and tsunamis that every other later documentary source has used, invented these events, adapting reports of Late Roman chroniclers of earthquakes and tsunamis affecting the Mediterranean.

Furthermore, Andrade *et al.* (2016) argues that the dismissal of these events agrees with recent onshore geological evidences of tsunami inundation in the Algarve, where only one deposit resulting from an extreme marine event has been

unequivocally associated with a tsunami inundation (*AD* 1755). According to these authors, the study of other additional sandy layers attributed by several other authors to tsunami inundations in Algarve lowlands, is so far incomplete, either lacking the establishment of marine sediment source for the sediment, or not addressing other possibilities for their origin, such as changes in the sediment depositional patterns occurring in subtidal to intertidal domains.

2.1.3 26th January 1531

On January of 1531 two earthquakes occurred in Portugal: the first, smaller, on the 7th January; and a second event, larger, on the 26th of the same month at dawn, lasting for a "creed" – 20 sec (*cf.* Pereira *et al.*, 1986), triggered a tsunami inundation in the Tagus estuary (Justo and Salwa, 1998). Original references to the January 1531 Lisbon earthquake can be found in the work of Resende (1554), Sandoval (1560-1620), Garibay (1628), Couto (1778), Babinet (1861) and Osório (1919 in Justo and Salwa, 1998) (further details in Appendix A3).

Based on the earthquake effects and their relationship with geological bedrock (Justo and Salwa, 1998) and macroseismic data (Martins and Victor, 2001 in Baptista and Miranda, 2009) the authors suggested the location of the epicenter in the Tagus Estuary, close to Vila Franca de Xira town. This location was subsequently supported by results of tsunami modelling by Miranda *et al.* (2012). Baptista and Miranda (2009) attribute a tsunami intensity of VII, classified as a damaging tsunami. However, given that there are no reports of inundation and that the only effects observed were the destruction of ships within the estuary (namely in the Lisbon harbour), an intensity of V (strong tsunami) would be more appropriate (*cf.* Papadopoulos and Imamura, 2001).

2.1.4 27th December 1722

On the 27th December 1722, from 5 to 6 *P.M.*, an earthquake occurred affecting the Algarve (S Portugal) and lasting less than one "hail Mary" - 8-15 sec (*cf.* Pereira *et al.* (1986). The newspaper Gazeta de Lisboa (Mascarenhas, 1723) reported several effects associated with this earthquake, never explicitly mentioning a tsunami inundation. However, there is a reference to the river disappearing, leaving a

caravel, originally sailing up-river, sitting on the river bed (further details in Appendix A4). Mendonça (1758), citing Mascarenhas (1723), presents a slightly different account, in which the caravel was exiting the river. Almost one century later, Silva Lopes (in this work referred as Lopes, 1841), presents a description similar to Mendonça (1758), also not mentioning its origin, but this time, the caravel is given as crossing the inlet[1], sailing towards the sea (further details in Appendix A4).

In the reports of Sousa (1916) and Rodriguez (1932-40), the authors specifically wrote "*the documents do not mention a tsunami*" and "*there was no seaquake*", respectively. Baptista and Miranda (2009) state that "*the flooding of Tavira area is well documented and persisted in the collective memory of the population*", although the only original document that points toward a tsunami is the work of Belem (1750), in which the author states: "*Some churches, convents, towers, walls[2], and countless houses are ruined, completely collapsed or with cracks and uninhabitable, even some ships were left without water beneath at sea. (…) This religious procession repeats every ear at the same day, the 27th December, with the assistance of the senate, communities, and large attendance of the people, to recall such luck; in spite of the great loss, the city could have been submerged".* Despite the evidences that might indicate the existence of a tsunami, such as a ship suddenly resting in the river bottom and the risk of submersion, there is no clear report of a tsunami inundation.

Baptista and Miranda (2009) attributed a tsunami intensity of VI, classified as a slightly damaging tsunami, however, given that there are no reports of inundation or ship destruction, an intensity of IV (largely observed tsunami) would be more appropriate (*cf.* Papadopoulos and Imamura, 2001).

There seems to be no consensus regarding the location and characteristics of the source location for the earthquake and tsunami (Baptista *et al*., 2007). All authors, that used isoseismal maps constructed on the basis of damages described in the historical records, locate the epicenter either onshore, E of Tavira, or offshore the

[1] Presumably the Tavira inlet, which separates Ria Formosa lagoon from the open sea.
[2] Belonging to fortifications

Algarve coast, SE of Tavira (*cf.* Rodriguez, 1932-40; Mezcua, 1982; Pereira *et al.*, 1986; Campos, 1991; Baptista *et al.*, 2007).

2.1.5 1st November 1755

The well-known earthquake and tsunami of 1st November 1755 has been described by many authors as the most destructive event that affected Europe. Its effects were felt in Portugal, Spain, Morocco, France and many other European countries (Mendonça, 1758). The earthquake occurred at about 9h30 AM and lasted for 6 to 7 minutes (Mendonça, 1758).

Pereira de Sousa (in this work referred as Sousa, 1919) made an extensive compilation of documentary records of the effects of the earthquake and constructed the correspondent isoseismic map, attributing an intensity of X-XI to the regions of Lisbon, Setúbal and most part of the Algarve.

From the analysis of historical records, Campos (1991) identified at least three tsunami waves reaching the coastline of Cadiz and Ceuta at high tide, which maximized the inundation effects. Moreover, in some places, the first manifestation was a withdrawal of the sea in excess of 2 km. According to this author the tsunami inundation reached maximum heights of 18-20 m in Cadiz and 11 m in Tarifa (Spain).

Baptista *et al.* (1998a, b) estimated the tsunami parameters mainly based on their reanalysis of the answers to the inquiry conducted by the Marquis of Pombal. According to these authors, the tsunami waves reached 5 m in Lisbon, over 10 m in cape S. Vicente, 15 m in Cadiz and 1.2 m in Porto.

Several authors have suggested different tsunamigenic sources for the *AD* 1755 Lisbon earthquake, almost all located SW of mainland Portugal. These locations were based on tsunami modelling of the research of tectonic and morphological structures identified in the western and southern continental margins offshore mainland Portugal (*cf.* Moreira, 1988; Baptista *et al.*, 1996; 1998a; b; 2003; Zitellini *et al.*; 2001; 2009; Barkan *et al.*, 2009; Muir-Wood and Mignan, 2009). A discussion on the possible sources presented in the literature is beyond the scope of this study. Regardless the source, the effects of the tsunami inundations were much more

devastating in the Algarve when compared to other locations further N. Baptista and Miranda (2009) attribute to the *AD* 1755 tsunami an intensity of XI, classifying it as a devastating tsunami.

Some transcriptions of historical records of the *AD* 1755 tsunami inundation were selected to better perceive changes in inundation height and distance along the Portuguese coastline. For this purpose, records containing contrasting locations and within contrasting geological settings (sediment-starved rocky and cliffed coasts and lowlands) were selected. Furthermore, historical records of the tsunami inundation with explicit references to boulder transport were also selected (see Appendix A5 for the original records). General location of the selected descriptions is presented in Figure 2.

Quarteira is located over an outcrop of Pliocene and Pleistocene poorly consolidated sandy deposits in the central Algarve coast (Marques, 1997), next to a lowland with an average altitude below 6 m amsl, where estuarine/alluvium sediments deposited throughout the Holocene. The maximum height and distance locally reached by the *AD* 1755 inundation were 13.2 m and 3000 m, respectively.

Armação de Pêra sits to the west of a wide bay where a continuous sand beach accumulated, developing along approximately 6 km, backed by sand dunes developing up to 8-17 m amsl height, interrupted only by the outlet of the two small streams. This wide bay is limited by soft pending cliffs cut in Miocene calcareous rocks, sandstones and siltstones (Rocha *et al.*, 1989). Further inland, muddy fluvial sediments almost fully chocked the Alcantarilha palaeoestuary and actively infill the Salgados lagoonal system (Costa *et al.*, 2016b). Sedimentological and morphological evidences of inundation have been identified within the estuarine and lagoonal sediments and in the sand dunes, respectively, and attributed to the *AD* 1755 tsunami (Costa *et al.*, 2012; Costa *et al.*, 2016a). Maximum inundation height and distance reached by the *AD* 1755 tsunami inundation reported in historical document were 10 m amsl and 3000 m, respectively.

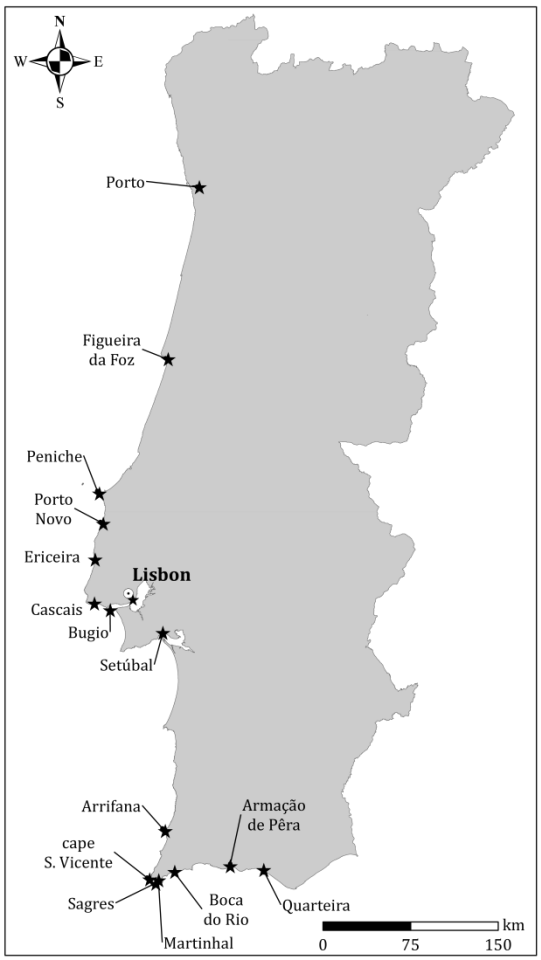

Figure 2: Location of historical records presented along the coastline of mainland Portugal

Boca do Rio lowland is a flat-floored valley, cut in Jurassic and Cretaceous limestones, and corresponds to the outlet of a confluence of three small streams (Rocha *et al.*, 1983). This lowland area consists of an active supratidal floodplain, occasionally flooded during the rainy season and separated from the sea by a shingle and sandy beach (Hindson *et al.*, 1996). A sandy tsunami deposit has been identified within the recent infilling of the valley and extensively characterized by several authors (*e.g.* Dawson *et al.*, 1995; Hindson *et al.*, 1996; 1999; Hindson and Andrade, 1999; Allen, 2003; Cunha *et al.*, 2010), and attributed to deposition by the *AD* 1755 tsunami inundation. According to historical reports of the inundation, maximum height and distance reached in this location were of 11-13.2 m and 3000 m, respectively.

Martinhal lowland comprises a small lagoon/alluvial plain and beach, facing SE, located immediately E of Sagres. A sand sheet has been described within the estuarine/lagoonal sediments and attributed to deposition by the *AD* 1755 tsunami

inundation by Kortekaas and Dawson (2007) and Cunha *et al*. (2010). Historical records of the tsunami inundation in Martinhal do not mention inundation height, but reported distances reach 3000 m, which is highly unlikely since this lowland reaches a maximum length of 1 km inland.

Sagres village sits on a rocky Pleistocene raised marine platform at about 40 m amsl limited by plunging cliffs cut in Jurassic limestone (Rocha *et al.*, 1979). Maximum reported inundation height reached 130-170 m and there are no records of inundation distance.

In cape S. Vincente, located to the W of Sagres village at 60 m amsl, maximum reported inundation height reached 66 m, and similarly to Sagres, there are no records of inundation distance.

Arrifana forms a natural headland above 50 m amsl, S of the Aljezur stream, which presents an ESE-WNW general direction. The cliffs limiting the headland present steep slopes and are cut in Carboniferous greywackes and shales, partially covered by Holocene dune deposits (Ribeiro *et al.*, 1987). Maximum inundation height reported in Arrifana reached 45 m with no record of inundation distance.

Setúbal is located further N, about 30 km SW of Lisbon, on the northern margin of the Sado river estuary. The estuary mouth consists of a 2-km wide inlet confined to the N by the W-E elongated Arrábida chain and to the S by the tip of the Tróia sand spit (Rebêlo *et al.*, 2013). The city of Setúbal develops along a natural amphitheatre, with low-lying areas comprising Holocene alluvium deposits developing along a stream which outlets in Sado estuary, and are backed by progressively higher Pleistocene clastic formations and Miocene and Jurassic limestone and marls (*cf.* Zbyszewski *et al.*, 1965). Inundation height in Setúbal reached 8 m and inundation distance 330-1500 m.

When arriving at the Tagus estuary, the *AD* 1755 tsunami wave hit Bugio's castle, a fortified lighthouse located on a sand bank in the outer Tagus estuary, reaching 5 m in height. Shortly after, the tsunami struck Lisbon, with maximum inundation height and distance reported in low-lying estuarine margins, of 6 m and 250 m, respectively.

Further N, and to the W of Lisbon, in a small stream valley within Cascais village, maximum inundation height and distances were of 6 m and 400 m, respectively.

Further N, in the W-facing coast, is Ericeira, sitting on top of a 30-m high rocky cliff that limits a small bay. Here, a minimum inundation height of 5-6 m was inferred from the historical records.

Porto Novo is in the western cliffed coast, N of the study area, in the outlet of a small stream, which widens up inland to form a flat floored valley. This outlet is interrupted by a long narrow beach, backed by a 25 m-high cliff in the S margin, and by a vertical cliff averaging 50 m in height in the N margin. There are no values for inundation distance in the historical records; however, an unexpected height of 20 m was reported for the inundation height at this location. The inundation height of ~20 m is mentioned in a record of Priest António Duarte (in Sousa, 1928) at least twice (see Appendix A5 for the original records). Although it seems unexpectedly high when compared with the inundation height of 6 m in Lisbon, one should take in consideration that, in general, reported inundation heights in rocky cliff contexts are consistently higher when compared to those occurring in low lying areas.

Peniche town developed over the rocky end of a tombolo. Based on the historical records of the tsunami inundation in Peniche, minimum inundation height and distance were of 3 m and 100 m respectively.

Figueira da Foz is a coastal village located at low altitude, facing WSW, and limited to the N by a natural promontory, the Boa Viagem ridge, that reaches a height of 100 m amsl. Maximum inundation height of the *AD* 1755 tsunami in Figueira da Foz interpreted by Baptista and Miranda (2009) and Santos *et al*. (2011) from historical records spanned from 10 m to 36 m, respectively. No reports of inundation distance have been found.

The city of Porto is in the northern margin of Douro river and estuary, approximately 3-4 km inland of the river mouth. Maximum inundation height reported in historical records was of 1.2-1.5 m.

Table II presents a summary of maximum inundation heights and distances in different coastal locations of Mainland Portugal and within different geomorphological contexts, obtained from the analysis of the historical records. Figueira da Foz was excluded due to discrepancies in inundation heights interpreted by the authors and to difficulties in accessing the original documents.

Table II: Maximum inundation heights and distances of the *AD* 1755 tsunami in various locations along the Portuguese coastline

LOCATION	INUNDATION HEIGHT	INUNDATION DISTANCE	GEOMORPHOLOGICAL CONTEXT
Quarteira	13.2 m	~3000 m	Lowland in cliffed coast
Armação de Pêra	>10 m	~3000 m	Lowland in cliffed coast
Boca do Rio	11-13.2 m	~3000 m	Lowland in cliffed coast
Martinhal	-	~3000 m	Lowland in cliffed coast
Sagres	130-170 m	-	Cliff
Cape S. Vicente	66 m	-	Cliff
Arrifana	45 m	-	Cliff
Setúbal	>8 m	330-1500 m	Natural amphitheatre within an estuary
Bugio	~5 m	-	Outer Tagus estuary
Lisbon	6 m	250 m	Estuary
Cascais	6.5 m	400 m	Stream valley
Ericeira	> 5-6 m	-	Cliff
Porto Novo	20 m	-	Lowland in cliffed coast
Peniche	> 3 m	> 100 m	Rocky island connected to land by a tombolo
Porto	1.2-1.5 m	-	Estuary

The extremely high inundation-heights reported in Sagres and cape S. Vicente might correspond to an absolute maximum of the vertical reach of water, like the more frequently observed very high jets produced when long-period waves hit vertical cliffs. The description obtained in the available compilations may be somewhat exaggerated, nevertheless the mention of uncommon and landward boulder transport by the tsunami in a rocky coastline context is very clear, and unusual

details, such as fish being thrown on top of the cliff indicate authenticity of the reported facts (see appendix A5 for original record of the tsunami inundation in Sagres fortress).

As anticipated, inundation height and distance inferred from the documentary record present maximum values closest to the tsunami source location (the Portuguese margin offshore SW of cape S. Vicente). Maximum values of inundation height were reported in Sagres village, and decrease towards N, except for Porto Novo. All the lowlands in the Algarve were affected in the same way, presenting identical inundation height of around 10-13 m and distance of 3000 m. Altogether, there was a clear difference in the *AD* 1755 tsunami inundation depending on the geomorphological context: lowlands were extensively inundated and cliffed coasts showed maximum inundation heights.

2.1.6 16th November 1755

In the 16th November 1755, at 3h30 *P.M.*, an earthquake was felt in Galicia causing a tsunami classified with a reliability of 2 on a 0-4 scale (0 is a very improbable and a 4 is a definite tsunami) by Baptista and Miranda (2009). The authors attribute this event to an earthquake with epicenter in the SW Iberian Transpressive Zone, containing active tectonic structures (*e.g.* Gorringe Bank, Horseshoe, Marques de Pombal and Portimão Bank faults), S of Sines (*cf*. Zitellini *et al*., 2009), but the coordinates for the epicenter correspond to a location offshore Galicia (Figure 1). Campos (1991) attributes the same source as the 1st November 1755 event. Baptista and Miranda (2009) attribute a tsunami intensity of III, classified as a weak tsunami, although the historical records state "*with great damage, caused not only by the earthquake, but also by the extraordinary flux and reflux of the sea*", which would imply a minimum intensity of V (strong tsunami).

2.1.7 29th March 1756

On the 29th March 1756, an earthquake was felt in Lisbon causing a tsunami also classified with a reliability of 2 by Baptista and Miranda (2009). The authors attribute this event to a local earthquake with epicenter in Tagus estuary, generating an intensity III tsunami (weak tsunami). In contrast, Campos (1991) attributed this

event to an earthquake with the same source as the *AD* 1755 event, offshore SW Portugal.

2.1.8 31st March 1761

On the 31st March 1761, at noon, an earthquake occurred lasting for five minutes, and affecting Portugal, Spain, Ireland, the United Kingdom and several other locations (*cf.* Baptista and Miranda, 2009).

Baptista *et al.* (2006) proposed a source location for this event at about 500 km SW of Portugal (Figure 1), using tsunami information extracted from historical records and backward ray-tracing methods. Baptista and Miranda (2009) attributed a tsunami intensity of VI to this event (slightly damaging tsunami). However, given that there are no reports of inundation, an intensity of IV (largely observed tsunami) is proposed (*cf.* Papadopoulos and Imamura, 2001).

2.1.9 Recent tsunamis

All tsunami events occurring recently, from 1929 to 1975, were grouped in this section. They are small amplitude events (< 0.30 m) with tsunami intensities of II and III (weak and largely observed tsunamis) detected at tide gauge stations located along the Portuguese mainland coast (*cf.* Baptista and Miranda, 2009). A summary of these occurrences can be found in Table I. Given the low magnitude of these events it was considered that they were unable to have generated significant sediment transport. After 1975 there are no records of tsunamis affecting mainland Portugal in any of the consulted tsunami catalogues (*cf.* Baptista and Miranda, 2009; Maramai *et al.*, 2014; National Geophysical Data Centre/World Data Service, 2016).

2.1.10 Additional events in tsunami catalogues

By searching historical tsunami databases containing records of events spanning from 6150 BC to the present (*cf.* Maramai *et al.*, 2014; National Geophysical Data Center/World Data Service, 2016) several events are listed as having affected the Portuguese coast, other than those depict in Table I. Some were sourced and felt only in the region of the Azores archipelago, with no references of effects in the mainland Portuguese coast, and were excluded in this work.

Other events depicted in the National Geophysical Data Center/World Data Service (2016) catalogue (occurring on 26-12-1746, 28-04-1752, 2-11-1755, 21-12-1755 and 04-07-1809) exclusively appeared in seismic catalogues in Iberia (*e.g*. Perrey, 1847; Rodriguez, 1932-40) and were not mentioned in any sources of the Portuguese archives. Moreover, they were considered unreliable events by Baptista and Miranda (2009) and excluded from the Portuguese catalogue.

The National Geophysical Data Center/World Data Service (2016) catalogue lists two other events having allegedly affected the Portuguese coast and occurring shortly after the *AD* 1755 earthquake and tsunami, on the 2-11-1755 and 21-12-1755. The source of information of these events was attributed to the 2009 version of the Northeast Atlantic and Mediterranean Region Tsunami Catalogue. However, the updated version of this catalogue, described by Maramai *et al*. (2014), no longer contains these entries.

The 18th December 1926 Lisbon tsunami event, listed in Baptista and Miranda (2009), was excluded in this work, because despite eyewitness reports of agitation in the Tagus river, there was no identifiable waveform recorded in the Cascais tide gauge station (*cf*. Baptista and Miranda, 2009).

Three other events were listed in the National Geophysical Data Center/World Data Service (2016) catalogue (210 BC, 5-04-1504 and 26-12-1764). They were originally cited in the seismic catalogues of Mezcua and Solares (1983) and Mendonça (1758) and were excluded from this work for either not having reference to a tsunami occurrence, or due to unclear and difficult to access source documents.

2.2 Sea storms

Although rarely witnessed, transport inland of boulder-sized particles by storm waves does occur and has been documented in research articles and newspapers. In Portugal, it has been mostly associated with:

1. The destruction of man-made structures and transport of stones inland by the sea (*e.g*. in a description of the effects of a major storm in Lisbon that occurred in 19th November 1724 - *cf.* Dominguez-Castro *et al*., 2013);

2. The destruction of support walls, houses, railings, fences, ramps (*e.g.* effects of the 1941 windstorm in Sesimbra - *cf*. Freitas and Dias, 2013);
3. The partial destruction of coastal protection structures (*e.g.* effects of a major storm in Sines pier, with H_s reaching 8.5 m, on the 25/26 February of 1978– *cf*. Daveau *et al*., 1978);
4. And with wave overtopping of breakwaters originating inland transport of concrete blocks (*e.g.* effects of Christina storm, with H_s reaching 9 m, between January 5th and 7th 2014 in Terceira Island, Azores – *cf.* Santos *et al.*, 2014; Diogo *et al*., 2014a).

These effects are always associated with energetic winter storms which are considered as abnormal events by the media/community. However, there is no knowledge of threshold wave parameters, or of their recurrence, beyond which a storm generates a significant impact in the coastline. This is mainly because the determination of threshold wave parameters that cause maximum run-up values, overwash, flooding and destruction of infrastructures along coastal areas depend of local specificities, such as storm surge, tides, available sediment, bathymetry, *etc.*, that influence how offshore waves affect the coast (*cf.* Ferreira *et al.*, 2010; Ciavola *et al*., 2011; Diogo *et al*., 2014a, b).

Regardless local specificities, extreme marine events capable of generating boulder transport with significant wave heights above 8.5 m, such as these, are quite common, occurring in the western coast of Portugal with recurrence periods below 5 years (Table III).

Table III: Extrapolated significant wave heights affecting the central W Portuguese coastline for different return periods (R_P), obtained by fitting an exponential-Poisson distribution to peaks over threshold (H_s 4 m and 5 m), to a 6-year significant wave height time-series (from 1974 to 1980). Extracted from Pires and Pessanha (1986)

THRESHOLD	EXTRAPOLATED H_S				
	R_P=5 yr.	R_P=10 yr.	R_P=25 yr.	R_P=50 yr.	R_P=100 yr.
H_s > 4m	9.5	10.4	11.4	12.4	13.1
H_s > 5m	9.8	10.7	11.8	12.7	13.7

However, when considering large time-scales, frequency and magnitude of storms are not stationary, following complex patterns which vary both in space and time. Weather patterns, especially in what relates to changes in storminess, have been

addressed using two distinct methods, both focusing on different time scales. Hindcast models have been used to evaluate weather patterns and to better understand how the magnitude/frequency of storms changes at decennial to centennial time scales and relationships with large scale pressure systems. Larger time scales analysis of single storm events or periods of increased storminess have been based in the geological record using overwash sand deposits and aeolian sediments corresponding to dune development pulses affecting the western European coastline during the middle to late Holocene.

Several authors detected significant fluctuations in storminess intensity in the North Atlantic over the past 130 years through the analysis of hindcast time series of wind speed and significant wave height, and its relationship with the North Atlantic Oscillation (NAO) (*e.g.* Wang and Swail, 2001; Dodet *et al.*, 2010; Wang *et al.*, 2011; Matulla *et al.*, 2008). The NAO index is based on the monthly averaged difference of normalized sea level pressure between Lisbon, Portugal, and Stykkishólmur, Iceland, since 1864, and 1821 if Reykjavík is used instead of Stykkishólmur and Gibraltar instead of Lisbon (IPCC, 2007). Periods of positive NAO index are related to higher and long-period waves induced by strong westerly winds at northern latitudes; and to smaller waves travelling from a narrow NW window at southern latitudes (Dodet *et al.*, 2010). Conversely, periods of negative NAO index are related with a larger directional spreading of waves affecting the NE Atlantic coast; waves with smaller H_s and T_p occuring at northern latitudes; and waves with higher H_s at southern latitudes (Dodet *et al.*, 2010).

Besides the aforementioned spatial variability in storminess, significant changes is wind speed have been detected since 1880 and described by Dawson *et al.* (2007), Matulla *et al.* (2008) and Wang *et al.* (2011). These fluctuations show different patterns throughout W Europe showing one similar attribute, except for the North Sea area, storm intensity and frequency has reached in the past higher values than those registered in the last half century.

Long time scale studies of storminess based on geological evidences have been found all over the W Europe coastlines. Sorrel *et al.* (2012) compiled evidences of increased storminess in the North Atlantic throughout the mid- to late Holocene,

recorded in sedimentary archives of northern France, England, Scotland, Ireland, The Netherlands, Denmark and Sweden. These evidences include high energy event deposits incorporated in the sedimentary sequences accreting in low-energy environments (estuaries and bays) and sand bodies and discontinuities formed during pulses of coastal dune development. They interpret these deposits as resulting from reinforced wind activity, in turn associated with a more frequent passage of cyclones. The scale of the coastal area addressed in this study allowed to define a sequence of storm periods (HSPI to HSP V) as the most widespread stormy intervals during the mid- to late Holocene impacting the North Atlantic European shores, occurring at 4500-5500; 4500-3950; 3300-2400; 1900-1050 and 600-250 yr. cal BP (3850-3550 BC; 2550-2000 BC; 1350-450 BC; *AD* 50-900 and *AD* 1350-1700) (Figure 3). Age estimation of the deposits defining the stormy periods presented by Sorrel *et al.* (2012) do not overlap perfectly between various locations and storminess periods seem to have been defined mainly based on deposits related with coastal flooding rather than dune features.

González-Villanueva (2013) dated and interpreted washovers and aeolian sand bodies of two barrier-lagoon systems in Galicia (NW Spain) and used these data to identify five periods of increased storminess in the Holocene that are roughly coincident in age with the stormy periods proposed by Sorrel *et al.* (2012) (Figure 3).

Clarke and Rendell (2006) identified and dated to 394 BC - *AD* 26 and *AD* 336-706 coastal dune bodies formed between Nazaré and Porto (central/NW Portuguese coastline) in relation with intense winds blowing from the NW. In addition, they correlated the most recent dune accretion episodes in Portugal (*AD* 1770-1905) to periods of predominantly negative NAO index, asynchronous to increased sand mobilization episodes in France and UK (*AD* 1480-1750) (Figure 3).

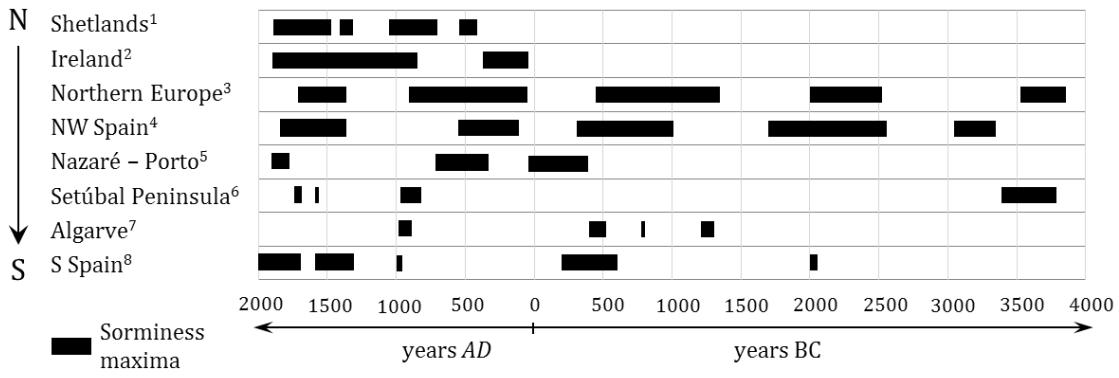

Figure 3: Holocene storminess maxima identified by various authors in deposits throughout W Europe. [1] Hall *et al.* (2006) and Hansom and Hall (2009); [2] Cox *et al.* (2012); [3] Sorrel *et al.* (2012): [4] González-Villanueva (2013); [5] Clarke and Rendell (2006); [6] Costas *et al.* (2012); [7] Andrade *et al.* (2004); [8] Zazo *et al.* (1994) and Borja *et al.* (1999)

Costas *et al.* (2012) identified phases of higher aeolian activity in the Setúbal Peninsula (W Portugal) related to enhanced westerly winds and storminess. Optically stimulated luminescence age estimation of the dune sets rendered ages of 12.6, 5.6, 1.2, 0.44 and 0.3 ka ago (before 2010) (10590 BC; 3590 BC; *AD* 810; *AD* 1570 and *AD* 1710) (Figure 3). These results disagree with results obtained by Clarke and Rendell (2006), but synchronous with dune accumulation periods along European shores, suggesting a common driving factor (*cf.* Costas *et al.*, 2012).

Andrade *et al.* (2004) identified and characterized sandy marsh detached beaches landward of Faro barrier island in Ria Formosa (Algarve, S Portugal). The authors attributed these features to multiple events of storm-induced overwash. ^{14}C age estimation of marsh sediment buried by the marsh detached beaches rendered ages of 1305-1205 BC; 805-780 BC; 515-400 BC and *AD* 880-990 (Figure 3).

In southern Spain, Zazo *et al.* (1994) identified erosional surfaces separating prograding spit bar units and associated these surfaces with more frequent and stronger storm waves that partly eroded beaches forming along spit bars. Age constrainment of these structures allowed the definition of erosive episodes rendering ages of approximately 4000 BP and 1000 BP (2050 BC and *AD* 950) (Figure 3). In the same coast and barriers, Borja *et al.* (1999) identified dune building phases which developed during the occurrence of the aforementioned erosional surfaces. Ages of dune development have been deduced from the ages of spit barrier systems with which they associate and from archaeological findings. Accumulation of the oldest aeolian system took place between the late 6th and early

2nd centuries BC; the intermediate system most probably developed between the 14th and 17th centuries *AD*; and the most recent aeolian system began developing around the early 17th century *AD* and continues to present (Figure 3), all of which were associated by Borja *et al*. (1999) with prevailing winds from the WSW.

Hall *et al.* (2006), Hansom and Hall (2009) and Cox *et al.* (2012) defined a storm chronology for cliff top storm deposits in the Shetland islands (N Scotland) and Ireland comprising boulder ridges, based in age estimations using ^{14}C and OSL of boring bivalves in boulders, and shell ash, peat and sand found beneath the boulders. Results rendered the following time intervals: *AD* 410-540, *AD* 710-1040, *AD* 1300-1400 and *AD* 1470-1880. In Ireland, Cox *et al*. (2012) completed their age estimation data of boring bivalves in boulders with additional results published by Scheffers *et al.* (2009), recalibrated to include local reservoir correction and rendering the following time intervals: *AD* 40-362; *AD* 848-1894 (Figure 3).

Considering the work summarized above, it becomes clear that storm intensity and frequency varied during the mid- to late Holocene, within the present-day sea level. Additionally, and despite the general increase in storminess detected in northern Europe, geological and instrumental data indicate that storminess has reached in the past higher values than those observed recently. Thus, it is reasonable to conclude that storm impacts have also been larger than those identified nowadays. Ultimately, high energy deposits formed along, or landward of, the Portuguese shoreline, and elsewhere, above the reach of ordinary storms can be related to prior storminess maxima within the present-day sea level, other than a consequence of tsunami inundation or even an inheritance of a higher sea-level stand during past interglacial periods.

2.3 Summary

Among the numerous events captured by the tsunami catalogues addressing the mainland Portuguese coast, 12 tsunamis are reported to have affected that coast. The 1st November 1755 Lisbon tsunami singles out due to highest wave amplitude and devastation caused in Portuguese, Spanish and Morocco Atlantic coastlines. The *AD* 1755 event was a transoceanic event, as shown by the records of inundation in

Cornwall (England), Azores and the Caribbean (*cf.* Affleck and Gray, 1755-1756; Muir-Wood and Mignan, 2009; Santos and Koshimura, 2015).

More recent events were identified in records of mareographic stations along the Portuguese coast, with measured wave amplitudes lower than 0.30 m, and low intensities (< III). These tsunamis were clearly unable to generate significant, if any, sediment transport and deposition onshore.

Two regional tsunamis (~60 BC and *AD* 382) with high intensities (≥ VI) (the 26 January 1531 and 27 December 1722 were local tsunamis) share seismic sources offshore cape S. Vicente and within the Iberian continental margin. These events predate mareographic stations and, except for the *AD* 1755 tsunami, lack detailed historical descriptions in varying locations much needed to precisely infer on source location and intensity. Moreover, there is a strong possibility that these events were invented by Brito (1595; 1607), as suggested by Andrade *et al*. (2016) in an historical and sedimentological review of tsunamis affecting the S Portuguese coast.

Although the Portuguese mainland presents a high tsunamigenic risk, the geological, historical and instrumental records of tsunamis indicate that, during the past ~5000, years only one destructive tsunami capable of generating boulder transport inland occurred, the *AD* 1755 Lisbon tsunami. Furthermore, there are major differences in the descriptions of the *AD* 1755 inundation reach and height along the Portuguese coastline in contrasting geomorphological contexts (lowlands and cliffed coasts). Inundation heights and distances are highest close to the tsunami source and decrease with increasing distance towards N, except for Porto Novo region. In general, maximum inundation heights occur in rocky coastline contexts and maximum inundation distances are reported in lowlands.

In contrast, extreme marine inundations generated by storms present much higher frequency. In rocky coast contexts, they may generate equally destructive effects and entrain and transport large-sized rock fragments inland, just like tsunamis. Actually, the analysis of the pattern of storminess along the European shores indicates that storm impacts may have been larger in several periods throughout the Holocene than in present times. Consequently, high energy coarse clastic deposits resulting from unknown extreme marine events, accumulated along the mainland Portuguese

shoreline, that are apparently inaccessible to present-day storms are not necessarily related to tsunamis and could be related to prior storminess maxima within the present-day sea level context.

3

Coarse deposits related with extreme marine events

In general, coastal coarse deposits are associated with temporally restricted transport either (1) landward, and driven by extreme marine events such as cyclone-generated swell, extra-tropical storms or tsunamis, or (2) seaward, and driven by gravity associated with slope mass movements, such as topples and landslides affecting coastal cliffs (Paris *et al*., 2011). This chapter contains a review about coarse deposits related to extreme marine events, showing landward and/or upward displacement.

The classification of individual coarse clasts (grain-size classification) and of coarse clastic deposits (in morphological and location terms) is presented. A brief description of deposits identified and characterized worldwide is subsequently made. This is followed by a more detailed review on coastal coarse deposits in mainland Portugal. Finally, the key issues associated with the interpretation of these deposits, such as their age estimation, influences of regional and local geomorphology in their characteristics and processes leading to their formation, are presented.

3.1 Classification

Classical grain size classification based on the Udden-Wentworth scale reduces all particles coarser than "cobble" to "boulder". Within the scientific community studying deposits of coarse particles related to extreme marine events, the term "megaclast" has been abundantly but somewhat loosely used to designate large clast. Williams (2010) constrained the meaning of "megaclast" to particles larger than 0.256 m (in coincidence with the lower limit of the Udden-Wentworth's "boulders") but noted that they are usually at least on a meter scale and consist of rock displaced from its point of origin and showing little or no evidence of rounding. More recently, Terry and Goff (2014) suggested the incorporation of the term "megaclast" in the Udden-Wentworth scale to encompass particles larger than the boulder category (> 4.1 m).

In this work, the term megaclast was avoided due to its generic meaning in dimensional terms. Instead, coarse particle nomenclature will be based on the extended Udden-Wentworth scale as proposed by Blair and McPherson (1999) (Table IV).

Table IV: Modified Udden-Wentworth grain-size scale proposed by Blair and McPherson (1999)

Particle length (b-axis)			Class	Fraction	
m	mm	ϕ		Unlithified	Lithified
65.5		-16	...	Megagravel	Mega-conglomerate
			Block		
4.1	4096	-12	Boulder	Gravel	Conglomerate
0.26	256	-8	Cobble		
	64	-6	Pebble		
	4	-2	Granule		
	2	-1	Sand	Sand	Sandstone
	0.063	4	Silt	Mud	Mudstone or Shale
	0.004	8	Clay		

The use of sieves in grain size analysis dictates that the intermediate axis (b-axis) of a particle determines its size classification (Blair and McPherson, 1999). Terms like "large particle", "coarse clast", *etc.* refer to: (1) coble, when the b-axis is larger than 0.064 m and smaller than 0.26 m; (2) boulder, when the b-axis is larger than 0.26 m

and smaller than 4.1 m; (3) block, when the b-axis is larger than 4.1 m and smaller than 65.5 m.

Boulder accumulations can also be classified based on their location. Paris *et al.* (2011) defined: offshore boulders (located in the infratidal zone); platform boulders (located on intertidal and supratidal littoral platforms); and cliff-top boulder deposits (deposited at high elevations – above 10m in Iceland, Ireland or Scotland) (Figure 4).

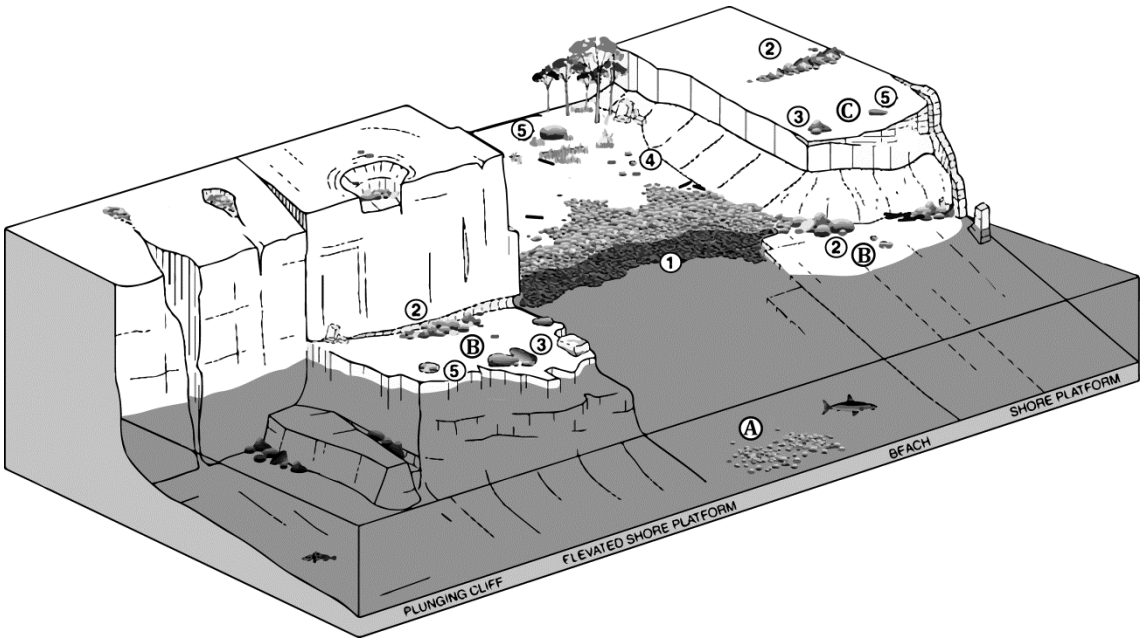

Figure 4: Schematic representation of different classifications of boulder accumulations. Classification based on location: A-offshore boulders, B-platform boulders; C- cliff-top boulder deposits. Morphological classification: ① Boulder beach; ② Boulder ridge; ③ Boulder cluster; ④ Boulder field; ⑤ Isolated boulder. Modified after Paris *et al.* (2011)

Classification of coarse clast deposits can also be based on the morphology and location of the deposits. There is a vast range of morphologies of coarse clast accumulations deposited by wave action described in specialized bibliography, showing different degrees in internal organization (Figure 4) (*cf.* Paris *et al.*, 2011): (1) boulder beaches (*e.g.* Oak, 1984; Scheffers *et al.*, 2009; Etienne and Paris, 2010; Pérez-Alberti *et al.*, 2012); (2) ridges or ramparts (*e.g.* Williams and Hall, 2004; Hall *et al.*, 2006, 2008; Morton *et al.*, 2006; Hansom and Hall, 2009; Suanez *et al.*, 2009; Cox *et al.*, 2012); (3) boulder clusters (*e.g.* Jones and Hunter, 1992; Paris *et al.*, 2009; Mhammdi *et al.*, 2008); (4) boulder fields (*e.g.* Bourrouilh-Le Jan and Talandier, 1985; Goto *et al.*, 2007; 2009a; b; 2010a; b, c; 2011; Paris *et al.*, 2010; Etienne *et al.*, 2011; Bahlburg and Spiske, 2012; Ramalho *et al.*, 2015); (5) isolated boulders (*e.g.*

Süssmilch, 1912; Bourrouilh-Le Jan and Talandier, 1985; Hearty, 1997; Goto *et al.*, 2011; Oliveira *et al.*, 2011).

Boulder beaches generally share the following sedimentary characteristics (Oak, 1984): up-beach fining trend; abundant and widespread particle breakage; positively skewed particle size distribution; absence of shape zoning and sphericity grading; and low foreshore slopes (7°-12°). Furthermore, these accumulations occur in embayments (*cf.* Etienne and Paris, 2010; Pérez-Alberti *et al.*, 2012) and most sediment is comprised within the intertidal zone (Paris *et al.*, 2011).

Ridges or ramparts are frequently described in the literature as morphological features associated with extreme events. Morton *et al.* (2006; 2008) described a ridge as an isolated, narrow and low, shore-parallel feature comprising an accumulation of clasts in contact with one another, and exhibiting packed fabric that can be either matrix- or framework-supported. Moreover, the largest clasts concentrate on the seaward side of the ridge and platy shaped clasts are commonly imbricated and dip seaward (Morton *et al.*, 2008).

Etienne and Paris (2010) and Paris *et al.* (2011) considered a minimum threshold height as a criterion for a deposit to be considered a ridge. They defined a ridge as a deposit similar to a boulder beach, located above the highest astronomical tide in a way that the lower seaward part of the ridge is higher than the MHWL (mean high water line).

Williams and Hall (2004), Hall *et al.* (2008), Williams (2010) and Cox *et al.* (2012) described boulder ridges as well-organized structures with asymmetrical cross-sections, consisting of a steep seaward face (~20°) with the largest clasts showing pronounced imbrication, and a gentle down-flow slope (~5°). Furthermore, these authors observed a landward (down-flow) reduction in clast size.

Although most boulder ridges described in the literature are shore-parallel (*cf.* Hall *et al.*, 2006; Morton *et al.*, 2006; 2008; Hansom and Hall, 2009; Richmond *et al.*, 2011b), some exceptions exist. Knight *et al.* (2009) identified storm-related shore-normal ridges on an intertidal rock platform in the NW coast of Ireland, with

alignment resulting from deposition controlled by lateral emplacement by the swash resulting from an oblique wave attack.

Ridges can be organized in ridge complexes, which sometimes exhibit ridge and swale topography, they can be flat-crested or wedge-shaped, generally with the highest elevation near the ocean (Morton *et al*., 2006). Furthermore, Morton *et al*. (2008) consider ridge complexes as generally stable landforms that aggrade seaward as additional material accumulates on their seaward side. According to these authors, these features represent the accumulation of many depositional events. They result from long-term multi-event reworking and coalescence of several deposits, including former isolated ridges. Morphologic, sedimentologic and stratigraphic attributes, such as ridge complex morphologies, lateral and vertical textural trends, internal stratification and large volume of accumulated sediment, favour the association of ridge complexes to multiple and high-frequency, intense wave events (storms) (Morton *et al*., 2008).

Paris *et al.* (2011) also associated supra-tidal boulder ridges and boulder beaches to storm waves because "*the organization of coarse clasts into supra-tidal ridges requires repeated reworking by waves rather than the single impact of a tsunami wave*". This indication is further supported by Etienne *et al.* (2011) which stated that there are no published accounts of extensive boulder ridge formation by a tsunami in any case studies of recent events.

Boulder ridges have been reported in various locations and geomorphological contexts, such as intertidal to supratidal littoral platforms and structural ramps (*cf*. Knight *et al*., 2009; Etienne and Paris, 2010), cliff-tops (*cf*. Etienne and Paris, 2010; Williams and Hall, 2004; Hall *et al*., 2006, 2008; Hansom and Hall, 2009; Williams, 2010; Cox *et al*., 2012) and in the landward limit of, or alternating with, boulder beaches (Scheffers *et al.*, 2009; Etienne and Paris, 2010).

Boulder clusters have been described as groups of boulders often in contact with one another, or even piled, frequently presenting imbrication facing seaward (*cf.* Bourrouilh-Le Jan and Talandier, 1985; Noormets *et al*., 2002; Mastronuzzi and Sansò, 2004; Paris *et al*., 2009; Scicchitano *et al*., 2007; Switzer and Burston, 2010; Barbano *et al*., 2010). These boulder accumulations have been attributed to both

contemporary tsunamis (*e.g*. Paris *et al*., 2009) and storms (*e.g.* Hall, 2011). Moreover, they have been observed near the base of boulder ridges (in cliff-top platforms) and within joint-defined gullies that act as sediment trap in both cliff-tops and shore platforms (*cf.* Knight *et al*., 2009; Hall *et al*., 2008).

Clusters of aligned boulders, or boulder trains, have also been described, sometimes showing imbrication, both the boulders and imbrication following the general flow direction responsible for their deposition. This has been observed in contemporary tsunami deposits (Bahlburg and Spiske, 2012) and also in palaeodeposits attributed to tsunami inundations (Nott, 1997; Mastronuzzi and Sansò, 2004).

Boulder fields consist mainly of clasts scattered across a surface; the particles are separated from each other and their position does not influence subsequent movement of one another (Morton *et al*., 2008). Boulder fields generated by storms have been observed to occur in association with boulder ridges (located further inland of the latter), in places where boulder accumulations are not limited landward by steep slopes (*cf*. Etienne and Paris, 2010, Pérez-Alberti *et al*., 2012). Most boulder deposits resulting from contemporary tsunamis are boulder fields. They have been described scattered on reefs' surfaces, the particles having been sourced in reef rocks, and across coastal plains, with the clasts having been sourced in seawalls and other man-made constructions (*e.g*. Goto *et al*., 2007; Paris *et al*., 2010).

Isolated boulders have been observed in atolls, and next to the edge of cliff-tops and structural benches, and have been attributed to storms, typhoons and cyclones (*e.g.* Süssmilch, 1912; Bourrouilh-Le Jan and Talandier, 1985; Hearty, 1997; Goto *et al*., 2011, Oliveira *et al*., 2011). Furthermore, these conspicuous clasts have also been observed in shore platforms, lowlands and reefs and were mostly attributed to tsunamis (*e.g.* Scicchitano *et al*., 2007; Paris *et al*., 2010; Goto *et al*., 2010c).

3.2 Coastal coarse deposits worldwide

Coarse deposits related to extreme events (either storm or tsunami) have been described by several authors worldwide (Figure 5), from the Eastern Atlantic (Williams and Hall, 2004; Hall *et al*., 2006; 2008; Hansom and Hall, 2009; Knight *et*

al., 2009; Suanez *et al*., 2009; Williams, 2010; Etienne and Paris, 2010; Hall, 2011; Fichaut and Suanez, 2011; Costa *et al.,* 2011; Oliveira *et al*., 2011; Knight and Burningham, 2011; Cox *et al.*, 2012; Pérez-Alberti *et al.,* 2012) to the Mediterranean sea (Mastronuzzi and Sansò, 2000; Morhange *et al*., 2006; Gracia *et al*., 2006; Mastronuzzi *et al*., 2007; Scicchitano *et al*., 2007; Scheffers and Scheffers, 2007; Vött *et al*., 2008; Scheffers *et al*., 2008; Maouche *et al*., 2009; Barbano *et al*., 2010; Dalal and Torab, 2013), in the Western Atlantic (Jones and Hunter, 1992; Scheffers, 2004; Morton *et al*., 2006; 2008), in the Indian Ocean (Goto *et al*., 2007; 2009a; 2010b; Paris *et al*., 2007; 2009; 2010; Etienne *et al*.; 2011), and in the Pacific (Bourrouilh-Le Jan and Talandier, 1985; Young *et al*., 1996; Nott, 1997; 2003; 2004; Lange *et al*., 2006; Goto *et al*., 2009b; 2010a).

Most coarse deposits generated by extreme events occur within rocky geomorphological contexts, with some exceptions found in Indonesia and Japan related to storms (*e.g.* Goto *et al*., 2011) and to the 2004 Indian ocean tsunami (IOT) and 2009 South Pacific tsunami (SPT) (*cf.* Goto *et al.*, 2007; Paris *et al.*, 2009; Etienne *et al*., 2011); and in atoll islands in the South Pacific Ocean probably related to cyclones (*cf.* Bourrouilh-Le Jan and Talandier, 1985; Harmelin-Vivien and Laboute, 1986).

In contrast with frequent studies addressing contemporary tsunami deposits in low-lying coasts, there is scarce information regarding the impact of recent tsunamis in coastal cliff contexts. The only reference found so far by the author has been on the displacement of one small basaltic boulder from a cliff edge in Savaii, Samoa, and further transport inland with undisputable origin in the 2009 SPT, made by Etienne *et al.* (2011).

Contemporary tsunamis have generated numerous coarse deposits and their study gives the opportunity to better understand the generation of boulder accumulations by these events. Goto *et al.* (2007; 2010b) identified a field of scattered boulders in the intertidal zone at Pakarang Cape, Thailand. The boulders were sourced in reef rocks and coral colonies, and dispersed as a result of the 2004 IOT inundation. The authors found no clear evidences indicating monotonous landward fining/coarsening trends. However, they have found variable orientations of the long

axes of boulders due to local undulations, but showing an overall dominant N-S direction, consistent with an E-W propagation direction of the tsunami wave. This result is compatible with results obtained from numerical modelling of the inundation.

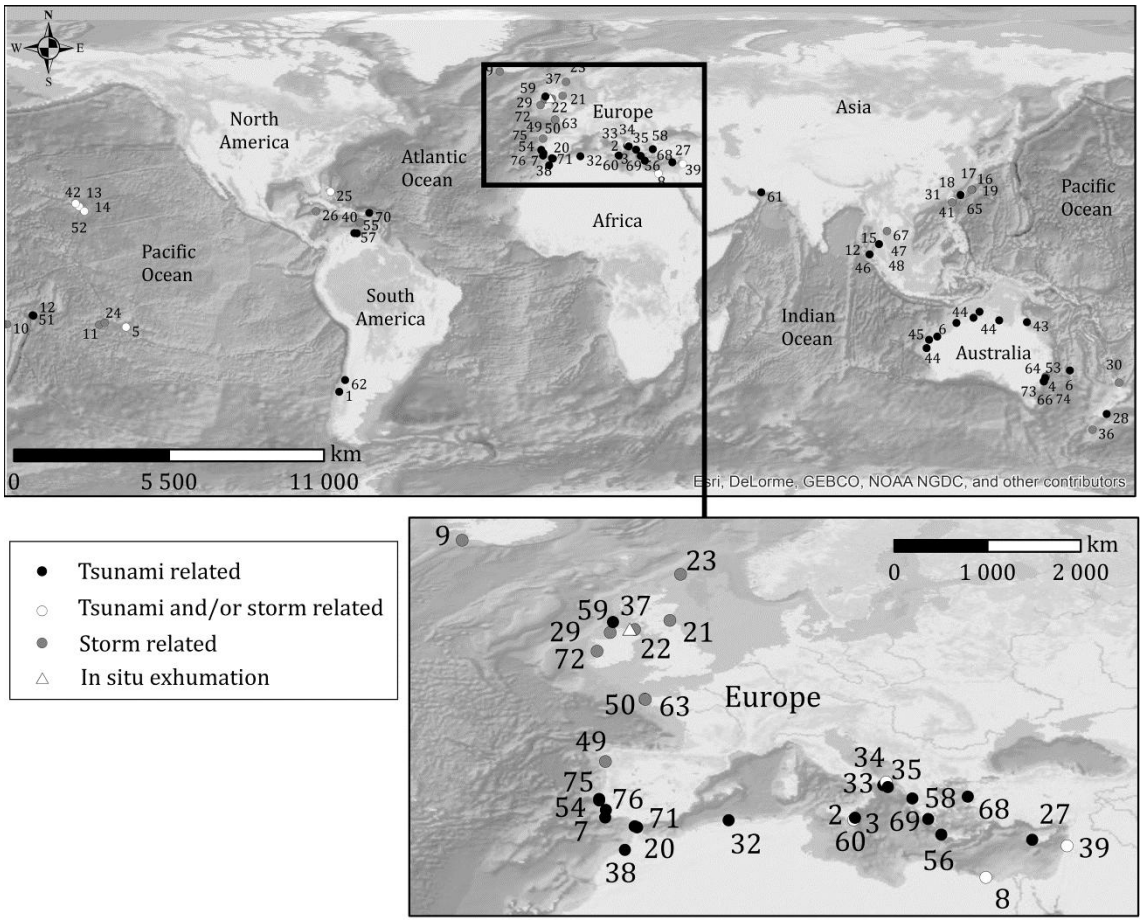

Figure 5: Location of coastal coarse clast deposits worldwide (numbers represent references in footnote[3]). World Ocean Basemap from Esri®ArcMap™

[3] [1]Bahlburg and Spiske (2012); [2]Barbano *et al.* (2010); [3]Barbano *et al.* (2011); [4]Bishop and Hughes (1989); [5]Bourrouilh-Le Jan and Talandier (1985); [6]Bryant and Nott (2001); [7]Costa *et al.* (2011); [8]Dalal and Torab (2013); [9]Etienne and Paris (2010); [10]Etienne and Terry (2012); [11]Etienne (2012); [12]Etienne *et al.* (2011); [13]Felton (2002); [14]Goff *et al.* (2006a); [15]Goto *et al.* (2007, 2009b, 2010c); [16]Goto *et al.* (2009a); [17]Goto *et al.* (2010a); [18]Goto *et al.* (2010b); [19]Goto *et al.* (2011); [20]Gracia *et al.* (2006); [21]Hall (2011); [22]Hall *et al.* (2006) and Hansom and Hall (2009); [23]Hall *et al.* (2008); [24]Harmelin-Vivien and Laboute (1986); [25]Hearty (1997); [26]Jones and Hunter (1992); [27]Kelletat and Schellmann (2002); [28]Kenedy *et al.* (2007); [29]Knight and Burningham (2011) and Knight *et al.* (2009); [30]Lange *et al.* (2006); [31]Lau *et al.* (2015); [32]Maouche *et al.* (2009); [33]Mastronuzzi and Sansò (2000); [34]Mastronuzzi and Sansò (2004); [35]Mastronuzzi *et al.* (2007); [36]McFadgen and Yaldwyn (1984); [37]McKenna *et al.* (2011); [38]Mhammdi *et al.* (2008); [39]Morhange *et al.* (2006); [40]Morton *et al.* (2006, 2008); [41]Nakamura *et al.* (2014); [42]Noormets *et al.* (2002); [43]Nott (1997); [44]Nott (2000); [45]Nott (2003, 2004); [46]Paris *et al.* (2007); [47]Paris *et al.* (2009); [48]Paris *et al.* (2010); [49]Perez-Alberti *et al.* (2012); [50]Regnauld *et al.* (2010); [51]Richmond *et al.* (2011a); [52]Richmond *et al.* (2011b); [53]Saintilan and Rogers (2005); [54]Scheffers and Kelletat (2005); [55]Scheffers and Scheffers (2006); [56]Scheffers and Scheffers (2007); [57]Scheffers (2004); [58]Scheffers *et al.* (2008); [59]Scheffers *et al.* (2009); [60]Scicchitano *et al.* (2007); [61]Shah-hosseini *et al.* (2011); [62]Spiske and Bahlburg (2011); [63]Suanez *et al.* (2009) and Fichaut and Suanez (2011); [64]Süssmilch (1912); [65]Suzuki *et al.* (2008); [66]Switzer and Burston (2010);

Similar boulder fields were recognized in Lhok Nga, west Banda Aceh (Sumatra, Indonesia), as a result of the same tsunami event (2004 IOT), by Paris *et al.* (2010). Again, no clear boulder-size gradient was found within the deposit. Additional surveys undertaken in this area resulted in the identification of other boulder deposits resulting from the same event: coral boulders deposited inland and originated in the fringing reef; calcareous boulders derived from a previously existing seawall; imbricate clusters and one solitary boulder eroded by the tsunami in a rocky platform and covering a distance of only a few meters from its source (Paris *et al.*, 2009; 2010; Etienne *et al.*, 2011). In most deposits, there was no clear relationship between boulder size/weight and distance from the shoreline. Similarly to what was described in Pakarang Cape by Goto *et al.* (2007; 2010b), the boulders' long axis were tangent to the direction of approach of the tsunami wave.

Spiske and Bahlburg (2011) and Bahlburg and Spiske (2012) described deposits from the 27 February 2010 Chile Tsunami in coastal plains in both Bucalemu (central Chile) and Isla Mocha. They identified boulder trains oriented perpendicularly to the coastline and boulder fields originated in an artificial pile of cobbles and boulders put there for construction purposes some days before the tsunami. In both deposits, a landward fining trend was not present. Furthermore, clasts in the boulder field were arranged into groups partially determined by the local topography and showing preferable deposition in morphological depressions.

The effects of the 2009 South Pacific tsunami (2009 SPT) in Samoan Islands (Upolu Island) were observed and described by Richmond *et al.* (2011a). These authors recorded the position, axis dimensions and a-axis direction of isolated boulders and boulder fields. They found no strong trend in boulder size distribution; however, they found that most of the boulders were aligned with their a-axis perpendicular to the dominant flow direction. They further observed a non-uniform distribution of the deposits resulting from highly variable and complex tsunami flow patterns, which were a result of the interaction between multiple tsunami waves and locally

[67]Terry *et al.* (2016); [68]Vacchi *et al.* (2012); [69]Vött *et al.* (2008); [70]Watt *et al.* (2012); [71]Whelan and Kelletat (2005); [72]Williams and Hall (2004), Williams (2010) and Cox *et al.* (2012); [73]Young *et al.* (1996); [74]Oak (1984); [75]Oliveira *et al.* (2011); [76]Ramos-Pereira *et al.* (2009).

complex topography and bathymetry. Along steep coasts, they observed traces of high inundation heights, limited inundation distances and strong return flow.

Many boulder accumulations described in the literature have an unknown origin and are interpreted as a result of tsunami inundations. Cliff-top and platform boulder ridges, ridge complexes and imbricate boulder clusters are present in numerous coastal locations in E, N and W Australia (Young *et al*., 1996; Nott, 1997; 2000; 2004; Bryant and Nott, 2001). These features were considered anomalous by those authors and with emplacement well above the limit of modern storm waves. Based on these considerations, together with results obtained from hydrodynamic approaches, they indicated tsunamis as the most probable cause for the transport and deposition of these boulders. Furthermore, based on thermo-luminescence and ^{14}C age estimation of finer materials trapped beneath the boulders, Young *et al*. (1997) interpreted these deposits as a consequence of at least 5 major tsunamis that struck the Australian coast during the Holocene.

Over low rocky cliffs and shore platforms of Apulia and Sicily, southern Italy, Mastronuzzi and Sansò (2000; 2004), Mastronuzzi *et al.* (2007), Scicchitano *et al.* (2007) and Barbano *et al.* (2010) described small ridges, imbricate boulder clusters, boulder trains, boulder fields and isolated boulders. Age estimation of boulder emplacement was based on ^{14}C dating of encrusting organisms attached to the boulders and accelerator mass spectrometry radiocarbon dating of marine shells found beneath the boulders. The authors also used hydrodynamic approaches to discriminate tsunami from storm origins. Boulder emplacement was mainly attributed to recent historical tsunamis (~*AD* 1100 onwards); however, boulder reworking by subsequent storms was also detected in some cases (Mastronuzzi and Sansò, 2004; Barbano *et al.*, 2010).

Scheffers (2004) described extensive rubble ridges and ridge complexes, rampart formations and boulder assemblages in the Caribbean Sea (Aruba, Curaçao and Bonaire). This author observed that boulder assemblages coincided in space with nearly vertical cliffs containing narrow supratidal zones, and that the amount of the debris increased in broader supratidal areas with more convex cliff profiles. Minimum age estimation of the deposits was based on qualitative assessment of the

size of weathering depressions and additional age estimation was based on radiocarbon dating of vermetids attached to the boulders. Scheffers (2004) excluded storm or hurricane-induced deposition based on field observations and relative and absolute age estimation results, indicating several tsunami events as the origin of these deposits, occurring at approximately 500, 1500 and 3500 BP.

In some cases, doubts in the identification of the event responsible persist. Morton *et al*. (2006; 2008) presented a detailed description of coarse deposits related to extreme marine events found in several islands of the Caribbean sea (Bonaire, Jamaica, Puerto Rico and Guadeloupe), including some of the coarse deposits studied by Scheffers (2004). Contrarily to the interpretations made by Scheffers (2004), Morton *et al*. (2006; 2008) attributed ridge formation to multiple high-frequency intense-wave events (storms) that have accumulated for a few centuries or millennia. These conclusions were based on morphologic, sedimentologic, lithostratigraphic, and chronostratigraphic evidences, such as the fitted fabric, clast imbrication in the seaward face of ridges and internal structure that characterize these deposits, which are similar to modern gravel beaches.

Other authors inferred that both tsunami and storm events have contributed to build the same boulder accumulation. Regnauld *et al.* (2010) observed boulder movement due to a major storm, occurring on March 2010, in pre-existing boulder fields in Ushant Island, offshore western France. The three largest boulders identified by the authors were dislocated during the storm, but their original location prior to the storm was unknown. Given their size, the application of hydrodynamic equations for boulder detachment rendered unrealistic storm wave heights, suggesting that only a tsunami could have detached these boulders from their original location. The authors interpreted this deposit as having a polygenetic origin: the boulders having been originally displaced by a tsunami (possibly the *AD* 1755 Lisbon tsunami) and subsequently moved by severe storm waves.

More recently, efforts have been made to find characteristics that discriminate storm from tsunami boulders in locations affected by both types of events. With this purpose, Goto *et al*. (2009a; 2010a; 2011) investigated offshore boulder fields and isolated boulders located in reef flats and cliff-top boulders, related to storms and

tsunamis in a number of Japanese Islands (Okinawa, Ishigaki, Kudaka and Tsuken). The discrimination of storm from tsunami origin was based on the observation of aerial photographs taken from 1977 onwards (Goto *et al.*, 2009a; b), on eyewitness accounts and previous work by others (*cf.* Goto *et al.*, 2011), added by ^{14}C age estimation of coral boulders (Goto *et al.*, 2010a). The authors found that the average direction of the a-axis of the largest boulders unequivocally associated with storms was parallel to the reef edge whereas orientations of small boulders varied greatly, depending on local topo-bathymetrical undulations (*cf.* Goto *et al.*, 2009a; 2011). Moreover, grain size distribution of these boulders showed an exponential shoreward fining trend (*cf.* Goto *et al.*, 2009a; 2010a). This trend was not observed in boulders deposited by tsunamis and was associated with the exponential decrease in height of storm waves propagating over the reef flat after breaking (Goto *et al.*, 2010a).

Many boulder accumulations have been exclusively attributed to storms, particularly those located in northern Europe (Figure 5). Etienne and Paris (2010) studied 17 boulder accumulations related to storms in Reykjanes Peninsula, Iceland. They found that the morphology of boulder accumulations was related to local geomorphology: boulder beaches were restricted to embayments, and turned into boulder fields further inland ("washover boulders") in the absence of backing cliffs; structural ramps and shore platforms mainly contain boulder ridges occurring in association with boulder fields further inland ("washover boulders"), also in the absence of backing cliffs; benched cliffs contained boulder ridges and cliff-top boulders (heterometric material composed of one layer of boulders); and plunging cliffs were mainly characterized by cliff-top boulders.

Hall *et al.* (2006; 2008) and Hansom and Hall (2009) described cliff-top storm deposits (CTSD) in plunging cliffs of Scotland and Ireland. They associated these deposits with recent storms based on ^{14}C age estimation of mixed shell content found within boulder ridges, and OSL age estimation of sand found below boulders (see 2.2 Sea storms for further details). CTSD deposits were mainly composed of locally-derived coarse clastic debris arranged as asymmetrical ridges aligning parallel to the coast, sheets, clusters and isolated clasts (Hall *et al.*, 2006). The seaward face of the CTSD boulder ridges was formed by imbricate clasts dipping

seaward, and normal to ridge orientation (Hall *et al*., 2006). These accumulations were generally found away from the cliff edge, behind rock surfaces that were clear of debris due to storm wave activity. Boulders originated in fracture-bound particles removed from stepped overhangs on the upper part of the cliff (Hall *et al*., 2008).

Hall (2011) monitored boulder accumulations along a shore platform backed by cliffs in Scotland. These accumulations comprise scattered boulders along the shore platform, boulder clusters showing imbrication facing seaward and boulder trains. Boulder source was identified in the seaward edge of the platform, which showed angular sockets and detachment sites. The author observed rapid reduction in clast size inland, which was consistent with dispersal of wave energy across the platform. However, Hall (2011) also identified a sharp longshore variation in boulder size indicating a significant spatial variability in storm wave current velocities across the platform due to changes in topography.

Williams and Hall (2004) and Cox *et al*. (2012) described cliff-top boulder deposits mainly consisting of asymmetrical boulder ridges, with steeper seaward face, sitting up to ~50 m amsl in the Aran Islands (Ireland). The deposits were well imbricated on the seaward face of the ridges, with boulders predominantly pending to the SW and SSW, matching the prevailing storm wave-direction. Cox *et al.* (2012) presented evidence for recent (decadal to centennial) movement of both individual blocks and ridges during major storms based on: (1) photo comparisons showing block movement between 2006 and 2012; (2) eye-witness accounts of megagravel movement during a storm in 1991; (3) geographical information system (GIS) analysis of 19th century maps and 21st century orthophotos showing landward migration of large sections of a ridge system. Moreover, Cox *et al*. (2012) further presented a storm chronology for cliff-top storm deposits comprising boulder ridges based on ^{14}C age estimations of boring bivalves in boulders, which provided maximum ages for boulder emplacement ranging from about *AD* 100 to post 1950 (see 2.2 Sea storms for further details).

Knight *et al*. (2009) and Knight and Burningham (2011) described storm-related boulder ridges, boulder clusters and isolated boulders in the upper intertidal zone of a shore platform in NW Ireland. Boulder ridges were described as triangular in

section with apices located centrally and separated by a boulder-free platform surface. Cluster accumulations preferably occurred within joint-defined gullies which act as sediment traps (Knight *et al*., 2009; Knight and Burningham, 2011).

Suanez *et al*. (2009) and Fichaut and Suanez (2011) identified boulder clusters, isolated boulders, ridges and ridge complexes developing parallel to coastline configuration along low cliff edges and at the rear of gently sloping embayments in Banneg Island, off the NW tip of Brittany, France. Monitoring of storm conditions and boulder transport indicated a recurrence period of 2 years for the occurrence of wave height with capability to generate boulder movement. Moreover, the authors observed the concentration of bores along channels, forming in discontinuities enlarged by marine erosion, which are compared to "launching pads" that enhance potential for boulder movement. Geomorphological influence on boulder spatial distribution was further observed in imbrication, which mainly reflected the shape of the bay. In cases where the coast was linear, imbrication coincided with dominant wind-driven wave direction (Suanez *et al*., 2009; Fichaut and Suanez, 2011).

Jones and Hunter (1992) studied boulder clusters irregularly distributed along cliffs in the southern coast of Grand Cayman Island in the northern Caribbean Sea. Regardless of the event responsible for these deposits, they observed that boulders preferably occurred inland of indentations developed along solution-widened joints affecting the cliffs. Moreover, field observations showed that incoming waves were funnelled into these indentations creating differential energy levels along a short stretch of coastline.

An alternative explanation for the existence of boulder deposits well above the reach of modern storms, besides tsunami inundations associated with the current sea-level stand, is the preservation of features generated by high energy events contemporaneous of pre-Holocene higher sea-level stand. This is the case of a boulder accumulation described by Kennedy *et al*. (2007), occurring at ~7.5 m amsl, on the SE coast of the S Island of New Zealand, containing partially buried imbricated boulders. These boulders were found in the seaward edge of a marine isotopic age 5 (MIS 5) terrace, which extends a few hundred meters landward where it meets a former sea cliff, and over a planar erosion surface. Directly landward of

the boulders, surrounding some of the smaller particles, and occurring at a similar stratigraphic level, a well-sorted laminated sand unit overlies the same eroded bedrock surface. Age estimation of this laminated sand using OSL rendered 81.9±11.7 ka, compatible with the MIS 5. The authors attributed this deposit to a pre-Holocene tsunami based on results obtained by hydrodynamic models.

Hearty (1997) described 7 isolated boulders on the top of cliffs in N Eleuthera Island, Bahamas. The boulders were sitting on entisols (immature soils), corresponding to the youngest MIS 5 unit represented in the area, and were further encrusted by calcrete and paleosoil, formed during sea-level regression. Based on this stratigraphic setting, the author interpreted these boulders as a result of major storms or tsunami events occurring after substage 5e, when sea level was still relatively high.

Pérez-Alberti *et al.* (2012) studied boulder accumulations (boulder beaches and one isolated boulder) along profiles surveyed on granite littoral platforms in Galicia, NW Spain. Boulder beaches showed a predominance of boulders oriented towards the S and SE, corresponding to the direction of the storm waves affecting that area. Additionally, backshore deposits, accumulated 4-5 m above high tide (6-7 m amsl), comprising two populations: 1) the first, containing immobile discoloured boulders partially covered with vegetation and lichen, was interpreted as MIS 5 in age; 2) the second population, containing fine boulders with freshly abraded surfaces, was interpreted has having been deposited more recently. The authors interpreted this boulder accumulation as a probable result of both recent and Eemian storms and excluded tsunami origin based on the absence of seismic tsunami sources nearby, except for the *AD* 1755 tsunami source, which generated only a slight swell in Galicia and caused no damage in this region.

3.3 Coastal boulder deposits in Portugal

Several boulder accumulations identified as having resulted from extreme marine events have been identified and described in mainland Portugal, and mostly attributed to the *AD* 1755 tsunami inundation (Figure 6 and Table V).

Oliveira *et al.* (2011) described two parallelepiped limestone boulders showing evidence of transport against gravity, with mass of 8 ton and 14 ton, sitting on a rocky structural platform at 1.8 m and 3.5 m amsl respectively, N of Praia das Maçãs beach, in the W coast of Portugal (Figure 6). Time of boulder transport was constricted between 1965 and 1975 based on the comparison of aerial photographs. The more probable event responsible for the detachment and transport of these boulders was the most intense storm event affecting the Portuguese coastline between 1965 and 2009, which occurred on 17th January of 1973, with significant wave heights of 13 m, corresponding to maximum wave heights of approximately 22 m.

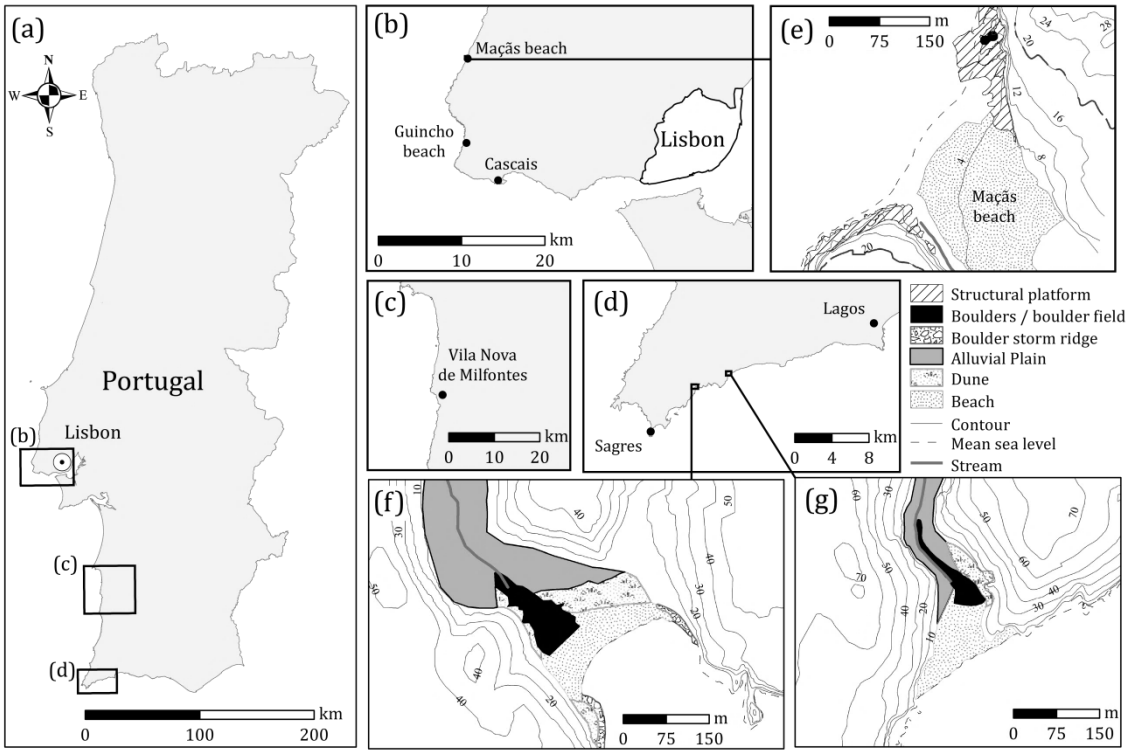

Figure 6: (a) Location of coastal boulder deposits in Mainland Portugal described in the literature. (b) Two boulders N of Praia das Maçãs, and several boulder accumulations located W of Cascais and depicted in Figure 7. (c) Isolated boulders in the SW coast of Portugal depicted in Figure 8. (d) Lowlands in the S coast of Portugal comprising cobble/boulder fields. (e) Geomorphological sketch of the Praia das Maçãs area (modified after Oliveira *et al.*, 2011). (f) Geomorphological sketch of Barranco beach (modified after Costa *et al.*, 2011). (g) Geomorphological sketch of Furnas beach (modified after Costa *et al.*, 2011)

Further S, in the coastal sector located between Cascais and Guincho beach (Figure 6 and Figure 7), several boulder accumulations, as well as other evidences of inundation by extreme marine events were identified and described by Scheffers and Kelletat (2005). Some of the evidences N of Praia do Guincho indicated by these authors comprise vegetation scars at 20-50 m amsl, smaller boulders (50-300 kg) of

varying nature (granite, basalt, quartzite, sandstone, limestone, diabase, *etc.*) embedded in a sandy matrix, well-rounded quartz pebbles at 30 m amsl and beach pebbles and sand above 50 m amsl.

Table V: Summary of boulder characteristics identified in the Portuguese coastline

LOCATION	BOULDER CHARACTERISTICS			ORIGIN	AUTHOR
	MASS (ton)	HEIGHT	COMPOSITION		
Praia das Maçãs	8-14	1.8-3.5 m	limestone	Storm between 1965-1975	Oliveira *et al.* (2011)
Coastal sector between Guincho and Cascais	>100	4-12 m	limestone	Tsunamis (*AD* 1755; 2440 BP; 6000-7000 BP)	Scheffers and Kelletat (2005)
N Vila Nova de Milfontes	0.09-19	12-20 m	unknown	*AD* 1755 tsunami	Ramos-Pereira *et al.* (2009)
Barranco and Furnas beaches	0.005-1.1	2.7-3.4 m	limestone	*AD* 1755 tsunami	Costa *et al.* (2011)

In this coastal ribbon and facing W, Scheffers and Kelletat (2005) indicate several boulder alignments at a height of 14 m amsl, as well as substantial amounts of sand with shell fragments of limpets (*Patella* sp.) and marine gastropods, deposited over the marine sculptured shore platform. In the coast facing S, these authors mainly found isolated boulders and boulder fields, sometimes showing imbrication, with mass ranging from 10 ton to 20 ton and sitting on intensely karstified raised shore platforms, found up to 20 m amsl and 50 m inland. Boulder transport from the SW and SSW (landward) was inferred based on imbrication and boulder size reduction trends.

Based in these indicators, maximum inundation heights of 50 m were suggested in the western coastline N of Praia do Guincho, and of 20 m in the southern coastline (Scheffers and Kelletat, 2005). These authors attributed the evidences of extreme marine inundation to the *AD* 1755 tsunami and to two other possible tsunamis, one occurring at 2440 BP and another dated from the Middle Holocene, around 6000-7000 BP. Age estimations were based on ^{14}C and electron spin resonance (ESR) of 4 gastropod shells found within the sand, as well as other, more subjective, indicators (soil development, degree of karstification, weathering intensity on dislocated boulders and vegetation and soil development around them).

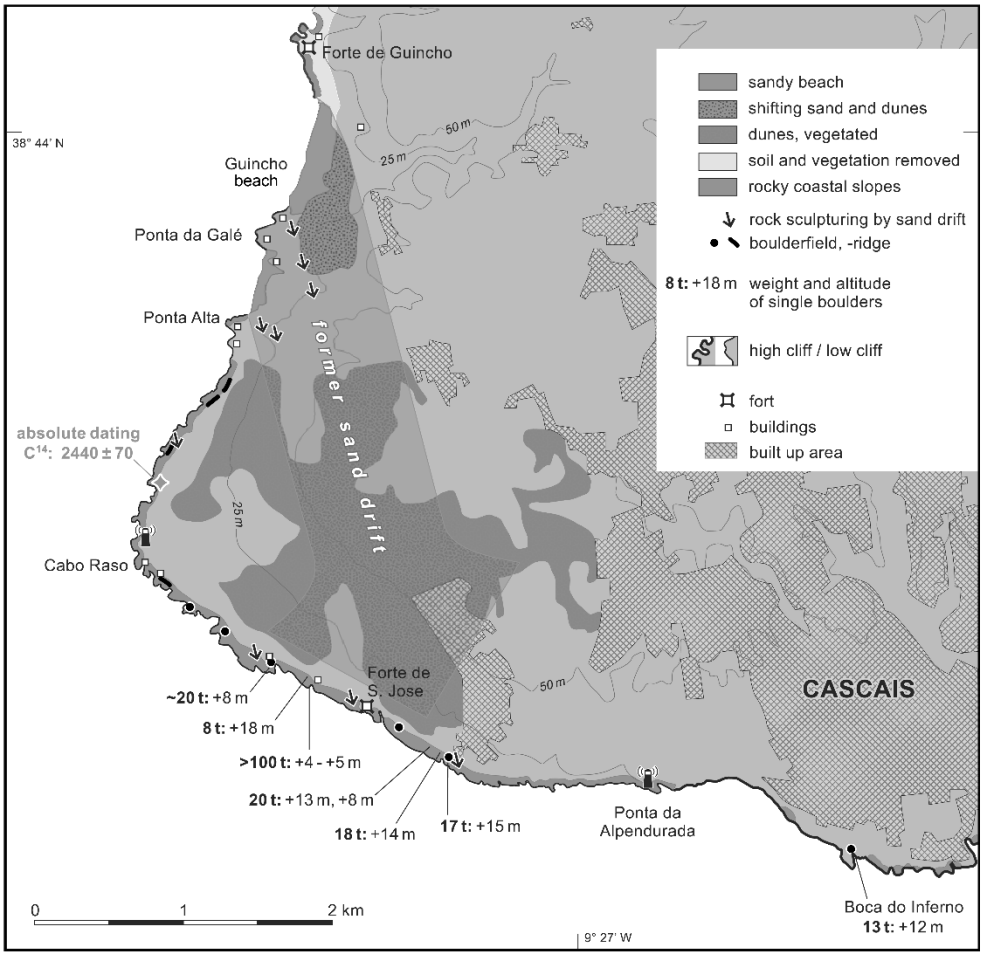

Figure 7: Location of features identified by Scheffers and Kelletat (2005). Modified after Scheffers and Kelletat (2005)

Observation of some of these boulder accumulations during field surveys and analysis of work done in this location by other authors lead to the conclusion that some of the evidences of tsunamigenic marine inundation presented by Scheffers and Kelletat (2005) are feeble. Depositional evidences of marine origin described by Scheffers and Kelletat (2005) N of Praia do Guincho beach are compatible with the general location and description of several marine terraces located next to Ponta da Galé (< 25 m) and E of Cabo Raso (> 50 m) and dated from the Pleistocene by Ramalho *et al.* (2001). Besides containing beach sand and pebbles, these deposits also contain abundant well-rounded pebbles and stone tools resulting from human activity and dated from the Palaeolithic to Roman epochs. These artefacts were found at 4-6 m, 15 m, 30 m and 60 m amsl (Ramalho *et al.*, 2001).

Despite recognizing the existence of a sand drift corridor, trending NNW-SSE and fed by Guincho beach sand, Scheffers and Kelletat (2005) theorize about the possibility

that the substantial amounts of sand existing between Cascais and Cabo Raso and covering the raised rocky platform might have been originated by tsunami waves incoming from SW, that transported finer sediments from the Tagus outlet. Actually, this large amount of tsunamigenic sand corresponds to two dune systems developing over a wide raised shore platform, from Guincho beach towards the S-facing coast. These dune systems are aligned along a well-known aeolian corridor and contain an active dune system connected to Guincho beach; and also a consolidated dune of Pleistocene age located further SE, that has been studied by several authors (*cf.* Ramalho *et al*.; 2001; Ramos-Pereira and Angelucci, 2004; Soares *et al*., 2006; Prudêncio *et al*., 2007). This corridor has been intermittently active since the Late Pleistocene until present, so there is no need to find an additional sediment source further S (as well as an additional transport mechanism of tsunamigenic nature) to justify the volume and geometry of the sandy deposits developing over that platform.

Boulder accumulations described in the S-facing coast were not undoubtedly proven to be of tsunamigenic origin. The largest boulder with estimated mass above 100 ton located west of Forte de S. José identified in Scheffers and Kelletat's (2005) study, is part of an *in situ* dismantled limestone layer. This block is tilted due to differential erosion of surrounding layers of marl and volcanic dikes and does not show any evidence of transport against gravity. Other boulder accumulations identified by these authors comprise irregularly distributed clasts with mass below 20 ton, sitting on a raised platform at maximum heights of 12 m amsl. They appear to have been recently deposited but, in the cases observed, transport against gravity cannot be assured.

Ramos-Pereira *et al*. (2009) described a boulder field containing 42 boulders sitting on a littoral platform cut in a Pleistocene aeolianite, in the Portuguese coastline between Vila Nova de Milfontes and Malhão beach (Figure 6 and Figure 8). This platform is partially covered by a dune field and is limited by a 20-m high plunging cliff and a ramp pending seawards (Figure 8). Boulders were found from the cliff-top edge towards inland, at heights ranging from 12 m to 20 m amsl and masses ranging from 0.09 ton to 19 ton (Ramos-Pereira *et al*., 2009). The largest boulders were found clustered near the landward edge of the ramp. These boulders were

attributed to the *AD* 1755 tsunami event by Ramos-Pereira *et al.* (2009), based on unrealistic storm wave heights obtained when applying hydrodynamic equations developed by Nott (1997; 2003). Boulder origin and source location were not described.

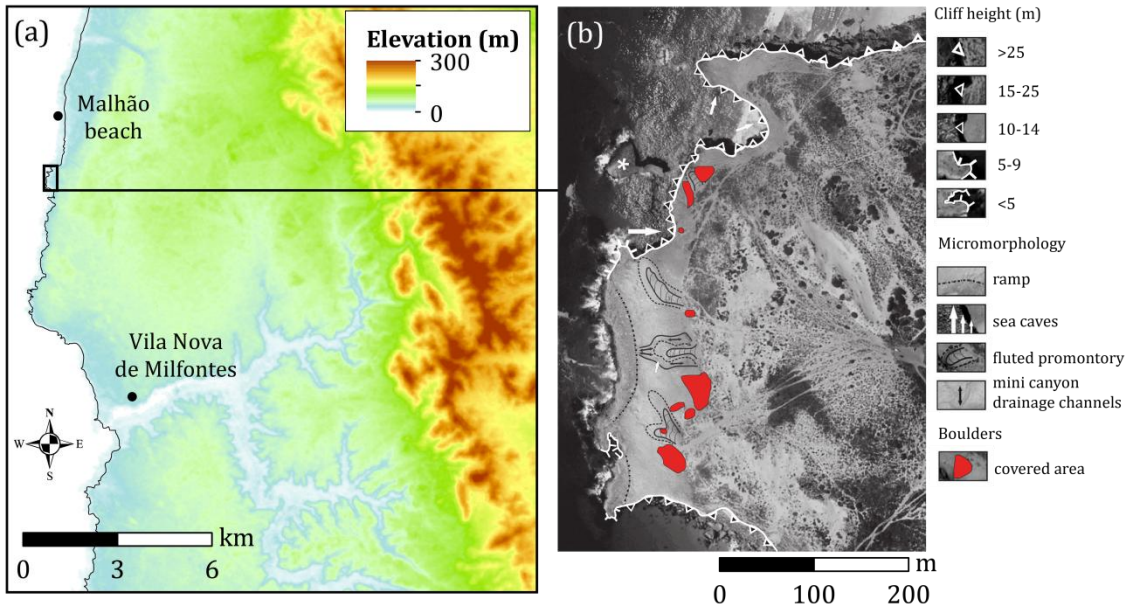

Figure 8: (a) Location of the littoral platform studied by Ramos-Pereira *et al.* (2009). ASTER Global Digital Elevation Model property of METI and NASA (available in http://reverb.echo.nasa.gov/reverb/); (b) Morphology of the littoral platform (modified after Ramos-Pereira *et al.*, 2009)

Costa *et al.* (2011) identified two limestone cobble-boulder fields in the S coast of Portugal with origin attributed to the *AD* 1755 tsunami. The clasts were well-rounded with ellipsoidal cross-section and a-axis ranging from 0.3 m to 1.6 m. They were found sitting at the bottom of two narrow flat-floored valleys, which end in pocket beaches (Barranco and Furnas beaches) in the coastal sector located between Sagres and Lagos (Figure 6).

Cobbles and boulders rest above or are partly mixed with beach sand and alluvial deposits and were found inland up to 250 m of the coastline at average heights of 2.7-3.4 m amsl. Their surface was pitted due to marine bioerosion by endolithic bivalve organisms, some still presenting *in situ* preserved shells, indicating an origin within the subtidal coastal domain and suggesting a single transport pulse, excluding saltation or rolling mechanisms (Costa *et al.*, 2011). The age estimation of boulder transport was based on ^{14}C dating of bivalve shells and showed compatibility with the *AD* 1755 tsunami inundation (Costa *et al.*, 2011).

3.4 Interpreting boulder deposits

The key issues regarding the study of boulder deposits transported by extreme marine events have been: (1) how to extract information regarding flow characteristics; (2) how to differentiate between tsunami and storm origins; (3) how much influence does local geomorphology have on boulder deposit characteristics; (4) how to accurately estimate the age of the depositional event(s).

3.4.1 Inference of flow characteristics

The study of boulder characteristics, and of their spatial distributions, such as cluster alignment, ab surface (boulder surface comprising the a- and b-axis) dip direction, a-axis direction and sediment source have been used to infer on flow characteristics by several authors.

Boulder cluster alignment has been reported as occurring in accordance with the direction of the wave approach by Mastronuzzi and Sansò (2004) in deposits attributed to two paleotsunamis in the Adriatic coast of Apulia, southern Italy. In contrast, many other authors have recognized boulder ridges developing parallel to the shoreline with alignments resulting from interactions between storm waves and local morphology.

Flow direction has also been inferred from the ab surface dip direction (or imbrication axis in the case of imbricated boulders) and a-axis direction. Regarding this subject, there is a general agreement in that elongated boulders come to rest with their long axis aligned orthogonally to the flow direction, and that the imbrication axis and ab dip direction align with flow direction (*e.g.* Mastronuzzi and Sansò, 2000; 2004; Hall *et al.*, 2006; Mastronuzzi *et al.*, 2007; Goto *et al.*, 2007; Scicchitano *et al.*, 2007; Barbano *et al.,* 2010; Williams, 2010; Cox *et al.*, 2012; Pérez-Alberti *et al.*, 2012). Williams and Hall (2004) further differentiate flow direction based on boulder shape: when the a-axis is much larger than the b-axis, the orthogonal of the a-axis is representative of flow direction; when both axes are of similar dimensions, the dip of the ab surface is representative of flow direction.

One other way to infer on flow direction is by identifying boulder source and thus defining the shortest transport paths. Goto *et al*. (2007) studied an extensive boulder field in Pakarang Cape, Thailand, deposited by the 2004 IOT, and inferred on wave direction near the coast by matching information regarding location of source and final deposition, together with the spatial orientation of boulder long-axis.

3.4.2 Distinction between storm and tsunami

The distinction of storm versus tsunami origins of coastal boulder deposits is a subject at the cutting edge of research and has been critically discussed by many authors who attempted to differentiate between these origins using: (1) inferences on the flow velocity and wave height required to transport large particles, based on the application of balance equations, that allow for the computation of height of tsunami and storm waves capable of generating boulder movement (Nott, 1997; 2003); (2) boulder deposit dimensions, such as the inland extension of the deposit (*e.g*. Goto *et al*., 2010a); (3) sedimentological characteristics, such as size grading inland or particle imbrication (*e.g.* Paris *et al*., 2009; Goto *et al.*, 2010a); and (4) presence/absence of specific morphological features, such as organization in linear ridges versus scattered deposits (*e.g.* Morton *et al*., 2008; Williams and Hall, 2004; Etienne and Paris, 2010).

Computations of wave height of both tsunami and storm waves capable of generating boulder movement using balance equations derived by Nott (1997; 2003) are based on boulder size and mass and on an initial probable scenario (submerged, subaerial or joint-bounded boulder). Many authors have attempted to distinguish tsunami from storm origin of palaeodeposits by using these equations (Mastronuzzi and Sansò, 2004; Mastronuzzi *et al*., 2007; Scicchitano *et al*., 2007; Maouche *et al*., 2009), but this approach has generated much controversy due to the simplistic method and implicit generalizations and assumptions (see chapter 4 Numerical solutions of boulder movement).

Based on the comparison between tsunami and storm boulder deposits at Ishigaki Island, Japan, Goto *et al*. (2010a) suggested that the transport distance of boulders inland should be used to discriminate transport by tsunamis and storms, due to the significant difference in wave period, rather than wave height, characterizing both

types of waves. This was further confirmed by Watanabe *et al*. (2014), which state that tsunami waves are capable of transporting boulders to larger distances inland (~1500 m) when compared to storms (~300 m).

In contrast to storm-related boulder deposits, which present distinct landward fining trends (*cf.* Williams, 2010; Etienne and Paris, 2010; Cox *et al*., 2012; Pérez-Alberti *et al.*, 2012), one characteristic generally observed in boulder deposits originated by recent tsunami events, such as the 2004 IOT and the 2009 SPT, is that they rarely show size grading in space, such as landward fining (Goto *et al*., 2007; 2010a). In fact, exponential shoreward fining trends were detected in storm deposits by Goto *et al*. (2010a) and related to the decrease in intensity of the forces associated to broken storm waves acting on the boulders. However, Goff *et al*. (2006b) described landward fining in boulder deposits, extending from 50 to 300 m inland and up to 10.4 m amsl, in Apua Point, Hawaii, related to the 1975 Kalapana tsunami inundation. In contrast with other tsunami deposits, the absence of impact marks in these marine boulders was interpreted as indicative of reduced clast-clast interference during transport. The contrast between this and other deposits has led to the interpretation that the chaotic nature imparted in most boulder deposits is related to clast interference during entrainment (Goff *et al*., 2006b).

Most boulder accumulations generated by contemporaneous tsunamis are represented by fields of scattered boulders, which preferentially show their long axis oriented perpendicularly to flow (Goto *et al*., 2007; Paris *et al*., 2009; Etienne *et al*., 2011), although Paris *et al*. (2009) also described imbricate boulder clusters and solitary clasts associated with the erosion of a rocky platform by the 2004 IOT in the NW coast of Sumatra.

Watt *et al.* (2012) used a-axis orientation, weight distribution and directional trends in clast spacing to infer the direction of flow responsible for cobble and boulder transport on Anegada, British Virgin Islands, associated with a unique landward thinning and fining sand sheet. This deposit has been associated with a tsunami event, evidenced by morphology of the boulder deposit and comparison of flow velocities obtained from numerical modelling of tsunami and storm inundation with

those necessary to generate boulder movement (*cf.* Buckley *et al.*, 2012; Watt *et al.*, 2012).

3.4.3 Geomorphological controls

Another point to consider when making interpretations about flow direction and velocity based on boulder deposits is the influence of local and regional geomorphology (bathymetry and topography) in the way a storm or tsunami bore disperses energy when approaching and reaching the coastline.

Tsunami waves, due to their long wavelength, are greatly affected by regional bathymetry, which controls both the distribution of maximum wave and inundation heights and travel times (Iglesias *et al.*, 2014; Matsuyama *et al.*, 1999). Maximum inundation heights occur due to wave focusing, which can result from funnelling effects in concave morphologies and wave refraction due to differentiated shoaling effects (decrease of tsunami wavelength and velocity and increase of wave height) (Iglesias *et al.*, 2014; Matsuyama *et al.*, 1999). The significance of the shoaling effect changes according to the shape and depth of every slope and shelf. In terms of tsunami hazard, a wide continental shelf induces a strong shoaling effect that can translate into a late arrival time to the coastline but also into a larger inundation height (Iglesias *et al.*, 2014).

Furthermore, the presence of a submarine canyon incised into the continental shelf originates a greater longshore variability in wave and associated potential inundation heights along the adjacent coastline, with lower values in the coastal stretch just shoreward of the canyon head, and higher at both sides of that stretch (Iglesias *et al.*, 2014). Based in all these evidences it becomes clear that seabed morphological attributes are critical to accurately model tsunami propagation

Besides large-scale sea-bottom morphological features, local geomorphology also influences flow direction and velocity. Goff *et al.* (2006a) evaluated the impacts of the 26 December 2004 transoceanic tsunami in Sri Lanka. Given the differences of the observed impacts and of the extensive eye witness accounts collected over this island, the authors concluded that morphological features controlled the tsunami impacts, so that the headlands blocked tsunami inundation and prevented landward

damage, whereas the embayments focused the waves and increased the height and inundation distance.

Etienne and Terry (2012) identified boulders showing evidence of recent transport (while others remained immobile) by cyclone Tomas (March 2010) on Taveuni Island, Fiji. The authors further observed that signs of rock dismantlement preferentially appeared on headlands.

Canelas *et al.* (2014) used a hydrodynamic numerical model to evaluate the influence of micro to meso-scale geomorphological conditions in rocky coastal contexts in the capability of waves to entrain and transport boulder upwards and inland. They concluded that a concave planar geometry (embayment), together with an overhanging configuration of the impacted cliff generate a local concentration of energy and maximize the chance of boulder dislodgement and transport.

Additional geomorphological/topographical controls of inundation and boulder distribution have been observed worldwide and are cited in section 3.2 (Coastal coarse deposits worldwide), such as: (1) preferable location of boulder accumulations in specific geomorphological features such as landward of vertical cliffs with narrow supratidal zones (Scheffers, 2004), inland of coastal indentations (Suanez *et al.*, 2009; Fichaut and Suanez, 2011; Jones and Hunter, 1992), within joint-defined gullies (Knight *et al.*, 2009; Knight and Burningham, 2011); (2) preferable deposition in morphological depressions (Spiske and Bahlburg, 2011); (3) changes in boulder distributions related to topography (Hall, 2011); (4) morphology of boulder accumulations varying with local geomorphology (Etienne and Paris, 2010); (5) high inundation heights, limited inundation distances and strong return flow along steep coasts (Richmond *et al.*, 2011a).

3.4.4 Age estimation

Age estimation of boulder deposition by extreme marine events is a major challenge and has been mainly achieved indirectly through: 1) the comparison of aerial photographs and cartography with different dates (*e.g.* Oliveira *et al.*, 2011; Cox *et al.*, 2012); 2) ^{14}C age estimation of boring bivalves and biogenic encrustations attached to the boulders, assuming that death occurred by dislocation from their

living environment (*e.g*. Mastronuzzi and Sansò, 2004; Scheffers *et al*., 2009; Costa *et al*., 2011); 3) ^{14}C age estimation of marine shells and coral fragments found beneath boulders (*e.g.* Nott, 2000; Mastronuzzi *et al*., 2007; Scheffers *et al*., 2009); 4) OSL age estimation of marine sand surrounding boulders (*e.g*. Kennedy *et al*., 2007). The transport of coral boulders can also be dated with ^{14}C (*e.g.* Jones and Hunter, 1992; Nott, 1997; Suzuki *et al*., 2008) or uranium/thorium (U/Th) age-dating (*e.g.* Terry *et al*., 2016), a technique also based in the assumption that the death of the corals occurred by dislocation from their living environment.

Lichenometry is another approach of surface boulder age estimation that has been extensively used, together with other techniques (absolute age estimation from ^{14}C and relative age estimation from soil development, weathering rind, vegetation cover, *etc.*), in the study of Holocene glacier recession through moraine sequences (*e.g.* Mahaney, 1973; Carrara and Andrews, 1975; Hansen, 2008). This technique has also been used in the determination of recurrence intervals for debris-flows and slush avalanches (*e.g.* Innes, 1983; André, 1990; Jonasson *et al.*, 1991), earthquakes (*e.g.* Bull., 2014) and boulder transport caused by major floods and river incision (*e.g.* Mass and Macklin, 2002; Gob *et al.*, 2003).

Lichenometry is based on the following assumptions (McCarthy, 1999): an individual is not older than the surface on which it is growing; the larger individuals in a population grow under optimal conditions and provide a minimum estimate of the amount of time of exposure of the substrate on which they grow. This technique is based on the principle that the largest the individual, the older the exposure of the surface. It is usually used as a calibrated age estimation method, but in the absence of a calibration curve, it serves as a relative age estimation technique (Noller and Locke, 2000). This calibration curve relates lichen size (or cover area) with time elapsed and must be specifically built for the species (or genus) used in the study as well as for the general environmental conditions in which the deposits to be dated occur (air temperature, day length, aspect, latitude, altitude, moisture, *etc*.) (*cf.* Innes, 1985; Lowe and Walker, 1984).

The upper limit of applicability is determined by senescence or by competition for available space by either individual of the same species or others (Noller and Locke,

2000). Although some species are reported to be 5000 years old, in most cases, this method is most useful for dating the past 500 years (Beschel, 1961; Innes, 1985; Armstrong, 2004).

Lichenometry has been developed and mainly used in silicate rocks colonised by a specific group of crustose lichens from the *Rhizocarpon* genus (Innes, 1985; McCarthy, 1999; Armstrong, 2004). Although rare, the studies of lichen growth in calcareous rocks exist *(e.g.* Trudgill *et al.*, 1979; Mass and Macklin, 2002). Better results can be obtained when the studied species is slow-growing and circular in shape (Innes, 1985; Noller and Locke, 2000).

The application of this technique to coastal boulder deposits has been attempted by Williams and Hall (2004) and Hall *et al.* (2006; 2008) to obtain relative ages. The authors mapped the distribution of spray-tolerant lichen on CTSD deposits, cliffs and platforms in Scotland and Ireland, to separate boulder populations with different ages and to evaluate the stability of rock surfaces on cliff faces and tops.

For further details about lichenometric methods and range of applications please refer to the work of Innes (1985), McCarthy (1999) and Noller and Locke (2000).

3.5 Summary

Contemporary tsunamis mainly comprise boulder fields, and less frequently boulder trains, mostly accumulated in lowlands and reef flats. Generally, these deposits do not show landward fining trends and individual particles come to rest with their a-axis perpendicular to the dominant flow. Storm deposits comprise varied morphological arrangements (boulder beaches, ridges, clusters, isolated boulders and boulder fields), frequently showing imbrication, which agrees with the dominant wave-driven flow direction in linear coasts and reflects the shape of the bays when the coastline is irregular.

Influence of regional and local geomorphology has been observed in both tsunami and storm boulder deposits, as summarized below:

1. For a given location, the amount of accumulated material increases with decreasing profile slope;

2. Boulder fields frequently occur in uncliffed coasts, boulder beaches in embayments and boulder ridges develop in every context (cliffs, embayments and platforms);
3. Along steep coasts, inundation heights are higher, inland penetration distances are lower and return flow has maximum transport capability;
4. Boulder accumulations preferably occur in topographic lows and joint-defined gullies which act as sediment traps;
5. Indentations in the coastline create funnelling effects, enhancing the potential for boulder movement and preferential accumulation inland of those indentations;
6. Cliff-top boulder deposits are mainly sourced in the upper part of the cliffs, and especially where loosened overhanging blocks have been previously detached by weathering;
7. The presence of submarine canyons originates reduced maximum wave heights in the coastal stretch just shoreward of the canyon head, and increases height at both sides of that stretch.

Age estimation of boulder deposits is an extremely challenging task, and has been essentially achieved by indirect age estimation using OSL and ^{14}C of materials attached or located beneath the boulders. Lichenometry has also been used in coastal boulder accumulations, but so far, only relative age estimation of boulder movement has been achieved.

There are many numerical solutions available to aid in the differentiation of tsunami and storm boulder accumulations. The use of these approximations is frequently acritical and may generate incorrect interpretations on the origin of boulder deposits. To more adequately apply these approximations, a detailed analysis of the underlying principles is required. Additionally, the application of these approximations to boulder deposits with known origin provides a mean to evaluate their functionality within different contexts. Both the analysis of the available numerical solutions and of their application to known boulder deposits are undertaken in the next chapter.

Numerical solutions of boulder movement

The development of numerical solutions of boulder movement by storm and tsunami waves is a complex subject, which has been discussed in published work throughout the past 20 years. Besides calculating flow velocities required to entrain large particles, the main challenge has been to reconstruct the nature of the extreme event (storm or tsunami) driving the transport and to calculate physical parameters (*e.g.* wave height, extent of the inundation) associated with the event responsible for displacement and deposition of boulders.

The use of measurable large-sized particle characteristics in boulder deposits generated by storms or tsunamis, and reconstruction of wave parameters argued to have been responsible for their transport and deposition made the focus of published work undertaken at a global scale, mainly addressing rocky coastline contexts (*e.g.* Nott, 1997; 2003; Mastronuzzi and Sansò, 2004; Noormets *et al.*, 2004; Etienne *et al.*, 2011; Nandasena *et al.*, 2011a; Oliveira *et al.*, 2011). Results sometimes show inconsistencies between storm condition inferred from boulder attributes and the observed prevailing wave regime. Many times, these

inconsistencies do not imply a tsunami origin, but are frequently related to the straightforward use of numerical approximations, that generally render minimum flow velocities necessary to generate boulder movement, which are uncritically used to reconstruct wave parameters departing from boulder properties, regardless of their position in relation to the breaking point.

Straightforward numerical solutions predicting boulder movement are mainly based on solutions that do not consider distance travelled neither local (micro to meso-scale) geomorphological conditions, which strongly control the capability of waves to entrain and transport large particles (Canelas *et al*., 2014). Moreover, the study of recent boulder deposits with known storm origin showed that local conditions largely influence potential inundation heights and distances of boulder transport (*e.g*. local and regional bathymetry, coastline configuration, slope, sediment availability, *etc.*). For this reason, the identification of extreme events (storm or tsunami) and extrapolated wave parameters based on these approximations are sometimes not compatible with the events responsible for boulder deposition (*cf.* Williams and Hall, 2004; Oliveira *et al*., 2011, Cox *et al*., 2012). Thus, straightforward approaches for modelling boulder transport should be applied with caution, especially when interpreting coastal boulder accumulations of unknown origin (Nandasena *et al.*, 2011b).

There are several approaches available to model boulder movement, with varying degrees of complexity. Simple solutions are easy to apply and need minimum information; however, because simulated physical processes are far from simple, interpretation of results must be carefully made (Lorang, 2011). For each degree of complexity added in the formulations, more information and variables become necessary for computations, such as boulder source location and wavelength/period of the waves responsible for the transport. More recently, validation of predictive formulations using case studies where transport has been measured revealed that some solutions, sometimes, provide a good approximation of reality (*e.g.* Lorang, 2000).

In this section, an attempt was made to review straightforward solutions available in the bibliography, each bringing something new to the pre-existing work by the

inclusion of additional variables/processes, allowing a better description of the specificities associated with the case studies. A general description of the approximations is made and equation derivation is presented in Appendix D trough G. Moreover, the identification and corrections of inconsistencies and clarification of contexts in which they may be used is also made. Each approximation is explained separately and applied to a specific boulder data-set (listed in Appendix H) resulting from boulder accumulations with different origins (storm and tsunami) and resting in geomorphological contexts, also described in the literature (Table VI).

Table VI: Boulder data-sets used in the application of different numerical solutions and presented in Appendix H

LOCATION	SETTING	ORIGIN	AUTHORS
S Portugal	Embayment	*AD* 1755 tsunami	Costa *et al.* (2011)
W Portugal	Structural platform	Storm occurring between 1965 and 1975	Oliveira *et al.* (2011)
Sumatra, Indonesia	Coastal plain	2004 IOT	Nandasena *et al.* (2011b)
Okinawa Island, Japan	Cliff-top	Typhoon in 1990	Goto *et al.* (2011)
Scotland	Rocky platform	Storm	Hall (2011)
Reykjanes Peninsula (Iceland)	Platforms, embayments and cliff-tops	Storms	Etienne and Paris (2010)
Chile	Coastal plain	2010 Chile tsunami	Spiske and Bahlburg (2011)

This chapter is subdivided in four sections: (1) empirical solutions used to estimate the weight of blocks required to provide stability to rubble revetments in breakwaters, for a given design wave (Hudson and van deer Meer formulae); (2) balance equations used to account for relevant forces acting on a boulder as a result of water flow (equations developed by Nott, Hansom *et al.*, Nandasena *et al.* and Noormets *et al.*); (3) wave competence approaches considering wave height and period, based on a combination of the balance of moments, geometric settings, linear and non-linear shallow water wave theory and empirical relationships (Benner's and Lorang's equations); (4) a summary of the approaches, comparing results obtained with different solutions, focusing on input and output parameters and on strengths and limitations associated with each approximation.

Letter symbols used in this work are defined in the text where they first appear and arranged alphabetically in Appendix B. All expressions given in this work consider a boulder positioned with the ac surface facing flow direction, as depicted in Figure 9.

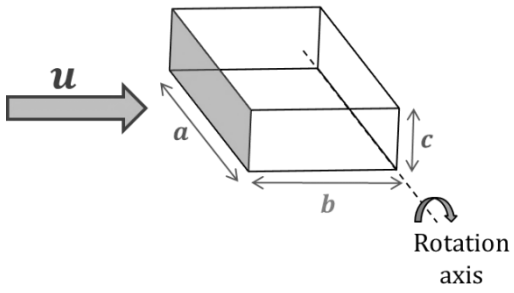

Figure 9: Boulder position relative to flow direction. Shaded boulder surface (comprising a and c axes) is directly exposed to a moving flow with velocity u

4.1 Empirical solutions

4.1.1 Hudson formula

Empirical approaches are based on experiments undertaken in flumes and in the field. Regarding the movement of large particles, the most known and commonly used empirical relationship is the Hudson formula. This formula is widely used in coastal engineering to determine the mass (M) of particles required to provide stability to rubble coastal defence structures for a given design wave height (U.S. Army Corps of Engineers, 1984), herewith resolved for wave height:

$$H = \sqrt[3]{\frac{MK_D\left(\frac{\rho_s}{\rho_w} - 1\right)^3 \cot\beta}{\rho_s}} \qquad \textbf{Equation 1}$$

Where H is the wave height, here represented by the design wave H_{10} (average of the highest 10% of all waves), as suggested by the U.S. Army Corps of Engineers (1984), β represents slope, ρ_s and ρ_w are rock and water mass density, respectively, and K_D is a dimensionless coefficient that depends on the armour unit shape, method of placement, location on the structure (head or trunk), and whether the incident wave breaks on the structure face or not (U.S. Army Corps of Engineers, 1984).

Conversion of H_{10} to significant wave height (H_s), assuming that a Rayleigh distribution adequately describes the distribution of water levels at high frequency

during a brief period of observations, uses the following expression, (U.S. Army Corps of Engineers, 2008):

$$H_{10} = 1.27H_s \qquad \textbf{Equation 2}$$

The slope parameter considered in the following computations corresponds to an approximate value, and is based on the vertical and horizontal distances from each boulder considered to the mean sea level (msl) contour line, and does not consider variations along pronouncedly stepped cross-shore profiles. It is thus an "equivalent slope" estimation. Moreover, the rough parallelepiped shape of most storm boulders used in this review chapter, and their location above mean sea level, has led to the use of the breaking wave parameter for angular quarrystone located in the head of the breakwater. Platform boulders, cliff-top boulders and boulder fields, observed in the accumulations described by Oliveira *et al.* (2011), Hall (2011), Goto *et al.* (2011) and Etienne and Paris (2010) were considered equivalent to an armour layer comprising a thickness of 2 units, while boulder beach and ridges, described by Etienne and Paris (2010), were considered as equivalent to > 3 units-thick armour layers. The U.S. Army Corps of Engineers (1984) advises the use of K_D values listed in Table VII for waves breaking on a structure with slopes ranging from 18° to 45°, given that some tests indicate a K_D-slope dependence.

Table VII: Suggested K_D values for use in determining armor unit weight for armour unit shape similar to a rough angular quarrystone. *comprising the thickness of the armour layer. From U.S. Army Corps of Engineers (1984)

UNIT	NUMBER OF UNITS*	HEAD	
		K_D	COT β
Rough angular quarrystone	2	1.9	1.5
		1.6	2.0
		1.3	3.0
	>3	2.1	-

The application of the Hudson formula to boulders with storm origin described in Appendix H, renders a broad range of results, represented in Figure 10. The application of this equation to a 13 300-kg boulder transported upward and landward between 1965 and 1975 in the western Portuguese rock coastline, and described by Oliveira *et al.* (2011), rendered significant wave heights of 4.4 m. This threshold is commonly observed and exceeded, and well below the H_s~13 m,

indicated as characterizing the 1973 storm waves that were responsible for transport and deposition of that particle.

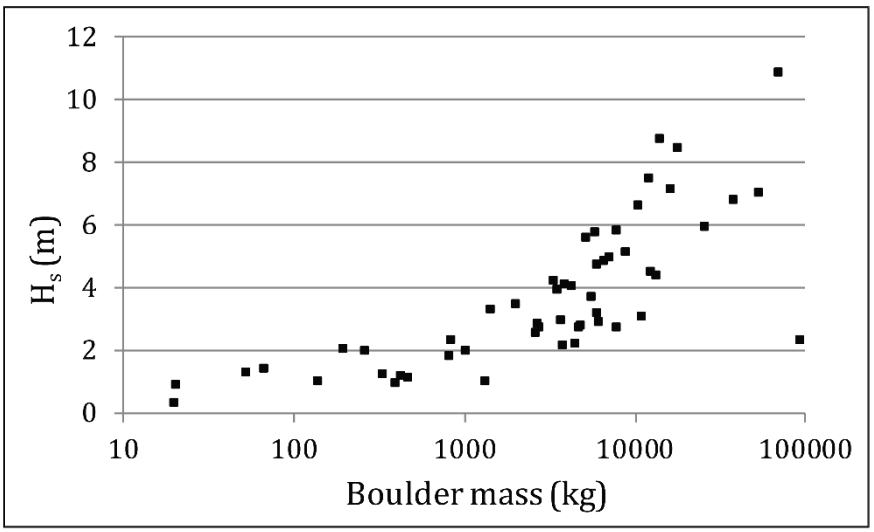

Figure 10: Scatter plot showing significant wave heights required to generate boulder movement based on the Hudson formula, against boulder mass, applied to particles in Appendix H

The heaviest boulder in the dataset corresponds to a 94 000-kg cliff-top boulder in Okinawa Island, Japan, which suffered inland transport during a typhoon in 1990 (Goto *et al.*, 2011). A significant threshold wave height of 2.3 m was obtained using the Hudson formula, which is much lower than the significant wave height of 9.2 m indicated for this typhoon (*cf.* Goto *et al.*, 2011).

Application of the Hudson formula to boulders transported during a storm on 30-03-2010 in Scotland, rendered significant wave heights of 2.0 m, which correspond to a maximum wave height (H_{max}) of about 3.3 m (considering roughly equal to $1.67H_s$), and this is compatible with recorded wave heights of 5.8 m (*cf.* Hall, 2011).

Finally, maximum significant wave heights reaching 10.8 m were obtained for the dataset corresponding to boulder deposits from Iceland, where H_s has exceeded 15 m (*cf.* Etienne and Paris, 2010).

Lower, but commonly observed, significant wave height values inferred from Hudson's formula are possibly related with two main causes: 1) inadequate parametrization of K_D values that was developed for slopes ranging from 18° to 45°, but applied, in this work, to case studies that mostly present lower slopes; 2) the development of the Hudson formula and K_D values consider only non-breaking and

breaking wave action, the forces produced by broken waves being usually negligible and not considered (U.S. Army Corps of Engineers, 1984). Therefore, significant wave heights obtained with the application of this equation corresponded, in this case, to waves breaking at a structure. Most storm boulders in the dataset were transported by waves which have broken at significant distances offshore from the original location of the boulders. Consequently, the application of the Hudson formula to boulder transport above mean sea level in rocky coastline contexts can result in underestimated threshold values of significant wave height.

4.1.2 van der Meer formulae

Other empirical formulas used in the evaluation of stability of breakwaters under wave attack are the van der Meer formulae, derived for both plunging and surging waves (van der Meer, 1988; 1998), here resolved for significant wave height:

Plunging: $$H_s = \left[6.2P^{0.18}\left(\frac{S}{\sqrt{N}}\right)^{0.2}\Delta D_n(\tan\beta)^{\frac{-1}{2}}\left(\frac{2\pi}{gT_m{}^2}\right)^{\frac{1}{4}}\right]^{4/3}$$ **Equation 3**

Surging: $$H_s = \left[P^{-0.13}\left(\frac{S}{\sqrt{N}}\right)^{0.2}\Delta D_n(\tan\beta)^{P-\frac{1}{2}}\left(\frac{2\pi}{gT_m{}^2}\right)^{\frac{-P}{2}}\right]^{1/1.05}$$ **Equation 4**

Where Δ represents the relative buoyant mass density;· D_n is the nominal diameter; P is the notional permeability factor; S assesses the damage level; N is the number of waves; T_m is the average zero up-crossing wave period (variables described in detail in Appendix C). The slope (β) considered in these computations was based on the vertical and horizontal distances from each boulder to the msl contour line, and does not consider slope variations along pronouncedly stepped cross-shore profiles.

The damage level S is defined by (van der Meer, 1988; 1998):

$$S = \frac{A_e}{D_n{}^2}$$ **Equation 5**

where A_e represents the cross-sectional eroded area.

One major contribution of these formulas is the incorporation of wave period, but assumptions must be made regarding the number of waves (N) and initial position

of the boulder to calculate the damage level (S). In this work, and following Reeve *et al.* (2004), the number of waves corresponding to a 3-hour storm duration was considered, and the cross-sectional eroded area used corresponds to the product of the boulder's *b* and *c*-axes.

The van der Meer formulas were applied to boulders with storm origin described in Appendix H with the exception of cases in where computed variables fell outside the range of application of the formulas (defined in Table XXIX of Appendix C). Moreover, wave periods used in the computations correspond to maximum values, yielding values for N within the range of application of the van der Meer formulas (between 1000 and 7500), considering a 3-hour storm duration.

Significant wave heights obtained with the application of the van der Meer formulae to known storm boulder deposits are presented in Figure 11 and predict low H_s values (< 7 m), when compared with the wave heights observed during the events responsible for their transport: H_s of 5.6-6.3 m *vs* the 13 m-high storm waves described by Oliveira *et al.* (2011); 2.1-2.3 m *vs* the 9.2 m-high waves generated by a typhoon described by Goto *et al.* (2011).

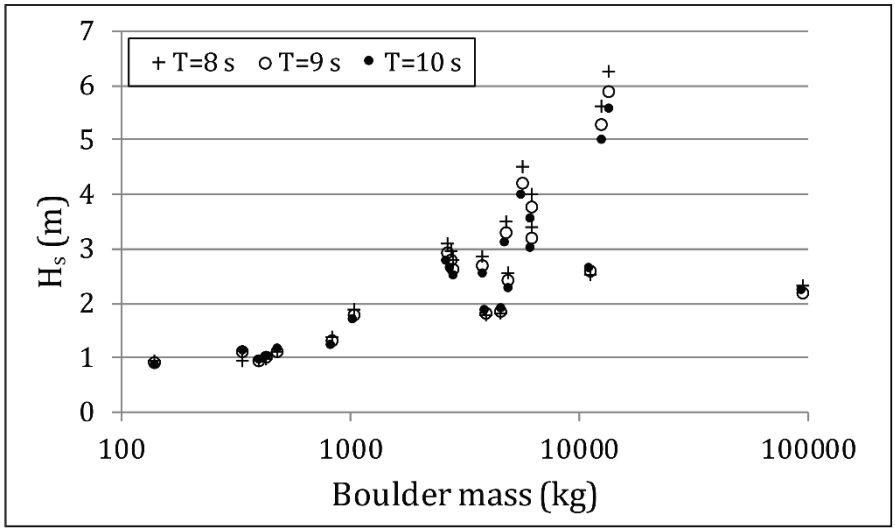

Figure 11: Significant wave heights of waves required to generate boulder movement, based on the van der Meer formula for plunging and surging waves applied to some of the boulders transported by storms listed in Appendix H

The stability equations by van der Meer presented above were developed for deep water wave conditions at the toe of the structure (van der Meer, 1998). Therefore, significant wave heights obtained with the application of the van der Meer formulas to transport boulders sitting above mean sea level in rocky coastline contexts, by

broken waves, underestimate the threshold values of H_s required to displace these particles.

4.2 Force/moment/energy balance equations

4.2.1 Nott's equations

Massel and Done (1993) modelled the forces induced by broken and unbroken storm waves acting on submerged corals at the Great Barrier Reef (East coast of Australia). Furthermore, the authors deduced an equation based on the balance of moments generated by a wave passing over weakly attached or detached coral colonies, allowing to compute the flow velocities necessary to originate rotation of coral-particles around a pivot point. Nott (1997) simplified and adapted these expressions to calculate flow velocities necessary to originate overturning of a submerged boulder and Nott (2003) changed these equations to also consider sub-aerial and joint-bounded-block boulder scenarios.

The expressions presented below were deduced based on Nott's (1997; 2003) conceptual model. However, they present differences when compared to these in the original works. Changes mainly reflect different initial boulder position relative to flow direction (Figure 9) and, consequently, different axes considered in the definition of forces and moments, as well as corrections to irregularities detected in the original work, some already detected by Benner *et al*. (2010) and Nandasena *et al*. (2011a). Moreover, boulder volume, needed for the computation of restraint and inertia forces, and frequently included in the balance equations as the product of the a, b and c axes, was maintained as an independent variable.

Boulders will overturn when moments of forces with horizontal component are equal or larger than those with vertical component (Massel and Done, 1993). Based on Nott's reasoning, the forces to be taken in consideration depend on the initial scenario (submerged, sub-aerial or joint-bounded block) (Figure 12) resulting in three balance equations.

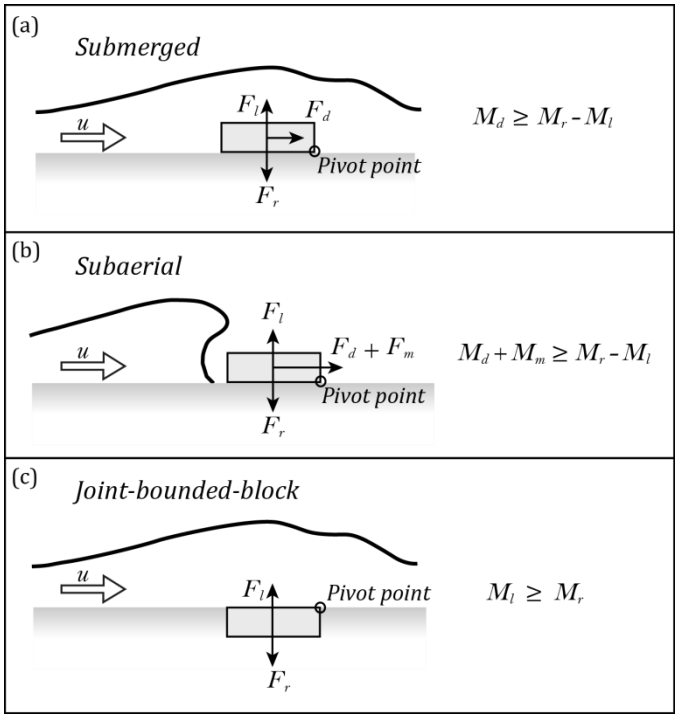

Figure 12: Forces acting on a boulder in different initial scenarios as defined by Nott (1997; 2003) and corrected expressions representing the balance of moments for an overturning boulder

Substituting moments of forces in the balance equations for the three scenarios above (Equation 45 through Equation 52, deduced in Appendix D), and resolving for u, leads to flow velocities necessary to overturn a boulder positioned as exemplified in Figure 9, according to expressions presented in Table VIII.

Table VIII: Corrected expressions for computing flow velocities required to generate boulder overturning in distinct initial as scenarios defined by Nott (1997; 2003)

SCENARIO	FLOW VELOCITY
SUBMERGED	$u \geq \sqrt{\frac{2\left(\frac{\rho_s - \rho_w}{\rho_w}\right) V g \frac{b}{a}}{C_d c^2 + C_l b^2}}$
SUB-AERIAL	$u \geq \sqrt{\frac{2V\left[\left(\frac{\rho_s - \rho_w}{\rho_w}\right) g \frac{b}{a} - C_m \ddot{u} \frac{c}{a}\right]}{C_d c^2 + C_l b^2}}$
JOINT-BOUNDED	$u \geq \sqrt{\frac{2\left(\frac{\rho_s - \rho_w}{\rho_w}\right) V g}{C_l a b}}$

In these formulas ρ_w and ρ_s are fluid and boulder mass density respectively, V is boulder volume; b and c represent the intermediate and the smallest boulder axis, respectively; C_d, C_l, and C_m (taken as 2, 0.178 and 1-2, respectively) represent the drag, lift and mass coefficients, respectively; g represents the gravitational acceleration, $\ddot{u}$ the instantaneous flow acceleration (taken as 1 m·s^{-2}) and u the average flow velocity.

Flow velocities used in the computation of drag correspond to depth-averaged values, whereas lift is computed using near-bottom velocities (Nott, 2003). However, the turbulent nature of flow induced by a storm wave during and after breaking, as well as that of a tsunami wave, generate minimum differences between average and near-bottom velocities, and, for simplification purposes, they can be considered equal in magnitude (Nott, 2003).

Threshold flow velocities required to generate boulder overturning were applied to boulder deposits described in Appendix H. Results indicate minimum differences between the submerged and subaerial scenarios (Figure 13). The latter yielded slightly lower velocities due to the incorporation of inertia moment in the balance equation. In both the submerged and subaerial case scenarios, and for boulders with mass under 1000 kg, overturning occurs when flow velocities are under 4 m·s^{-1}. For heavier boulders (mass>10 ton) flow velocities of 4-8 m·s^{-1} are required to generate overturning.

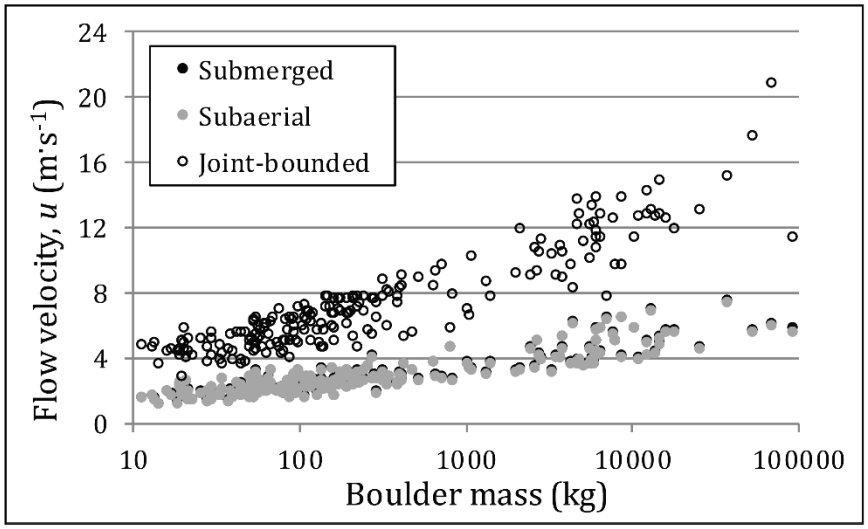

Figure 13: Comparison between flow velocities obtained for different scenarios, based on Nott's approximation (submerged, subaerial and joint bounded boulder), and applied to boulders and cobbles listed in Appendix H

Transport of joint bounded boulders requires much larger (more than double) flow velocities due to the absence of drag. In this scenario, boulders with mass under 1000 kg require flow velocities between 4 m·s^{-1} and 10 m·s^{-1}, and heavier boulders (mass>10 ton) require flow velocities above 11 m·s^{-1}, reaching values as high as 21 m·s^{-1}.

For the conversion of flow velocity into tsunami wave height, Nott (1997) uses the following expression (Camfield, 1980):

$$u = 2\sqrt{gH_t} \qquad \textbf{Equation 6}$$

Where H_t represents tsunami wave height.

In the case of storm waves, Nott (1997) used the following approximation for mean horizontal velocity in broken storm waves suggested, by experimental studies of Hedges and Kirgoz (1981 in Massel and Done, 1993):

$$u \approx 0.5\sqrt{gH_{storm}} \qquad \textbf{Equation 7}$$

Where H_{storm} represents storm wave height. Later, Nott (2003) used a different expression, which renders maximum values for mean flow velocity, and only applies when the wave commences to break and transport of boulders is initiated:

$$u = \sqrt{gH_{storm}} \qquad \textbf{Equation 8}$$

Nott (2003) discouraged the use of Equation 7 stating that it does not hold in the surf zone, where boulder transport occurs.

Following the application of these equations, submerged boulders with mass under 1000 kg would overturn when acted by a current with velocity slightly under 4 m·s^{-1} generated by a 6.5 m broken storm wave, a 1.6 m breaking wave and a 0.4 m tsunami wave (Figure 14). These values increase to 14.6 m (broken storm wave), 3.7 m (breaking storm wave) and 0.9 m (tsunami wave), when considering boulders with mass ~10 ton and average critical flow velocities of 6 m·s^{-1}.

Overturning of the lightest joint bounded boulders (< 1000 kg) requires broken storm waves with heights mostly between 6.5 m and 41 m, breaking waves with heights between 1.6 m and 10 m and 0.4-2.5 m-high tsunami waves. Maximum

velocities of 21 m·s^{-1}, required for overturning the heaviest boulders, are generated by 180 m-high broken waves, 45 m-high breaking waves and tsunami waves higher than 11 m. Given that all storm boulders used in this review are located above msl, the conversion into broken wave height is considered more adequate. Storm wave heights inferred considering the joint-bounded boulder scenario are unrealistic, surpassing the highest ocean wave ever measured of 33.5 m (*cf*. Whitemarsh, 1934 in Denny *et al*., 2003). Moreover, boulder accumulations used in this chapter, and described in Appendix H, do not comprise joint-bounded particles, therefore, the conversion to tsunami and storm wave heights was excluded for this scenario.

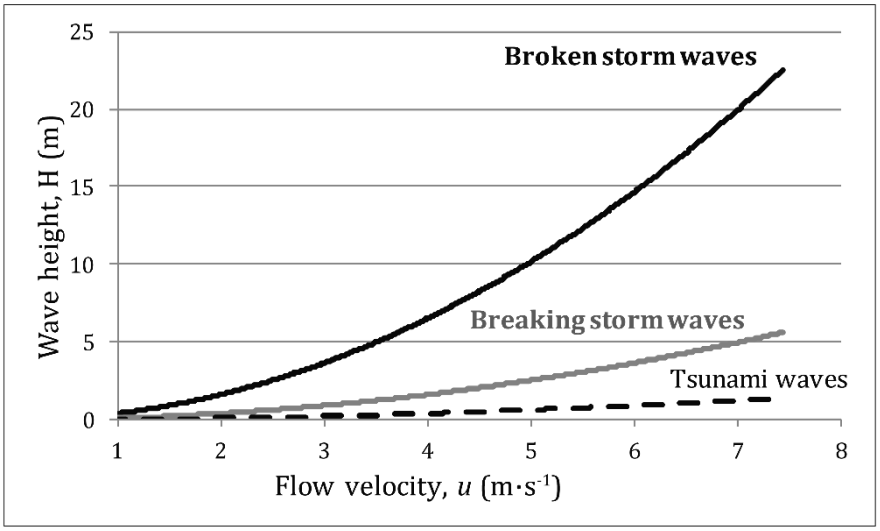

Figure 14: Comparison between computed storm and tsunami wave heights

Wave heights required to generate boulder overturning by a tsunami are smaller than 1 m for all the tested tsunami deposits (Figure 15). Large discrepancies between required (computed) and observed tsunami wave heights in the cases addressed here (observed tsunami wave height of 10 m in relation with the *AD* 1755 and 2004 IO tsunamis) are attributed to particle size limitations instead of wave capability to generate transport. A wide range of computed storm wave heights can be observed, with minimum values of 1.5 m (H_s of 0.9 m), especially for cases where all boulder data was considered, not only the largest particles. These wave heights are very common in all the locations contemplated in this review, and if results are true, boulder transport by storms should be an everyday occurrence.

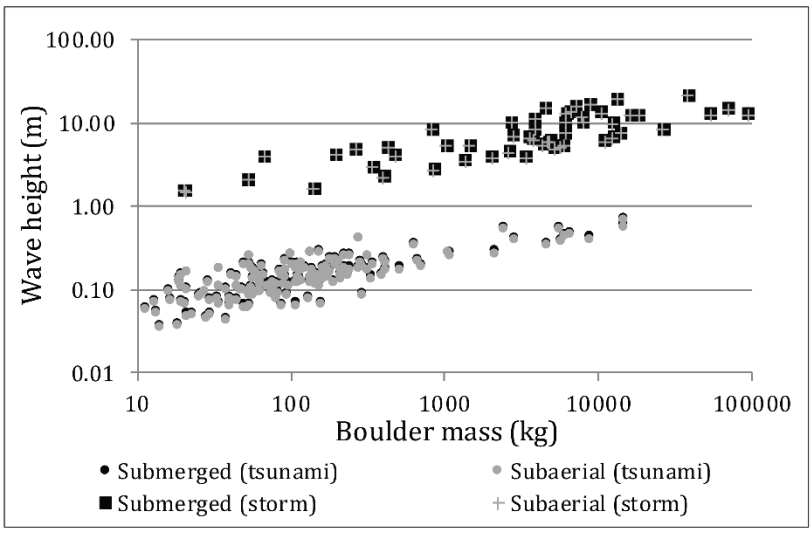

Figure 15: Tsunami and storm wave heights computed for storm and tsunami boulder deposits considering the submerged and subaerial boulder scenarios

Validation of Nott's equations using known recent case studies of submerged and subaerial boulders in Oliveira *et al.* (2011) rendered threshold storm wave height of 19.2-19.8 m, which agrees with modelled maximum wave heights of 22.1 m of the storm indicated as responsible for the transport of that boulder (*cf.* Oliveira *et al.*, 2011). The cliff-top boulder described by Goto *et al.* (2011) would require a broken wave height of 12.3-13.8 m, which is compatible with a maximum wave height of 15.4 m (recorded H_s of 9.2 m). Wave heights necessary to generate transport of the largest platform boulders described by Hall (2011) reach 4.8-4.9 m, also compatible with maximum recorded wave heights for the storm, of 5.8 m. Finally, maximum wave heights of 22.5 m were obtained for the largest boulders located in Iceland, which is somewhat below H_{max} of 25 m, corresponding to significant wave heights of 15 m and recorded in the North Atlantic Ocean (Etienne and Paris, 2010), taking $H_{max} \approx 1.67 H_s$ (*cf.* U.S. Army Corps of Engineers, 2008).

4.2.2 Hansom's et al. equations

Hansom *et al.* (2008) used a balance of forces/moments approach and considered four different modes of transport (Figure 16): 1) sliding over an unobstructed surface; 2) rolling over a low obstacle; 3) rolling over a high obstacle; and 4) extraction of a cliff-top boulder by a bore.

Based on measurements of wind flow over buildings, Hansom *et al.* (2008) applied corrections to drag and lift coefficients, as well as to the axis and consequently to the

surface areas subject to flow, which vary with mode of transport and boulder orientation. The equations presented in this work pertain to a boulder with a-axis normal to flow direction (Figure 9).

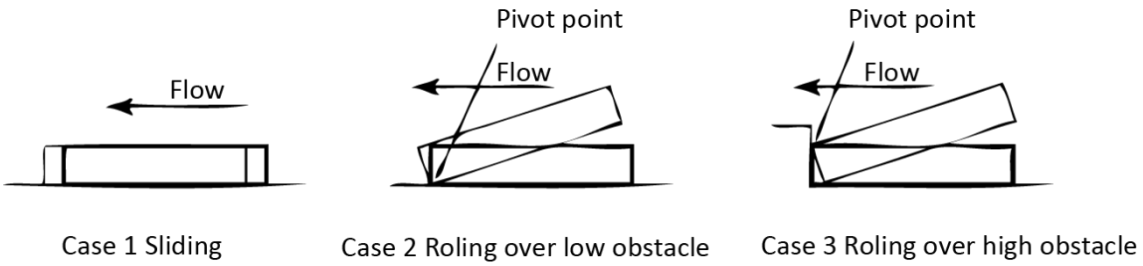

Figure 16: Modes of transport defined by Hansom *et al.* (2008). Modified after Hansom *et al.* (2008)

Due to larger velocities near the leading edge of the particle, derived from recirculation affecting a length of $c/2$, adjustments to pressure coefficients were made by the definition of two lift coefficients (C_{l_1} and C_{l_2}) (Figure 17).

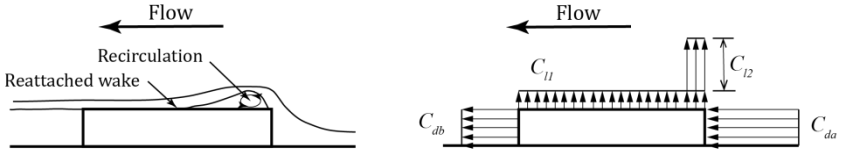

Figure 17: Flow circulation around the boulder and effects in pressure coefficients. Modified from Hansom *et al.* (2008)

Due to three dimensional flows that occur over the boulder, Hansom *et al.* (2008) suggested a correction to the a axis and included information regarding the width of the boulder:

$$a' = a - \frac{b}{2} \qquad \textbf{Equation 9}$$

Including the corrections suggested by Hansom *et al.* (2008) in the computation of drag and lift forces yields:

$$F_d = \frac{1}{2}\rho_w C_d (a'c) u^2 \qquad \textbf{Equation 10}$$

$$F_l = \frac{1}{2}\rho_w a' \left(bC_{l_1} + \frac{c}{2}C_{l_2}\right) u^2 \qquad \textbf{Equation 11}$$

For sliding, boulder movement will occur when the drag force is greater than or equal to the frictional force (F_f) (Hansom *et al.*, 2008):

$$F_d \geq F_f \qquad \textbf{Equation 12}$$

and

$$F_f = \mu(F_r - F_l) \qquad \textbf{Equation 13}$$

where μ is the coefficient of static friction (Nandasena *et al.*, 2011a).

In the case of a boulder rolling over a low obstacle, transport occurs when drag and lift overturning moments exceed the moment of restraint, similarly to the submerged boulder case defined by Nott (2003). In the case of a boulder rolling over a high obstacle, the balance of moments is identical to the preceding case, but a reduction of the drag force to 60% is included, because it acts only on the upstream face, and the block now must pivot about its top. Finally, for extraction of a cliff-top boulder, the authors equate this scenario with sliding, but remove lift and reduce drag to an indicative value of about 40%.

Resolving for u, yields the expressions presented in Table IX. Again, there are some differences between these expressions and those originally presented by the authors. In the first and fourth case scenarios (sliding and extraction of a cliff-top boulder) the authors excluded the friction coefficient from the final equation and in the third case (rolling over a high obstacle) the drag force was multiplied by -0.6, which will result, at times, in negative square roots making it impossible to calculate flow velocity. Furthermore, the final expressions for rolling over low and high obstacles, deduced from the descriptions given in Hansom *et al.* (2008), present additional differences to those presented in the author's original work. As in previous approximations, boulder volume was maintained as an independent variable in the final expressions.

The coefficients suggested by Hansom *et al.* (2008), are $C_d = 1.8$ for a boulder positioned perpendicularly to flow direction and $C_{l_1} = 0.1$ and $C_{l_2} = 0.8$. Regarding the friction coefficient (μ) the authors do not attribute a specific value; however, to achieve identical results to those presented in the cited work, a value of 0.7 must be assumed.

Table IX: Corrected flow velocity expressions obtained for different transport scenarios defined by Hansom *et al.* (2008) and modified expression for rolling over a high obstacle

MODE OF TRANSPORT	FLOW VELOCITY
SLIDING	$u \geq \sqrt{\frac{2\mu\left(\frac{\rho_s - \rho_w}{\rho_w}\right)Vg}{a'\left[cC_d + \mu\left(bCl_1 + \frac{c}{2}Cl_2\right)\right]}}$
ROLLING OVER A LOW OBSTACLE	$u = \sqrt{\frac{2\left(\frac{\rho_s - \rho_w}{\rho_w}\right)Vgb}{a'\left(C_d c^2 + C_{l_l} b^2 + C_{l_2}\frac{bc}{2}\right)}}$
ROLLING OVER A HIGH OBSTACLE	$u = \sqrt{\frac{2\left(\frac{\rho_s - \rho_w}{\rho_w}\right)Vgb}{a'\left(0.6C_d c^2 + C_{l_l} b^2 + C_{l_2}\frac{bc}{2}\right)}}$
EXTRACTION OF A CLIFF-TOP BOULDER	$u \geq \sqrt{\frac{2\mu\left(\frac{\rho_s - \rho_w}{\rho_w}\right)Vg}{0.4C_d a' c}}$

Hansom's *et al.* (2008) equations were differently applied to particles, depending on the preferable mode of transport interpreted from descriptions in the original work, as specified in Appendix H. Results show that sliding is the mode of boulder transport that requires less energy, followed by rolling over a small obstacle, rolling over a large obstacle and, finally, extraction of a cliff-top boulder (Figure 18a). Boulders with mass <1000 kg, roll over a small obstacle (overturn) when flow velocities reach 4-6 m·s^{-1}, and boulders with mass ~10 ton will overturn when u~5-9.7 m·s^{-1}.

Conversion of flow velocity in tsunami wave height for larger boulders resulting from tsunami inundations described in Appendix H indicate a critical tsunami wave height of 1.3 m to induce transport by overturning over a high obstacle (Figure 18b). Again, these results are well below observed tsunami heights for most case studies.

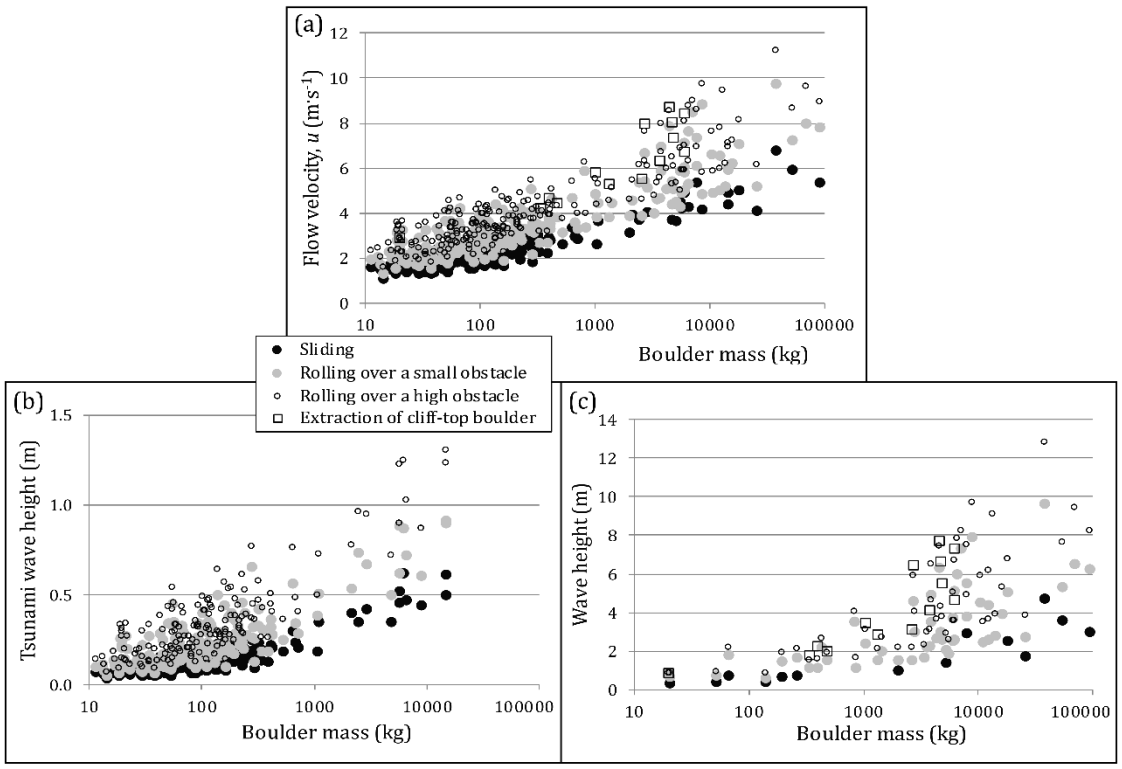

Figure 18: Scatter plots showing boulder mass against flow velocity/wave height obtained for different modes of transport according to Hansom *et al.* (2008) and applied to boulders and cobbles listed in Appendix H: (a) flow velocity; (b) tsunami wave height; (c) wind wave height following Hansom *et al.* (2008) suggestions

For incident waves overtopping the cliff edge, and based on flume experiments, Hansom *et al.* (2008) suggested an indicative conversion of flow velocity into storm wave height equal to the one reported in Nott (2003) for a breaking wave (Equation 8). Application of this conversion to the largest boulders listed in Appendix H indicates critical wave heights of 12.8 m and 9.6 m needed to roll the largest boulders over a large and a small obstacle, respectively; 7.7 m to extract them from a cliff-top and 4.7 m to move them by sliding, selectively applied to different boulder accumulations according to their context (Figure 18c). In some cases, especially for smaller boulders, wave heights obtained were as low as 0.6-1 m, regardless of the mode of transport considered.

The specific case study described by Oliveira *et al.* (2011), refers to a boulder transported up-slope 1 m, previously located on the edge of the structural platform and ending up over it, in an upside-down position, which is equivalent to a boulder rolling over a large obstacle. The application of the approximations suggested by Hansom *et al.* (2008) results in a storm wave height of 9.1 m (H_s of 5.5 m), which is relatively frequent offshore the Portuguese W coastline.

The transport of a 94-ton boulder horizontally on the top of a 15-m cliff, approximately 3 m inland, described by Goto *et al*. (2011), most likely occurred by sliding or rolling over a small obstacle. This corresponds to relatively low wave heights ranging from 2.9 m to 6.2 m (H_s of 1.7 m and 3.7 m, when compared to observed H_s of 9.2 m) (Figure 18d).

Transport of boulders over a shore platform (at ~1 m amsl) described by Hall (2011) most probably occurred by sliding or rolling over small obstacles. Application of the approximations suggested by Hansom *et al*. (2008) resulted in wave heights of 0.7-1.8 m (Figure 18d), which correspond to low significant wave heights of 0.4-1.1 m when compared to maximum observed wave heights for that storm (H_{max} of 5.8 m).

4.2.3 Nandasena's et al. equations

Nandasena *et al*. (2011a) used balance equations for submerged/subaerial and joint-bounded boulders, and considered sliding, rolling and saltation transport modes. Furthermore, they included slope in the balance equations, by decomposing the forces involved in x and y components, allowing to consider boulders sitting on an inclined plane (equations deduced in Appendix E).

Resolving the equations for velocity in all case scenarios (sliding, rolling and saltation for submerged and subaerial boulders and saltation for joint-bounded boulders) yields the expressions presented in Table XI. As in previous approximations, boulder volume was maintained as an independent variable. The coefficients suggested by Nandasena *et al.* (2011a) were $C_d = 2$, $C_l = 0.18$ and μ, which represents the coefficient of static friction, taken as 0.7.

Application to the boulder accumulations described in Appendix H renders different critical flow velocities, depending on the mode of transport (Figure 19). Sliding is the mode of transport requiring less energy and flow velocity, followed by rolling and by saltation. Boulders with mass under 1000 kg require flow velocities just under 3 $m \cdot s^{-1}$ to initiate sliding, of 4.7 $m \cdot s^{-1}$ for rolling and 9.7 $m \cdot s^{-1}$ to be transported by saltation. Heavier boulders, with mass above 10 ton are transported by sliding,

rolling and saltation when flow velocities fall within 3.5-5.4 m·s^{-1}, 4.3-7.6 m·s^{-1} and 11-20.8 m·s^{-1}intervals, respectively.

Table X: Flow velocity expressions obtained for the different scenarios defined by Nandasena *et al.* (2011a)

SCENARIO	MODE OF TRANSPORT	FLOW VELOCITY EXPRESSIONS
SUBMERGED AND SUBAERIAL	SLIDING	$u \geq \sqrt{\frac{2\left(\frac{\rho_s - \rho_w}{\rho_w}\right) Vg(\mu \cos\beta + \sin\beta)}{a(C_d c + \mu C_l b)}}$
	ROLLING	$u \geq \sqrt{\frac{2\left(\frac{\rho_s - \rho_w}{\rho_w}\right) Vg[b \cos\beta + c \sin\beta]}{a(C_d c^2 + C_l b^2)}}$
	SALTATION	$u \geq \sqrt{\frac{2\left(\frac{\rho_s - \rho_w}{\rho_w}\right) Vg \cos\beta}{abC_l}}$
JOINT-BOUNDED	SALTATION	$u \geq \sqrt{\frac{2\left(\frac{\rho_s - \rho_w}{\rho_w}\right) Vg(\cos\beta + \mu \sin\beta)}{abCl}}$

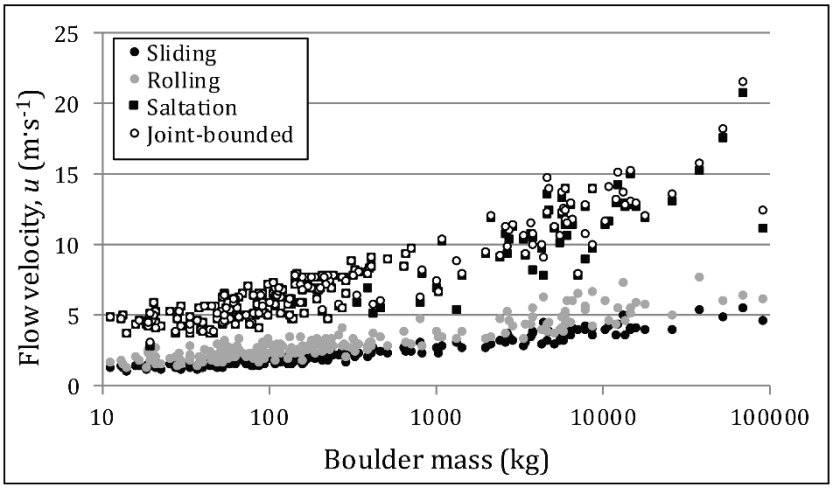

Figure 19: Comparison between flow velocities obtained for modes of transport (sliding, rolling, saltation and saltation when joint-bounded) and applied to boulders and cobbles listed in Appendix H

Saltation of a boulder lying on a plane and saltation of a joint-bounded boulder require similar critical flow velocities, because both modes of transport are essentially governed by forces with relevant vertical components (lift and restrain forces) (see Appendix E for details). The inclusion of friction force in the balance equation does not generate significant differences in most tested cases.

Nandasena *et al.* (2011a) further devised a plot (the boulder transport histogram) containing information regarding all modes of transport for each boulder. In general, boulders and cobbles attributed to tsunami inundations (fields 1, 2 and 3 in Figure 20) need lower flow velocities to be transported than those attributed to storms (fields 4, 5 and 6 in Figure 20). This is considered a coincidence due to smaller boulders in tsunami-related deposits in data-sets available in the bibliography.

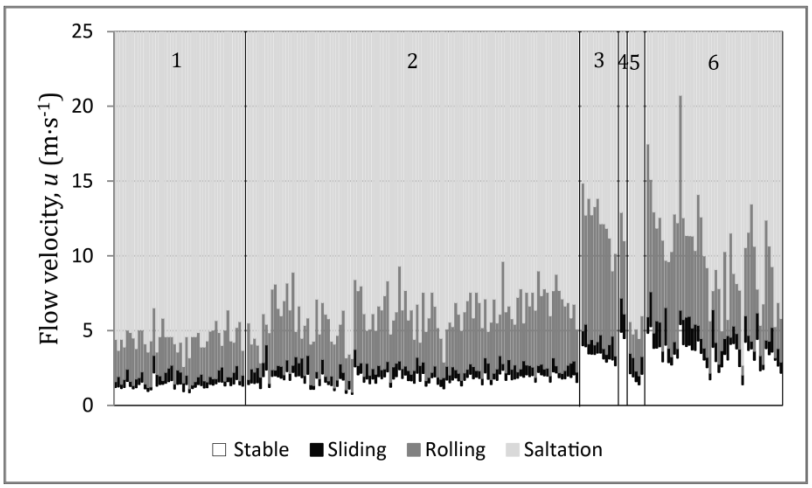

Figure 20: Boulder transport histogram containing boulder data listed in Appendix H: 1- data from Costa *et al.* (2011); 2-data from Spiske and Bahlburg (2011); 3- data from Nandasena *et al.* (2011b); 4- data from Oliveira *et al.* (2011) and Goto *et al.* (2011); 5-data from Hall (2011); 6- data from Etienne and Paris (2010)

4.2.4 Noormets' et al. equations

Noormets *et al.* (2004) computed hydrodynamic forces using linear wave theory and empirical relationships between pressure exerted on vertical walls, wave height and water depth. Computations were applied to a case study in Oahu, Hawaii, comprising a shore platform limited seaward by a submerged cliff, developing from mean sea level to a depth of approximately 10 m. They defined balances of forces/moments generated by waves in three stages of movement of a wedge-shaped boulder: dislodgement, emplacement and transport. Moreover, they distinguish breaking from broken swell waves and from tsunami waves using different empirical

relationships involving the estimate of pressure acting on the cliff-face. Boulder dislodgement and entrainment are not described in detail in this review due to specificities associated with the approximations, presented below.

According to Noormets *et al.* (2004), dislodgement is partially controlled by the existence of pre-impact fractures surrounding the boulder, and for that reason, additional forces acting on the lower fracture plane are needed to adequately describe this occurrence. This approach is unique in the bibliography; however, some clarification regarding the computation of these forces is needed to adequately replicate the results presented by the authors.

In what regards boulder entrainment, the balance equation presented by Noormets *et al.* (2004) is valid exclusively for wedge-shaped boulders, and cannot be applied to the boulder dataset being used herein.

Balance equations for boulder transport by sliding and rolling, described by Noormets *et al.* (2004), can be applied to the boulder dataset addressed in this study and are described henceforth. In the case of sliding, the balance of forces can be expressed by Equation 14; in the case of rolling, the balance of moments is described by Equation 15 (Noormets *et al.*, 2004):

$$F_d + F_l + F_m = F_r \qquad \textbf{Equation 14}$$

$$M_d + M_l + M_m = M_r \qquad \textbf{Equation 15}$$

To obtain the flow velocity necessary to generate boulder emplacement and transport (by sliding and rolling) as defined by Noormets *et al.* (2004), balance equations were resolved in order of u and final expressions are presented in Table XI. As for the remaining numerical solutions, boulder volume was maintained as an independent variable in the final expressions.

The expression describing transport by rolling is equal to that of Nott's equations for the overturning of a subaerial boulder. Noormets *et al.* (2004) advise the use of a lift coefficient (C_l) of 0.178, a mass (or inertia) coefficient (C_m) of 2, fluid acceleration ($\ddot{u}$) of 1 m·s^{-2} and drag coefficient (C'_d) extracted visually from a graph presented by Helley (1969) relating drag coefficient of particles resting on a bed with shape factor for turbulent flow.

Table XI: Flow velocity expressions for sliding and rolling based on balance equations defined by Noormets *et al.* (2004)

MODE OF TRANSPORT	FLOW VELOCITY
SLIDING	$u = \sqrt{\frac{2\,V\left[\left(\frac{\rho_s - \rho_w}{\rho_w}\right) g - C_i \ddot{u}\right]}{C'_d\, ac + C_l\, ab}}$
ROLLING	$u = \sqrt{\frac{2\,V\left[\left(\frac{\rho_s - \rho_w}{\rho_w}\right) gb - C_i \ddot{u} c\right]}{C'_d\, ac^2 + C_l ab^2}}$

Results obtained are presented in Figure 21 and show, in most cases, a small difference between velocities required to generate boulder movement by both modes of transport, indicating sliding as the easier mode of transport. Boulders with mass under 1000 kg and above 10 ton require flow velocities below 4.5 m·s^{-1} and of 4.3-11.8 m·s^{-1}, respectively, to be transported.

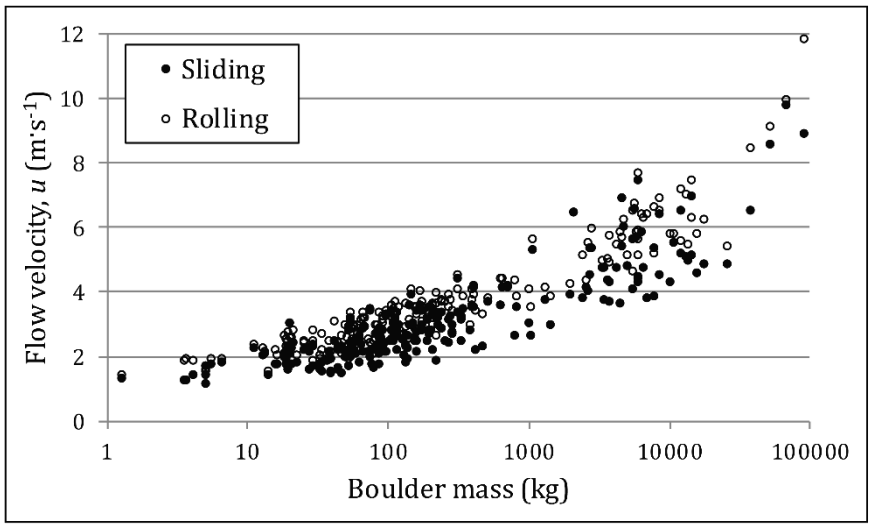

Figure 21: Comparison between flow velocities obtained for boulder sliding and rolling using Noormets *et al.* (2004) balance equations applied to particles listed in Appendix H

Another approach used by Noormets *et al.* (2004) accounts for height reduction due to turbulent energy dissipation of a bore propagating a given distance over the platform by using the following expression by (Cox and Machemehl, 1986), here solved for $[R_u - E]$:

$$R_u - E = \left(\sqrt{H} + \frac{5X}{T\sqrt{g}}\right)^2 \quad \textbf{Equation 16}$$

where $[R_u - E]$ represents the difference between run-up elevation (R_u) and revetment crest height (E) or bore height at the cliff, X represents the horizontal distance over the littoral platform, T is the wave period and H represents bore height as a function of X (Figure 22).

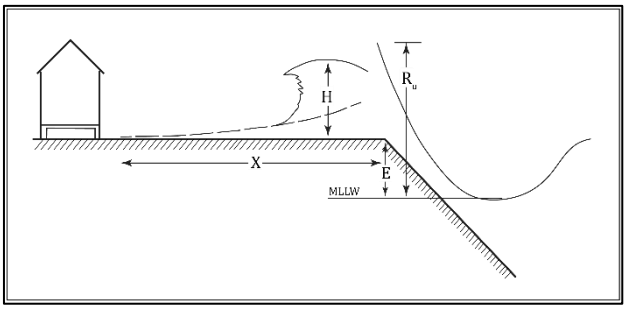

Figure 22: Definition sketch of wave overtopping a berm. MLLW stands for mean lower low water. Modified after Cox and Machemehl (1986)

Conversely, travelled distances can be calculated by resolving the same equation for X:

$$X = \frac{T\sqrt{g}\left(\sqrt{R_u - E} - \sqrt{H}\right)}{5} \quad \textbf{Equation 17}$$

When calculating height reduction of a bore due to turbulent energy dissipation, one can use wave heights and velocities occurring in the final stage of emplacement, when lift and inertia forces are not important, as the clast is no longer fully submerged and the flow is steady (Noormets *et al.*, 2004, Barbano *et al.*, 2011). In this case, boulder movement ceases when the fluid drag is equal or lower than net friction, F_μ, and the following equations apply (Noormets *et al.*, 2004):

$$F_\mu = \mu M g \quad \textbf{Equation 18}$$

$$F_d = \frac{1}{2} C_d \rho_w A_n u^2 \quad \textbf{Equation 19}$$

$$u = \left(\frac{2\mu M g}{C_d A_n \rho_w}\right)^{\frac{1}{2}} \quad \textbf{Equation 20}$$

Where A_n represents the area of the boulder directly exposed to the incoming flow.

It is possible to calculate flow velocity in the final stage of boulder transport by using Equation 20 and convert it to wave height by using Equation 6 to Equation 8. Based on this approach, Barbano *et al.* (2010; 2011) devised plots describing the attenuation of wave energy associated with specific events and boulder deposits. Such plots are exemplified in Figure 23, using the conversion of flow velocity into wave height of a broken wave as suggested in Hedges and Kirgoz (1981 in Massel and Done, 1993), and refer to cases described in Nandasena *et al.* (2011b), Costa *et al*. (2011), Oliveira *et al*. (2011) and Spiske and Bahlburg (2011).

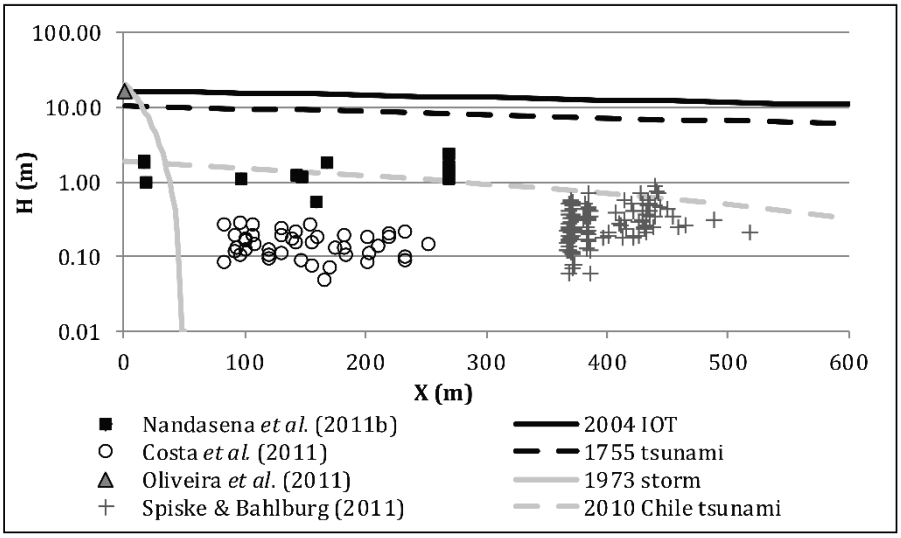

Figure 23: Attenuation curves for different events and attributed boulder deposits. Data regarding clasts is listed in Appendix H. Wave parameters used in the computation of attenuation curves for the 2004 IOT were extracted from Paris *et al*. (2009), for the *AD* 1755 tsunami from Lopes (1841), for the 2010 Chile tsunami from Bahlburg and Spiske (2012) and for the 1973 storm from Oliveira *et al*. (2011). For conversion of flow velocity into wave height for storms, a broken wave condition was assumed

The attenuation of wave height computed with Cox and Machemehl's (1986) expression agrees with velocities of broken storm and tsunami waves occurring in the final stage of boulder emplacement, in all case studies. The rapid attenuation of storm wave height exemplified by the 1973 storm contrast with the low attenuation associated with all tsunami waves, occurs due to differences in wave period.

4.2.5 Benner's et al. equations

Benner *et al.* (2010) suggested an approximation to boulder entrainment and transport based on the maximum force exerted by a wave as it strikes a sub-aerial boulder, by using the linear momentum equation and assuming that: (1) the boulder is positioned on a horizontal surface; (2) it is subject to a water flow with uniform

velocity at the *ac* boulder face (position depicted in Figure 9); and (3) the water mass is deflected perpendicularly to the boulder exposed face.

When the wave strikes, the net force exerted on the *ac* face of a static boulder can be expressed by the following expression (Benner *et al.*, 2010) (see Appendix F for formula derivation):

$$F = \rho_w acu^2 \qquad \textbf{Equation 21}$$

If the force acting on the boulder (F) is higher than the friction force (F_f), shifting (sliding) of the boulder will occur.

$$F_f = \mu F_g = \mu\, \rho_s V\, g \qquad \textbf{Equation 22}$$

The symbol μ represents the friction coefficient taken as 0.6 for bulk materials and 0.65-0.8 for concrete over gravel (according to Oumeraci, 2008 in Benner *et al.*, 2010).

For known flow velocities, boulder movement can be evaluated by comparing both forces. Additionally, by equating the forces defined above and resolving for u, flow velocities necessary to generate boulder movement can be estimated by using the following expression (Benner *et al.*, 2010):

$$u = \sqrt{\frac{\mu V g \rho_s}{ac\rho_w}} \qquad \textbf{Equation 23}$$

Flow velocities required to transport a boulder by sliding, obtained from the expression suggested by Benner *et al.* (2010) are mostly under 5.5 m·s^{-1} and reach 6.8 m·s^{-1} (Figure 24).

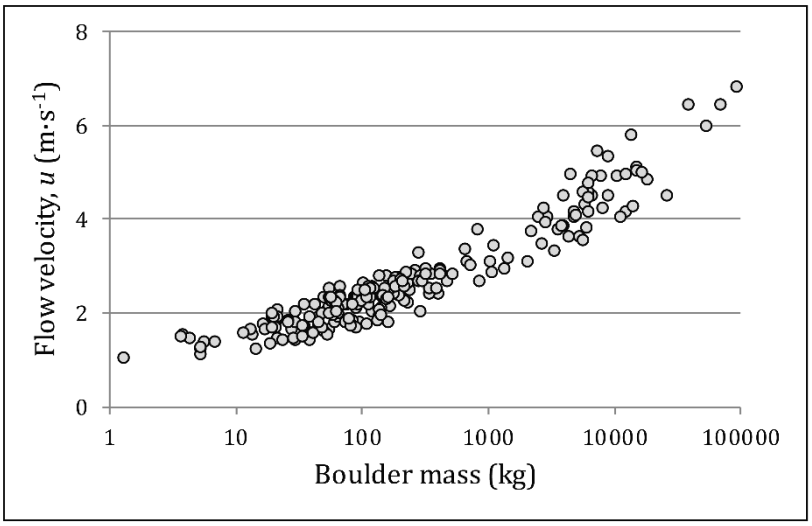

Figure 24: Flow velocities necessary to originate boulder movement by sliding based on linear momentum applied to boulders and cobbles listed in Appendix H

4.3 Wave competence approaches

In most approximations described above, boulder entrainment is predicted as a function of wave height and boulder characteristics. However, the ability to entrain boulders depends on wave competence and should be related not only to wave height but also to wave power (Lorang, 2000).

4.3.1 Benner's et al. equation

Benner *et al.* (2010) developed a set of equations to calculate maximum values for horizontal and vertical boulder transport distances based on conservation of energy principles (Equation 24):

$$\sum E_t = constant \qquad \textbf{Equation 24}$$

When a boulder is uplifted, wave energy (E_{wave}) transformed into "vertical energy" [*sic*] (E_{height}, relative to height) and, when a boulder is transported up-slope, energy loss occurs due to friction ($E_{friction}$) (Benner *et al.*, 2010):

$$E_{wave} = E_{height} + E_{friction} \qquad \textbf{Equation 25}$$

The authors presented alternatives to compute wave energy, one more adequate for tsunami waves (Equation 26, see Appendix F for formula derivation) and another for storm waves (Benner *et al.*, 2010) (Equation 27):

$$E_{tsunami\ wave} = \frac{1}{2}\rho_w acu^3 t$$ **Equation 26**

$$E_{storm\ wave} = \frac{1}{8}\rho_w g H^2 L$$ **Equation 27**

where ρ_w represents fluid mass density, a and c the largest and smallest boulder axes respectively, u is flow velocity, t time, g the acceleration of gravity, and H and L wave height and length, respectively.

To simplify calculations, the expression used to compute the tsunami energy assumes a constant velocity (u) over the whole wave period, and only the energy of a mass of water acting during that time-window upon the ac surface of the boulder is considered (Benner *et al.*, 2010).

Regarding the expression used to calculate the energy of a storm wave, the value obtained corresponds to the total wave energy in one wavelength per unit crest width (*cf.* U.S. Army Corps of Engineers, 2008).

Vertical energy and energy loss due to friction depend of distances travelled by the boulder and of its weight, which in turn depend of the scenario of submerged or subaerial boulder (Table XII, see Appendix F for formula derivation) (*cf.* Benner *et al.*, 2010).

Table XII: Expressions suggested by Benner *et al.* (2010) to calculate vertical energy and energy loss due to friction

SUBMERGED BOULDER	SUBAERIAL BOULDER
$E_{height} = V(\rho_s - \rho_w)g\Delta z$ $E_{friction} = \mu V(\rho_s - \rho_w)gX$	$E_{height} = V\rho_s g\Delta z$ $E_{friction} = \mu V\rho_s gX$

where V represents boulder volume, ρ_s boulder mass density, ρ_w fluid mass density, g is the acceleration due to gravity, Δz vertical distance traveled by the boulder, μ is a friction coefficient and X the upslope distance travelled by the boulder (Figure 25).

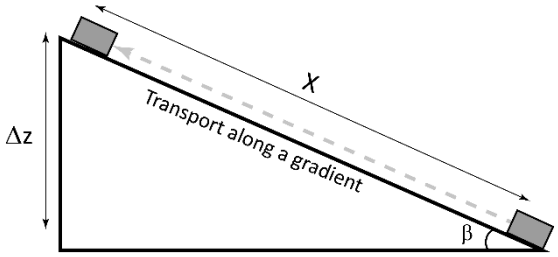

Figure 25: Schematic representation of boulder transport up a slope. Modified after Benner *et al.* (2010)

By substituting the expressions in Table XII in Equation 25, and resolving for Δz, it is possible to obtain maximum values for vertical transport distances in different initial scenarios, and considering different waves and slope angles, α.

For storm waves, Benner *et al.* (2010) further divided the boulder mass by boulder a-axis length (mass per 1 m edge length), so that the values obtained can be compared with total wave energy per unit crest width (Table XIII).

Table XIII: Expressions suggested by Benner *et al.* (2010) to calculate maximum vertical boulder transport for different scenarios and waves

CASE SCENARIO		MAXIMUM VERTICAL TRANSPORT
STORM WAVE	SUBMERGED BOULDER	$\Delta z = \frac{\rho_w H^2 L}{8\frac{V(\rho_s - \rho_w)}{a}\left(1 + \frac{\mu}{\sin\beta}\right)}$
	SUBAERIAL BOULDER	$\Delta z = \frac{\rho_w H^2 L}{8\frac{V\rho_s}{a}\left(1 + \frac{\mu}{\sin\beta}\right)}$
TSUNAMI WAVE	SUBMERGED BOULDER	$\Delta z = \frac{\rho_s acu^3 t}{2V(\rho_s - \rho_w)g\left(1 + \frac{\mu}{\sin\beta}\right)}$

Maximum horizontal travelled distances can be computed using the geometric relationship:

$$\sin\beta = \frac{\Delta Z}{X} \qquad \textbf{Equation 28}$$

The projection of measured against computed vertical and horizontal distances of boulder transport by known tsunamis and storms (Figure 26a, b) show that, for these case studies, Benner's *et al.* (2010) equations based on conservation of energy

render unrealistic results. In fact, Benner *et al.* (2010) emphasized that travelled distances correspond to theoretical maximum values and that real values may be assumed as roughly being half (or less) of the computed values. However, most values are much higher than double, in cases reaching more than 400 times the measured values in the boulders with tsunami origin (both vertical and horizontal distances) and reaching 99000 times and 63000 times (vertical and horizontal distances, respectively) in boulders of storm origin. Given these discrepancies, and without further testing, results obtained with this approximation are considered unreliable.

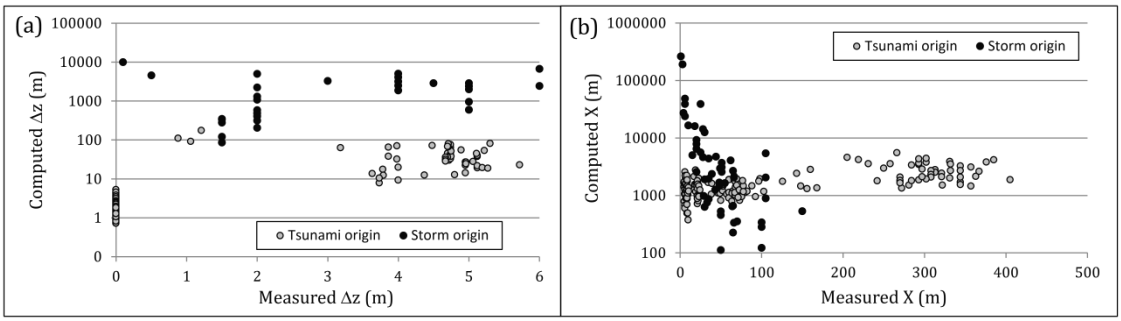

Figure 26: Comparison between measured and calculated vertical (a) and horizontal distances (b) by applying Benner's *et al.* (2010) expressions for a tsunami wave, lasting 300 s, and broken storms waves with a wave period of ~15 s (considering a subaerial boulder scenario), to the boulders and cobbles listed in Appendix H

4.3.2 Lorang's equations

Lorang (2011) forwarded a contribution to the debate on differentiating tsunami from storm boulder deposits, using a wave competence approach. He suggested the use of wave period instead of wave height as a differentiating variable, mainly because the difference between tsunami and storm wave period is at least of one order of magnitude.

For this purpose, Lorang (2011) used an expression derived in previous work (Lorang, 2002) to estimate the height of a boulder beach crest, solved for the wave period, coupled with wave height, estimated from other approximations, such as Nott's equations or the Hudson formula.

Following observations made by Bagnold (1940 in Lorang, 2002) regarding the formation of beach crests, Lorang (2002) concluded that, in a beach face, boulders

are transported in a mode of high saltation, not rolling, and that the elevation of the beach crest equals the height reached by swash surging up the beach face.

By equating the wave force acting on an individual particle with the immersed weight force, which describes the minimum critical threshold condition, and assuming that run-up equals the height of the beach crest (h_c), and solving for wave period, T, Lorang (2002; 2011) obtained the following expression (see Appendix G for formula derivation):

$$T = \frac{2}{g}\left(\frac{\rho_w}{\rho_s - \rho_w}\right)\left(\frac{C_d}{\tan\beta}\right)\left(\frac{h_c}{D_i}\right)U_{max} \qquad \textbf{Equation 29}$$

Where D_i is the intermediate particle diameter, U_{max} represents the maximum swash velocity and C_d represents the drag coefficient, which assumes a value of ~2 for large boulders and of 0.2 to 0.5 for cobbles and small boulders (Lorang, 2011). This equation allows estimating the wave period required to transport a specific boulder, thereby aiding in the differentiation between driving waves. Wind-generated waves of storm origin, are characterized by periods between 10 and 40 seconds, and tsunami waves by periods in the range of hours to tens of minutes (Lorang, 2011).

Maximum swash velocity is given by the shallow water wave equation, and considered by Lorang (2011) an appropriate estimator of swash/bore velocity for both storm and tsunami waves:

$$U_{max} = \sqrt{g(h_i + H_i)} \qquad \textbf{Equation 30}$$

where h_i represents water depth and H_i wave height.

Tsunamis and storms wave height (H_i) can be estimated using Nott's equations, or another formula deemed appropriate. Water depth for storm waves can be estimated using the breaking criteria for solitary waves (Lorang, 2011):

$$h_b = \frac{H_b}{0.78} \qquad \textbf{Equation 31}$$

where h_b refers to the water depth and H_b represents wave height at the breaking point.

Regarding the estimation of tsunami water depth, Lorang (2011) suggests a conservative approach by equating the inundation distance to the backwash, hence ignoring spreading and loss of water prior to the backwash. To estimate the backwash water depth, he used a flow competence approach developed for palaeoflood applications (Komar, 1989 in Lorang, 2011) and the Shields criterion. For a given threshold entrainment condition, the tsunami water depth during backwash can be crudely estimated by (Lorang, 2011):

$$h_t = \theta \left(\frac{\rho_s - \rho_w}{\rho_w}\right)\left(\frac{D_i}{S_e}\right) \qquad \textbf{Equation 32}$$

where $\theta = 0.03$ and S_e represents the energy gradient, assumed to be equal to the slope determined by the ratio of the boulder displacement height over the displacement distance (h_c/THD) (Lorang, 2011) (Figure 27).

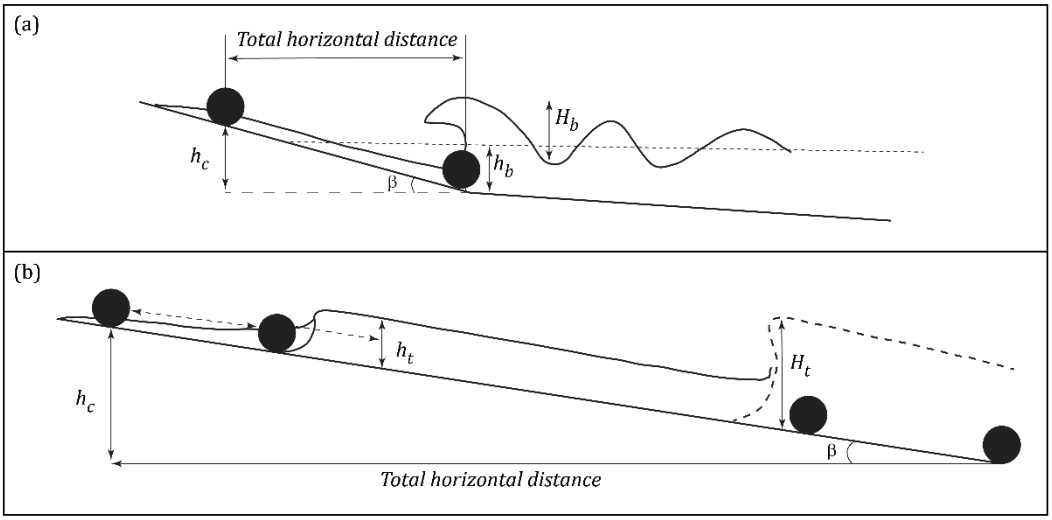

Figure 27: Conceptual model showing storm versus tsunami processes. (a) storm wave breaking on a boulder beach, entrainment, transport and deposition of a boulder by the wave breaking and swash, reaching an arbitrary total horizontal distance (THD) and elevation h_c above and inland its original position; (b) boulder entrainment due to a tsunami-generated swash bore and boulder deposition at an elevation h_c and total horizontal distance above and inland of its original position. Modified after Lorang (2011)

This wave competence approach considers not only the size and density of displaced boulders, but also the distance and height of displacement, whenever the initial location of the particle entrained can be determined, which must be ascertained during field work.

Lorang (2011) emphasizes the use of these equations as rough estimators, helping in the determination of likelihood of one causal mechanism over the other (storms *vs*

tsunamis) and that the use of Equation 29 as a diagnostic tool is only possible due to the significant difference between wave periods. Additionally, the author suggests that results should be interpreted together with other pieces of information gained from stratigraphy, imbrication, and morphology of boulder deposits, as well as data collected from age estimation techniques, allowing for time correlation with known storms and tsunamis.

To calculate wave period, one must first calculate wave height using an approximation of their choosing, and then calculate maximum swash velocity and water depth accordingly, depending on the storm or tsunami hypothesis. Wave period has been calculated for boulders listed in Appendix H with known transport distance, which sums up to all tsunami-related boulder accumulations and to storm boulders described by Oliveira *et al*. (2011) and by Goto *et al*. (2011). Wave period was computed considering two possible approximations for wave height: 1) Nott's approximation for breaking storm waves applied to storm boulders; 2) and Nott's approximation for tsunami waves applied to tsunami boulders.

Results show a direct relationship between computed wave period and travelled horizontal distance (Figure 28). Wave period computed for boulders transported by tsunamis shows a wide range, from 14 s to ~1500 s, with approximately 55% of boulders rendering wave periods above 100 s (Figure 28). The application of Lorang's equation to storm boulder with known transport distances resulted in low wave periods <10 s.

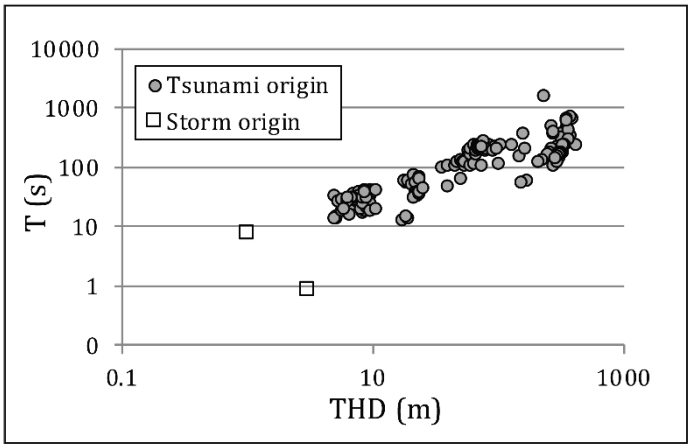

Figure 28: Wave period (*T*), calculated with Lorang's formula, projected against total horizontal distance (THD) of the boulders and cobbles listed in Appendix H with known transport distance

Although tsunami boulders present a higher computed wave period than storm boulders, there is a considerable number of boulders transported by a tsunami with T<40 s (~30%). Results show that wave period computed with Lorang's equation mostly depends on distances travelled by the boulders, which can correspond to inundation by several waves, instead of only one.

4.4 Summary

In this summary, results obtained with different approximations described above are compared and a synthesis is presented with incidence on comparing the results obtained. Finally, the most adequate numerical solutions will be selected to apply to the boulder accumulation under study.

There is always a trade-off between using robust approaches, that attempt to address all factors regulating a given physical process, and simpler approaches that try to explain a substantial portion of the natural variance using a restricted number of variables (Lorang, 2002). Different approximations presented above require different input variables and produce varying results (Table XV). Furthermore, some expressions were specifically designed addressing boulder beach contexts, whereas others considered breakwater design. In this chapter, they were applied to deposits located in various geomorphological contexts, such as lowlands, pocket beaches, boulder beaches, cliffed coasts and intertidal to supratidal rocky coasts.

Hudson's formula is simple to apply but mostly rendered underestimated critical wave heights when applied to boulders within rocky coastline contexts, sitting near and above the mean sea level. This empirical formula is valid in the design of breakwaters and should preferably be used within intertidal to supratidal rocky platform contexts with slopes ranging from 18-45°.

Formulae developed by van der Meer (1988; 1998) include significant wave height and period and were developed for both plunging and surging waves. Again, application of these formulae to the largest boulders of the cases addressed in this study, rendered underestimated critical significant wave heights, 2 to 3 times lower than the values obtained using the Hudson formula (Figure 29).

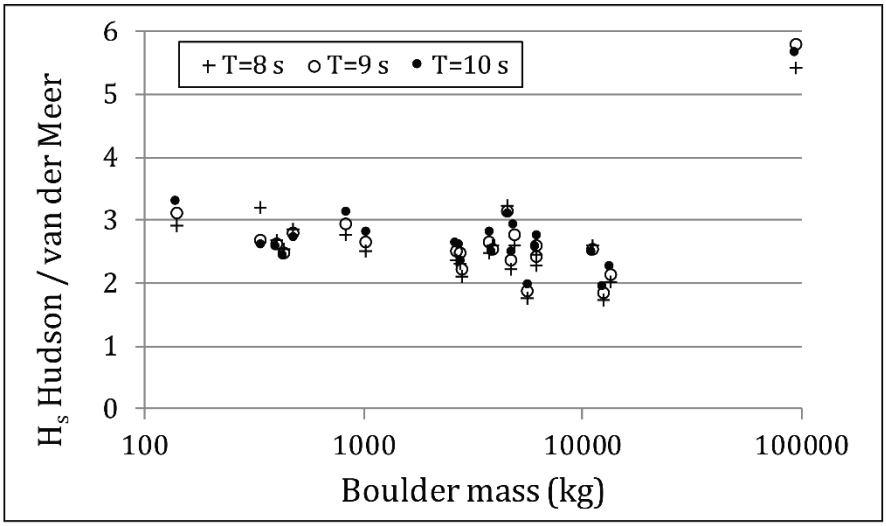

Figure 29: Scatter plot of the ratio between H_s computed with the Hudson and the van der Meer formulae against boulder mass, applied to boulder deposits generated by storms listed in Appendix H which fall within the range of application of both approximations

These low wave heights, obtained with the application of the Hudson and van der Meer formulae, might be related to the field of application of these stability equations, which were developed for waves breaking at the structure. This is not the case for most storm-related boulders used to validate these approximations within these contexts. For this reason, both the Hudson's and van der Meer formulae were not further used in this work.

Nott's (1997, 2003) work and solutions triggered a discussion on boulder transport, mainly in what concerns their use to discriminate the type of event responsible for boulder transport, storm or tsunami. Validation with largest boulders in deposits with known storm origin agree well with critical wave heights obtained with the subaerial and submerged scenarios. However, application of the joint-bounded boulder equation rendered unrealistically high wave heights. Tsunami wave heights required to generate boulder movement, computed with Nott's equations, were well below observed tsunami wave heights, which was attributed to particle size limitations in the cases addressed.

Noormets *et al.* (2004), Hansom *et al.* (2008) and Nandasena *et al.* (2011a) further developed Nott's approximations to include slope and other modes of transport besides rolling, such as sliding, rolling over a high obstacle and saltation. Furthermore, Benner *et al.* (2010) presented a different approach to calculate flow velocity capable of initiating sliding by using the linear momentum equation.

Comparison of minimum threshold flow velocities required to induce sliding predicted by these approaches (Figure 30) indicates that maximum values are obtained when applying Noormets *et al.* (2004) solutions. The higher values are related with the consideration of a variable shape-dependent drag coefficient, which is mostly lower than the constant value of 1.8-2 used by Nott (1997), Hansom *et al.* (2008) and Nandasena *et al.* (2011a). Minimum flow velocities for sliding were computed with Nandasena's *et al.* (2011a) equation. Hansom's *et al.* (2008) and Benner's *et al.* (2010) approximations yielded similar and intermediate flow velocities.

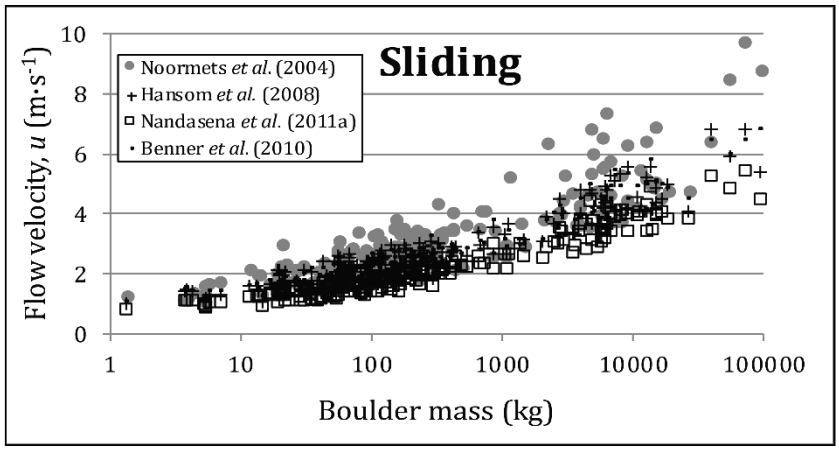

Figure 30: Threshold flow velocities necessary to generate boulder movement by sliding when applying different approximations to boulders and cobbles listed in Appendix H

In what regards flow velocities necessary to generate boulder overturning (rolling), higher values are obtained when applying Noormets *et al.* (2004), also due to the lower drag coefficients, and when applying Hansom's *et al.* (2008) approximation, due to corrections to axes and coefficients (Figure 31). Nott's (1997) and Nandasena's *et al.* (2011a) approximations yielded lower and similar results, the slight differences resulting from the inclusion of slope in the latter approach.

Results obtained when applying different approximations to known case studies describing storm-related boulder accumulations, considering distinct transport modes are summarized in Table XIV.

Application of Nott's and Nandasena's *et al.* solutions of sliding and rolling to boulders in deposits of known storm origin indicate the use of the subaerial case-scenario coupled with conversion of flow velocity into broken wave height, as the

best combination yielding wave heights in agreement with observed values offshore, when applied to the largest particles in the dataset. Given that Nandasena's *et al.* (2011a) solutions include an additional and relevant variable (slope), for both sliding and rolling, these have been considered as the most adequate.

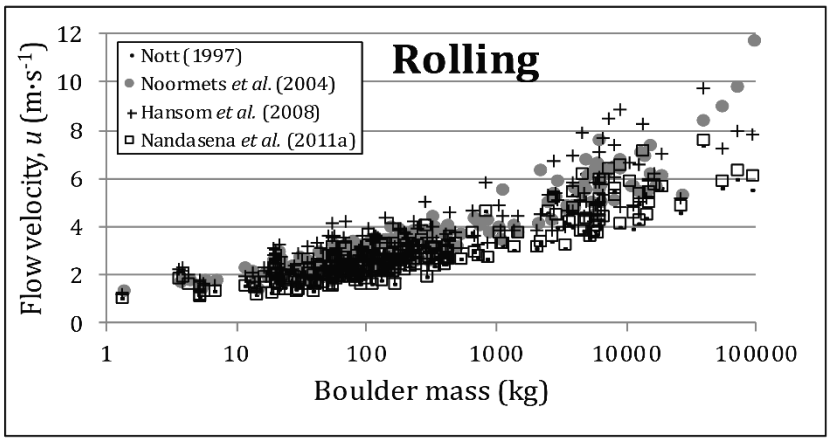

Figure 31: Threshold flow velocities necessary to generate rolling when applying different approximations to boulders and cobbles listed in Appendix H

When considering rolling over a large obstacle and extraction of a cliff top boulder by Hansom *et al.* (2008) heights obtained for broken waves were consistently above maximum recorded offshore wave heights and, for breaking waves, correspond to commonly observed values. For these transport modes, either the computation of flow velocity, or the conversion of flow velocity into wave height, or both, are inadequate. In fact, Hansom *et al.* (2008) referred to the difficulty in choosing the most appropriate expression to convert flow velocity into wave height. Moreover, laboratory and field experiments performed by Denny *et al.* (2003) showed that the interaction between complex topography and a bore could amplify flow velocities up to 1.6 times. Given these results and the fragilities associated with these solutions, results obtained with these approximations should be used with extreme caution.

Wave competence approaches, which include both wave height and period, include the work of Benner *et al.* (2010) and Lorang (2011). Vertical and horizontal distances travelled by boulders due to tsunami waves, obtained with Benner's *et al.* (2010) equations, yield unrealistically high values and for that reason were not further used in this work.

Table XIV: Significant and maximum wave heights responsible for known storm-related boulder accumulations and results obtained when applying distinct transport modes and numerical solutions: A – Nott (1997); B – Noormets *et al.* (2004); C – Hansom *et al.* (2008); D – Nandasena *et al.* (2011a); E – Benner *et al.* (2010). [1] applied to boulder beach and boulder ridge; [2] applied to cliff-top boulders and cliff-top ridges. Shaded cells correspond to computed values above maximum recorded wave heights

Case Study	H_s (m)	H_{max} (m)	Mode of transport	Numerical solution	Flow velocity (m·s^{-1})	Broken H (m)	Breaking H (m)
Oliveira *et al.* (2011)	13.0	22.1	Rolling	A	6.9	19.3	4.8
				B	6.9	19.7	4.9
				C	8.3	27.9	7.0
				D	7.2	21.1	5.3
			Rolling over a large obstacle	C	9.4	36.3	9.1
			Extraction of a cliff-top	C	9.9	39.5	9.9
Goto *et al.* (2011)	9.2	15.4	Sliding	B	8.8	31.7	7.9
				C	5.4	11.8	3.0
				D	4.5	8.2	2.1
				E	6.8	19.1	4.8
			Rolling	A	5.5	12.3	3.1
				B	11.8	56.4	14.1
				C	7.8	24.9	6.2
				D	6.1	15.3	3.8
Hall (2011)	8.5	5.8	Sliding	B	2.4	2.4	0.6
				C	2.6	2.8	0.7
				D	2.1	1.9	0.5
				E	2.9	3.4	0.9
			Rolling	A	3.4	4.8	1.2
				B	3.6	5.4	1.3
				C	4.1	6.7	1.7
				D	3.5	5.0	1.2
Etienne and Paris (2010)	15.0	25.0	Sliding (applied to platform boulders)	B	6.4	16.9	4.2
				C	6.8	18.8	4.7
				D	5.3	11.4	2.8
				E	6.4	16.9	4.2
			Rolling (applied to boulder field)	A	3.1	3.9	1.0
				B	4.2	7.2	1.8
				C	3.9	6.1	1.5
				D	3.2	4.2	1.1
			Rolling over a large obstacle[1]	C	9.8	38.9	9.7
			Extraction of a cliff-top[2]	C	8.7	30.9	7.7

Lorang (2011) derived a solution for estimating the period of waves responsible for the transport of boulders that could inform on their storm *vs* tsunami origin. To use this approximation, wave height must first be estimated using Nott's or equivalent expressions, based solely on boulder properties. The application of Lorang's equation to boulders and cobbles with known transport distance, listed in Appendix H, shows that, despite the low wave periods obtained, tsunami deposits associate to larger values when compared to storm deposits. Lorang's (2011) solution is the only approximation aiding in the differentiation of storms from tsunami deposits and will be applied to the boulder accumulation under analysis in this work.

In cases where the boulder dataset used was extensive and contained a wide range of boulder sizes, such as data from Etienne and Paris (2010) and Hall (2011), computed storm wave heights were equally wide-ranging. Although some approximations, such as Nandasena's *et al*. (2011a), rendered storm wave heights which agree quite well with the observed wave regime, this only applies to values obtained for the largest particles in the dataset. Low wave heights obtained for smaller particles frequently occur in the locations in question. With these results, one might think that those smaller waves can generate boulder transport in those locations, when clearly, they cannot. Because a wave capable of emplacing a 10-ton boulder is equally capable of transporting a 100-kg particle upwards and inland, the latter does not represent wave capability to generate boulder transport. Overall, computed wave heights in agreement with the observed wave regime were observed only when applied to the largest particles.

These results exposed relevant fragilities associated with the use of straightforward numerical solutions of boulder transport, regardless if they are based in empirical solutions, balance equations or wave competence approaches. These approximations should be applied with caution and their use as a tool to distinguish from storm or tsunami origin is not advised.

Table XV: Input and output parameters and relevant observations for the described numerical solutions for boulder transport presented in this study

AUTHORS	INPUT	OUTPUT	OBSERVATIONS
Hudson (in U.S. Army Corps of Engineers, 1984)	Boulder mass, general shape and location within the breakwater structure (head or trunk)	Design wave (H_{10}) height capable of removing a boulder from a breakwater structure, by breaking and non-breaking waves.	To be applied in the design of breakwaters, preferably used in intertidal rocky coastline contexts with slopes ranging from 18-45° and deep-water wave conditions at the toe of the slope. Renders underestimated wave heights.
van der Meer (1988;1998)	Boulder mass, density, b and c axis; profile slope; wave period and number of waves	Significant wave height, for plunging and surging waves, capable of generating boulder movement in a breakwater structure.	To be applied in the design of breakwaters, preferably used in intertidal rocky coastline contexts with slopes ranging from 10-33° and deep-water wave conditions at the toe of the slope. Renders underestimated wave heights.
Nott (1997; 2003)	Boulder axis and density	Flow velocity capable of generating boulder overturning (rolling) in three different pre-transport settings: submerged, subaerial and joint-bounded boulders. Conversion of flow velocity into wave height considering tsunami, broken and breaking storm waves.	Joint-bounded case renders unrealistically high wave heights due to the absence of drag. Subaerial case coupled with conversion of flow velocity into broken wave height indicated as the best combination, in agreement with observed values.
Hansom *et al.* (2008)	Boulder axis and density		Overestimated wave heights when using conversion of flow velocity into wave broken wave height.

Authors	Input	Output	Observations
Nandasena *et al.* (2011a)	Boulder axis and density; Profile slope	Flow velocities capable of generating boulder entrainment applied to three transport modes: sliding, rolling and saltation. Boulder transport histogram.	Flow velocities obtained for sliding and rolling, converted into broken wave height yielded realistic results, in agreement with observations.
Noormets *et al.* (2004)	Boulder axis and density	Flow velocities capable of generating boulder sliding and rolling.	Validation with known case-studies has sometimes yielded overestimated wave heights.
Benner *et al.* (2010)	Boulder axis and density	Flow velocities necessary to generate boulder sliding.	Based on the assumption that, after hitting the boulder face, the water mass is deflected perpendicularly. Validation with known case-studies has, on one occasion, yielded overestimated wave heights.
Benner *et al.* (2010)	Boulder axis and density; Profile slope; Storm wave height and wavelength; Tsunami velocity and time (taken as wave period)	Maximum vertical and horizontal distances of boulder transport generated by a storm wave for submerged and subaerial boulder; and by a tsunami wave for a submerged boulder.	This approximation yields unrealistically high values of travelled horizontal and vertical distances.
Lorang (2000; 2002; 2011)	Horizontal and vertical distance of boulder transport; Boulder diameter; Wave height (storm and tsunami).	Wave period of the event responsible for boulder transport.	Numerical solution developed for boulder beaches. Wave height must first be estimated using Hudson's, Nott's or equivalent expressions. Requires precise determination of initial location, prior to transport.

5

Study area

5.1 General settings

Coxos littoral area is in the Atlantic western-facing coast of Portugal, approximately 40 km NW of Lisbon and 5 km N of Ericeira (Figure 32). This area is a sediment-starved rocky coast, with an irregular coastline presenting a N-S general trend, where 20-50 m high cliffs alternate with pocket beaches, subtidal rocky platforms and structurally-controlled rocky platforms (a few corresponding to shore platforms) developing at the toe of the cliffs. The cliff edge limits a 10 km-wide plateau with maximum heights inland of 200 m, that gently slopes seaward.

The cliffs and littoral platforms are cut in a lower Cretaceous sedimentary sequence mainly comprising alternating claystone, sandstone, marl and limestone layers. In this area, the Cretaceous sequence is gently tilted towards SSW and is intercepted by faults, magmatic veins and, more frequently, by joints with metric spacing.

The coastline presents different geomorphological features, depending on the outcropping lithology. Sets of hard limestone and sandstone layers form subtidal and intertidal platforms, as well as vertical cliffs that evolve by rock fall. In places where they are interbedded with softer sandstone and mudstone layers, the cliff face undergoes differential erosion and develops an irregular profile (Figure 33) with

hard layers forming benches (Figure 34) and overhanging visors. Stepped surfaces correspond to bedding planes, that slope west (seaward) and southward. The steep faces of the steps correspond to WNW-ESE, NW-SE, NE-SW and ~N-S near-vertical fractures, and the height of each step is inherited from the thickness (0.5–1 m) of the harder layers.

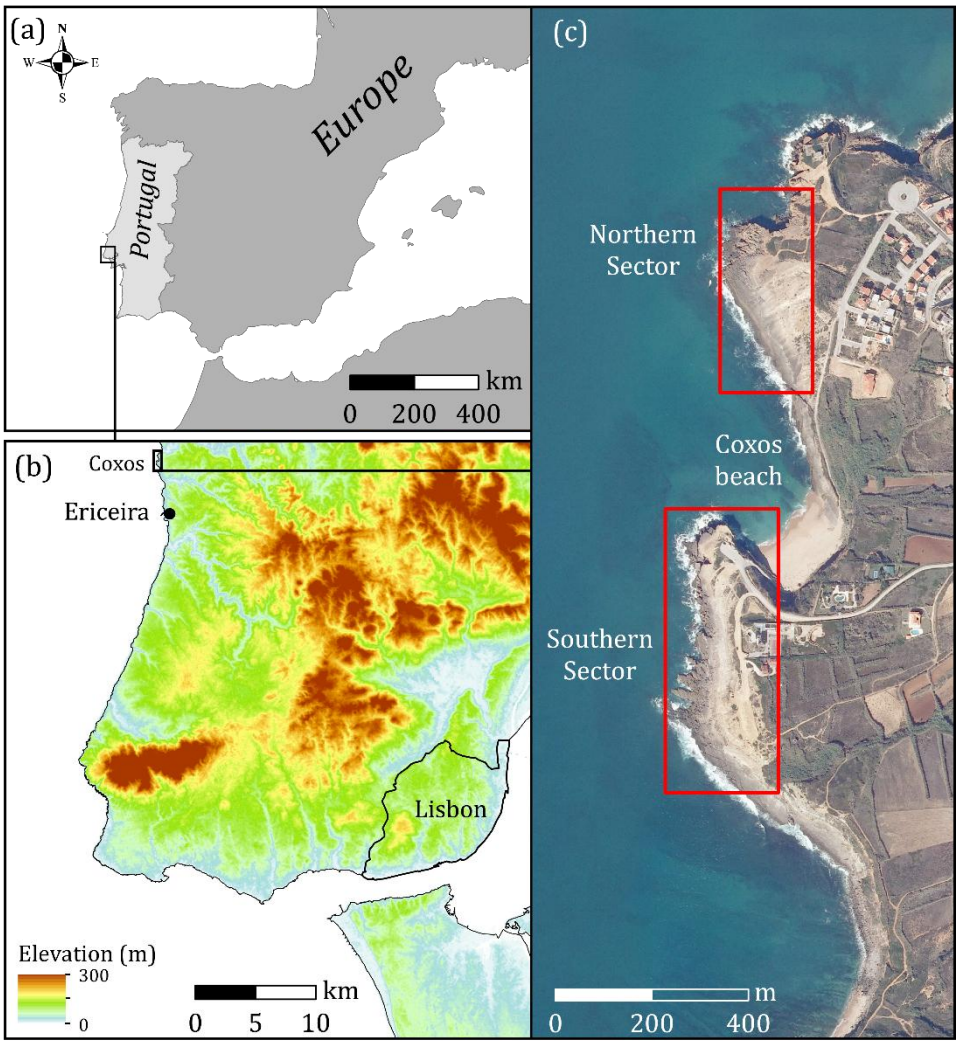

Figure 32: (a) Location of the study site in Europe; (b) location in the Lisbon area. Digital terrain model corresponds to ASTER Global Digital Elevation Model property of METI and NASA (available at http://reverb.echo.nasa.gov/reverb/); (c) location of Coxos beach and rocky platforms over 2010 digital orthophotos (IGEO, 2010). Northern and southern sectors of the study area are delimited by red rectangles

Breakdown of hard layers that protrude from the cliff and platform edges generates cobbles and boulders that eventually accumulate at the cliff and platform steps toes. These boulders and cobbles inherit their thickness from that of the hard layers and are further size-limited by the spacing between joints.

Low-sloping cliffs (<40°) develop in thick sequences of marls and claystones. These low-angle cliffs mainly evolve by gullying and mass wasting and generate colluvium deposits.

Figure 33: Photograph of the study area showing vertical cliffs with irregular and stepped profiles. Vertical scale is approximately 3 m

Figure 34: Photograph of the study area showing structural platforms with irregular and stepped profiles. Vertical scale is approximately 3 m

Several Pliocene and Pleistocene marine terraces cover the Cretaceous sedimentary sequence and are exposed at various altitudes. Pliocene marine terraces were described by Zbyszewski (1958) as scattered deposits of sand and gravel, found at plateaus above 100 m. Pleistocene marine terraces are more frequent and were described by Zbyszewski (1958; 1971) as poorly developed and scattered deposits infilling gullies that incised the Cretaceous bedrock and are found at various altitudes (80-95 m, 50-60 m, 40-60 m; 20-35 m; 15-20 m). This author characterized these deposits as consisting of dune sand, oxidized sand and gravel, sometimes interbedded with thin clay layers. Near the study area, several marine terraces like

those described by Zbyszewski (1958; 1971) were recognized at 14-17 m, 17-20 m, 25 m and 35-38 m. The similarity exhibited in altitudes and sediments indicate they are Pleistocene in age and of marine origin.

5.2 Lithostratigraphy

One criteria used to associate coarse clastic coastal deposits to extreme marine events, is the detection of a seaward sediment source, or of a source area resting at lower altitude, thus implying transport landward and against gravity. In the case of boulders, this can be done through the identification of the (source) layers from which the boulders originated, using, for example, lithological, textural, palaeontological and/or geometrical match. Thus, it is essential to investigate both the outcropping geological sequence, and the boulders, for those criteria.

The litho- and biostratigraphy of the Cretaceous outcropping along this coast, including the study area, was studied by several authors in the past century. Choffat (1904-1907) presented a detailed lithostratigraphic description of sediments outcropping in the region of Ericeira and discussed their relationship with Cretaceous materials outcropping in other locations in Portugal. Rey (1972) wrote a detailed stratigraphic analysis of the Lower Cretaceous of the central west area of Portugal. Kullberg *et al*. (2006) studied the stratigraphic units of the Mesozoic, outcropping in the western Portuguese coast, and up to approximately 20 km inland, and discussed their spatial and temporal relationship within the evolution of the Lusitanian Basin. Nevertheless, it was Rey (2007) who presented the most complete and detailed stratigraphic description of the Cretaceous sequences outcropping in the study area. Correlation between layers in structural platforms and cliffs found in the study area and those described by Rey (2007) was based on layer geometry, lithostratigraphy and macro-paleontological content. Given the high resolution of Rey's (2007) work, the lithostratigraphical description presented here will combine field observations with descriptions in that study and major units defined by that author were also maintained.

Layers outcropping in the study area uplifted and reshaped into cliffs and platforms, and were originally formed during a marine transgressive-regressive 2nd order cycle dated from the lower Cretaceous (Upper Valentinian-Upper Hauterivian - Rey *et al*.,

2003; Rey, 2007). Rey (2007) organized strata description in several sets, each set corresponding to a complete depositional sequence, *i.e.* a complete third-order sedimentary cycle representing 0.5 to 3 Ma. In this section, only four third-order sedimentary cycles dated from the lower Hauterivian are described. They are referred to, from the base to the top, as Ha 1, Ha 2, Ha 3 and Ha 4.

Each sequence is composed of two system tracts (Rey, 2007): a transgressive system tract (TST), corresponding to deposition in a rising sea level context; a highstand system tract (HST) corresponding to deposition within a stable sea level period, with rates of deposition exceeding rates of sea level rise (relative sea level rise decrease). These sets begin, at the base, with a sequence boundary (*SB*) of a transgressive system tract (*TST*), followed by a maximum flooding surface (*mfs*) and, finally by a highstand system tract (*HST*). Periods of lower sea level separate each sedimentary cycle, and are represented by an interruption of sedimentation or an erosive surface (Rey, 2007).

5.2.1 Ha 1

The first set, Ha 1, outcrops at the cliffs that limit the northern sector (Figure 32), and at the base of the cliffs of the southern sector. The sequence logged during field work, correlates well with the stratigraphic description presented by Rey (2007) and is presented in Figure 35. From the base to the top, it comprises: (1) a transgressive sequence, which begins with a thin layer of grey claystone/marl (L1), followed by a thick succession of yellowish fine sandstone with interbedded harder sandy limestone layers (L2-L8); (2) a maximum inundation surface expressed by a thin layer of claystone (L9); (3) a high sea-level stand sequence (L10 to L15) essentially corresponding to intensely bioturbated "packstone-wakestone" grey limestones containing scattered quartz grains. Colonial corals can also be found, as well as nodular bioturbation towards the top of the sequence (L15).

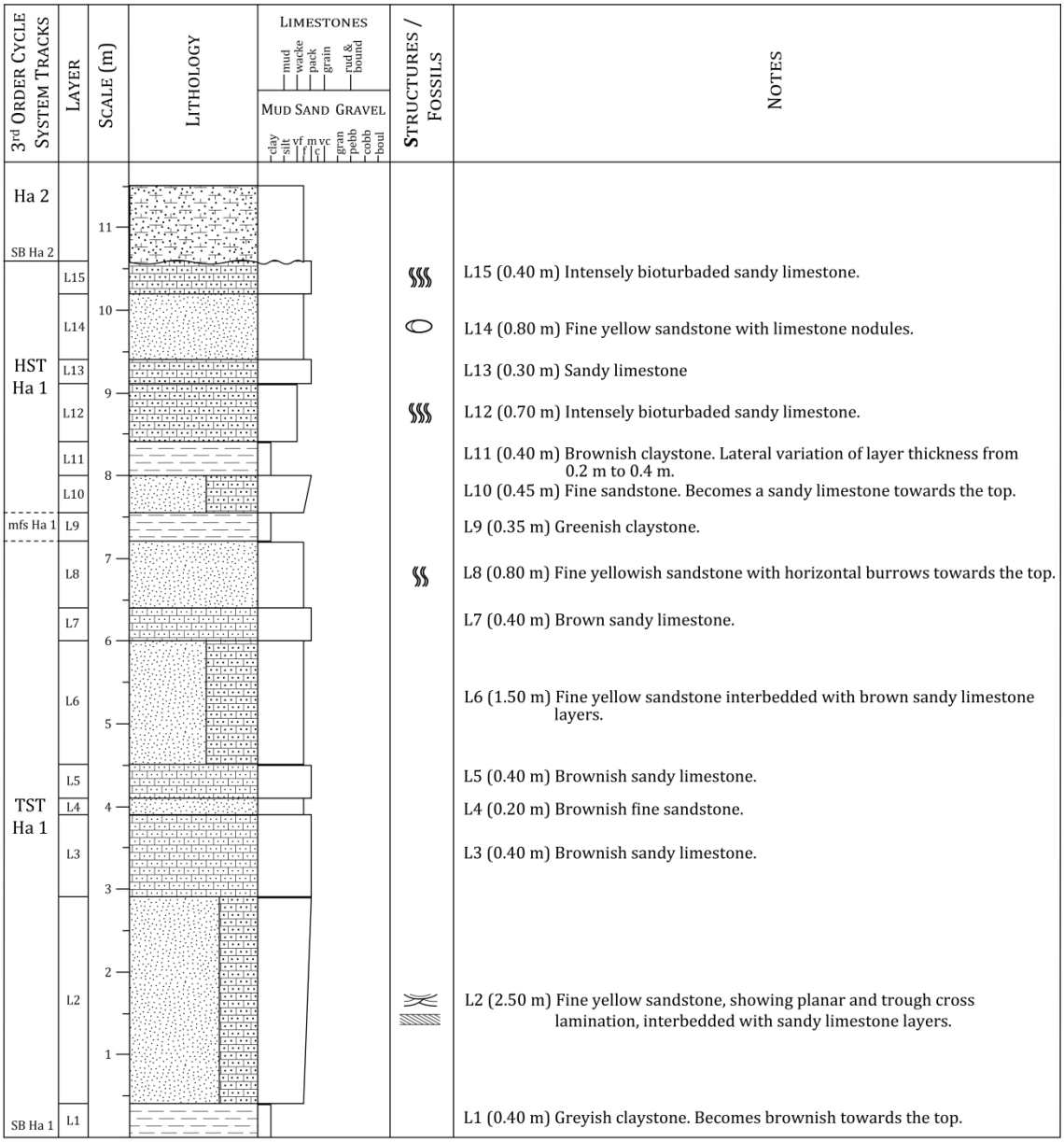

Figure 35: Sedimentary sequence Ha 1. Log-key in Figure 36

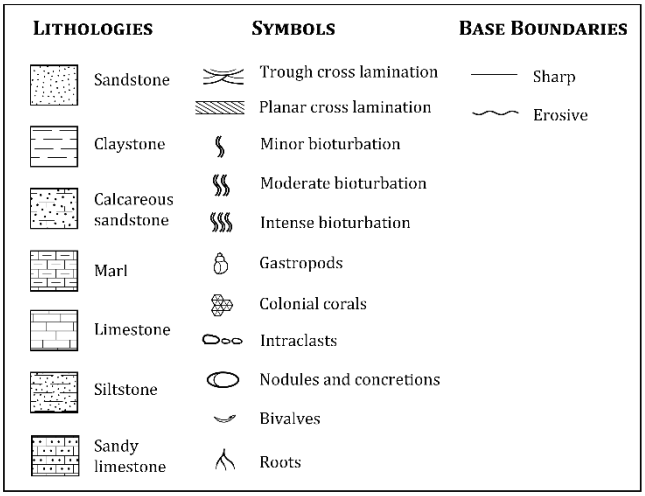

Figure 36: log key for Ha 1-Ha 4 sets

5.2.2 Ha 2

The second intermediate set, Ha 2, corresponds to hard layers that promoted the development of benches and structural platforms N and S of Coxos beach, where the boulder deposits described in this work are sitting. Once more, the field log surveyed under the scope of this work, correlates well with the stratigraphic description of Rey (2007), and is presented in Figure 37. From the base to the top, it comprises: (1) a basal contact with Ha 1, corresponding to an erosive surface cut in the sandy limestone layers of the previous highstand system tract, above which the Ha 2 transgressive sequence develops. This sequence is represented by calcareous sandstone to sandy limestone layers with varying thickness and rich in gastropod and bivalves towards the top (L16-L18); (2) the maximum inundation is expressed by a lamina of calcareous sandstone between layers L18 and L19; (3) the highstand system tract is composed of four to five hard "wakestone-packstone" limestone layers (layers L19, L21, L24, L26 and L28), intercalated by clayey limestone layers showing bioturbation. The limestone layers yielded a diversified fossil content (gastropods, bivalves, foraminifera and dispersed coral colonies). The surface of the uppermost limestone layer is oxidized and hardened (Rey, 2007) indicating subaerial exposure.

5.2.3 Ha 3

The third set, Ha 3, corresponds to a sequence comprising softer layers, that outcrop above, and inland of the vertical cliffs and stepped benches, N and S of Coxos beach. The field log surveyed in this work, correlates with the stratigraphic description of Rey (2007) and it is sketched in Figure 38 and summarized below.

The basal contact with Ha 2 consists of a hardened, oxidized surface, affected and armoured by an iron crust. The transgressive sequence accumulated above this surface is composed of two distinct groups: the lower group consist of green to red claystone layers that laterally grade into fine, well sorted sandstone showing trough cross-lamination, iron concretions and fossilized roots (L29-30). The sandstone corresponds to a lenticular body and can be traced as such alongshore, in the same stratigraphic location, indicating time and space-limited sediment input of terrestrial source into an otherwise shallow, carbonate-dominated marine platform.

The upper group contains beige to blue bioturbated “wakestone” clayey limestone, interbedded with claystone (L31).

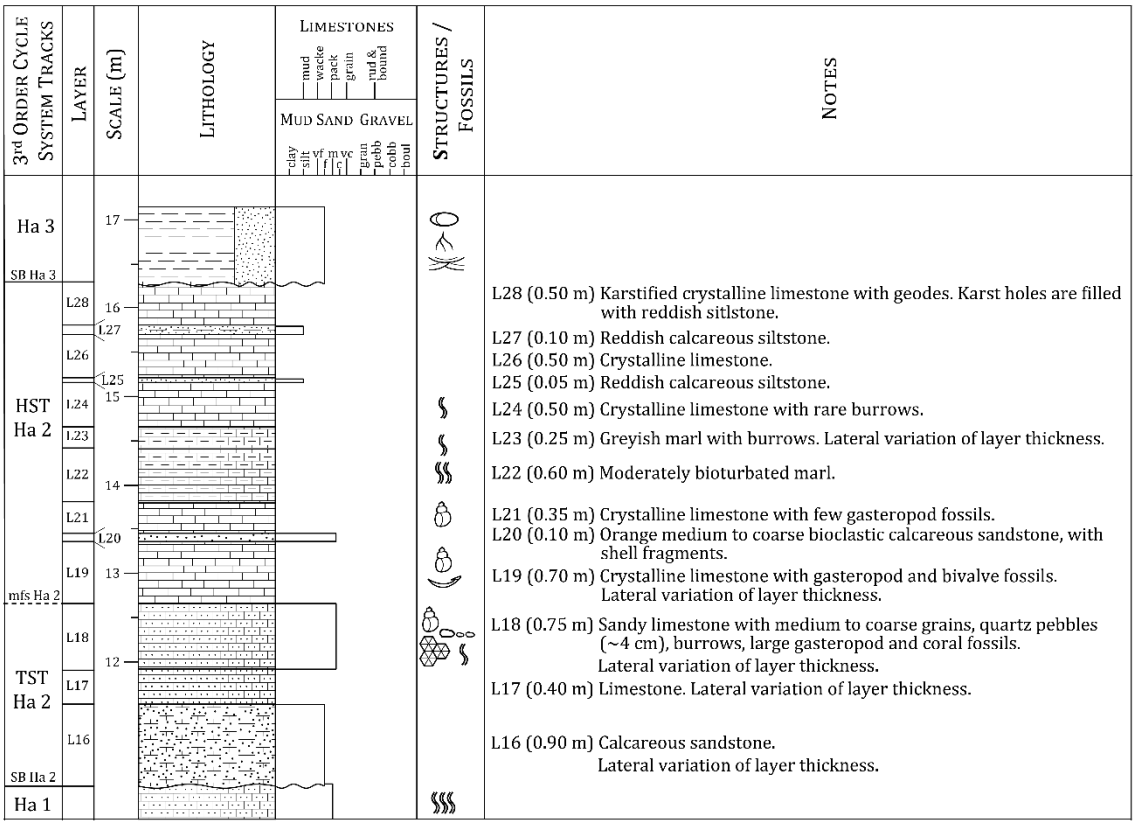

Figure 37: Sedimentary sequence Ha 2. Log-key in Figure 36

The surface of maximum inundation is represented by a sandy limestone layer limiting the transgressive sequence (L32). The highstand system tract is similar to the marls that top the transgressive sequence, but showing more intense bioturbation and higher and richer faunal density and diversity.

5.2.4 Ha 4

Ha 4 sedimentary set tops Ha 3 and outcrops in the cliffs backing Coxos beach and at the top of the cliffs limiting the structural benches that comprise the southern sector of the study area. In this region, only the lower part of the transgressive sequence outcrops and is represented in Figure 38. From the base towards the top, set Ha 4 comprises: (1) a dark claystone bed (L35) marking the change between sets Ha 3 and 4; (2) a fine yellowish to greyish sandstone sequence (L36, L37) showing internal trough cross-lamination. These detritic terms form the top of the sequence outcropping in the study area.

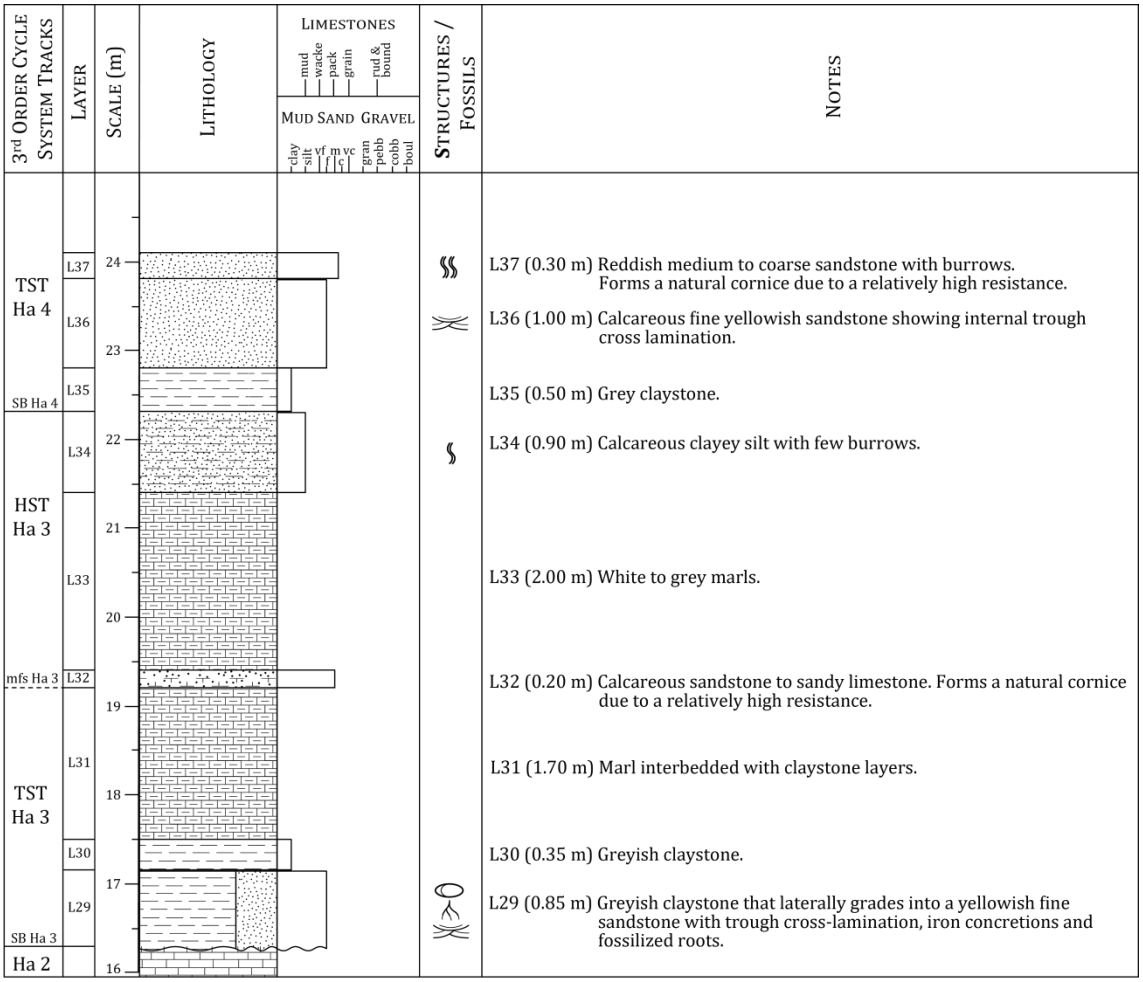

Figure 38: Sedimentary sequence Ha 3 and Ha 4. Log-key in Figure 36

5.3 Geomorphology

The geometry and lithostratigraphy of the outcropping sedimentary sequence described above, together with the presence of faults, flexures, joints and varying exposure to wave attack, control the development of different geomorphological features in the study area.

Identified geomorphological features are associated with specific lithological units that were defined according to their influence in the geomorphological development. Field observations of these geomorphological features and association with the lithostratigraphical sets defined above, allowed the definition of 5 different units (A to E). These units are separated by four surfaces (S I to S IV) which coincide with bedding planes, and with the top of harder layers controlling the development of structural benches and cliff-top surfaces.

The Cretaceous sequence is slightly tilted towards SW (S_0 = 280-300°, 6-10°SW) and its lateral continuity is interrupted by a NW-SE vertical fault limiting the cliffs S of Coxos beach. This fault generated a vertical offset of approximately 20 m, the northern block having subsided relatively to the southern block (Figure 39a). Additionally, several NNE-SSW faults identified in the northern sector generated smaller vertical offsets (<2 m). Some of these faults change laterally into flexures, visibly affecting Units C, D and E, (Figure 39a).

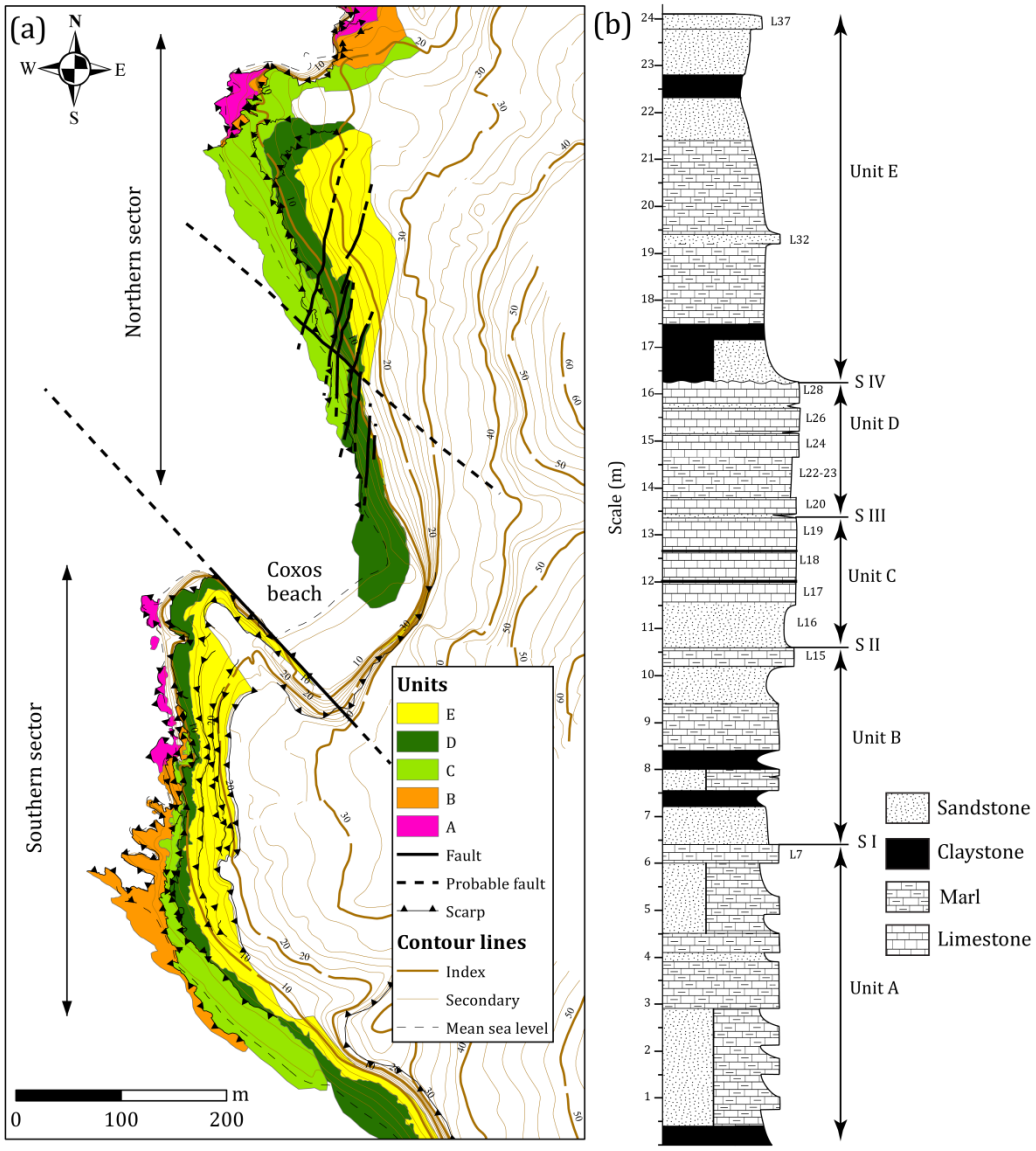

Figure 39: (a) Mapped units outcropping in the study area. (b) Schematic geologic log and definition of the units and limiting structural surfaces (S I-S IV)

5.3.1 Unit A

Unit A is the basal unit and contains the lower part of Ha 1. This unit outcrops at the base of the cliffs that limit the northern sector, and along the base of the cliffs of the southern sector (Figure 39a). It is mainly composed of fine sandstone interbedded with sandy limestone layers (Figure 39b).

The harder limestone layer L7 forms the lowest structural bench (surface S I), which is present in the northern region of both sectors, developing in the intertidal domain and, for this reason is rarely accessible due to wave action. The sandy layers outcropping above S I are more easily eroded and structural notches formed, which, in turn, generate irregular cliff profiles, developing by rockfalls of the sandy limestone protruding at higher altitudes. Thus, extensive boulder and block accumulations occur at the base of these cliffs.

5.3.2 Unit B

Unit B contains the upper part of Ha 1. This unit outcrops in the middle and top of the cliff face that limits the northern sector, and at the base of the structural benches of the southern sector (Figure 39a). It is mainly composed of fine sandstone interbedded with claystone and intensely bioturbated sandy limestone layers (Figure 39b).

The upper layer of this unit (L15) corresponds to a hard sandy limestone with nodular bioturbation that formed an intricate and resistant network of filled burrows (Figure 39b). Its top is a Cretaceous erosion surface that marks the transition from Ha 1 to Ha 2 and corresponds to the second structural surface (S II) This surface forms a wide bench in the southern sector (Figure 39a). Breakdown of unit B results in rock-fall and generates boulder and block accumulations at the cliff-toes. Joint sets affecting this unit preferably develop NNW-SSE and, less frequently, WNW-WSE. The average spacing between fractures was measured on aerial photographs (using the window method described in section 6.1) and corresponds to 3.5 m, although this number may include overestimation (Figure 40).

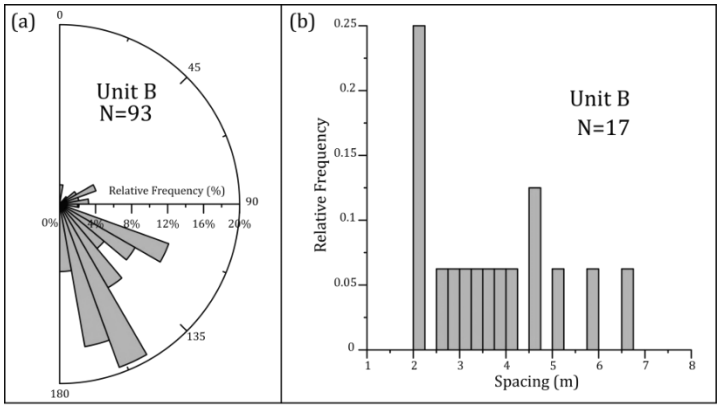

Figure 40: (a) Rose diagram of joints affecting unit B; (b) histogram of joint spacing acquired using virtual scanlines in a sampling window over aerial photographs

5.3.3 Unit C

Unit C contains the lower part of Ha 2. This unit outcrops along both sectors (Figure 39a). It is composed, from the base towards the top, of a calcarenite layer with varying thickness (L16), sandy limestone layers (L17-18) and a thick crystalline limestone layer (L19) (Figure 39b). In the southern sector, the top of the crystalline limestone forms a wide structural bench (surface S III), whereas in the northern sector, surface S III is narrower and prolonged seaward by secondary structural surfaces developing at the top of the underlying detritic limestone layers. This unit evolves by breakdown and dislodgement of boulders along bench edges due to wave action, and generates large boulders, reflecting larger bed thickness and low joint frequency. Lithological contrasts promote differential erosion and favour development of overhanging visors, notches, irregular profiles and stepped surfaces. Step faces correspond with NW-SE and NNW-SSE near-vertical joints showing average spacing of 1.75 m and higher frequency in the 0.5-0.75 m joint spacing class (Figure 41).

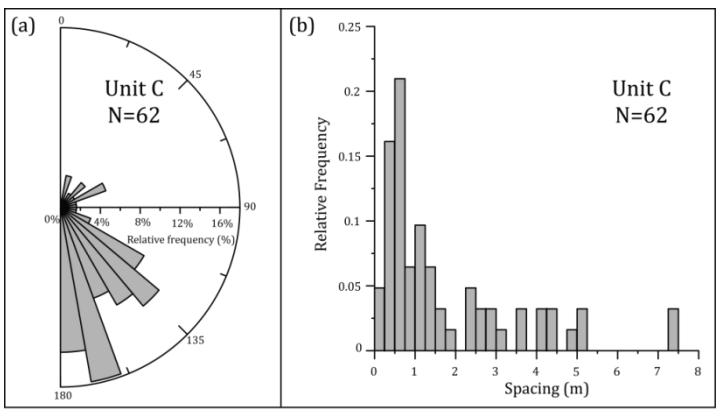

Figure 41: (a) Rose diagram of joints affecting Unit C; (b) histogram of joint spacing

5.3.4 Unit D

Unit D contains the upper part of Ha 2 and outcrops in both sectors (Figure 39a). It is composed of three limestone layers (L24, L26 and L28) interbedded with marls and thin siltstone layers, with increasing hardness towards the top (Figure 39b). The top of this sequence corresponds to a Cretaceous erosion surface marking the transition from Ha 2 to Ha 3 (surface S IV). Similarly to Unit C, it evolves by breakdown of platform edges due to wave action, generating boulders that reflect bed thickness and joint frequency. Lithological contrasts promote differential erosion and favour development of overhanging visors and notches, and of irregular profiles and stepped surfaces. Step faces correspond mostly with N-S to NNW-SSE and, less frequently, WNW-ESE and NW-SE near-vertical joints, showing average spacing of 0.7 m and higher frequency within the 0.5-0.75 m spacing class (Figure 42).

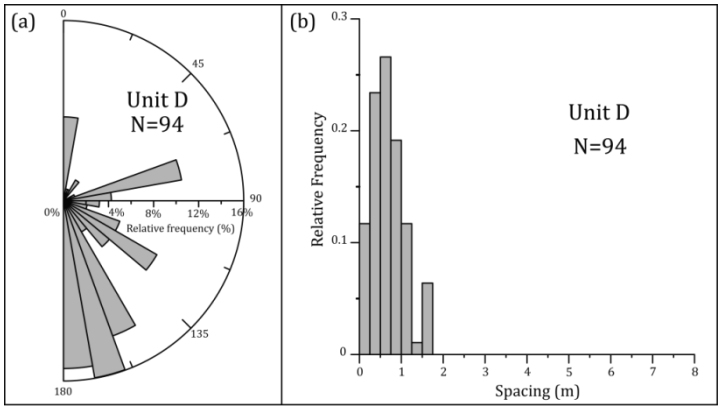

Figure 42: (a) Rose diagram of joints affecting Unit D; (b) histogram of joint spacing

5.3.5 Unit E

Unit E is the upper unit, and contains both Ha 3 and Ha 4 sets. It is composed of softer interbedded thin layers of claystone, sandstone and marl (Figure 39b). This unit outcrops farther inland of the underlying units in both sectors, due to differential and faster retreat of the low angle cliff face, and in the base of a vertical cliff that limits Coxos beach (Figure 39a). This differential erosion allowed for exposure of the rocky structural benches that developed in relation with the S IV structural surface.

Marls and claystones of Unit E form low-sloping cliffs that evolve by gullying and mass movement, generating colluvium deposits at the landward edge of surface S IV. These deposits consist of clay and silt with small contributions of sand, cobbles and boulders originated in layers L32 and L37 of Unit E. These layer clasts accumulate at the base of this slope. The horizontal (seaward) extension of the colluvium is limited by frequent washing out promoted by rain and wave swash.

Joint spacing and orientation, together with layer thickness, constrain boulder size and shape. Boulders originating in Units B and C are larger than those originating in Unit D, due to higher layer thickness and joint spacing. Regarding boulder shape, most frequent joint directions affecting both Units B and C (NW-SE and NNW-SSE) generate triangular and lozenge shaped parallelepipeds, whilst the additional modal direction in discontinuities present in Unit D (WSW-ENE) further constrains boulder shape, which is frequently rectangular parallelepiped.

5.4 Oceanographic climate

Tides along the central western coast of mainland Portugal are semidiurnal. The elevation reached by the sea surface of the ocean in highest astronomical spring tide condition is, on average, of 1.89 m amsl, and presents an average amplitude of 2.16 m, according to data from Instituto Hidrográfico (2010; 2011; 2012; 2013; 2014; 2015). In the exposed west coast near Lisbon, the maximum increment in height of the sea surface due to storm surge is typically less than 0.6 m, and averages 0.4 m (Vieira *et al.*, 2012; Taborda and Dias, 1992; Gama *et al.*, 1997).

The west coast of Portugal is exposed to high-energy swell generated in the Atlantic and sea storms occur during winter (October-March) with major incidence from November to March (Costa, 1994). Significant wave heights are larger in the N (mean $H_s \sim 2$ m) and decrease towards S (mean $H_s \sim 1.7$ m) with H_s >5 m representing 1 to 2% of total observations (Costa and Esteves, 2009). Average mean period (T_m) is contained in the 5-7 s class interval, with T_m>11 s representing less than 2% of observations (Costa and Esteves, 2009). Peak period (T_p) is approximately 11 s, with T_p>15 s representing less than 6% of observations. Wave

directions show higher occurrences from the NW sector (72-76%), followed by occurrences from the W (21-24%) and SW (< 3%) (Costa and Esteves, 2009).

The analysis of a 56 year long (1953-2009) hindcast time-series obtained by Dodet *et al.* (2010) in a simulation point located offshore the central west coast of Portugal (available at http://disepla.fc.ul.pt/Micore/WaveDownload.html) shows highest mean H_s travelling from the WSW (240°-260°) and highest mean periods of 9.5 s (mean T_p ~11.3 s) associated with a WNW direction (280°-300°) (Figure 43). The pattern of mean wave power distribution follows that of the mean significant wave height, showing maximum values associated with west-southwesterlies.

Storm climate along the Portuguese western coastline is highly energetic, the number of storms per year ranging from 9 to 12 (Ferreira *et al.*, 2009). Storms last 26 hours on average, reaching maximum significant wave heights of about 12-14 m and maximum peak periods above 20 s (Ferreira *et al.*, 2009). Most storm waves propagate from W to NW, although rare (<3%) southwesterlies also occur (Esteves *et al.*, 2010).

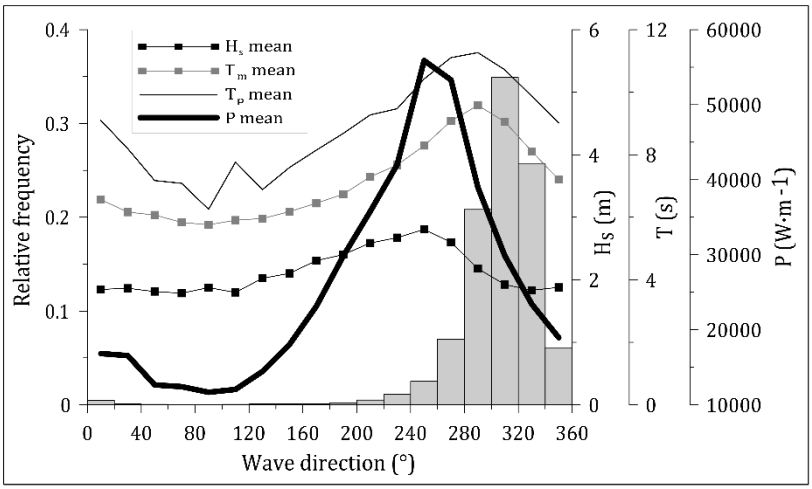

Figure 43: Histogram showing occurrences of wave direction (20° interval), mean values of H_s, T_m, T_p and wave power, P, associated with each direction interval. Wave data extracted from the hindcast time-series obtained by Dodet *et al.* (2010)

The maximum yearly values of H_s vary between 5.7 and 13.0 m, averaging 7.9 m with 45% of occurrences falling in the 6-9 m interval (Figure 44a). Wave direction for these records show highest frequencies associated with 280°-290° and the highest waves (H_s > 9 m) preferably travel from the WSW to WNW (250°-300°) (Figure 44b).

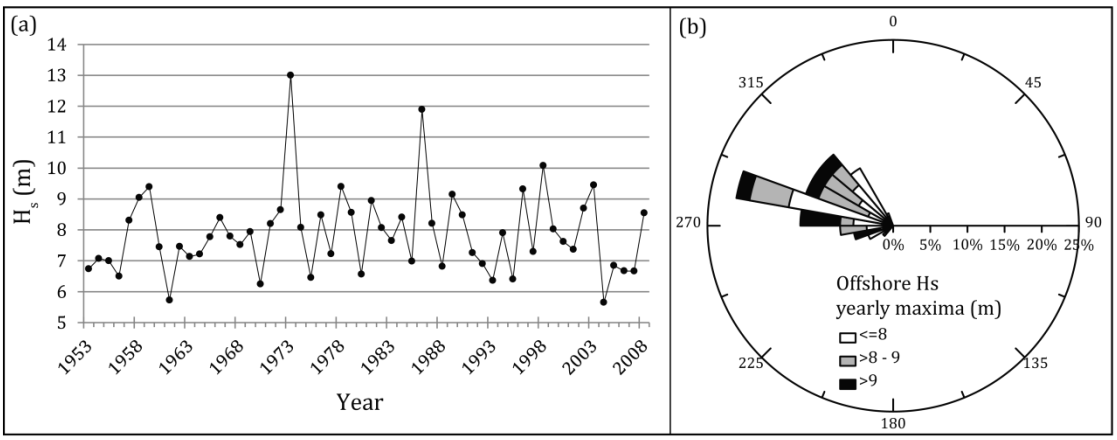

Figure 44 (a): H_s yearly maxima between 1953 and 2008; (b) wind-rose diagram for the same wave records associating H_s with wave direction. Wave data extracted from the hindcast time-series obtained by Dodet *et al.* (2010)

Yearly maxima of T_m vary between 14.1 s and 17.7 s, averaging 15.4 s, with 70% of occurrences falling in the 15-17 s interval (Figure 45a). Wave direction for these records shows highest frequencies associated with west-northwesterlies (290°-300°) and a relevant contribution from northwesterlies (300°-330°) (Figure 45b). Maximum peak period (T_p) ranges from 17.2 s to 22.7 s, averaging 19.1 s, with 42% of occurrences falling in the 18-20 s interval (Figure 45a). Wave direction for these records show highest frequencies associated with northwesterlies (modal class 300°-310°) and a relevant contribution from westerlies (260°-270°) (Figure 45c).

Comparison of yearly maximum records of significant wave height and wave period (mean and peak values) clearly indicates that higher waves are not necessarily the longer, although they both preferably associate with W to NW wave directions (Figure 44 and Figure 45).

Wave propagation of yearly maxima from the offshore to the nearshore, at a point about 1 km from Coxos beach (depth of 23 m below mean sea level), reveals an average reduction in wave height of about 85%, a counterclockwise rotation in wave direction averaging 17° and a decrease in directional dispersion due to wave refraction (Figure 46).

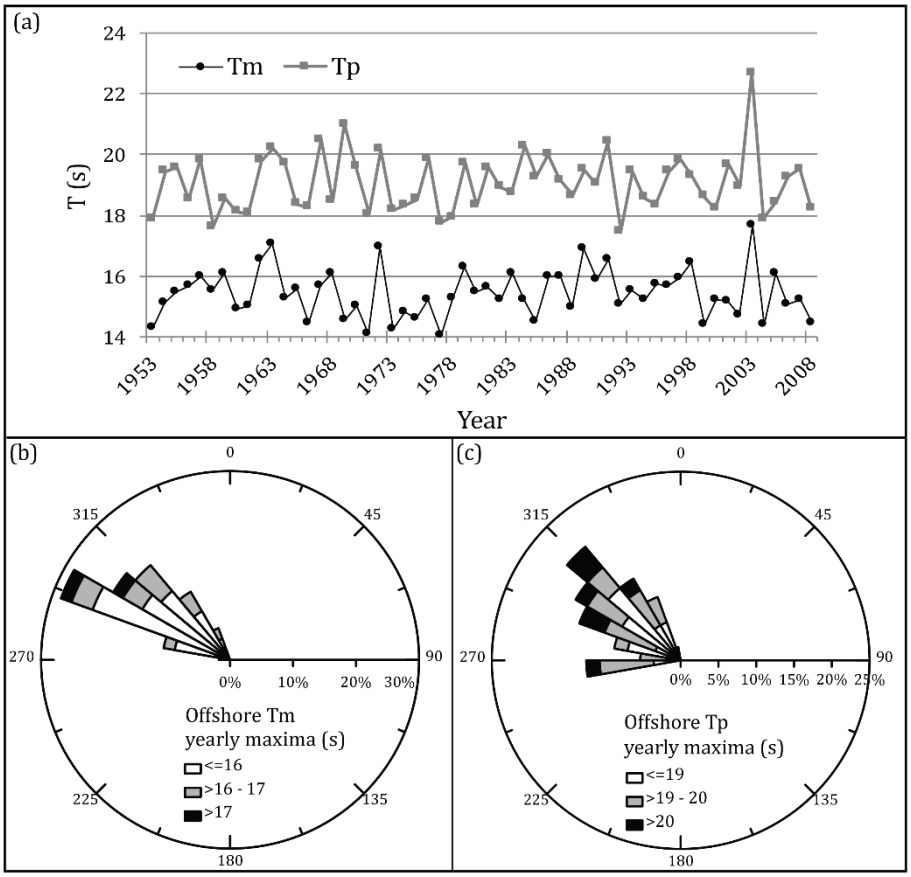

Figure 45 (a): T_m and T_p yearly maxima between 1953 and 2008; (b) Rose diagram associating maximum T_m with wave direction; (c) Rose diagram associating maximum T_p with wave direction. Wave data extracted from the hindcast time-series obtained by Dodet *et al.* (2010)

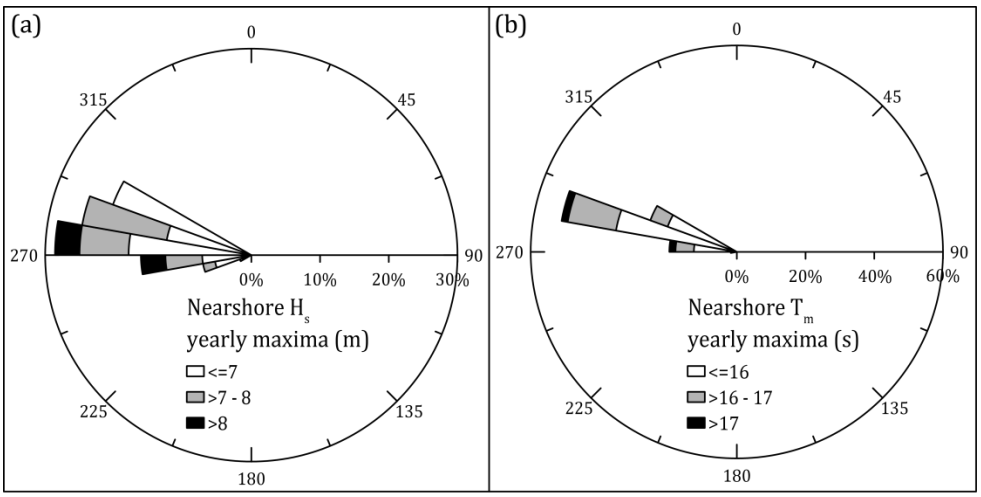

Figure 46: Wind-rose diagram showing nearshore wave direction and associated H_s (a) and T_m (b) based on the numerical propagation of yearly maxima data obtained by Dodet *et al.* (2010) for the period between 1953 and 2008

The interaction of long waves (T_m>15 s) travelling from NW to SW (240-320°) with the bathymetry, generate little energy dispersion in the sector comprising Coxos

beach, which is expressed by nearshore H_s values simillar to, or even slightly larger than (in a factor of ~1.1) the corresponding deep-water value (Figure 47). Furthermore, regardless the onshore wave direction, longer waves, will reach the study area travelling from the western octant SW-NW (more precisely 255°-295°) and shorter-period waves (T_m<10 s) reach the coastline with a 240°-310° direction.

This N-S aligned coastal stretch is thus characterized by an energetic wave regime due to a coincidence between modal direction of extreme storms and the wave direction for which energy concentration occurs in this coastline configuration.

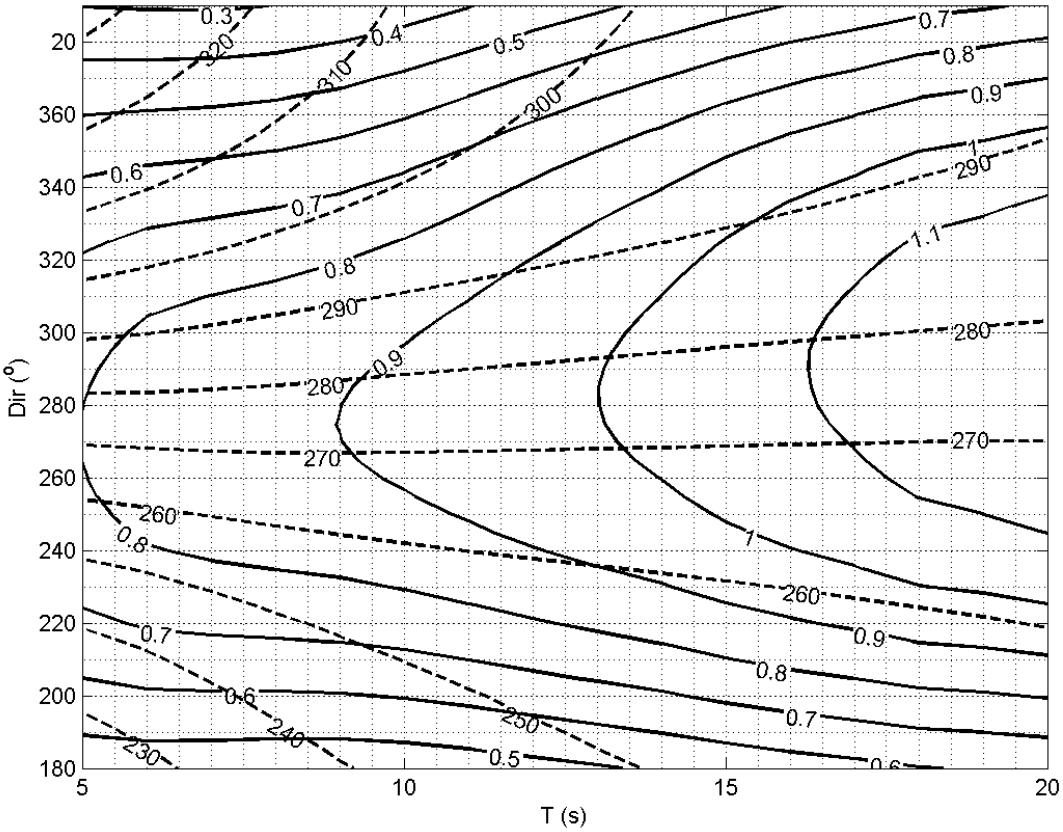

Figure 47: Wave height transformation matrix of nearshore Coxos beach (~10 deep) showing the ratio between nearshore and offshore H_s and changes in wave direction for different wave periods. Extracted from Silveira *et al.* (2013)

Methods

This chapter starts with a brief explanation of the methods used in the lithostratigraphic and geomorphological characterization of the study area (Section 6.1). Sections 6.2 and 6.3 address methods used in the characterization of the boulder accumulations and of finer deposits, respectively. These sections include a description of methods used during field work, laboratory work (measurement of rock mass density, grain-size analysis and morphoscopy) and data processing. Moreover, in section 6.2, the criteria used in the identification of boulder accumulations deposited by extreme marine events are explained. Subsequently, in section 6.4, techniques applied in wave data processing are briefly explained. These comprise methods used in the numerical modelling of storm waves propagation (6.4.1) and in statistical modelling of extreme values applied to wave parameters (6.4.2). The fifth section (6.5) enumerates approximations used in the computation of wave parameters based on validation presented in chapter 4. In the last section (6.6), the age estimation methods used (aerial photographs, lichenometry, downwearing rates and optically stimulated luminescence) are explained.

6.1 Characterization of the study area

Site characterization was firstly based in the observation of outcropping sedimentary sequences, development of a field log, and subsequent correlation with the stratigraphic description presented by Rey (2007). The macroscopic description of the layers included lithological, textural, palaeontological and geometrical characteristics (bedding plane attitude, lateral continuity, presence and type of sedimentary structures, such as cross lamination or load casts, and length, spacing and direction of joints affecting the layers). Distinct geomorphological features were identified (*e.g.* scarps, boulder accumulations, colluvium deposits, faults, flexures) and associated with the lithostratigraphic units previously identified. These units and geomorphological features were mapped using GIS software (Esri®ArcMap™) and based on the observation of 2010 aerial photographs, with 0.5 m resolution, using a SOKKISHA mirror Stereoscope and validated during field work, using Real Time Kinematic Global Positioning System (RTK-GPS) equipment.

Data from discontinuities (joints) affecting rocks outcropping in the study area were acquired in the field following the scanline sampling method proposed by Priest (1993). A measuring tape was pinned to the exposed rock surface (bedding plane), whenever possible along its strike, and another perpendicularly, along the line of maximum dip. Only discontinuities intersecting the measuring tapes were considered and intersection distance and orientation were recorded for each discontinuity (*cf.* Priest, 1993) (Figure 48a).

In situations where the rock surfaces were inaccessible, discontinuity data were collected with the aid of 2010 aerial photographs and orthophotos, both showing 0.5 m resolution, using GIS software and following the window sampling method proposed by Priest (1993). This method is essentially like the scanline sampling method, except in that all discontinuities visible inside a defined polygon of the rock face (or window) are measured (Priest, 1993) (Figure 48b). Orientation and length were directly measured and the intersection distance was extracted by measuring the distance along two virtual scanlines introduced over the window, following the layers' strike and perpendicularly, along the maximum dip. Comparison of data

acquired with the scanline and window sampling methods showed identical distributions of joint orientation but overestimation of joint spacing in the latter.

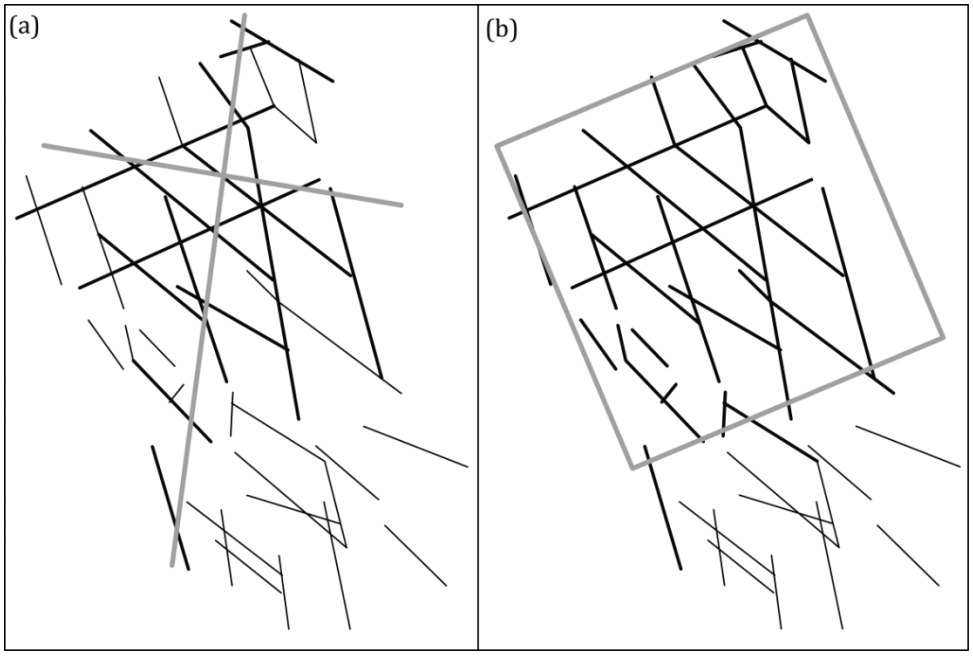

Figure 48: Discontinuity sampling methods. (a) Scanline method: grey lines represent scanlines and only discontinuities intersecting them, represented in bold black lines, are measured. (b) window method: grey square represents the sampling window and all discontinuities inside the window area are measured (bold black lines)

Analysis of discontinuity data collected in the field was separately made for each unit (represented by the upper layer exposed at each platform step). Data collected over the layers from the same unit was merged together. The spacing between joints, as defined in Priest (1993), was taken as the spacing between a pair of adjacent joints measured along the scanlines, and was represented in histograms to compute average, median and modal values. Graphical representation of the orientation of discontinuities was based in rose diagrams, which are particularly suited in cases where most discontinuities have angles of dip in excess of 60°, as suggested in Priest (1993). Identification of discontinuities sets was based on visual inspection of the resulting rose-diagrams.

6.2 Characterization of the boulder deposit

Boulder deposits in the shore zone have been associated with different transport and emplacement processes (McKenna *et al.,* 2011): (1) transport inland and upwards by waves (storm or tsunami); (2) transport by extreme marine events (either storms or tsunamis) contemporaneous of a higher than present sea level

generating deposits located at higher altitudes than recent deposits, contemporaneous of the present-day mean sea level; (4) slope mass movements, with emphasis on rock fall from cliffs; (5) glacial and paraglacial processes.

Distinguishing the mechanism responsible for transport is essential in the study of boulder deposits. Of utmost relevance is the ability to identify the signatures of marine processes and distinguish them from every remaining transport mechanisms, which comprises the base of demonstration of boulder emplacement landwards and against gravity.

In this study, boulder transport against gravity is considered to have existed when the following is observed: (1) source layer outcropping at lower altitudes from boulder position (Figure 49); (2) evidence of permanence at or below sea level prior to transport, such as boulder surface sculpturing and colonisation by macrofauna or biogenic encrustations (Figure 50) (*e.g.* Costa *et al.*, 2011; Mastronuzzi *et al.*, 2007).

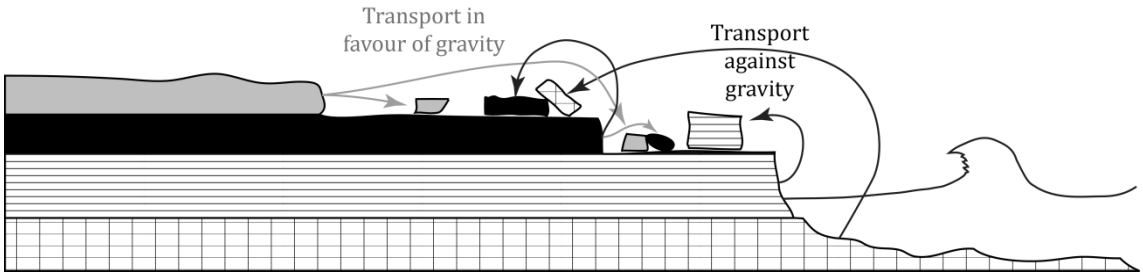

Figure 49: Schematic representation of structural benches containing four source layers, showing criteria used in the identification of boulders transported by extreme marine events based on relative position of a boulder and source layer. Grey arrows indicate transport in favour of gravity, black arrows indicate transport against gravity

Figure 50: Evidence of boulders permanence below mean sea level. (a) Biogenic perforation and sculpturing of a boulder surface (vertical scale is approximately 40 cm); (b): bioerosion and sculpturing (detail) showing preserved endolithic bivalves (coin's diameter is 2.5 cm); (c) biogenic encrustations of barnacles and vermetids (coin's diameter is 2.5 cm). Photos by M.C. Freitas

Identification of boulder source layer or/and original location was based on the following set of procedures applied to outcropping source layers and boulders: (1)

similarity in micro to macro geomorphological features, rock textures and lithologies; (2) similarity in fossil contents; (3) matching of socket and boulder geometric features.

The identification of a boulder's source layer was foremost based in lithology. Once restricted to a few possibilities, geometrical characteristics were used such as identical layer thickness and boulder height (generally corresponding to the c-axis). Surface sculpturing, which is preferably associated with specific layers was also relevant in the identification of boulder source (*e.g.* extensive bores on top of layer L28; network of burrows forming an irregular surface in layer L15). Furthermore, another distinguishing criterion was the presence of irregularities in the surfaces of boulders inherited from contact between layers (*e.g.* load cast on bedding planes generating undulating boulder surfaces).

Once a boulders' source layer has been identified, its location was compared to that of the closest outcrop, and transport was categorized as against or in favour of gravity. The former is considered a result of inundation by an extreme marine event and further characterized as described below.

All dislocated boulders sitting on surfaces S III and S IV of both northern and southern sectors in the study area, and originating in layers outcropping at lower altitudes, were marked and numbered. Measurements undertaken during field surveys were (Figure 51): 1) geographic location of the corners of each boulders' largest surface (comprising a and b-axes) acquired using a Real Time Kinematic Global Positioning System (RTK-GPS) equipment with an accuracy <5 cm; 2) boulder thickness (usually the c-axis); 3) dip direction (taken as the angle between the magnetic N and the horizontal projection of the dip line) and dip angle (corresponding to the maximum slope line within the tilted surface) as illustrated in Figure 51b; 4) other relevant observations, such as composition, polarity, imbrication, degree of burial and source layer.

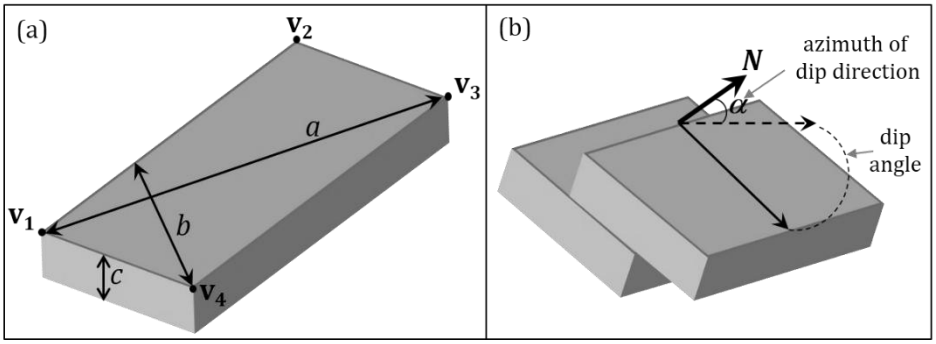

Figure 51: (a) Boulders' a, b and c-axis considered in this work. V1 to V4 represent the boulder vertices location acquired in the field surveys. (b) Schematic representation of imbricated boulders and dip measurement

Considering that most boulders in the study area have a parallelepiped shape, the data collected allowed to later reconstruct each boulder's absolute location, placement and dimensions as well as volume, main axis length and direction, with the aid of specific GIS (Geographical Information System) and 3D design software.

The information acquired in field surveys (vertices, thickness and dip) was processed using Geographical Information System (GIS) and 3-dimension computer-aided design (CAD) software, following the procedure listed below:

1. Conversion of points to 3D polygon, manually attribution of thickness and dip direction to each polygon;
2. Computation of polygon 3D surface area, volume (by multiplying area by thickness) and slope (dip) of the ab surface;
3. Creation of a polyline feature and manually attribution of major (a) and intermediate (b) axis, for each boulder, using CAD software, following the scheme represented in Figure 51;
4. Computation of axes length and direction using GIS software;
5. Shape classification of boulders based on axes ratios, following Zingg's classification (in Krumbein, 1941) (Table XVI and Figure 52);

Direction of the flow responsible for boulder transport and deposition was inferred, based on the following principles relating the orientation of particles with transport direction in aqueous media (Potter and Pettijohn, 1977):

1. The preferred orientation of disk-like particles transported in contact with a frictional substrate due to a combination of gravity plus current, results in imbrication with the plane surface (ab surface) facing flow provenance; the

long axis of such particles tends to be sub-horizontal and perpendicular to flow direction;

2. Under the same conditions, scattered, isolated, and elongate particles tend to rest with their long axis parallel to flow;
3. Particle shape and size, as well as local geometry of the substrate, can introduce some variations in the above generalizations; commonly, larger particles are better oriented than smaller ones, simple shapes better than complicated ones;
4. Orientation of the particles should always be related to the depositional surface – which may not be identical to local structural dip.

Table XVI: Zingg's classification of particle shape. After Krumbein (1941)

Class	b/a	c/b	Shape
I	>2/3	<2/3	disks
II	>2/3	>2/3	spherical
III	<2/3	<2/3	bladed
IV	<2/3	>2/3	rod-like

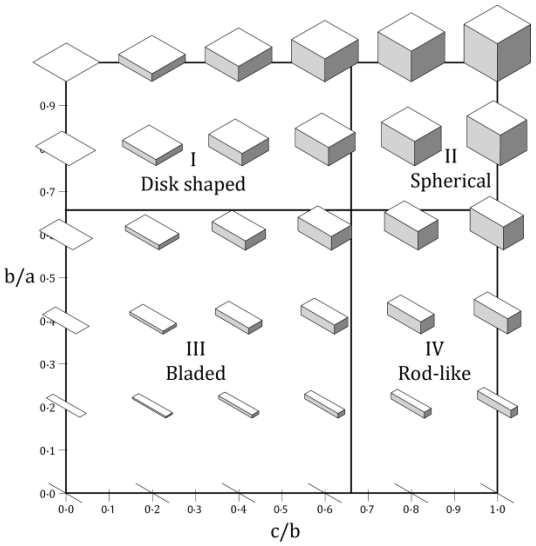

Figure 52: Zingg's classification of shapes. Modified after Blott and Pye (2008)

Disk, bladed and rod-like particles were favoured in this work as the use of spherical particles tends to increase variability and, in extreme cases, to obscure current direction (Potter and Pettijohn, 1977).

Surface dip and azimuth of the a-axis dip were grouped into 10-15° intervals, and further subdivided by boulder mass classes, and plotted in rose diagrams. Surface dip was represented by the dip direction of boulder surfaces comprising the a- and b-axes (ab surface), excluding isolated planar particles sitting sub-horizontally, with their ab surface paralleling the surface of rock benches. Azimuth of a-axis dip, or a-axis trend, was plotted considering all particles except those with vertical a-axis.

To evaluate the influence of other variables in boulder orientation, such as shape and imbrication, rose diagrams were constructed for partial sets of boulders, using the following criteria: (1) location: distinct plots were constructed with data from only the northern and southern sectors; (2) only disk-shaped, bladed and rod-like boulders were considered, spherical boulders having been disregarded; (3) imbricated boulders alone, regardless their shape, which better reflect flow direction than individual boulders that may adjust to substrate morphology.

The extent of boulder burial was ranked in four classes: 1) completely exposed; 2) slightly buried with all axis completely visible; 3) partially buried, with one or more axis partially covered, but, still allowing to define the ab surface; 4) almost completely buried, with an impossible to define ab surface.

Rock samples of sediment layers that indisputably generated boulders were collected to evaluate rock mass density and to further compute boulder mass. For this purpose, 3 to 6 samples per layer were collected, oven-dried and their mass was measured with a decimal weighing scale. The samples were boiled in water for approximately 10 minutes, to remove air in pores and the saturated samples were placed in a graduated cylinder containing a known volume of water. The displaced volume of water, corresponding to the volume of the rock sample, was measured up to 0.5 cm^3. Mass density, herein referred to as density, was calculated for each sample by dividing the mass by its volume and averaged for each source layer. In cases where boulder lithology was not accurately identified, boulder density was calculated based on the average of density values of possible layers from which it may have originated.

Extensive photographic record of all boulders and morphologies of boulder accumulations, such as imbricated clusters and boulder ridges, was undertaken. Boulder movement by storms, when detected, was monitored by GPS field surveys for boulders' scalar and directional properties, distance and direction of transport.

6.3 Characterization of finer deposits

Three samples were collected from a sand patch found beneath a boulder accumulation on the upper structural platform of the southern sector, exposed after

major storms (Figure 53a and b): one was processed for grain-size analysis and morphoscopy and the remaining two samples were sent to Doctor Ronald Goble for sample preparation and analysis in the Department of Earth & Atmospheric Sciences, University of Nebraska-Lincoln for age estimation by OSL (further described in section 6.6.4). Sample collection occurred in October of 2014 and involved the horizontal insertion of two 30x5 cm opaque PVC cylinders in the sand patch, for age estimation purposes, ~35 cm below the boulder topping it; and manual collection of a discrete sample at the same depth, reaching approximately 30 cm inside the outcrop to avoid textural changes due to exposure, as suggested by Carvalho (2005), for grain-size analysis and morphoscopy.

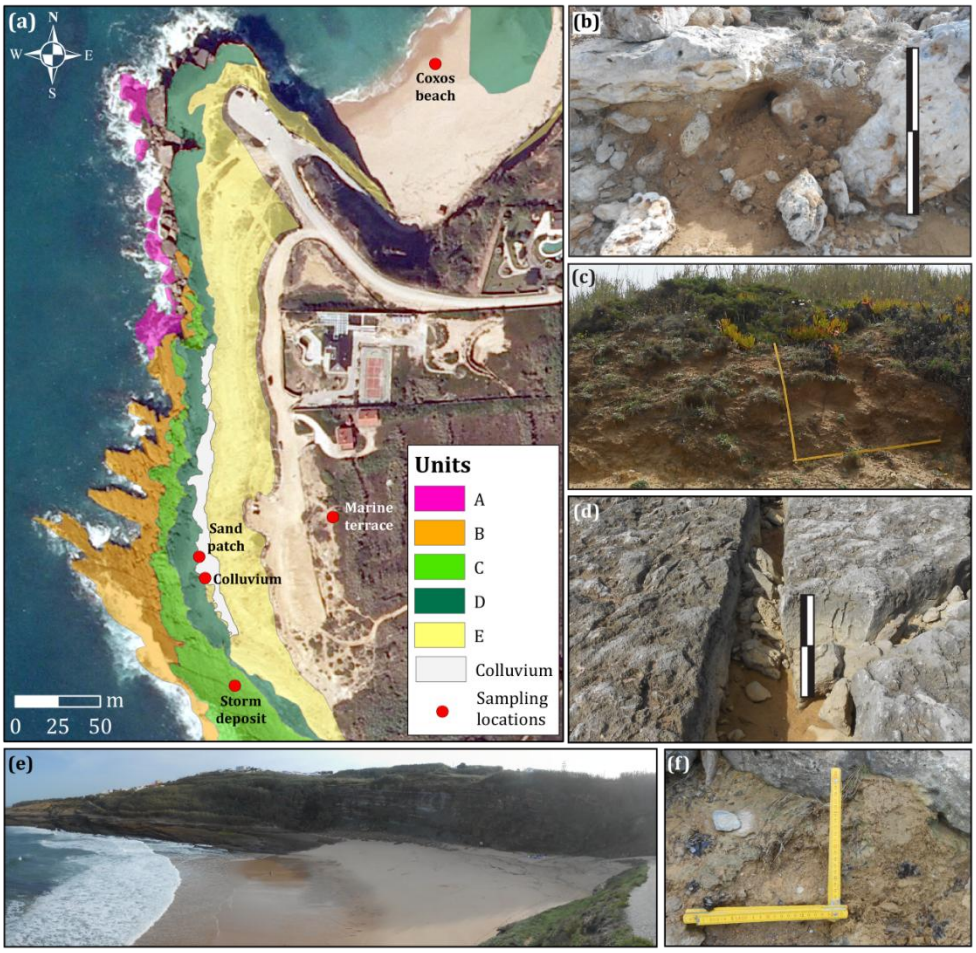

Figure 53: (a) Sampling locations in the study area over mapped units and a digital orthophoto from 2010 (IGEO, 2010). (b) Sampled sand patches found beneath a boulder accumulation; vertical scale corresponds to ~0.5 m. (c) Marine terrace outcropping at 25 m amsl, inland of the boulder accumulation; vertical and horizontal scales correspond to 0.6 m. (d) Widened joints partially filled with sand; vertical scale corresponds to ~0.5 m. (d) Northwards view of Coxos beach. (e) Sampled colluvium deposit; vertical and horizontal scales correspond to 0.2 m

The identification of the sediment source of the sand patch found beneath the boulder accumulation was made by comparison with other deposits identified

within the study area (Figure 53a, c, d, e and f), namely: (1) Coxos beach-face; (2) sandy material found after storms partially filling widened joints affecting S III; (3) colluvium deposit overlying S VI; (4) and marine terrace inland of the boulder accumulation in the southern sector, at 25 m amsl.

6.3.1 Grain-size analysis

Sediment discrete samples were processed in the laboratory for grain-size analysis and morphoscopy. Samples were dried in an oven at 60°C and subsampled with a sample splitter to obtain 50-100 g, the mass being measured with a decimal weighing scale.

Subsamples were wet-sieved using tap water and a 4 ϕ (63 μm) mesh to separate sand from finer fractions. The sand fraction was dried in an oven at 100°C, weighted and dry-sieved using a column of ASTM sieves at 0.5 ϕ intervals. The mass of the sand fraction and of individual fractions resulting from dry-sieving was measured with a decimal weighing scale.

The previously measured mass of different sand fractions was used to compute relative and cumulative frequencies and plotted in histograms and probability graphs, respectively, to evaluate the grain-size distribution and to identify different sub-populations. Moreover, the computer software GranGraph V2.0β (GranGraf V 2.0β Program for treatment of granulometric data, 1998) was used to compute grain-size graphical parameters (graphical mean, inclusive graphic standard deviation, inclusive graphic skewness and kurtosis) based on the cumulative frequency curve and to classify the sediment according to Folk and Ward (1957).

6.3.2 Morphoscopy

Morphoscopy consists in the observation of the surface of quartz grains under a binocular microscope (Carvalho, 2005). The 0.5 ϕ and 1 ϕ sand fractions, previously separated through dry sieving, were selected for morphoscopic analysis. The two fractions were mixed together and subsampled with a sample splitter until obtaining the desirable amount of sand (<30 g) to undergo mineral separation by density. This

procedure was repeated for the 1.5 ϕ and 2 ϕ to aid in the distinction between sub-populations for both the colluvium, marine terrace and sand patch samples.

Mineral separation by density was undertaken using a heavy liquid (Bromoform), with density 2.89 $g \cdot cm^{-3}$, using a separatory funnel and following the procedure indicated in Carvalho (2005). This technique allowed separation of translucent lighter minerals, such as quartz, from denser, such as zircon and tourmaline, to undergo morphoscopic analysis.

The surface of at least 100 quartz grains from the 0.5-1 ϕ fraction per sample were observed using an OLYMPUS SZX12 binocular microscope following the procedure indicated in Dias (2004) and Carvalho (2005). For each quartz grain the following characteristics were registered: (1) estimated roundness and sphericity based on the visual comparison chart by Powers (in Graham, 1988) (Figure 54); (2) surface lustre classification in polished, unpolished or frosted (Folk, 1974); (3) presence or absence of coatings covering the grains (*e.g.* oxidized iron coatings); (4) nature of the grains observed until reaching 100 quartz grains (quartz, bioclast, lithoclast, other).

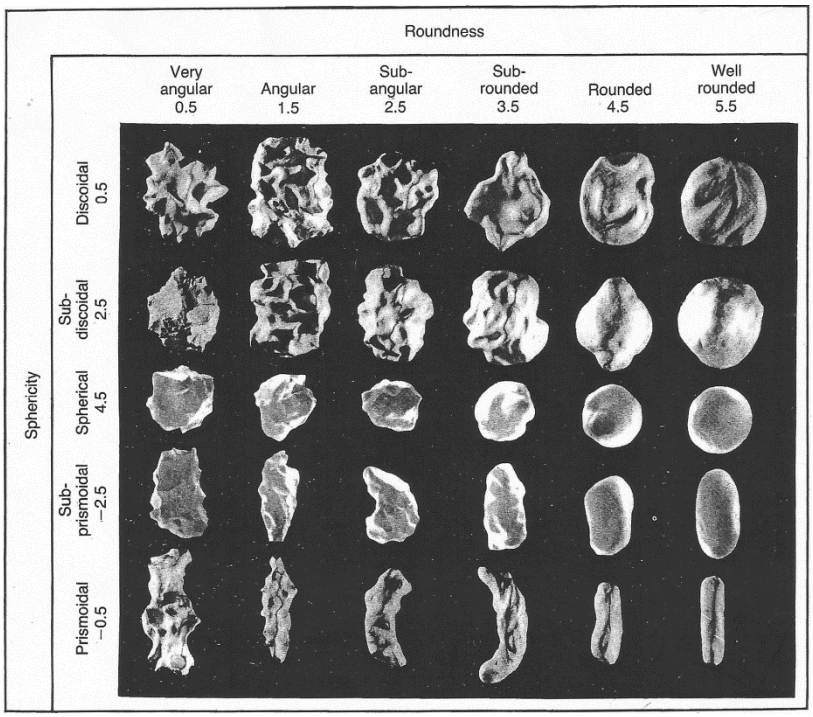

Figure 54: Visual comparison chart for estimating roundness and sphericity. From Powers (in Graham, 1988)

Roundness, sphericity, lustre, presence/absence of coatings and nature identified in the observed sand fractions, of at least 100 quartz grains, were plotted in histograms combining data from all samples.

6.4 Wave data

The wave data used in this work corresponds to a 56 year long (1953-2009) hindcast time-series obtained by Dodet *et al.* (2010). Moreover, wave parameters of storms which have generated boulder transport in the study area were also collected and used in this work. These datasets were used to model both wave propagation and statistical extreme events, following the methods described hereafter.

6.4.1 Storm wave propagation

Modelling wave propagation from the offshore to the nearshore of Coxos beach was undertaken for the yearly maxima of H_s and T_m records, filtered from the long hindcast time-series. Moreover, wave propagation of specific storms affecting the study area, and described in detail in section 7.2.2 (Present-day storms capable of generating boulder movement), were also modelled. Construction of the necessary topobatimetric meshes and a general explanation of the model and parameters used in simulating wave propagation are described in sections 6.4.1.1 and 6.4.1.2, respectively.

6.4.1.1 Topobatimetric meshes

Two topobatimetric meshes were constructed with distinct resolution and extents, to run the simulations with two distinct objectives: a regional mesh to be used in the propagation of offshore wave records to the nearshore (Figure 55a); and a local mesh to be used in the propagation of the resulting nearshore records along the study area (Figure 55d).

The regional mesh, presenting a 200 m resolution (Figure 55b and Table XVII), was built from 250 m resolution bathymetric data of the Hidrographic Institute of the Portuguese Navy (available at http://www.hidrografico.pt/download-gratuito.php), and 30 m resolution topographical data from the global digital elevation model

ASTER (Advanced Spaceborne Thermal Emission and Reflection Radiometer), product of the Japanese Ministry of Economy Trade and Industry (METI) and NASA (National Aeronautics and Space Administration) (available at http://reverb.echo.nasa.gov/reverb/).

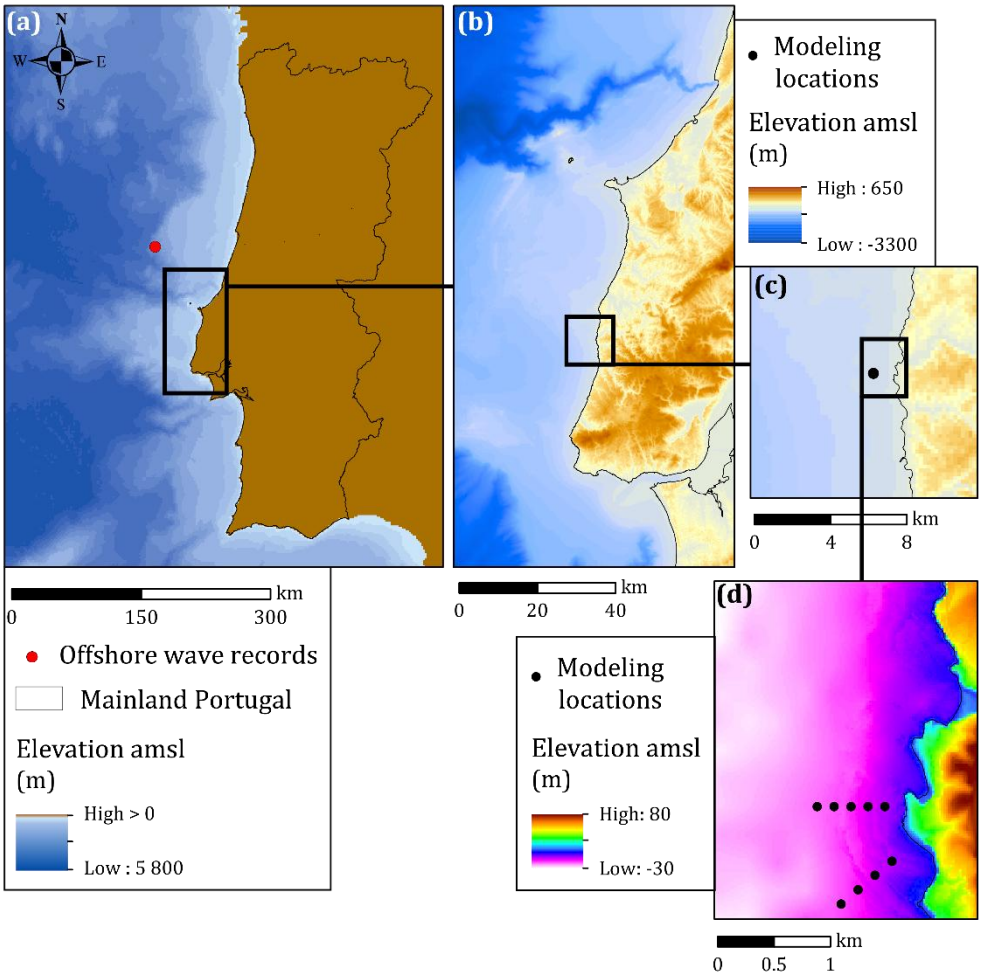

Figure 55: (a) Location of the regional mesh and of the offshore wave records used in most simulations. (b) Regional mesh. (c) Location of the point in the nearshore used in the simulations; (d) Local mesh

Table XVII: Details of the meshes built and used in wave propagation modelling. * ETRS89 PT-TM06 Coordinate System

MESH	RESOLUTION (m)	COORDINATES* (bottom left corner)		EXTENT (width×length m)
		x	y	
Regional	200	-148800	-131600	72000×144000
Local	20	-113800	-74000	2500×3000

The local mesh, with a resolution of 20 m, was based on bathymetric data from the Portuguese Hidrographic Institute and a 2-m resolution topo-batimetric LiDAR

(Light Detection and Ranging) mesh of the littoral stretch with a width of approximately 1 km (Figure 55d and Table XVII).

6.4.1.2 Wave propagation

Wave propagation was undertaken using SWAN© (Simulating WAves Nearshore) (Booij *et al.*, 1999) version 40.85, developed by the Delft University of Technology. Settings used in the simulations followed suggestions based on the SWAN model validation to a location in the W Portuguese coastline performed by Ribeiro (2013). Simulations were performed in stationary mode with significant wave height, mean period and mean direction as input wave parameters, following different procedures, depending on the objectives.

The first objective was to determine changes in extreme waves' direction as they approach the study area. Yearly maxima of significant wave height and mean period were selected for modelling wave propagation and filtered from the 56 year-long (1953-2009) hindcast time-series obtained by Dodet *et al*. (2010). The selected dataset comprised a total of 112 records, presented above, in the description of the study area (section 5.4 Oceanographic climate). Propagation of these waves was undertaken using the regional mesh, from the offshore to the nearshore, to a point about 1 km from Coxos beach (Figure 55b and c).

The second objective was the comparison of directional characteristics observed in boulders transported by known events, with wave characteristics in the nearshore. For this purpose, maximum wave parameters registered in wave-buoys and extracted from the website http://www.hidrografico.pt/boias-ondografo.php (presented in section 7.2.2), were selected for numerical modelling of wave propagation. Modelling was firstly undertaken using the regional grid to obtain boundary conditions to be subsequently used in wave propagation modelling over the local grid. Wave parameters were computed in several points located along two cross-shore sections in front of the southern sector, where most data from boulder monitoring exists (Figure 55d).

6.4.2 *Statistical modelling of extreme events*

The modelling of extreme marine-borne storm waves is particularly important in the analysis and prediction of destructive events. Statistical tools, such as the fitting of extreme value functions to wave-height datasets, have been extensively used in studies addressing long-term prediction of extreme wave-heights (Kamphuis, 2000). Soares and Henriques (1994) illustrate applications of such methods for the Portuguese coast. Pires and Pessanha (1986) fitted a log-normal distribution to data of significant and maximum wave heights and zero crossing period to estimate return levels for 1, 5, 10, 25, 50 and 100 years, based on a 6-year time series of instrumental data collected in several locations in the western coast of Portugal. Long datasets of instrumental wave records are not available and thus, application of these methods has been mostly undertaken on short datasets.

Estimation of extreme values is described by the extreme value theory (EVT) which focuses on the statistical behaviour of maximum values, M_n, over n time units (Coles, 2001):

$$M_n = max\{X_1, \dots, X_n\} \qquad \textbf{Equation 33}$$

where $X_1, \dots, X_n$, is a sequence of independent random variables having a common distribution function. Generally, X_i represents values of a process measured on a regular time-scale (Coles, 2001).

EVT stipulates that maximum values follow one of three distributions: type I or Gumbel; type II or Fréchet; and type III or Weibull. These three distributions can be represented as members of a unique family, with the following distribution function, known as the generalized extreme value (GEV) function (Kotz and Nadarajah, 2000; Coles, 2001):

$$G(x) = e^{\left\{-\left[1+\xi\left(\frac{x-\mu}{\sigma}\right)\right]^{-\frac{1}{\xi}}\right\}}, 1 + \xi\left(\frac{x-\mu}{\sigma}\right) > 0, -\infty < \xi < \infty, \sigma > 0 \qquad \textbf{Equation 34}$$

in which μ represents the location parameter, σ represents the scale parameter and ξ represents the shape parameter. When $\xi > 0$, the distribution assumes a type II

class; for $\xi < 0$ the distribution becomes a type III; and when ξ tends to $-\infty$ or ∞, the power function $1/\xi$ tends to zero and the distribution becomes a type I function.

GEV fitting to yearly maxima was done by using R statistical software (R: A language and environment for statistical computing, 2016), more specifically, the statistical package extRemes (Gilleland and Katz, 2011), which estimates function parameters by maximum likelihood. Depending on estimated shape parameter, a specific function is then selected (Gumbel, Fréchet or Weibull) to calculate return levels. GEV fitting was applied to maximum yearly values of H_s, T_m and wave power, P, (computed as described in Komar, 1976) from the 56 year hindcast time-series (from 1953 to 2008) obtained by Dodet *et al.* (2010), offshore central west Portugal (described in section 5.4). Data from 2009 was excluded because this year contained only 3 months of records. Extreme return levels and corresponding 95% confidence intervals were computed for return periods of 2, 5, 10, 20, 50, 100 and 200 years. The script used for data filtering, function parameters estimation and extraction of return levels is presented in Appendix I.

6.5 Computation of wave parameters

The application of numerical solutions of boulder transport to any case-study requires knowledge of the specific contexts for which the solutions were developed and of their limitations. In this work, the main objective of applying numerical solutions was the identification of the most probably type of waves (storm and/or tsunami) responsible for generating the boulder accumulation identified north of Ericeira and the approximate reconstruction of their parameters.

Based on results obtained with the validation of different numerical solutions to boulder accumulations of known origin, presented in chapter 4, flow velocity was extrapolated using Nandasena's *et al.* (2011a) equations for the transport mode of rolling. Conversion of flow velocity into broken storm wave tsunami wave heights was based in Nott's (1997, 2003) equations. Computed threshold wave heights corresponded to maximum values (H_{max}) and were converted to significant wave heights (H_s) using the following relationship (U.S. Army Corps of Engineers, 2008):

$$H_{max} \approx 1.67 H_s \qquad \textbf{Equation 35}$$

Lorang's (2002; 2011) approximation was applied to aid in the differentiation from tsunami and storm origin. Travelled distances considered when applying Lorang's expression were: (1) vertical distance between source layer and boulder position; and (b) the shortest horizontal distance from the seaward bench edge to the current boulder position. When boulder source layer was unknown, the lowest most probable layer was assumed, corresponding to a maximum vertical boulder transport.

6.6 Age estimation

Age estimation of boulder deposition is an essential part in the study of extreme marine events. This knowledge contributes with information regarding the frequency of these events, the identification of the type of event responsible for generating boulder transport and deposition by comparing with tsunami catalogues and wave records and finally, their recurrence periods. This task is often impossible to perform in boulder accumulations due to the absence of elements that retain information about the passage of time.

The chronology of boulder emplacement was evaluated with the aid of several methodologies: (1) comparison of aerial photographs and orthophotos of different dates; (2) lichenometry; (3) extrapolation of downwearing rates of a sandstone layer, measured beyond a limited shadow zone provided by a large boulder sitting on the exposed surface, being actively eroded; (4) OSL age estimation of marine sands found beneath boulders within a boulder ridge.

6.6.1 Aerial photographs

Recent movement of individual boulders and changes in boulder accumulations were assessed through the observation of aerial photographs taken in different dates. The oldest aerial photographs available for the study area were dated from 1948 and were made available in photographic paper, at ~1:7500 scale. More recent aerial photographs, dated from 2010 and with a resolution of 0.5 m, were available in digital format. Aerial photographs of 1948 were digitized and, together with the 2010 aerial photographs, were georeferenced by superimposition with 2010 digital orthophotos. Images were adjusted and corrected using at least 30 control points

and a 3rd order polynomial solutions, rendering total root mean square errors below 1 m (Figure 56).

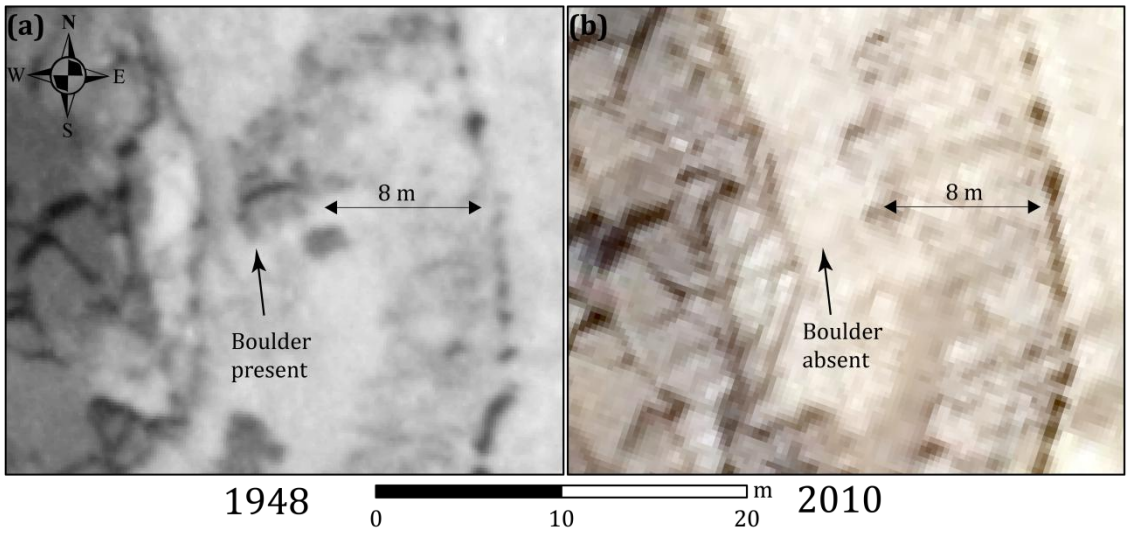

Figure 56: Comparison of 1948 and 2010 aerial photographs. A boulder visible in the 1948 aerial photograph, indicated by the arrow, is absent in the 2010 image

Boulder accumulations, colluvium and, whenever possible, individual boulders, were mapped over the georeferenced aerial photographs with the aid of a SOKKISHA mirror Stereoscope and GIS software. Moreover, when clearly identified, bench and cliff edges were also mapped. Additional elements such as oblique photographs from 1991 and 2010 and orthophotos from 2010 were also used to aid in the identification of geomorphological features. The position of individual boulders identified in the 2010 aerial photographs was defined based on field surveys and stereoscopic analysis of aerial photographs. All the remaining information, presented for both dates were mapped exclusively with stereoscopic analysis of aerial photographs.

Mapped geomorphological features with different dates were compared to identify changes. Boulder movement was considered to have taken place when changes in absolute boulder position surpassed 2 m (Figure 56), which corresponds to the sum of georeferencing errors obtained for the 1948 and 2010 aerial photographs. Changes in relative distances between boulders and other fixed elements in the images, larger than 2 m, were also considered as indicating movement. Moreover, evidences of boulder rotation (regardless of the distances involved), by opposition to simple translation, were also considered as displacement.

6.6.2 Lichenometry

To extend the time interval further, age estimation of the exposure of boulder surfaces was undertaken using lichenometry, based on the lichen size and cover of the species *Opegrapha durieui* Mont. (Roux and Egea, 1992). The conversion from relative to absolute age estimation was based on a growth model built for that species, using control points collected along the Portuguese coastline. Methods used in the collection of lichen data and the establishment of a lichen growth model are explained and justified henceforth.

Lichenometry is an age estimation technique based on the relationship between lichen size and time. This technique has been used to estimate age of surface exposure, assuming that if the time lag before colonisation of a substratum by a lichen is known, and lichen age can be estimated, then a minimum date can be obtained for the exposure by measuring size-related properties of the largest lichens present (Armstrong, 2015a).

There are several ways to measure lichen size: linear growth (length×time^{-1}), area growth (area×time^{-1}) and mass growth (mass×time^{-1}) (Hill, 2002). The choice of measurement depends on the growth form (morphology) of the thallus and, in lichens with circular crusts, both linear and area growths are likely to be successful (Hill, 2002).

Regarding linear growth, there are two possibilities when choosing the distance to be measured in individual thallus (Figure 57): diameter of the largest inscribed circle and largest diameter. The use of the diameter of the largest inscribed circle is more adequate in species showing circular growth and is frequently used when authors want to avoid overestimation of lichen size due to coalescence (*cf.* Innes, 1986).

Lichenometry can be used as a relative or an absolute age estimation technique, depending on the existence/absence of a calibration curve, also known as lichen growth curve (Noller and Locke, 2000).

Lichen growth curves can either be directly established, by frequent measurement of the same individuals, or indirectly, by measuring the size of thallus in surfaces of known age, named control points (*cf.* Beschel, 1961; Innes, 1985; Armstrong, 2004). Direct measurement of lichen growth shows that individuals present different growth rates depending on their size (age) (*cf.* Armstrong, 2015a). Additional fluctuation in lichen growth rates associate with environmental conditions, such as rainfall, temperature, light intensity, moisture or even properties related to the substrate, such as rock chemistry, texture and porosity (Armstrong, 2015b).

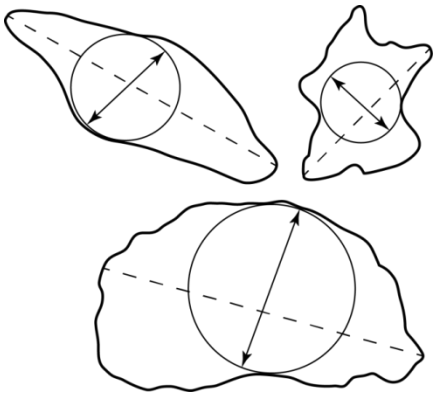

Figure 57: Alternative ways of measuring a lichen thallus: diameter of largest inscribed circle (arrows) and largest diameter (hatched lines). Modified after Innes (1985)

By choosing an indirect method to build a lichen growth curve, based on control points taken in locations with identical environmental conditions, the fluctuations in growth rates resulting from environmental factors and age are included as well as the unknown period of colonisation.

In this work, lichen growth curves were established indirectly, based on control points. These control points were collected in structures with known age containing the lichen species *Opegrapha durieui*. These comprise well dated coastal structures along the Portuguese coastline and, closer to the study area, recent (< 70 years) rock-falls (further described in Appendix L). For this purpose, a slope mass-movement inventory of the study area based on observation of aerial photographs and field validation was provided by Sónia Queiroz (inventory developed under the scope of the Faculdade de Ciências da Universidade de Lisboa/Instituto Dom Luiz/Agência Portuguesa do Ambiente, I.P. project "Creation and implementation of a Costal Monitoring System for the jurisdiction area of Administração da Região Hidrográfica do Tejo IP").

Following suggestions by Innes (1985), the age estimator used in this work was the average diameter of the largest enclosed circle obtained from the 5 larger individuals colonising the sample surfaces (Figure 58a). The selection of these individuals was based on visual inspection and their measurement to the closest millimetre was performed with a ruler. Care was taken in choosing individuals with clear boundaries and, whenever possible, showing no evidence of competitive restriction, as any coalescence with other individuals can invalidate age determination (*cf.* Beschel, 1961; Innes, 1985).

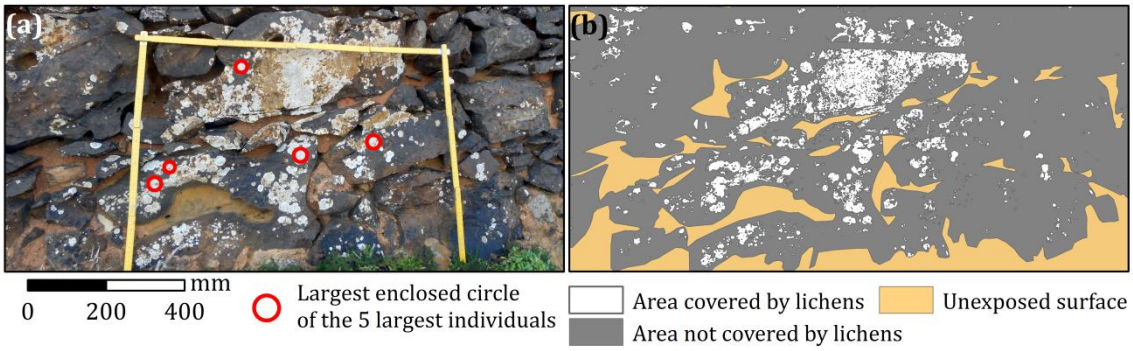

Figure 58: Methods used in Lichenometry. (a) Representation of the largest enclosed circles of the 5 larger individuals. (b) Same extent as represented in (a) with identification of areas covered and not covered by lichens

Besides linear, area growth measurements were also undertaken. Surfaces chosen for measuring the area covered by lichen thalli were those presenting the highest lichen cover, based on visual inspection, that were generally facing North. These surfaces were scaled and photographed in sections to maintain the best possible resolution for subsequent mosaic construction and quantification of lichen cover.

Mosaics were constructed using photo stitching software (using Adobe® Photoshop® or Hugin version: 2013.0.0.0d404a7088e6 built by Matthew Petroff) and scaled in GIS software (Esri®ArcMap™) (Figure 58a). Lichen cover area was extracted with photo editing software (Adobe® Photoshop®). Scaled mosaics containing extracted areas were automatically classified and converted into polygons with automatic image classification tools from GIS software (Figure 58b). Area not covered by lichens was obtained by subtracting covered area from total surface area and absolute values of area and percentage of lichen cover were then computed.

This procedure was applied to every studied surface containing the lichen species of interest, consisting of both the control points and the boulders to be dated, as indicated by Noller and Locke (2000). In the case of control points used in the construction of the lichen growth curve and model, sampling was undertaken in the surface showing the highest lichen cover. In the case of boulders to be dated, although all surfaces containing lichens were sampled, only those showing maximum growth were used in age estimation computations. For each sampled surface, strike and dip were measured with a compass and other relevant information was collected, such as the presence of competing species, shadowing, *etc.*

The construction of the lichen growth model using lichen control points and estimation of calendar ages was made with the best fitting function to lichen parameters and time, computed with R statistical software (R: A language and environment for statistical computing, 2016). The script used for function fitting is presented in Appendix M.

Most lichen species used for geochronology are circular in form and have slow growth rates to maximize the time range (Noller and Locke, 2000). The circular and slow growing species *Opegrapha durieui* was used in this study due to its abundance in both the boulders and substrate surfaces of the narrow coastal fringe where the boulder deposits are sitting (Figure 59).

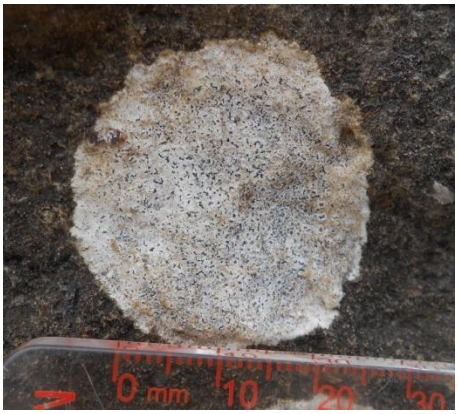

Figure 59: Photograph of a thallus of the species *Opegrapha durieui* in a boulder transported by an extreme marine event located in the southern sector of the study area

Species identification of collected voucher samples of lichens used in this work was undertaken by Doctor Esteve Llop Vallverdú (Unit of Botany, University of Barcelona, Spain).

Opegrapha durieui colonises calcareous rocks in the supra-littoral fringe subject to sea spray, in the Mediterranean and adjacent Atlantic coasts of Morocco and Portugal (Roux and Egea, 1992; Sipman and Raus, 1999). It generally occurs in N vertical and overhanging humid cliffs and it is absent in near-horizontal or softly pending dry surfaces with high exposure to sun-light (Roux and Egea, 1992).

Disadvantages associated with the use of the diameter of the largest inscribed circle reported in Innes (1986) were considered as minor given that this species shows a remarkably circular shape, regardless the size of the thalli (age). However, coalescence was frequent in surfaces with high lichen cover. The use of these individuals was avoided whenever possible.

6.6.3 Downwearing rates

Another approach to estimate the age of deposition of one large limestone boulder, also containing the lichen species *Opegrapha durieui*, was based on the extrapolation of downwearing rates of a cretaceous siltstone layer beneath the boulder, which is actively being eroded by surface run-off. Erosion estimations were obtained by regularly measuring vertical distances to a fixed point with a micro-erosion meter (MEM), from 2012 to 2015.

The presence of this boulder has created a shelter effect and prevented erosion of the siltstone layer to occur beneath the boulder. This sheltering effect has generated a pedestal of approximately 13 cm (Figure 60). The pedestal represents the amount of vertical downwearing of the siltstone that occurred since boulder deposition. If the erosion rate of the siltstone is known, time elapsed since boulder deposition can be inferred. The erosion rate was measured over the siltstone layer in several locations beyond the shadow area offered by the boulder.

The MEM consists of an equilateral triangular sturdy metal base, with three legs located at each corner, and a dial gauge located eccentrically, with a spindle extending through the base plate (Stephenson and Finlayson, 2009). Each leg has a

different base, referred to as wedge, a cone and a flat (forming a Kelvin lock), which allows a precise relocation of the device over three pre-installed bolts fixed on the rock surface (Figure 61) (Smith, 1978). Due to an off-centre spindle of the dial gauge, three readings can be made on each measurement site by rotating the instrument 120° (Stephenson and Finlayson, 2009; Moses *et al.*, 2014).

Figure 60: Pedestal of approximately 13 cm generated by the sheltering effect of a boulder, locally preventing downwearing of the underlying siltstone layer. Vertical scale in the inset is 20 cm; in the larger picture is 1 m long

Figure 61: MEM measurements over three pre-installed bolts fixed on the siltstone in the southern sector of the study area. Photo by R. González-Villanueva

Minimum values are read when the profile gauge is fully extended. Hence, a decrease in measurements corresponds to an increase in the distance between the gauge and the layers' surface. The lowering of the surface between time-separated measurements corresponds to the difference between dial gauge readings with an accuracy of ±0.01mm. Rate of erosion integrated throughout several measurements corresponds to the slope of a linear trendline adjusted to the readings *vs* time elapsed between them.

Three measurement sites were installed over the siltstone in January and February 2012 by inserting three round-head bolts in each sampling location. Field measurements were undertaken seasonally, whenever possible and following suggestions made by Smith (1978):

1. The MEM was carefully placed onto the bolts, commencing with the cone;
2. Once firmly positioned, the probe was gently lowered until touching the ground;
3. The dial was read to the nearest 10^{-2} mm;
4. The probe was raised and the sequence repeated for the remaining positions;
5. More than one reading was taken for each measurement and mean values computed;
6. Before and after each field survey, measurements over a test plate (plate of stainless steel with fixed reference bolts) were done to ensure that the instrument did not suffer damage between sample runs.

6.6.4 Optically stimulated luminescence

Two samples of clean sand, found beneath boulders of a boulder ridge were collected for age determination by OSL. These sand accumulations were exposed by heavy rains and wave swash storms that lasted over a month in January/February 2014, due to removal of overlying material (boulders and colluvium). Ages obtained with this technique correspond to minimum age of deposition of boulders sitting on top of the sand patches.

Sample preparation and analysis was performed by Doctor Ronald Goble (Department of Earth & Atmospheric Sciences, University of Nebraska-Lincoln). Sample preparation was carried out under amber-light conditions. Samples were wet sieved to extract the 90 – 150 μm fraction, and then treated with HCl to remove carbonates, and with hydrogen peroxide to remove organics. Quartz and feldspar grains were extracted by flotation using a 2.7 $gm \cdot cm^{-3}$ sodium polytungstate solution, then treated for 60 minutes in 48% HF, followed by 30 minutes in 47% HCl. The sample was then re-sieved and the <90 μm fraction discarded to remove residual feldspar grains. The etched quartz grains were mounted on the innermost 2 mm or 5 mm of 1 cm aluminium disks using Silkospray.

Chemical analyses were carried out using a high-resolution gamma spectrometer. Dose-rates were calculated using the method of Aitken (1998) and Adamiec and Aitken (1998). The cosmic contribution to the dose-rate was determined using the techniques of Prescott and Hutton (1994).

Optically stimulated luminescence analyses were carried out on Risø Automated OSL Dating System Models TL/OSL-DA-15B/C and TL/OSL-DA-20, equipped with blue and infrared diodes, using the Single Aliquot Regenerative Dose (SAR) technique (Murray and Wintle, 2000). Early background subtraction (Ballarini *et al*., 2007; Cunningham and Wallinga, 2010) was used. Preheat (240° C/10 s) and cutheat (220° C/0 s) temperatures were based upon preheat plateau tests between 180° and 280° C. Dose-recovery was within 2-sigma of 100% and thermal transfer within 2-sigma of 0 Gy (Murray and Wintle, 2003). Sample growth curves were below saturation (D/Do<2; Wintle and Murray, 2006). Optical ages are based upon a minimum of 50 aliquots (Rodnight, 2008). Individual aliquots were monitored for insufficient count-rate, poor quality fits (*i.e.* large error in the equivalent dose, De), poor recycling ratio, strong medium *vs* fast component (Durcan and Duller, 2011), and detectable feldspar. Aliquots deemed unacceptable based upon these criteria were discarded from the data set prior to averaging.

Results and interpretation

This chapter encloses four sections, starting with the description of the boulder accumulations (section 7.1) combining field observations and results obtained from the analysis of general attributes (lithology, burial, imbrication), scalar (mass) and directional (ab dip direction and a-axis trend) properties of individual boulders. Results are firstly presented separately for the northern (7.1.1) and southern sectors (7.1.2) and are followed by a comparison between their characteristics and interpretations (7.1.3).

The second section (7.2) comprises the description of recent boulder movement detected in the study area associated with specific storms. Moreover, these storms are described, focusing on tidal level, significant wave height, period and wave direction offshore and nearshore, resulting from modelling storm wave propagation in two cross-sections in the study area. Finally, the parameters of storms capable to generate boulder movement are compared with results obtained with statistical modelling of extreme values for significant wave height, wave periods and wave power, to ascertain the frequency of these events.

The third section (7.3) presents results obtained with the application of numerical solutions for boulder transport and inferred wave parameters.

In the last section of this chapter (7.4), results obtained with the application of age estimation techniques are presented. They include comparison of aerial photographs, lichenometry, erosion rates obtained with MEM's and OSL dating of a marine sand deposit found within a boulder cluster.

7.1 Boulder deposit

The boulder deposit of Coxos comprises 1613 boulders that accumulated in two sectors, located N and S of Coxos beach. All the elements considered in this deposit were sourced in layers outcropping at lower altitudes. Mass density measured in samples collected from these layers rendered similar values, between 2484 $kg \cdot m^{-3}$ and 2671 $kg \cdot m^{-3}$, listed in Appendix J.

7.1.1 Northern sector

The deposit located N of Coxos beach contains 34 boulders with mass ranging from 100 kg to 26 ton, located at 3.7-10.1 m amsl, and mostly between 6 m and 10 m amsl (Figure 62a). The deposit presents a N-S general alignment, mimicking both the coastline trend and the bench edge (Figure 62a). Boulders are located at the top of a low stepped cliff facing NW, and in the middle of a SW facing ramp, both developed in layers of Unit C (Figure 62b and f).

Source layer has been identified for all 34 boulders, most having originated in layer L19 (53%), followed by L15 (25%), L16 (16%) and finally L18 (6%) (Figure 62c). In some cases, boulders were composed of more than one layer, making it simpler to establish origin and polarity. In the example presented in Figure 62e, boulders originated in layers L18-L19, are upside down and probably originated from lateral extensions of *in situ* layers.

Larger boulders (mass > 2.5 ton) were sourced in layers L15-L16 (transition between Units B and C) and L19 (Unit C), the exception being the largest boulder in this sector (mass~26 t), which was sourced in layer L16 (Unit B). The latter leans against a small bench step on the top of the NW-facing cliffed section (Figure 62a, b and d).

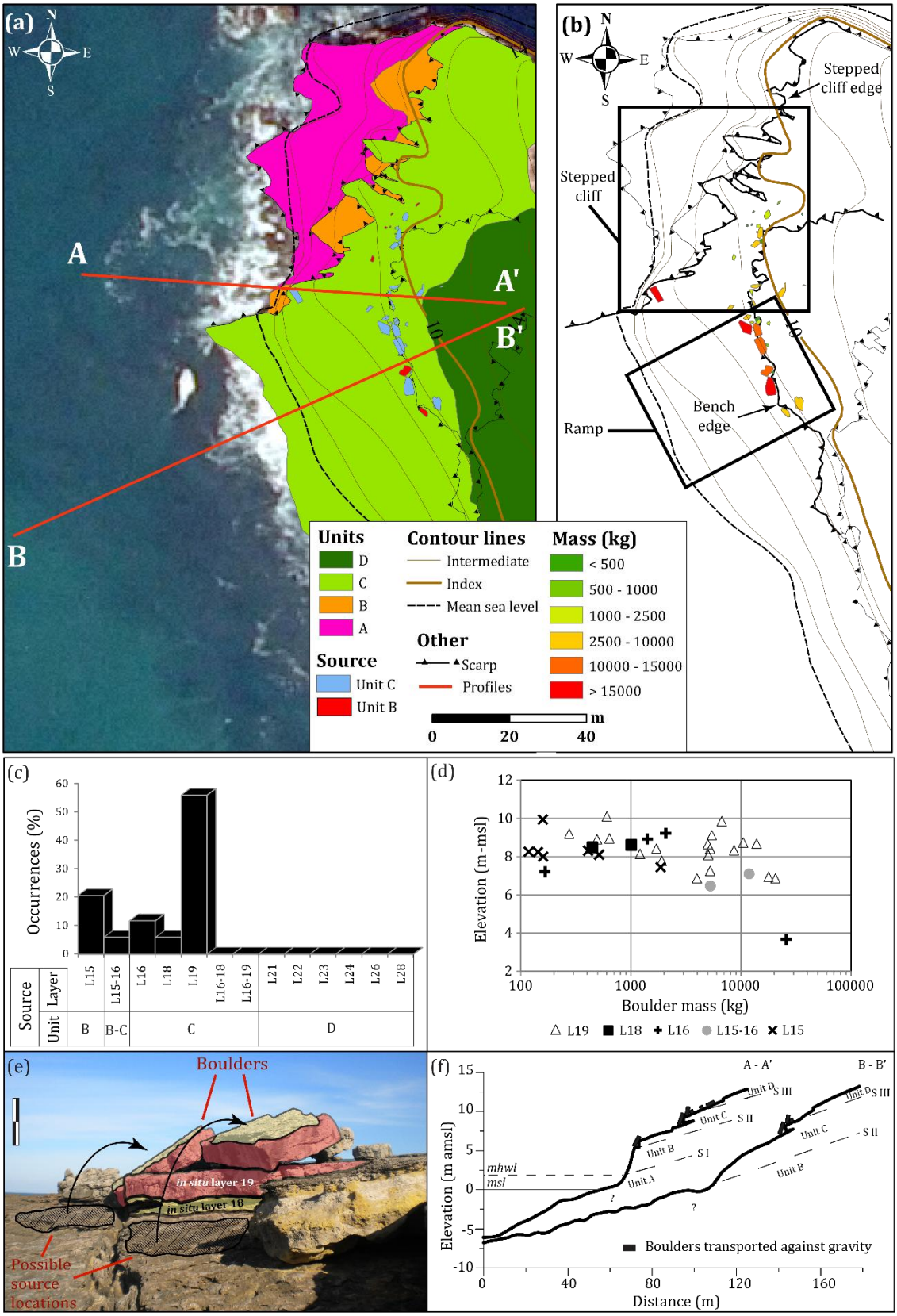

Figure 62: Boulder deposit in the N sector. (a) Location and source units of boulders in the northern sector; (b) spatial variation of boulder mass; (c) Source layers of boulders identified in the northern sector; (d) scatter plot of boulder mass against elevation grouped by source layer; (e) example of current position, possible source location and stratigraphical origin of boulders in the northern sector (vertical scale is approximately 1 m); and (f) Profiles A-A' and B-B' (see (a) for location)

The remaining population of larger boulders can be further subdivided according to their mass and position. Those with mass above 10 ton align and lean against a N-S to NW-SE trending bench edge developing on surface S III. They formed by the detachment of particles from the fracture-controlled edge of *in situ* layer L19 (Unit C). Boulders with mass ranging from 2.5 ton to 10 ton, were found sitting on surface S III, up to 5 m landward of the bench edge, and scatter along structural surfaces outcropping seaward and below surface S III (Figure 62b). The remaining (smaller) boulders, with mass under 2.5 ton, originated in layers L15, L16, L18 and L19, and occur scattered along structural surfaces outcropping seaward and below surface S III.

The plot of boulder mass against height of emplacement (Figure 62d) suggests a general fining trend with increasing elevation. Up to 2.5 ton, boulder elevation seems unrelated to boulder mass, as indicated by the elongation of the point cloud, paralleling the x-axis. The spatial variation of boulder mass indicates landward and northward fining trends (Figure 62b and d).

Although most boulders lean against bench edges, no evident imbrication of particles was observed in the N sector. Boulders are fully exposed, no marine sand or other finer materials where found in association with the boulders and no vegetation is growing around them either. All the boulders originating in layer L19 are partially covered with lichens of the species *Opegrapha durieui* (further details about lichen size and cover are described in section 7.4.2.2).

The analysis of particle shape, defined by b/a and c/b axes ratios, reveals larger frequencies of blade-shaped boulders (50.0%), equal occurrences of disk and rod-like boulders (23.5%) and smaller representation of spherical boulders (3%, corresponding to just one case) (Figure 63a and b). Although some associations between source layer and boulder shape may be suggested in Figure 63b (*e.g.* rod-like shapes preferably associate with boulders originating in layers L15 and L19), the small number of particles in this sector inhibits to derive correlations between shape and source layer.

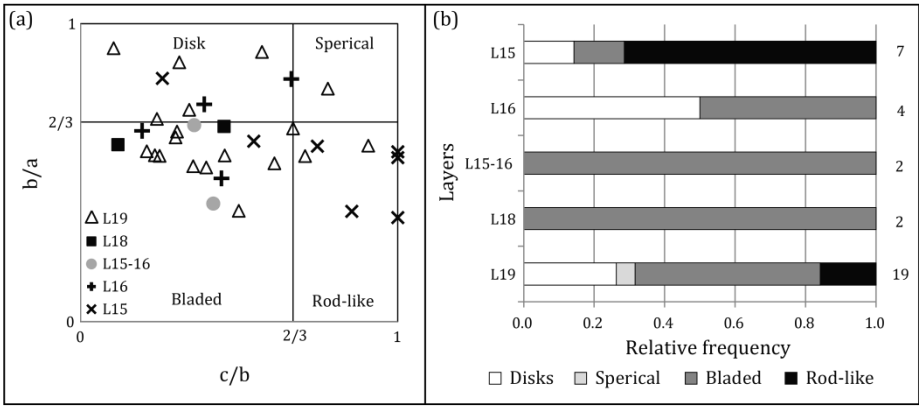

Figure 63: Diagrams shopwing boulder shape in the N sector. (a) Scatter plot of boulders' axes ratios b/a and c/b, (Zingg's shape classification diagram) grouped by source layer; (b) relative frequency of boulder shape for each layer (numbers to the right correspond to sample size)

The frequency distribution of axes' length is represented in Figure 64. Results obtained for a- and b-axes, show a unimodal population, asymmetric and positively skewed (tail towards larger dimensions) with an identical modal size-class interval of 1-1.5 m. The c-axis distribution is also unimodal and asymmetric, but it is negatively skewed and the mode is contained in the size-class interval of 0.5-0.75 m.

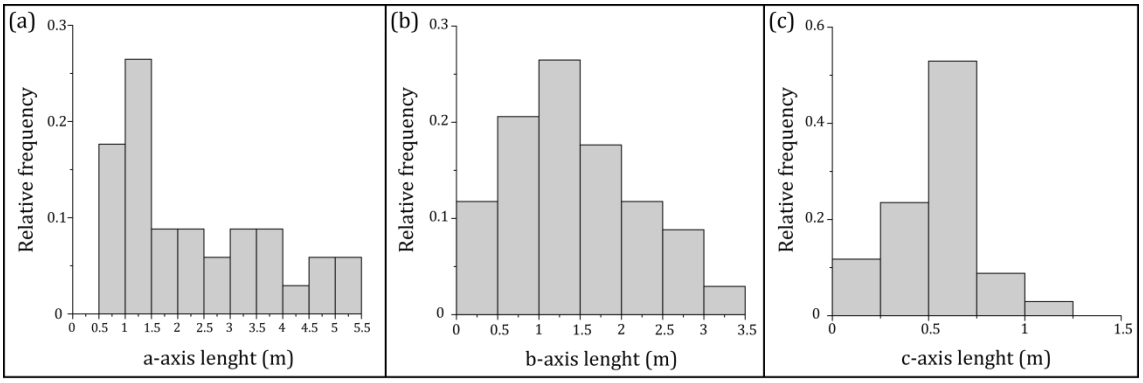

Figure 64: Histograms of boulder axes' length in the N sector (N=34): (a) a-axis; (b) b-axis; and (c) c-axis

Directional properties of disk-shaped, bladed and rod-like boulders identified in the northern sector, are represented in Figure 65. The ab surface preferably dips towards the W quadrant, evidencing two main directional sub-populations of 220°-260° (SW-WSW) and 260°-300° (W-WNW), containing 67% of particles and subdivided in minimum frequency classes (Figure 65a). In general, heavier boulders follow the same directional tendency, with higher frequency of tilt towards the WNW (280°-290°). The a-axis trend of disk-shaped, bladed and rod-like boulders located in the N sector shows two directional clusters: 220°-270° (SW-WSW) and 310°-340° (NW-NNW), containing 63% of particles (Figure 65b).

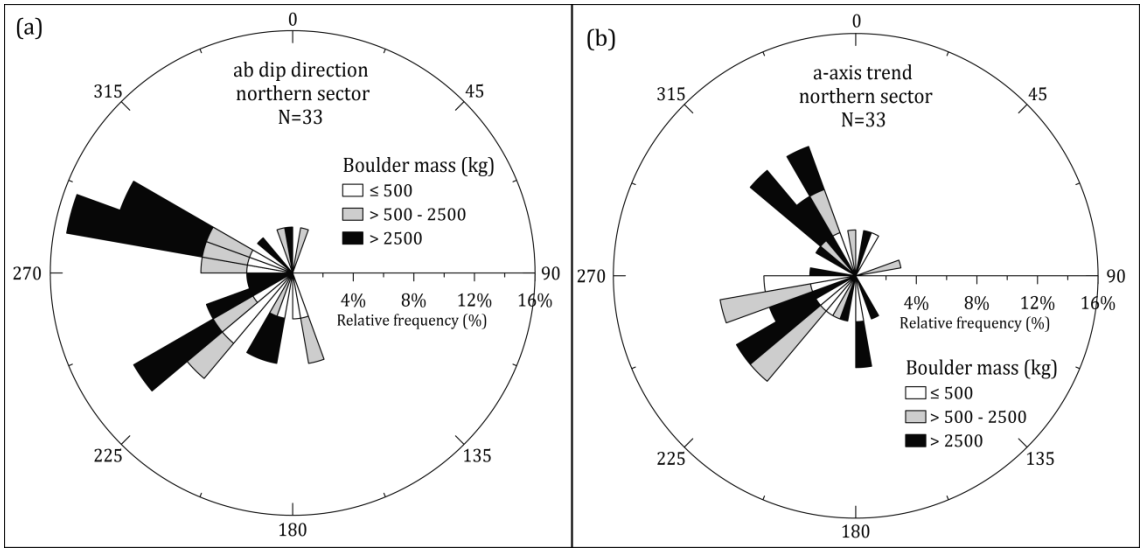

Figure 65: Rose diagrams projecting directional properties from boulders in the N sector: (a) ab surface dip direction; and (b) a-axis trend

In general, the spatial distribution of the ab surface dip, represented in Figure 66a, does not show a clear pattern, except for a cluster containing the largest boulders in the southernmost segment of the northern deposit. These particles consistently dip towards the SW, roughly corresponding to the orthogonal of the bench edge upon which they lean. The spatial variation of the a-axis direction of all boulders in the N sector shows a preferable NNW-SSE to NNE-SSW alignment, following the direction of both the bench step limiting surface S III, and the coastline (Figure 66b).

The identification of the boulders' source layer and of specific pre-transport locations can be used to trace shortest travelled paths, and thus infer on the direction of the flow responsible for boulder transport. In the N sector, possible source location of boulders indicates two transport directions, roughly aligned cross-shore (ENE-WSW) and along-shore (NW-SE) (Figure 67a and b).

Largest boulders sourced in layer L19 (mass > 10 ton) leaning against or at the bench edge topped by surface S III, suffered minimum vertical and horizontal displacement, the transport being equal or smaller than the size of the boulder. Some of these boulders were not pushed over the 1-2 m step, indicating that the flow was only capable of slightly lifting and/or rotating them (Figure 62e). Boulders also originated in layer L19 with mass ranging from 2.5 ton to 10 ton were transported up to 5 m landward of their possible source location, suggesting inland cross-shore transport (Figure 67b).

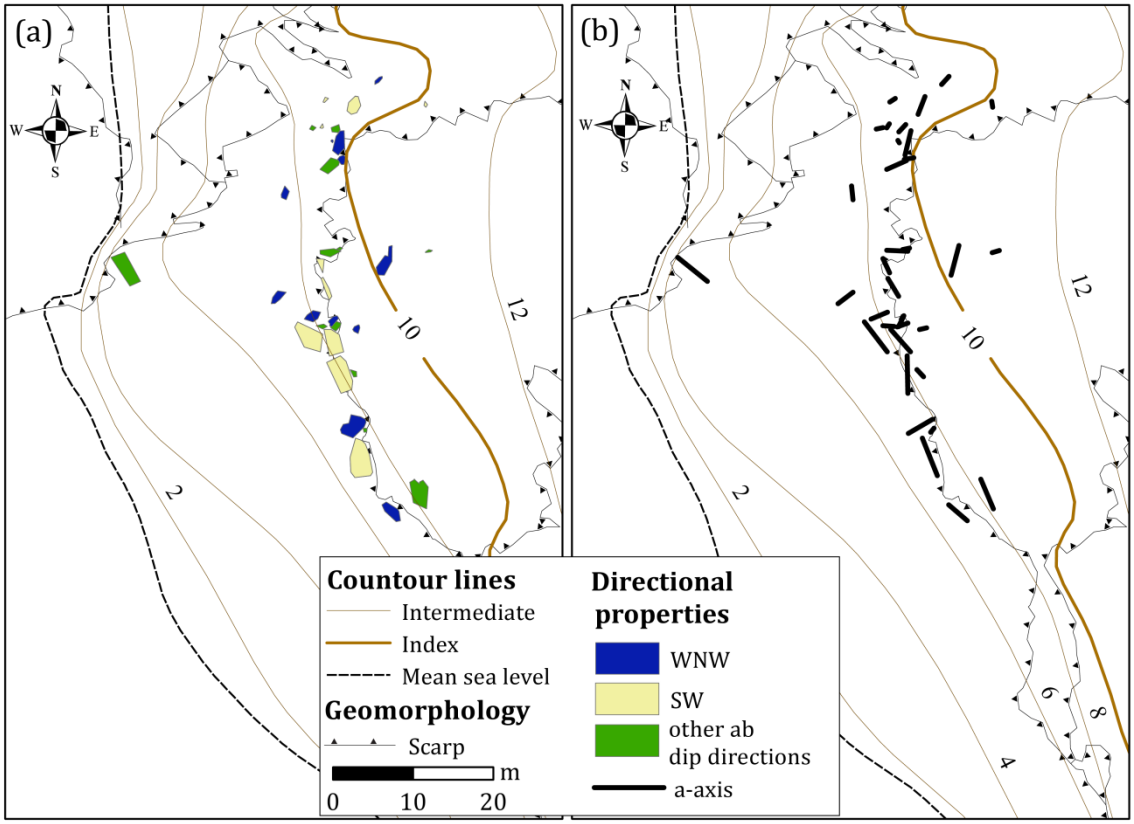

Figure 66: Mapped directional properties of boulders in the N sector. (a) Disk-shaped, bladed and rod-like boulders in the N sector dipping towards three directional clusters: SW (220°-260°), WNW (260°-300°) and other directions. (b) representation of the boulders' a-axis in the N sector

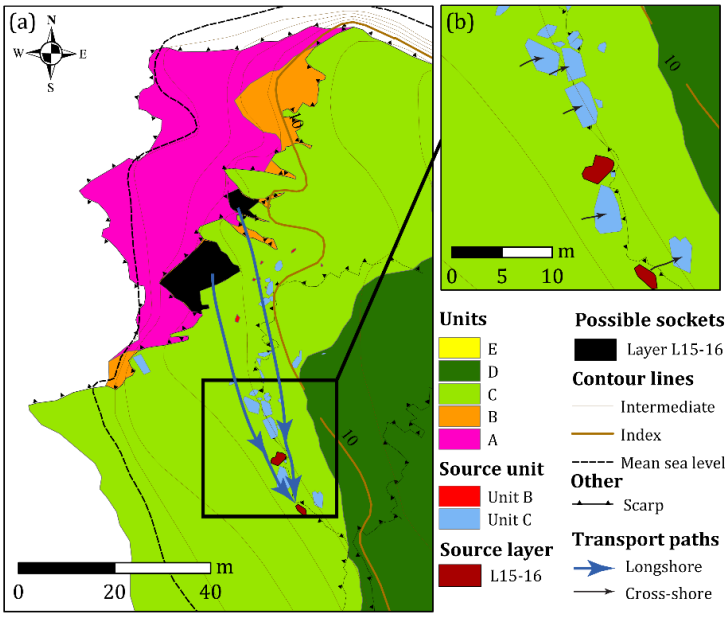

Figure 67: Location of boulders sourced in layer L15-16 and possible sockets where they originated from

Along-shore transport towards S is suggested by two boulders, with 5 ton and 12 ton each, sourced in layers L15-16 (Units B and C), their possible sockets outcropping 35 m to 65 m N and NW of their present location (Figure 67). The ab

surface of these particles dips towards W and SW, although their sediment source is indicative of transport from NNW to SSW.

7.1.2 Southern sector

The deposit located south of Coxos beach contains over 1500 boulders sitting on sub-horizontal structural surfaces from 1.8 m to 12.8 m amsl, developing along an indented 300 m stretch of rocky coastline (Figure 68). These surfaces decrease in elevation and increase in width towards S, following the geometry of the outcropping Cretaceous sequence. This coastal sector comprises varied cross-shore profiles, ranging from low and vertical (Figure 69a) to irregular cliffs (Figure 69b and c) to stepped sub-horizontal structural platforms (Figure 69d), on the top of which boulder accumulations and colluvium deposits occur.

The source layers of 409 out of 1579 boulders were identified in the S sector (Figure 70). Similarly to the northern sector, the most frequent source material corresponds to the layer topped by the surface upon which boulders sit: layer L28 (Unit D) for boulders sitting on surface S IV (78%) and layer L19 (Unit C) for boulders sitting on surface S III (~10%) (Figure 68, Figure 70 and Figure 71a and b). Boulders originating in layers L16-18 and L16-19 correspond to approximately 5% of the deposit.

Uncertainty in the identification of source layers occurs in boulders sitting on surface S IV and forming boulder ridges. These particles are generally small and lack micro-morphological or geometrical features enabling correlation with their source layer. However, the number of probable source layers was reduced to L19, L22, L24, L26 and L28 (15-20%) using the principles defined in section 6.2.

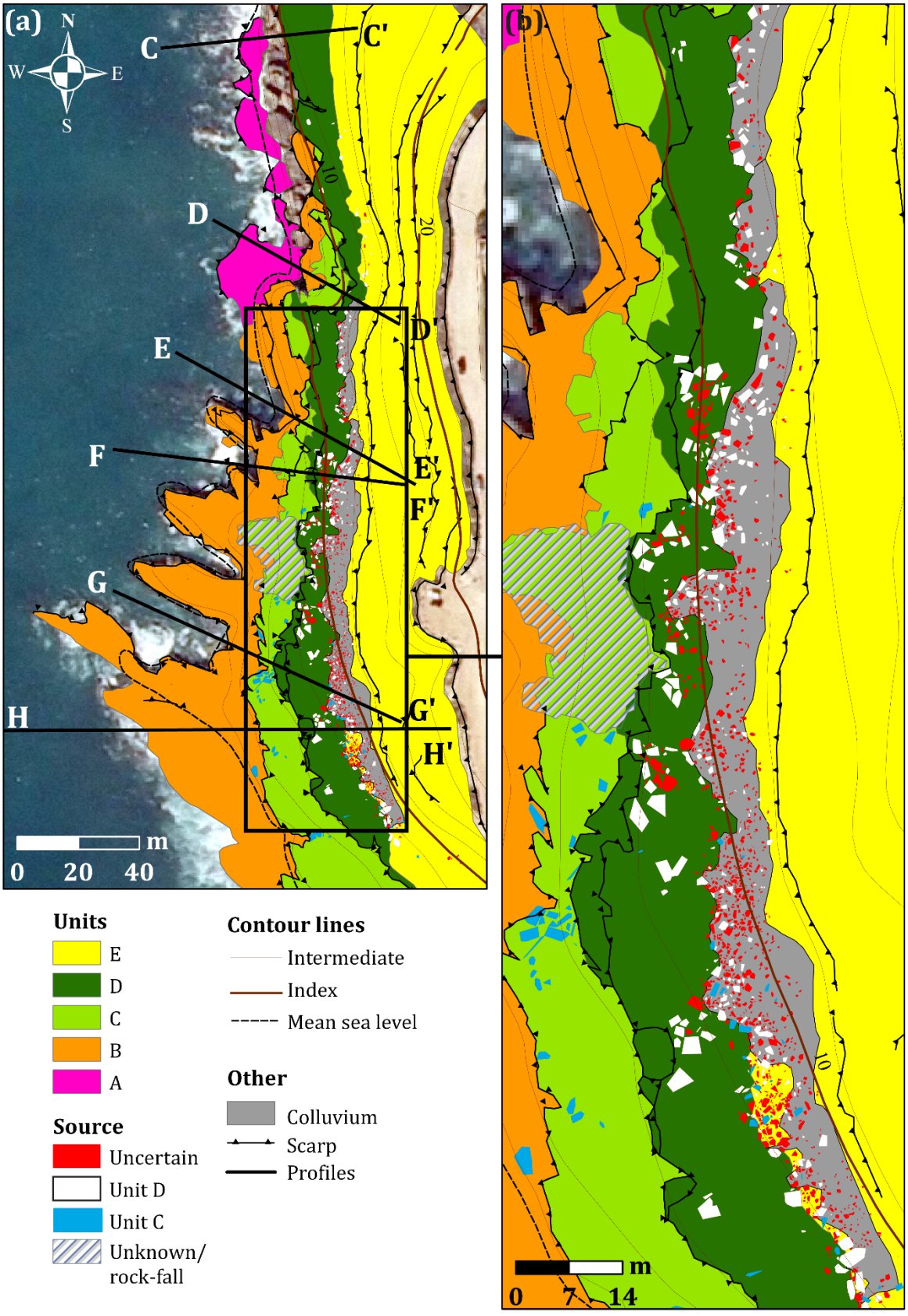

Figure 68: Map showing outcropping units, colluvium and boulders in the S sector (classified by source layer) and the location of profiles presented in Figure 69

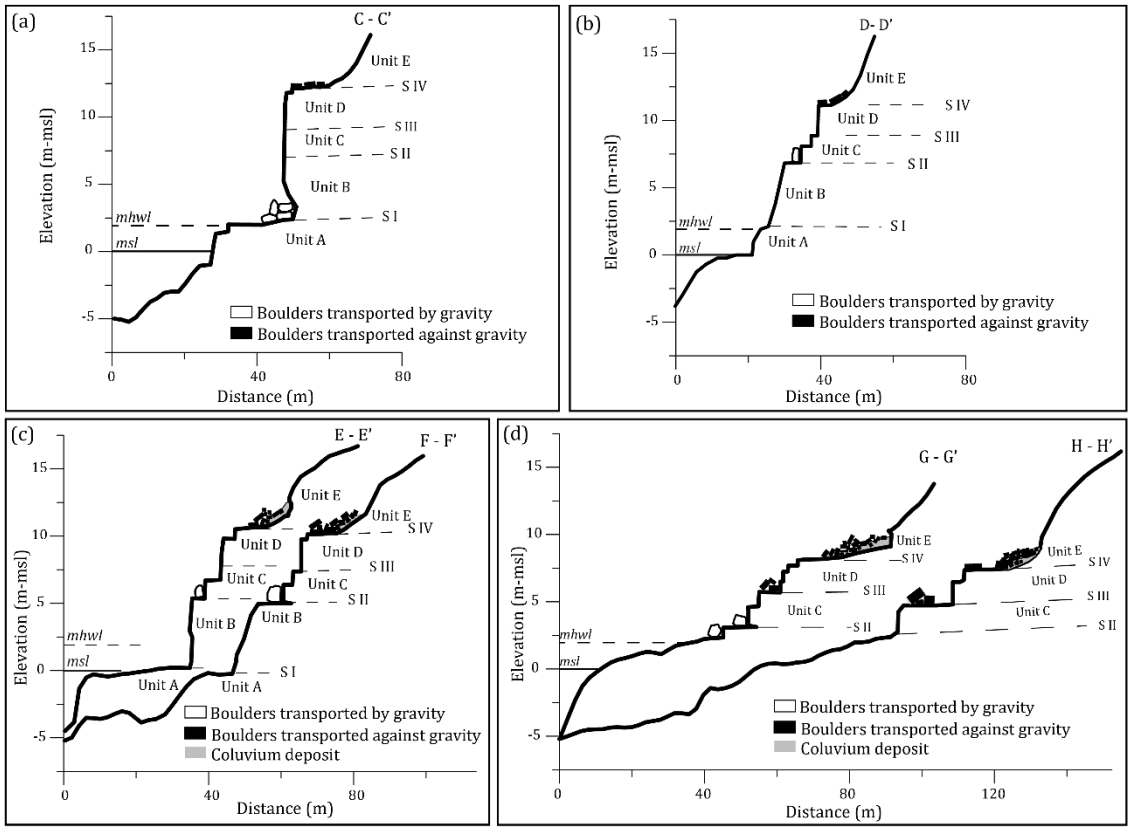

Figure 69: Cross-sections of the S sector. (a) Profile C-C'; (b) Profile D-D'; (c) Profiles E-E' and F-F'; (d) Profiles G-G' and H-H' (see Figure 68a for location)

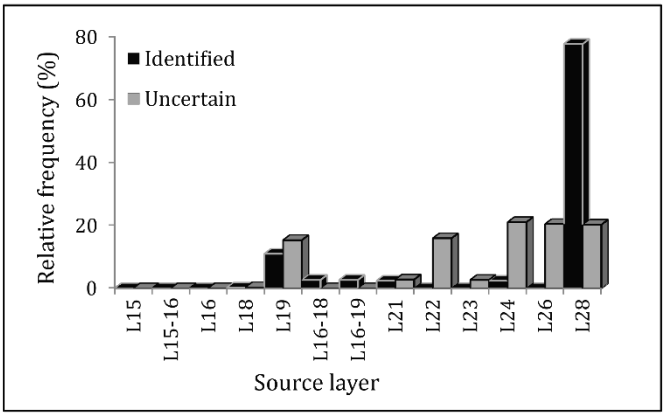

Figure 70: Source layers of boulders identified in the S sector

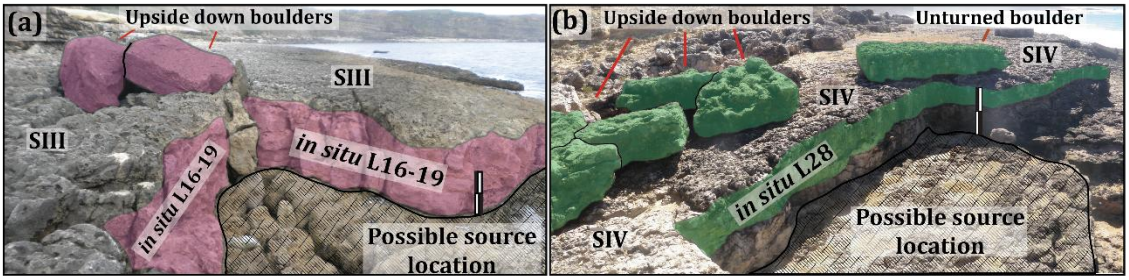

Figure 71: Boulder sockets in the S sector. (a) Current position, possible source location and stratigraphical origin of boulders sourced in Unit C and sitting on surface S III; (e) Current position, possible source location and stratigraphical origin of boulders sourced in Unit D and sitting on surface S IV (photo by T.M. Silveira). Vertical scales correspond to ~1 m

Larger boulders, with mass ranging from 10 ton to 30 ton, form one sub-population, and are mostly found over or leaning against the bench edge topped by surface S III (Figure 71a and Figure 72a), frequently reached by storm waves during high tide. They were all sourced in Unit C and their size relates with higher layer thickness and lower joint spacing characterizing this unit, as well as with the occurrence of boulders comprising more than one layer (L16-18 and L16-19). A second sub-population sitting on surface S III consists of smaller boulders (mass ranging from 2.5 ton to 10 ton), generally arranged in clusters and sometimes showing imbrication.

Boulders sitting on surface S IV are here subdivided in three sub-populations based on field observations, mass, source layer, distance from the bench edge and morphology of boulder accumulations. In locations where boulder frequency is higher, these sub-populations merge into a continuous accumulation.

1. Isolated boulders or boulder clusters sitting near the bench edge mostly sourced in layer L28 (topmost layer of Unit D). These range in mass from 2.5 ton to 10 ton, and show parallelepiped shape and straight edges. In some cases, they are located close to sockets (< 2.5 m) from which they originated (Figure 71b and Figure 72b).
2. Boulders clustering closer to the landward edge of surface S IV, sometimes forming ridges (Figure 72b and Figure 73a). These particles present variable shapes, rounding and size (including cobbles) with mass up to 1 ton and, in broad terms, show fining upward and inland trends. They were mostly sourced in layers from Unit D or in unidentified layers and they rest over and/or are partially covered by colluvium deposits. Boulder ridges attach by their northern tips to the low-sloping cliffs affecting Unit E. They are aligned N-S to NE-SW and show poorly defined crests (Figure 73a). The boulders comprising the ridges sometimes show imbrication, but this feature is limited to a few particles within clusters (Figure 73b).
3. The third sup-population comprises boulders sourced in layers L28 and L19 with a wide mass range (1-10 ton). They align in elongated clusters bordering the second innermost sub-population, and in cases merge with the seaward tip of the ridges (Figure 72b and Figure 73c). These aligned boulders function

as a barrier blocking the washing out by rain or wave swash/backwash of the colluvium deposited further inland. In locations where the rocky bench is wider, there is a barren band between this boulder sub-population and the first.

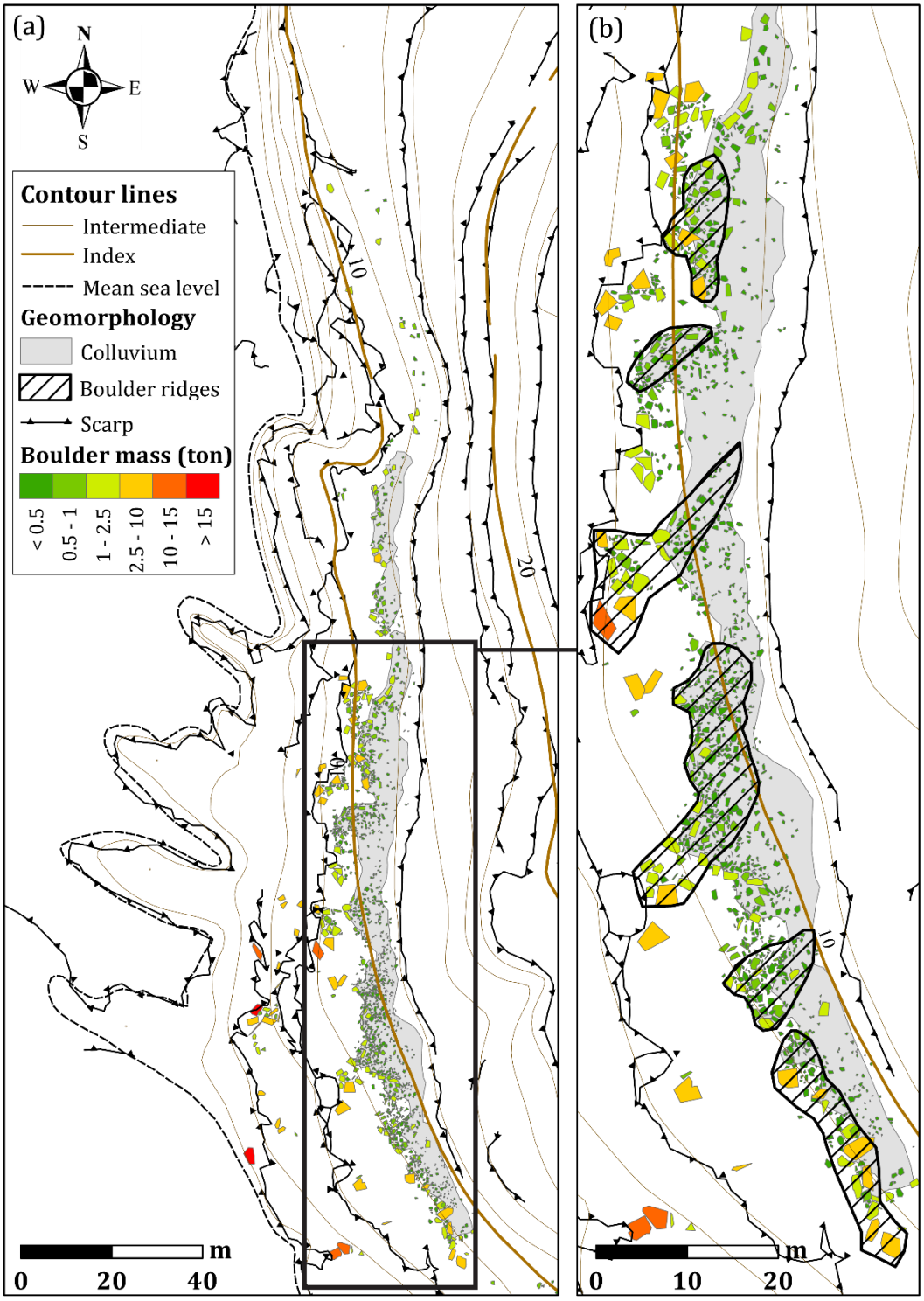

Figure 72: Mapped boulder mass in the S sector. (a) Spatial variation of boulder mass; (b): Spatial variation of boulder mass over surface S IV and delimitation of boulder ridges

The spatial variation of boulder mass shows a landward and northwards fining trend, similarly to the northern sector. The projection of boulder mass against height of emplacement (Figure 73d) suggests a fining upward trend that is particularly evident for boulders with mass larger 300 kg. Up to 300 kg, emplacement elevation is unrelated to boulder mass, as indicated by the elongation of the point cloud, paralleling the x-axis.

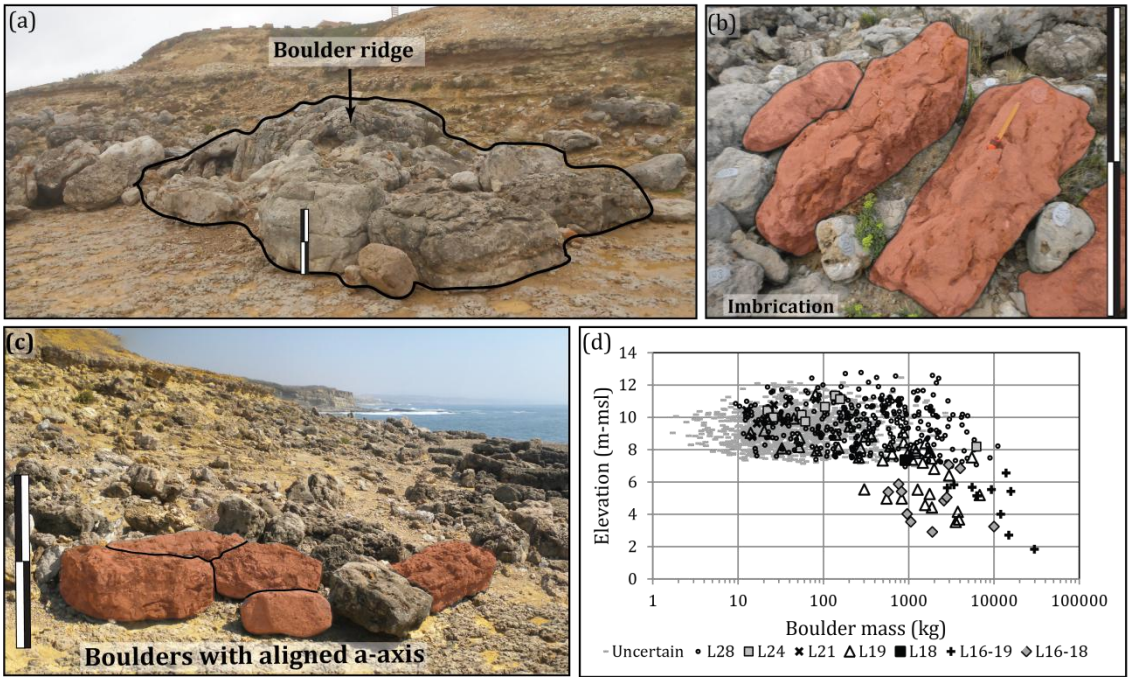

Figure 73: (a) Cross-sectional view of a boulder ridge aligned NE-SW; (b) Boulder imbrication within a boulder ridge, partially covered by colluvium, in the S sector; (c) Boulders with aligned a-axis, paralleling and limiting the colluvium; (d) Scatter plot of boulder mass against elevation grouped by source layer. Vertical scales correspond to ~1 m

Development of the colluvium deposits partially buries some of the boulders of the previously mentioned second and third sub-populations sitting on surface S IV. In the S sector, most boulders are fully exposed or slightly buried (69%), 29% are partially buried and only 2% are almost completely buried (Figure 74). Given that mass is calculated based on boulder volume and density, underestimation of that scalar property can be expected in some cases.

Besides the five boulder sets described above (2 sub-populations covering surface S III and 3 sub-populations over surface S IV), there is a highly mobile boulder/cobble deposit located in the middle of the southern section. This accumulation partially covers surfaces S II and S III at 4 -8 m amsl, and forms an active ridge with WSW-ENE general alignment, where boulder reworking and

transport by waves frequently occurs (mapped in relation to an unknown- or rock-fall- source in Figure 68a). It comprises rounded boulders from undetermined source and larger parallelepiped boulders originating in rock-fall from layers outcropping at higher altitudes (Figure 75). Difficulty in identifying source layers was due to rounding and intense abrasion that obliterated original layer geometry and morphology. Besides information regarding the approximate location of this accumulation, boulder individual position and characteristics were not collected.

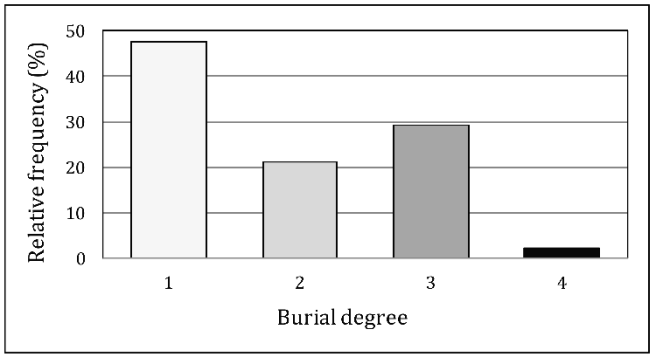

Figure 74: Relative frequency of burial degree in boulders from the S sector

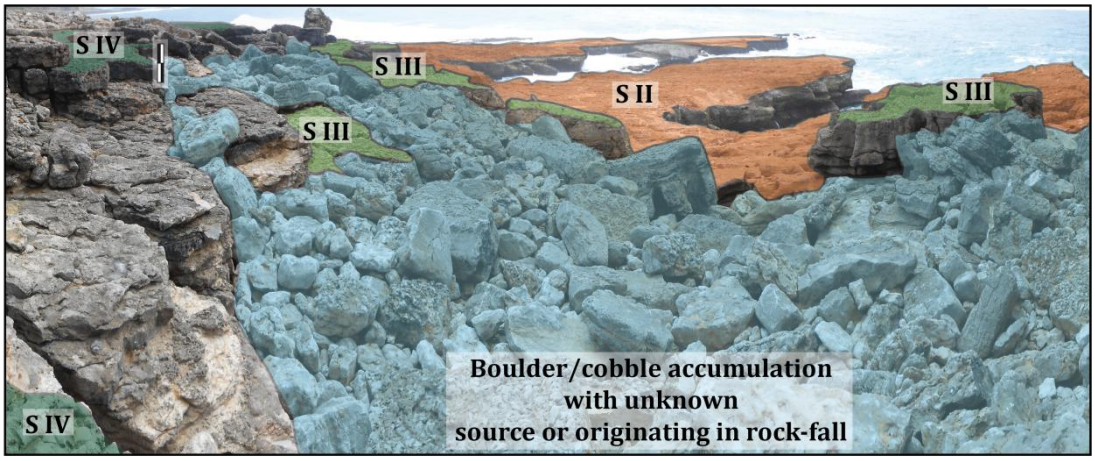

Figure 75: Boulder and cobble accumulation over S II and S III with unknown source layers or sourced in rock-fall. Vertical scale corresponds to ~1m

Results of shape classification of boulders located in the S sector reveal larger frequencies of disk and blade-shaped boulders (35.2 and 32.1%, respectively), followed by rod-like boulders (23.1%), and by a smaller representation of spherical boulders (9.3%) (Figure 76a). This pattern is repeated for boulders originated in layer L28 (N=319) (Figure 76b). Contrary to the remaining layers, boulders originating in layer L19 (N=45) are more frequently spherical than disk-shaped or bladed. Remaining cases lack statistical significance due to the small number of particles (N≤11). However, it appears that higher probability of producing spherical-

shaped boulders is associated with the thickest layers. Given that joint spacing controls the size of a and b axes and that, for Units C and D, higher frequency of joint spacing is within the 0.5-0.75 m, then layers with thickness within that interval (L28 and L19) should (and do) produce a larger number of spherical boulders, when compared to the remaining layers.

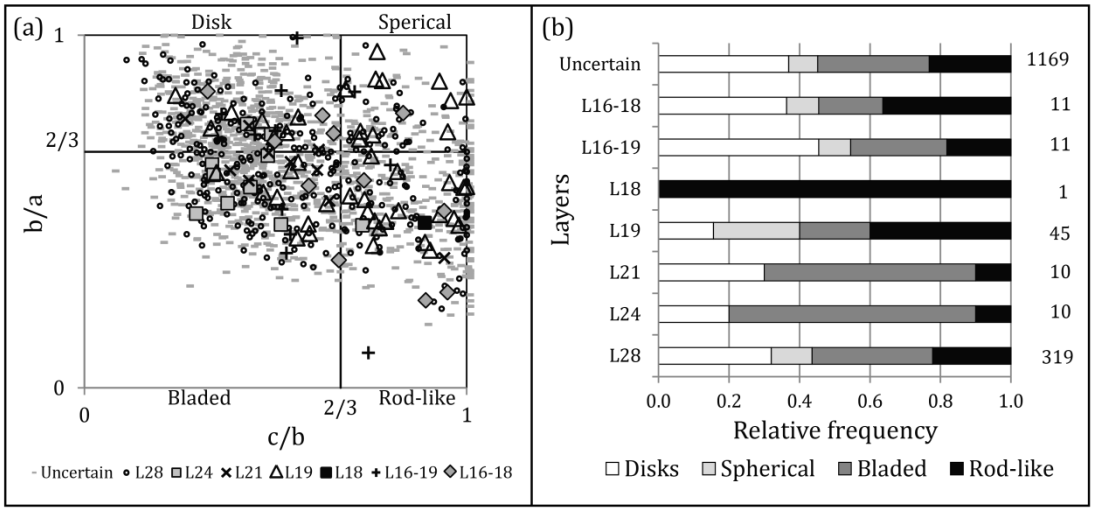

Figure 76: Diagrams showing boulder shape in the S sector. (a) Scatter plot of boulders' axes ratios b/a and c/b, (Zingg's shape classification diagram) grouped by source layer for particles identified in the S sector; (b) relative frequency of boulder shape for each layer (numbers to the right correspond to sample size)

Frequency distribution of the boulders' axes in the S sector is represented in Figure 77. The distribution of all axes is unimodal, asymmetric and positively skewed. Modal size intervals correspond to the lowest size-classes: 0-0.5 m in the case of a- and b-axes and 0-0.25 m in the case of c-axis.

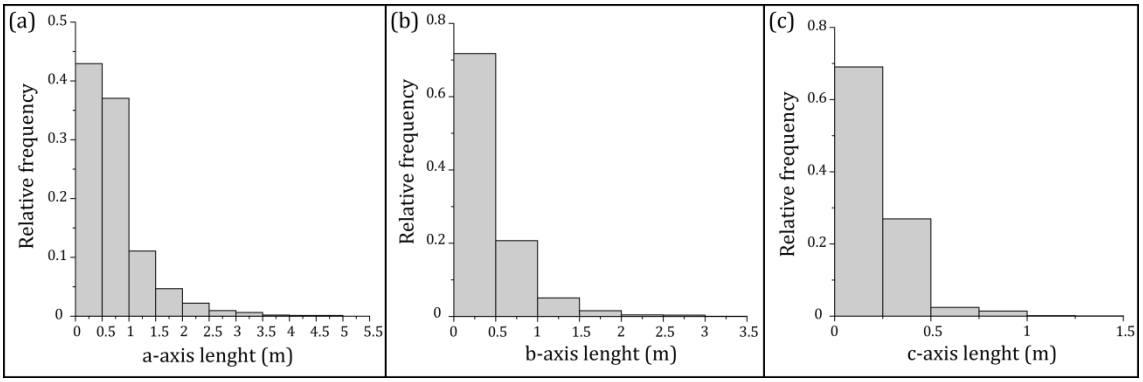

Figure 77: Histograms of boulders' axes from the S sector (N=1579): (a) a-axis; (b) b-axis; and (c) c-axis

Directional properties of disk-shaped, bladed and rod-like boulders identified in the S sector are represented in Figure 78. Boulders preferably dip towards the western quadrant, presenting three clear directional modes: 220°-230° (SW), 260°-270° (W)

and 290°-300° (WNW). Heavier boulders are present in almost all modal directional classes, but preferably dip towards 160°-210° (S-SSW), 240°-270° (WSW) and 280°-310° (WNW) (Figure 78a).

The projection of the ab dip direction of all non-spherical boulders allowed the identification of three directional sub-populations containing over 65% of occurrences: NW (275° to 355°); WSW (245° to 275°); and SW (195° to 245°). The definition of the limits between sub-populations was based on the shape of the frequency curve and corresponds to minima in frequency.

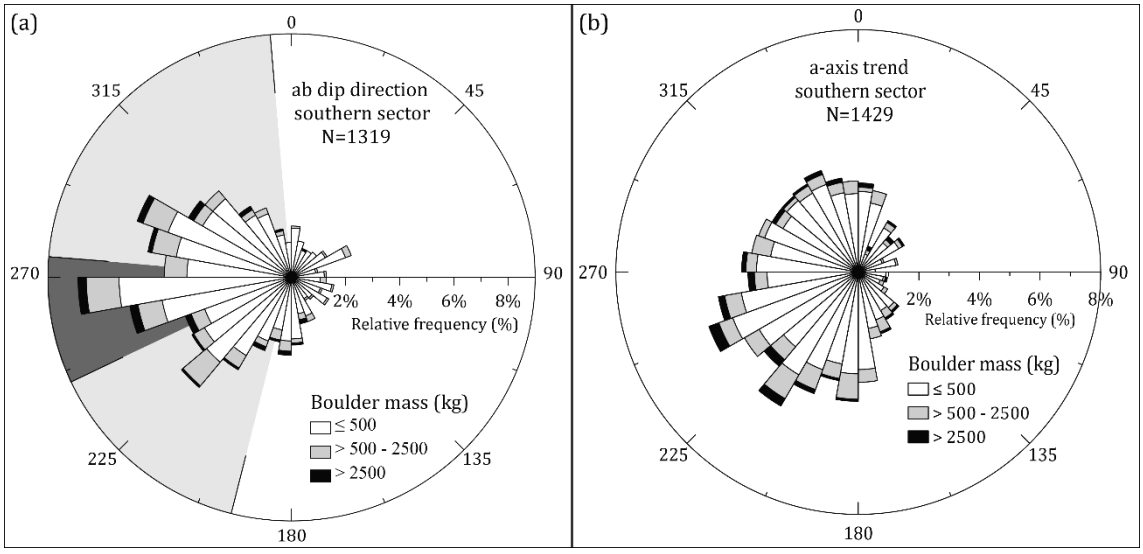

Figure 78: Rose diagrams projecting directional properties from disk-shaped, bladed and rod-like boulders of the S sector: (a) ab surface dip direction; and (b) a-axis trend

The a-axis trend shows high directional range with higher frequency of tilt towards the SW quadrant, presenting three main directional modes: 180°-190° (S), 210°-220° (SW) and 240°-250° (WSW). Heavier boulders are represented in all directional modes, concentrating in the SW and WSW maxima (Figure 78b).

The spatial variation of the ab dip direction of non-spherical particles in the S sector, grouped by directional sub-populations, suggests that boulders occur preferably organized in clusters. This is particularly evident in the case of boulders pending towards the NW and WSW. Particles in these clusters dip orthogonally to the alignment of the boulder ridges they incorporate (Figure 79a, c and d).

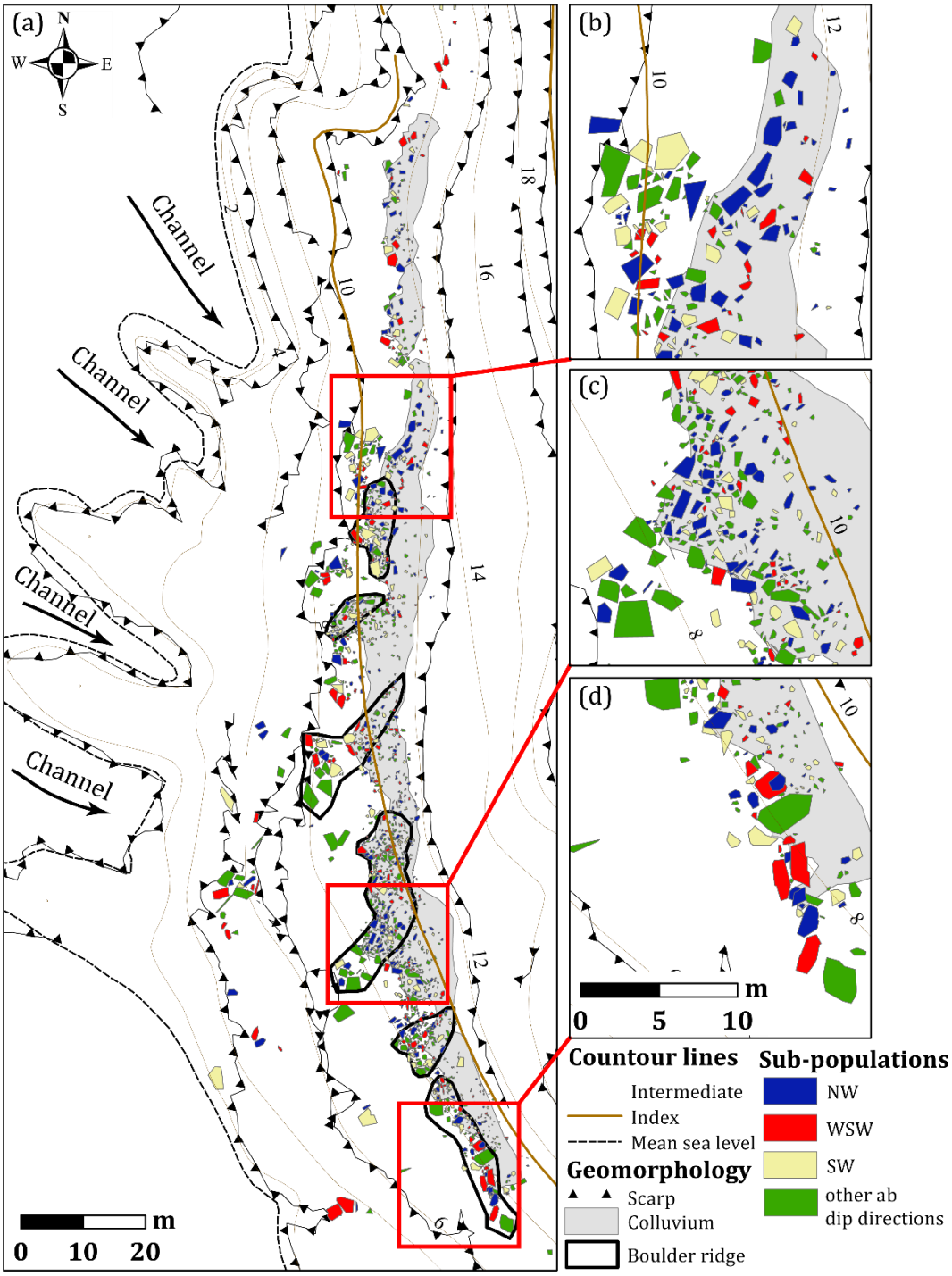

Figure 79: Mapped spatial variation of ab surface dip direction boulders in the S sector

Furthermore, these clusters essentially occur inland of channels corresponding to pronounced indentations in the lower section of the rocky structural platforms, which are in alignment with the ab surface dip of the boulders (Figure 79b and c).

Directional properties of imbricated boulders were also analysed, regardless of their shape. Imbricated boulder clusters in the southern sector (49 clusters containing 125 boulders) present ab surfaces dipping towards four main directional modes:

345°-360° (N); 300°-315° (NW); 255°-270° (W); and 60°-75° (ENE) (Figure 80a). The a-axis trend of these boulders mainly aligns and dip towards W, and, less frequently towards the SW and NW (Figure 80b).

The projection of the average ab dip direction of particles in each cluster allowed the identification of four directional sub-populations containing over 95% of occurrences. These sub-populations, defined based on the shape of the frequency curves with limits corresponding to minima in frequency, comprise the following directional intervals (Figure 80a): 330°-360° (N-NNW); 277.5°-330°(W-NNW); 225°-277.5°(W-SW); and 45°-120° (E-NE).

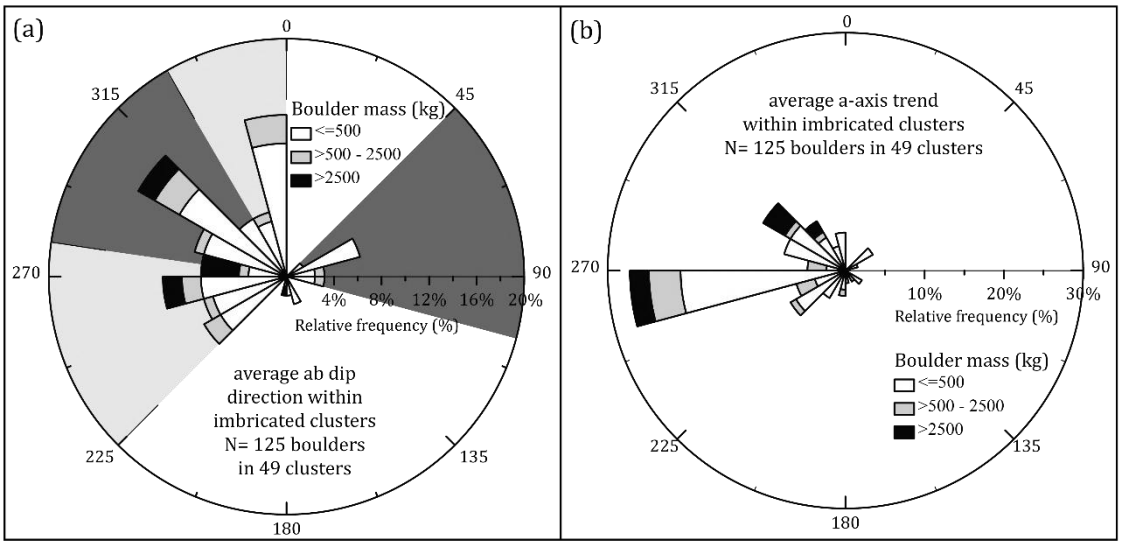

Figure 80: Rose diagrams projecting directional properties of imbricated boulders from the S sector: (a) average ab dip direction within imbricated clusters (shaded areas correspond to directional sub-populations-see text for explanation); and (b) a-axis trend

The spatial variation of the directional properties of imbricated boulders is depicted in Figure 81. Imbricated particles sitting over the lower structural platform (S III) mostly developing below ~6 m amsl, preferably dip towards W-SW and NNW-W (identified by red and blue colours, respectively, in the left part of Figure 81a). Over the upper structural platform (S IV), developing above 8 m amsl, imbricated boulder clusters were found within the colluvium deposit or leaning against boulder ridges. In the northernmost segment, they are found bordering the colluvium or near the bench edge, pending towards W-SW (red polygons in Figure 81). Many imbricated boulder clusters have been found further S, dipping towards all modal classes, with higher frequency towards NNW-NW and N-NNW, lacking any evident spatial pattern (blue and orange polygons in Figure 81b). Imbricated clusters dipping landwards

(45°-120°) preferably rest in the landward slope of the ridges (landward of the ridge crest) and of other boulder clusters (white polygons in Figure 81b).

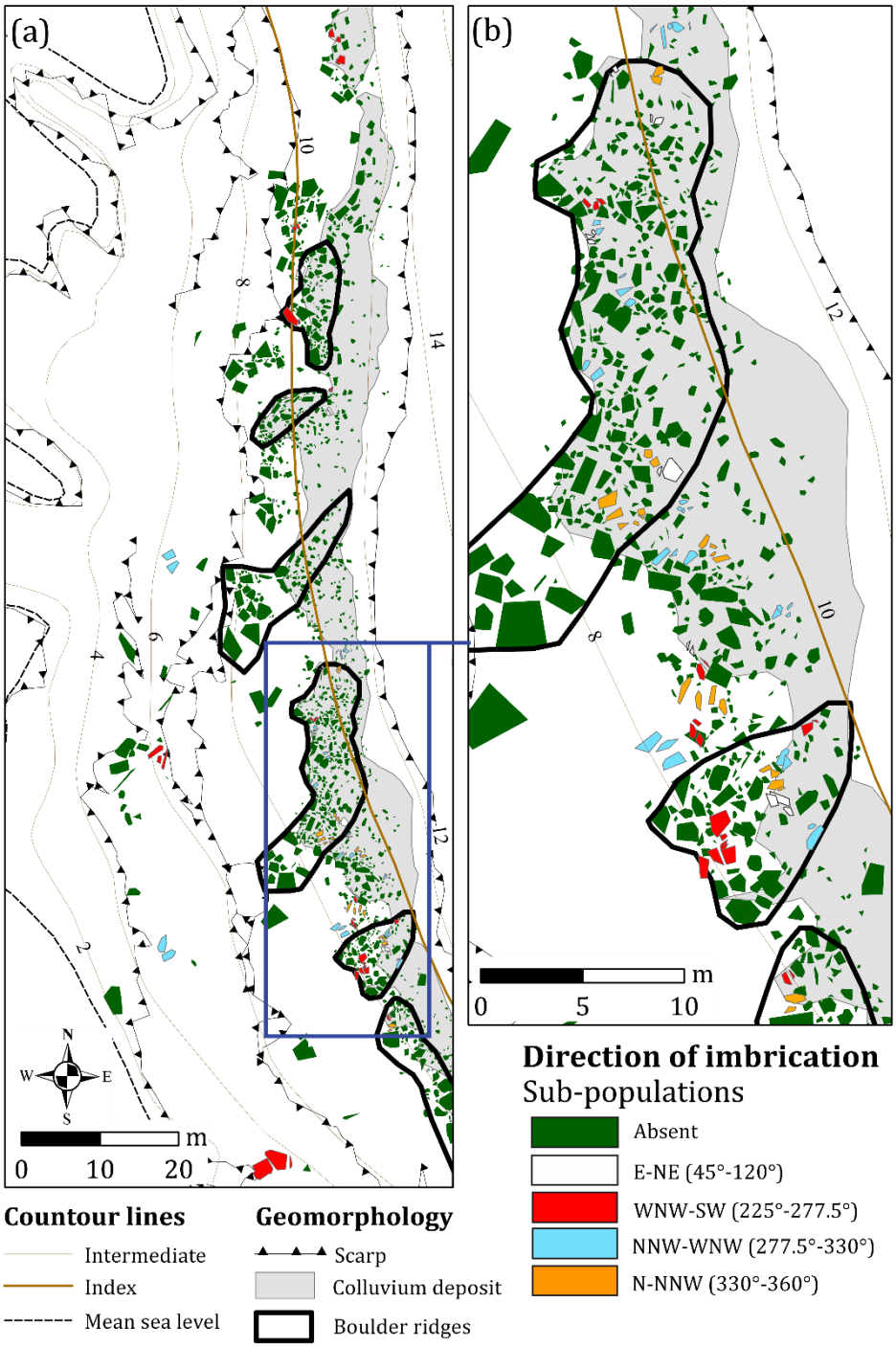

Figure 81: Sub-populations of ab surface dip direction of imbricated boulder clusters in the S sector

The spatial variation of the direction of the a-axis in the S sector shows three main alignments, depending on their location. Boulders resting over the lower structural surface (S III, in the western segment of the southern sector, below 6-8 m amsl) are

preferably aligned with the bench edge, represented by the scarp in Figure 82a, and are roughly orthogonal to the NW-SE direction.

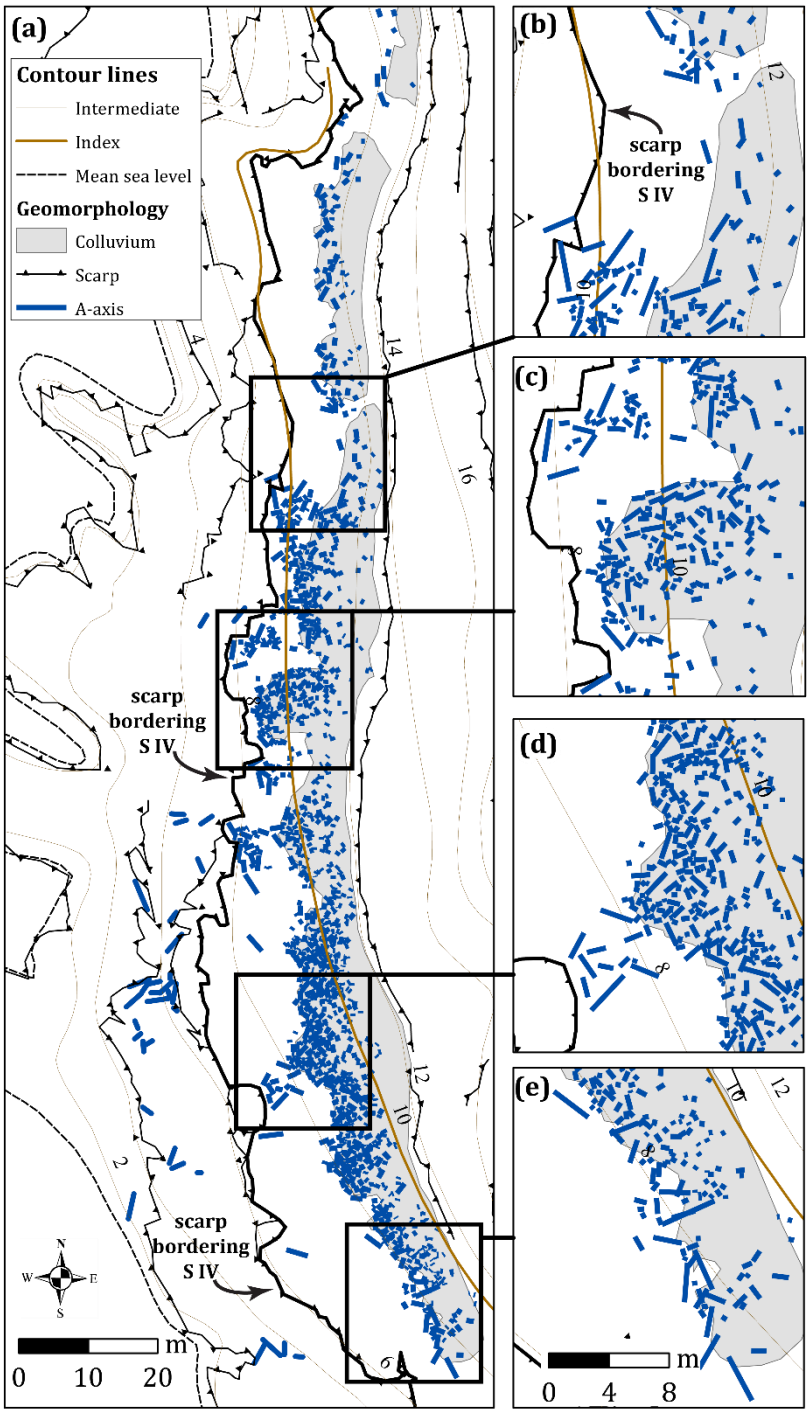

Figure 82: Representation of the a-axis of boulders in the S sectors

Over the upper structural surface (S IV), above 10 m amsl, and in the northernmost segment of this sector, boulders are arranged in aligned arcuate clusters roughly parallel to indentations in the rocky platforms, with their a-axis mirroring the development of the platform edge (represented by the scarp in Figure 82b).

Although reflecting the bench edge/scarp, aligned clusters are located at some distance from that feature.

In the central and southernmost segments of the S sector, where boulder ridges develop, the a-axis of particles are parallel to the ridges' general elongation (Figure 82c, d and e). In boulder accumulations occurring closer to the bench scarp, and in all segments of the upper structural surface, the a-axis alignment is more variable, sometimes showing a NE-SW orientation in boulders of the coastal segments facing W and NW (Figure 82b, c and d) and a NW-SE orientation in boulders directly facing SW (Figure 82e).

Identification of boulder sockets in the S sector is less revealing due to the substantial number of boulders and sockets, which makes biunivocal matching difficult, and to the extremely short transport distances. Many boulders located on the edge of surfaces S III and S IV were deposited near their sockets, evidencing short cross-shore transport, with paths essentially directed towards land. For boulders sitting in the inner region of surface S IV, the size and shape diversity precluded clear identification of boulder-socket relationships.

The 2014 storms caused inland retreat of up to 5 m of the outer limit of the boulder ridges and of the colluvium, and scarped the latter materials. This exposed and irregular patches of sand located at 9 m amsl within the first boulder sub-population described above, the innermost deposit sitting on surface S IV (Figure 83) (for further information regarding the effects of these storms see section 7.2 Monitoring boulder transport). Under macroscopic observation these patches correspond to clean, well sorted marine sand with tiny shell fragments, and are limited by both the boulders and the colluvium deposit, which provided sheltering against erosion by surface run-off and wave swash. Sand samples were collected in this location for OSL age estimation. Results are presented in section 7.4.4.

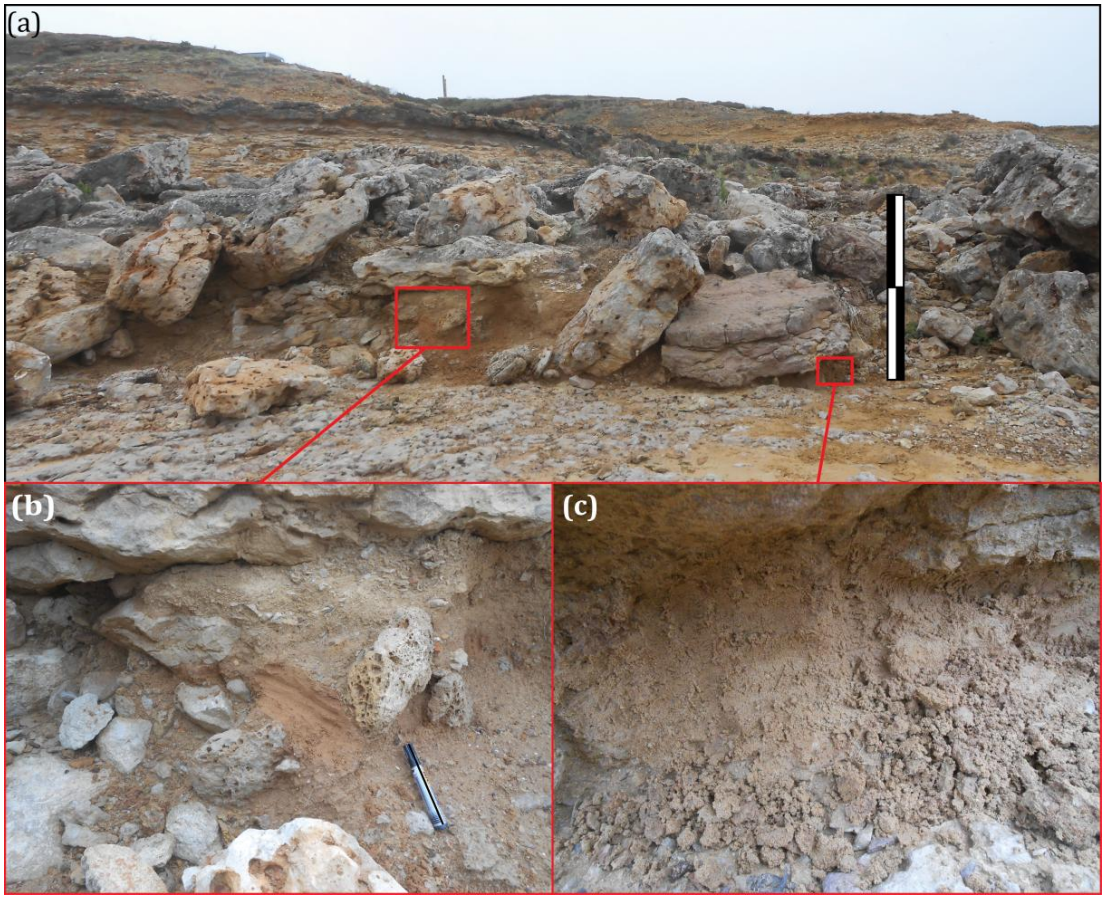

Figure 83: (a) Colluvium deposit partially covering boulders and sand patches exposed during the 2014 storms at ~9m; (b) and (c) detail of the sand patches. Vertical scale corresponds to 1 m

Grain size analysis of the sand in the patches and of possible source sediments is summarized in Table XVIII, and relative frequency histograms and cumulative distribution curves are presented in Figure 84a and b. Particle morphology and surface features investigated under the binocular morphoscopic over the]0-1 ϕ] fraction are represented in Figure 84c, d, e, f and g, and over the]1-2 ϕ] fraction in Figure 85.

Coxos beach sand shows a unimodal distribution with modal class in the 0-0.5 ϕ interval (Figure 84a and b). Beach sediments consist of well sorted coarse sand (MZ=0.47ϕ and σ_I=0.38) with a mesokurtic distribution curve (KG=1.04) and a tail towards the finer fraction (positive-skewed, SKI=0.12). Beach sand mainly comprises clean and polished sub-rounded and spherical quartz grains (Figure 84c, d, e, f and g). Heavy minerals comprise 12% of the]0-2 ϕ] fraction. The lighter portion of the]0-1 ϕ] fraction contains 83% quartz, 6% bioclasts, 1% lithoclasts and 10% calcite and other minerals (Figure 84g).

Table XVIII: Grain size data, graphic parameters and classification of sediment samples collected

SAMPLE		GRAPHIC MEAN (MZ) (ϕ)	INCLUSIVE GRAPHIC STANDARD DEVIATION (σ_I) (ϕ)	INCLUSIVE GRAPHIC SKEWNESS (SKI)	KURTOSIS (KG)	<63μm (%)	HEAVY MINERAL OF THE 0-2ϕ FRACTION (%)
Present-day	Beach	0.47	0.38	0.12	1.04	0.2	12.1
		Coarse sand	Well sorted	Positive-skewed	Mesokurtic		
	Storm	0.72	0.76	0.09	1.22	0.9	13.2
		Coarse sand	Moderately sorted	Nearly Symmetrical	Leptokurtic		
Colluvium		1.87	2.47	-0.60	0.72	39.6	2.2
		Medium sand	Very poorly sorted	Very negative-skewed	Platykurtic		
Marine terrace		2.60	1.65	-0.21	1.43	20.1	0.3
		Fine sand	Poorly sorted	Negative-skewed	Leptokurtic		
Sand patch		2.32	1.09	0.14	1.05	11.2	0.6
		Fine sand	Poorly sorted	Positive-skewed	Mesokurtic		

Sediments collected after a storm and captured inside wide and open joints affecting the topmost layer of surface S III mostly show a unimodal distribution with modal class in the 0.5-1 ϕ interval (Figure 84a and b). These sediments, deposited by storms, comprise moderately sorted coarse sand (MZ=0.72ϕ and σ_I=0.76) with a nearly symmetrical and leptokurtic distribution curve (SKI=0.09 and KG=1.22). They mostly comprise clean and polished, well rounded and spherical quartz grains (Figure 84c, d, e and f). Heavy minerals comprise 13% of the]0-2 ϕ] fraction. The lighter fraction of the]0-1 ϕ] fraction contains 77% quartz and 17% bioclasts, 1% lithoclasts and around 5% of other minerals (Figure 84g).

The sediment sample collected from the colluvium deposit comprises a modal class in finer material (<63 μm~40%). The size classification is of medium sand (MZ=1.87 ϕ) with a tail in the distribution curve towards the coarser fraction (very negative skewness, SKI=-0.60), despite the subequal amounts of sediment throughout the remaining size-classes (Figure 84a). The heterometric character of this deposit is reflected in very low sorting (σ_I=2.47) and a platykurtic curve (KG=0.72). The colluvium deposit primarily contains clean and frosted, sub-angular and spherical quartz grains (Figure 84c, d, e and f). The]0-2 ϕ] fraction contains 2%

of heavy minerals and the lighter portion of the]0-1 ϕ] fraction contains 56% quartz, 6% bioclasts, 38% lithoclasts and about 1% of other minerals (Figure 84g). The]1-2ϕ] fraction contains 64% clean and polished sub-angular to sub-rounded quartz grains, 31% lithoclasts, 2% bioclasts and approximately 3% other minerals.

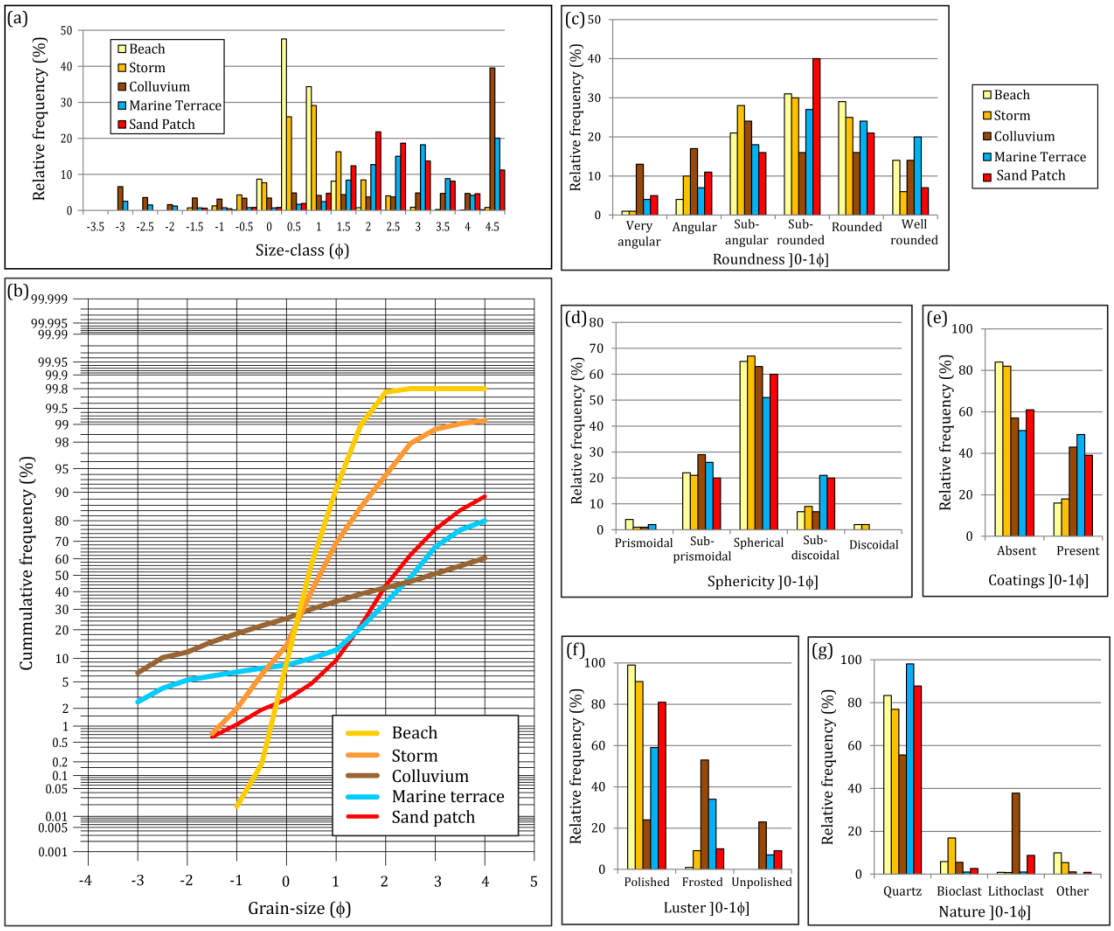

Figure 84: Grain-size and morphoscopy results of finer sediments. (a) Grain-size relative frequency histogram. (b) Grain-size cumulative distribution curves. Particle morphology and surface features obtained with morphoscopic analysis of the]0-1 ϕ] fractions: (c) roundness; (d) sphericity; (e) coatings; (f) lustre; and (g) nature

Sediments from the Pleistocene marine terrace show a multimodal distribution with a modal class in the finer fraction (<62 μm~20%), another in the 2.5-3 ϕ interval (~18%) and another mode comprising only 2.5% of the sediment in the coarsest interval (-3.5 ϕ to-3 ϕ) (Figure 84a). This sediment consists of poorly sorted fine sand (MZ=2.60ϕ and σ_I=1.65) with a leptokurtic distribution curve (KG=1.43), a tail towards the coarser fraction (negative-skewed, SKI=-0.21) and comprises two sub-populations intersecting at 1 ϕ (Figure 84b). The]0-2 ϕ] fraction contains less than 1% of heavy minerals. The lighter portion of the]0-1 ϕ] fraction essentially

comprises 1% bioclasts, 1% lithoclasts and 98% sub-rounded and spherical polished quartz grains, showing coatings and clean surfaces in equal proportions (Figure 84c, d, e, f and g). In what respects the lighter portion of the]1-2 ϕ] fraction, it consists of 1% bioclasts, ~6% other minerals and 93% sub-rounded, spherical, cleaned and polished quartz grains (Figure 85).

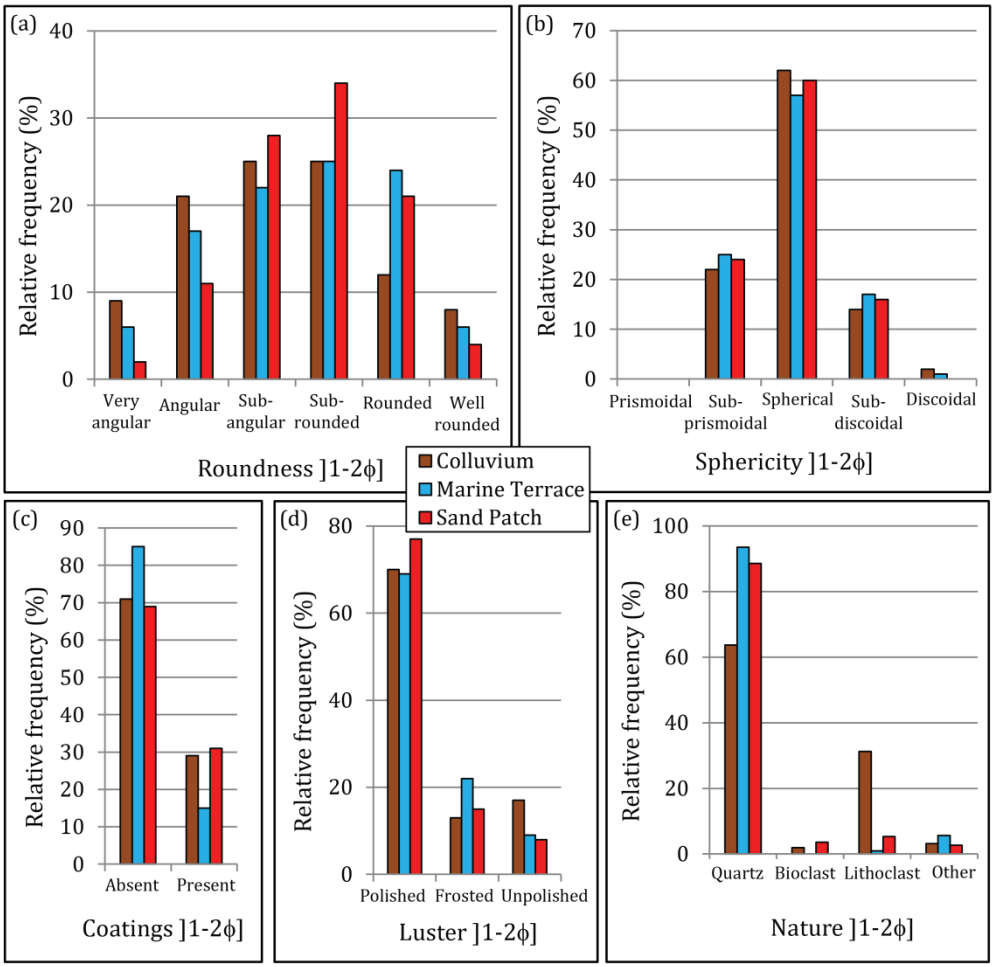

Figure 85: Particle morphology and surface features obtained with morphoscopic analysis of the]1-2 ϕ] fractions: (a) roundness; (b) sphericity; (c) coatings; (d) lustre; and (e) nature

The sand patch collected beneath boulders partially covered by the colluvium, and exposed during the 2014 storms, shows a bimodal distribution with modal classes in the finer fraction (<62 μm~11%) and another in the 1.5-2 ϕ interval (22%) (Figure 84a). It consists of poorly sorted fine sand (MZ=2.32ϕ and σ_I=1.09) with a mesokurtic distribution curve (KG=1.05), a tail towards the finer fraction (positive-skewed, SKI=0.14). The sand patch comprises two subpopulations intersecting at approximately 1 ϕ (Figure 84b). Also, the]0-2 ϕ] fraction contains less than 1% of heavy minerals. The lighter portion of the]0-1 ϕ] fraction essentially comprises 4%

bioclasts, 11% lithoclasts and 84% sub-rounded and sub-discoidal, coated quartz grains, mostly showing a frosted aspect (Figure 84c, d, e, f and g). In what respects the lighter portion of the]1-2 ϕ] fraction, it consists of 4% bioclasts, 5% lithoclasts, 88% clean and polished sub-rounded and spherical quartz grains, and approximately 3% of other minerals (Figure 85).

7.1.3 Summary and interpretations

7.1.3.1 Geomorphological setting

All characteristics of both N and S sectors, and respective boulder accumulations, are summarized and presented separately for each sector in Table XIX.

The two sectors present some differences in general orientation, exposure and geomorphology. The N sector comprises a low cliff facing NW, developing into a ramp aligned NW-SE, being less exposed to wave attack from the NW and more exposed to wave attack from the SW. Furthermore, in this sector, Units B and C show higher exposure to wave attack, Unit D outcropping further inland and upwards.

The S sector presents a N-S general alignment, the northernmost and central segments being more exposed to waves from the NW and W and the southernmost segment to waves from the SW. There is another equally important contrast in the geomorphological complexity of the southern sector: it presents both cross-shore and longshore irregularities, low vertical and irregular cliffs, stepped sub-horizontal surfaces and the development of a colluvium deposit in the landward edge of surface S IV. In addition, the N-S alignment is closer to the general pending of the sedimentary sequence towards SW, resulting in the outcropping of more diverse source layers closer to mean sea level, implying a higher exposure of Unit D to wave attack. Correspondingly, the boulder accumulation found in the S sector is more complex than that of the N sector.

Table XIX: Summary of the characteristics of boulder accumulations identified in the N and S sectors

SECTOR / CHARACTERISTICS	NORTHERN	SOUTHERN
Geomorphology	Low lying cliff facing NW and SW facing ramp. S III is the topmost surface containing boulders transported against gravity.	Low vertical to irregular cliffs and stepped sub-horizontal structural platforms facing W. Colluvium development along the landward edge of S IV. SIV is the topmost surface containing boulders transported against gravity.
Number of boulders	34	1579
Elevation (m amsl)	3.7-10.1	1.8-12.8
Mass range (kg)	100 - 26000	~1 - 30000
Main source layer	L19 (53%)	L28 (78%)
Morphology of boulder accumulations	Aligned boulder clusters (boulder trains); scattered boulders; and isolated boulders.	Boulder ridges; boulder clusters, sometimes showing imbrication; aligned boulder clusters (boulder trains); scattered boulders; and isolated boulders.

SECTOR / CHARACTERISTICS	NORTHERN	SOUTHERN
Sub-populations	Mass > 10 ton: boulders lean against the bench edge topped by surface SIII forming a cluster of aligned boulders; 2.5 ton > Mass < 10 ton: scattered boulders over S III near the bench edge, and over secondary structural surfaces seaward of S III; Mass < 2.5 ton: scattered boulders over secondary structural surfaces seaward of S III.	Boulders on S III - 10 ton<Mass<30 ton: sitting over or leaning against the bench edge of that surface; 2.5 ton<Mass<10 ton: boulder clusters, sometimes showing imbrication. Boulders on S IV: 2.5 ton<Mass<10 ton: isolated boulders or boulder clusters located near the bench edge, showing straight edges and parallelepiped shape; 1 ton<Mass<10 ton: aligned boulder clusters bordering the colluvium and boulder ridges; Mass<1 ton: Boulder ridges and scattered boulders resting over and/or partially covered by the colluvium.
Boulder shape	Disk-shaped:23.5%; Bladed: 50.0%; Rod-like: 23.5% Spherical: 3.0%	Disk-shaped: 35.2% Bladed: 32.1% Rod-like: 23.1% Spherical: 9.3%

SECTOR / CHARACTERISTICS		NORTHERN				SOUTHERN			
Axis length (m)	Statistics	Minimum	Average	Maximum	Standard deviation	Minimum	Average	Maximum	Standard deviation
	a	0.73	2.43	5.33	1.41	0.17	0.73	4.56	0.54
	b	0.30	1.38	3.28	0.79	0.08	0.46	3.03	0.35
	c	0.12	0.54	1.14	0.22	0.02	0.22	1.53	0.15
Directional properties of disks blades and rods	ab dip direction	Modes: 230°-240° (SW) and 280°-290° (WNW). Sub-populations. 220°-260° (SW-WSW) and 260°-300°(W-WNW)				Modes: 220°-230° (SW), 260°-270° (W-WSW) and 290°-300° (WNW). Sub-populations: 195°-245° (SW), 245°-275° (WSW) and 275°-355° (NW).			
	a-axis trend	Clusters around 220°-260° (SW) and 310°-340° (NW-NNW)				High directional dispersion, preferably trending towards the SW quadrant showing three directional modes: 180°-190° (S); 210°-220 (SW); and 240°-250° (WSW).			

SECTOR / CHARACTERISTICS		NORTHERN	SOUTHERN
Spatial analysis	ab dip direction	Cluster of largest boulders: ab surface dips towards SW, orthogonally to the bench edge.	Boulders preferably occur in directional clusters inland of channels corresponding to indentations in lower units closest to the msl. The ab dip direction preferably aligns orthogonally to the elongation of boulder ridges.
	a-axis trend	NNW-SSE to NNE-SSE, following the direction of the bench step and the coastline.	Arcuate aligned boulder clusters (and a-axis), arranged around indentations, mirroring the bench edge in the northernmost segment of S IV and in S III; In the inner part of S IV, boulders' a-axis are parallel to the ridges elongation. Closer to the bench edge a-axis is more variable. Further inland, a-axis preferably aligns with the bench edge, directly facing W and NW, in the northern and central segments, and W-SW, in the southern segment.

SECTOR / CHARACTERISTICS		NORTHERN	SOUTHERN
Imbricated boulder sets	ab dip direction	Boulder imbrication not observed.	Modes: 345°-360° (N), 300°-315° (NW), 255°-270° (W) and 60°-75° (ENE). Sub-populations: 330°-360° (N-NNW), 277.5°-330° (NNW-WNW), 225°-277.5° (WNW-SW) and 45°-120° (E-NE).
	Spatial analysis		Exposed imbricated boulders in S III preferably dip towards W-SW and NNW-W; Imbricated boulders located in the southernmost segment of the sector, over S IV, dip towards all modal classes, with higher frequency towards NNW-NW and N-NNW; Imbricated boulders dipping inland (45°-120) are preferably located in the landward slope of boulder ridges.

SECTOR / CHARACTERISTICS	NORTHERN	SOUTHERN
Transport paths	Cross-shore: approximately ~1 m vertical displacements and <5 m horizontal displacement observed in boulders leaning upon or near the bench edge, close to sockets. Longshore: transport towards S-SE with short vertical displacement (~2 m) and large horizontal displacement (35-65 m).	Cross-shore: vertical and horizontal displacement of ~2 m and 15-20 m, respectively, observed in boulders over structural surface S IV.

7.1.3.2 Boulder deposit

The contrast in geomorphological complexity between sectors is reflected in the number of particles, in the variety of morphologies exhibited by boulder accumulation, number of sub-populations (identified using directional and other properties), spatial variation of directional properties, and in wider range of mass and height of emplacement values.

The joint analysis of the morphology of boulder accumulations, boulder characteristics (source layer, mass, position, placement) and spatial distribution in both sectors provides clues regarding flow magnitude and direction over the structural platforms. Boulder characteristics are summarized and discussed below, focusing on deducing flow characteristics over the structural platforms and on identifying the controlling factor in boulder characteristics (nearshore wave regime *vs* local geomorphology).

Boulder source layer, boulder mass and spatial distribution provide clues pertaining to the relative magnitude of the event(s) responsible for transport and deposition. In both sectors, most boulders originate in the uppermost layer, topped by the surface where they sit: over 50% of boulders in the N sector are sourced in L19 and they all sit or lean against S III (top of Unit C); about 80% of boulders in the S sector are sourced in L28 and sit or lean against S IV (top of Unit D). These observations indicate short vertical and horizontal displacement associated with cross-shore transport, following boulder detachment and mobilization by incoming waves. This is also indicative of short-lived (eventually repetitive) events (low wave period with limited inland inundation capability), such as storm waves rather than tsunami.

Average and benchmark values of boulder mass and position may reflect the capability of flow to generate boulder movement. The analysis of boulder height of emplacement *vs* boulder mass indicates that the average flow reaching the structural platforms was capable of generating emplacement of boulders up to ~14000 kg within the 7-11 m amsl height range (Figure 86). Moreover, the upper mass limit for the landward and upward transport of boulders by waves was 3×10^4 kg in the S sector and 2.6×10^4 kg in the N sector.

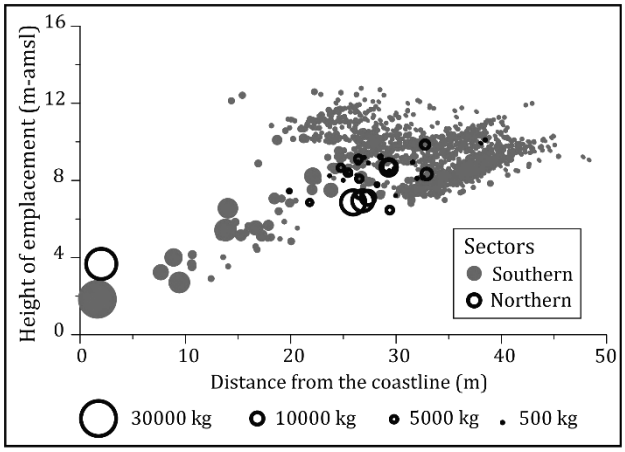

Figure 86: Scatter plot showing boulder height of emplacement against distance from the coastline. The diameter of the circles representing the boulder is based on their mass

Differences between boulder position *versus* boulder mass of large particles observed in both sectors reveal that heavier boulders are generally further up and inland in the N sector, when compared to boulders with similar mass in the S sector (Figure 86). This difference can represent one or a combination of the following possibilities:

1. Higher flow velocities reach the N sector, associated with different waves reaching each sector. This hypothesis implies that the WSW-facing coastline in the N sector has been reached by more energetic waves, when compared to the (mostly) W-facing coast in the S sector.
2. Near- and on-shore geomorphology controls energy dissipation and, regardless the offshore wave direction, a wave bore produced by the same wave is more energetic in the N sector.
3. A strong influence of local geomorphology which reflects in longshore change of initial boulder location and mass, and height of the bench. The layers producing the larger boulders from Unit C in the N sector outcrop at higher elevations (7-8 m amsl) than in the S sector (4-7 m). Thus, in the N sector, initial boulder position is higher and the vertical up-bench distance that boulders are required to overcome is smaller (1 m in the northern sector against 2 m in the southern sector). As a result, the same waves impacting both sectors would have been more capable of producing transport of large boulders in the N sector due to a lower bench step.

Local geomorphology does constrain boulder size and the geometry of the structural platforms, which supports geomorphology as a dominant factor in the boulder position *vs* mass. The combination of larger source layer thickness and lower joint frequency generates the largest boulders in the study area. As a result, boulders sourced in Unit C (average layer thickness of 0.75 m and joint spacing of 1.75 m) are generally larger than those sourced in Unit D (average layer thickness of 0.45 m and joint spacing of 0.7 m). Accordingly, the discrepancy in boulder size range between sectors is attributed to the larger diversity of source layers in the S sector, which includes Unit D as a major supplier. An additional factor controlling boulder size is the probable removal of smaller boulders by the backwash in the N sector. The higher seaward pending of the structural ramp in that sector favours boulder removal (and washing out), in contrast with the sub-horizontal structural platforms of the S sector, which favour boulder preservation.

It is not possible to further select and/or exclude any of the three possibilities based on boulder mass and position alone. Additional information regarding boulder characteristics (spatial variation of boulder mass and directional attributes) is discussed below and may provide information regarding the direction of the flow responsible for boulder deposition. This information can further contribute in establishing differences and similarities between boulder accumulations observed in the N and S sectors, identifying the controlling factors and explaining those differences.

The spatial variation of boulder mass in both sectors (Figure 62b and Figure 72b) indicates landward and northwards fining trends. These trends could indicate reduction in flow competence (capability to generate boulder movement) in the same directions (northwards and inland). If all boulders had been emplaced by a SW broken wave, a similar distribution pattern of boulder mass would occur. However, the inland and northwards fining trend could be interpreted as a consequence of coastline morphology rather than flow direction. In fact, in both sectors, the elevation increases inland and northwards, which results in a decrease of the ability of any broken wave to emplace boulders, in the same directions. Although a straightforward approach in evaluating spatial distribution of boulder mass indicates transport by event(s) reaching the coastline from the SW, the increasing

platform and cliff height might very well be a controlling factor of wave competence and of mass of transported boulders. Such uncertainty can be clarified using information regarding the directional properties of boulders.

Directional attributes include the ab dip direction and the a-axis trend of both individual boulders and imbricated clusters, and the alignment of boulder accumulations. The statistical and spatial analysis of the ab surface dip direction of individual boulders indicates two main directions in the N sector (WNW and SW) and three main directions in the S sector (W-WNW, WSW and SW). The a-axis, assumed perpendicular to the flow direction, tends to align roughly perpendicularly to the ab surface, especially in bladed boulders. It preferably aligns with NW and SW in the N sector, which roughly agrees with results obtained for the ab surface. In the S sector, the a-axis trend shows higher frequency of tilt towards the SW quadrant, indicating a flow mostly directed from the NW quadrant.

Differences in directional properties between sectors suggests a morphological inheritance of those characteristics. In fact, the spatial variation of the ab surface dip direction shows that boulders appear to be grouped in "directional clusters", pending towards the directional modes. The dip of the ab surface of particles in directional clusters aligns perpendicularly to the development of linear morphological features acting as obstacles, such as bench edges and boulder ridge crests. More specifically, in the S sector, directional clusters preferably occur inland of natural channels corresponding to pronounced indentations of the lower structural platforms and cliff face (see Figure 79). Here, the ab surface dip direction of the boulders in each cluster parallels the cross-shore axis of these indentations.

Among all boulder morphologies identified in both sectors, boulder ridges provide the most reliable information regarding flow direction (and changes in flow direction) over the structural surfaces. Six boulder ridges were identified in the S sector showing varying alignments: N-S, in the northernmost segment, occurring inland of a large indentation affecting the cliff and the lower section of the structural platform, and roughly aligned with the vertical scarp limiting surface S IV; NE-SW, in the central segment (including 4 ridges), also occurring inland and developing

orthogonally to indentations in the cliff and structural platform; NW-SE, in the southernmost segment, paralleling both the scarp limiting Unit D and the coastline.

Directional properties of imbricated boulders (exclusively found in the S sector) show four directional sub-populations: NNW-WNW and WNW-SW spread throughout the whole sector; E-NE and N-NNW specifically found within the boulder ridges over surface S IV. The SW directional mode observed in individual boulders scattered in the study area and absent in imbricated boulders, supports a partial morphological inheritance in boulder position. This can also be observed in the E-NE directional sub-population found in imbricated boulders, which is interpreted as being associated with transport over the ridge crest and landing in the landward side of those accumulations, inheriting the general pending of the topographic surface. The N-NNW directional sub-population occurs exclusively over surface S IV and is interpreted as boulder transport by backwash, following the structural platform general South pending. The existence of imbricated boulder clusters facing north, and emplaced by backwash embedded within NW-facing ridges, implies that ridges must have increased in width seawards, with time. Those imbricated particles represent the activity of the backwash when the ridges were narrower. The analysis of directional properties of imbricated boulder clusters within ridges suggests transport and deposition by flow over S IV mostly directed from the N and NW.

To create a conceptual model showing most frequent flow directions over the structural platforms, a spatial analysis was made in which flow direction is assumed perpendicular to the direction of the a-axis, and to the alignment of boulder ridges or clusters (Figure 87). Flow direction appears to be variable over the structural platforms, directed from the W and NW in NW- and W-facing coastal stretches and directed from the SW in WSW-facing stretches.

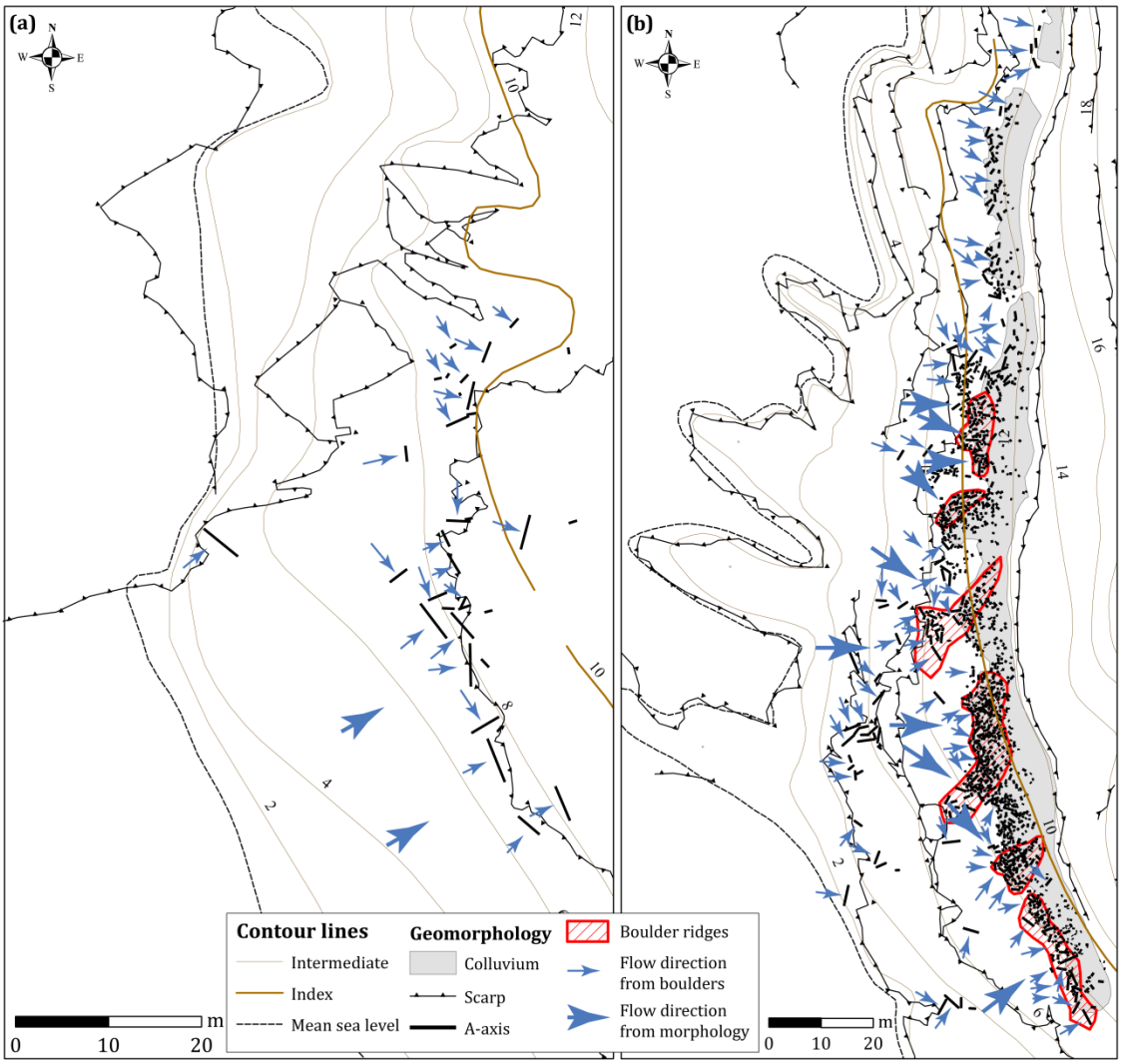

Figure 87: Flow direction inferred from the a-axis of individual boulders and from the alignment of boulder ridges: (a) N sector; (b) S sector

The relationships between the directional attributes of boulders, together with the alignment of boulder ridges and coastal morphology, suggests that geomorphological control plays a role in the development of these accumulations. Assuming that boulder ridges align perpendicularly to flow direction, as discussed above (see chapter 3), the importance of geomorphological *vs* hydrodynamic controls can be discussed invoking two different mechanisms, or a combination of both:

1. Waves with different directions reach different segments of the structural platform at different angles and generate differently aligned boulder ridges, according to a directional signal inherited from the nearshore wave direction. Directional properties show a flow from the NW quadrant, which roughly

agrees with the storm wave regime affecting the Portuguese coastline, and would be indicative of a storm origin for the boulder deposit, rather than tsunami.

2. Coastline configuration partly or essentially controls the direction of the flow reaching the structural platforms where boulders sit. When bores reach the coastline, they are channelled by indentations of the cliff and structural platforms, which function as corridors where flow velocity is enhanced and direction of incoming flow is also structurally controlled. This hypothesis reduces the weight of wave direction in determining the alignment of ridges and the directional properties of individual boulders.

It is possible that the flow responsible for boulder transport and deposition reaches different areas of structural platforms using natural geomorphological features facilitating or channelling the flow and minimizing energy dissipation, such as ramps, bays or indentations. Therefore, waves travelling from the SW could preferably reach the supratidal structural platforms at the southernmost segments of both sectors that face the same direction. Equally, waves travelling from the NW would preferably reach the northernmost segment of the N sector and regions located inland of the indentations in the S sector. Waves travelling from the W would essentially reach limited stretches of the cliffs and inland of wider indentations, in the northernmost and central segment of the S sector, respectively.

The backwash flow of incoming storm waves most probably follows the slope of the structural platform, which is directed seawards and southwards in the N sector, and towards South in the S sector. The backwash current developing along the southern structural platform justifies the existence of N-facing imbricated boulder clusters, observed close to and within some of the ridges (Figure 88). Furthermore, the geomorphological context of the N sector promotes boulder removal by backwash, which, together with the preferably large size of boulders produced, justifies the absence of smaller boulders.

Further clarification of the factors controlling boulder transport and deposition (local geomorphology *vs* nearshore wave direction) will be provided with observed

boulder transport by present-day storms and numerical modelling of associate waves, described and discussed in section 7.2.

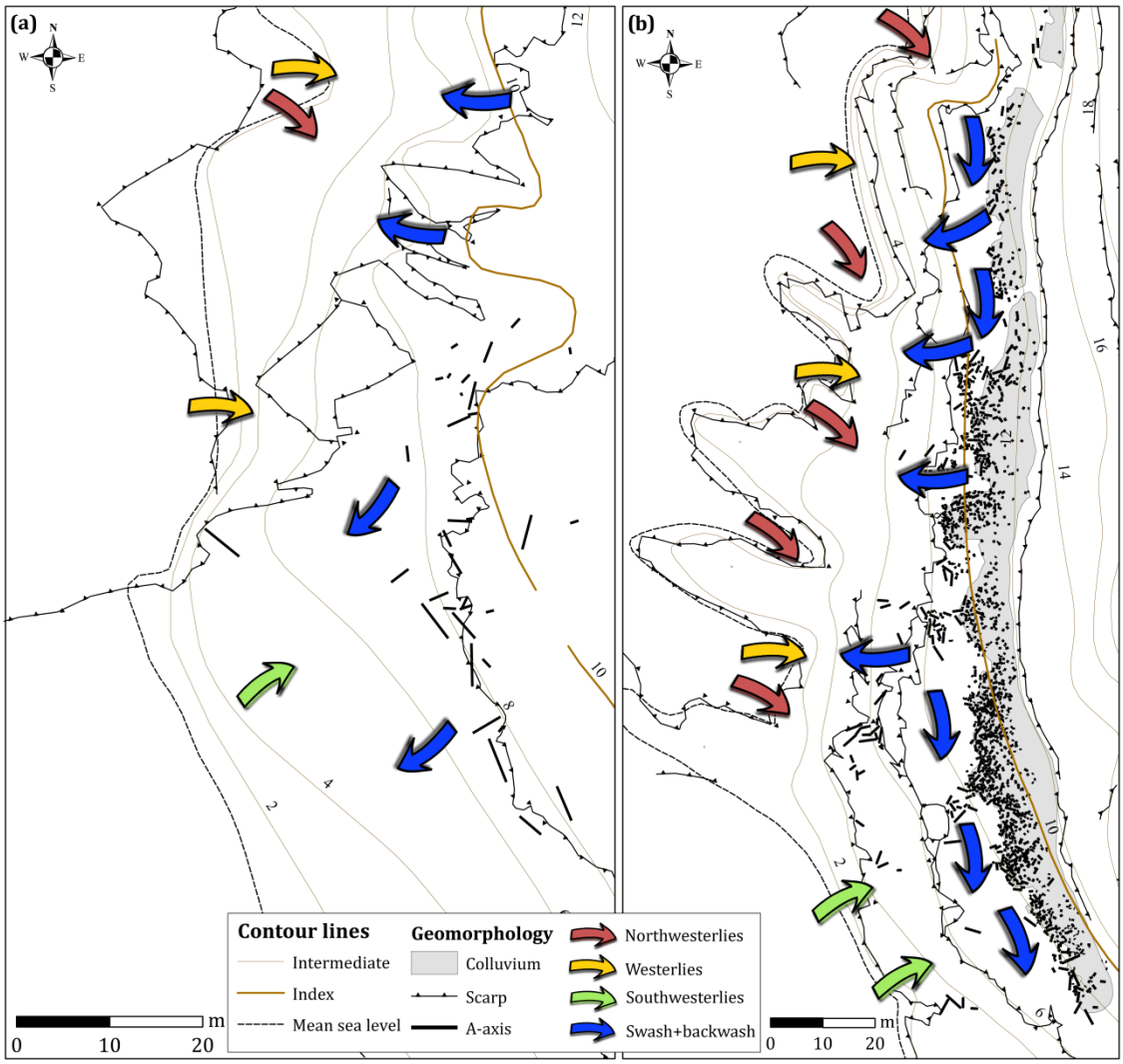

Figure 88: Schematic representation of wave direction affecting different segments of the structural platforms and resulting swash and backwash flow

7.1.3.3 Finer deposits

The analysis of the textural characteristics of the finer sediments collected in the study area indicate three major groups, which reflect, in part, sediment source and the depositional environment: one group includes the beach and storm deposits; another, the marine terrace and sand patch deposits; and the third group contains the colluvium deposit.

The present-day beach and storm deposits consist of moderate to well sorted coarse sands, largely comprising a unique population, with relevant percentage of heavy

minerals. The main characteristic separating these two deposits is the higher percentage in bioclasts found in the storm deposit (17% against 6% found in the beach sand). The coarse character of these sediments, associated with an insignificant content in finer (<63 μm) fraction, reflects the high energy associated with the transport. The high sorting index, together with the composition and lustre of quartz grains reflect transport in an aqueous media with repetitive character. These characteristics reflect continuous reworking of sediments by wind waves (storm and permanent wave regime) responsible for the transport and deposition of these materials in the beach face and in the rocky structural platform forming surface S III. Moreover, the high energy impedes the deposition of particles finer than 63 μm, or these materials do not exist in relevant proportions in the source area, located landward of the closure depth of the coastal zone.

The marine terrace and sand patch contain poorly sorted fine sand which include two sub-populations intersecting at 1 ϕ. These sediments present a relevant content in the <63 μm fraction (20% in the marine terrace and 11% in the sand patch. Morphoscopic analysis of both the]0-1ϕ] and]1-2ϕ] size fractions show similar characteristics of both deposits, the sand patch showing rounder and more polished (less frosted) quartz grains. Moreover, the marine terrace essentially comprises quartz grains (93-98%), whereas the sand patch contains relevant content of bioclasts, lithoclasts and other minerals (~12%). These results suggest that the source sediment of both deposits is the same, with differences in composition and surface aspect of the grains reflecting the passing of time since deposition. In this sense, bioclasts and lithoclasts are mostly absent in the marine terrace due to dissolution over time and frosted surfaces have a larger representation due to longer exposure of the surface of the quartz grains to chemical weathering processes. A possible sediment source for both the sand patch and the marine terrace deposits is the nearshore area, rather than the subaerial beach.

The colluvium material comprises very poorly sorted medium sand, with a platykurtic distribution curve, reflecting a proximal sediment source. This deposit mainly results from the incorporation of heterometric particles deriving from the physical and chemical weathering of the layers outcropping at higher altitudes and transported by gravity and surface run-off. A varied sediment source is reflected in

the high content of the <63 μm fraction (~40%) and in the diversity of the lustre observed in quartz grains inherited from different source layers. This interpretation is further supported by a high percentage of lithoclasts in the]0-1ϕ] and]1-2ϕ] size fractions (38% and 31%, respectively). Overall, this deposit is mostly derived from a nearby terrestrial source, contrasting with the remaining deposits that reflect a marine source area.

7.2 Monitoring boulder transport

Monitoring boulder transport by present-day storms is of extreme importance as it contributes to better understand how boulder transport occurs, and to constrain threshold values of wave parameters capable of generating boulder movement. It allows to: (1) retracing boulder displacement paths; (2) evaluating how offshore wave parameters of specific storms influenced boulder transport, final position and placement; (3) and calculating recurrence intervals for storms responsible for boulder transport.

7.2.1 Observations of boulder movement during storms

Transport and emplacement at ~4 m amsl of one specific boulder of unknown origin in the southern edge of surface S III (S sector), was witnessed by surfers. They have dated this event to 10th March 2003 (Figure 89), in relation to an "intense swell". Photographic record and measurements of that boulder were undertaken in 2007 by P. Figueiredo. The shape of the boulder was approximately that of a triangular parallelepiped, with a-axis of 5 m, b-axis of 2 m and c-axis of 1.7 m (P. Figueiredo 2010, personal communication, 26 September). By September 2010 the boulder had been washed out.

The observation of boulder characteristics in photographs, such as the number of layers and their thickness, indicates a probable origin in layers L16-19; layers' arrangement and surface features indicate that the boulder was turned upside down and its mass was estimated to 22 tons (average density ~ 2600 kg/m^3; volume ~ 8.5 m^3).

A possible socket has been identified, located 3-4 m seaward of the boulders' location and ~2 m lower, in the inner region of the lower bench developed in Unit C (Figure 90). The possible socket was identified based on: (1) presence of relatively fresh and smooth surfaces in a small area, compatible with the boulder size and shape, lacking major dissolution features, and contrasting with the general aspect of the surrounding surface; (2) compatibility with boulder face geometry; and (3) proximity to boulder position after transport.

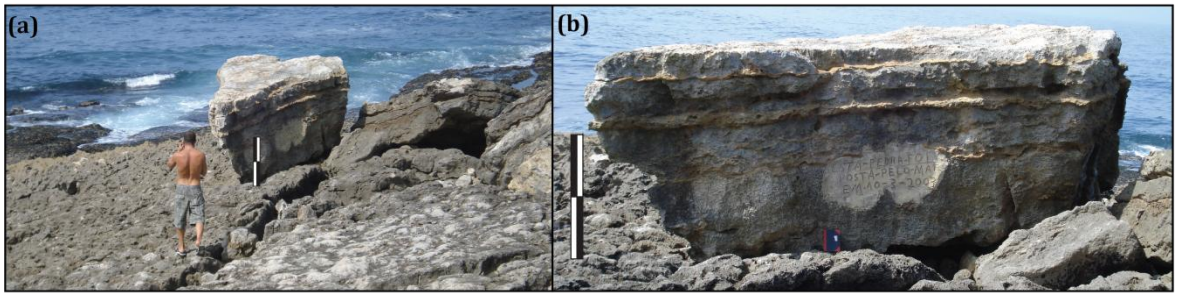

Figure 89: a) General view of the boulder transported and emplaced in 2003; b) side view of the same boulder. Vertical scale corresponds to ~1 m. Photographs were taken in 2007. Photos by P.M. Figueiredo

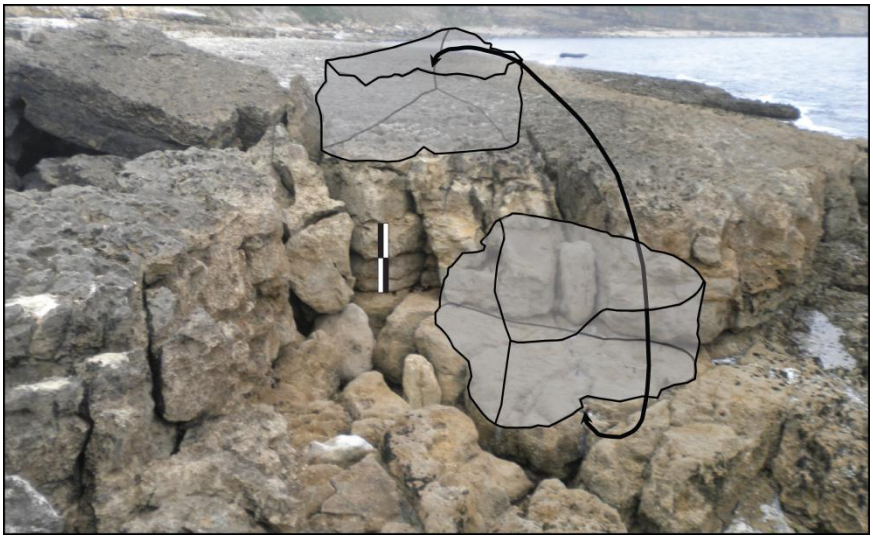

Figure 90: Probable original boulder location and schematic representation of boulder movement, initial and final positions. Vertical scale corresponds to ~1 m

Recent landward boulder movement in both sectors of the study area has also been detected in association with several winter storms that lasted over a month, with emphasis on "Christina" (3-7 January 2014) and "Nadja" (1-2 February 2014) events. Besides boulder movement, waves pronouncedly eroded and washed out particles located in the colluvium deposit in the S sector. Figure 91 to Figure 93 illustrate changes observed in relation with these storms. Details regarding individual boulders affected by these storms are listed in Appendix K.

Monitoring campaigns mainly focused on acquiring positions of particles displaced during these storm, previously identified in earlier field campaigns, and georeferencing "new" particles, *i.e.* boulders detached and emplaced by waves during this period. Movement was detected and transport distances computed by comparing original and post-storm boulder positions. Regarding "new" boulders, and whenever possible, the scar from which they originated was also mapped. The source location of "new" boulders emplaced during the storms was identified in 9 (out of 27) cases. In some cases, these boulders corresponded to partially loosened particles limited by well-developed opened joints prior to transport. They were extracted from the topmost layer of the bench edge and placed at varying distances from their source.

Not all boulder movements were detected given the substantial number of particles originally mapped. In addition, and especially in the central segment of the S sector, numerous tags identifying particles were obliterated, precluding evaluation of changes. For these reasons, monitoring campaigns were mainly conducted in the northernmost and southernmost segments of the S sector.

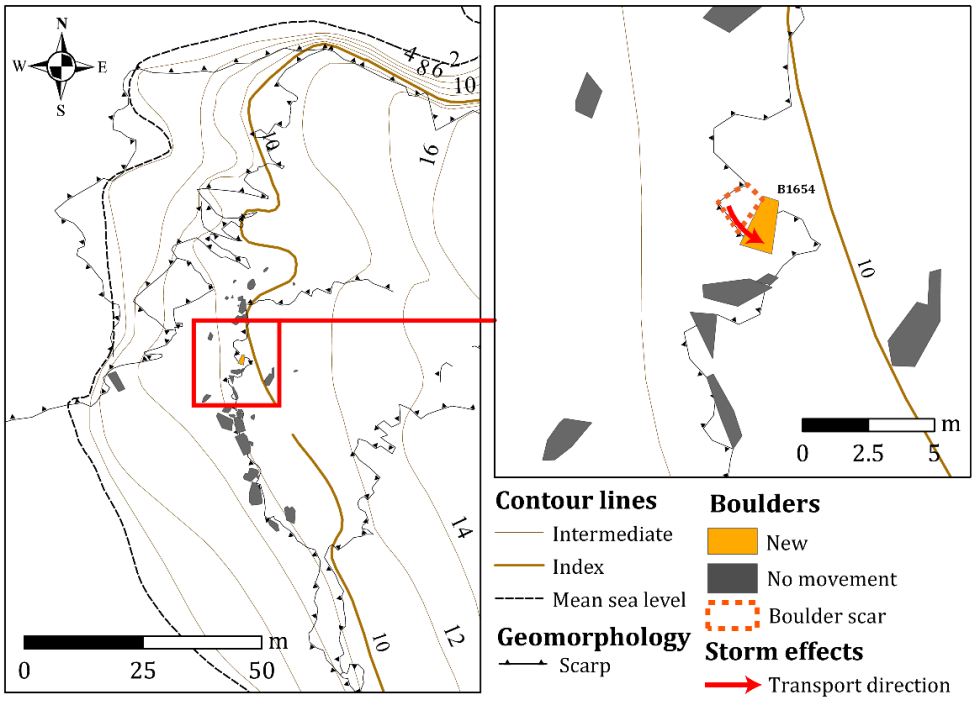

Figure 91: Boulder movement induced by January/February 2014 storms in the N sector

In the N sector, only the transport of one boulder was detected (Figure 91). This boulder, sitting at ~6 m amsl with mass over 3000 kg, suffered short landward

cross-shore transport, having been flipped upside down and pushed against the bench edge, next to its original position.

In the S sector, boulders sitting at 3-13 m amsl and with mass up to 14 tons, were moved cross-shore and alongshore (Figure 92 and Figure 93). As referred above, these storms also induced inland retreat (up to 5 m) of the colluvium foot and removed and washed out boulders formerly embedded in this deposit.

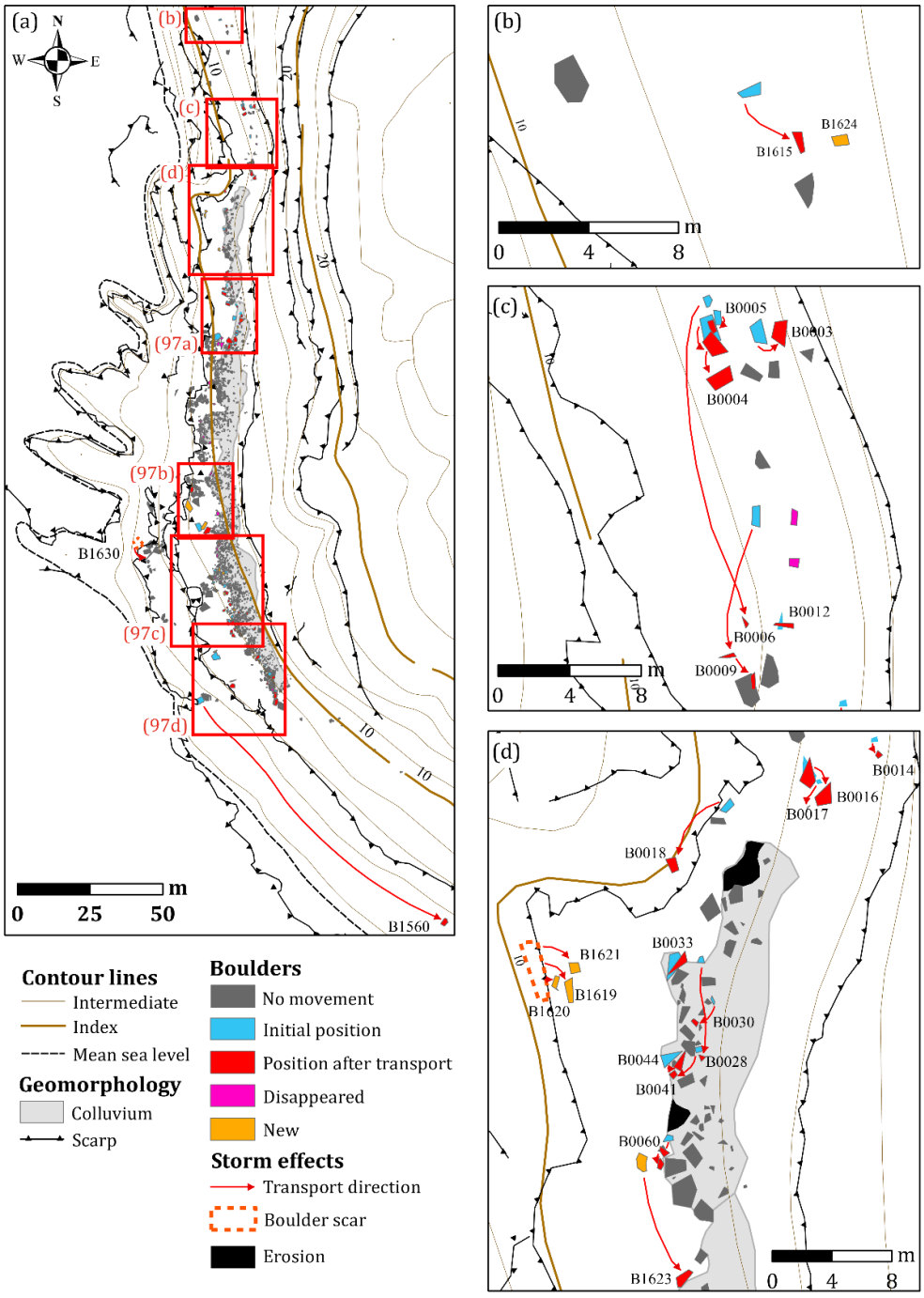

Figure 92: Boulder movement and erosion of the colluvium induced by the January/February 2014 storms in the S sector

In some cases, boulder transport appeared to have been initiated by the impact of another boulder (B0041 pushed by B0028; B0921 pushed by B1649, B0913 pushed by B1629; B1030 pushed by B1653; B1238 pushed by B1234), the impacting boulder occupying the location of the impacted particle.

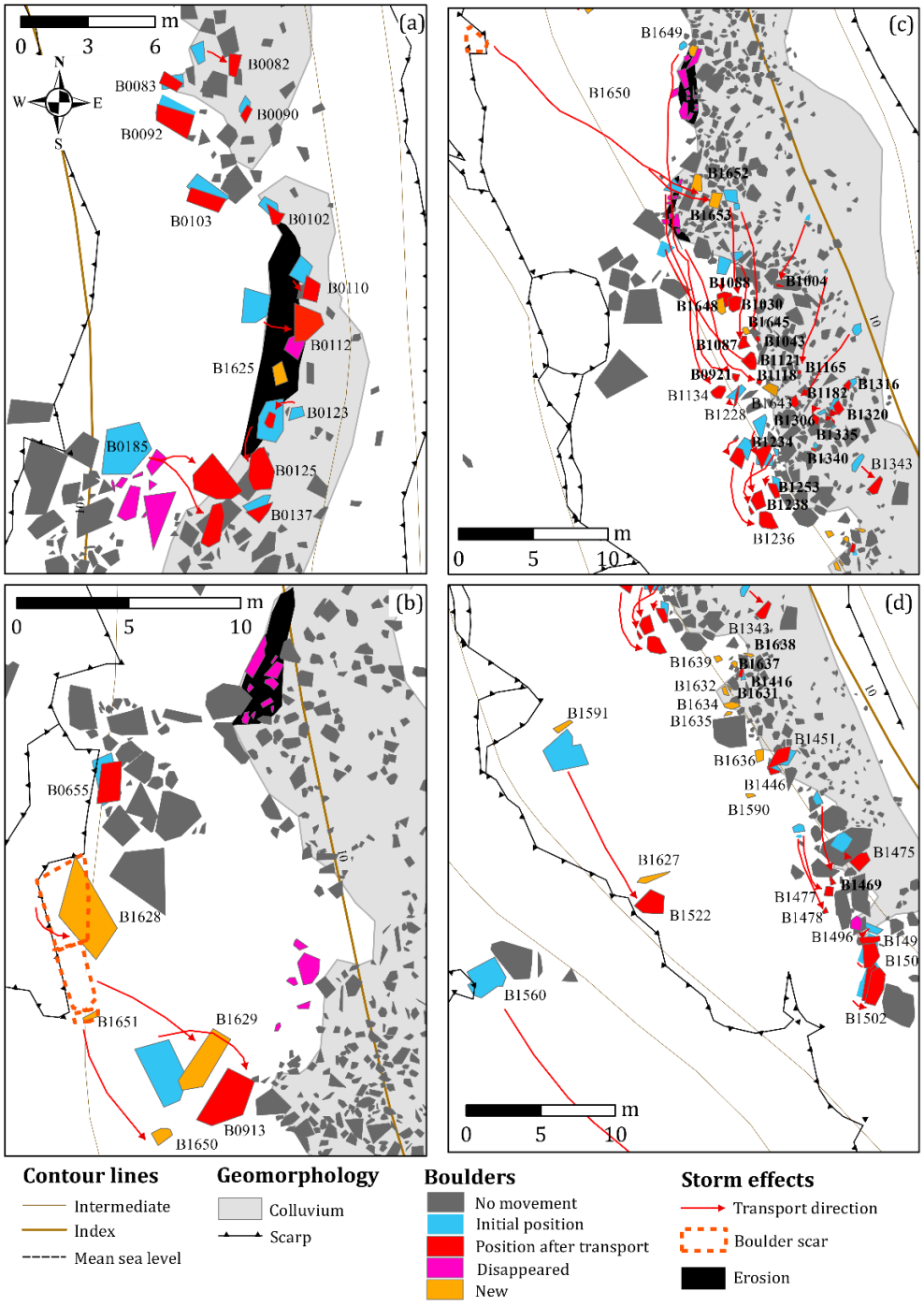

Figure 93: Boulder movement and erosion of the colluvium induced by the January/February 2014 storms in the S sector

Cross-shore transport during these storms produced maximum horizontal displacements of 20 m over S IV and 6 m over S III, and vertical displacements of 2 m

on S IV and over 3 m on S III. Longshore transport associated with minimum vertical displacements mostly occurred in favour of gravity, and reached maximum horizontal distances of 110 m over S III (Figure 92a) and 23 m on S IV (Figure 93c).

The ab surface dip direction of all boulders displaced by these storm waves shows a distribution similar to that of the overall boulder population previously mentioned and represented in Figure 78a. Boulders were placed facing four directional modes: NW, W, SW and S (Figure 94a). The a-axis of all boulders preferably trending towards the S-SW (Figure 94b).

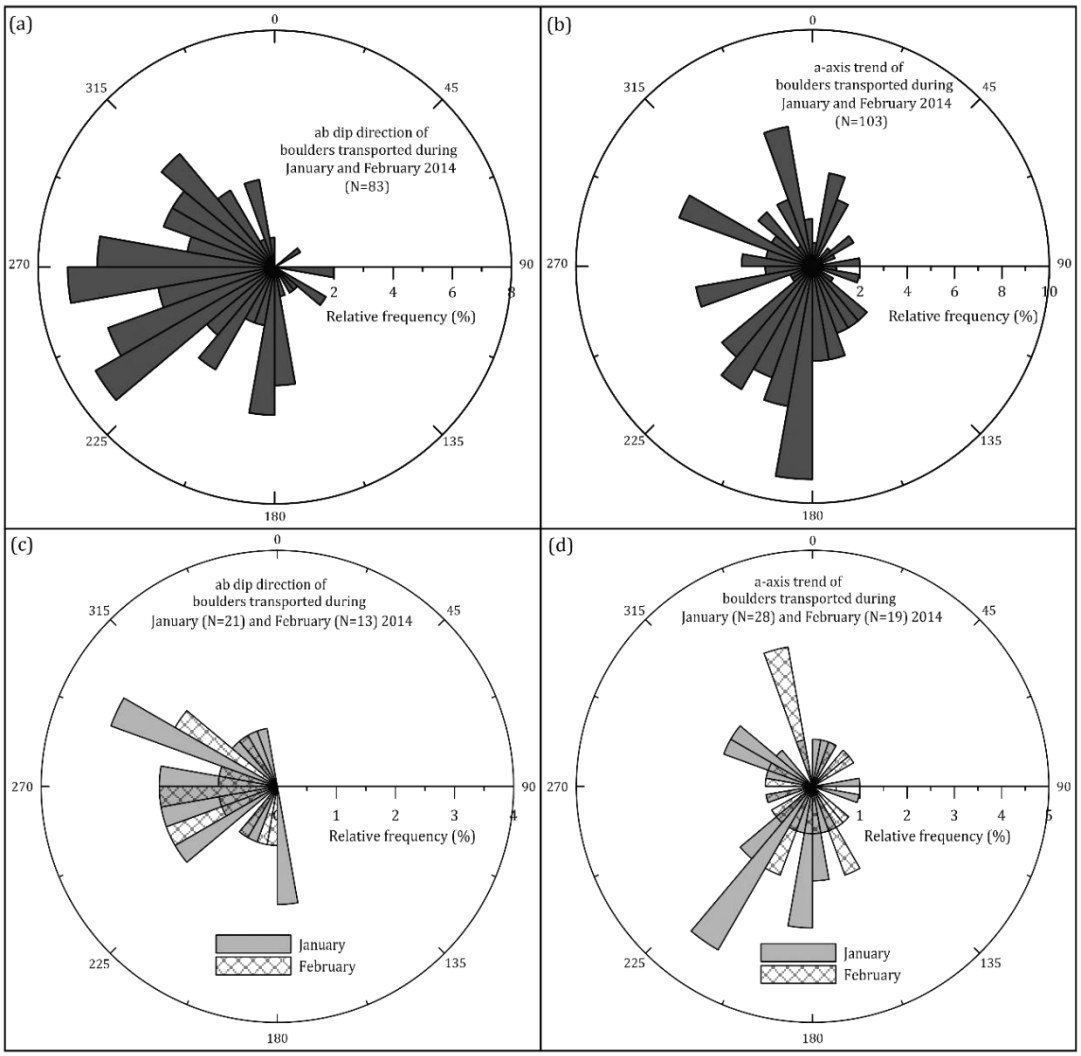

Figure 94: Rose diagram showing of directional properties of boulders transported during 2014 storms: (a) ab surface dip direction and (b) a-axis trend of all boulders transported during storms occurred in January and February 2014; (c) ab surface dip direction and (d) a-axis trend of boulders where transport could be unequivocally attributed to storms occurring either in January or February 2014

Boulder movement detected during January 2014 affected particles ranging in mass from 50 kg to 3170 kg (averaging 740 kg), which suffered vertical displacements

from 2.1 m down-slope to 0.6 m up-slope, and horizontal displacements of 0.7-7.6 m (average of 2.6 m). The movement of particles occurred in the following manner: cross-shore transport, mostly up-bench, up-ridge and/or colluvium, and directed towards E-SE (23%); alongshore transport, generally over the surface where boulders originally sat, maintaining their initial height of emplacement or occurring in favour of gravity, and directed towards SE-SW (40%); *in situ* boulder rotation, mostly affecting larger boulders (20%); the remaining 17% correspond either to "new" boulders with unknown origin, or washed-out boulders, both with untraceable direction of movement. Particles transported during January presented a varied ab surface dip direction with higher frequency of cases facing W and S, and a-axis preferably trending towards S and SW (Figure 94c and d).

Boulders affected by February storms range in mass from 200 kg to 13890 kg (averaging 2630 kg). They suffered vertical displacements from 0.3 m down-slope to 3.2 m up-slope, and horizontal displacements of 0.3-19 m (average of 5.0 m). Boulder movement attributed to February 2014 storms occurred in the following manner: cross-shore transport, mostly up-bench, up-ridge and/or colluvium, and directed towards E-SE (53%); alongshore transport, generally over the surface where boulders originally sat, maintaining their initial height of emplacement or occurring in favour of gravity, and directed towards SW-SE (37%); the remaining 11% correspond to "new" boulders with unknown origin and untraceable direction of movement. Particles transported exclusively during February mostly face NW-SW, their a-axis preferably trending towards N and scattering around S (Figure 94c and d).

On average, differences between boulder mobilization occurred in January and February include: (1) larger particles were transported in February; (2) higher vertical and horizontal transport distances were detected in February; (3) cross-shore transport was more frequent than alongshore transport in February, the opposite having occurred during January; (4) a-axis trend of boulders transported during January cluster around S and SW, whereas, in boulders transported during February, the a-axis trend clusters around N. These differences must be associated with distinct wave regimes affecting this coastline during January and February, which is verified the following section.

7.2.2 *Present-day storms capable of generating boulder movement*

The transport and emplacement of the boulder during the 2003 swell, detected and observed by surfers, and mentioned above, occurred in March 10th, 2003. Wave data extracted from the hindcast time-series obtained by Dodet *et al.* (2010) reveal maximum values of H_s ~6 m occurring from 6 AM to noon of March 10th, associated with T_p ~19.5 s and corresponding to NW (~300°) swell (Figure 95). During that day, tidal level reached a maximum elevation of +0.64 m amsl, close to the high (astronomical) tide level during neap tides (averaging +0.67 m amsl).

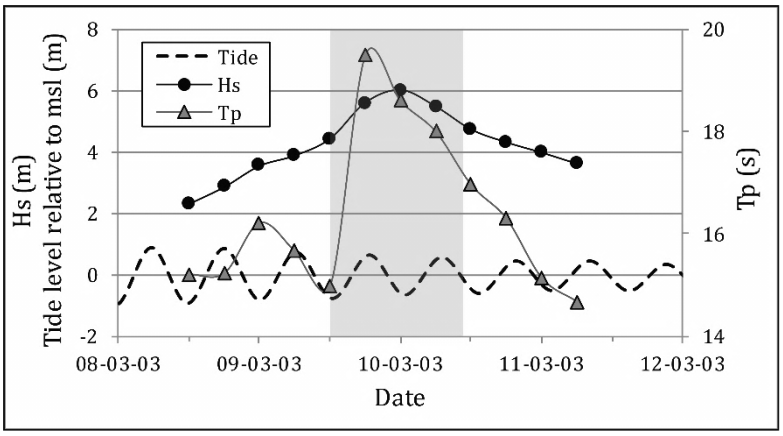

Figure 95: H_s, T_p and tide level data for March 9th to 11th 2003. Shaded area corresponds to March 10th, 2003, when boulder transport occurred. Wave data extracted from the hindcast time-series obtained by Dodet *et al.* (2010) and tide level data available in http://www.hidrografico.pt/previsao-mares.php

The significant wave height observed during this swell event (~6 m) is relatively common in the west-facing coast of Portugal. However, this event generated a not so common up-bench vertical displacement of ~2 m and emplacement of a 22-ton boulder. The unusual character of this event is probably associated with a coincidence in occurrence of high tide with maximum peak period of 19.5 s. The former generated an increase in water level allowing for waves to reach closer to the coastline without breaking, and the latter implied a significant increase in the energy associated with these waves, together with longer time of landward-directed flow related with larger wave length.

More recently, "Christina" (3-7 January 2014) and "Nadja" (1-2 February 2014) storms caused major effects in coastal areas (Aon Benfield, 2014a; b). In the W coast of Portugal most important effects comprised beach and dune erosion, overwash and flooding of coastal areas, damages in coastal protection structures and buildings

(Diogo *et al.*, 2014a). Boulder dislodgement and transport in both cross-shore and alongshore directions were detected in the study area, as previously described (section 7.2.1).

Wave data (significant and maximum wave heights and zero-crossing and maximum periods) during "Christina" storm was extracted from the http://www.hidrografico.pt/boias-ondografo.php website, for the Leixões wave-buoy. To compare this data with that of the remaining storms, values for peak period had to be extrapolated. The following linear relationship between zero-crossing period (T_m) and peak period (T_p) has been obtained using the hindcast time-series produced by Dodet *et al.* (2010), and further used to infer values of T_p of "Christina" and "Nadja" waves (Figure 96):

$$T_p = 1.06T_m + 1.23 \qquad \textbf{Equation 36}$$

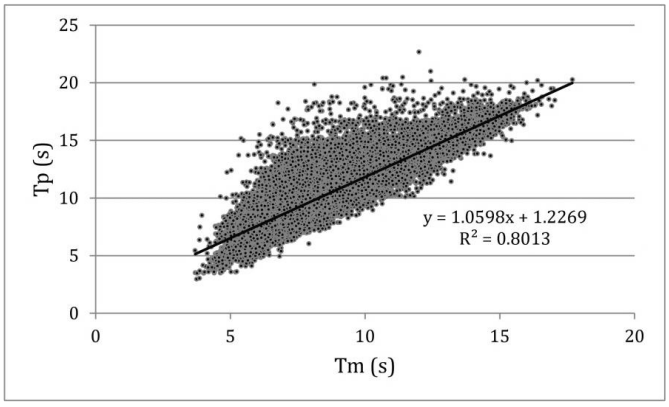

Figure 96: Scatter plot of T_m *vs* T_p and linear relationship between both variables

Wave parameters registered in buoys located offshore the Portuguese coastline show that "Christina" raised significant wave heights to 9 m, peak period up to 16.7 s (Figure 97) with the highest waves travelling from the WNW. When maximum significant wave height and period occurred, in the afternoon of 6th January 2014, the tide was approximately at mean sea level, but the following high tide (+1.12 m amsl) occurred still during the storm, in association with slightly lower values of significant wave height and peak period.

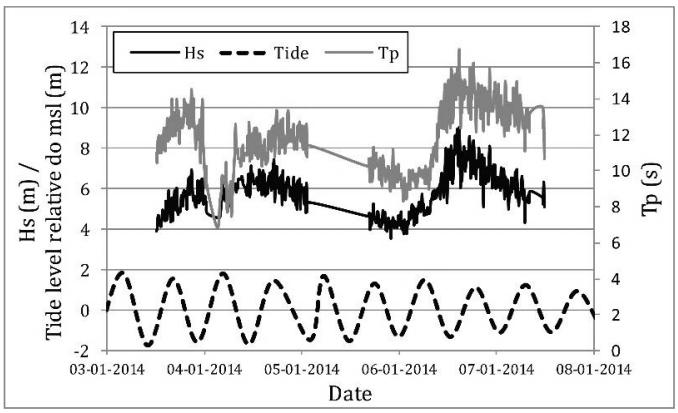

Figure 97: H_s, T_p and tide level data during Christina storm from January 3rd to 7th 2014. Wave data extracted from the website http://www.hidrografico.pt/boias-ondografo.php at the time of the storm and tide level data available at http://www.hidrografico.pt/previsao-mares.php

In what concerns "Nadja", wave parameters reported by the Leixões wave-buoy, accessed days after that storm (http://www.hidrografico.pt/boias-ondografo.php), indicate maximum significant wave heights above 9 m, zero-crossing wave period of 14 s (corresponding to T_p of ~16 s), the wave direction varying from NW to WNW (Figure 98).

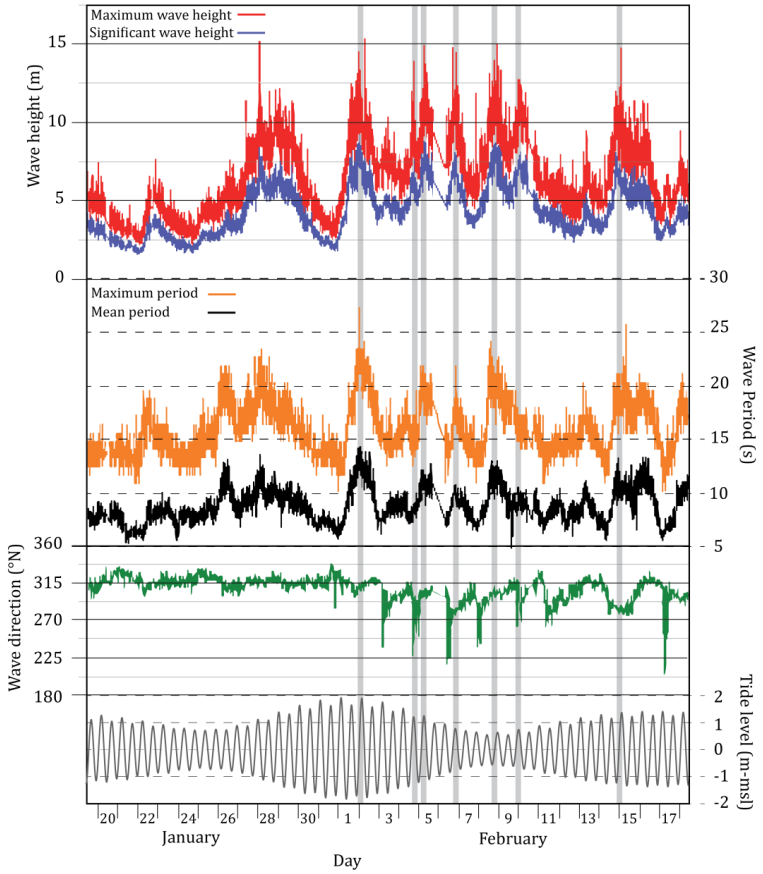

Figure 98: Wave data from Leixões buoy during January and February and tidal levels. Grey bands mark relevant peaks in significant wave height and mean period. Graphics containing wave parameters were modified after plots produced by Instituto Hidrográfico (accessed in 18-02-2014). Tide level data available at http://www.hidrografico.pt/previsao-mares.php

Moreover, on the 2nd February 2014, maximum H_s and T_p values coincided with high spring tide, that reached +1.9 m amsl. Following "Nadja" decline, boulder transport continued to occur and several relevant peaks in wave height and period were registered, showing varying wave directions, ranging from NW to SW (Figure 98).

Approximate time, wave parameters and tidal level information (available in http://www.hidrografico.pt/previsao-mares.php) on the 10th March 2003 event, as well as on "Christina", "Nadja" and other relevant storms occurred during February 2014 (identified from graphical data presented in Figure 98) are listed in Table XX.

Table XX: Wave parameters and tidal level of the 10th March 2003, "Christina", "Nadja" and from other relevant storms affecting the western Portuguese coastline during February 2014

DAY / TIME	H_s (m)	T_m (s)	T_p (s)	DIRECTION (°N)	WAVE POWER ($W \cdot m^{-1}$)	TIDAL LEVEL amsl (m)
10-03-2003	6	17.2	19.5	300	558 286	0.64
06-01-2014 / 14:50 ("Christina")	9	14.6	16.7	292.5	953 426	0
02-02-2014 / 04:00 ("Nadja")	9	14	16.07	304	886 430	1.9
04-02-2014 / 18:00	7.5	9	10.77	225	307 234	1.21
05-02-2014 / 06:00	8.75	12	13.95	304	638 681	1.25
06-02-2014 / 20:00	8	11	12.89	281.25	461 973	0.78
08-02-2014 / 24:00	8.5	13	15.01	292.5	693 394	0
09-02-2014 / 24:00	8	11	12.89	270	461 973	0.74
15-02-2014 / 05:00	8.5	13	15.01	281.25	683 394	0

Numerical modelling of wave propagation undertaken using SWAN© to several points along two cross-shore profiles in front of the west-facing and southwest facing segments of the S sector (methods described in section 6.4) for the events described in this section, and listed in Table XX, rendered results showed in Figure 99.

As waves approach the study area, wave direction converges into the western octant, regardless the offshore wave direction. The further away they are from the W, the larger is the difference between the offshore and the nearshore wave direction, showing maximum counter-clockwise refraction-induced changes in direction of 29° and a clockwise change of 32°. Nearest to the coastline, waves arrive at both the west- and southwest-facing segments of the southern sector travelling from the W. However, for these storms, refraction-induced changes in direction are

not sufficient to completely obliterate the directional differences between them, which reaches values of 21° in the west-facing segment and 25° in the southwest-facing segment.

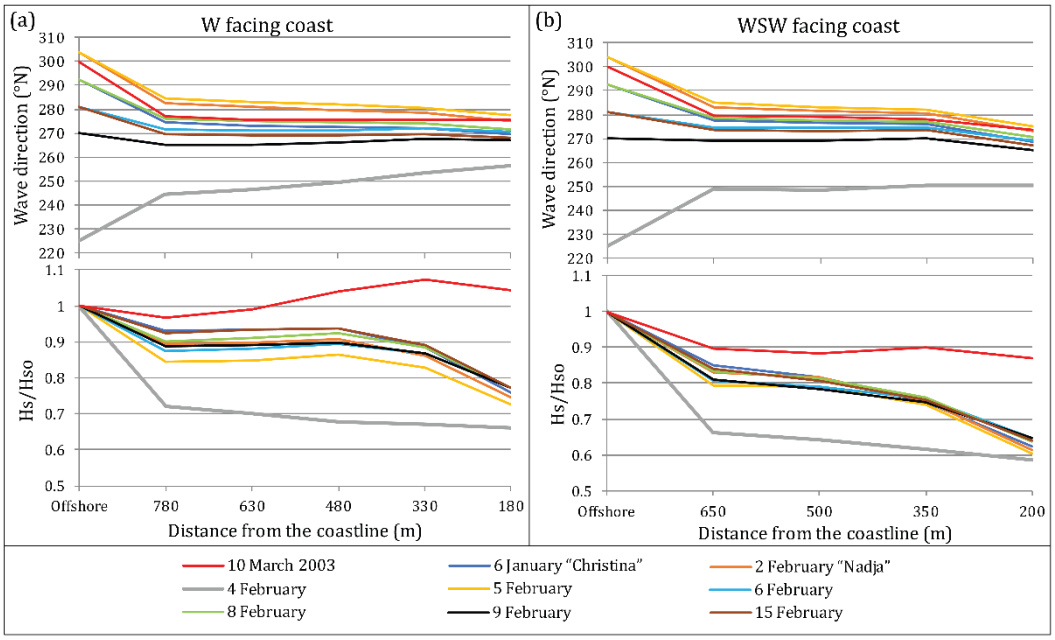

Figure 99: Wave direction and ratio between nearshore and offshore significant wave height (H_s/H_{so}), offshore and in the target points located along cross-shore profiles in the (a) west-facing segment of the S sector (b) southwest-facing segment of the S sector

Results of numerical modelling show a general decrease in wave height when they approach the coastline (distances of 800-200 m), except for the 10th March 2003 event. This decrease appears to be unrelated to wave direction, it partly depends of wave period and is larger in the SW- than in the W-facing segment of the southern sector. Longer waves, such as those occurring on 10th March 2003 (T_m=17.2 s), show an increase in the ratio between nearshore and offshore significant wave height (H_s/H_{so} of 1.07) in the W-facing segment and a decrease (0.9) in the WSW-facing segment. Conversely, waves with shorter period, such as those occurring on 4th February 2014 (T_m=9 s), show a decrease in H_s/H_{so} of 0.6 in both segments.

Summarizing, the following conclusions can be extracted from numerical modelling of present-day storms: (1) refraction-induced changes in direction are not sufficient to completely obliterate the directional difference between storms, which reaches 25°; (2) the decrease in wave heights is unrelated to wave direction, it partly depends of wave period and is larger in the WSW-facing segment; (3) long-period waves suffer minimum wave height decrease or even slight increase. Besides wave

parameters, it is also important to consider the influence of tidal levels and storm surge, which can increase, on average, the sea surface in 2.16 m and 0.4 m, respectively. These results are integrated and further discussed in what respects interpretations of boulder accumulations, in section 7.2.4 (Summary and interpretations).

7.2.3 Statistical modelling of extreme values

Storms responsible for boulder entrainment, transport and placement described above raised maximum significant wave heights of 6-9 m and maximum mean periods of 9-17.2 s. The generalized extreme value (GEV) function was fitted to yearly maxima of significant wave heights (data plotted in Figure 44) and mean periods (data plotted in Figure 45) extracted from the hindcast time-series presented in Dodet *et al.* (2010) (further details about GEV fitting in 6.4.2 Statistical modelling of extreme events). Estimated return levels and confidence bounds are presented in Table XXI.

Table XXI: Estimated H_s and T_p with 95% confidence intervals for different recurrence periods

Recurrence period (years)	Significant wave height (m)			Wave Period (s)		
	Lower confidence bound	Estimate	Upper confidence bound	Lower confidence bound	Estimate	Upper confidence bound
2	7.33	7.66	7.99	15.15	15.37	15.59
5	8.34	8.82	9.31	15.80	16.08	16.36
10	8.93	9.60	10.26	16.16	16.50	16.84
20	9.42	10.34	11.27	16.41	16.86	17.30
50	9.90	11.31	12.73	16.64	17.28	17.92
100	10.16	12.05	13.93	16.73	17.56	18.39
200	10.33	12.78	15.22	16.79	17.82	18.85

Based on the GEV fitting of yearly maxima, made separately for both H_s and T_m, these events present recurrence intervals of 2-10 years and 2 to 50 years, respectively. To evaluate the joint probability of occurrence of a combination of values of H_s and T_m, producing a magnitude identical to that of the events described in this work, the computation of recurrence intervals for wave power was

undertaken, which incorporates both wave height and period in the computation (Table XXII).

Table XXII: Estimated *P* with 95% confidence intervals for different recurrence periods

Recurrence period (years)	Wave Power ($W \cdot m^{-1}$)		
	Lower confidence bound	Estimate	Upper confidence bound
2	400 541	444 705	488 869
5	538 646	612 519	686 393
10	625 801	738 916	852 032
20	699 416	873 048	1 046 680
50	774 261	1 067 595	1 360 929
100	811 221	1 230 617	1 650 012
200	827 843	1 409 375	1 990 907

Most storms described above, all of which having been responsible for boulder transport in the study area, present wave power of 400 000-600 000 $W \cdot m^{-1}$, and occur on average once every 2-5 years. However, events such as "Christina" and "Nadja", responsible for generating significant changes in the boulder deposit, present wave power above 880 000 $W \cdot m^{-1}$, and occur on average only once every 20 years.

7.2.4 Summary and interpretations

The observation of the effects of present-day storms in the study area provided invaluable information regarding how boulder transport occurs. The identification of "new" boulders, pre-transport setting and transport paths suggests that boulders incorporated in the deposit correspond to loosened, joint-bounded pieces of the top-most layer of the bench edges, directly exposed to the wave swash. Larger particles suffer minimum cross-shore displacement and rotation, remaining near their socket, sometimes in an up-side down position. Smaller particles are transported further inland and upwards, sometimes being directly placed on the top of boulder ridges or along their landward facing slope.

After emplacement over the structural platform, when boulders are large enough, they either remain as isolated boulders near the bench edge, or are broken into several smaller particles. When they reach a transportable size, are transported by sliding or rolling over and along the structural platforms, and pushed against obstacles (*e.g.* larger boulders, boulder ridges or colluvium), and remain for long-periods of time. These particles end up incorporating boulder clusters or ridges and, when located next to the landward edge of the structural platforms, can be partially covered by the developing colluvium. However, they can also be transported alongshore, towards SW-SE, and finally removed by the backwash, mostly near the southernmost of both sectors.

The effects of present-day storms in the N and S sectors presented a sharp contrast: only a 3000-kg boulder was moved in the N sector, while in the S sector, the transport of over 100 boulders with mass up to 14 ton was detected. Furthermore, also in the S sector, a contrast in boulder movement can be observed between different segments. This is revealed by the obliteration of tags identifying the boulders mapped in earlier field campaigns, by boulder transport frequency and by significant erosion of the colluvium deposit (together with particles embedded within) in the W-facing segments of that sector. Also in the S sector, but in the WSW-facing segment, the storms mainly induced deposition of small boulders and slightly displaced larger boulders, inducing an increase in packing of boulder accumulations, corresponding to active development of an incipient boulder ridge. This discrepancy indicates that the dissipation of energy by storm waves in W and WSW-facing segments is very different, the former being much more exposed to the present-day wave regime than the latter.

Directional properties of boulders placed during January and February 2014 are similar to the bulk of the initially mapped boulder accumulation, strongly suggesting a storm-origin for the larger deposit under analysis. Wave refraction affects the waves as they approach the nearshore, generating a concentration in wave direction around the western octant, which explains the larger frequency in the western directional mode found in boulders.

Differences between boulder transport and placement during January and February of 2014 comprise both magnitude and direction (mostly visible in dissimilar a-axis trends). The average mass of displaced boulders is significantly larger in February, reflecting a higher destructive power of the "Nadja" storm. Given that wave parameters of "Christina" and "Nadja" were identical, differences in transport magnitude must be related with the coincidence of peak in storm intensity with peak tide levels. Higher tide levels increase sea surface height and, consequently, the reach of waves, thus increasing boulder transport capability. Larger frequency and magnitude in boulder transport occurring during "Nadja" might also be related to the mechanical effects of waves during previous events (namely "Christina"), which could have facilitated layer breakdown and boulder detachment, making them available to be transported in the following storms.

Comparison of transport paths and a-axis trend of boulders indicates a counterclockwise rotation in the main transport direction. Storms occurring during January preferably generated longshore transport associated with NW flow over the structural platform. During February, significant boulder detachment and cross-shore transport was detected, apart from the longshore transport, associated with a larger W-E flow direction over the structural platform.

Although refraction-induced changes in storm wave direction are not sufficient to completely obliterate the directional difference between them, there is an evident narrowing in wave direction. Modelling of wave propagation shows that present-day storms responsible for boulder transport have reached the coastline with wave directions ranging from 250° to 280°. These results confirm that directional attributes of boulders do not exclusively represent nearshore wave direction, but are influenced by the interaction of the flow reaching the structural platforms with morphological features, such as the indentations in the lower structural platforms. Moreover, contrasts in transport direction and a-axis trends associated with the "Christina" and "Nadja" storms, must be related with a dominance of swash (preferably associated with cross-shore) over backwash (preferably associated with alongshore transport) in the latter, due to the higher tidal levels and consequent reach of the waves.

Long-period waves, such as the 10th March 2003 storm, suffer minimum wave decrease or even slight increase as they approach the coastline. These waves present a large potential to generate boulder transport, as the wave power is significant, even when wave height is low.

The recurrence intervals for events with the magnitude of storms observed in January and February 2014 is high (more than 20 years). However, boulder transport in the study area occurs with lower magnitude and more frequent events, which occur at least once every 5 years. In conclusion, events affecting this coastal sector are more common than initially foreseen and present a sedimentological signature identical to that observed in the boulder accumulation studied. In retrospective, there is no need to invoke a catastrophic event, such as a tsunami, to explain such deposits, thus suggesting a storm origin for the Coxos boulder accumulation.

7.3 Numerical solutions for boulder transport

7.3.1 Application to the boulder deposit

Approximations described in section 6.5 (Computation of wave parameters) were separately applied to boulders in the N and S sectors, and to boulders transported by the 2013/2014 (B1619 onwards) and 2003 storms.

Significant wave heights capable of generating boulder movement obtained with the Nandasena's *et al*. (2011a) equations are presented in Figure 100a. These values are higher for boulders located in the northern sector, reaching 12.8 m, and 11.5 m in the southern sector. Significant wave heights computed for smaller boulders are much lower, with particles requiring a H_s lower than 3 m corresponding to 74% of particles in the N sector, and 87% in the S sector. The boulder transported during the 2003 storm described in section 7.2.1 (Observations of boulder movement) would require a significant wave height of 5 m to be dislodged. Regarding boulders transported during the 2013/2014 storms, significant wave heights reach 9 m, but are below 3.8 m for most particles.

Maximum values of tsunami wave heights, represented in Figure 100b, were obtained for boulders in the northern sector, reaching 1.3 m, followed by maximum tsunami wave heights of 1.2 m for boulders in the southern sector. For comparison purposes, tsunami wave heights necessary to generate boulder movement were also calculated for recent known storm boulders. In this case, a tsunami wave of 0.5 m would suffice to transport the boulder associated with the 2003 storm and 0.9 m for the largest boulder transported during the 2013/2014 storms.

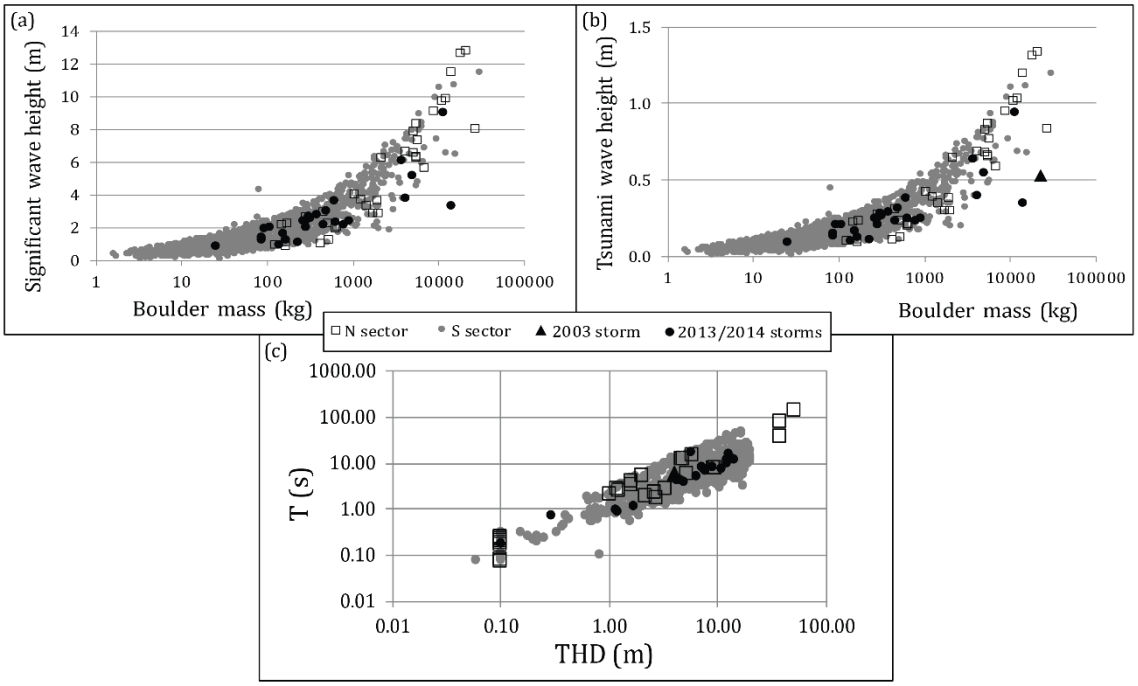

Figure 100: Scatter plots showing critical wave parameters necessary to generate boulder movement: (a) H_s inferred from Nandasena's *et al.* (2011a) equation for rolling; (b) tsunami wave height obtained with Nott's (1997, 2003) equation for subaerial boulders; (c) wave period obtained with Lorang's (2002; 2011) equation

Results obtained with Lorang's (2002; 2011) approximation using wave height computed with Nott's equation for threshold flow velocity in a subaerial context and further converted to breaking wave height, are represented in Figure 100c. Maximum wave periods of 80 and 150 s were obtained for two boulders in the northern sector with maximum transport distances of 38-50 m towards S-SSE. Wave periods obtained for the remaining boulders were under 47 s.

7.3.2 Summary and interpretations

The application of the numerical solution developed by Nandasena *et al.* (2011a) to the larger boulders transported by storms with known wave parameters, rendered

significant wave heights of broken waves below maximum offshore modelled/recorded values: computed H_s of 5 m for the 2003 storm (offshore significant wave heights during the storm reached 6 m); computed H_s obtained for larger boulders and offshore recorded H_s of the storms occurring during January/February of 2014 of 9 m.

When applied to the bulk of the Coxos accumulation this solution predicts significant wave heights up to 12.8 m for the largest boulders in the N sector and up to 11.5 m in S sector. These values are lower than maximum modelled values of 13 m in the offshore the Portuguese coastline from 1953 to 2008 (described in section 5.4 Oceanographic climate). Computed tsunami wave heights reach 1.3 m, which are well below the *AD* 1755 tsunami inundation height over of 5-6 m near Ericeira (described in section 2.1.5 1st November 1755). Computed wave periods are mostly under 40 s, except for two boulders transported towards S-SE, showing long horizontal displacements of 35 m and 65 m, thus indicating a storm origin for most of the particles in Coxos accumulation.

Significant wave heights are computed for broken waves when energy dissipation and flow velocity are near its maximum. Inland of the breaking point, flow velocities decrease until reaching zero when arriving at the coast. Given that the pre-transport location of boulders addressed in this study is above msl, computed wave heights should be underestimated. In addition, results obtained from modelling present-day storms, presented in section 7.2.2 (Present-day storms capable of generating boulder movement), and the wave height transformation matrix in front of Coxos beach (Figure 47 in section 5.4 Oceanographic climate), showed that, in many cases there is a relevant deacrese in significant wave height in front of the study area. This implies that computed H_s values could be even more underestimated than expected. However, validation of the available approximations to known boulder accumulations described in chapter 4 (Numerical solutions of boulder movement) and results obtained for boulder transported during present-day storms, considering only the largest boulders, rendered significant wave heights consistently close to, and below, maximum values observed offshore. Considering this, these approximations should only be applied to the largest boulders, as they represent the competency of the largest waves, they should be used with caution as

rough estimators for wave height and their use as a tool to differentiate storm from tsunami origin in not advised.

Computed significant wave heights are essentially larger for boulders in the N sector. This suggests that the transport of boulders in the N sector required events of larger magnitude than those of the S sector, and recently observed. These interpretations are further supported by the contrast in boulder transport frequency between sectors observed during the 2013/2014 storms. These storms severely affected the southern sector, but were only capable to transport a 3000-kg boulder in the northern sector. Therefore, larger boulders in the northern sector must have been transported by more energetic events, such as storms with return periods larger than 20 years or to tsunami events. To clarify which interpretation is more accurate, age estimation of boulder transport was attempted and described in the following section (6.6).

7.4 Age estimation

Age estimation results obtained by applying the methodologies described in section 6.6 (Age estimation) are presented in this section, including comparison of aerial photographs, lichenometry, downwearing rates and OSL dating.

The comparison of aerial photographs was initially undertaken as a tool to estimate the age of boulder movement. However, results pertaining to changes in geomorphological features from 1948 to 2010 allowed only to identify generic boulder movement in different segments of the study area during this period, which can only be attributed to storms. Age estimation of specific boulders was achieved using lichenometry through the construction of a lichen growth curve and model and application to the boulder deposit, described in sub-sections 7.4.2.1 and 7.4.2.2. Results obtained with lichenometry were further tested by comparison with another chronology proxy based on downwearing rates. More specifically, the age of deposition of one single boulder was estimated based on the erosion of the underlying layer using a MEM, and is presented in the following sub-section. Finally, OSL age estimation of marine sand patches collected beneath of boulders, which correspond to a minimum age for their deposition, will be shown in the last sub-section.

7.4.1 Aerial photographs

The comparison between the cartography performed over the 1948 aerial photographs with that of the 2010 photographs in the N sector shows many similarities (Figure 101a and b). The boulder accumulation extending for approximately 40 m, and roughly aligned ENE-WSW mapped over the 1948 photographs and absent in the 2010 images, corresponds to boulders generated by break-down of layer L19. They rest close to its edge, and not show evidence of transport against gravity. Although these boulders still exist, they were not mapped in field campaigns because the basic criteria of transport against gravity was not observed. This was also the case of 3 large boulders roughly aligned NNW-SSE along the bench edge and shown in the 1948 photographs. Only one large-sized boulder, sitting closest to the cliff edge, further west, was identified during both the field surveys and in the 2010 aerial photographs, and not visible in the 1948 photographs.

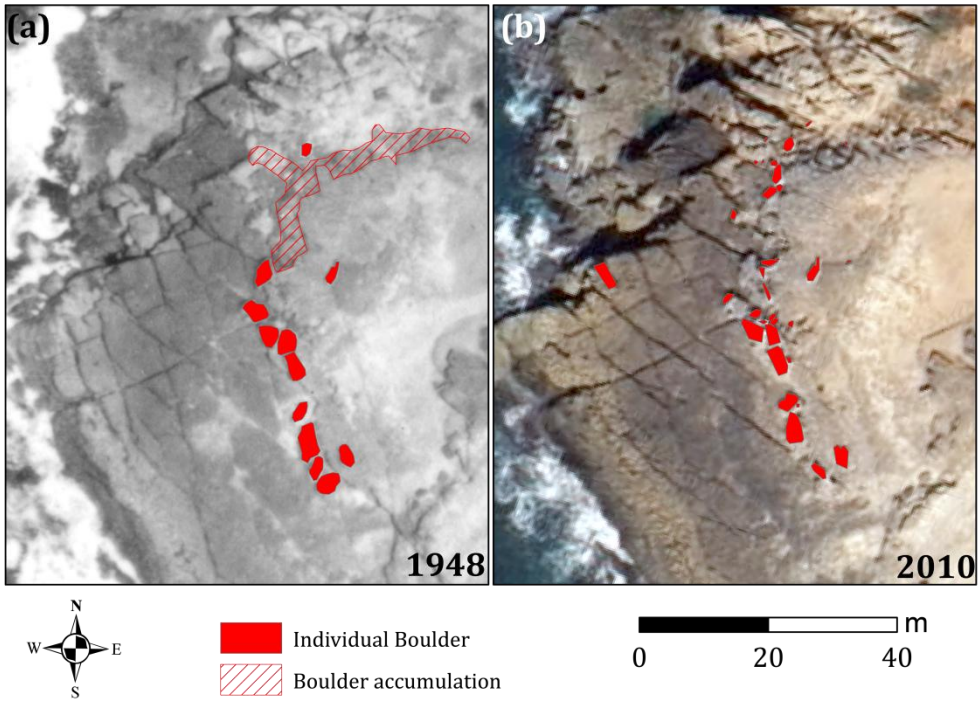

Figure 101: Mapped individual boulders and boulder accumulations using stereoscopic analysis of aerial photographs in the N sector, over: (a) 1948 aerial photographs; (b) 2010 aerial photographs

Boulder sizes, as mapped in the 1948 photographs, are larger than sizes acquired during field work, and corresponding to the 2010 cartography. These differences are related with the methods applied: boulders mapped over the aerial photographs

correspond to their outline as visible from the angle of the photograph, while boulders mapped in field surveys correspond to the horizontal projection of their ab surfaces.

Results from the comparison of the 1948 and 2010 aerial photographs of the S sector are presented in three segments, from N to S, sequentially. In this sector, the ability to distinguish individual boulders on aerial photographs was compromised, due to low resolution of the images, the considerable number of boulders in close proximity and their small size. An additional drawback was the difficulty in resolving features in the colluvium from boulders over the 1948 photograph. However, individual boulders and accumulations were separately mapped whenever boulder size (larger boulders), concentration (isolated boulders) and location (not contained within the colluvium) allowed to definitely identify these elements.

Several equidistant boulders were identified in the northernmost segment of the S sector, in 2010, located near the cliff edge, which were absent in 1948 (Figure 102a and b). According to local fishermen, these boulders have been placed to prevent cars from getting too close to the cliff edge. Further south, significant changes in the width of the colluvium were detected, the deposit showing larger cross-shore development in the 1948 photograph.

The upper structural platform of the central segment of the S sector shows significant changes in boulder position and development of the colluvium deposit, which cannot be attributed to human activities, given the inaccessibility to vehicles (Figure 103a and b). Over that surface, most particles mapped in 1948 images as individual boulders cannot be recognized in the 2010 photographs implying that they have been displaced, washed out or buried by the colluvium. However, although boulder movement between 1948 and 2010 in this area is clear, the clusters mapped in both images display the same general cross- and alongshore locations. There are significant changes observed in the cross-shore development of the colluvium deposit. In some places, the colluvium presents a regular width in 1948, whereas it shows indentations in the 2010 cartography (Figure 103a and b).

In what concerns the lower structural platform, although some differences can be found in boulder accumulations, they roughly occupy the same position. Differences between individual boulder positions are: larger particles mapped as individual boulders disappeared in the more recent image; and several "new" boulders detected in the 2010 image seem to correspond to breakdown of the bench edge.

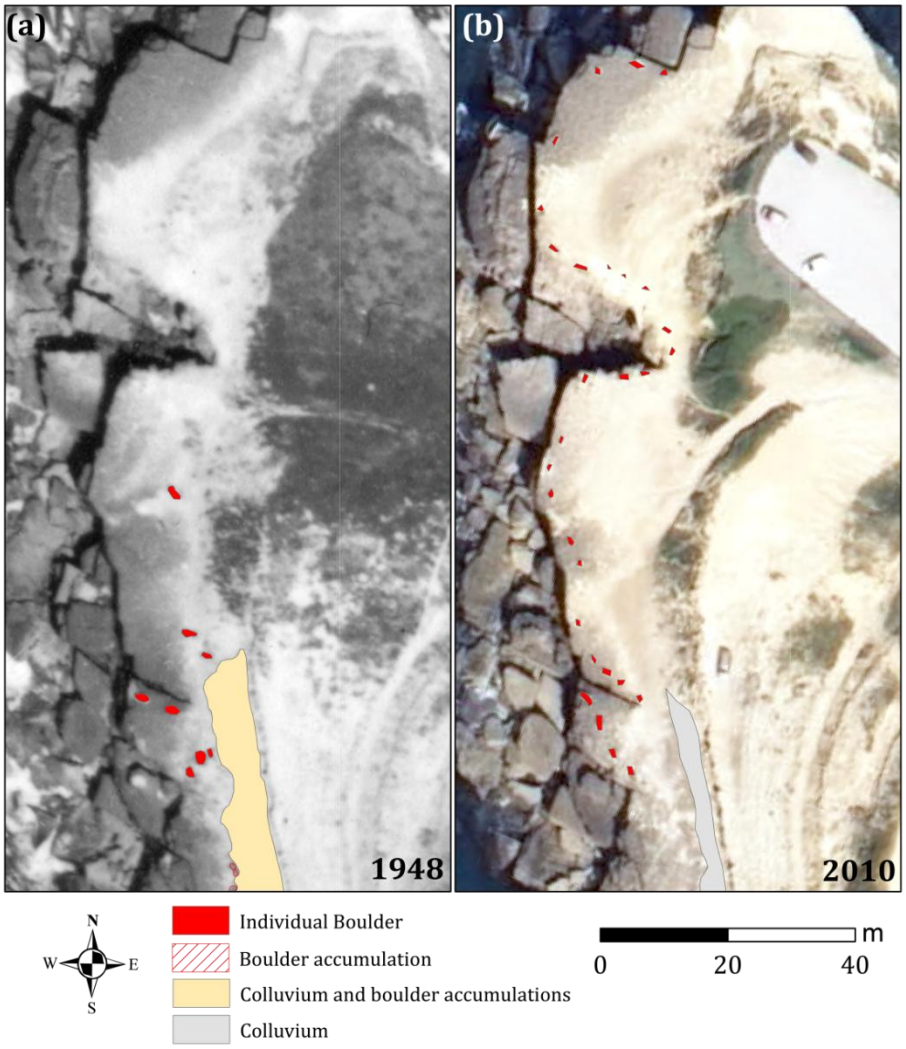

Figure 102: Mapped individual boulders detected with using aerial photographs in the northernmost segment of the S sector, over: (a) 1948 aerial photographs; (b) 2010 aerial photographs

The southernmost segment shows many similarities between 1948 and 2010 (Figure 104a and b). In the lower structural platform, most individual boulders can be identified and are in the same location in both photographs. In places where they could not be separately mapped over the 1948 photography, boulder accumulations were limited and perfectly overlap individual boulders mapped over the 2010 photograph.

In what concerns the upper structural surface, larger individual boulders are also in the same locations in both photographs. Moreover, clusters of larger boulders in the 2010 cartography overlap boulder accumulations mapped over the 1948 aerial photographs. Finally, colluvium development is almost identical in both dates.

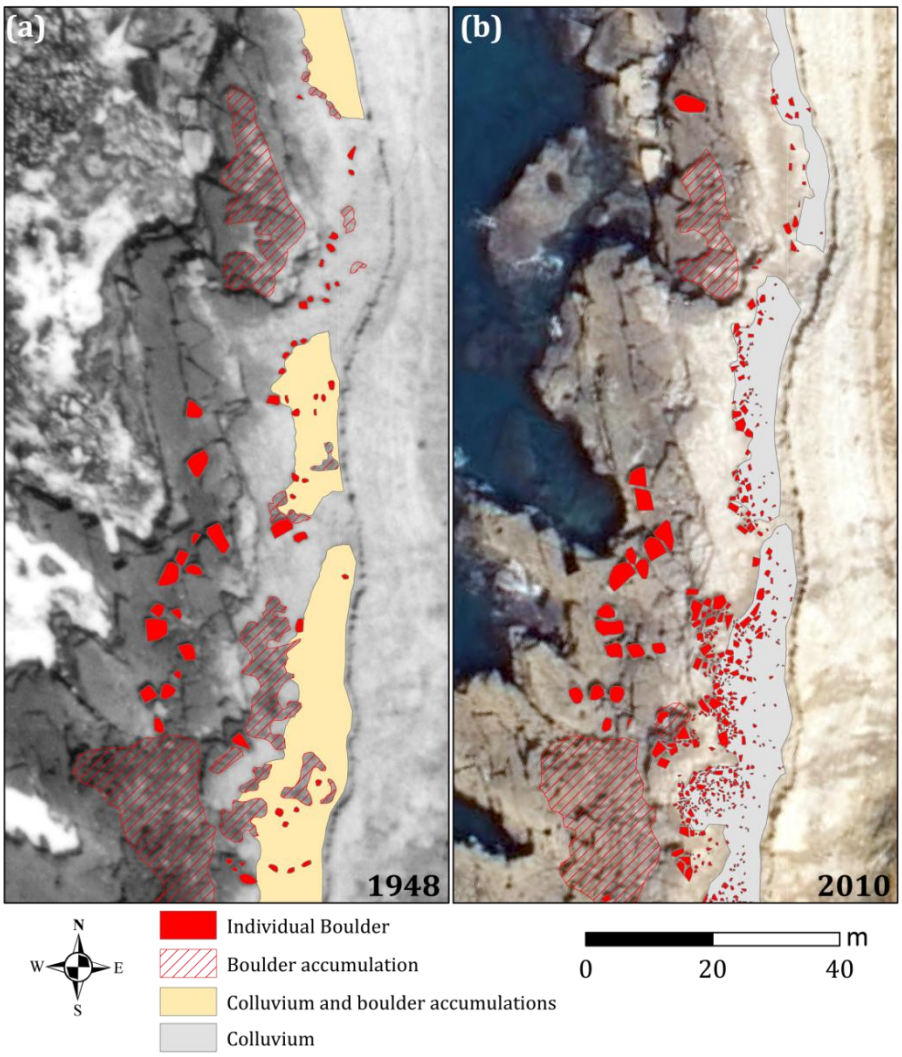

Figure 103: Mapped individual boulders, boulder accumulations and colluvium detected with stereoscopic analysis of aerial photographs in the central segment of the S sector, over: (a) 1948 aerial photographs; (b) 2010 aerial photographs

Summarizing, many boulders have moved between 1948 and 2010, but others, however, did not. In the N sector, all but one of the larger boulders identified during field surveys overlap perfectly with boulders observed in the 1948 aerial photographs. In the northernmost segment of the S sector significant changes in boulder position were detected and attributed to human activities. In the central segment of the same sector, boulder transport and changes in the colluvium deposit are evident, indicating that most boulders in the accumulations were emplaced more

recently than 1948. Despite these differences, the general cross-shore and longshore distribution of accumulations are approximately the same. The southern segment is more stable, larger individual boulders having remained in the same position since 1948.

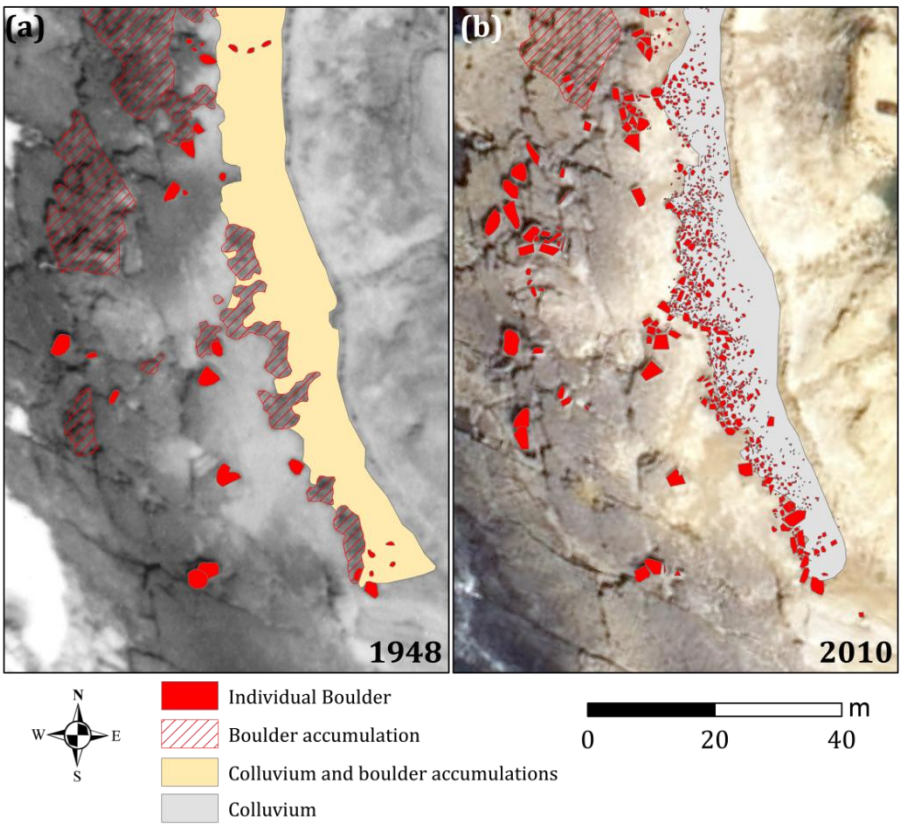

Figure 104: Mapped individual boulders, boulder accumulations and colluvium detected with stereoscopic analysis of aerial photographs in the southernmost segment of the S sector, over: (a) 1948 aerial photographs; (b) 2010 aerial photographs

7.4.2 Lichenometry

Results regarding the lichen growth curves, which correlate lichen data and time, are firstly presented, followed by the distribution of lichen size in the boulder deposit and, finally, results obtained with the application of the lichen growth model to individual boulders will be presented.

7.4.2.1 Lichen growth curve

The lichen *Opegrapha durieui* was found covering substrate developed in marls, sandy to crystalline limestone and concrete. These materials show different

physical, mineralogical, textural and chemical characteristics, but all contain calcium carbonate in high proportions, in the form of calcite.

A total of 14 control points were obtained from lichens colonising rock surfaces along a coastal ribbon extending from Nazaré to Boca do Rio, located in forts, other artificial structures and rock scars developed in relation with slope mass movements (Figure 105). Information about the control points, date and properties measured in the field is summarized in Table XXIII. Data on lichen size and cover and detailed information about the control points are presented in appendix L. Results regarding lichen cover and size are summarized in Table XXIV and Table XXV, respectively, and presented in chronological order.

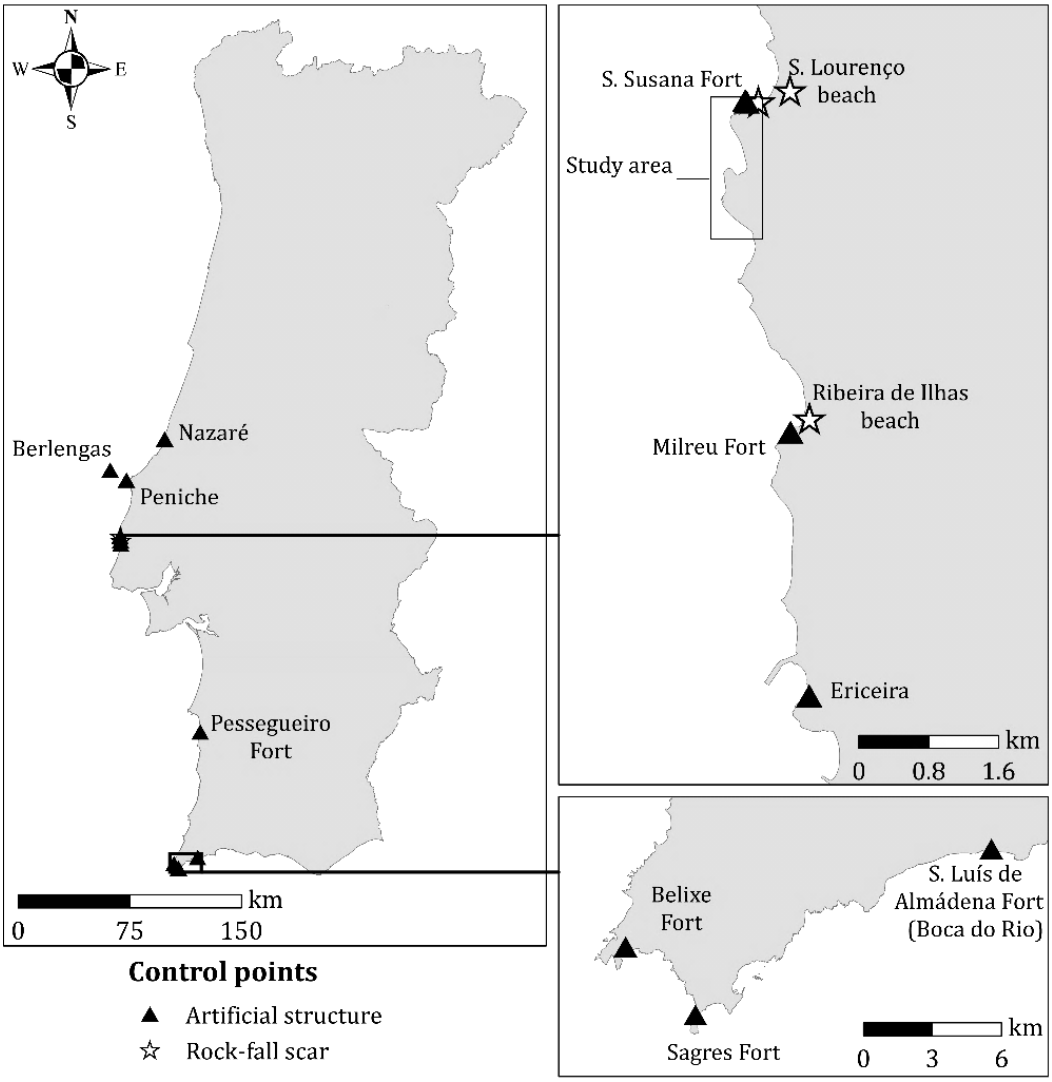

Figure 105: Location along the Portuguese coastline and type of structure containing control points used in the construction of the growth curves for the lichen species *Opegrapha durieui*

Table XXIII: Control points used to build the lichen growth curve (species *Opegrapha durieui*). Z corresponds to elevation. * Time of exposure ended before date of measurement due to cleaning of stone, probably during reconstruction works

CONTROL POINT	TYPE	Z (m amsl)	YEAR OF EXPOSURE	DATE OF MEASUREMENT	TIME (years)	PROPERTY
L05	Rock-fall	14.5	Between September 2011 and 30-05-2012	20-09-2013	1.7	Lichen size and cover
L01	Rock-fall	8.6	Between 1-11-2005 and 10-06-2006	20-09-2013	7.6	Lichen size and cover
Ericeira wall	Artificial structure	14	Between 24-05-1980 and 24-02-2000	18-02-2014	23.9	Lichen size and cover
L12	Rock-fall	37	Between 24-05-1980 and 18-04-1989	07-11-2013	29.0	Lichen size and cover
S. Susana Fort (CC03)	Artificial structure	18	Between 1944 and 1949	26-12-2013	67	Lichen size and cover
S. Miguel Arcanjo Fort (Nazaré)	Artificial structure	15	1645	13-11-2015	370	Lichen size and cover
São João Baptista Fort (Berlengas)	Artifical structure	5	1678	31-07-2016	338	Lichen size and cover
Baluarte Redondo (Peniche)	Artificial structure	14	1558	17-06-2015	457	Lichen cover
				05-08-2016	458	Lichen size
S. Susana Wall (CC04)	Artificial structure	17	Between 1657 and 1777	26-12-2013	296	Lichen size and cover
Milreu Fort	Artificial structure	21	Between 1777 and 1657	30-01-2014	297	Lichen size
			1657	07-11-2013	356	Lichen cover
Pessegueiro Fort	Artificial structure	13	1690	09-02-2014	324	Lichen cover
				03-08-2016	326	Lichen size
Belixe Fort	Artificial structure	52	1632	26-01-2014	382	Lichen cover
				03-08-2016	384	Lichen size
Sagres Fort	Artificial structure	37	1793*	26-01-2014	157	Lichen cover
				03-08-2016		Lichen size
S. Luís de Almádena Fort	Artificial structure	69	1632	26-01-2014	382	Lichen cover
				03-08-2016	384	Lichen size

Lichen coalescence was frequently observed in surfaces with longer time of exposure, making the identification and measurement of individual lichens complex. These were the cases of S. Luís de Almádena Fort, Pessegueiro Fort, Milreu Fort and Baluarte Redondo (Peniche). Furthermore, in some forts, lichens were found and measured only in unplastered limestone stones, such as Santa Susana, Milreu, S. Luís de Almádena and Pessegueiro. Unplastering resulted from deterioration of plaster originally covering the construction material. However, it was considered that exposure occurred immediately after construction, except for Milreu and Santa Susana forts, where 18th century (historical) information on the state of preservation of the forts aided to constrain age of exposure of stones originally under plaster. For this reason, age of exposure may have been overestimated in some cases.

Table XXIV: Percentage of lichen cover of control surfaces and age of exposure

CONTROL PONT	TIME (years)	% COVER (100×100mm)
L05	1.7	0
L01	7.6	2.68
Ericeira wall	23.9	22.11
L12	29.0	6.15
S. Susana Fort (CC03)	67	93.47
Sagres Fort	157	90.01
S. Susana Wall (CC04)	296	82.36
Pessegueiro Fort	324	72.73
S. João Baptista Fort (Berlengas)	338	94.89
Milreu Fort	356	93.68
S. Miguel Arcanjo Fort (Nazaré)	370	100
Belixe Fort	382	71.44
S. Luís de Almádena Fort	382	96.80
Baluarte Redondo (Peniche)	457	98.07

In Sagres and Baluarte Redondo, the limestone stones used to build the door-frames have been partially cleaned; this is evidenced by a large population of dead organisms and stone discoloration. In both forts, the exact date of the last cleaning operations is unknown. In the case of Sagres, lichens were assumed to have stopped growing following major reconstruction works undertaken around 1950 (between 1940 and 1960). Maintenance of Baluarte Redondo occurred repeatedly, due to the continuous use of this defensive structure, precluding to establish a date for the last cleaning of the stones (see appendix L for more information).

The percentage of lichen cover in a 100x100 mm area computed in all control points, is summarized and organized chronologically in Table XXIV, and represented in Figure 106.

Lichen cover rapidly reaches percentages above 70% after ~70 years of surface exposure. After 70 years, most control points present lichen cover percentages above 80% except for Pessegueiro and Belixe forts (Figure 106). The exceptionally high values of lichen cover observed in at least two structures (Santa Susana Fort-CC03 and Sagres Fort) indicate that this variable is conditioned by unknown additional factors, other than time (Table XXIV and Figure 106). These unknown factors are most probably related to the species ecology, such as optimal temperature, moisture content, substrate, *etc.*

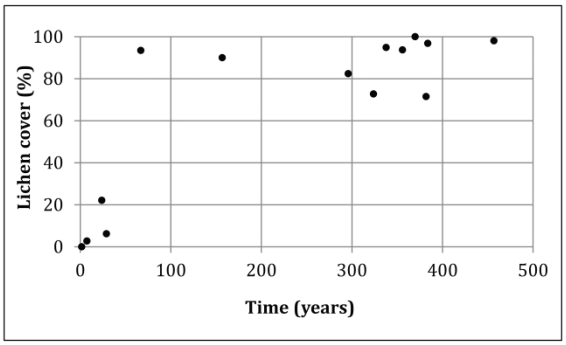

Figure 106: Lichen growth curve based on the percentage of lichen cover, considering a 100x100 mm sampling area

The use of this parameter as an age estimator requires the inclusion of additional ecological parameters which would explain changes in lichen cover. Such an investigation is beyond the scope of this work and thus lichen cover was not further used as an age estimator.

Average diameter of the 5 largest thalli identified in each control point, the area of an equivalent circle, as explained below, and age of exposure are summarized and organized chronologically in Table XXV. Growth of thalli can be represented in two ways: (1) by plotting the average diameter of the largest thalli (five, in this case) against age of exposure (Figure 107a); (2) or by plotting the corresponding area, considering an equivalent circular shape, against age of exposure (Figure 107b).

Table XXV: Average diameter of the 5 largest lichen thalli covering the control surfaces and age of exposure used in the construction of the lichen growth curve. The area parameter *A* represents the area of a circle with a diameter equal to the average of the 5 largest thalli

CONTROL POINT	TIME (years)	AVERAGE DIAMETER, Ø (mm)	AREA OF EQUIVALENT CIRCLE, *A* (mm²)
L05	1.7	0	0
L01	7.6	5	20
Ericeira wall	23.9	13.2	137
L12	29.0	11	95
S. Susana Fort (CC03)	67	24.4	468
Sagres Fort	157	29.6	668
S. Susana wall (CC04)	296	31.4	774
Milreu Fort	297	34.8	951
Pessegueiro Fort	326	31.6	784
S. João Baptista Fort (Berlengas)	338	33.0	855
S. Miguel Arcanjo Fort (Nazaré)	370	38.8	1182
Belixe Fort	384	34.0	908
S. Luís de Almádena Fort	384	37.2	1087
Baluarte Redondo (Peniche)	458	37.6	1110

Lichen thalli of the species *Opegrapha durieui* become visible under macroscopical observation after 1.7 to 7.6 years of surface exposure. Lichen diameter increases rapidly during the first ~70 years, at a rate of 0.36-0.66 mm·year^{-1}, averaging 0.49 mm·year^{-1}. The increase in size after 70 years and at least until reaching the maximum observed age of 458 years, progresses at a slower rate, of 0.08-0.19 mm·year^{-1}, averaging 0.11 mm·year^{-1} (Figure 107a). These changes in lichen growth rate over time are also observed when the area of the equivalent circle is plotted against time (Figure 107b). However, in this case, the contrast between the two growth stages is less obvious. Altogether, the plot of size *versus* time follows a logarithmic curve, similar to the ones obtained by other authors investigating lichen growth (*c.f.* Bradwell, 2001; Gob *et al.*, 2003; Benedict, 2009; Armstrong, 2015a).

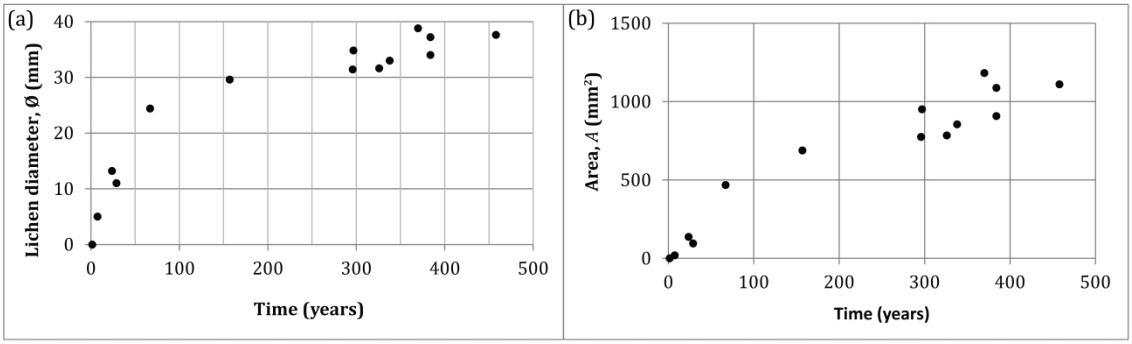

Figure 107: Lichen growth curves for the species *Opegrapha durieui* showing: (a) the average diameter of the 5 largest individuals measured in the control points plotted against time; (b) area of the equivalent circle plotted against time

To infer the age of surface exposure of an individual based on lichen size (diameter and area of the equivalent circle), and prediction intervals as indicated in Freund *et al.* (2006) and Moore *et al.* (2009), the best fit to the observed data sets, was obtained using a linear regression model, following a logarithmic transformation of the dependent variable (time) in the case of Ø diameter. The plot of ln(time) *vs* lichen diameter (Equation 37 and Figure 108a) yielded $R^2 = 0.96$ and of time *vs* area (Equation 38 and Figure 108b) yielded $R^2 = 0.91$.

$$\ln(time) = 0.13\emptyset + 1.25 \quad \ll\!=\!\gg \quad time = 3.49e^{0.13\emptyset} \qquad \textbf{Equation 37}$$

$$time = 0.38A - 19.33 \qquad \textbf{Equation 38}$$

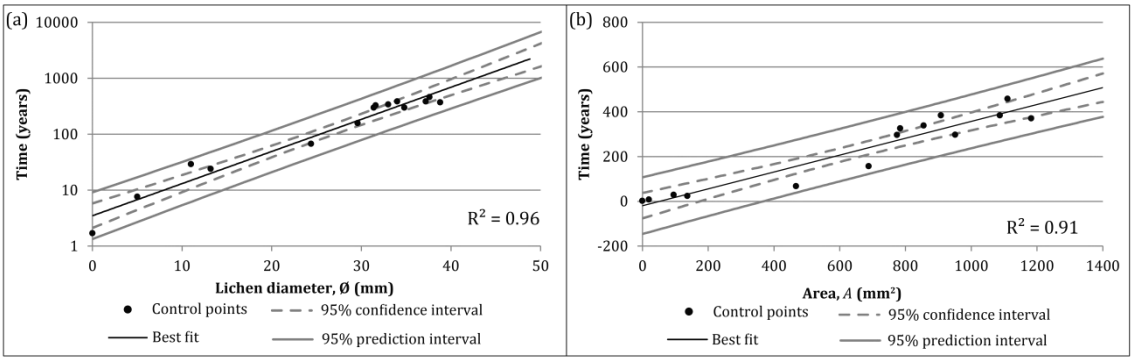

Figure 108: Lichen growth models and 95% confidence and prediction intervals for the data set: (a) ln(time) *vs* the average of the 5 largest thalli; (b) time *vs* area of the equivalent circle

The lichen growth models, depicted in Figure 108, yielded high R^2 values indicating high goodness of fit. In perspective, R^2 values obtained for the Ø based model, may indicate that this model is the best fit, and, at first glance, the best proxy of age of exposure of a given surface. This is further strengthened by results obtained from age estimation of younger surfaces based on the *A*-model, which may render negative values, indicating that the latter model is inadequate for small lichen thalli (Figure 109a). However, the use of lichen diameter as an age estimator is not without difficulties. Due to the exponential relationship between time and lichen diameter, the amplitude of prediction intervals becomes increasingly larger, in cases reaching the double of predicted ages (Figure 109b). On the contrary, at approximate ages of 200 years and larger, amplitudes of prediction intervals based on *A* remain constant and around 235 years, while those based on Ø continue to increase (Figure 109c and d).

Given the age estimations and amplitude of prediction intervals obtained, a combined approach making use of both models was adopted. The growth model based on Ø was used for Ø values lower than 30 mm (roughly corresponding to ~200 years), and for larger thalli, age estimation of surfaces was inferred using the growth model based on *A* (Figure 109d). For thalli larger than 40 mm, predictions lie outside the range of the control values used to constrain the models and correspond to extrapolations. In this case, and for the reasons stated above, the growth model based on *A* was also used.

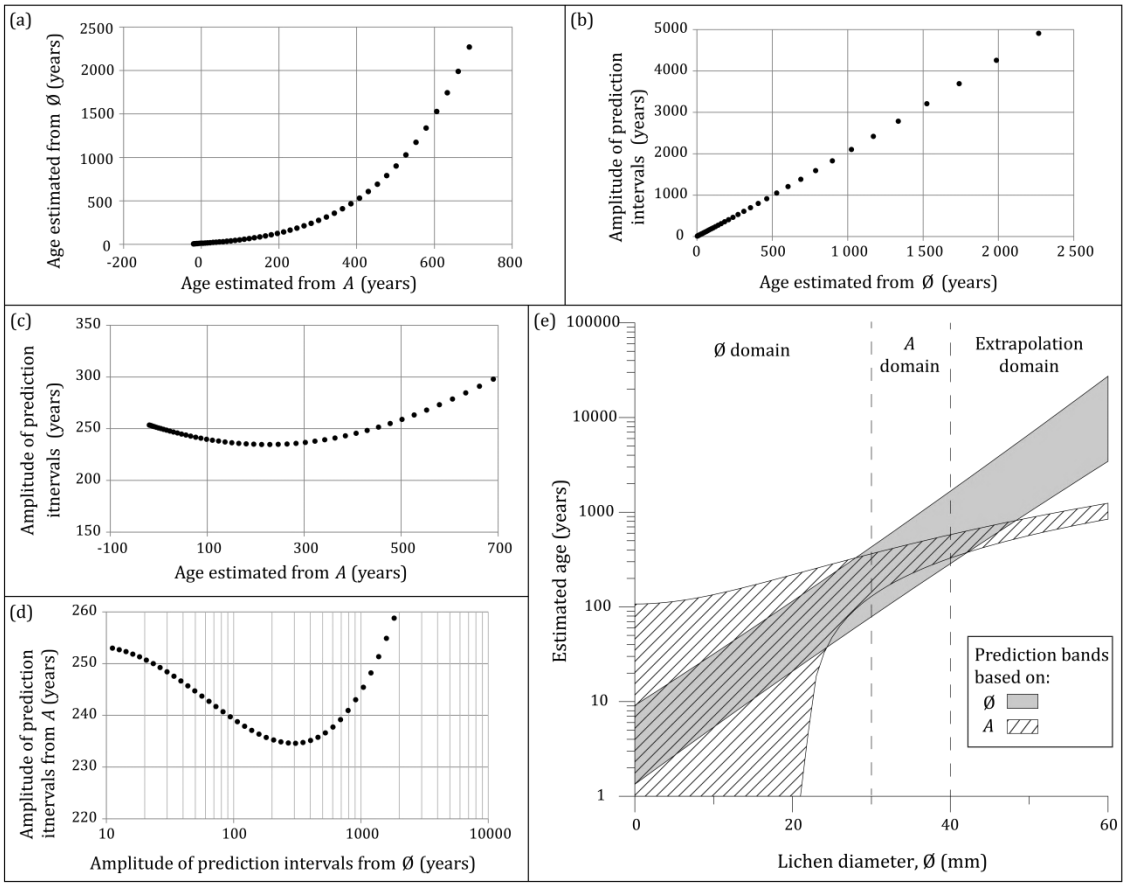

Figure 109:Estimated ages and amplitude of prediction intervals for Ø and *A* growth models. (a) Scatterplot comparing estimated ages obtained with different growth parameters. (b) Scatterplot showing the amplitude of prediction interval against age estimated from the Ø growth model. (c) Scatter plot showing the amplitude of prediction interval against age estimated from the *A* growth model. (d) Scatter plot comparing the amplitude of prediction intervals. (e) Prediction bands for both growth models and definition of site domains to be used in age estimation

7.4.2.2 Application to the boulder deposit

Among the over 1500 boulders identified in both the northern and southern sectors, 35 were covered by lichens from the species *Opegrapha durieui* (Figure 110a and b).

All boulder faces showing living lichens face N-NE or are partially sheltered by boulders that protect them from direct exposure to sunlight.

In some cases, both dead and living lichen populations were found covering the surfaces of boulders. Generally, both populations presented similar sizes, but sometimes the living specimens were larger than the dead and in other cases the dead were larger than the living. In cases where the latter was observed, living lichens consistently overlapped dead forms (Figure 111b). Moreover, some of the boulder surfaces showing well developed and living lichen colonies in 2012, when the first lichen measurement campaign was undertaken, contained exclusively dead forms in the latest campaigns (2016). This was observed in coastal sections showing frequent boulder movement due to storms.

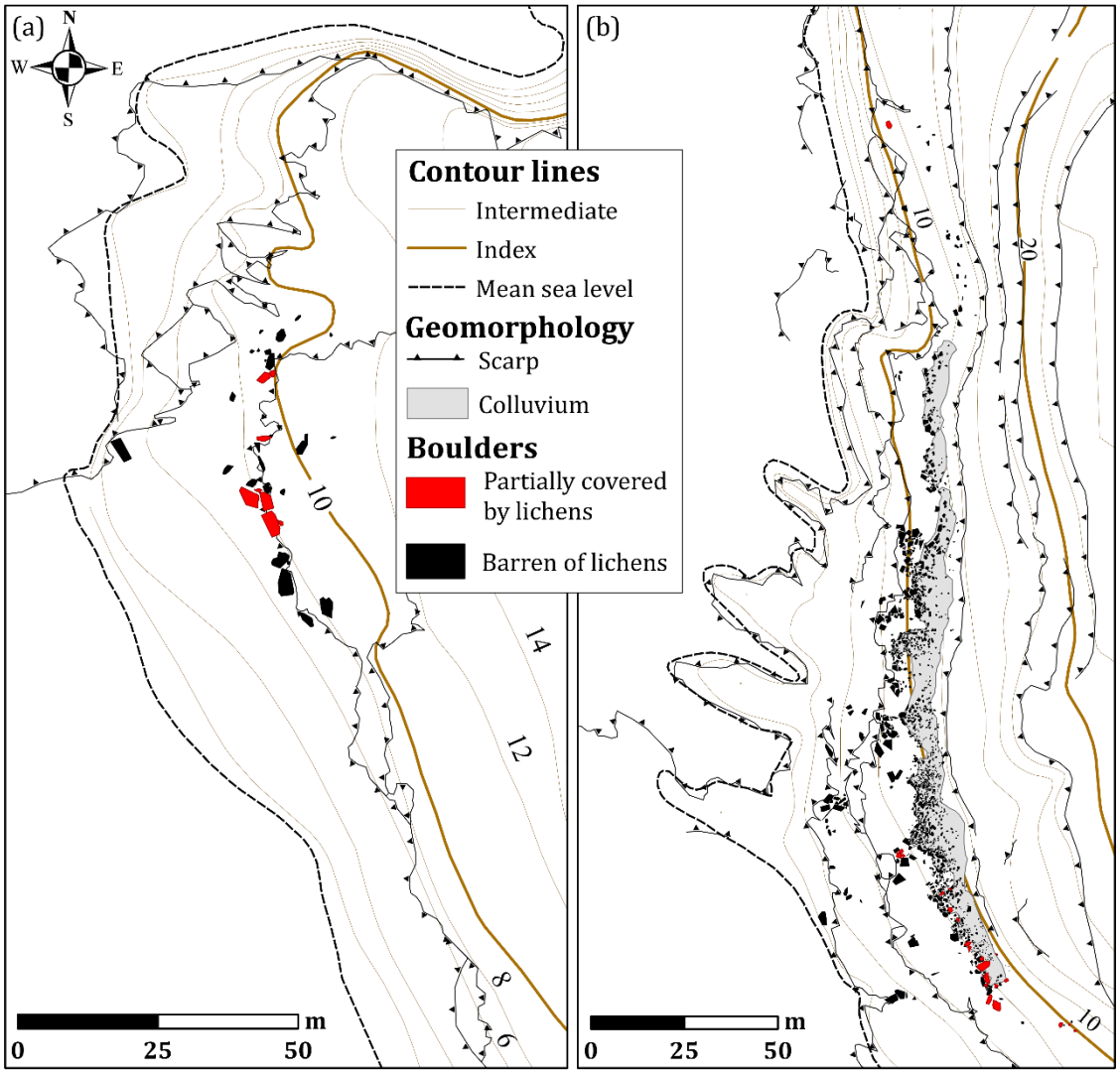

Figure 110: Location of boulders partially covered by lichens in the northern (a) and southern (b) sectors

The death of these lichens is due to temporary burial by the colluvium deposit, by atypical inrushes of salt water or by direct exposure to sunlight of the surface where they have been developing. Exposure occurs due to the movement of colonised boulders, or by removal of overlying particles, which were providing shade and humidity conditions required for lichen development. The re-growth of new lichen thalli covering the older (and now dead) lichen is attributed to the regaining of optimal conditions necessary for lichen development.

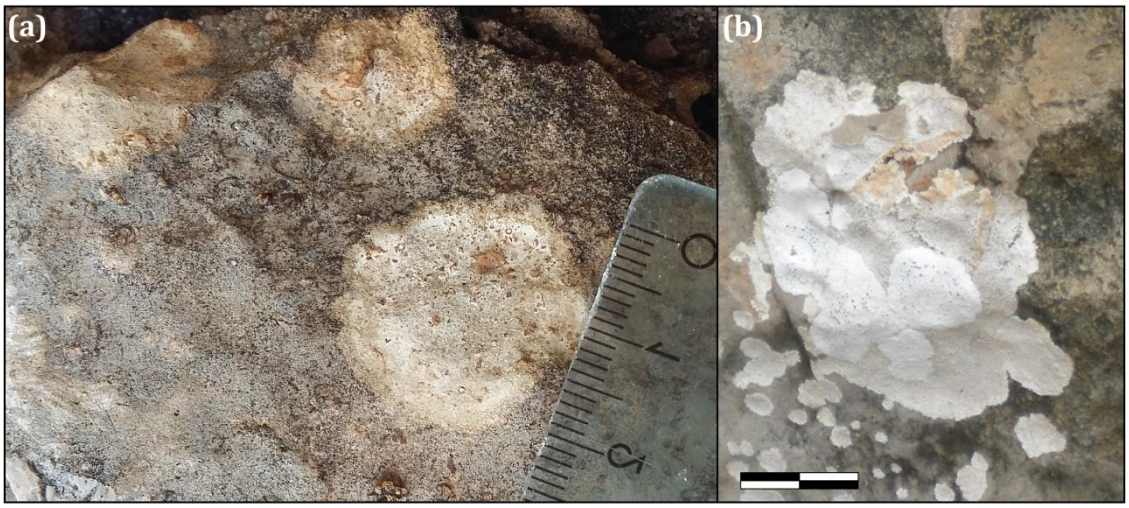

Figure 111: Photographs of dead and living lichen specimens. (a) Slightly discoloured round thalli with rough surfaces and lacking visible apothecia, interpreted as dead *Opegrapha durieui* lichens; (b) Living lichen overlapping the dead population. Scale corresponds to 2 cm

When two lichen populations with different sizes were identified containing living *Opegrapha durieui* significantly smaller and overlaying larger thalli of dead lichens, the size of the living thalli was interpreted as corresponding to time passed since the event responsible for the death of the former population. Complementary, the size of the thalli of dead lichens was interpreted as corresponding to the time elapsed between initial lichen growth and the event responsible for their death. To estimate the age associated with initial lichen growth, which corresponds to a minimum age of boulder placement, the largest 5 individuals of both populations were measured. Dead lichens were carefully selected to avoid non-circular thalli, which might result from coalescence. Due to the exponential relationship between lichen diameter and time, the attribution of lichen size parameters could not be based on the sum of lichen diameters of both populations, and were instead based on the sum of the equivalent areas occupied by both populations. The diameter of the circle corresponding to that area was then computed.

In the N sector, 11 boulders were colonised by the lichen species under analysis, 10 of which were sourced in layer L19 and one in layer L18. These boulders are located more than 25 m inland of the coastline, at 6.8-9.2 m amsl, next to the bench edge and over surface S III (Figure 110a). In only one case, living and dead lichens were found over the same boulder. Besides boulders, and exclusively in the N sector, *Opegrapha durieui* living specimens were found colonising *in situ* layers. They were found in N and N-NE facing vertical faces corresponding to joints or karst features protected from direct sunlight. To guarantee that size of lichens covering boulders in this sector was not contaminated by growth preceding boulder transport and deposition, only originally upward facing surfaces in inverted boulders were considered for lichenometry. This lead to the exclusion of 3 boulders from the 11 previously identified, 8 remaining.

In the southern sector, 24 boulders (preferably sourced in layer L28) were colonised by *Opegrapha durieui*. In this sector, 10 of the colonised boulders presented only slightly discoloured round thalli with rough surfaces and lacking visible apothecia (reproductive structures) (Figure 111a). Although unequivocal species identification was not possible, and given that *Opegrapha durieui* was the only species identified in 92% of the boulders, these cases were interpreted as representing dead lichens from the same species. In 3 cases, boulders were found showing both living and dead specimens of *Opegrapha durieui*. These were mostly located in the southernmost segment of the S sector, at 6.8-8.9 m amsl and more than 27 m inland of the coastline, away from direct exposure to sea spray (Figure 110b). One boulder in the northernmost segment of this sector, resting close to the cliff edge, at 12.4 m amsl and distanced 15 m from the mean sea level contour line, showed well developed living individuals of *Opegrapha durieui* (Figure 110b). The remaining 10 boulders colonised by living lichens were also found in the southernmost segment of the S sector.

Date of field data acquisition, average diameter of the 5 largest thalli and corresponding circular areas measured in boulders from both the N and S sectors are presented in Table XXVI.

Table XXVI: *Opegrapha durieui* size data acquired during field surveys in the N and S sectors of Coxos boulders. * data from dead lichens; ** data from the combination of dead and living populations

BOULDER	SECTOR	POPULATIONS	YEAR OF FIELD SURVEY	AVERAGE Ø (mm)	AREA *A* (mm^2)
B1532	N	Living	2016	18.2	260
B1533	N	Living overlying dead	2015	6.6	34
B1533*				19.0	284
B1533**				~20.1	318
B1536	N	Living	2015	39.2	1207
B1540	N	Living	2015	46.4	1691
B1556	N	Living	2015	31.6	784
B1542	N	Living	2015	27.0	573
B1544	N	Living	2015	25.0	491
B1543	N	Living	2016	36.4	1041
B1614	S	Living	2015	48.2	1825
B1144	S	Dead	2012	5.8	26
B1140	S	Dead	2012	14.8	172
B1143	S	Living	2012	12.6	125
B1306	S	Living	2016	25.6	515
B1333	S	Living overlying dead	2016	8	50
B1333*				18.6	272
B1333**				~20.2	322
B1280	S	Living	2016	13.0	133
B1264	S	Dead	2012	3.6	10
B1406	S	Dead	2012	8.8	61
B1451	S	Living	2012	12.2	117
B1452	S	Dead	2012	8.8	61
B1362	S	Dead	2012	19.2	290
B1473	S	Dead	2012	23.4	430
B1481	S	Living	2012	13.0	133
B1492	S	Living	2012	20.6	333
B1493	S	Dead	2012	16.8	222
B1367	S	Living	2012	16.2	206
B1496	S	Dead	2012	17.0	227
B1504	S	Living overlying dead	2012	16.2	206
B1504*				21.6	366
B1504**				~27.0	573
B1502	S	Living	2012	7.6	45
B1509	S	Living overlying dead	2012	17.2	232
B1509*				31.0	755
B1509**				~35.5	987
B1512	S	Living	2012	12.4	121
B1515	S	Dead	2012	6.2	30
B1517	S	Living	2012	18.2	260

The distribution of lichen size-parameters (Ø and *A*, represented in Figure 112a and b) differ, due to the logarithmic increase of Ø *vs* linear increase of *A*, with time. Thus, the observation of the distribution of smaller lichens is more detailed when using the Ø parameter, and of larger lichens when using *A*.

The observation of both distributions shows that: (1) maximum occurrences in lichen size of all boulders (total data) occur in the Ø=10-20 mm interval; (2) maximum occurrences in lichen size of particles in the southern sector (S sector data) occur in the Ø=10-20 mm interval and no occurrences were found in the class interval of A=1095-1460 mm^2; maximum occurrences in lichen size of boulders in the northern sector (N sector data) occur in the Ø=20-40 mm interval.

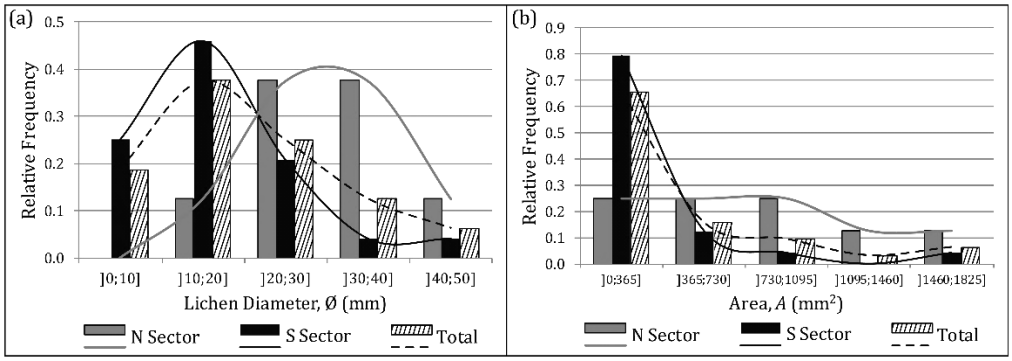

Figure 112: Histograms showing the distribution of lichen size: (a) average diameter of the 5 largest lichen thalli (Ø); (b) area of equivalent circle

Age estimation and 95% prediction intervals based on the application of the growth models to lichen data covering boulders, in the northern and southern sector, are presented in detail in Appendix N. The overall distribution of predicted ages (not considering prediction intervals) is presented in Figure 113a, and indicates that: (1) most boulders (more than 80%) were emplaced within the past 140 years (since ~1875), and more than 65% within the past 60 years (since ~1957); (2) the time window *AD* 1740-1875 (past 140 to 272 years) is not represented in boulders colonised by lichens and is overlapped by the *AD* 1755 tsunami event; (3) there is a small number of boulders (~19%) emplaced before 272 years ago and back to 450 years (~1560-1740); (4) age estimation of the remaining lichens fall in the extrapolation domain, showing indicative ages of emplacement of ~600-700 years ago (14th-15th centuries). The overlap between the gap in boulder emplacement and the *AD* 1755 tsunami could be attributed to erosion by that event and is further discussed in 7.4.5 - Summary and interpretations.

When uncertainty intervals are considered, these values slightly change but the overall tendency is maintained, the large frequency of estimated lichen age within the youngest size-class remaining evident: 66% of boulder were emplaced since *AD* 1875, 34% since *AD* 1957, and only 9% before *AD* 1740. However, ages near the

chronological limits (vertical dashed lines and vertical strip in Figure 113b) are statistically not distinguishable and the gap in boulder emplacement observed from *AD* 1740 to *AD* 1875 disappears.

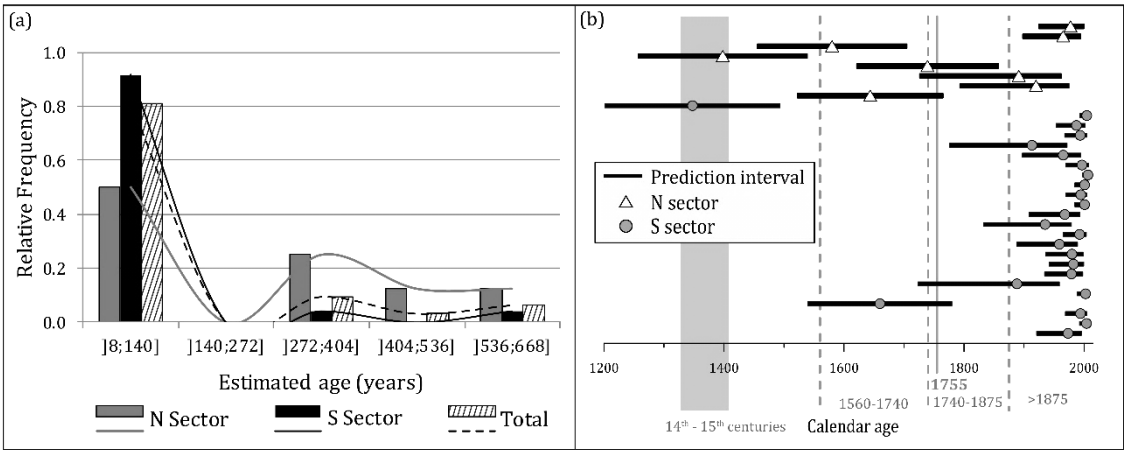

Figure 113: Estimated ages. (a) Histograms showing distribution of estimated lichen age obtained for the northern and southern sectors. (b) Estimated values of lichen age and 95% prediction intervals. Data are sorted from N to S. Gray vertical dashed lines and vertical strip correspond to limiting ages described in the text. Gray line corresponds to the *AD* 1755 tsunami

Estimated ages and 95% prediction intervals allowed to identify 5 boulders whose time of emplacement is compatible with the *AD* 1755 tsunami: 3 are in the N sector (Figure 114a) and 2 in the S sector (Figure 114b, c, d and e).

The 3 boulders in the northern sector (B1542, B1543 and B1556) sit within a conspicuous boulder cluster at 6.9-8.9 m amsl and comprise particles with varying mass, ranging from 0.6 ton to 20.5 ton. Moreover, this accumulation also comprises boulders B1544 and B1540, with estimated ages of 1793-1974 and 1257-1538, respectively (Figure 114a and Figure 115a, b and c). The varying mass, position and age indicates that their deposition was asynchronous.

The date of *AD* 1755 intersects age uncertainty intervals of 2 boulders in the southern sector. These boulders sit at 7-8 m amsl and range in mass from 1 to 5 ton (Figure 114b, Figure 115b and c). Only one particle, sitting on the cliff-top at ~12.4 m amsl in the northernmost segment, has rendered an age of emplacement older than this date (Figure 114c). The remaining boulders are in the southernmost segment. They comprise both NE-SW and NW-SE aligned ridges and have been emplaced in the past ~200 years.

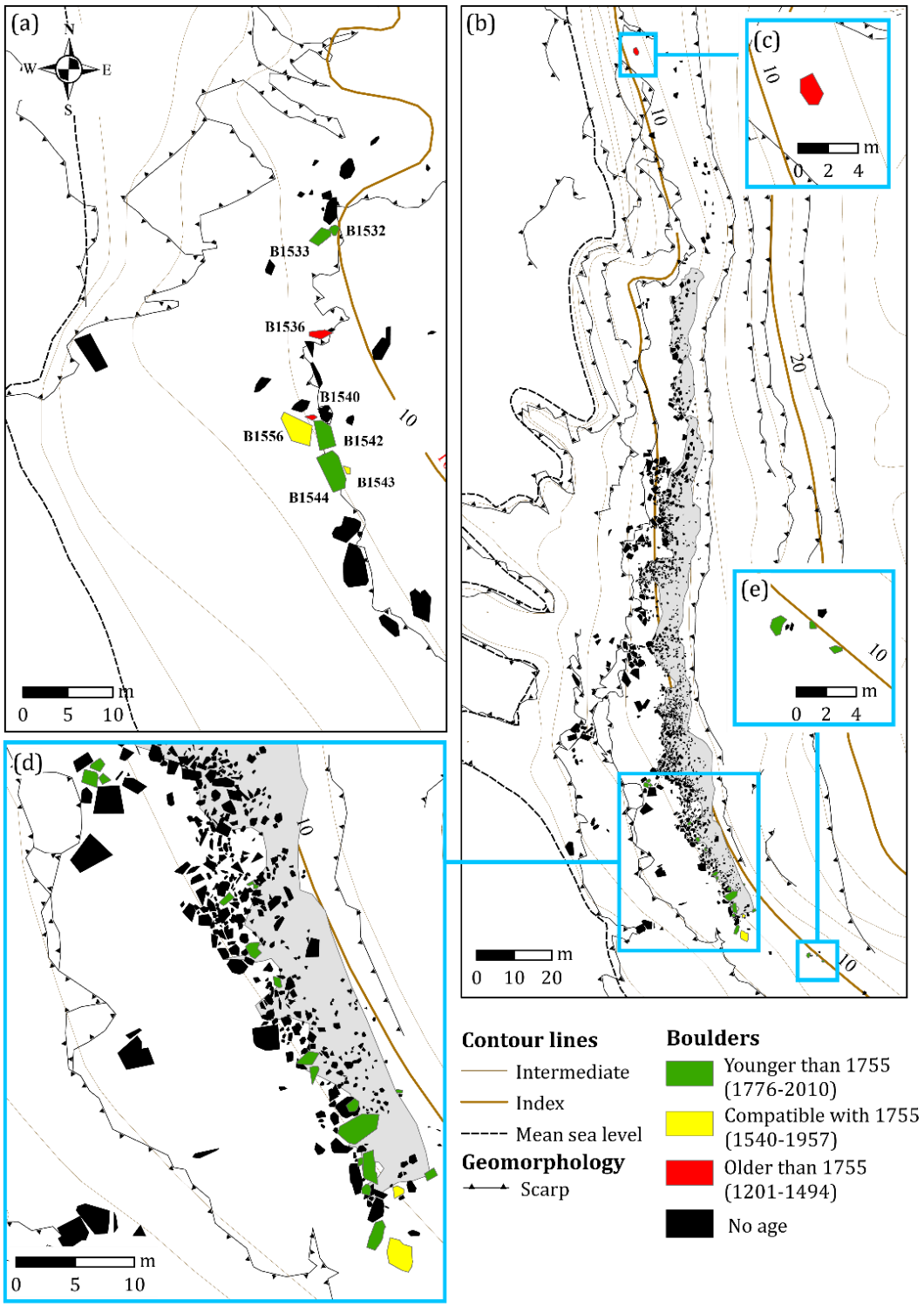

Figure 114: Map of boulders classified according to age in: (a) the N sector; and (b, c d and e) S sector

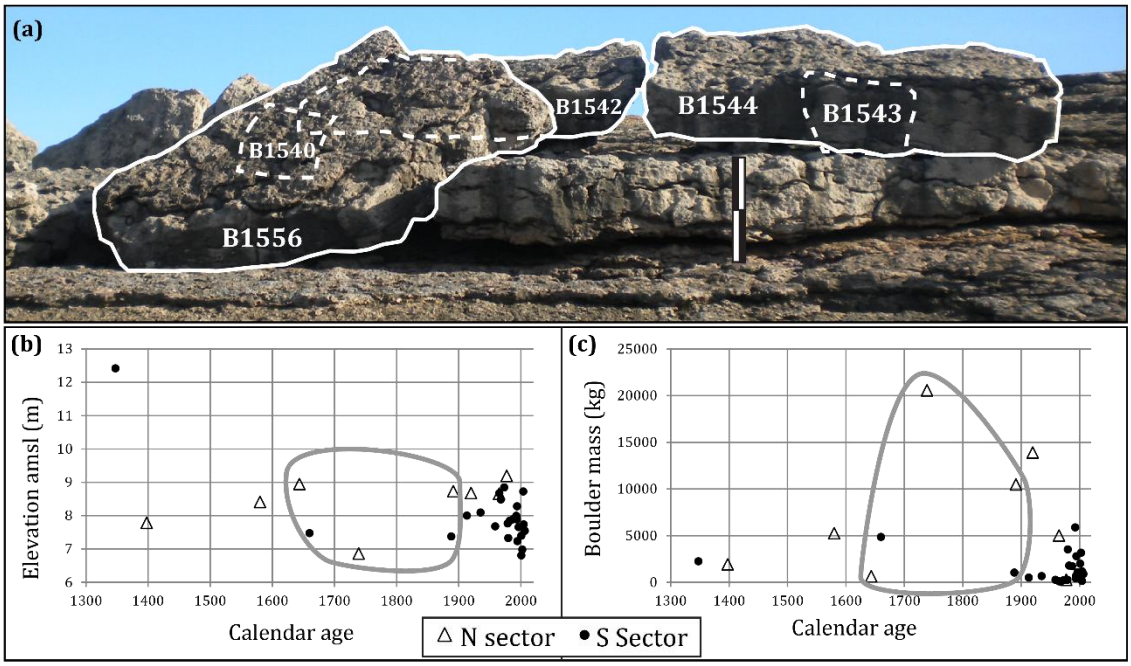

Figure 115: (a) Photograph looking ENE showing the boulder cluster of the northern sector mentioned in text; vertical scale corresponds to ~1 m. (b) Scatter plots showing lichen ages from the N and S sectors against boulder elevation and (c) boulder mass. Boulders containing lichens with ages statistically compatible with the *AD* 1755 tsunami event are outlined in grey

Figure 116 represents the distribution of calendar ages of living and dead lichen specimens in the study area, considering the time window extending from 1957 onwards. One immediate observation revealed by these distributions is the similarity between their shapes. They are both multimodal, the frequency (represented by counts in Figure 116) showing a general decrease with increasing age. Furthermore, the distribution of peaks is shifted of 1 to 2 time-class intervals (corresponding to 10-20 years), the living population being older than the dead. The similarity between these populations suggests that lichen development occurred at the same time and that the 10-20 years of time deviation between peaks corresponds to the average time passed between their death and field measurements.

Peaks in the distribution represent periods of maximum number of available exposed surfaces ready to be colonised by lichens, and roughly occurring during *AD* 1887-1897, *AD* 1957-1967 and *AD* 1987-1997. These periods are separated by phases of minimum to absent lichen colonisation, occurring during *AD* 1897-1907, *AD* 1927-1947, *AD* 1967-1977 and *AD* 1997-2007.

The determination of periods associated with lichen death was undertaken by estimating the age of the overlapping living lichen populations, which resulted from re-growth. Two ages were obtained for events generating the death of lichens in 4 boulders, containing both living and dead lichen populations (represented by asterisks in Figure 116): *AD* 1978-1982 in the S sector; and *AD* 2006-2007 in both sectors. These ages are roughly coincident with periods of minimum lichen colonisation.

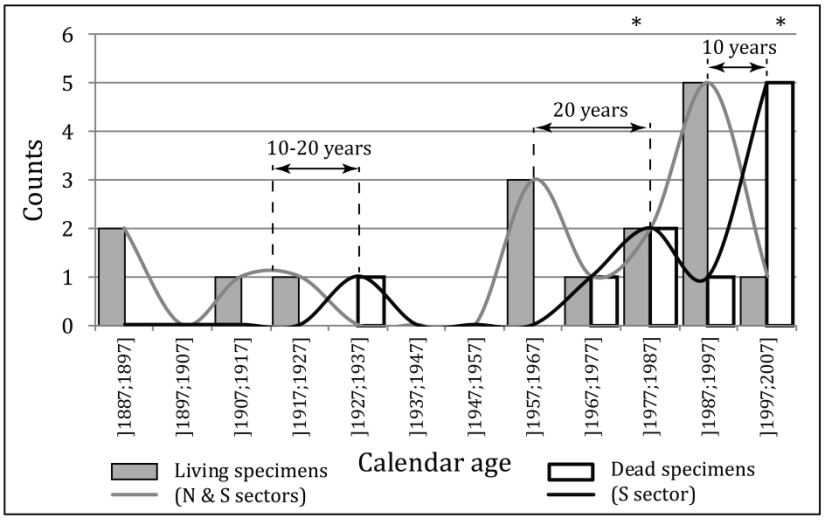

Figure 116: Histogram showing distribution of calendar ages obtained for living and dead lichens in the study area. * events which generated lichen death, followed by re-growth

As observed during field work, and stated before, lichen death has been associated with atypical inrushes of salt water and with boulder movement (however slight) due to storms, and could be associated with an increase in storm frequency/magnitude. This possibility is further supported by the overlapping between phases of minimum lichen colonisation and dated events which generated lichen death.

Summarizing, boulders with lichens were mostly found in WSW-facing coastal segments. Oldest ages of boulder emplacement were of *AD* 1348 [1201–1494] in the southern sector and of *AD* 1398 [1257–1538] in the northern sector, the oldest boulders in the data-set having been preferably found in the latter. Age of emplacement does not correlate with boulder height nor mass. When uncertainty is considered, over ⅔ of the boulders were emplaced after 1875 and over ⅓ after 1957. Minimum to absent lichen colonisation occurred during the 15th until the middle of the 16th centuries, from the mid-18th until the mid-19th centuries, and

more recently in *AD* 1897-1907, *AD* 1927-1947, *AD* 1967-1977 and *AD* 1997-2007. Finally, a considerable number of lichens have died in the past 10-20 years, indicating a recent increase in storm activity.

7.4.3 Downwearing rates

The emplacement of the limestone boulder B1509 over the exposed surface of a Cretaceous siltstone layer (L29), outcropping at the southern tip of the southern sector, generated localized shelter regarding the downwearing of the siltstone beneath the cap-rock. This resulted in the development of a vertical ledge approximately 13 cm-long. Erosion rates of the siltstone surface were inferred based on repetitive measurements of surface downwearing in three distinct locations (Figure 117a) using a micro-erosion meter (MEM), and are presented in Appendix O, and represented in Figure 118a, b and c.

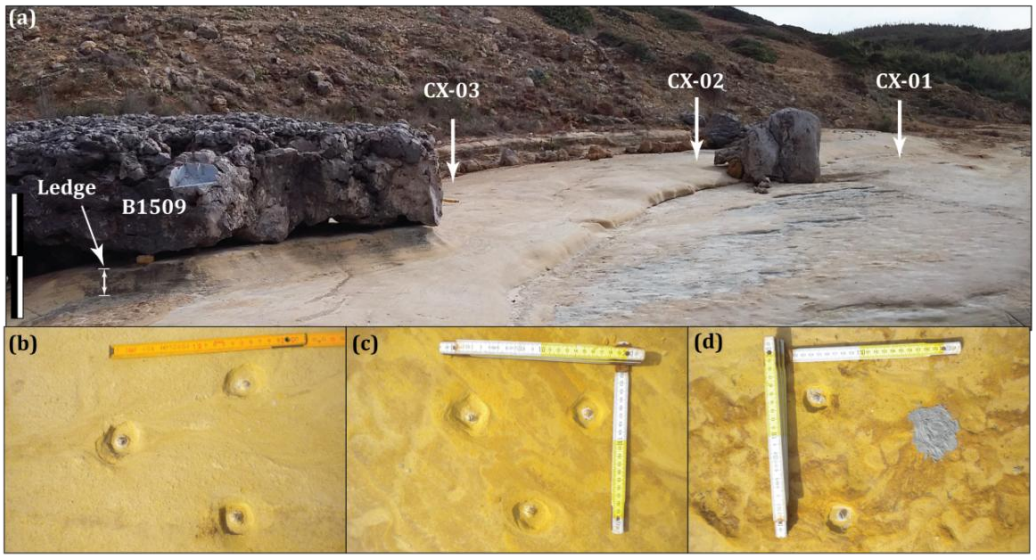

Figure 117: (a) Location of the ledge beneath boulder B1509 and of the MEM stations over the siltstone layer (L29) in the southern sector (vertical scale corresponds to ~0.5 m). (b) Photograph of MEM stations CX-03; (c) CX-02; and (d) CX-01. Scales correspond to 0.2 m

The MEM station CX-01, located further away from the ledge, was installed in a lower stratigraphic position (Figure 117a and d). MEM stations CX-02 and CX-03 were installed closer to and at the same stratigraphic position of the ledge. Station CX-O1 produced three valid readings (Figure 118a), and yielded erosion rates ranging from 0.037 mm·year^{-1} (0.0002 mm·day^{-1}) to 0.292 mm·year^{-1} (0.0008 mm·day^{-1}), averaging 0.134 mm·year^{-1} (0.0004 mm·day^{-1}). Station CX-02 provided only one valid data-set, and shows a consistent increase in the distance

between the MEM and the siltstone, and a higher erosion rate of 0.329 mm·year^{-1} (0.0009 mm·day^{-1}) (Figure 118b). Erosion rates reach maximum values in station CX-03, closest to the ledge (Figure 117), ranging from 0.510 mm·year^{-1} (0.0014 mm·day^{-1}) to 0.657 mm·year^{-1} (0.0018 mm·day^{-1}), and averaging 0.584 mm·year^{-1} (0.0016 mm·day^{-1}) (Figure 118c).

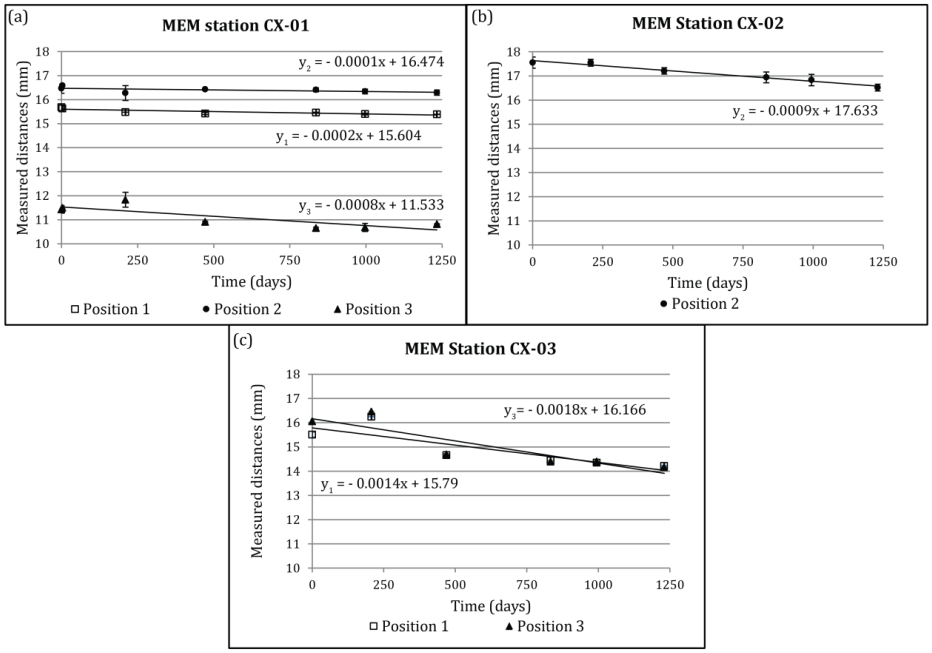

Figure 118: Average distances (and error bars) between the MEM and the siltstone measured in several positions during more than 3 years in: (a) CX-01 station; (b) CX-02 station; and (c) CX-03 station

In all stations, distances from the MEM to the siltstone exposed surface generally increased with time, at different rates. However, an unexpected decrease in distances between the MEM and the siltstone, in all stations, was observed in the second survey, approximately 200 days after the initial (reference) measurement. This decrease is spurious for this study and is related to swelling of the topmost sub-millimetric siltstone laminae following intense rainfall. The micro-mounds so formed became separated from the underlying laminae by air-pockets. This generated an ephemeral swelling of the surface of the siltstone, before complete disruption, detachment and erosion of siltstone flakes by running water (Figure 119).

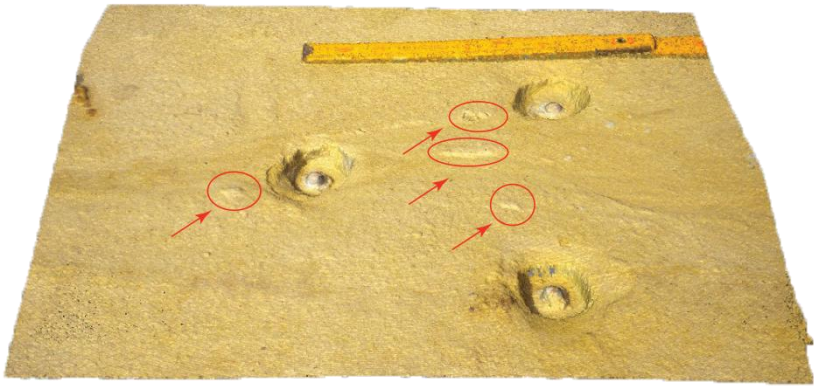

Figure 119: Perspective view of MEM station CX-03, based on photographs taken in the second survey. Examples of micro-mounds related with swelling of the top-most siltstone laminae are outlined in red. Scale corresponds to app. 20 cm. Dense cloud obtained with Agisoft PhotoScan Professional© Version 1.2.6

MEM-inferred age results for boulder emplacement, considering that the 13 cm-high siltstone ledge equals in length the thickness of siltstone removed by surface downwearing since boulder B1509 was emplaced, are presented in Table XXVII.

Table XXVII: Average erosion rates computed for MEM stations and time required in each location to erode 130 mm of the siltstone

LOCATION	EROSION RATE ($mm \cdot year^{-1}$)	TIME REQUIRED TO ERODE 130 mm (year)
CX-01	0.134	971
CX-02	0.329	396
CX-03	0.584	223

The data shows that erosion rates in layer L29 are variable, due to the layer's changes in resistance to erosion. This layer is characterized by very low-angle cross-lamination which produces a complex and varying geometry. Furthermore, it contains iron concretions and fossilized roots (further details in 5.2 Lithostratigraphy), scattered across the layer's exposed surfaces. Lower erosion rates occur in MEM CX-01, in relation with higher iron concentrations (Figure 117d) that armour patches of the surface exposed to weathering and erosion. MEM stations CX-02 and CX-03, installed at the stratigraphic level where the boulder is sitting and the ledge is developing, show higher erosion rates. Erosion rates of MEM stations CX-02 and CX-01 were used and averaged to date emplacement of boulder B1509, yielding 310 years (223-396 years), corresponding to a calendar age of *AD* 1702 (*AD* 1616-1789).

7.4.4 *Optically stimulated luminescence*

Age estimation of two marine sand samples found beneath the boulders and within the colluvium deposit in the southern sector provides a minimum age for their deposition. Results from the OSL age estimation of this sand are presented in Table XXVIII and detailed in Appendix P (Optically stimulated luminescence results). Calculation of De values was carried out using the Minimum Age Model (Galbraith *et al.*, 1999) because the De distribution (asymmetric distribution; decision table of Bailey and Arnold, 2006), indicated that this model was more appropriate than the Central Age Model (Galbraith *et al.*, 1999).

Table XXVIII: Luminescence dating results when applying the Minimum Age Model (Galbraith *et al.*, 1999) (OSL ages in years before 2014). Error on De is 1 standard error. Error on age includes random and systematic errors calculated in quadrature

Sample	Lab ID	Burial depth (m)	Cosmic (Gy)	Dose Rate (Gy/ka)	De (Gy)	No of Aliquots	Age (ka)	Cal. Age (*AD*)
Q20 CxS	UNL4003	0.35	0.20	2.66±0.10	0.60±0.06[b]	75	0.23±0.02[b]	1784
Q21 CxS	UNL4004	0.35	0.20	2.63±0.10	0.77±0.13[b]	72	0.29±0.05[b]	1724

Sand grains rendered OSL age estimations of 230±20 and 290±50 years before 2014, corresponding to calendar ages of 1784 and 1724, respectively.

7.4.5 *Summary and interpretations*

Results regarding the age of boulders' emplacement as well as interpretations concerning their origin are summarized and presented in the same order as the results.

Results obtained from the comparison of aerial photographs taken in 1948 and 2010 illustrate distinct behaviours in different segments of the study area, and are summarized below:

1. The N sector shows little movement of larger boulders in this time window and, except for one boulder, their accumulation predates 1948. Smaller boulders could not be differentiated in photographs due to limited image resolution;

2. The northernmost segment of the S sector shows boulder movement occurring from 1948 to 2010 due to human activities. Boulders were moved and placed bordering the cliff edge to prevent cars from reaching it;
3. The central segment of the S sector shows significant movement of individual boulders and changes in the development of the colluvium deposit. Clusters, and especially ridges, remained in the same locations and show similar shape and extent, although individual boulders may have been replaced;
4. The southernmost segment of the S sector has been mostly stable over the past 60 years and apart from the movement of a few isolated boulders, the bulk of this deposit predates 1948.

The dynamics of large particles in the study area changes considerably depending on the coastal segment considered. Segments facing W-SW show lower frequency in boulder movement by extreme storms, whereas segments facing W and W-NW show higher frequency in boulder movement. Although the northernmost segment of the S sector is directly exposed to the W, it is limited by vertical ~13m-high cliffs, that are reached mainly by the vertical swash of storm waves, which have limited boulder transport capability.

These interpretations are supported by both the observation of boulder movement associated with present-day storms and by the presence of lichens covering boulders in the less dynamic segments. Boulders colonised by well-developed lichens were found in the N sector and in the northernmost and southernmost segments of the S sector. Boulders deposited in more dynamic segments do not offer the conditions necessary for lichen colonisation and development, either due to higher concentrations of salt, associated with more frequent and stronger marine inrushes, or due to higher frequency in boulder movement and consequent absence of the stability during the time necessary for lichens to develop. These observations also suggest that lichen development indicates reduction or absence of boulder movement due to a persistence of optimal development conditions associated with low storminess periods, and that lichen ages correspond to minimum age of emplacement of boulders.

Age estimation results based on lichenometry show that:

1. Most lichens are younger than *AD* 1875 (66%) and over 34% of boulders colonised by lichens were emplaced from 1957 onwards;
2. Maximum lichen development occurred between *AD* 1987 and *AD* 1997;
3. Two episodes of lichen death and regrowth were detected in both sectors using data from living specimens overlapping dead populations and dated to *AD* 1978-1982 and *AD* 2006-2007;
4. Lichenometry was unable to find boulder emplacement from *AD* 1740 to *AD* 1875, if ages considered estimated values rather than the predicted intervals;
5. Older lichens ranging from *AD* 1875 back to the 14th century comprise ~19% of dated boulders.

The shift of approximately 10-20 years observed in the frequency distribution curves of living and dead specimens indicates that the event(s) generating lichen death occurred recently, from approximately 1997 onwards. This is mostly attributed to an increase in storminess which generated boulder movement, exposing the lichens to direct sunlight, and to possible physical and chemical changes related with burial by the colluvium and frequent inundations. Stability of the area occupied by the colluvium in the segments containing boulders colonised by lichens and the inexistence of tsunamis since 1997, suggests that lichen death resulted from storm activity. This interpretation is further supported by field observations undertaken during the past 4 years, that marked as dead the same lichen colonies found alive four years before. This specially occurred in boulders showing evidence of movement that induced exposure to sunlight of surfaces covered by lichens. The distribution and age estimation of both living and dead lichens indicates an increase in boulder movement since ~1997, related to an increase in storminess. This increase followed a period of lower storm frequency or intensity, and of larger stability of boulders in this coastal area from 1957 onwards, with maximum lichen development (thus, minimum storm activity) occurring between 1987 and 1997.

It was previously shown (chapter 2.1 Tsunamis) that the only tsunami event affecting the western Portuguese coastline in the past 5000 years and capable of generating boulder transport was the *AD* 1755 tsunami. And yet, the time between

the *AD* 1740 and *AD* 1875 is scarcely represented in lichenometry data. This apparent paradox may be solved as follows:

1. The extreme *AD* 1755 tsunami event, generated an atypical and significant inrush of water and sediment, drowning the boulder surfaces addressed in this study, and generating the death of most lichens;
2. The same inundation generated significant erosion and was eventually responsible for the removal of lichen-bearing boulders, with few exceptions, and eventually for the emplacement of others;
3. The dynamic character of the W-facing segments in the study area does not allow for boulder immovability for extended periods, which rarely exceeds 100-200 years (maximum residence period). Eventually, a storm capable of generating boulder movement occurs and lichens growing on their surfaces die. Boulders deposited prior to *AD* 1875 are currently located in places protected from both the development of the colluvium and/or the reach of storm waves.

Conceptually, the few boulders with lichens broadly contemporaneous to the *AD* 1755 tsunami emplaced in the N and S sectors, could have been deposited by storms, by tsunamis, or both. Results obtained with the application of numerical solutions of boulder transport together with observed boulder movement suggests that events with higher magnitude than those occurring nowadays were responsible for boulder transport in the N sector. Moreover, the WSW-facing segment in which they sit is prone to a tsunami inundation from S, such as the *AD* 1755 event. However, boulders in the N sector with ages compatible with this event occur together with other (both older and younger) boulders, showing that the emplacement of the complete set was not synchronous. In addition, and however possible, it is unlikely that a single tsunami stroke was capable to generate the transport and deposition of 10-20 ton boulders, but unable to remove an older and smaller (2 ton) particle. Altogether, the above strongly suggests a storm origin for this cluster.

The patches of marine sand located beneath and above boulders with estimated ages of 230±20 and 290±50 years strongly indicate that the *AD* 1755 tsunami reached and affected the study area. In the S sector, there are only three boulders containing

lichens with estimated ages older than or roughly contemporaneous of *AD* 1755. One sits in the northernmost segment of this sector, at 13 m amsl, and predates *AD* 1494. Both the age and location, together with the absence of visible dead lichens, strongly suggests that the *AD* 1755 inundation was unable to reach this location. This reasoning allows to place an upper limit of 13 m amsl for the inundation height of that tsunami in this location. The other two boulders are surrounded by younger boulders and sit at 7-8 m amsl, an elevation range that could have been reached by the *AD* 1755 tsunami and the hypothesis that these particles were placed by that event cannot be discarded.

Although a tsunami origin for some boulders preserved in both the N and S sector cannot be discarded, the most probable scenario is that the marine events responsible for detachment, entrainment and emplacement of most boulders in both sectors are storm related. It is more likely that the *AD* 1755 tsunami generated significant boulder removal up to a height contained within the 9-13 m amsl range. This implies that boulders deposited prior to the *AD* 1755 tsunami event correspond to remnants of pre-existing and diachronic storm-related deposits just like it must have happened from the mid-18th century onwards.

Low occurrences of boulders older than 1875 in the S sector is most probably related with the highly dynamic character of the W-facing segment of this coastal stretch in relation with storms. Here, storms waves induce frequent boulder movement in the seaward part of the structural platforms, this erosive effect having been further enhanced by the *AD* 1755 tsunami inundation. In contrast, the N sector and the southernmost segment of the S sector, where oldest boulders were found, are less dynamic and show limited boulder movement. This interpretation is supported by observations of aerial photographs from 1948 to 2010, by the time-scattering ages of boulder emplacement, especially in the N sector, and by observation of boulder movement by present-day storms.

Despite the indication of a storm origin by the overall results, the possibility that the Coxos boulder accumulation has a polygenic origin cannot be rejected at the present state of knowledge.

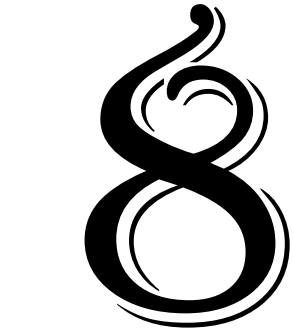

Discussion

In this chapter interpretations previously presented are discussed and compared with work forwarded by other authors. Foremost, a discussion of the morphology of the boulder accumulations is presented, focusing on storm *vs* tsunami signatures. Interpretations regarding flow direction inferred from boulders' location, characteristics and movement by storms, follows. The integration of boulder properties, observation of boulder transport by present-day storms and numerical modelling resulted in a conceptual model, explaining boulder detachment, emplacement and transport over the structural platforms in the study area. Afterwards, a brief discussion about the sediment source of the marine sand found beneath the boulders is made. Also, results obtained from the application of numerical solutions of transport, are addressed. Finally, the age of emplacement is constrained and the most probable processes involved in the generation of the accumulations are identified based on the overall integration of proxies.

8.1 Morphology of the accumulations, boulder properties and storm *vs* tsunami origin

The boulder deposit of Coxos contains isolated boulders, boulder clusters (sometimes aligned or showing imbrication) and boulder ridges, sometimes

gradually changing into each other. For instance, boulder ridges turn into boulder alignments in a longshore direction, whereas, in a cross-shore direction, ridges turn into clusters, which further seaward turn into isolated boulders, closer to bench edges and cliff-tops. The six boulder ridges identified in the southern sector develop in N-S, NE-SW and NW-SE directions, sometimes oblique to, and sometimes mimicking, the coastline trend.

A similar interchangeable character of the morphology of boulder accumulations within rocky coastline contexts was observed by Etienne and Paris (2010) in storm deposits of Iceland, and interpreted in the case addressed here as indicating a storm-related origin. The multidirectional flow generated by varying magnitudes of storm waves associated with the regional wave regime affecting the coastline, results in diverse morphologies of related boulder accumulations. According to Morton *et al.* (2008), ridges and ridge complexes represent the accumulation of several depositional events, and result from long-term reworking and addition of material on their seaward side, by storm waves.

Boulder ridges in the study area present different alignments, depending on their location. WSW-facing coastal segments (N sector and southernmost segment of the S sector) comprise boulder alignments and incipient boulder ridges paralleling the coastline (NNW-SSE). In contrast, boulder ridges located in the central segment of the S sector develop with a N-S elongation, also paralleling the coastline and with a NE-SW elongation inland of, and orthogonally to, the indentations of the lower structural platforms. Most boulder ridges studied by several authors have been found preferably developing in a shore-parallel direction (*cf.* Hall *et al.*, 2006; Morton *et al.*, 2006; 2008; Suanez *et al.*, 2009; Richmond *et al.*, 2011b; Fichaut and Suanez, 2011), indicating, in most cases, an orthogonal relationship between flow direction and ridge alignment.

The complex morphologies of boulder accumulations especially observed in the S sector, together with the preferable NW-W flow direction interpreted from the alignment of boulder ridges (which is compatible with the prevailing wave regime), suggests a storm origin for this deposit. However, interpretations based on the properties of individual boulders suggest that geomorphological controls may play a

non-negligible role in the development of boulder accumulations, as further discussed below.

The systematic analysis of general attributes (such as relative locations of source layer/area and of displaced elements) and of scalar properties (such as mass) of particles may be used to infer directional derivatives or gradients of those attributes which, when mapped, have paleocurrent significance (Potter and Pettijohn, 1977).

Source layers and shortest transport paths identified in Coxos boulders indicate both frequent cross-shore and inland-directed and alongshore, southwards-directed, movement. However, the spatial distribution of scalar properties of boulders, such as mass, reveals a fining inland and northwards pattern in both sectors.

Although transport paths inferred from source-sink criteria indicate flow directions from N and W, inland and northwards fining trends observed in both sectors, reveal a mass gradient which, without further context or validation, could indicate flow direction from the SW. Moreover, boulders in the N sector are larger than those located in the S sector, which opposes mass trends locally observed in each sector. Ultimately, contrasting boulder sizes between sectors is explained by higher joint spacing affecting the thicker layers outcropping closer to the mean sea level and directly exposed to wave swash. The inland and northward fining trends detected within sectors is interpreted as mostly related to the general geomorphology of the structural platforms of the study area. In fact, in both locations, the SW dip of Cretaceous strata generates a topographic surface which increases in height northward and inland. Therefore, the fining trends are considered a result of an increase in both elevation and distance from mean sea level, and thus, reduction of transport capability of wave swash or wave bores in the same directions. In conclusion, interpretations of flow direction based in boulder mass criteria should be cautiously made and do not apply in this case.

In what concerns vectorial properties, flow direction may imprint individual boulders in agreement with guiding principles for the orientation of particles following transport in aqueous media, summarized in Potter and Pettijohn (1977). The ab surface preferably faces flow provenance and their long axis tend to be sub-horizontal and perpendicular to flow direction when they come to rest.

Biunivocal relations between particle orientation and flow direction have been observed worldwide, and in diverse morphologies, originated by both tsunami and storm events. Such particles show long axis aligned orthogonally to flow direction, with their ab surfaces facing it (*e.g.* Mastronuzzi and Sansò, 2000; 2004; Hall *et al*., 2006; Mastronuzzi *et al*., 2007; Goto *et al*., 2007; Scicchitano *et al*., 2007; Barbano *et al.,* 2010; Williams, 2010; Cox *et al.*, 2012; Pérez-Alberti *et al*., 2012; Richmond *et al*., 2011a).

Following these principles, the statistical analysis of directional properties of boulders in both the N and S sectors indicates transport by flows travelling from the NW-WNW and the SW. In the S sector, there is an additional and well defined directional mode reflecting dominant flow from the WSW. The spatial distribution of vectorial properties of Coxos boulder accumulations shows that they organize in directional clusters, either mimicking the coastline trend or facing pronounced indentations in the lower structural platforms. Significant variation in boulder properties (source layer, mass and direction), between and within the sectors, suggests a strong geomorphological control in flow direction over the structural platform, and hence, in boulder characteristics.

The issue of geomorphological inheritance has been addressed by several authors who detected spatial trends in storm-generated boulder characteristics and distribution due to local changes in topography. Hall (2011) associated variations in boulder size to changes in topography. Jones and Hunter (1992) and Suanez *et al*. (2009) noticed preferable boulder deposition inland of indentations affecting the coastline. The influence of geomorphological features in flow characteristics has also been described in tsunami deposits. Goto *et al.* (2007) detected changes in the orientation of the a-axis of boulders due to local undulations in the bathymetry, disturbing an overall trend compatible with flow direction. Goff *et al*. (2006b) reported focusing of waves and increased reach of inundation and run-up during the 2004 IOT in Sri Lanka, associated with small scale coastal embayments and blockage of tsunami inundation associated with headlands. Accordingly, numerical modelling of extreme marine events simulate localized piling up of water due to wave refraction and funnelling effects related to irregular morphologies developing at different spatial scales, such as submarine canyons and alternating coastal

embayments and headlands (*e.g.* Matsuyama *et al.*, 1999; Iglesias *et al.*, 2014; Canelas *et al.*, 2014).

The answer to que question "do boulder characteristics represent wave direction and magnitude or the geomorphology of the coastal sector where accumulations develop?" is not simple. In a significant number of cases, both controls leave their signature on the same deposit and the extent to which each control prevails may vary in space (during the same event) and time (according to differences in oceanographic forcing).

The presence of several directional signatures found in boulder clusters sitting inland of pronounced indentations of the rocky platforms in Coxos boulder accumulations, and in boulders transported by present-day storms mostly travelling from W-NW, are indicative of local effects prevailing over nearshore wave parameters. However, the tidal level and the wave period did influence the amount of energy arriving at the structural platforms and preferential direction of boulder transport. Higher tides generated an increase in sea surface height and a relative increase of cross-shore boulder transport by swash, to the detriment of longshore boulder transport by backwash. Furthermore, in the study area, and for waves travelling from 220°-350° (over 90% of occurrences), the ratio between nearshore and offshore wave height is highly dependent of wave period, with long-period waves ($T_m > 15\ s$) experiencing minimum energy dissipation (*cf.* wave height transformation matrix represented in Figure 47, section 5.4 Oceanographic climate).

There is, however, an undeniable difference in boulder transport and boulder properties in different segments of the coastline, which is a result of the control by natural structures, which can either facilitate (ramps and indentations in the lower structural surfaces) or counter (cliffs) marine inundations. WSW-facing segments have shown little boulder movement by present-day storms, but preferably contain larger boulders with directional attributes indicating a flow from the SW. W- to NW-facing coasts have shown frequent boulder movement, and generally contain smaller boulders indicating flow from various directions.

Ultimately, the answer to the aforementioned question is "yes to both parts". Storm waves in the nearshore present a narrow directional spread around the western

octant, preferably traveling from WNW, and this is reflected by the dominant directional mode of ab surface dip direction and a-axis trend of individual boulders, in both sectors.

Various stages of boulder detachment, emplacement and transport have been detected following present-day storms, and observations agree with some of the earlier interpretations exclusively based on boulder attributes.

Particles are added to the structural platforms and pre-existing boulder accumulation by detachment of loosened and joint-bounded pieces of the top-most layer at the bench edge (stage 1 in Figure 120). This process is (much) facilitated in places where the (cracked or fractured) source-layer protrudes from the underlying scarp or there is excavation of the softer materials beneath the source layer. This differential boulder transport capability associated with overhanging boulder geometry has been demonstrated in numerical simulations presented by Canelas *et al.* (2014) and described in boulder transport by storms in the Shetlands by Hall *et al.* (2008). Once detached, boulders generally suffer short landward cross-shore transport, rotation and end up next to their original position, sometimes up-side down. This short-lived transport has been interpreted from the statistical and spatial analysis of source layers of boulders comprising the bulk of the deposit.

When these particles are large enough, they either remain as isolated boulders near the bench edge, or are broken into several smaller boulders. Breakage happens at the moment of landing or later, by subsequent wave reworking or impact by other particles. When reaching a moveable size, they are transported by sliding or rolling over and along the structural platforms, where they can be pushed against obstacles (larger boulders, boulder ridges or colluvium). Here, they remain for extended periods of time (stage 2 in Figure 120), or may be transported alongshore (following the general pending). Eventually, they are finally removed by backwash and washed back into the sea (stage 3 in Figure 120). When particles remain docked against obstacles, they end up incorporating boulder clusters or ridges and, when pushed against the landward edge of the structural platforms, they can be partially covered by the colluvium. Additionally, smaller particles detached from the bench edge, can

suffer cross-shore transport by wave swash and be directly placed in boulder clusters and ridges, thus contributing to their development in both height and width.

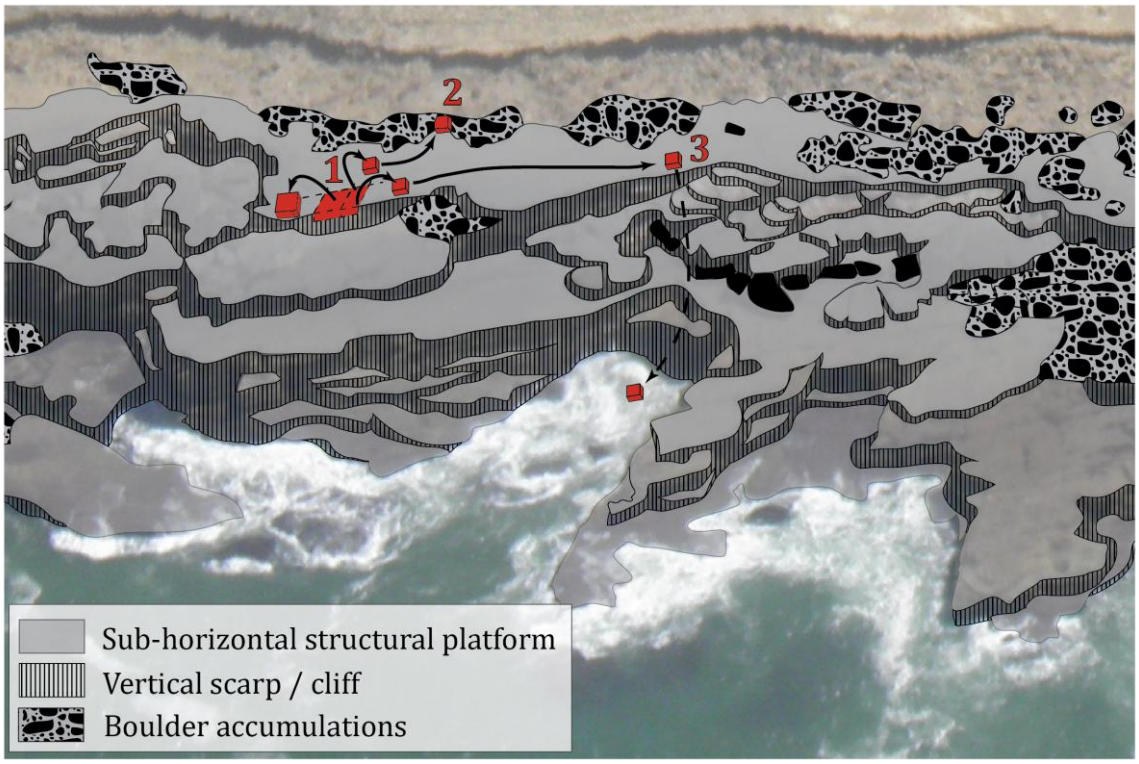

Figure 120: Conceptual model, explaining boulder detachment, emplacement and transport over the structural platforms. Stages 1, 2 and 3 are explained in text

The incorporation of particles in boulder ridges occurs by both cross-shore and alongshore transport, and this is reflected in the directional attributes of imbricated boulder clusters. Boulders suffering longshore transport by backwash will generate N-facing imbricated boulder clusters. In contrast, boulders suffering cross-shore to oblique boulder transport by wave swash, will produce NW-facing boulder clusters. Boulders transported up-ridge and over the ridge crest, end up on its land-facing slope and inherit their pending, thus generating landward-facing imbricated clusters.

These observations are congruent with descriptions of the dynamics of storm-related cliff-top boulder accumulations in Ireland by Williams (2010) and Cox *et al.* (2012). These authors have observed that boulders sitting in the seaward and landward faces of boulder ridges show distinct tilt and mention pronounced imbrication in boulders sitting in the seaward margin of these accumulations, coinciding with the dominant direction of wind waves. Moreover, the temporary

stay of loose material standing between the boulder ridges and the ocean has been observed by Cox *et al*. (2012), which stated that this material was either incorporated into the ridges or, eventually, removed back to the sea.

Several evidences indicate storm origin for most of the boulders in the accumulation under analysis: (1) similarity with properties of the particles transported during the January and February 2014 storms; (2) similarity with descriptions of storm-related boulder deposits by various authors; (3) short-lived transport indicative of short-lived events, with limited inland inundations.

8.2 Sediment source of the sand underneath the boulders

The comparison of textural and morphoscopic characteristics of beach, storm, colluvium, and marine terrace deposits with the sand patch identified beneath boulders following removal of boulders and colluvium by major storms, show a larger similarity of that sand with the marine terrace deposit. Given textural and morphological characteristics, the sediment source of both deposits is interpreted as marine and from the same general submarine source area, most probably the nearshore. This interpretation agrees with data of Balsinha (2008), that studied the inner shelf sediment until approximately 40 m depth in front of the study area. This shelf area is characterized as sediment-starved, with numerous rocky outcrops, and patches of fine, moderately sorted and negatively skewed sand.

8.3 Numerical solutions for boulder transport

Based on the validation of available numerical solutions, undertaken in chapter 4 (Numerical solutions of boulder movement), the equations developed by Nandasena *et al*. (2011a), coupled with Nott's (1997) approach to relate flow velocity with broken wave height, were applied to Coxos boulder deposit and boulders transported by present-day storms in the study area and elsewhere. Computed significant waves heights of broken waves required to transport larger boulders were close to, and lower than, maximum observed offshore values: computed H_s of 5 m for the boulder transported during the the 2003 storm; H_s of 9 m for the boulders transported during the storms of January/February of 2014; H_s of 12.8 m for boulders in the northern sector; and of 11.5 m for boulders in the southern

sector. Computed tsunami wave heights required to generate the same flow velocities, when applied to boulders of Coxos, were well below the values reported in historical records of the inundation in a location near the study area (computed tsunami wave heights reached maximum values of 1.3 m, against observed tsunami wave height over 5 m). Wave periods computed using Lorang's (2011) approximation, to differentiate storm from tsunami origin, were under 40 s for most boulders in the study area, except for two particles in the northern sector, which rendered wave periods of 80 s and 150 s.

The pronounced contrast between inferred storm and tsunami wave heights has been used by many authors to attribute the origin of coastal boulder accumulations to tsunamis instead of storms, especially in coasts prone to tsunami inundations (*e.g.* Nott, 1997; 2000; 2004; Mastronuzzi and Sansò, 2000; 2004; Mastronuzzi *et al.*, 2007; Kennedy *et al.*, 2007; Scicchitano *et al.,* 2007; Maouche *et al.*, 2009; Barbano *et al.*, 2010; Shah-hosseini *et al.*, 2011).

Despite the ample use of Nott's (1997, 2003) equations to infer the nature of the mechanism responsible for coastal boulder deposits, computed wave heights must be underestimated, given that derivation of H_s from flow velocity is computed near the breaking point (thus seawards of most boulder deposits) where flow velocities and wave height are near maximum. Furthermore, and in the case addressed in this work, comparing offshore and nearshore wave heights is only valid for longer waves (T_m~15 s or larger) travelling from the western octant, which suffer minimum height deacrese or even slight increase (*cf.* Silveira *et al.*, 2013). The conversion of velocity into storm wave height is further complexified by the frequent amplification of flow velocities due to the interaction between the complex topography and the wave bore and due to the interaction of bores arriving at the shoreline with different directions, which can increase flow intensity up to a factor of 2 (*cf.* Denny *et al.*, 2003). Moreover, the propagation of bores in natural channels can generate relevant increases in flow velocities due the lateral squeeze of the flow by channel walls (*cf.* Denny *et al.*, 2003), such as the natural structures (indentations) found in the southern sector of the Coxos study area. Storm wave heights obtained using Nott's approach are based in assumptions that are not met in most cases.

In addition, both the initial (source) and final (deposit) position of boulders are located on supra-tidal rocky structural platforms, far away and landward of the breaking point of waves. Thus, and despite validation with boulder transport by known storms, the application of these equations to this geomorphological context lacks physical grounds.

Besides the conversion of flow velocity into wave heights, another problem is the assumption that boulder extraction and/or transport occurs because of a single wave attack and caution is required when interpreting boulder transport by events with numerous successive waves (Etienne and Terry, 2012). Either in the case of storms or tsunamis, there is always more than one wave hitting the coastline and generating changes in boulder attachment/position at each stroke.

Regardless, for boulder movement to occur in the N sector, more energy is required, when compared to the S sector. Transport in the former sector probably occurred by less frequent, and higher magnitude waves. This interpretation is based in computed flow velocities and wave heights and further supported by the transport of only one particle during the 2014 storms in this location, contrasting with movement of over 100 boulders having been detected in the S sector. This contrast is further discussed in the next section, together with age estimation results.

8.4 Age estimation

Age estimation of the Coxos boulder accumulations was based in the application of several proxies and the combined interpretation of results. Each proxy contributed with information that allowed the identification of distinct phases of development of the boulder accumulation, extending back in time up to 500 years.

The comparative analysis of aerial photographs of the study area, together with observed boulder movement during recent storms, and estimated ages of boulder colonisation by the lichen species *Opegrapha durieui*, clearly show that boulder movement has been quite frequent in the recent past (~60 years). This is especially true in the segments of the study area exposed to W and NW.

The application of lichenometry in specific boulders has allowed evaluating their age of movement and emplacement, or lack thereof. Lichen age was considered as proxy of minimum age of boulder transport and deposition, also allowing to identify time intervals associated with maximum and minimum occurrence of lichen-colonised particles. Maximum frequencies of lichen bearing boulders in the recent past are considered to indicate limited boulder movement due to periods of lower storm frequency and/or intensity. Conversely, minimum frequency within the same time intervals, and maximum in occurrences of particles exhibiting dead lichens, are attributed to increase in the frequency and/or magnitude of marine events (storminess) generating boulder movement. Based on this premise, a period of lower storminess affecting the study area was identified as having occurred from 1957 onwards, with incidence between 1987 and 1997. Following this time-period, storms capable of generating boulder movement were more frequent, from 1997 to 2007, originating the death of several lichens and infrequent colonisation of new surfaces.

Several authors reported considerable decadal fluctuations in European wave climate throughout the past 130 years (Wang and Swail, 2001; Dodet *et al.*, 2010; Wang *et al.*, 2011; Matulla *et al.*, 2008). Although a significant increase in storminess is reported for the European Northern Atlantic coast in the past 40-60 years, it has been accompanied by an absent or decreasing trend in the subtropical North Atlantic, in which Portugal is included, associated with a poleward shift of storm tracks (Wang and Swail, 2001; Dodet *et al.*, 2010; Wang *et al.*, 2011; González-Villanueva *et al.*, 2013). Regional trends in storminess agree with an increase in lichen colonisation and development observed in the study area in the past 60 years. Moreover, the analysis of local storminess trends based on wind time-series in the NW Iberia compiled and discussed by González-Villanueva *et al.* (2013) shows minimum average wind velocities around 1994, followed by a slight increasing trend since then, although never reaching values as high as those registered during 1940-1960.

Further back in time, the investigation of repetitive development of clifftop boulder deposits, overwash deposits and dunes along the Western Europe throughout the past 6000 years, indicates the existence of periods of storminess maxima during the

Holocene (*e.g.* Hall *et al*., 2006; Hansom and Hall, 2009; Cox *et al*., 2012; Sorrel *et al*., 2012; González-Villanueva, 2013; Clarke and Rendell, 2006; Costas *et al*., 2012; Andrade *et al*., 2004; Zazo *et al*., 1994; Borja *et al*., 1999). The absence of development of these deposits corresponds, at least in part, to periods of lower storminess, during which lichen development on boulder surfaces must not have been compromised. This same principle has been applied by González-Villanueva *et al*. (2013), which detected alternated expansion and decline of vegetation cover in dunes, associated with alternated decrease in wind speed and retreat of the shoreline.

Computed flow velocities required to generate boulder movement in the Coxos region and age estimation results obtained with aerial photographs and lichenometry sort out distinct boulder sub-populations comprising older, and sometimes larger particles in WSW-facing segments of the study area. A possible explanation is that boulder deposition in these segments are related with events of larger magnitude than those currently observed. At first glance, the coincidence between boulder transport associated with larger magnitude events in WSW facing segments, and a seismic tsunami source offshore SW Iberia, could indicate that the deposition of these boulders was generated by tsunami waves. However, only one destructive tsunami occurred in the past 3500 years, the *AD* 1755 event (*cf.* Andrade *et al*., 2016). The larger and older boulders in the N sector occur within a cluster containing particles with varying mass, position and age, indicating their deposition was asynchronous. In this case, although some boulders present estimated ages compatible with deposition by the *AD* 1755 tsunami, the asynchronous character of this cluster counters the tsunami hypothesis. Boulders in the southern sector contemporaneous to the *AD* 1755 tsunami are older than the surrounding particles, so transport and deposition by that event remains a possibility.

The presence of marine sand patches attributed to the *AD* 1755 tsunami inundation beneath boulders, over the S structural platform, at 9 m amsl, strongly suggests that this tsunami event has, in fact, reached the study area. The localized minimum inundation height of 9 m amsl, required to allow for extensive inundation and deposition of sand in the study area in relation with the *AD* 1755 tsunami, contrasts with values of approximately 5-6 m near this area reported in historical records (for

further details see section 2.1.5 1st November 1755). Such increase in the vertical reach of the *AD* 1755 tsunami is explained by both regional and local geomorphological constrains which modulate the longshore distribution of height of both tsunami and long-period storm waves. Relevant alongshore differences in wave run-up and boulder transport capability has been detected in field observations (*e.g.* Jones and Hunter, 1992; Goff *et al*., 2006a; Paris *et al*., 2009) in association with regional and local geomorphological changes. The influence of regional- to micro-scale morphological features in modulating the patterns of wave-energy distribution along the coast have been successfully recreated by complex numerical models. For example, Matsuyama *et al*. (1999) and Iglesias *et al*. (2014) investigated effects related with regional geomorphological features such as submarine canyons. Numerical simulations of the *AD* 1755 tsunami propagation presented by Oliveira *et al.* (2015) show energy convergence promoted by two mesoscale shelf morphological features in the Portuguese western continental margin (Estremadura Spur and Nazaré canyon), which resulted in energy concentration and consequent localized increase in flooding potential of the studied coast.

The question of whether the *AD* 1755 tsunami generated boulder transport in the study area or not, is no longer relevant, given that its vertical reach and velocity were capable to generate boulder movement. Numerical solutions for boulder transport indicate that a 1.5 m-high tsunami would suffice to generate flow velocities required to overturn all boulders in the Coxos deposit. Additionally, the distribution of estimated ages using lichenometry shows a void in boulder deposition within the time-frame including the *AD* 1755 event. These evidences suggest that, not only was this event capable of generating boulder movement, but that its signature was mostly erosive. Therefore, boulders deposited prior to the *AD* 1755 tsunami event, preferably located in WSW-facing segments of the study area, correspond to remnants of pre-existing storm-related deposits that have been extensively washed out by that 18th century extremest event.

Another not necessarily conflicting possibility, is that the highly dynamic character of the study area, especially in the case of the W- to NW-facing segments, does not allow boulder immovability for extended periods of time. Although boulder transport by storms is a continuous process, which must have occurred in this

location since the sea level rise stabilized, at least 6000 years ago (*cf.* Cearreta *et al.*, 2007), there is a limit in the number of boulders that the structural platforms are able to accommodate. These particles are deposited by storms, only to be later removed by the backwash, remaining over the structural platforms during a residence period rarely exceeding 200 years.

Regardless if boulder erosion occurred due to the *AD* 1755 tsunami or to storm waves occurring in the past 200 years, the WSW-facing segments of the study area have proven to be much less dynamic and show limited boulder movement. This interpretation is supported by observations of aerial photographs from 1948 to 2010, by the scattered age of boulder emplacement, especially in the N sector, and by results obtained from monitoring boulder movement by present-day storms. Deposition of large boulders by storms in these locations followed by extended period mostly characterized by immobility, suggests a prior occurrence of rare and extreme storm events, of higher magnitude than that observed in the past 70 years, most likely related with changes in large scale pressure systems.

For example, larger than average significant wave heights reaching the Portuguese coastline have been detected and associated with negative NAO index by Dodet *et al.* (2010), based on the analysis of a long-term hindcast time series (from 1953-2009) of wave data for the North-East Atlantic Ocean. Moreover, in the W-facing coast of central Portugal (Setúbal Peninsula) and going back further in time, Costas *et al.* (2012) identified phases of higher aeolian activity related to enhanced westerly winds and storminess compatible with prolonged periods of negative NAO index. Age determination of the correspondent dune sets indicated major phases of aeolian activity around 0.44 and 0.3 ka (1570 and 1710), that these authors related to increased storminess during the Little Ice Age.

In fact, maximum development of lichens in surfaces of boulders in the southern sector coincide with a continuous NAO+ period occurring from 1987 to 1995, thus supporting the interpretations stated above (Figure 121). Ultimately, it is conceivable that in the present study case, sub-populations comprising older and larger boulders could be coeval with transport and deposition during high storminess periods coincident with negative winter NAO index. If these

interpretations are correct, they provide grounds to suggest that in rocky coasts lichens may be used as an innovative proxy of storminess.

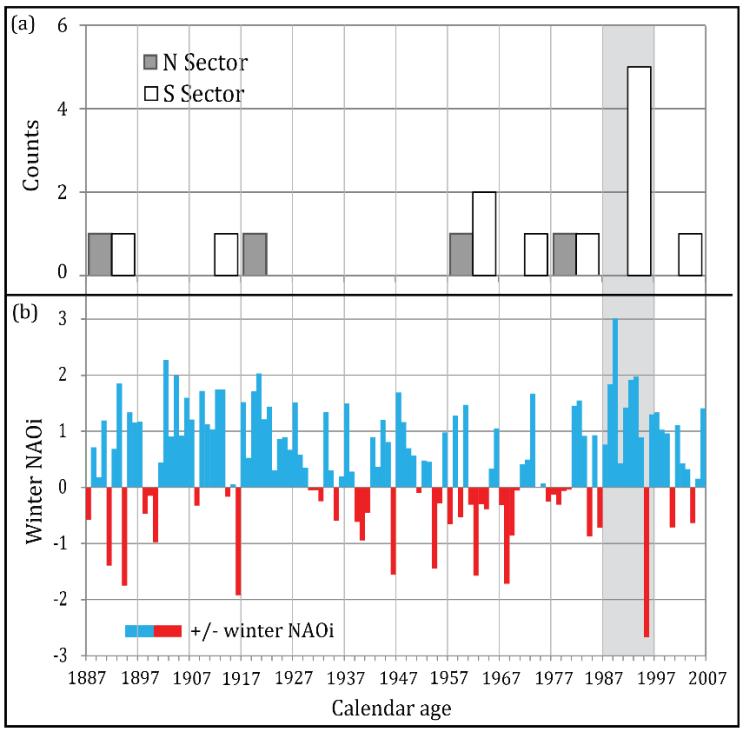

Figure 121: (a) Distribution of calendar ages obtain for lichens developing in the N and S sectors from 1887 onwards; (b) Winter NAOi computed with information from the North Atlantic Oscillation (NAO) database, made available by the Climatic Research Unit, University of East Anglia (https://crudata.uea.ac.uk/cru/data/nao/) under the Open Database License (ODbL) (http://opendatacommons.org/licenses/odbl/1.0/)

Summarizing, boulder transport and deposition in the study area has been a permanent process in the past ~5000 years, although discontinuous in time. Similarly to what has been observed in the past 70 years, boulders mostly originated in the top-most layer comprising the bench edges have been detached and emplaced over the structural surfaces. These particles are later remobilized and emplaced further inland, where they end up forming boulder clusters and ridges. Despite the remobilization of particles by successive storms, these structures mostly remain in the same position, reflecting the swash and backwash flow covering the structural surfaces, which, in turn, is mostly controlled by local geomorphological features, such as indentations in the lower structural platforms.

Prior to the *AD* 1755 tsunami inundation, the Coxos boulder accumulation must have resembled the deposit existing today, with minor differences in the position of individual boulders (Figure 122a to d).

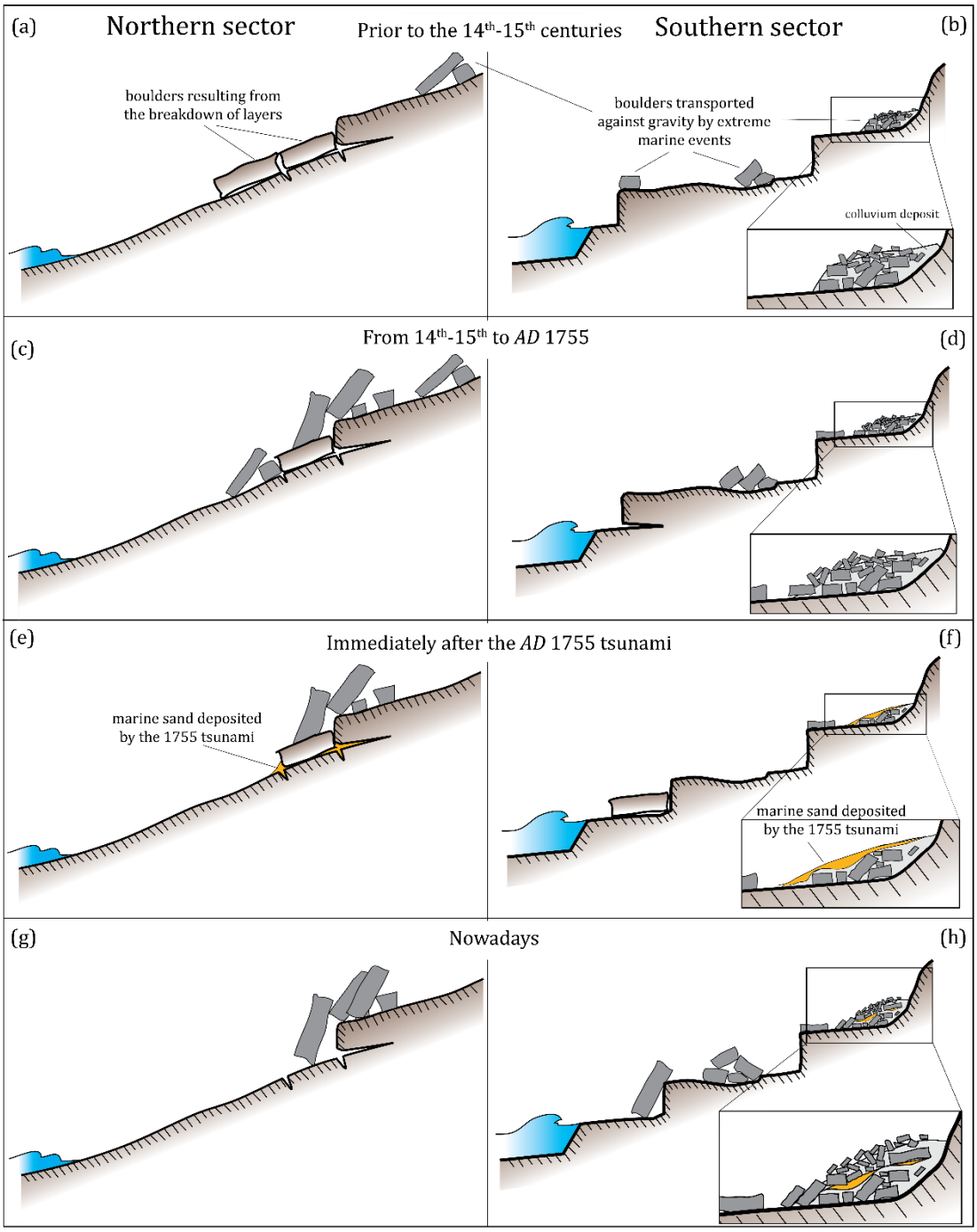

Figure 122: Schematic representation of the conceptual model showing the evolution of Coxos boulder accumulation in the northern and southern sectors

The *AD* 1755 event partially inundated the study area, with emphasis on the southern sector, reaching at least 9 m amsl and an upper limit of 13 m amsl. Ultimately, the tsunami was capable of significantly eroding most boulders comprising the boulder ridges, leaving a patched deposit of marine sand covering part of the remaining boulder accumulations and infilling the wider joints affecting the structural surfaces (Figure 122e and f). Although there is no evidence of the

marine sand in the northern sector, there is also no reason to believe that the tsunami exclusively deposited finer materials in the southern sector. The selective preservation of finer materials is attributed to the following contrasting geomorphological contexts: higher pending of the WSW-facing ramp in the northern sector favouring erosion by the backwash, contrasting with the sub-horizontal surfaces of the southern sector; minimum erosion of the tsunami sand in the southern sector due to the cover provided by the developing colluvium deposit.

From *AD* 1755 onwards, the Coxos accumulations developed by successive boulder transport and subsequent removal, more frequently during periods of negative winter NAO index, until reaching the configuration which can be observed at present (Figure 122g and h). Boulder transport is more frequent in the S sector, and generated by storms occurring every 2-5 years, while in the N sector, only storm waves such as those occurring during "Christina" or "Nadja" storms, associated with maximum tidal levels, are capable to generate movement, with return periods over 20 years.

In conclusion, the body of evidence collected and discussed in this study strongly suggests a storm origin of the Coxos boulder deposit. The *AD* 1755 tsunami event undoubtedly reached the study area but with mostly erosive effects on the previously existing and storm-related boulder accumulation. Given these evidences, a polygenic origin of the boulder deposit cannot be disregarded.

9

Conclusions

A boulder deposit associated with high energy marine event(s) was detected in the central western Portuguese coast, near Ericeira, within a rocky sand-starved geomorphological context. The boulder deposit was at first thought to be related to tsunami events, given the large size of some of the boulders and height of boulder emplacement, apparently beyond the reach of modern-day storms.

The rocks outcropping in this location consist of a Cretaceous sedimentary sequence encompassing five units (from A to E) separated by four structural surfaces (from S I to S IV) roughly described from the base towards the top as: Unit A includes layers L1 to L7 and is composed of fine sandstone interbedded with sandy limestone layers and topped by a resistant sandy limestone layer which forms the lowest littoral bench in the study area and structural surface S I; Unit B comprises layers L8 to L15 and mainly consists of fine sandstone interbedded with claystone and intensely bioturbated sandy limestone layers, topped by a more resistant layer forming a wide bench and surface S II; Unit C contains a calcarenite layer (L16), a sandy limestone layer (L17-18) and a thick crystalline limestone layer (L19), which forms the wider structural bench of the study area, topped by surface S III; Unit D incorporates layers L20 to L28, corresponding to crystalline limestone layers interbedded with softer marls and thin siltstone layers, the sequence being topped by a hardened surface

where most boulders in the deposit sit (surface S IV); Unit E includes layers L29 to L37 and is composed of less resistant interbedded thin layers of claystone, sandstone and marls, forming a low-sloping cliff outcropping inland of the more resistant underlying units.

The study area was subdivided into two sectors, northern and southern, showing differences in geomorphology and in both individual properties of boulders and accumulations. Several proxies were applied to identify the direction, magnitude and age of the event, or events, responsible for the entrainment, transport and deposition of the boulders. The proxies included the statistical and spatial analysis of boulders' characteristics, such as source layer, mass, height of emplacement, distance from the coastline and directional properties (source-sink travel paths, dip of the ab surface, and trend of the a-axis of individual and imbricated particles). One of the main objectives of this approach was to apply paleocurrent analysis procedures, some of which have been successfully used in the study of fluvial deposits. Additionally, frequently used numerical solutions for boulder entrainment, frequently applied to coastal boulder accumulations deposited by extreme marine events were critically discussed and applied to the deposit under scope. A major challenge was to determine the age of the emplacement of particles in the deposit, and different techniques were used to decipher the processes involved in its origin.

The northern sector comprises a low cliff facing W-NW and a seaward sloping ramp facing W-SW. Larger source-layer thickness and joint spacing of layers from Unit C outcropping in this sector generate the largest boulders in the study area. The southern sector is much more complex. It is roughly aligned N-S, but it contains low cliffs and cross-shore and longshore irregularities, such as stepped sub-horizontal surfaces, mostly developing in Units C and D, and presenting a pronouncedly indented shoreline subject to incoming waves.

The boulder deposit contains isolated boulders, boulder clusters (sometimes aligned or showing imbrication) and boulder ridges. All these morphological types have been described in modern-day storm-related deposits and some in tsunami-related accumulations. The whole deposit was subdivided in four sub-populations, each

sharing common characteristics, such as source layer, mass morphology of the accumulations and prevailing mode of transport, as outlined below:

1. Sub-population SP1 comprises the largest boulders of the deposit, with mass over 10 ton, mostly sourced in Unit C and leaning against the bench edges of S III. Boulders were rarely completely pushed up-slope having been detached and slightly uplifted.
2. Sub-population SP2 includes isolated boulders resting frequently up-side down over, and sourced in, the top-most layer defining the structural platforms (L19 and S III in both sectors and L28 and S IV exclusively in the southern sector), next to the bench edge. They range in mass from 2.5 ton to 10 ton and have been detached, rotated and transported for short vertical and horizontal distances.
3. Sub-population SP3 is composed of boulder clusters, including particles with mass from ranging from 1 to 2.5 ton, but occasionally reaching 10 ton. These particles border and armour boulder ridges as well as the landward edge of surface S IV and colluvium. They have been transported for diverse distances by sliding and rolling.
4. Sub-population SP4 comprises the smallest boulders in the deposit, with mass under 1 ton, and exclusively occurs in the southern sector forming six boulder ridges. These boulders are sometimes weathered and rounded evidencing mechanical abrasion due to repetitive transport by rolling and sliding until reaching the base of the ridges and rolling over larger obstacles or saltation when travelling up-slope the ridge.

The spatial distribution of boulder and mass reveal an overall fining inland and upward trend which reflect the coastline morphology. Short vertical and horizontal displacement reflected in the distribution of boulders' source layer suggest a rapid energy dissipation, associated with storm waves, rather than tsunami. This conclusion is further supported by the existence of multiple ridges which have been found worldwide forming boulder deposits of indisputable storm origin in rocky coastline contexts and are associated with the repetitive reworking of boulder by storms waves.

The alignment of boulder ridges and from directional properties of boulders suggests that the flow over the structural platforms is mostly controlled by local geomorphological features. Exposure to wave attack changes within each segment, depending on local coastline trend and geomorphological features, such as indentations in the lower structural platforms and cliffs, that function as natural channels, constraining the direction of incoming bores and increasing the run-in and run-up of incoming broken waves. Nonetheless, dominant flow directions extracted from the boulder deposit are consistent with the prevailing nearshore storm wave regime, travelling from the W-NW.

The addition of particles and development of the boulder accumulations in the Coxos area occurs in the following manner:

1. Loosened particles corresponding to joint-bounded pieces of the top-most layer of the bench edge, and exposed to wave attack, are pushed upward and inland by wave swash. They suffer short-lived cross-shore transport and end up over the structural platforms, next to their original position. These particles form isolated boulders, sometimes turned upside down, and bordering the bench and cliff edges;
2. When these particles have movable sizes, they are subsequently transported both cross- and along-shore, over the structural platforms, by sliding or rolling. When they hit an obstacle, they remain in the same location, incorporating boulder clusters and ridges;
3. Whenever an obstacle is not met or is ineffective to stop the movement, the particles continue or resume alongshore movement, until they are finally removed by backwash into the ocean.

The incorporation of age estimation results with the remaining proxies allowed drawing the following conclusions regarding the origin of the Coxos boulder accumulations:

1. The boulder deposit dates back from at least *AD* 1500, the oldest boulders in the northern sector having been deposited during periods of enhanced storminess associated with larger than average wave height. Storms capable

of generating boulder movement in the southern sector occur once every 2-5 years, and in the northern sector once every 20 years;

2. The *AD* 1755 tsunami inundation reached approximately 9 m amsl and did not surpass 13 m amsl in the study area, especially affecting the southern sector, having had an essentially erosive effect on the previously existing boulder accumulation, which was almost totally obliterated;
3. After the *AD* 1755, the deposit regained its volume and shape by the repetitive addition and removal of boulders by storms;
4. Once a boulder is placed on the structural surfaces, its stay rarely exceeds 200 years, especially in the more exposed W- and NW-facing segments.

Flow velocities and wave heights required to generate boulder movement are higher in the N sector, suggesting that wave-related events responsible for boulder transport and deposition in that location, are of higher magnitude than generated by present-day storms. It is hypothesized that those events could associate with periods of prevailing negative winter NAO index.

Strong and congruent evidences suggest a storm origin for the boulder deposit under analysis. However, given that the *AD* 1755 tsunami did reach the study area with flow velocities capable of generating boulder movement, and that the range of elevations reached by that inundation encompasses the elevation range of most of the deposit, a polygenic origin of this accumulation cannot be fully discarded.

In summary, major contributions of this work are:

1. The proposal and testing of field and data processing methodologies developed to acquire the maximum possible information on attributes of a large number of particles in the least amount of time;
2. The computation of return levels for recurrence periods of 2, 5, 10, 20, 50, 100 and 200 years for significant wave height and wave period and wave power offshore the western coast of Portugal;
3. Approximate recurrence periods for boulder transport in the study area from 2-5 years in the southern sector and above 20 years in the northern sector;
4. The identification of tidal level and wave period, besides the frequently considered wave height, as wave parameters which greatly influence the

amount of energy reaching the deposit and control the direction of the flow generating boulder transport and deposition over the structural platforms;

5. The discovery of new values of inundation height of the *AD* 1755 tsunami in the western Portuguese coastline, based on field evidences, and the attribution of an essentially erosive effect, rather than depositional, to that event;
6. New insights about the effects of both storm and tsunami waves in rocky coastline contexts;
7. An average residence period of two centuries for boulders in the Coxos deposit, forwarded by data collected in this study;
8. The construction of a lichen growth model for the species *Opegrapha durieui* which allows to estimate the age of exposure of limestone surfaces in coastal areas of the Portuguese coast, from Nazaré to Boca do Rio, where this species develops;

In conclusion, the local geomorphology significantly influenced boulder transport and deposition by waves in this rocky coastline. In the case addressed, no unique proxy *per se* has given a satisfactory answer regarding what processes were involved in the origin of this boulder accumulation. Especially in irregular coastlines where complex processes occur, such as the study area, it is essential to have an wholistic approach, integrating information from historical records of tsunami inundation, wave records, geomorphology, direct observation and numerical modelling of physical processes and age estimation techniques to develop a complete conceptual model explaining how and when boulder transport by extreme waves occur.

References

Adamiec, G. and Aitken, M. (1998). Dose-rate conversion factors: update. *Ancient TL*, 16, pp. 37-50.

Affleck and Gray C. (1755-1756). An account of the agitation of the sea at Antigua, Nov 1 1755. By Capt. Affleck of the Advice Man of War, Communicated by Charles Gray Esq FRS in a Letter to William Watson FRS, *Transactions of the Royal Society of London*, 49, pp. 668-670.

Aitken, M.J. (1998). An introduction to Optical Dating - The Dating of Quaternary Sediments by the use of photon-stimulated Luminescence. New York, United States of America: Oxford University Press, p. 280.

Allen, H.D. (2003). A transient coastal wetland: from estuarine to supratidal conditions in less than 200 years – Boca do Rio, Algarve, Portugal. *Land Degradation & Development,* 14, pp. 265-283.

Almeida, J. (1946). Roteiro dos monumentos militares portugueses. Vol II Distritos de Aveiro, Coimbra, Leiria e Santarém. Lisboa, Portugal: J. Almeida, p. 342.

Andrade, C., Freitas, M.C., Moreno, J. and Craveiro, S.C. (2004). Stratigraphical evidence of Late Holocene barrier breaching and extreme storms in lagoonal sediments of Ria Formosa, Algarve, Portugal. *Marine Geology*, 210, pp. 339-362.

Andrade, C. Freitas, M.C., Oliveira, M.A. and Costa, P.J.M. (2016). On the sedimentological and historical evidences of seismic-triggered tsunamis in the Algarve coast of Portugal. In: J. Duarte and W. Schellart, ed., Plate Boundaries and Natural Hazards - Geophysical Monograph 219, 1st edition, New Jersey, United States of America: American Geophysical Union and John Wiley and Sons, Inc, pp. 219-238.

André, M.-F. (1990). Frequency of debris flows and slush avalanches in Spitsberg: a tentative evaluation from lichenometry. *Polish Polar Research*, 11 (3-4), pp. 345-363.

Aon Benfield (2014a). January 2014 Global Catastrophe Recap. London, United Kigndom: Impact Forecasting, p. 9. Available at: http://www.aon.com [Accessed 8 August 2014].

Aon Benfield (2014b). February 2014 Global Catastrophe Recap. London, United Kigndom: Impact Forecasting, p. 10. Available at: http://www.aon.com [Accessed 8 August 2014].

Armstrong, R. (2004). Lichens, Lichenometry and Global Warming. *Microbiologis*t, 5 (3), pp. 32-35.

Armstrong, R.A. (2015a). Lichen growth and lichenometry. In: D.K. Upreti; P.K. Divakar; V. Shukla and R. Bajpai, ed., Recent Advances in Lichenology - Modern methods and approaches in biomonitoring and bioprospection, Volume 1, 1st edition. New Delhi, India: Springer-Verlag, pp. 213-227.

Armstrong, R.A. (2015b). The Influence of Environmental Factors on the Growth of Lichens in the Field. In: D.K. Upreti, P.K. Divakar, V. Shukla and R. Bajpai, ed., Recent Advances in Lichenology Modern Methods and approaches in biomonitoring and bioprospection, Volume 1, 1st edition, New Delhi, India: Springer-Verlag, pp. 1-18.

Arquivos do Ministério do Reino (1756). Documentacão sobre o tremor de terra de 1 de Novembro de 1755, Maço no 638. Lisboa, Portugal: Arquivo Nacional da Torre do Tombo.

Babinet, J. (1861). Sur le désastre de Lisbonne de 1531. *Comptes Rendus des séances de l'Académie des Sciences*, tome 52, pp. 369-370.

Bagnold, R.A. (1940). Beach formation by waves: some model experiments in a wave tank. *Journal of the Institution of Civil Engineers*, 15 (1), pp. 27–52.

Bahlburg, H. and Spiske, M. (2012). Sedimentology of tsunami inflow and backflow deposits: key differences revealed in a modern example. *Sedimentology*, 59, pp. 1063-1086.

Bailey, R.M. and Arnold, L.J. (2006). Statistical modeling of single grain quartz De distributions and an assessment of procedures for estimating burial dose. *Quaternary Science Reviews*, 25, pp. 2475-2502.

Ballarini, M., Wallinga, J., Wintle, A.G. and Bos, A.J.J. (2007). A modified SAR protocol for optical dating of individual grains from young quartz samples. *Radiation Measurements*, 42, pp. 360-369.

Balsinha, M. (2008). Sedimentary dynamics of Portuguese continental shelf between Nazaré submarine canyon and Ericeira. Master Dissertation, Universidade de Lisboa, p. 175.

Bansal, R.K. (2010). A Textbook of Fluid Mechanics and Hydraulic Machines (in S.I. Units). Revised 9th edition. New Delhi, India: Laxmi Publications, p. 1093.

Baptista, M.A. and Miranda, J.M. (2009). Revision of the Portuguese catalog of tsunamis. *Natural Hazards and Earth System Sciences*, 9, pp. 25-42.

Baptista, M.A., Miranda, P.M.A., Miranda, J.M. and Victor, J.M. (1996). Rupture Extent of the 1755 Lisbon Earthquake Inferred from Numerical Modeling of Tsunami Data. *Physics and Chemistry of the Earth*, 21 (12), pp. 65-70.

Baptista, M.A., Heitor, S., Miranda, J.M., Miranda, P. and Victor, L.M. (1998a). The 1755 Lisbon tsunami; Evaluation of the tsunami parameters. *Journal of Geodynamics*, 25 (2), pp. 143-157.

Baptista, M.A., Miranda, P.M.A., Miranda, J.M. and Victor, L.M. (1998b). Constrains on the source of the 1755 Lisbon tsunami inferred from numerical modelling of historical data on the source of the 1755 Lisbon tsunami. *Journal of Geodynamics*, 25 (2), pp. 159-174.

Baptista, M.A., Miranda, J.M., Chierici, F. and Zitellini, N. (2003). New study of the 1755 earthquake source based on multi-channel seismic data and tsunami modeling. *Natural Hazards and Earth System Sciences*, 3, pp. 333-340.

Baptista, M.A., Miranda, J.M., and Luís, J.F. (2006). In Search of the 31th March 1761 Earthquake and Tsunami Source. *Bulletin of the Seismological Society of America*, 96 (2), pp. 713–721.

Baptista, M.A., Miranda, J.M., Lopes, F.C. and Luís, J. (2007). The source of the 1722 Algarve earthquake: evidence from MCS and Tsunami data. *Journal of Seismology*, 11, pp. 371-380.

Barbano, M.S., Pirrota, C. and Gerardi, F. (2010). Large boulders along the south-eastern Ionian coast of Sicily: Storm or tsunami deposits? *Marine Geology*, 275, pp. 140-154.

Barbano, M.S., Gerardi, F. and Pirrota, C. (2011). Differentiation between boulders deposited by tsunamis and storm waves along the south-eastern Ionian coast of Sicily (Italy). *Bollettino di Geofisica Terica ed Applicata*. 52 (4), pp. 707-728.

Barkan, R., ten Brink, U.S. and Lin, J. (2009). Far field tsunami simulations of the 1755 Lisbon earthquake: Implications for tsunami hazard to the U.S. East Coast and the Caribbean. *Marine Geology*, 264, pp. 109–122.

Barreiro, F.J. (1838). Memoria sobre os pesos e medidas de Portugal, Espanha, Inglaterra, e França, que se empregão nos trabalhos do Corpo de Engenheiros e da Arma de Artilharia; e noticia das principais medidas da mesma espécie, usadas para fins militares em outras nações. Lisboa, Portugal: Tipografia da Academia Real das Sciencias, p. 80.

Belem, F.J. (1750). Chronica Serafica da Santa provincia dos Algarves, Parte Primeira. Oficina de Inácio Rodrigues, p.286.

Benner, R., Browne, T., Brückner, H., Kelletat, D. and Scheffers, S. (2010). Boulder transport by waves: progress in physical modelling. *Zeitschrift für Geomorphologie*, 54 (3), pp. 127-146.

Benedict, J.B. (2009) A Review of Lichenometric Dating and Its Applications to Archaeology. *American Antiquity*, 74 (1), pp. 143-172.

Beschel, R.E. (1961). Dating rock surfaces by lichen growth and its application to glaciology and physiography (lichenometry). *Geology of the Arctic*, 2, pp. 1044-1062.

Bishop, P. and Hughes, M. (1989). Imbricate and fitted fabrics in coastal boulder deposits. *Geology*, 17, pp. 544–547.

Blair, T.C. and McPherson, J.G. (1999). Grain-size and textural classification of coarse sedimentary particles. *Journal of Sedimentary Research*, 69 (1), pp. 6-19.

Blott, S.J. and Pye, K. (2008). Particle shape: a review and new methods of characterization and classification. *Sedimentology*, 55, pp. 31-63.

Booij, N., Ris, R. and Holthuijsen, L. (1999). A third-generation wave model for coastal regions. I Model description and validation. *Journal of Geophysical Research*, 104, pp. 7649–7666.

Borja, F., Zazo, C., Dabrio, C.J., del Olmo, F.D., Goy, J.L. and Lario J. (1999). Holocene aeolian phases and human settlements along the Atlantic coast of southern Spain. *The Holocene*, 9 (3), pp. 333-339.

Bourrouilh-Le Jan, F.G. and Talandier, J. (1985). Sedimentation et fracturation de haute energie en milieu recifal: Tsunamis, ouragans et cyclones et leurs effets sur la sedimentologie et la geomorphologie d'un atoll: Motu et hoa, a rangiroa, Tuamotu, Pacifique SE. *Marine Geology*, 67 (3-4), pp. 263–272, 277–323, 327–333.

Bradwell, T. (2001). A New Lichenometric Dating Curve for Southeast Iceland. *Geografiska Annaler. Series A, Physical Geography*, 83 (3), pp. 91-101.

Brito, F.B. (1595). Monarquia Lusitana, Parte Primeira, contém as histórias de Portugal desde a criação do mundo até o nascimento de nosso senhor Jesus Cristo. 1597 Edition. Alcobaça, Portugal: impressa no Insigne Mosteiro de Alcobaça por mandado do R.^{mo} Padre Geral Frey Francisco de S. Clara com licença e privilégio Real, p. 415.

Brito, F.B. (1607). Segunda Parte da Monarquia Lusitana em que se continuam as histórias de Portugal desde o nascimento do nosso salvador Iesu Christo até ser

dado em dote ao Conde Dom Henrique. 1690 Edition. Lisboa, Portugal: Na Impressão Craedbeeckiana, p. 558.

Bryant, E.A. and Nott, J. (2001). Geological indicators of large tsunami in Australia. *Natural Hazards*, 24, pp. 231– 249.

Buckley, M.L., Wei, Y., Jaffe, B.E. and Watt, S.G. (2012). Inverse modeling of velocities and inferred cause of overwash that emplaced inland fields of boulders at Anegada, British Virgin Islands. *Natural Hazards*, 63, pp. 133-149.

Bull, W.B. (2014). Using earthquakes to assess lichen growth rates. *Geografiska Annaler: Series A, Physical Geography*, 96, pp. 117–133.

Camfield, F.E. (1980). Special Report 6 - Tsunami Engineering. Washington, United States of America: U.S. Army Corp. Eng. Coastal Eng. Res. Cent., p. 222.

Campos, M.L. (1991). Tsunami Hazard on the Spanish Coasts of the Iberian Peninsula. *Science of Tsunami Hazards*, 9, pp. 83-90.

Canelas, R., Oliveira, M.A., Crespo, A., Neves, R., Costa, P., Freitas, M.C., Andrade, C. and Ferreira, R. (2014). Mathematical simulation of boulder dislodgement by high-energy marine flows in the western coast of Portugal. In: Geophysical Research Abstracts from the European Geosciences Union General Assembliy 2014 (EGU2014), Vol. 16. Vienna, Austria: European Geosciences Union, pp. 16081.

Carrara, P.E. and Andrews, J.T. (1975). Holocene glacial/periglacial record; Northern San Suan Mountains.Southwestern Colorado. *Zeitschrift für Gletscherkunde und Glazialgeologie*, 2 (2), pp. 155-174.

Carvalho, A.M.G. (2005). Geologia Sedimentar Volume II – Sedimentologia. Lisboa, Portugal: Âncora editora, p. 475.

Cearreta, A., Alday, M., Freitas, M.C. and Andrade, C. (2007). Postglacial foraminifera and paleoenvironments of the Melides Laggon (SW Portugal): towards a regional model of coastal evolution. *Journal of Foraminiferal Research*, 37 (2), pp. 125-135.

Çengel, Y.A. and Cimbala, J.M. (2006). Fluid Mechanics: Fundamentals and Applications. New York, United States of America: McGraw-Hill, p. 929.

Choffat, P. (1904-1907). Le Cretacique dans L'Arrabida et dans la Contrée D'Ericeira. *Communicações da Commissão do Serviço Geologico de Portugal*, Tomo VI, pp. 1-55.

Ciavola, P., Ferreira, Ó., Haerens, P., Koningsveld, M.V. and Armaroli, C. (2011). Storm impacts along European coastlines. Part 2: Lessons learned from the MICORE project. *Environmental Science & Policy*, 14, pp. 924-933.

Clarke, M.L. and Rendell, H.M. (2006). Effects of storminess, sand supply and the North Atlantic Oscillation on sand invasion and coastal dune accretion in western Portugal. *The Holocene*, 16 (3), pp. 341-355.

Coles, S. (2001). An Introduction to Statistical Modeling of Extreme Values. London, Great Britain: Springer-Verlag, p. 208.

Costa, A.G. (1997). Os fortes costeiros de Santa Susana e S. Pedro de Milreu, no concelho de Mafra. *Boletim Cultural da Câmara de Mafra*, 96, pp. 105-132.

Costa, M.D.S. (1994). Agitação marítima na costa Portuguesa. *Anais do Instituto Hidrográfico*, 13, pp. 35-40.

Costa, M. and Esteves, R. (2009). Clima de agitação marítima na costa Oeste de Portugal Continental. In: Comunicações das XI Jornadas Técnicas de Engenharia Naval. Lisboa, Portugal: Instituto Superior Técnico, p. 15.

Costa, P.J.M., Andrade, C., Freitas, M.C., Oliveira, M.A., da Silva, C.M., Omira, R., Taborda, R., Baptista, M.A. and Dawson, A.G. (2011). Boulder deposition during major tsunami events. *Earth Surface Processes and Landforms*, 36, pp. 2054–2068.

Costa, P.J.M., Andrade, C., Freitas, M.C., Oliveira, M.A., Lopes, V., Dawson, A.G., Moreno, J., Fatela, F. and Jouanneau, J.-M. (2012). A tsunami record in the sedimentary archive of the central Algarve coast, Portugal: Characterizing sediment, reconstructing sources and inundation paths. *The Holocene*, 22 (8), pp. 899-914.

Costa, P.J.M, Costas, S., González-Villanueva, R., Oliveira, M.A., Roelvink, D., Andrade, C., Freitas, M.C., Cunha, P.P., Martis, A., Buylaert, J.-P. and Murray, A. (2016a). How did the 1755 CE tsunami impact on sand barriers across the southern coast of Portugal? *Geomorphology*, 268, pp. 296-311.

Costa, P.J.M., Oliveira, M.A., González-Villanueva, R., Andrade, C. and Freitas, M.C. (2016b). Imprints of the AD 1755 tsunami in Algarve (South Portugal) lowlands and post-impact recovery. In: V. Santiago-Fandino, H. Tanaka and M. Spiske, ed., Tsunami and Earthquakes in Coastal Environments Significance and Restoration, 1st Edition. Basel, Switzerland: Springer, pp. 17-30.

Costas, S., Jerez, S., Trigo, R.M., Goble, R. and Rebêlo, L. (2012). Sand invasion along the Portuguese coast forced by westerly shifts during cold climate events. *Quaternary Science Reviews*, 45, pp. 15-28.

Coutinho, V. (1997). Castelos Fortalezas e Torres da região do Algarve. Faro, Portugal: Algarve em Foco Editora, p. 199.

Couto, D. (1778) Da Ásia - Dos feitos, que os Portuguezes fizeram na conquista, e descubrimento das terras, e mares do Oriente, Década 4-Parte Segunda. Lisboa, Portugal: Na Regia Officina Topografica, p. 461.

Cox, J. and Machemehl, J. (1986). Overload Bore Propagation Due to an Overtopping Wave. *Journal of Waterway, Port, Coastal, and Ocean Engineering*, 112 (1), pp. 161–163.

Cox, R., Zentner, D.B., Kirchner, B.J. and Cook, M.S. (2012). Boulder Ridges on the Aran Islands (Ireland): Recent Movements Caused by Storm Waves, Not Tsunamis. *The Journal of Geology*, 120, pp. 249-272.

Cunha, P.P., Buylaert, J.-P., Murray, A.S., Andrade, C., Freitas, M.C., Fatela, F., Munhá, J.M., Martins, A.M. and Sugisaki, S. (2010). Optical dating of clastic deposits generated by an extreme marine coastal flood: the 1755 tsunami deposit in the Algarve (Portugal). *Quaternary Geochronology*, 5, pp. 329–335.

Cunningham, A.C. and Wallinga, J. (2010). Selection of integration time intervals for quartz OSL decay curves. *Quaternary Geochronology*, 5, pp. 657-666.

Dalal, N. and Torab, M. (2013). Large boulders deposits on the coast of Ras El Hekma, NW coast, Egypt. Storm or tsunami. In: The 2nd International Symposium on Kaz Mountains (Mount Ida) and Edremit: Human - Environment Interactions and Ecology of Mountain Ecosystems. İzmir, Turkey: Meta Basım, pp. 505-511.

Daveau, S., Almeida, G., Feio, M., Rebelo, F., Silva, E. and Sobrinho, A. (1978). Os temporais de Fevereiro / Março de 1978. *Finisterra*, 13 (26), pp. 236-260.

Dawson, A.G., Hindson, R., Andrade, C., Freitas, C., Parish, R. and Bateman, M. (1995). Tsunami sedimentation associated with the Lisbon earthquake of 1 November AD 1755: Boca do Rio, Algarve, Portugal. *The Holocene*, 5 (2), pp. 209-215.

Dawson, A.G., Dawson, S. and Ritchie, W. (2007). Historical climatology and coastal change associated with the "Great Storm" of January 2005, South Uist and Benbecula, Scottish Outer Hebrides. *Scottish Geographical Journal*, 123 (2), pp. 135-149.

Dean, R.G. and Dalrymple, R.A. (2002). Coastal Processes: with Engineering Applications. Cambridge, United Kingdom: Cambridge University Press, p. 475.

Denny, M.W., Miller, L.P., Stokes, M.D., Hunt, L.J.H. and Helmuth, B.S.T. (2003). Extreme water velocities: Topographical amplification of wave-induced flow in the surf zone of rocky shores. *Limnology and Oceanography*, 48(1), pp. 1-8.

Dias, A.M.A. (2004). A análise sedimentar e o conhecimento dos sistemas marinhos. Faro, Portugal: Published by the author. Available at http://w3.ualg.pt/~jdias/JAD/eb_Sediment.html [accessed 10-12-2016].

Diogo, Z., Bastos, A., Lira, C., Taborda, R., Andrade, C., Silveira, T. M., Ribeiro, M., Silva, A.N., Carapuço, M.M., Pinto, C.A. and Freitas, M.C. (2014a). Morphological impacts of Christina storm on the beaches of the central western portuguese coast. *Comunicações Geológicas*, V101 (III), pp. 1445-1448.

Diogo, Z.S., Lira, C., Bastos, A.P., Silva, A.N., Carapuço, A.M., Taborda, R., Andrade, C.F. and Freitas, M.C. (2014b). Impacto da tempestade Christina nas praias da APA, I.P./ARH Tejo. Supplementary report of the project "Creation and implementation of a Costal Monitoring System for the jurisdiction area of Administração da Região Hidrográfica do Tejo IP. Lisboa, Portugal: Centro de Geologia & Instituto Dom Luiz, p. 78.

Direção Geral dos Edifícios e Monumentos Nacionais (1953). Boletim da Direção Geral dos Edifícios e Monumentos Nacionais nº 74 – Forte da Berlenga. Porto, Portugal: Ministério das Obras Públicas, p. 27.

Direção Geral dos Edifícios e Monumentos Nacionais (1960). Boletim da Direção Geral dos Edifícios e Monumentos Nacionais nº 100 - Monumentos de Sagres. Porto, Portugal: Ministério das Obras Públicas, p. 42.

Dodet, G., Bertin, X. and Taborda, R. (2010). Wave climate variability in the North-East Atlantic Ocean over the last six decades. *Ocean Modelling*, 31, pp. 120-131.

Dominguez-Castro, F., Trigo, R.M., and Vaquero, J.M. (2013). The first meteorological measurements in the Iberian Peninsula: evaluating the storm of November 1724. *Climate Change*, 118, pp. 443-445.

Durcan, J.A. and Duller, G.A.T. (2011). The fast ratio: A rapid measure for testing the dominance of the fast component in the initial OSL signal from quartz. *Radiation Measurements*, 46, pp. 1065-1072.

Ellicot, J. (1755-1756). Extract of Letter VIII to Tilman Henkel concerning the earthquake at Oporto in Portugal. *Philosophical Transactions*, 49, pp. 418-419.

Emery, K.O. and Kuhn, G.G. (1982). Sea cliffs: Their processes, profiles, and classification. *Geological Society of America Bulletin*, 93 (7), pp. 664-654.

Engenheiro, F. (1999). O terramoto de 1755 e outros que, ao longo dos séculos, se fizeram sentir em Peniche. *A Voz do Mar*, 1017, pp. 29.

Engenheiro, F. (2005). Quando o mar galgou a terra em 1755, não poupou Peniche. *A Voz do Mar*, 1150, pp. 8.

Esteves, F. (2011). A Dimensão Marítima e Piscatória do Porto da Ericeira no Século XIX. In: Actas do XIII Curso de Verão da Ericeira. Ericeira, Portugal: ICEA and Academia de Marinha, p. 15.

Esteves, R., Silva, F.S., Pinto, J.P. and Costa, M. (2010). Caracterização de eventos extremos de agitação marítima em Portugal Continental. In: Actas das 1as Jornadas de Engenharia Hidrográfica. Lisboa, Portugal: Instituto Hidrográfico, pp. 205-208.

Etienne, S. (2012). Marine inundation hazards in French Polynesia: geomorphic impacts of Tropical Cyclone Oli in February 2010. In: J. P. Terry and J. Goff, ed., Geological Society Special Publications 361 - Natural Hazards in the Asia–Pacific Region: Recent Advances and Emerging Concepts. Ist edition. Bath, United Kingdom: The Geological Society of London, pp. 21–39.

Etienne, S. and Paris, R. (2010). Boulder accumulations related to storms on the south coast of the Reykjanes Peninsula (Iceland). *Geomorphology*, 114, pp. 55–70.

Etienne, S. and Terry, J.P. (2012). Coral boulders, gravel tongues and sand sheets: Features of coastal accretion and sediment nourishment by Cyclone Tomas (March 2010) on Taveuni island, Fiji. *Geomorphology*, 175-176, pp. 54-65.

Etienne, S., Buckley, M., Paris, R., Nandasena, A.K., Clark, K., Strotz, L., Chagué-Goff, C., Goff, J. and Richmond, B. (2011). The use of boulders for characterizing past tsunamis: lessons from the 2004 Indian Ocean and 2009 South Pacific tsunamis. *Earth Science Reviews*, 107, pp. 76-90.

Felton, E.A. (2002). Sedimentology of rocky shorelines: 1. A review of the problem, with analytical methods, and insights gained from the Hulopoe Gravel and the modern rocky shoreline of Lanai, Hawaii. *Sedimentary Geology*, 152, pp. 221-245.

Ferreira, Ó., Vousdoukas, M. and Ciavola, P. (2009). MICORE Report D.14 - Review of climate change impacts on storm occurrence. MICORE team, p. 123 Available at http://www.micore.eu. [Accessed 21-02-2017]

Ferreira, Ó., Almeida, L.P., Rodrigues, B., and Matias, A. (2010). Determination of thresholds for storm impacts. In: Avances de la Geomorfologia en España, 2008-

2010, XI Reunión Nacional de Geomorfologia. Solsona, Spain: Sociedad Española de Geomorfologia, pp. 35-42.

Fichaut, B. and Suanez, S. (2011). Quarrying, transport and deposition of cliff-top storm deposits during extreme events: Banneg Island, Brittany. *Marine Geology*, 283, pp. 36–55.

Folk, R.L. (1974). Petrology of Sedimentary Rocks. Austin, United States of America: Hemphill Publishing Company, p. 182.

Folk, R.L. and Ward, W.C. (1957). Brazos river bar: a study in the significance of grain size parameters. *Journal of Sedimentary Petrology*, 27 (1), pp. 3-26.

Freitas, J.G. and Dias, J.A. (2013). 1941 windstorm effects on the Portuguese Coast. What lessons for the future? *Journal of Coastal Research*, SI65, pp. 714-179.

Freund, R.J., Wilson, W.J. and Sa, P. (2006). Regression Analysis, statistical Modeling of a Response Variable. 2nd edition. Burlington, MA, United States of America: Academic Press, p. 480.

Galbraith, R.F., Roberts, R.G., Laslett, G.M., Yoshida, H. and Olley, J.M. (1999). Optical dating of single and multiple grains of quartz from Jinmium Rock Shelter, Northern Australia: Part I, experimental design and statistical models. *Archaeometry*, 41, pp. 339-364.

Gama, C., Taborda, R. and Dias, J.A. (1997). Sobreelevação do nível do mar de origem meteorológica (storm surge) em Portugal continental. In: G.S. Carvalho, F.V. Gomes and F.T. Pinto, ed., Colectânea de Ideias sobre a Zona Costeira de Portugal. Porto, Portugal: Associação Eurocoast-Portugal e Instituto da Água, pp. 131-149.

Garibay, E. (1628). Compendio historial de las chronicas y universal historia de todos los reynos de Espanã, donde se ponen en suma los Condes, Senõres de Aragon, con los Reyes del mesmo Reyno: y Condes de Barcelona, y reyes de Napoles y Sicilia, tomo quatro. Barcelona, Spain: impresso por Sebastian de Cormellas, p. 430.

Gelfenbaum, G. and Jaffe, B. (2003). Erosion and sedimentation from the 17 July, 1998 Papua New Guinea tsunami. *Pure and Applied Geophysics*, 160, pp. 1969-1999.

Gilleland, E. and Katz, R.W. (2011). New software to analyze how extremes change over time. *EOS*, 92(2), pp. 13-14.

Gob, F., Petit, F., Bravard, J.-P., Ozer, A. and Gob, A. (2003). Lichenometric application to historical and subrecent dynamics and sediment transport ofa Corsican stream (Figarella River-France). *Quaternary Science Reviews*, 22, pp. 2111–2124.

Goff, J., Dudley, W.C., deMaintenon, M.J., Cain, G. and Coney, J.P. (2006a). The largest local tsunami in 20th century Hawaii. *Marine Geology*, 226, pp. 65-79.

Goff, J., Liu, P L.-F., Higman, B., Morton, R., Jaffe, B.E., Fernando, H., Lynett, P., M.EERI, Friz, H., Synolakis, C. and Fernando, S. (2006b). Sri Lanka Field Survey after the December 2004 Indian Ocean Tsunami. *Earthquake Spectra*, 22(S3), pp. S155-S172.

González-Villanueva, R. (2013). Origin, evolution and processes controlling Holocene barrier-lagoon systems (NW Spain). Doctoral Dissertation. Universidade de Vigo, p. 199.

González-Villanueva, R., Costas, S., Pérez-Arlucea, M., Jerez, S. and Trigo, R.M. (2013). Impact of atmospheric circulation patterns on coastal dynamics, NW Spain. *Geomorphology*, 185, pp. 96-109.

Goto, K., Chavanich, S.A., Imamura, F., Kunthasap, P., Matsui, T., Minoura, K., Sugawara, D. and Yanagisawa, H. (2007). Distribution, origin and transport process of boulders deposited by the 2004 Indian Ocean tsunami at Pakarang Cape, Thailand. *Sedimentary Geology*, 202, pp. 821-837.

Goto, K., Okada, K. and Imamura, F. (2009a). Characteristics and hydrodynamics of boulders transported by storm waves at Kudaka Island, Japan. *Marine Geology*, 262, pp. 14–24.

Goto, K., Okada, K. and Imamura, F. (2009b). Importance of the initial waveform and coastal profile for the tsunami transport of boulders. *Polish Journal of Environmental Studies*, 18, pp. 53–61.

Goto, K., Kawan, T. and Imamura, F. (2010a). Historical and geological evidence of boulders deposited by tsunamis, southern Ryukyu Islands, Japan. *Earth-Science Reviews*, 102, pp. 77-99.

Goto, K., Miyagi, K., Kawamata, H. and Imamura, F. (2010b). Discriminatiion of boulders deposited by tsunamis and storm waves at Ishigaki Island, Japan. *Marine Geology*, 269, pp. 34-45.

Goto, K., Okada, K. and Imamura, F. (2010c). Numerical analysis of boulder transport by the 2004 Indian Ocean tsunami at Pakarang Cape, Thailand. *Marine Geology*, 268, pp. 97–105.

Goto, K., Miyagi, K., Kawana, T., Takahashi, J. and Imamura, F. (2011). Emplacement and movement of boulders by known storm waves - Field evidence from the Okinawa Islands, Japan. *Marine Geology*, 283, pp. 66–78.

Gracia, F.J., Alonso, C., Benavente, J., Anfuso, G., and Del-Río, L. (2006). The different coastal records of the 1755 tsuanmi waves along the south Atlantic Spanish coast. *Zeitschrift für Geomorphologie*, Suppl.-Vol 146, pp. 195-220.

Graham, J. (1988). Collection and analysis of field data. In: M.E. Tucker, ed., Techniques in Sedimentology. Oxford, United Kingdom: John Wiley and Sons Ltd, pp. 5-62.

GranGraf V 2.0β Program for treatment of granulometric data (1998). Faculdade de Ciências da Universidade de Lisboa, Portugal: Developed by Carlos Carvalho.

Guedes, L.C. (1989). Aspectos do Reino de Portugal nos séculos XVI e XVII, A "Descripção de Alexandre Massaii (1621), Tratado II. Lisboa, Portugal: Arquivo Histórico Militar, p. 215.

Hall, A.M. (2011). Storm wave currents, boulder movement and shore platform development: a case study from East Lothian, Scotland. *Marine Geology*, 283, pp. 98–105.

Hall, A.M., Hansom, J.D., Williams, D.M. and Jarvis, J. (2006). Distribution, geomorphology and lithofacies of cliff-top storm deposits: Examples from the high-energy coasts of Scotland and Ireland. *Marine Geology*, 232, pp. 131–155.

Hall, A.M., Hansom, J.D. and Jarvis, J. (2008). Patterns and rates of erosion produced by high energy wave processes on hard rock headlands: The Grind of the Navir, Shetland, Scotland. *Marine Geology*, 248, pp. 28-46.

Hamilton, H.C. (1854). The Geography of Strabo, Volume I. London, United Kingdom: John Childs and Son (Bungay), p. 519.

Hansen, E.S. (2008). The application of lichenometry in dating of glacier deposits. *Geografisk Tidsskrift-Danish Journal of Geography*, 108 (1), pp. 143-151.

Hansom, J.D. and Hall, A.M. (2009). Magnitude and frequency of extra-tropical North Atlantic cyclones: A chronology from cliff-top storm deposits. *Quaternary International*, 195, pp. 42-52.

Hansom, J.D., Barltrop, N.D.P. and Hall, A.M. (2008). Modelling the processes of cliff-top erosion and deposition under extreme storm waves. *Marine Geology*, 253, pp. 36-50.

Harmelin-Vivien, M.L. and Laboute, P. (1986). Catastrophic impact of hurricanes on atoll outer reef slopes in the Tuamotu (French Polynesia). *Coral Reefs*, 5, pp. 55-62.

Hearty, P. (1997). Boulder deposits from large waves during the Last Interglaciation on North Eleuthera Island, Bahamas. *Quaternary Research*, 48, pp. 326-338.

Hedges T.S. and Kirkgoz M.S. (1981). An experimental study of the transformation zone of plunging breakers. *Coastal Engineering*, 5, pp. 353-370.

Helley, E.J. (1969). United States Geological Survey Professional Paper 562-G - Field measurement of the initiation of large bed particles motion in Blue creek near Klamath, California. Washington, United States of America: United States Government Printing Office, p. 19.

Hendricks, A., Subramony, L. and van Blerk, C. (1999). Physics for Engineering. Cape Town, South Africa: Juta and Company Ltd, p. 429.

Hill, D.J. (2002). Measurement of lichen growth. In: I. Kranner, R. Beckett and A. Varma, ed., Protocols in lichenology culturing, biochemistry, ecophysiology and use in biomonitoring. Heidelberg, Germany: Springer, pp. 255-278.

Hindson, R.A. and Andrade, C. (1999). Sedimentation and hydrodynamic processes associated with the tsunami generated by the 1755 Lisbon earthquake. *Quaternary International*, 56, pp. 27-38.

Hindson, R.A., Andrade, C. and Dawson, A.G. (1996). Sedimentary processes associated with the tsunami generated by the 1755 Lisbon earthquake on the Algarve coast, Portugal. *Physics and Chemistry of the Earth*, 21 (12), pp. 57-63.

Hindson, R., Andrade, C. and Parish, R. (1999). A microfaunal and sedimentary record of environmental change within the late Holocene sediments of Boca do Rio (Algarve, Portugal). *Geologie en Mijnbouw*, 77, pp. 311-321.

Hills, E.S. (1970). Fitting, fretting, and imprisoned boulders. *Nature*, 226, pp. 345-347.

IGEO (2010). Ortophotos. Available at WMS server http://mapas.igeo.pt/ortos/2010? [Accessed on 1 May 2016].

Iglesias, O., Lastras, G., Souto, C., Costa, S. and Canals., M. (2014). Effects of coastal submarine canyons on tsunami propagation and impact. *Marine Geology*, 350, pp. 39-51.

Innes, J.L. (1983). Lichenometric dating of debris-flow deposits in the Scottish Highlands. *Earth Surface Processes and Landforms*, 8, pp. 579-588.

Innes, J.L. (1985). Lichenometry. *Progress in Physical Geography*, 9(2), pp. 187-254.

Innes, J.L. (1986). Dating Exposed Rock Surfaces in the Arctic by Lichenometry: The Problem of Thallus Circularity and Its Effect on Measurement Errors. *Arctic*, 39 (3), pp. 253-259.

Inquéritos do Marquês de Pombal (1756). Respostas Paroquiais ao Inquérito do Marquês de Pombal. Arquivo do Ministério do Reino, Maço N. 638. Lisboa, Portugal: Arquivo Nacional da Torre do Tombo.

Instituto Hidrográfico (2010). Tabelas de Maré 2010 - Capítulo III - Informação Suplementar sobre Marés. Lisboa, Portugal: Instituto Hidrográfico, p. 6. Available at: http://www.hidrografico.pt/download-tabelas-mare.php [Accessed 6-11-2012]

Instituto Hidrográfico (2011). Tabelas de Maré 2011 - Capítulo III - Informação Suplementar sobre Marés. Lisboa, Portugal: Instituto Hidrográfico, p. 6. Available at: http://www.hidrografico.pt/download-tabelas-mare.php [Accessed 6-11-2012].

Instituto Hidrográfico (2012). Tabelas de Maré 2012 - Capítulo III - Informação Suplementar sobre Marés. Lisboa, Portugal: Instituto Hidrográfico, p. 6. Available at: http://www.hidrografico.pt/download-tabelas-mare.php [Accessed 6-11-2012].

Instituto Hidrográfico (2013). Tabelas de Maré 2013 - Capítulo III - Informação Suplementar sobre Marés. Lisboa, Portugal: Instituto Hidrográfico, p. 6. Available at: http://www.hidrografico.pt/download-tabelas-mare.php [Accessed 6-11-2012].

Instituto Hidrográfico (2014). Tabelas de Maré 2014 - Capítulo III - Informação Suplementar sobre Marés. Lisboa, Portugal: Instituto Hidrográfic, p.12. Available at: http://www.hidrografico.pt/download-tabelas-mare.php [Accessed 6-11-2012].

Instituto Hidrográfico (2015). Tabelas de Maré 2015 - Capítulo III - Informação Suplementar sobre Marés. Lisboa, Portugal: Instituto Hidrográfico, p. 14. Available at: http://www.hidrografico.pt/download-tabelas-mare.php [Accessed 6-11-2012].

Intergovernmental Oceanographic Commission (2013). Tsunami Glossary - IOC Technical Series 85. Revised Edition. Paris, France: UNESCO, p. 42.

IPCC (2007). Climate Change 2007: The Physical Science Basis. Contribution of Working Group I to the Fourth Assessment Report of the Intergovernmental Panel on Climate Change. New York, United States of America: Cambridge University Press, p. 996.

IPCC (2012). Managing the Risks of Extreme Events and Disasters to Advance Climate Change Adaptation. A Special Report of Working Groups I and II of the Intergovernmental Panel on Climate Change. New York, United States of America: Cambridge University Press, p. 582.

Jaffe, B.E. and Gelfenbaum, G. (2007). A simple model for calculating teunami flow speed from tsunami deposits. *Sedimentary Geology*, 200, pp. 347-361.

Jonasson, C., Kot, M. and Kotarba, A. (1991). Lichenometrical Studies and Dating of Debris Flow Deposits in the High Tatra Mountains, Poland. *Geografiska Annaler. Series A, Physical Geography*, 73 (3/4), pp. 141-146.

Jones, B. and Hunter, I.G. (1992). Very large boulders on the coast of Grand Cayman: the effects of giant waves on rocky coasts. *Journal of Coastal Research*, 8 (4), pp. 763-774.

Justo, J. L. anf Salwa, C. (1998). The 1531 Lisbon earthquake. *Bulletin of the Seismological Society of America*, 88, pp. 319–328.

Kamphuis, J.W. (2000). Introduction to Coastal Engineering and Management. Singapore: World Scientific, p. 447.

Kelletat, D. and Schellmann, G. (2002). Tsunamis on Cyprus-field evidences and ^{14}C dating results. *Zeitschrift für Geomorphologie*, NF 46 (1), pp. 19-34.

Kennedy, D.M., Tannock, K.L., Crozier, M.J. and Rieser, U. (2007). Boulders of MIS 5 age deposited by a tsunami on the coast of Otago, New Zealand. *Sedimentary Geology*, 200, pp. 222–231.

Knight, J., and Burmingham, H. (2011). Boulder dynamics on an Atlantic-facing rock coastline, northwest Ireland. *Marine Geology*. 283 (1–4), pp. 56–65.

Knight, J., Burningham, H. and Barret-Mold, C. (2009). The geomorphology and controls on development of a boulder-strewn rock platform, NW Ireland. *Journal of Coastal Research*, SI56, pp. 1646-1650.

Komar, P.D. (1976). Beach Processes and Sedimentation. 2nd edition. Englewood Cliffs, United States of America: Prentice-Hall, Inc., p. 429.

Komar, P.D. (1989). Flow-competence evaluations of the hydraulic parameters of floods: an assessment of the technique. In: K. Beven and P. Carling, ed., Floods: Hydrological, Sedimentological, and Geomorphological Implications. Chichester, United Kingdom: John Wiley and Sons, pp. 107–133.

Kortekaas, S. and Dawson, A.G. (2007). Distinguishing tsunami and storm deposits: An example from Martinhal, SW Portugal. *Sedimentary Geology*, 200, pp. 208-221.

Kotz, S. and Nadarajah, D. (2000). Extreme value distribution, Theory and applications. London, United Kingdom: Imperial College Press, p. 196.

Krumbein, W.C. (1941). Measurement and geological significance of shape and roundness of sedimentary particles. *Journal of Sedimentary Petrology*, 11 (2), pp. 64-72.

Kullberg, J.C., Rocha, R.B., Soares, A.F., Rey, J., Terrinha, P., Callapez, P. and Martins, L. (2006). A Bacia Lusitaniana: Estratigrafia, Paleogeografia e Tectónica. In: R. Dias, A. Araújo, P. Terrinha and J.C. Kullberg, ed., Geologia de Portugal no contexto da Ibéria. Évora, Portugal: Universidade de Évora, pp. 317-368.

Kusky, T.M. (2010). Rocky Coasts. In: Encyclopedia of Earth and Space Science. New York, United States of America: Facts of File, pp. 98-99.

Lange, W.P, Lange, P.J. and Moon, V.G. (2006). Boulder transport by waterspouts: An example from Aorangi Island, New Zealand. *Marine Geology*, 230, pp. 115-125.

Lau, A.Y.A, Terry, J.P., Switzer, A.D. and Pile, J. (2015). Advantages of beachrock slabs for interpreting high-energy wave transport: Evidence from Ludao Island in south-eastern Taiwan. *Geomorphology*, 228, pp. 263-274.

Leal, A.S.A.V.P. (1874). Portugal antigo e moderno; diccionario geographico, estatistico, chorographico, heraldico, archeologico, historico, biographico e etymologico de todas as cidades, villas e freguezias de Portugal e de grande numero

de aldeias, Volume 2. Lisboa, Portugal: Livraria editora de Mattos Moreira & Companhia, p. 494.

Lopes, J.B.S. (1841). Corografia ou Memória Económica, Estatística e Topográfica do Reino do Algarve. Lisboa, Portugal: Typografia da Academia das Sciencias de Lisboa, p. 528.

Lorang, M.S. (2000). Predicting threshold entrainment mass for a boulder. *Journal of Coastal Research*, 16 (2), pp. 432-445.

Lorang, M.S. (2002). Predicting the crest heights of a gravel beach. *Geomorphology*, 48, pp. 87-101.

Lorang, M.S. (2011). A wave-competence approach to distinguish between boulder and megaclast deposits due to storm waves versus tsunamis. *Marine Geology*, 283, pp. 90-97.

Lowe, J.J. and Walker, M.J.C. (1984). Reconstructing Quaternary Environments. 1st Edition. London, United Kingdom: Longman, p. 404.

Machado, J.L.S. (2009). O Forte de S. Miguel Arcanjo, Monumento Histórico-Militar do séc. XVII. Lisboa, Portugal: Edições Colibri and Câmara Municipal da Nazaré, p. 94.

Mahaney, W.C. (1973). Neoglacial chronology in the Fourth of July Cirque, Central Colorado Front Range. *Geological Society of America Bulletin*, 84, pp. 161-170.

Maouche, S., Morhange, C. and Meghraoui, M. (2009). Large boulder accumulation on the Algerian coast evidence tsunami events in the western Mediterranean. *Marine Geology*, 262, pp. 96-104.

Maramai, A., Brizuela, B. and Graziani, L. (2014). The Euro-Mediterranean Tsunami Catalogue. *Annals of Geophysics*, 57 (4), pp. S0435.

Maria, F. S. (1744). Anno historico, Diario portuguez, noticia abreviada de pessoas grandes, e cousas notaveis de Portugal, Tomo I. Lisboa, Portugal: Na Officina e à custa de Domingos Gonsalves, p. 735.

Marques, F.M.S.F. (1997). As Arribas do Litoral do Algarve – Dinâmica, processos e mecanismos. Doctoral Dissertation, Universidade de Lisboa, p.556.

Marques, M.S. (2001). Cartografia antiga: tabela de equivalências de medidas: cálculo de escalas e conversão de valores de coordenadas geográficas. Lisboa, Portugal: Biblioteca Nacional, p. 102.

Martins, I. and Victor, L. A.M. (2001). Contribution to the Study of Seismicity in the West Margin of Iberia. Lisboa, Portugal: Universidade de Lisboa and IGIDL Pub 25.

Mascarenhas, J.F.M. (1723) Algarve Villa nova de Portimão 3 de janeiro. *Gazeta de Lisboa*, nº2, pp. 15-16.

Mascarenhas, J.F.M. (1756). Ericeria. *Gazeta de Lisboa*, nº11, pp. 87.

Mass, G.S. and Macklin, M.G. (2002). The impact of recent climate change on flooding and sediment supply within a mediterranean mountain catchment, soutwestern Crete, Greece. *Earth Surface Processes and Landforms*, 27, pp. 1087-1105.

Massel, S.R. and Done, T.J. (1993). Effects of cyclone waves on massive coral assemblages on the Great Barrier Reef: meteorology, hydrodynamics and demography. *Coral Reefs*, 12, pp. 153-166.

Mastronuzzi, G. and Sansò, P. (2000). Boulders transport by catastrophic waves along the Ionian coast of Apulia (southern Italy). *Marine Geology*, 170, pp. 93-103.

Mastronuzzi, G. and Sansò, P. (2004). Large boulder accumulations by extreme waves along the Adriatic coast of southern Apulia (Italy). *Quaternary International*, 120, pp. 173–184.

Mastronuzzi, G., Pignatelli, C., Sansò, P and Selleri, G. (2007). Boulder accumulations produced by the 20th of February, 1743 tsunami along the coast of southeastern Salento (Apulia region, Italy). *Marine Geology*, 242, pp. 191-205.

Mateus, M.F.R.C. (1999). Fortificações da região de Peniche. Master Dissertation. Universidade de Lisboa, p. 224.

Matsuyama, M., Walsh, J.P. and Yeh, H. (1999). The effect of bathymetry on tsunami characteristics at Sisano Lagoon, Papua New Guinea. *Gephysical Research Letters*, 26 (23), pp. 3513-3516.

Matulla, C., Schöner, W., Alexandersson, H., von Storch, H. and Wang, X.L. (2008). European storminess: late nineteenth century to present. *Climate Dynamics*, 31 (2), pp. 125-130.

McCarthy, D.P. (1999). A biological basis for lichenometry? *Journal of Biogeography*, 26, pp. 379-386.

McFadgen, B.G. and Yaldwyn, J.C. (1984). Holocene sand dunes on Enderby Island, Auckland Islands. *New Zealand Journal of Geology & Geophysics*, 27, pp. 27-33.

McKenna, J., Jackson, D.W.T. and Cooper, J.A.G. (2011). In situ exhumation from bedrock of large rounded boulders at the giant's Causeway, Northern Ireland: An alternative genesis for large boulders (mega-clasts). *Marine Geology*, 283, pp. 25-35.

Mendonça, J.J.M. (1758). Historia Universal dos terremotos que tem havido no mundo de qua há noticia, desde a sua creação até o seculo presente: com huma narraçam individual do terremoto de Novembro de 1755, e noticia verdadeira dos seus effeitos em Lisboa, todo Portugal: E huma dissertação physica sobre as causas geraes dos terremotos, seus effeitos, differenças e Prognosticos; e as particularidades do ultimo. Lisboa, Portugal: Na Offic. De Antonio Vicente da Silva, p. 272.

Mesquita, J.C.V. (2000). Sagres um lugar na história e no património universal. 1st edition. [pdf] Faro, Portugal: AJEA Edições, p. 19. Available at http://sapientia.ualg.pt/handle/10400.1/4514 [acessed 8 July 2016].

Mezcua, J. (1982). Catalogo general de isossiestas de la Peninsula Ibérica. Madrid, Spain: Instituto Geografico Nacional, p. 61.

Mezcua, J. and Solares, J.M.M. (1983). Sismicidad del Area Ibero-Mogrebi. Presidencia del Gobierno. Madrid, Spain: Instituto Geografico Nacional, p. 210.

Mhammdi, N., Medina, F., Kelletat, D., Ahmamou, M. and Aloussi, L. (2008). Large boulders along the Rabat coast (Morocco): Possible emplacements by the November, 1st, 1755 A.D. tsunami. *Science of Tsunami Hazards*, 27 (1), pp. 17-30.

Mineiro, A.C. (2005). A propósito das medidas de remediação e da opção política de reedificar a Cidade de Lisboa sobre os seus escombros, após o sismo de 1 de Novembro de 1755: Reflexões. In: FLAD and PÚBLICO ed., O grande terramoto de Lisboa, Volume 1 Descrições. Lisboa, Portugal: FLAD and PÚBLICO, pp. 188-217.

Miranda, J., Batlló, J., Ferreira, H., Matias, L.M. and Baptista, M.A. (2012). The 1531 Lisbon earthquake and tsunami. In Proceedings of the 15 World Conference on Earthquake Engineering. Lisboa, Portugal: IAEE, p. 9. Available at http://www.iitk.ac.in/nicee/wcee/article/WCEE2012_0685.pdf [Accessed 19 September 2016]

Molloy, Mr. (1761). Another Account of the Same Earthquake: In a Letter from Mr. Molloy, Dated There April 3, 1761, to Keane Fitzgerald, Esq; F. R. S. *Philosophical Transactions*, 52, pp. 142-143.

Moore, D.S., McCabe, G.P. and Craig, B.A. (2009). Introduction to the practice of statistics. 6th edition. New York, United States of America: W.H. Freeman and Company, p. 709.

Moreira, V.S. (1988). Historical and recent tsunamis in the European Area. *Science of Tsunami Hazards*, 6, pp. 37-42.

Morhange, C., Marriner, N. and Pirazzoli, P.A. (2006). Evidence of Late-Holocene tsunami events in Lebanon. *Zeitschrift für Geomorphologie*, NF 146, pp. 81-95.

Morton, R.A., Richmond, B.M., Jaffe, B.E. and Gelfenbaum, G. (2006). Reconnaissance investigation of Caribbean extreme wave deposits – preliminary observations, interpretations, and research directions, Open-File Report 2006-1293. [online]. St. Petersburg, United States of America: U.S. Geological Survey, p. 41. Available at https://pubs.usgs.gov/of/2006/1293/ [Acessed 8 February 2016].

Morton, R.A., Richmond, B.M., Jaffe, B.E. and Gelfenbaum, G. (2008). Coarse-clast ridge complexes of the Caribean: A preliminary basis for distinguishing tsunami and storm-wave origins. *Journal of Sedimentary Research*, 78, pp. 624-637.

Moses, C., Robinson, D., and Barlow, J. (2014). Methods for measuring rock surface weathering and erosion: A critical review. *Earth-Science Reviews*, 135, pp. 141-161.

Muir-Wood, R. and Mignan, A. (2009). A Phenomenological Reconstruction of the Mw9 November 1st 1755 Earthquake Source. In: L.A. Mendes-Victor, C.S. Oliveira, J. Azevedo and A. Ribeiro, ed., The 1755 Lisbon Earthquake: Revisited. Cham, Switzerland: Springer, pp. 121-146.

Murray, A.S. and Wintle, A.G. (2000). Luminescence dating of quartz using an improved single-aliquot regenerative-dose protocol. *Radiation Measurements*, 32, pp. 57-73.

Murray, A.S. and Wintle, A.G. (2003). The single aliquot regenerative dose protocol: potential for improvements in reliability. *Radiation Measurements*, 37, pp. 377-381.

Nakamura, M., Arashiro, Y. and Shiga. S. (2014). Numerical simulations to account for boulder movements on Lanyu Island, Taiwan: tsunami or storm? *Earth, Planets and Space*, 66 (1), pp. 1-20.

Nandasena, N.A.K., Paris, R. and Tanaka, N. (2011a). Reassessment of hydrodynamic equations: Minimum flow velocity to initiate boulder transport by high energy events (storms, tsunamis). *Marine Geology*, 281, pp. 70-84.

Nandasena, N.A.K., Paris, R. and Tanaka, N. (2011b). Numerical assessment of boulder transport by the 2004 Indian ocean tsunami in Lhok Nga, West Banda Aceh (Sumatra, Indonesia). *Computers & Geosciences*, 37(9), pp. 1391-1399.

National Geophysical Data Center/World Data Service (2016): Global Historical Tsunami Database. National Geophysical Data Center, NOAA. Available at https://www.ngdc.noaa.gov/metaview/page?xml=NOAA/NESDIS/NGDC/MGG/Hazards/iso/xml/G02151.xml&view=getDataView&header=none [Accessed 27 October 2016]

Noller, J.S. and Locke, W.W. (2000). Lichenometry. In: J.S. Noller, J.M. Sowers and W.R. Lettis, ed., Quaternary Geochronology Methods and Applications, AGU Reference Shelf 4. Washington, United States of America: American Geophysical Union, pp. 261-272.

Noormets, R., Felton, E.A. and Crook, K.A.W. (2002). Sedimentology of rocky shorelines: 2 Shoreline megaclasts on the north shore of Oahu, Hawaii-origins and history. *Sedimentary Geology*, 150, pp. 31-45.

Noormets, R., Crook, K.A.W. and Felton, E.A. (2004). Sedimentology of rocky shorelines: 3. Hydrodynamics of megaclast emplacement and transport on a shore platform, Oahu, Hawaii. *Sedimentary Geology*, 172, pp. 41–65.

Nott, J. (1997). Extremely high wave deposits inside the Great Barrier Reef, Australia: determining the cause-tsunami or tropical cyclone. *Marine Geology*, 141, pp. 193–207.

Nott, J. (2000). Records of prehistoric tsunamis from boulder deposits evidence from Australia. *Science of Tsunami Hazards*, 18 (1), pp. 3-14.

Nott, J. (2003). Waves, coastal boulder deposits and the importance of the pre-transport setting. *Earth and Planetary Science Letters*, 210, pp. 269-276.

Nott, J. (2004). The tsunami hypothesis—comparisons of the field evidence against the effects, on the Western Australian coast, of some of the most powerful storms on Earth. *Marine Geology*, 208, pp. 1 – 12.

Nozes, J. (1990). The Lisbon earthquake of 1755-British accounts: Anthology of accounts of the XVIIIth century. Lisboa, Portugal: The British Historical Society of Portugal & Lisóptima, Lda., p. 277.

Oak, H.L. (1984) The Boulder Beach: A Fundamentally Distinct Sedimentary Assemblage. *Annals of the Association of American Geographers*, 74 (1), pp. 71-82.

Oliveira, M.A., Andrade, C., Freitas, M.C., Costa, P., Taborda, R., Janardo, C. and Neves, R. (2011). Transport of large boulders quarried from shore platforms of the Portuguese west coast. *Journal of Coastal Research*, SI64, pp. 1871-1875.

Oliveira, M.A., Luis, J.F., Andrade, C.F., Costa, P.J.M. and Freitas, M.C. (2015). Extreme marine event transport and deposition: Crossing historical, geological and oceanographic records with tsunami modelling. In: XIX International Union for Quaternary Research (INQUA) Congress. Nagoya, Japan: INQUA, p. 1.

Osório, B. (1919). O terramoto de Lisboa de 1531, Separata do Boletim da Segunda Classe, volume XII. Coimbra, Portugal: Imprensa da Universidade, p. 12.

Oumeraci, H. (2008). Solutions for Coastal Engineers. Available at www.lwi.tu-bs.de.

Papadopoulos, G.A. and Imamura, F. (2001). A proposal for a new tsunami intensity scale. In: Proceedings of the 2001 International Tsunami Symposium. [online] Seattle, United States of America: ITS 2001, pp. 569–577. Available at http://nthmp-history.pmel.noaa.gov/its2001/Separate_Papers/5-01_Papadopoulos.pdf [Acessed 23 July 2014]

Paris, R., Lavigne, F., Wassmer, P. and Sartohadi, J. (2007). Coastal sedimentation associated with the December 26, 2004 tsunami in Lhok Nga, west Banda Aceh (Sumatra, Indonesia). *Marine Geology*, 238, pp. 93-106.

Paris, R., Wassmer, P., Sartohadi, J., Lavigne, F., Barthomeuf, B., Desgages, E., Grancher, D., Baumert, P., Vautier, F., Brunstein, D. and Gomez, C. (2009). Tsunamis as geomorphic crises: Lessons from the December 26, 2004 tsunami in Lhok Nga, West Banda Aceh (Sumatra, Indonesia). *Geomorphology*, 104, pp. 59-72.

Paris, R., Fournier, J., Poizot, E., Etienne, S., Morin, J., Lavigne, F. and Wassmer, P. (2010). Boulder and fine sediment transport and deposition by the 2004 tsunami in Lhok Nga (western Banda Aceh, Sumatra, Indonesia): A coupled offshore–onshore model. *Marine Geology*, 268, pp. 43–54.

Paris, R., Naylor, L.A. and Stephenson, W.J. (2011). Boulders as a signature of storms on rock coasts. *Marine Geology*, 283, pp. 1-11.

Pereira, J., Monteiro, V. and Oliveira, C.S. (1986). A sismicidade Histórica e a Revisão do Catalogo Sísmico. Lisboa, Portugal: Laboratório Nacional de Engenharia Civil, p. 192.

Pérez-Alberti, A., Trenhaile, A.S., Pires, A., López-Bedoya, J., Chaminé, H.I. and Gomes, A. (2012). The effect of boulders on shore platform development and morphology in Galicia, north west Spain. *Continental Shelf Research*, 48, pp. 122–137.

Perrey, A. (1847). Sur les tremblements de terre de la Péninsule Ibérique. *Annales des sciences physiques et naturelles, d'agriculture et d'industrie*, Tome X, pp. 461–514.

Pires, H.N.O. and Pessanha, L.E.V. (1986). Estima da distribuição de probabilidade dos valores extremos, utilizando séries climatológicas curtas. *Separata da Revista do Instituto Nacional de Meteorologia e Geofísica*, 4 (3-4), pp. 3-25.

Potter, P.E and Pettijohn, F.J. (1977). Paleocurrents and basin analysis. Heidelberg, Germany: Springer-Verlag, p. 425.

Prescott, J.R. and Hutton, J.T. (1994). Cosmic ray contributions to dose rates for luminescence and ESR dating: large depths and long-term time variations. *Radiation Measurements*, 23, pp. 497-500.

Priest, S.D. (1993). Discontinuity Analysis for Rock Engineering. Hong Kong, China: Springer-Science & Business Media, p. 473.

Prudêncio, M.I., Marques, R., Rebelo, L., Cook, G.T., Cardoso, G.O., Naysmith, P., Freeman, S.P.H.T., Franco, D., Brito P., and Dias, M.I. (2007). Radiocarbon and blue optically stimulated luminescence chronologies of the Oitavos consolidated dune (western Portugal). *Radiocarbon*, 49 (2), pp. 1145-1151.

Quaresma, A.M. (2007). Alexandre Massai, a "escola italiana" de engenharia militar no litoral Alentejano (séculos XVI e XVII). Sines, Portugal: Centro Cultural Emmerico Nunes, p. 95.

R: A language and environment for statistical computing (2016). Vienna, Austria: R Foundation for Statistical Computing. Available at https://www.R-project.org/ [Accessed 24 February 2017].

Ramalho, M.M., Rey, J., Zbyszewski, G., Alvez, C.A.M., Palácios, T., Almeida, F.M., Costa, C. and Kullberg. M. (2001). Notícia explicativa da folha 34-C Cascais. Lisboa, Portual: Instituto Geológico e Mineiro, p. 104.

Ramalho, R.S., Winckler, G., Madeira, J., Helffrich, G.R., Hipólito, A., Quartau, R., Adena, K. and Schaefer, J.M. (2015). Hazard potential of volcanic flank collapses raised by new megatsunami evidence. *Science Advances*, 1(9), p. 10.

Ramos-Pereira, A. and Angelucci, D.E. (2004). Formações dunares no litoral português, do final do plistocénico e inícios do Holocénico, como indicadores paleoclimáticos e paleogeográficos. In A. A. Tavares, M. J. Ferro Tavares e J. L. Cardoso, ed., Evolução geohistórica do litoral português e fenómenos correlativos. Geologia, História, Arqueologia e Climatololgia. Lisboa, Portugal: Universidade Aberta, pp. 221-256.

Ramos-Pereira, A., Trindade, J., Neves. M. and Borges, B. (2009). Indicadores geomorfológicos de tsunamino Parque Natural do SW Alentejano e Costa Vicentina (Malhão). *Publicações da Associação Portuguesa de Geomorfólogos*, VI, pp. 51-56.

Reeve, D., Chadwick, A. and Fleming, C. (2004). Coastal Engineering: Processes, theory and design practice. Abingdon, United Kingdom: Spon Press, p. 461.

Rebêlo, L., Costas, S., Brito, P., Ferraz, M., Prudêncio, M.I. and Burbidge, C. (2013). Imprints of the 1755 tsunami in the Tróia Peninsula shoreline, Portugal. *Journal of Coastal Research*, SI65, pp. 814-819.

Regnauld, H., Oszwald, J., Planchon, O., Pignatelli, C., Piscitelli, A., Mastronuzzi, G. and Audevard, A. (2010). Polygenetic (tsunami and storm) deposits? A case study from Ushant Island, western France. *Zeitschrift für Geomorphologie*, 54 (Suppl.), pp. 197–217.

Resende, G. (1554). Miscelânia e Variedade de Histórias, Costumes, casos e cousas que em seu tempo aconteceram. 1917 Edition. Coimbra, Portugal: França Amado Editor, p. 165.

Rey, J. (1972). Recherches géologiques sur le Crétacé inferieur de l'Estremadura (Portugal). *Memórias dos Serviços Geológicos de Portugal*, Nova Série 21, p. 477.

Rey, J., 2007. Stratigraphie séquentielle et séquences de dépôt dans le Crétacé inférieur du Bassin Lusitanien. *Ciências da Terra (UNL)*. Vol Esp VI, p. 120.

Rey, J., Gracinsky, P.C. and Jacquin, T. (2003). Les sequences de depot dans le Crétacé inférieur du Bassin Lusitanien. *Comunicações do Instituto Geológico e Mineiro*, 90, pp. 15-42.

Ribeiro, A., Oliveira, J.T., Ramalho, M., Ribeiro. M.L. and Silva, L. (1987). Notícia Explicativa da Folha 48-D Bordeira da carta geológica de Portugal na escala de 1/50000. Lisboa, Portugal: Serviços Geológicos de Portugal, p. 30.

Ribeiro, M.S.A. (2013). Advance training course Report: Wave propagation modelling. Lisboa, Portugal: Faculdade de Ciências da Universidade de Lisboa, p. 25.

Richmond, B.M., Buckley, M., Etienne, S., Chagué-Goff, C., Clark, K., Goff, J., Dominey-Howes, D. and Strotz, L. (2011a). Deposits, flow characteristics, and landscape change resulting from the September 2009 South Pacific tsunami in the Samoan islands. *Earth-Science Reviews*, 107 (1-2), pp. 38-51.

Richmond, B.M., Watt, S., Buckley, M., Jaffe, B.E., Gelfenbaum, G. and Morton, R.A., (2011b). Recent storm and tsunami coarse-clast deposit characteristics, southeast Hawai'i. *Marine Geology*, 283 (1-2), pp. 79-89.

Rocha, R.B., Ramalho, M.M., Manuppella, G., Zbyszewski, G. and Coelho, A.V.P. (1979). Notícia explicativa da Folha 51-B Vila do Bispo da carta geológica de Portugal na escala de 1/50000. Lisboa, Portugal: Serviços Geológicos de Portugal, p. 118.

Rocha, R.B., Ramalho, M.M., Antunes, M.T. and Coelho, A.V.P. (1983). Notícia explicativa da Folha 52-A Portimão da carta geológica de Portugal na escala de 1/50000. Lisboa, Portugal: Serviços Geológicos de Portugal, p. 57.

Rocha, R.B., Marques, B.L., Antunes, M.T. and Pais, J. (1989). Notícia Explicativa da Folha 52-B Albufeira da carta geológica de Portugal na escala de 1/50000. Lisboa, Portugal: Serviços Geológicos de Portugal, p. 36.

Rodnight, H. (2008). How many equivalent dose values are needed to obtain a reproducible distribution? *Ancient TL*, 26, pp. 3-9.

Rodriguez, J.G. (1932-40). Catálogo sísmico de la zona comprendida entre los meridianos 5º E. y 20º W. de Greenwich y los paralelos 45º y 25º N, Tomo I. Madrid, Spain: Dirección General del Instituto Geográfico, Catastral y de Estadística, p. 807.

Roux, C. and Egea, J.M. (1992). L'opegraphetum durieui Egea et Roux ass. Nov., une association lichénique saxicole-calcicole, Halophile. Cryptogamie - Bryologie *Lichenologie*, 13 (2), pp. 105-115.

Saintilan, N., and Rogers, K. (2005). Recent storm boulders on the Beecroft Peninsula, New South Wales, Australia. *Geographical Research*, 43, pp. 429-432.

Sanches, A.N.R. (1757). Tratado da conservaçam da saude dos povos. Paris, France: Oficina de Joseph Filippe, p. 568.

Sandoval, F.P. (1560-1620). Historia del Emperador Carlor V, Rey de España., Tomo V, Livro XIX. 1847 Edition. Madrid, Spain: Est tipográfico-Literario-Universal, p. 394.

Santos, A. and Koshimura, S. (2015). The Historical Review of the 1755 Lisbon Tsunami. *Journal of Geodesy and Geomatics Engineering*, 1, pp. 38-52.

Santos, A., Zêzere, J., L. and Agostinho, R. (2011). O tsunami de 1755 e a avaliação da perigosidade em Portugal continental, In: Actas do VIII Congresso da Geografia Portuguesa, Repensar a Geografia para Novos Desafios: Competências, Investigação, Acção. Lisboa, Portugal: APG, p. 6.

Santos, A., Mendes, S. and Corte-Real, J. (2014). Impacts of the storm Hercules in Portugal. *Finisterra*, XLIX (98), pp. 197-220.

Scheffers, A. (2004). Tsunami imprints on the Leeward Netherlands Antilles (Aruba, Curaçao, Bonaire) and their relation to other coastal problems. *Quaternary International*, 120, pp. 163-172.

Scheffers, A. and Kelletat, D. (2005). Tsunami relics on the coastal landscape west of Lisbon, Portugal. *Science of Tsunami Hazards*. 23 (1), pp. 3-16.

Scheffers, A. and Scheffers, S. (2006). Documentation of the impact of hurricane Ivan on the coastline of Bonaire (Netherlands Antilles). *Journal of Coastal Research*, 22, pp. 1437–1450.

Scheffers, A. and Scheffers, S. (2007). Tsunami deposits on the coastline of West Crete (Greece). *Earth and Planetary Science Letters*, 259, pp. 613–624.

Scheffers, A., Kelletat, D., Vött, A., May, S.M. and Scheffers, S. (2008). Late Holocene tsunami traces on the western and southern coastlines of the Peloponnesus (Greece). *Earth and Planetary Science Letters*, 269, pp. 271–279.

Scheffers, A., Scheffers, S., Kelletat, D. and Browne, T. (2009). Wave-emplaced coarse debris and megaclasts in Ireland and Scotland: Boulder transport in a high-energy littoral environment. *The Journal of Geology*, 117, pp. 553-573.

Scicchitano, G., Monaco, C. and Tortorici, L. (2007). Large boulder deposits by tsunami waves along the Ionian coast of south-eastern Sicily (Italy). *Marine Geology*, 238, pp. 75-91.

Severino, C.M.M. (2014). De Sagres a Tróia - Fortalezas 1580-1680. Master Dissertation, Universidade de Évora, p. 119.

Shah-hossini, M., Morhange, C., Beni, A.N., Marriner, N., Lahijani, H., Hamzeh, M. and Sabatier, F. (2011). Coastal boulders as evidence for high-energy waves on the Iranian coast of Makran. *Marine Geology*, 290, pp. 17-28.

Sillmann, J. (2009). Extreme climate events and Euro-Atlantic atmospheric blocking in present and future climate model simulations. Doctoral Dissertation, Max Planck Institute for Meteorology, p. 89.

Silva, J.d'O.L. (2002). Anais da Vila da Ericeira. Mafra, Portugal: Câmara Municipal de Mafra, p. 177.

Silva, P.F.T. (2013). O restauro da Fortaleza de Sagres no Estado Novo, *VOX MUSEI arte e patrimônio*, 2 (3), pp. 190-198.

Silveira, T., Taborda, R., Andrade, C., Silva, A.N, and Carapuço, A.M. (2013). Caracterização do clima de agitação junto à costa. Relatório Técnico, Projeto Criação e implementação de um sistema de monitorização no litoral abrangido pela área de jurisdição da Administração da Região Hidrográfica do Tejo. FFCUL/APA, I.P., p. 53. Available at: http://sniamb.apambiente.pt/infos/geoportaldocs/Politicas/Agua/Ordenamento/SistemasMonitorizacaoLitoral/E_1.1.7.b_Clima_agitao_costa.pdf [Accessed 25-04-2017].

Sipman, H. and Raus, T. (1999). A lichonological comparison of the Paros and Santorini island groups (Aegean, Greece), with annotated checklist. *Willdenowia*, 29, pp. 239-297.

Smith, D.I. (1978). The micro erosion meter: its application to the weathering of rock surfaces. In: Proceedings of the International Workshop on the Conservation of Rock Art. Perth, Australia: Institute for the Conservation of Cultural Material, pp. 44-53.

Soares, A. M., Moniz, C. and Cabral, J. (2006). A Duna Consolidada de Oitavos (a Oeste de Cascais - Região de Lisboa) - a sua Datação pelo Método de Radiocarbono. *Comunicações Geológicas*, 93, pp. 105-118.

Soares, C.G. and Henriques, A.C. (1994). Long term predictions of significant wave heights at Sines and Faro. In: Proceedings of the LITTORAL 94, Vol. I: Lisboa, Portugal: EUROCOAST Association, pp. 343-356.

Sorrel, P., Debret, M., Billeaud, I., Jaccard, S.L., McManus, J.F. and Tessier, B. (2012). Persistent non-solar forcing of Holocene storm dynamics in coastal sedimentary archives. *Nature Geoscience*, 5 (12), pp. 892-896.

Sousa, F.L.P. (1916). Sur les mègasismes au XVIIIe siècle dans les environs de l'effondrement en ovalse lusitano-hispano-marocain. *Comptes Rendus de l'Académie des Sciences de Paris*, T163, pp. 709-711.

Sousa, F.L.P. (1919). O terremoto do 1º de Novembro de 1755 em Portugal e um estudo demográfico: Volume I Distritos de Faro, Beja e Évora. Lisboa, Portugal: Serviços Geológicos, p. 277.

Sousa, F.L.P. (1928). O terremoto do 1º de Novembro de 1755 em Portugal e um estudo demográfico: Volume III Distrito de Lisboa. Lisboa, Portugal: Serviços Geológicos, p. 472.

Sousa, M.F. (1678-80). Evropa Portuguesa. Segvnda Edicion Correta, ilvstrada e Añadida en santos lugares, y com tales que os labor nueva, Tomo I. Lisboa, Portugal: en la Officina de Antonio Craesbeeck de mello Impressor de sua Alteza, p. 491.

Spiske, M. and Bahlburg, H. (2011). A quasi-experimental setting of coarse clast transport by the 2010 Chile tsunami (Bucalemu, Central Chile). *Marine Geology*, 289, pp. 72-85.

Stephenson, W.J. and Finlayson, B.L. (2009). Measuring erosion with the micro-erosion meter-Contributions to understanding landform evolution. *Earth-Science Reviews*, 95, pp. 53–62.

Suanez, S., Fichaut, B. and Magne, R. (2009). Cliff-top storm deposits on Banneg Island, Brittany, France: Effects of giant waves in the Eastern Atlantic Ocean. *Sedimentary Geology*, 220, pp. 12–28.

Süssmilch, C. A. (1912). Notes on some recent marine erosion at Bondi. *Royal Society of New South Wales Journal and Proceedings*, 46, pp. 155-158.

Suzuki, A., Yokoyama, Y., Kan, H., Minoshima, K., Matsuzaki, H., Hamanaka, N. and Kawahata, H. (2008). Identification of 1771 Meiwa Tsunami deposits using a combination of radiocarbon dating and oxygen isotope microprofiling of emerged massive Porites boulders. *Quaternary Geochronology*, 3, pp. 226-234.

Switzer, A.D. and Burston, J.M. (2010). Competing mechanisms for boulder deposition on the southeast Australian coast. *Geomorphology*, 114, pp. 42-54.

Taborda, R. and Dias, J.M.A. (1992). Análise da sobreelevação do nível do mar de origem meteorológica durante os temporais de Fevereiro/Março de 1978 e Dezembro de 1981. *Geonovas*. Nº Especial 1 "A Geologia e o Ambiente", pp. 89-97.

Terry, J.P. and Goff., J. (2014). Megaclasts: Proposed revised nomenclature at the coarse end of the Udden-Wentworth grain-size scale for sediment particles. *Journal of Sedimentary Research*, 84, pp. 192-197.

Terry, J.P., Dunne, K. and Jankaew, K. (2016). Prehistorical frequency of high-energy marine inundation events driven by typhoons in the Bay of Bangkok (Thailand), interpreted from coastal carbonate boulders. *Earth Surface Processes and Landforms*, 41, pp. 553–562.

Trudgill, S.T., Crabtree, R.W. and Walker, P.J.C. (1979). The age of exposure of limestone pavements - a pilot lichenometric study in Co. Clare, Eire. *Transactions of the British Cave Research Association*, 6 (1), pp. 10-14.

U.S. Army Corps of Engineers (1984). Shore Protection Manual, Volume II. Washington, United States of America: Coastal Engineering Research Center, p. 644.

U.S. Army Corps of Engineers (2008). Coastal Engineering Manual, Part II, Chapter 1 – Water Wave Mechanics. Washington, United States of America: U.S. Army Corps of Engineers, p. 127.

Unknown (1761). An Account of the Earthquake at Lisbon, 31st March 1761: In a Letter from Thence, Dated the 2d April 1761, to Joseph Salvador, Esq; F. R. S. *Philosophical Transactions*, 52, pp. 141-142.

Vacchi, M., Rovere, A., Zouros, N. and Firpo, M. (2012). Assessing enigmatic boulder deposits in NE Aegean Sea: importance of historical sources as tool to support hydrodynamic equations. *Natural Hazards and Earth System Sciences*, 12, pp. 1109-1118.

van der Meer, J.W. (1987). Stability of Breakwater Armour Layers - Design Formulae. *Coastal Engineering*, 11, pp. 219-239.

van der Meer J.W. (1988). Rock slopes and gravel beaches under wave attack. Doctoral Dissertation. Delft University of Technology, p.152.

van der Meer, J.W. (1998). Application and stability criteria for rock and artificial units. In: K. Pilarczyk ed., Dikes and Revetments: Design, Maintenance and Safety Assessment. Rotterdam, the Netherlands: A. A. Balkema, pp. 191-216.

Vieira, R., Antunes, C. and Taborda, R. (2012). Caracterização da sobreelevação meteorológica em Cascais nos últimos 50 anos. In: Actas das 2as Jornadas de Engenharia Hidrográfica. Lisboa, Portugal: Instituto Hidrográfico, pp. 175-178.

Vött, A., Brückner, H., May, M., Lang, F., Herd, R. and Brockmüller, S. (2008). Strong tsunami impact on the Bay of Aghios Nikolaos and its environs (NW Greece) during classical-Hellenistic times. *Quaternary International*, 181, pp. 105-122.

Wang, X.L. and Swail, V.R. (2001). Changes of Extreme Wave Heights in Northern Hemisphere Oceans and Related Atmospheric Circulation Regimes. *Journal of Climate*, 14 (10), pp. 2204-2221.

Wang, X.L., Wan, H., Zwiers, F.W., Swail, V.R., Campo, G.P., Allan, R.J., Vose, R.S., Jourdain, S. and Yin, X. (2011). Trends and low-frequency variability of storminess over Western Europe, 1878-2007. *Climate Dynamics*, 37 (11), pp. 2355-2371.

Watanabe, M., Goto, K, Imamura, F and Hongo, C. (2014). Numerical method to differentiate tsunami. In: Abstract book of the 19th International Sedimentological Congress. Geneva, Switzerland: Université de Genève and International Association of Sedimentologists, pp. 741.

Watt, S., Buckley, M. and Jaffe, B. (2012). Inland fields of dispersed cobbles and boulders as evidence for tsunami on Anegada, British Virgin Islands. *Natural Hazards*, 63, pp. 119-191.

Whelan, F. and Kelletat, D. (2005). Boulder deposits on the southern Spanish Atlantic coast: possible evidence for the 1755 AD Lisbon tsunami? *Science of Tsunami Hazards*, 23, pp. 25-38.

Williams, D.M. (2010). Mechanisms of wave transport of megaclasts on elevated cliff-top platforms: Examples from western Ireland relevant to the storm-wave versus tsunami controversy. *Irish Journal of Earth Sciences*, 28, pp. 13-23.

Williams, D.M. and Hall, A.M. (2004). Cliff-top megaclast deposits of Ireland, a record of extreme waves in the North Atlantic-storms or tsunamis? *Marine Geology*, 206, pp. 101–117.

Wintle, A.G. and Murray, A.S. (2006). A review of quartz optically stimulated luminescence characteristics and their relevance in single-aliquot regeneration dating protocols. *Radiation Measurements*, 41, pp. 369-391.

Whitemarsh, R.P. (1934). Great sea waves. *U.S. Naval Institute Proceedings*, 60, pp. 1094–1103.

Young, R. W., Bryant, E. A. and Price, D. M. (1996). Catastrophic wave (tsunami?) transport of boulders in southern New South Wales, Australia. *Zeitschrift für Geomorphologie*, NF 40, pp. 191–207.

Young, R.W., Bryant, E.A., Price, D.M., Dilek, S.Y. and Weeler, D.J. (1997). Chronology of Holocene Tsunamis on the Southerastern Coast of Australia. *Transactions of the Japanese Geomorphological Union*, 18, pp. 1-19.

Zazo, C., Goy, J.-L., Somoza, L., Dabrio, C.-J., Belluomini, G., Improta, S., Lario, J., Bardaj, T. and Silva, P.-G. (1994). Holocene Sequence of sea-level fluctuations in relation to climatic trends in the Atlantic-Mediterranean linkage coast. *Journal of Coastal Research*, 10 (4), pp. 933-945.

Zbyszewski, G. (1958). Le Quaternaire du Portugal. *Boletim da Sociedade Geológica de Portugal*, Separata do Vol XIII, p. 227.

Zbyszewski, G. (1971). Notícia explicativa da carta geológica do Quaternário de Portugal na escala 1/1000000. Lisboa, Portugal: Serviços geológicos de Portugal, p. 39.

Zbyszewski, G., Ferreira, O.D., Manuppella, G. and Assunção, C.T. (1965). Notícia explicativa da Folha 38-B Setúbal da carta geológica de Portugal na escala 1/50000. Lisboa, Portugal: Serviços Geológicos de Portugal, p. 134.

Zitellini, N., Mendes, L.A., Cordoba, D., Danobeitia, J., Nicolich, R., Pellis, G., Ribeiro, A., Sartori, R., Torelli, L., Bartolome, R., Bortoluzzi, G., Calafato, A., Carrilho, F., Casoni, L., Chierici, F., Corela, C., Correggiari, A., Della Vedova, B., Gracia, E., Jornet, P., Landuzzi, M., Ligi, M., Magagnoli, A., Marozzi, G., Matias, L., Penitenti, D., Rodriguez, P., Rovere, M., Terrinha, P., Vigliotti, L. and Ruiz, A.Z. (2001). Source of 1755 Lisbon Earthquake and tsunami Investigated, *EOS*, 82 (26), pp. 289-291.

Zitellini, N., Gràcia, E., Matias, L., Terrinha, P., Abreu, M.A., DeAlteriis, G., Henriet, J.P., Dañobeitia, J.J., Masson, D.G., Mulder, T., Ramella, R., Somoza, L. and Diez, S. (2009). The quest for the Africa-Euroasia plate boundary west of the Strait of Gibraltar. *Earth and Planetary Science Letters*, 280, pp. 13-50.

Appendixes

A. Commented transcription/translation of historical records of tsunami inundations affecting the Portuguese coastline

1. ~60 BC

Based on texts that Brito (1595) allegedly translated to Portuguese from a codex in Latin he attributed to Pedro Alladio, the author describes the effect of the ~60 BC earthquake and tsunami affecting the coast of Portugal and Galicia:

"Around this time[4], or a bit earlier, a notable earthquake occurred in the coast of Portugal and Galicia, by which many places were ruined, and many people died, others left the villages and ran, parents forgot their children, husbands forgot their wives: each just hoping to save their one life (…). And the sea surged out of its limits in some places, occupied dry land, and uncovered never seen land in other places."

2. AD 382

The oldest reference to the *AD* 382 event was found in the work of Brito (1607), which allegedly resulted from a translation of (unknown) texts by other authors. The author reports damages that resulted from major earthquakes in Sicily, Greece, Palestine and Portugal and describes the effect of a tsunami in the coast of Portugal:

"What happened in Portugal during the time of these two Emperors[5] was buried in the generalized silence of Writers, which, occupied by changes in the Empire[6], neglected other things, we can only read in Ammiano Marcelino, Imperial vicar in Spain when Julian was emperor, one certain captain named Venusto, and Paulo Orosio and others that we know of, that a universal earthquake occurred from which many Cities were subverted, and the sea, leaving its natural course, flooded some lands, which were previously inhabited, and uncovered other lands that were navigable; Laymundo described this sea flood (…) almost saying, the earthquake generated damages not only in Sicily, Greece, and Palestine, but also in the maritime lands of Spain, the growing sea subverted some dry land, and covered some islands, which were previously inhabited, and rocks remained in the middle of the sea, striped of soil, that can be seen, close by,

[4] 63 BC
[5] Valentinian II and Gratian
[6] Roman empire

or in the middle of the Ocean, mainly in cape S. Vincente, where small signs of a certain ancient island remain, and others along the same coast of the Ocean sea, that continues towards North. From these words we can conjecture that the ancient island named Eritreia was destroyed (…) which, according to Pomponius Mela, was in Lusitania coast; and I can't stop imagining that the island named Berlengas, and others, located at sea near the island, are traces left along the coastline that continues towards North, all of which the people imagine was once dry land, connected to a long cape seen today opposite of Farelhões at a small distance, and just as it caused these changes in a known location, will cause much more in others, of which there is no notice"

The existence of the islands mentioned in the previous text are corroborated by a reference to three small islands, each one with a harbour, in front of cape S. Vicente, made in the first century description of Iberia by Strabo (translation by Hamilton, 1854):

"The promontory which projects into the sea[7], Artemidorus (who states that he has himself been at the place) compares to a ship; three little islands [he says,] each having a small harbour, contribute to give it this form; the former island resembling the beak of the ship, and the two latter the beams on each side of the ship's bows."

3. 26th January 1531

There are many original descriptions of the January 1531 Lisbon earthquake. Resende (1554) wrote a rhymed historical narration, in which the author describes this event, roughly translating:

"And in January of the year[8]
that followed amazing signs
were observed, from which
there is human ingenuity
capable to describe;
before Thursday morning

[7] cape S. Vicente
[8] 1531

a massive earthquake
occurred in Portugal,
unlike any other seen,
nor desired by God.

(…) It lasted for the duration of a creed,
if longer it would have destroyed
everything, collapse into nothing,
those who lived would have died,
most were merged
in one point,
it happened in the whole of Portugal,
stronger in Estremadura (…).

Rifts and holes
were opened in the ground,
from which water and sand came out,
smelling of sulphur,
this was observed in Almeirim (…)

It was also felt in the sea,
without wind tides rose,
ships touched the bottom,
and were adrift (…).”

In his chronicles, Garibay (1628) wrote:

“(…) in the first of the year[9] of 1531, a very strong earthquake happened in the city of Lisbon, this was not its first earthquake, as we have seen, or the last, and with astonishment of the people, and other villages of the kingdom shook, especially Santarem, Almeirim, Azambuja, and other villages, which, due to the never seen earthquake, suffered great damage, buildings were demolished, and people died. Tagus river grew so high with the sea currents, that the water sucked in many ships: The fury

[9] January, the first month of the year

of the sea was so great, that in some descriptions it is written, that Tagus river opened by its middle, leaving the middle dry and without water (...)"

The reports of Couto (1778) restrict sunken ships to the Lisbon harbour:

"(...) the storm in the sea was so strong, that broke every ship in Lisbon harbour, and it is stated that Tagus River opened by its middle, the waters departed leaving a path, where the sand appeared. (...)"

Babinet (1861) translated a description made by Laurent Surius in 1567, describing the effects of the 1531 earthquake in Lisbon: *"Some ships were swallowed by the swirls of a raised and turbulent sea".*

In a letter to Marquis of Tarifa, the following translated quotation was found: *"Seaman say the ships rose to the heavens and struck the rocks; and, according to some seamen who were near, the waters parted and closed in the river-bed, and at Azambuja the waters withdrew in the middle and the land appeared from below"* (Osório, 1919 in Justo and Salwa, 1998).

4. 27th December 1722

The oldest report of the 27th December 1722 event was published in the newspaper Gazeta de Lisboa (Mascarenhas, 1723):

"It has been reported that this movement came from cape S. Vincente and spread throughout the whole Kingdom[10]; affecting more violently Albufeira and Loulé towns, and Faro and Tavira cities. In the latter city, the effects caused were unfortunate, and it ended in a bang, larger than the most formidable thunder. Many buildings collapsed, others were ruined, and are supported by small props to stop them from collapsing. Only one person remained in his house near the square. Everyone else fled out of the houses; and some were buried by the ruins. The river water was separated by the earthquake, in such a way that a caravel going up-river was left without water for some time; and everyone sailing in it ran towards land on foot; from where they saw the vessel turn-over several times, until, after the earthquake ended, the ship resumed floating. (...) Also in Faro many houses collapsed, and some people died; and the houses

[10] Algarve kingdom

still standing are full of cracks (…). The earth absorbed the river water leaving a boat and the fishes without water. People say that the hills in Albufeira moved by the earthquake."

Mendonça (1758) cites Mascarenhas (1723) describing similar effects, except for the caravel by Tavira, which, this time, is described as exiting, instead of going up-river. Moreover, the author adds a report of an explosion at sea, but does not explain it:

"This big earthquake occurred together with the sudden explosion of fire in the sea, between Faro and Tavira; because many people saw the flames ascending between the water, roaring as a storm"

5. 1st November 1755

Mendonça (1758) gives the following (general) description of the effects of the 1st November 1755 earthquake and tsunami:

"A little after nine hours and thirty minutes in the morning (…) the earth began to shake pulsing from within towards the surface, and with increasing impulse continued to shake swinging from one side to the other, from north to south, damaging building (…). Due to the earth impulses the sea withdrew, exposing the bottom of the sea along its margins, as never seen before, and rippling and forming very high waves, the sea threw itself over the coastal villages with such plunge that it seemed it was trying to submerge them, extending its limits. Three major bursts rushed inland, besides other smaller ones, the sea destroying many buildings and taking many people within its waters. (…) The whole kingdom of Algarve suffered many damages with the earthquake because it had a coastline exposed to the sea, has it happened many times before. (…) The sea in that coastline rose so many poles above its ordinary surface that flooded many fields, and when it receded destroyed fortresses and the whole town of Albufeira, leaving many fishes in the bushes. (…)

The movement of the water was one of the colossal effects of the earthquake, in some ports the withdrawal of the sea came first, such as in Cadiz uncovering the beach more than half a league[11]; and in others, the inflow came without the withdrawal. In the port

[11] 1 Portuguese terrestrial league = 6173 m (Barreiro, 1838; Marques, 2001) ⇒ ½ league = 3086 m

of Santa Maria (in Cádiz) the sea flooded three leagues[12] inland. In the coasts of Portugal, and of the Algarve, the sea entered a great distance inland and caused many deaths, and ruined many buildings."

Lopes (1841) reports similar effects of the waves:

"The sea withdrew in some places more than 20 fathoms[13], leaving the beaches without water; and rushing immediately towards land with such momentum, that it entered inland more than a league, overtopping the highest rocks; withdrawing and coming back again three times in just a few minutes, the sea flux and reflux dragging huge pieces of cliffs and of buildings, and levelling almost every coastal villages."

Effects of the tsunami in specific coastal locations were compiled and are presented from E to W and S to N, starting with the Algarve coastline.

Sousa (1919) transcribes the following effects in Quarteira:

"After the earthquake, the sea surged out of its limits 5 times, causing in the first and second wave the described damage, along half a league[16] inland over the hills, 6 fathoms[14] high (...)".

Sousa (1919) and Lopes (1841) present the following description in Armação de Pêra:

"(...) in the above described Armação, the fortress was destroyed by the sea, and due to its impetus, took the church of Santo António leaving only a few stones, as also sixty-two people, that the sea took and afterwards threw them dead; however the fortress and church have been repaired and are now better and stronger than before (...)"
Sousa (1919).

"Pera Debaixo or Armação, located in the beach ¼ of league [15]from another village named Pera. The sea left one house standing in the earthquake; rushed more than ½

[12] ~18500 m
[13] 1 Portuguese fathom = 2.2 m (Barreiro, 1838; Marques, 2001) ⇒ 20 fathoms = 44 m
[14] 13.2 m
[15] 1543 m

league [16]inland, flooding everything, leaving salt water lakes in the lowlands, creating islands and drowning 84 people (...)" (Lopes, 1841).

The church of Santo António, located inside the fortress is assumed to be in a similar location to the original church and sits at present at a height of 10 m amsl, measured in the field using RTK-GPS equipment.

Lopes (1841) presented the following description of the tsunami inundation in Boca do Rio:

"In the day of the earthquake, the sea invaded the fresh water creek that outlets there into the sea, for more than ½ league with a water height of 10-12 "varas"[17] destroying some large sand "médãos[18]" and carrying along 50 of the heaviest anchors more than ¼ league inland. The backwash uncovered great and noble buildings in the beach, next to the coastline, of which no memory existed".

The effects of the tsunami in Martinhal were described by Lopes (1841):

"The sea flooded a beach called Mortinhal[19], facing eastward[20], by about ½ league ripping off vineyards and leaving the land as a beach, covered with several types of fish and big stones of which one, weighting more than 300 arrobas[21] showed many shellfish stuck on its surface. Three times the sea struck and withdrew, the first wave being the largest (...)".

Although this description provides details that indicate authenticity, such as the case of the boulder with encrusted fauna, it is very unlikely that the extension of inland inundation reached 3 km, as the Martinhal lowland presents a maximum length of 1 km (measured upstream along the central axis of valley developing below 10 m amsl).

Lopes (1841) presented the following description of the tsunami effects in Sagres village:

---

[16] 3086 m
[17] 1 "vara" translated to pole = 1.1 m (Barreiro, 1838; Marques, 2001) ⇒ 10-12 poles = 11-13.2 m
[18] Foredunes
[19] Martinhal beach, west of Sagres
[20] of Sagres village
[21] *ca.* 4.4 ton

"The sea withdrew about one league drying out all bays in which ships anchored; the sea returned afterwards with such a thrust, that by the North and East overtopped cliffs standing at a height of 60 and 80 fathoms[22], respectively, throwing many fishes and big stones into Sagres fort; and the backwash ripped off the vegetation."

Effects of the tsunami in cape S. Vicente were described by Lopes (1841) in the following manner:

"6 or 7 minutes after the earthquake the sea withdrew; however, although from the N the sea lowered about 6 fathoms[23], it didn't exceed its limits; from the E, in a distance of ½ league seaward, the seafloor dried up entirely to a depth of up to 8 fathoms[24]; and rose afterwards with such a fury, that levelled with the cliffs and walls of the fort of Beliche, which should have some 30 fathoms[25] of height. There were 3 major sea pulses".

Lopes (1841) presented the following historical records of the tsunami inundation in Arrifana:

"One league south of Aljezur stream stands a ruined fortress named fortress of Arrifana. Due to the earthquake, the sea withdrew about 30 fathoms[26], striking immediately after, with such thrust, that from the south of the tip rose to an enormous height and from the north, which sits at about 30 fathoms, rose merely two[27], repeating the same flux and reflux three times within a few minutes. In the reflux, the sea dragged big rocks, and split a stone in half (…)".

The ruined fortress of Arrifana mentioned in this description, sit at ~42 m, in the westernmost tip of the Arrifana headland.

Mendonça (1758) quotes the following eye witness accounts in Setúbal:

"Setúbal suffered the most. The earthquake ruined most of the temples, convents and houses. The sea rushed inland with such might that took down the city walls and many

[22] ~130 m and 170 m
[23] 13.2 m
[24] 17.6 m
[25] 66 m
[26] 66 m
[27] 4.4 m

buildings. People watched, in admiration, two yachts, and other ships, that the water brought 500 passos[28] inland".

Sousa (1928) described the following effects, reported by a priest:

"Almost half the town, which is one of the largest in this kingdom, was levelled by the earthquake and similarly to Lisbon there was also a fire, burning a street and the sea took down the city walls and rushed inland in the town and in the fields, almost a quart of a league[29], ant put ships in the streets (...)".

The tsunami inundation height in the city of Setúbal can be extracted in the detailed descriptions presented by Sousa (1928):

"(...) the sea rushed inland, its movement causing such horror and ruins, with bigger damage than usual, caused the death of two thousand people, and placed boats inland, in distant places (...) the convent of Nossa Senhora do Livramento was ruined by the earthquake, but its church only suffered the effects of the sea inrush (...) the water exceeded its natural limits and flooded dry land at places, reaching the first floor of some buildings."

The convent of Nossa Senhora do Livramento no longer exists, but its original location was in a main avenue[30] in the city of Setúbal. At present, this location rests at a minimum height of 8 m amsl.

Nozes (1990) presented an anonymous report written by a British citizen that witnessed the effects of the earthquake and tsunami from a boat anchored near Lisbon downtown:

"I observed the sea at the bar to break feather white, as if agitated by a storm. The castle of Rugio[31] was so far overcome by the water, that the garrison fired several guns as signals for help, and were obliged to retire to the upper part of the tower. By my best

[28]"passo" translates to pace and can either pertain to "passo geométrico" (geometric pace), which is 1.65 m, or "passo andante" (walking pace), which is 0.66 m (*cf*. Barreiro, 1838; Marques, 2001). 500 "passos" is either 330 m or 825 m
[29] approximately 1500 m
[30]http://www.igespar.pt/pt/patrimonio/pesquisa/geral/patrimonioimovel/detail/73702/
[31] Bugio Castle

judgment the water rose in five minutes about 16 feet[32], and fell in the same time for three times and at two the tide returned to its natural course."

The tsunami waves struck Lisbon affecting low-lying river margins, where many people concentrated to avoid frequent building collapses due to the earthquake. In a letter written by an English merchant residing in Lisbon, to a friend, in England, the following description can be found (Unknown, in Nozes, 1990):

"(…) the water of the river rose at once above twenty feet[33] perpendicular, and subsided again to its natural pitch in less than a minute's time."

The following description was found in an anonymous letter, also compiled by Nozes (1990):

"I found myself safe and unhurt in the large open space before St. Paul's Church (…) In an instance appeared at some small distance a vast body of water, rising as it were, like a mountain, it came on foaming and roaring, and rushed towards the shore with such impetuosity that tho' we all immediately ran for our lives as fast as possible, many were swept away. The rest were above their middles in water, a good distance from the banks."

The church of S. Paulo is nowadays located at approximately 300 m from the present-day river margins. Accordingly, Mineiro (2005) states that the tsunami rushed inland an estimated distance of approximately 250 m in Lisbon downtown with further advances having been blocked by the Fernandine defence wall surrounding Lisbon.

Two historical records regarding the *AD* 1755 tsunami inundation of Cascais village were found:

"*The sea, withdrew from its bed threw the boats from the bay towards the Alto-do-Poço-Velho, the highest point in the village! More than 300 people were killed in this catastrophe. (…) The people ran to the chapel of Nossa Senhora da Conceição dos Inocentes, located in a small peninsula East of the village, which, although appeared it*

[32] 1 foot = 30.48 cm (*cf.* Marques, 2001) ⇒ 16 feet=4.88 m
[33] Approximately 6 m

would be the first to be submerged by the waves, it was not reached and those that took shelter in it escaped death" (Leal, 1874).

This record is about two distinct locations in Cascais village, The Alto-do-Poço-Velho and the Chapel of Nossa Senhora da Conceição dos Inocentes. They still exist today, they are 300 m apart, and stand at the exact same height of 6.5 m amsl. The location farther away of the coastline is Alto-do-Poço-Velho, approximately 400m from the beach.

The fishing harbour of Ericeira has existed since before the *AD* 1755 tsunami, with references found in documents from 1507 (*cf.* Silva, 2002). Effects on the tsunami inundation in this location were reported by Mascarenhas (1756) in the newspaper Gazeta de Lisboa:

"*In the last week of October the sea was notably infuriated; and the fishermen, being afraid of some big storm, took their boats to the top of the cobble street that goes from the beach to the village. In the first of November, between 9 and 10 am we felt for about six minutes a violent earthquake, which caused the town people to run away from their homes and from the churches without knowing where to flee. All the buildings were ruined, the chapels and churches without serious damage, but the sea was so high that in the backwash took some of the boats, located on the cobble street, and like this continued all day."*

The cobble street mentioned in the transcription still exists and its lower reach develops between 4 and 18 m amsl. So far, the exact location of the section of that cobble street affected by the tsunami is unknown. This fishing harbour is fully exposed to the sea and, at the time, had no artificial protection from waves. According to Esteves (2011) the sea reached the base of the cobbled street in high tide and, during storms, the waves would break when reaching that street, at approximately 5-6 m amsl. Assuming the boats were placed above the normal reach of storm waves, then the *AD* 1755 tsunami inundation height would have to have been higher.

The *AD* 1755 tsunami inundation in Porto Novo was described by Priest António Duarte (in Sousa, 1928):

"News came about the sea, from Povoa and Porto-Novo of Penafirme, which limit this parish (A-dos-Cunhados) from the sea, about half a league from land, it raised high as a mountain and some people saw several colours in the water, which caused enormous astonishment and fear to everyone in the neighbourhood, imagining that it was final judgment day, fled to this place (A-dos-Cunhados) and church, just as they were, well or poorly dressed and left their houses without closing the door or bringing their things of value, where they stayed in the afternoon of the second day of November. A mountain of sea dwelled voraciously towards land and fought the cliffs at a height of 9 to 10 fathoms[34]. (…) the extraordinary flux and reflux occurred three times, reaching distances inland of which there is no memory."

The extraordinary inland inundation mentioned in the final part of the document must pertain to the floodplain developing inland of the Porto Novo stream outlet.

The effects of the tsunami inundation in Peniche have been collected and described by Engenheiro (1999; 2005) based on ancient official documents of both the city council and of a well-established Portuguese charity (Santa Casa da Misericórdia).

"About the most prominent building, the church of Misericórdia, it is important to mention that the water rose with such speed and quantity that reached the feet of a statue in the altar, not surpassing it" (Engenheiro, 2005).

The church of Misericórdia still exists today, at approximately 100 m from the city walls that separate the town from the moat directly connected to the sea, and its entrance is at 2.7 m amsl. There is no way of knowing how high the altar was at the time, so, for Peniche, the inundation height considered in this study is of > 3 m amsl and the inundation distance of > 100 m.

So far, no original records of the *AD* 1755 tsunami inundation in Figueira da Foz have been found. However, Baptista and Miranda (2009) and Santos *et al*. (2011) have collected, translated and cited the following observations:

"(…) however the biggest new was on the sea (…) by 10 o'clock and a quarter of the day, it started rising such water mounts (…) growing above the natural order 44

[34] Approximately 20 m

palms[35]*, more or less (…) for 3 or 4 times (…) uncovering rocks and sand never seen before (…)"* (Arquivos do Ministério do Reino, 1756 in Baptista and Miranda, 2009).

"(…) the flux of the sea was seen 20 fathoms[36] *more or less up the beach."* (Inquéritos do Marquês de Pombal, 1756 in Santos *et al.*, 2011).

Ellicot (1755-1756) describes the effects of the tsunami in the Douro estuary in a section of a letter written to Mr Timan Henkel, a merchant in London:

"What frightened the people, was the river, which rose and fell surprisingly every quarter of an hour, for upwards of 4 hours at least, 4 or 5 feet[37]*, and sometimes more; and some saw the river in some places open, and throw out a vast deal of wind, which was very terrifying".*

6. 16th November 1755

The oldest report found is authored by Sanches (1757), who stated the following:

"The 16th November, was felt in Compostella, and Coruña, with great damage, caused not only by the earthquake, but also by the extraordinary flux and reflux of the sea".

Mendonça (1758), citing Sanches (1757), gives a similar description, adding: "*At about three hours and thirty minutes in the afternoon a big explosion occurred*". Perrey (1847) presents the following description:

"The 16th, three hours and thirty minutes in the evening, at Lisbon, the earth lowered, making the same effect as a sailing ship; the sea swelled prodigiously."

7. 29th March 1756

The oldest report was found in Perrey (1847), and again in Rodriguez (1932-40), stating the following:

"The 29th, in the morning, at Lisbon, one violent shock; the water of Tagus moved considerably".

[35] 1 Portuguese palm = 0.22 m (*cf.* Barreiro, 1838; Marques, 2001) ⇒ 44 palms = 9.68 m
[36] 44 m, although Santos *et al.*, (2011) convert that value to 36 m
[37] 1 foot = 30.48 cm (*cf.* Marques, 2001) ⇒ 4-5 feet =1.22–1.52 m

8. 31st March 1761

Effects of this earthquake were described in several letters published in the Philosophical Transactions journal:

"The earthquake happened the 31st last month, precisely at twelve o'clock, and lasted full five minutes, with a smart and equal vibration. It exceeded all the others, except that of the first November 1755. Thank God it was attended with no other consequences, but that of alarming the inhabitants, throwing down some ruins, and rending some houses. About an hour and a quarter afterwards, the sea began to flow and ebb, about eight feet[38] perpendicular, every six minutes, and continued till night (…)" (Unknown, 1761).

"(…) The agitation of the sea was very great, during the time of the tremor; and, for some hours after it, the waters ebbed and flowed many feet perpendicularly, several times in the space of every six minutes. Ships at anchor in the rivers, though riding in some fathoms of water, were left dry at some intervals (…)" (Molloy, 1761).

Perrey (1847) presented the following additional information regarding the effects of the tsunami:

"(…) At Cape Finisterre, the sea water was agitated with extraordinary fluxes and refluxes; I think a boat was damaged; it was twelve hours and fifteen minutes. The boats, in the sea, at some distance of Lisbon, experienced two shocks at 11 hours and 45 minutes and at 11 hours and 50 minutes in the morning (…)."

[38] 2.44 m

B. Variable symbols and description

$Ø$	Average lichen diameter
a	Particle long axis
A	Area of the equivalent circle
a'	Corrected a-axis
A_e	Cross-sectional eroded area
A_n	Area of the boulder directly exposed to incoming flow (boulder surface normal to flow direction)
b	Particle intermediate axis
β	Slope
c	Particle short axis
C_d	Drag coefficient
C'_d	Drag coefficient of particles resting on a bed in turbulent flow
C_l	Lift coefficient
C_{l_1} and C_{l_2}	Corrected lift coefficients
C_m	Mass coefficient
Δ	Relative buoyant mass density
D	Distance to msl
D_i	Intermediate particle diameter, equivalent to the b-axis
D_n	Nominal diameter
Δ_x	Distance travelled by a water mass
Δ_z	Vertical distance
E	Revetment crest height
$E_{friction}$	Energy loss due to friction
E_{height}	"Vertical energy" [sic] when a boulder is uplifted (Benner *et al.*, 2010)
$E_{kinetic}$	Kinetic energy
$E_{storm\ wave}$	Energy associated with a storm wave
E_t	Total energy
$E_{tsunami\ wave}$	Energy associated with a tsunami wave
E_{wave}	Wave energy
F	Net force exerted on a static boulder
f	Wave frequency (inverse of wave period, $1/T$)
f_{BF}	Frictional resistance between the swash and the surface of a boulder beach
F_d	Force of drag
F_f	Frictional force
F_g	Weight
F_l	Force of lift
F_m	Force of inertia or momentum
F_μ	Net friction
F_r	Force of restrain

F_{rx}	x component of the force of restrain
F_{ry}	y component of the force of restrain
F_{wav}	Wave force acting on an individual particle
g	Gravitational acceleration (9.81 m·s^{-2})
H	Wave height
H_{10}	Average of the highest 10% of waves
h_b	Water depth at the breaking point
H_b	Wave height at the breaking point
h_c	Height of the beach crests
h_i	Water depth
H_i	Wave height
H_{max}	Maximum wave height
H_s	Significant wave height
H_{storm}	Storm wave height
H_t	Tsunami wave height
I	Impulsion
K_D	Dimensionless coefficient in the Hudson formula
KG	Kurtosis
L	Wave length
M	Mass
μ	Coefficient of static friction
$\dot{m}$	Amount of mass flowing through a cross-section per unit time
M_d	Moment of drag
M_l	Moment of lift
M_m	Moment of inertia
M_r	Moment of restrain
M_{rx}	x component of the moment of restrain
M_{ry}	y component of the moment of restrain
M_Z	Graphic mean
N	Number of waves
P	Notional permeability factor
θ	Shield's parameter
R_u	Wave run-up
ρ_s	Rock mass density
ρ_w	Water mass density
σ_I	Inclusive graphic standard deviation
S	Damage level
S_e	Energy gradient
SKI	Inclusive graphic skewness
S_{om}	Wave steepness

t	Time period
τ_{BF}	Fluid stress applied to a beach face
THD	Total horizontal distance
T	Wave period
T_m	Average zero up-crossing wave period
u	Average flow velocity
$\ddot{u}$	Instantaneous flow acceleration
U_{avg}	Average flow velocity
U_{max}	Maximum swash velocity
V	Particle volume
X	Horizontal distance
x	Abscissa in a two-dimensional rectangular space
ξ_m	Breaker or surf similarity parameter
y	Ordinate in a two-dimensional rectangular space
z	Height relative to msl

C. Description of the van der Meer formulae

Van deer Meer derived the following formulas to evaluate the stability of breakwaters for plunging and surging waves (van der Meer, 1988; 1998):

Plunging: $$\frac{H_s}{\Delta \cdot D_n} = 6.2P^{0.18}\left(\frac{S}{\sqrt{N}}\right)^{0.2}(\xi_m)^{-0.5}$$ **Equation 39**

Surging: $$\frac{H_s}{\Delta \cdot D_n} = 1.0P^{-0.13}\left(\frac{S}{\sqrt{N}}\right)^{0.2}\sqrt{\cot\theta}\,\xi_m{}^{P}$$ **Equation 40**

Where Δ represents the relative buoyant density (Equation 41);· D_n is the nominal diameter (Equation 42); ξ_m the breaker or surf similarity parameter (Equation 43); P the notional permeability factor (0.1 for impermeable surfaces); S the damage level (Equation 5); and N the number of waves.

Relative buoyant density, Δ, is described by (van der Meer, 1998):

$$\Delta = \frac{\rho_s}{\rho_w} - 1$$ **Equation 41**

The nominal diameter when using concrete units lacking size grading is obtained with (van der Meer, 1998):

$$D_n = \left(\frac{M}{\rho_s}\right)^{1/3}$$ **Equation 42**

Where M represents the mass of the stone/concrete units.

The surf similarity parameter defines which stability formula should be used. For $\xi_m < 3$ plunging waves are shown, and for $\xi_m < 3$ surging waves should be considered (van der Meer, 1987). The surf similarity parameter can be obtained using (van der Meer, 1998):

$$\xi_m = \frac{\tan\beta}{\sqrt{s_{om}}}$$ **Equation 43**

Where s_{om} represents wave steepness, defined by van der Meer (1988; 1998) as:

$$s_{om} = \frac{2\pi H_s}{g T_m{}^2} \qquad \textbf{Equation 44}$$

Where T_m represents the average zero up-crossing period.

Stability equations are valid and have been tested in engineering works for the range of governing variables presented in Table XXIX.

Table XXIX: List of governing variables for stability and possible range of application. Modified after van der Meer (1987, 1988; 1998)

VARIABLE	EXPRESSION	RANGE
Wave height parameter	$H_s / \Delta \cdot D_n$	1-4
Wave period parameter, wave steepness	s_{om}	0.01-0.06
Surf similarity parameter	ξ_m	0.7-7
Damage as a function of the number of waves	$S / \sqrt{N}$	< 0.9
Number of waves	N	1000-7500
Slope angle	$\cot \beta$	1.5-6

D. Derivation of Nott's (1997; 2003) equations

The various forces acting on a parallelepiped boulder subject to a moving flow are: drag (F_d), lift (F_l), restrain (F_r) and, in the case of sub-aerial boulders, inertia (F_m).

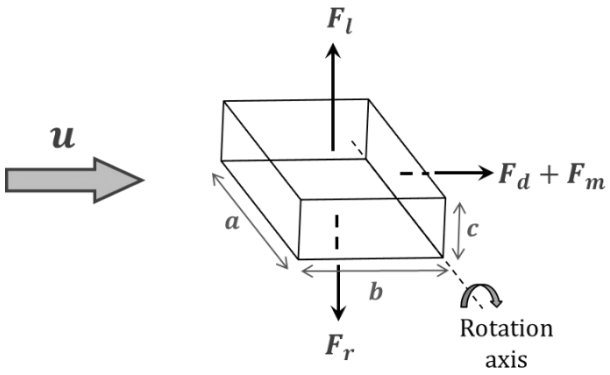

Figure 123: Schematic representation of different forces acting on a boulder subject to a moving flow

Drag force acts on the surface resting perpendicularly to flow direction (Dean and Dalrymple, 2002) (ac surface containing the a and c axes) and represents the force of the fluid in motion:

$$F_d = \frac{1}{2}\rho_w C_d (ac) u^2 \qquad \textbf{Equation 45}$$

in which ρ_w symbolizes fluid density, C_d the drag coefficient, a the largest boulder axis, c the smallest axis, and u the average flow velocity.

Lift force acts on the surface parallel to the flow (ab surface) and depends on the pressure gradient that the boulder generates when a wave goes over it (Dean and Dalrymple, 2002):

$$F_l = \frac{1}{2}\rho_w C_l (ab) u^2 \qquad \textbf{Equation 46}$$

in which C_l symbolizes the lift coefficient and b the intermediate boulder axis.

Restraint force (F_r) results from impulsion (I) and weight (F_g), with vertical component (Dean and Dalrymple, 2002):

$$F_r = F_g - I = \rho_s V g - \rho_w V g = (\rho_s - \rho_w) V g \qquad \textbf{Equation 47}$$

in which g represents the gravitational acceleration (9.81 m·s^{-2}) and ρ_s boulder mass density.

In the case of sub-aerial boulders, an additional force of inertia or momentum has been considered due to flow acceleration for a brief time as the wave crest impacts in the lee side of the boulder (Nott, 2003):

$$F_m = \rho_w C_m (abc)\ddot{u} \qquad \textbf{Equation 48}$$

in which C_m symbolizes the mass coefficient and $\ddot{u}$ the instantaneous flow acceleration.

The moment of a force or torque is a measure of the tendency of a force to cause rotation around an axis and its magnitude is the product of the force's magnitude and its moment arm (Hendricks *et al.*, 1999), and can be applied to boulder overturning in the following manner (Nott, 1997; 2003):

$$M_d = F_d \left(\frac{c}{2}\right) \qquad \textbf{Equation 49}$$

$$M_l = F_l \left(\frac{b}{2}\right) \qquad \textbf{Equation 50}$$

$$M_r = F_r \left(\frac{b}{2}\right) \qquad \textbf{Equation 51}$$

in which M_d represents the moment of drag, M_l the moment of lift and M_r the moment of restrain. The moment of inertia was not defined by Nott (2003) and in the balance of moments included the inertia force instead. As already pointed out by other authors (*e.g.* Benner *et al.*, 2010; Nandasena *et al.*, 2011a) this is not physically sound, it was considered an error and can be corrected by multiplying the force with the distance between its central point of application and the rotation axis. Given that inertia force acts in the same plane as drag (Nandasena *et al.*, 2011a), the distance considered is $c/2$ thus defining the moment of inertia as:

$$M_m = F_m \left(\frac{c}{2}\right) \qquad \textbf{Equation 52}$$

E. Derivation of equations by Nandasena *et al.* (2011a)

By decomposing forces in x and y components for a boulder in an inclined plane Nandasena *et al.* (2011a) included slope as a variable in the balance equations describing boulder movement (Figure 124).

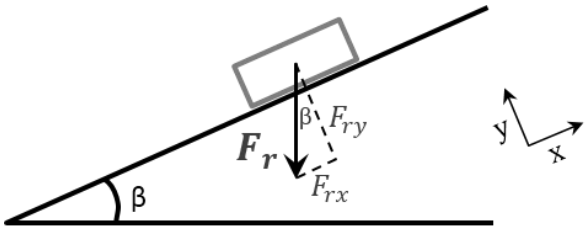

Figure 124: Decomposition of F_r into x and y components in an inclined plane

Restrain force (and moments) can be represented by the following components:

$$F_{rx} = F_r \sin\beta \rightarrow M_{rx} = F_r \sin\beta \left(\frac{c}{2}\right) \quad \textbf{Equation 53}$$

$$F_{ry} = F_r \cos\beta \rightarrow M_{ry} = F_r \cos\beta \left(\frac{b}{2}\right) \quad \textbf{Equation 54}$$

Sliding occurs, exclusively for submerged or subaerial boulders, when the following condition verifies (Figure 125) (Nandasena *et al.*, 2011a):

$$F_d \geq F_f + F_r \sin\beta \quad \textbf{Equation 55}$$

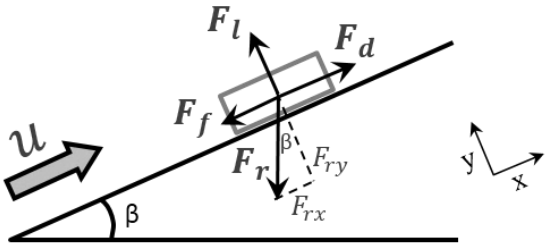

Figure 125: Forces acting on a boulder in an inclined plain

In which β represents the bed slope, μ represents the coeficient of static friction and F_f is the frictional force, computed with the following equation (Nandasena *et al.*, 2011a):

$$F_f = \mu(F_r \cos\beta - F_l) \quad \textbf{Equation 56}$$

The authors attempted to produce a balance equation for subaerial boulders by including the force of inertia, however for horizontal surfaces ($\beta = 0$), in some cases,

flow velocities present unrealistic low values. For this reason, Nandasena *et al.* (2011a) suggested the use of the same expression for both submerged and subaerial boulders, regardless the mode of transport.

In what concerns rolling (overturning around an axis), and given that boulders will overturn when moments of forces with horizontal component are equal or larger than those with vertical component, the balance equation becomes:

$$M_d - M_{rx} \geq M_{ry} - M_l \qquad \textbf{Equation 57}$$

Saltation is governed by forces with vertical components, and occurs when the following condition verifies (Nandasena *et al.*, 2011a):

$$F_l \geq F_r \cos\beta \qquad \textbf{Equation 58}$$

For joint-bounded boulders sliding or rolling could not be possible at the inception of motion, because boulder movement will be laterally restricted by adjacent rock faces (Nandasena *et al.*, 2011a). For this reason, forces must be used instead of moments. Also, for joint-bounded boulders, the friction force (F_f) is also considered. In this case, it acts in the lateral lower boulder face, it varies with the effective boulder weight, it is contrary to the movement and it is not significant if the joint bounded boulder lies in an horizontal platform (Figure 126 and Equation 59) (Nandasena *et al.*, 2011a).

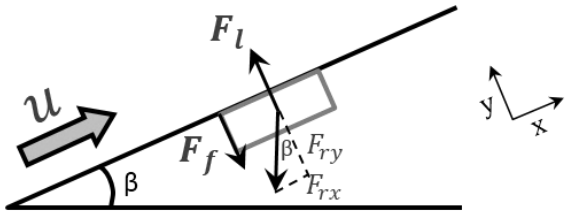

Figure 126: Forces acting on a joint-bounded boulder in an inclined plane

$$F_f = \mu F_r \sin\beta \qquad \textbf{Equation 59}$$

In this case boulders transport occurs when (Nandasena *et al.*, 2011a):

$$F_l \geq F_r \cos\beta + \mu F_r \sin\beta \qquad \textbf{Equation 60}$$

F. Derivation of equations by Benner *et al.* (2010)

1. *Conservation of momentum*

Linear momentum, or just momentum, of a body is the product of the mass and the velocity of that body and the rate of change of the momentum is equal to the net force acting on it (Çengel and Cimbala, 2006).

Based on conservation of momentum within a controlled volume containing a horizontal water flow hitting a boulder (Figure 127), the force that the water flow exerts on the particle can be computed by assuming that: 1) the boulder is sitting on an horizontal surface; 2) the flow of water is steady and hits the boulder at its front face ac: 3) after hitting the boulder the water will splatter in directions normal to the approach direction of the water flow; 4) vertical forces and momentum fluxes are not considered and have no effect on the horizontal reaction force; the force exerted by the water on the boulder will be (*cf.* Çengel and Cimbala, 2006; Benner *et al.*, 2010; Bansal, 2010):

$$F = rate\ of\ change\ of\ momentum\ in\ the\ direction\ of\ force$$

$$= \frac{Initial\ momentum - final\ momentum}{time}$$

$$= \frac{M}{t}(initial\ velocity - final\ velocity)$$

$$= \dot{m}(initial\ velocity - final\ velocity)$$

where $\dot{m}$ is the amount of mass flowing through a cross section per unit time, given by (Çengel and Cimbala, 2006):

$$\dot{m} = \rho_w u A_n \qquad \textbf{Equation 61}$$

in which u represents average velocity and A_n denotes the cross-sectional area normal to the flow direction (in this case ac). Final velocity in the direction normal to the flow will be zero, in which case the force exerted by the water on the boulder becomes:

$$F = \rho_w acu^2$$ **Equation 62**

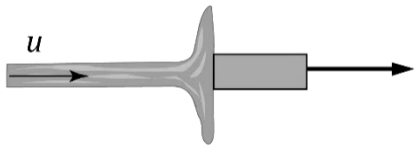

Figure 127: Schematic for a water flow striking a boulder

2. *Conservation of energy*

The kinetic energy of a fluid in motion is (Benner *et al.*, 2010):

$$E_{kinetic} = 0.5Mu^2$$ **Equation 63**

The kinetic energy of a mass of water acting on the boulder, namely affecting the surface area ac, is (Figure 128):

$$E_{kinetic} = 0.5Mu^2 = 0.5\rho_w Vu^2$$ **Equation 64**

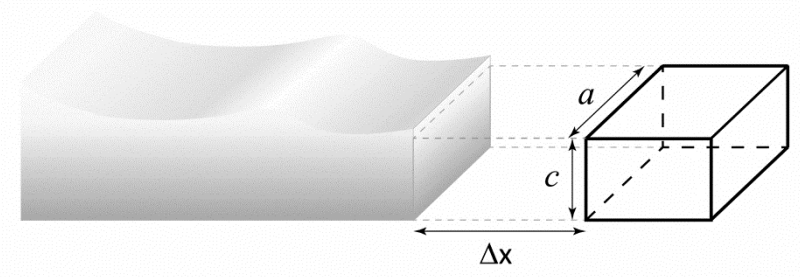

Figure 128: Schematic representation of the distances considered in the definition the mass of water hitting the boulder, comprising the a and c boulder axis and Δx

Assuming a constant flow velocity of u, over the whole time-period, t, it can be re-written as (*cf.* Benner *et al.*, 2010):

$$E_{kinetic} = 0.5\rho_w ac\Delta xu^2 = 0.5\rho_w acutu^2 = \frac{1}{2}\rho_w acu^3 t$$ **Equation 65**

Energy is defined as the product between force and distance (Benner *et al.*, 2010). Regarding boulder transport up-slope, wave energy is transformed into "vertical energy" [sic] when the boulder is uplifted a height Δz (E_{height}), and used to overcome friction when the boulder is transported a distance X (Figure 25) (Benner *et al.*, 2010).

$$E_{height} = F_r \Delta z$$ **Equation 66**

$$E_{friction} = \mu F_r X$$ **Equation 67**

For a subaerial boulder scenario, the restraining force (F_r) is the boulder weight, F_g:

$$F_g = Mg = V\rho_s g$$ **Equation 68**

For a submerged boulder scenario, the restraining force is the immersed weight:

$$F_r = F_g - I = V\rho_s g - V\rho_w g = V(\rho_s - \rho_w)g$$ **Equation 69**

Substituting in Equation 66 and Equation 67 renders (Table XXX):

Table XXX: Expressions suggested by Banner *et al.* (2010) to calculate vertical energy and energy loss due to friction

SUBMERGED BOULDER	SUBAERIAL BOULDER
$E_{height} = V(\rho_s - \rho_w)g\Delta z$ $E_{friction} = \mu V(\rho_s - \rho_w)gX$	$E_{height} = V\rho_s g\Delta z$ $E_{friction} = \mu V\rho_s gX$

G. Derivation of the height of a boulder beach crest by Lorang (2002)

Lorang (2002) derived an equation to predict the height of a beach crest based on wave forces and beach material. Following observations made by Bagnold (1940 *in* Lorang, 2002) the author concluded that boulder transport in the beach face occurs in a mode of high saltation, not rolling, and that the elevation of the beach crest (h_c) is equal to the height reached by swash surge up the beach face (or wave run-up).

Minimum critical threshold condition occurs when the wave force equals or exceeds the immersed weight force (Lorang, 2002). The wave force acting on an individual particle can be estimated by the following equation (Lorang, 2002):

$$F_{wav} = \tau_{BF} D_i^2 \qquad \textbf{Equation 70}$$

where D_i^2 is an approximation of the projected surface area of the particle being transported and τ_{BF} represents the fluid stress applied to the beach-face. As a first-order approximation to fluid stress, Lorang (2000) derived Equation 71 which incorporates the boundary shear stress for steady-state turbulent flows and the product of the fluid density (ρ_w) with mean flow velocity.

$$\tau_{BF} = f_{BF} \rho_w U_{max} R_u 2\mathrm{f} \cot\beta \qquad \textbf{Equation 71}$$

Where f_{BF} represents frictional resistance between the swash and the surface of a boulder beach, taken by Lorang (2011) as equal to the drag coefficient, R_u is the wave run-up which is equated to beach crest height (h_c), f represents wave frequency (inverse of wave period, T), and β represents the beach slope.

Because wave swash is a decelerating flow, instead of the square of mean velocity, the product of two velocity terms was used in Equation 71Equation 65: average (U_{avg}) and maximum (U_{max}) velocities. Average velocity is used to represent swash deceleration as a function of wave period and beach slope, geometrically defined by Lorang (2000) as:

$$U_{avg} = \frac{X}{t} = \frac{R_u \cot\beta}{1/2\,T} = R_u 2\mathrm{f} \cot\beta \qquad \textbf{Equation 72}$$

Immersed weight force is expressed as (Lorang, 2002):

$$I = (\rho_s - \rho_w)\, g\, D_i^3 \qquad \textbf{Equation 73}$$

By substituting τ_{BF} with Equation 71, f_{BF} with drag coefficient, C_d, and $R_u = h_c$, and resolving in order of h_c, yields (Lorang, 2002):

$$h_c = \frac{1}{2}\left(\frac{\rho_s - \rho_w}{\rho_w}\right)\left(\frac{g D_i T \tan\beta}{C_d U_{max}}\right) \qquad \textbf{Equation 74}$$

This equation represents the force balance equation relating directly to the physical factors describing the beach material, the wave frequency, swash velocity and associated drag as a function of the relative roughness of the beach face. Solving it for the wave period yields (Lorang, 2011):

$$T = \frac{2}{g}\left(\frac{\rho_w}{\rho_s - \rho_w}\right)\left(\frac{C_d}{\tan\beta}\right)\left(\frac{h_c}{D_i}\right) U_{max} \qquad \textbf{Equation 75}$$

H. Boulder and cobble data used in chapter 4

Table XXXI: Boulder and cobble data from various authors

Author	Location	Origin	Boulder axes (m)			ρ_s (kg. m^{-3})	Volume (m^3)	Mass (kg)	z (m amsl)	D (m)	Slope (°)	Transport distance (m)		Preferable mode of transport
			a	b	c							Δz	Δx	
Costa *et al.* (2011)	Furnas Beach, Algarve, S Portugal	*AD* 1755 Lisbon tsunami	0.44	0.30	0.23	2540	0.016	40	2.72	253	0.6	5.72	363	Sliding, rolling (over a small or large obstacle), or saltation
			0.40	0.33	0.16	2540	0.011	28	1.95	234	0.5	4.95	344	
			0.27	0.26	0.23	2540	0.008	21	1.95	234	0.5	4.95	344	
			0.56	0.30	0.18	2540	0.016	40	1.95	234	0.5	4.95	344	
			0.75	0.55	0.30	2540	0.065	165	2.12	221	0.5	5.12	331	
			0.44	0.33	0.28	2540	0.021	54	2.12	221	0.5	5.12	331	
			0.48	0.25	0.24	2540	0.015	38	1.8	212	0.5	4.8	322	
			0.60	0.30	0.17	2540	0.016	41	1.96	203	0.6	4.96	313	
			0.60	0.40	0.30	2540	0.038	96	1.96	203	0.6	4.96	313	
			0.60	0.50	0.30	2540	0.047	120	2.12	183	0.7	5.12	293	
			0.35	0.25	0.20	2540	0.009	23	2.12	183	0.7	5.12	293	
			0.40	0.18	0.15	2540	0.006	14	2.19	171	0.7	5.19	281	
			0.29	0.22	0.22	2540	0.007	19	2.27	162	0.8	5.27	272	
			1.60	1.00	0.50	2540	0.419	1064	2.3	156	0.8	5.3	266	
			0.48	0.36	0.15	2540	0.014	34	2.22	148	0.9	5.22	258	
			0.45	0.40	0.25	2540	0.024	60	2.11	140	0.9	5.11	250	
			0.76	0.40	0.40	2540	0.064	162	2.06	132	0.9	5.06	242	
			0.90	0.46	0.25	2540	0.054	138	1.89	121	0.9	4.89	231	
			0.80	0.54	0.25	2540	0.057	144	1.72	109	0.9	4.72	219	

Author	Location	Origin	Boulder axes (m)			ρ_s (kg·m^{-3})	Volume (m^3)	Mass (kg)	z (m amsl)	D (m)	Slope (°)	Transport distance (m)		Preferable mode of transport
			a	b	c							Δz	Δx	
Costa *et al.* (2011)	Barranco Beach, Algarve, S Portugal	*AD* 1755 Lisbon tsunami	0.45	0.25	0.20	2540	0.012	30	1.37	205	0.4	4.37	405	Sliding, rolling, rolling over a small or large obstacle, or saltation
			0.50	0.45	0.15	2540	0.018	45	0.78	185	0.2	3.78	385	
			0.52	0.44	0.21	2540	0.025	64	0.63	176	0.2	3.63	376	
			0.26	0.19	0.08	2540	0.002	5	0.79	167	0.3	3.79	367	
			0.57	0.41	0.25	2540	0.031	78	1.00	157	0.4	4	357	
			0.22	0.15	0.12	2540	0.002	5	1.00	157	0.4	4	357	
			0.33	0.26	0.25	2540	0.011	29	0.73	144	0.3	3.73	344	
			0.49	0.31	0.25	2540	0.020	51	0.73	144	0.3	3.73	344	
			0.50	0.40	0.28	2540	0.029	74	1.70	132	0.7	4.7	332	
			0.50	0.38	0.18	2540	0.018	45	1.70	132	0.7	4.7	332	
			0.51	0.28	0.18	2540	0.013	34	1.72	121	0.8	4.72	321	
			0.63	0.29	0.22	2540	0.021	53	1.72	121	0.8	4.72	321	
			0.53	0.41	0.29	2540	0.033	84	1.74	108	0.9	4.74	308	
			0.54	0.38	0.30	2540	0.032	82	1.74	108	0.9	4.74	308	
			0.62	0.42	0.38	2540	0.052	132	1.74	108	0.9	4.74	308	
			0.70	0.52	0.28	2540	0.053	136	1.74	102	1.0	4.74	302	
			0.67	0.53	0.19	2540	0.035	90	1.74	102	1.0	4.74	302	
			0.65	0.34	0.30	2540	0.035	88	1.74	102	1.0	4.74	302	
			0.92	0.50	0.48	2540	0.116	294	1.75	97	1.0	4.75	297	
			0.77	0.36	0.22	2540	0.032	81	1.75	97	1.0	4.75	297	
			0.65	0.43	0.21	2540	0.031	78	1.71	93	1.1	4.71	293	
			0.80	0.63	0.32	2540	0.084	214	1.71	93	1.1	4.71	293	
			0.59	0.38	0.37	2540	0.043	110	1.70	84	1.2	4.7	284	
			0.64	0.35	0.16	2540	0.019	48	1.70	84	1.2	4.7	284	

Author	Location	Origin	Boulder axes (m)			ρ_s (kg·m^{-3})	Volume (m^3)	Mass (kg)	z (m amsl)	D (m)	Slope (°)	Transport distance (m)		Preferable mode of transport
			a	b	c							Δ z	Δ x	
Oliveira *et al.* (2011)	Maçãs beach, W Portugal	1965-1975 Storm	2.80	2.00	0.94	2700	5.264	13371	3.3	20	9.4	0.5	1	Rolling over a large obstacle
Nandasena *et al.* (2011b) (values for transport distance were extracted from graphical content)	West Banda Aceh (Sumatra, Indonesia)	2004 IOT	2.35	1.75	1.50	2400	6.169	14805	0.88	17	3.0	0.88	17	Sliding, rolling (+ over a small or large obstacle)
			3.30	1.70	1.10	2400	6.171	14810	1.21	19	3.6	1.21	19	
			2.10	1.35	1.30	2400	3.686	8845	4.67	270	1.0	4.67	270	
			1.85	1.35	1.10	2400	2.747	6593	4.67	270	1.0	4.67	270	
			1.60	1.25	1.20	2400	2.400	5760	1.06	18	3.4	1.06	18	
			1.40	1.40	1.30	2400	2.548	6115	4.67	270	1.0	4.67	270	
			1.70	1.40	1.00	2400	2.380	5712	3.86	143	1.5	3.86	143	
			1.80	1.10	1.00	2400	1.980	4752	4.67	270	1.0	4.67	270	
			1.00	0.95	0.95	2400	0.903	2166	3.98	168	1.4	3.98	168	
			1.30	1.10	0.85	2400	1.216	2917	3.18	98	1.9	3.18	98	
			1.70	1.10	0.55	2400	1.029	2468	3.98	160	1.4	3.98	160	
			0.82	0.80	0.70	2400	0.459	1102	3.86	148	1.5	3.86	148	
Goto *et al.* (2011)	Okinawa Island, Japan	Typhoon in 1990	5.00	5.00	2.50	1504	62.5	94000	15	43	19.2	0.1	3	Sliding or rolling (+ over a small obstacle)
Hall (2011)	East Lothian, Scotland	Storm on 30-03-2010	0.88	0.58	0.22	2360	0.11	265	0-3	<100	0.6-3	<1	<100	Sliding or rolling (+ over a small or large obstacle)
			0.45	0.42	0.14	2550	0.03	67	0-3	<200	0.6-3	<1	<200	
			0.48	0.27	0.16	2550	0.02	53	0-3	<200	0.6-3	<1	<200	
			0.27	0.23	0.14	2360	0.01	21	0-3	<100	0.6-3	<1	<100	
			0.73	0.48	0.22	2550	0.08	197	0-3	<200	0.6-3	<1	<200	

Author	Location	Origin	Boulder axes (m)			ρ_s (kg·m^{-3})	Volume (m^3)	Mass (kg)	z (m amsl)	D (m)	Slope (°)	Transport distance (m)		Preferable mode of transport
			a	b	c							Δz	Δx	
Etienne and Paris (2010) (values for transport distance were equated to distance from msl)	Reykjanes Peninsula (Iceland)	Platform boulder	3.60	3.00	2.60	2400	22.46	53910	2	20	5.7	2	20	Sliding, rolling (+over a small and large obstacle)
			3.40	3.20	1.70	2599	14.8	38470	2	18	6.3	2	18	
			4.50	2.30	1.80	2701	9.73	26280	2	15	7.6	2	15	
			3.20	2.70	1.50	2700	6.77	18280	2	64	1.8	2	64	
			1.85	1.80	1.10	2700	2.93	7910	2	48	2.4	2	48	
			1.90	1.50	1.30	2696	1.94	5230	2	65	1.8	2	65	
		Boulder beach	2.40	2.40	0.80	2398	3.69	8850	3	44	3.9	3	44	Rolling (+over a small or large obstacle)
			1.70	1.70	1.20	2403	1.81	4350	2	29	3.9	2	29	
			1.60	1.30	1.20	2608	1.3	3390	2	30	3.8	2	30	
			2.70	1.90	1.65	2801	4.42	12380	2	35	3.3	2	35	
			1.70	1.60	1.50	2803	2.13	5970	2	33	3.5	2	33	
			3.50	3.10	3.00	2700	26.04	70310	6	65	5.3	6	65	
			3.70	1.85	1.10	2701	6.02	16260	8	105	4.4	8	105	
			3.00	1.80	0.90	2699	3.89	10500	4	66	3.5	4	66	
			1.90	1.80	0.90	2703	2.46	6650	5	51	5.6	5	51	
			2.10	1.50	0.90	2696	2.27	6120	5	51	5.6	5	51	
			1.60	1.50	0.75	2701	1.44	3890	5	51	5.6	5	51	
			2.10	1.90	1.50	2599	4.79	12450	4	20	11.3	4	20	
			3.00	2.00	1.60	2797	5.02	14040	2	50	2.3	2	50	
			2.40	1.50	1.15	2602	2.16	5620	5	30	9.5	5	30	
		Boulder field	1.45	1.10	0.90	2707	0.75	2030	8	150	3.1	8	150	Sliding or rolling (+over a small obstacle)
			0.65	0.45	0.35	2800	0.05	140	12	66	10.3	12	66	

Author	Location	Origin	Boulder axes (m)			ρ_s (kg·m^{-3})	Volume (m^3)	Mass (kg)	z (m amsl)	D (m)	Slope (°)	Transport distance (m)		Preferable mode of transport
			a	b	c							Δ z	Δ x	
Etienne and Paris (2010) (values for transport distance were equated to distance from msl)	Reykjanes Peninsula (Iceland)	Boulder ridge	3.00	2.50	0.50	2400	3	7200	6.5	105	3.5	6.5	105	Rolling (+over a small or large obstacle)
			2.20	1.20	0.70	2399	1.48	3550	6.5	105	3.5	6.5	105	
			1.05	0.85	0.70	2576	0.33	850	7	70	5.7	7	70	
			1.10	0.95	0.30	2688	0.16	430	4.5	10	24.2	4.5	10	
			1.40	1.20	0.80	2593	1.08	2800	5	25	11.3	5	25	
			1.45	1.10	0.25	2594	0.32	830	6	28	12.1	6	28	
			2.45	1.88	1.70	2702	4.09	11050	4	6	33.7	4	6	
			2.75	2.05	1.00	2695	2.95	7950	4	6	33.7	4	6	
			1.90	1.70	0.85	2706	1.43	3870	4	6	33.7	4	6	
			1.50	1.10	0.60	2788	0.52	1450	5	65	4.4	5	65	
		Cliff-top boulder	0.39	0.35	0.10	2000	0.01	20	11.5	35	18.2	11.5	35	Rolling (+over a small or large obstacle) or extraction of a cliff-top boulder
			2.10	1.70	0.80	2706	2.28	6170	8	30	14.9	8	30	
			2.30	1.30	0.95	2705	2.27	6140	7	35	11.3	7	35	
			1.30	1.30	1.30	2699	1.76	4750	7	28	14.0	7	28	
			1.70	0.90	0.80	2694	0.98	2640	8	48	9.5	8	48	
			2.30	1.90	0.50	2594	1.75	4540	12.2	25	26.0	12.2	25	
			1.20	0.85	0.35	2526	0.19	480	11.6	39	16.6	11.6	39	
			0.70	0.70	0.60	2667	0.15	400	12	20	31.0	12	20	
		Cliff-top ridge	1.50	1.30	1.20	2604	1.87	4870	7	20	19.3	7	20	
			1.82	1.16	0.86	2607	1.45	3780	11	49	12.7	11	49	
			1.45	1.40	0.65	2585	1.06	2740	11	62	10.1	11	62	
			1.20	1.00	0.80	2700	0.5	1350	10	4	68.2	10	4	
			1.20	1.15	0.55	2575	0.4	1030	11	55	11.3	11	55	
			0.90	0.70	0.40	2615	0.13	340	12	43	15.6	12	43	

Author	Location	Origin	Boulder axes (m)			ρ_s (kg·m^{-3})	Volume (m^3)	Mass (kg)	z (m amsl)	D (m)	Slope (°)	Transport distance (m)		Preferable mode of transport
			a	b	c							Δ z	Δ x	
Spiske and Bahlburg (2011)	Bucalemu, Central Chile	2010 Chile tsunami (GI)	0.32	0.20	0.18	2600	0.012	30	0.76	368	0.1	0	5.1	Sliding or rolling (+over a small or large obstacle)
			0.30	0.25	0.10	2600	0.008	20	0.76	368	0.1	0	5	
			0.27	0.23	0.12	2600	0.007	19	0.76	368	0.1	0	4.8	
			0.31	0.27	0.10	2550	0.008	21	0.76	368	0.1	0	4.9	
			0.20	0.15	0.05	2550	0.002	4	0.76	369	0.1	0	5.6	
			0.50	0.41	0.23	2550	0.047	120	0.76	368	0.1	0	5.2	
			0.90	0.68	0.18	2550	0.110	281	0.76	369	0.1	0	6	
			0.25	0.15	0.14	2600	0.005	14	0.76	370	0.1	0	6.6	
			0.57	0.40	0.37	2550	0.084	215	0.76	369	0.1	0	5.5	
			0.83	0.40	0.39	2600	0.129	337	0.76	369	0.1	0	6.2	
			0.44	0.38	0.25	2600	0.042	109	0.76	370	0.1	0	6.7	
			0.69	0.36	0.22	2550	0.055	139	0.76	370	0.1	0	6.8	
			0.34	0.30	0.29	2600	0.030	77	0.76	370	0.1	0	7	
			0.71	0.55	0.41	2550	0.160	408	0.76	370	0.1	0	7.3	
			0.37	0.30	0.25	2550	0.028	71	0.76	371	0.1	0	7.6	
			0.86	0.50	0.47	2600	0.202	525	0.76	370	0.1	0	7.2	
			0.60	0.44	0.15	2550	0.040	101	0.76	371	0.1	0	7.7	
			0.67	0.43	0.27	2550	0.078	198	0.76	370	0.1	0	7	
			0.44	0.40	0.12	2600	0.021	55	0.76	370	0.1	0	6.6	
			0.38	0.23	0.17	2600	0.015	39	0.76	370	0.1	0	6.5	
			0.60	0.49	0.21	2550	0.062	157	0.76	369	0.1	0	6.2	
			0.18	0.12	0.10	2600	0.002	6	0.76	369	0.1	0	5.7	

Author	Location	Origin	Boulder axes (m)			ρ_s (kg·m^{-3})	Volume (m^3)	Mass (kg)	z (m amsl)	D (m)	Slope (°)	Transport distance (m)		Preferable mode of transport
			a	b	c							Δ z	Δ x	
Spiske and Bahlburg (2011)	Bucalemu, Central Chile	2010 Chile tsunami (GI)	0.20	0.12	0.11	2600	0.003	7	0.76	369	0.1	0	5.8	Sliding or rolling (+over a small or large obstacle)
			0.55	0.34	0.30	2600	0.056	146	0.76	370	0.1	0	6.3	
			0.50	0.19	0.14	2550	0.013	34	0.76	372	0.1	0	8.5	
			0.53	0.47	0.28	2600	0.070	181	0.76	371	0.1	0	8.3	
			0.45	0.25	0.22	2600	0.025	64	0.76	371	0.1	0	8.2	
			0.20	0.20	0.20	2600	0.008	21	0.76	371	0.1	0	8.4	
			0.30	0.19	0.11	2600	0.006	16	0.76	371	0.1	0	8	
			0.20	0.10	0.10	2600	0.002	5	0.76	371	0.1	0	8.4	
			0.23	0.17	0.13	2600	0.005	13	0.76	372	0.1	0	8.7	
			0.40	0.36	0.18	2550	0.026	66	0.76	372	0.1	0	9	
			0.60	0.30	0.24	2600	0.043	112	0.76	372	0.1	0	9.4	
			0.12	0.07	0.06	2600	0.001	1	0.76	372	0.1	0	9.3	
			0.18	0.13	0.07	2600	0.002	4	0.76	373	0.1	0	9.5	
			0.10	0.06	0.06	2550	0.000	1	0.76	373	0.1	0	9.7	
			0.85	0.70	0.42	2600	0.250	650	0.76	372	0.1	0	8.2	
			0.60	0.45	0.36	2550	0.097	248	0.76	372	0.1	0	8.3	
			0.70	0.50	0.39	2550	0.137	348	0.76	372	0.1	0	8.9	
			0.35	0.26	0.23	2550	0.021	53	0.76	371	0.1	0	8.4	
			0.38	0.34	0.15	2600	0.019	50	0.76	372	0.1	0	8.6	
			0.23	0.23	0.16	2550	0.008	22	0.76	372	0.1	0	9.3	
			0.34	0.34	0.23	2550	0.027	68	0.76	373	0.1	0	10.3	
			0.22	0.23	0.15	2600	0.008	20	0.76	373	0.1	0	10.4	

Author	Location	Origin	Boulder axis (m)			ρ_s (kg·m^{-3})	Volume (m^3)	Mass (kg)	z (m amsl)	D (m)	Slope (°)	Transport distance (m)		Preferable mode of transport
			a	b	c							Δ z	Δ x	
Spiske and Bahlburg (2011)	Bucalemu, Central Chile	2010 Chile tsunami (GII)	0.59	0.40	0.27	2550	0.064	162	0.67	381	0.1	0	18	Sliding or rolling (+over a small or large obstacle)
			0.43	0.34	0.25	2550	0.037	93	0.67	381	0.1	0	17.5	
			0.72	0.39	0.33	2550	0.093	236	0.67	382	0.1	0	19.1	
			0.75	0.52	0.41	2600	0.160	416	0.67	383	0.1	0	19.9	
			0.20	0.16	0.14	2550	0.004	11	0.67	384	0.1	0	21.3	
			0.50	0.34	0.20	2550	0.034	87	0.67	385	0.1	0	21.6	
			0.45	0.41	0.24	2550	0.044	113	0.67	385	0.1	0	21.5	
			0.83	0.60	0.53	2550	0.264	673	0.67	385	0.1	0	22.1	
			0.40	0.35	0.25	2550	0.035	89	0.67	385	0.1	0	21.7	
			0.58	0.43	0.35	2600	0.087	227	0.67	385	0.1	0	21.8	
			0.38	0.30	0.20	2550	0.023	58	0.67	384	0.1	0	21.2	
			0.30	0.29	0.25	2550	0.022	55	0.67	384	0.1	0	21	
			0.25	0.25	0.12	2550	0.008	19	0.67	386	0.1	0	22.6	
			0.67	0.51	0.28	2550	0.096	244	0.67	386	0.1	0	22.8	
			0.41	0.30	0.11	2550	0.014	35	0.67	384	0.1	0	21.1	
			0.66	0.49	0.35	2550	0.113	289	0.67	385	0.1	0	21.7	
			0.30	0.18	0.15	2550	0.008	21	0.67	385	0.1	0	22.1	
			0.45	0.24	0.21	2550	0.023	58	0.67	384	0.1	0	21.1	

Author	Location	Origin	Boulder axes (m)			ρ_s (kg·m^{-3})	Volume (m^3)	Mass (kg)	z (m amsl)	D (m)	Slope (°)	Transport distance (m)		Preferable mode of transport
			a	b	c							Δ z	Δ x	
Spiske and Bahlburg (2011)	Bucalemu, Central Chile	2010 Chile tsunami (GII)	0.63	0.35	0.34	2600	0.075	195	0.67	386	0.1	0	23.2	Sliding or rolling (+over a small or large obstacle)
			0.46	0.38	0.26	2600	0.045	118	0.67	386	0.1	0	23.1	
			0.30	0.21	0.16	2600	0.010	26	0.67	386	0.1	0	22.9	
			0.32	0.17	0.12	2600	0.007	17	0.67	386	0.1	0	23.1	
			0.20	0.14	0.05	2600	0.001	4	0.67	387	0.1	0	24.4	
		2010 Chile tsunami (TZI)	0.44	0.32	0.16	2550	0.023	57	0.6	398	0.1	0	34.5	
			0.40	0.25	0.19	2550	0.019	48	0.6	401	0.1	0	38.3	
			0.43	0.32	0.17	2550	0.023	60	0.6	402	0.1	0	38.9	
			0.44	0.35	0.28	2600	0.043	112	0.6	407	0.1	0	44.4	
			0.40	0.28	0.22	2600	0.025	64	0.6	410	0.1	0	46.8	
			0.28	0.18	0.15	2600	0.008	20	0.6	413	0.1	0	49.8	
			0.50	0.30	0.24	2550	0.036	92	0.6	412	0.1	0	49.1	
			0.65	0.36	0.29	2600	0.068	176	0.6	415	0.1	0	52.2	
			0.44	0.45	0.34	2600	0.067	175	0.6	416	0.1	0	52.6	
			0.50	0.35	0.21	2550	0.037	94	0.6	416	0.1	0	53.3	
		2010 Chile tsunami (Group III)	0.50	0.37	0.34	2600	0.063	164	0.39	420	0.1	0	57.1	
			0.45	0.35	0.29	2550	0.046	116	0.39	423	0.1	0	59.9	
			0.31	0.20	0.16	2600	0.010	26	0.39	423	0.1	0	59.8	
			0.55	0.52	0.31	2550	0.089	226	0.39	423	0.1	0	59.9	
			0.41	0.35	0.15	2550	0.022	55	0.39	423	0.1	0	60	
			0.45	0.21	0.19	2550	0.018	46	0.39	427	0.1	0	63.5	
			0.40	0.32	0.30	2600	0.038	100	0.39	434	0.1	0	70.6	

Author	Location	Origin	Boulder axes (m)			ρ_s (kg·m^{-3})	Volume (m^3)	Mass (kg)	z (m amsl)	D (m)	Slope (°)	Transport distance (m)		Preferable mode of transport
			a	b	c							Δ z	Δ x	
Spiske and Bahlburg (2011)	Bucalemu, Central Chile	2010 Chile tsunami (Group III)	0.30	0.30	0.18	2600	0.016	42	0.39	433	0.1	0	69.9	Sliding or rolling (+over a small or large obstacle)
			0.50	0.48	0.22	2600	0.053	137	0.39	429	0.1	0	66.2	
			0.90	0.56	0.55	2600	0.277	721	0.39	428	0.1	0	64.7	
			0.45	0.30	0.24	2550	0.032	83	0.39	427	0.1	0	63.7	
			0.62	0.47	0.27	2550	0.079	201	0.39	429	0.1	0	66.2	
			0.39	0.31	0.20	2600	0.024	63	0.39	431	0.1	0	67.8	
			0.35	0.35	0.18	2550	0.022	56	0.39	431	0.1	0	67.6	
			0.40	0.34	0.31	2600	0.042	110	0.39	430	0.1	0	67.4	
			1.05	0.40	0.36	2600	0.151	393	0.39	430	0.1	0	67.2	
			0.51	0.39	0.18	2600	0.036	93	0.39	433	0.1	0	69.5	
			0.70	0.45	0.35	2550	0.110	281	0.39	435	0.1	0	72	
			0.45	0.40	0.27	2550	0.049	124	0.39	433	0.1	0	69.6	
			0.50	0.41	0.34	2600	0.070	181	0.39	436	0.1	0	72.7	
			0.35	0.25	0.24	2600	0.021	55	0.39	436	0.1	0	73.1	
			0.67	0.50	0.48	2600	0.161	418	0.39	441	0.1	0	78	
			0.78	0.45	0.33	2550	0.116	295	0.39	441	0.1	0	77.8	
			0.40	0.40	0.36	2600	0.058	150	0.39	443	0.1	0	79.8	
			0.59	0.41	0.35	2550	0.085	216	0.39	445	0.1	0	82.2	
			0.43	0.26	0.22	2550	0.025	63	0.39	439	0.1	0	75.7	
			0.64	0.55	0.36	2550	0.127	323	0.39	440	0.1	0	76.8	
			0.53	0.50	0.47	2550	0.125	318	0.39	441	0.1	0	77.8	
			0.46	0.35	0.35	2600	0.056	147	0.39	434	0.1	0	71.4	

Author	Location	Origin	Boulder axes (m)			ρ_s (kg·m^{-3})	Volume (m^3)	Mass (kg)	z (m amsl)	D (m)	Slope (°)	Transport distance (m)		Preferable mode of transport
			a	b	c							Δ z	Δ x	
Spiske and Bahlburg (2011)	Bucalemu, Central Chile	2010 Chile tsunami (TZII)	0.60	0.33	0.31	2550	0.061	157	0.51	456	0.1	0	92.6	Sliding or rolling (+over a small or large obstacle)
			0.69	0.34	0.27	2550	0.063	162	0.51	466	0.1	0	103	
			0.40	0.40	0.28	2600	0.045	116	0.51	451	0.1	0	88.2	
			0.50	0.39	0.21	2550	0.041	104	0.51	460	0.1	0	96.5	
			0.64	0.46	0.28	2550	0.082	210	0.51	489	0.1	0	125.7	
			0.28	0.26	0.16	2550	0.012	30	0.51	519	0.1	0	156	

I. Script used to estimate recurrence levels for H_s, T_m and P

```
#Load the packages that contain the necessary functions

library(aspace)
library(chron)
library(zoo)
library(plyr)
library(extRemes)

#Define the path for the wave records file in csv format, and
#the export directory

WRPath <- "G:/Wave data/input/"
WRFile <- "wavedata.csv"
ExportDir <- "G:/Wave data/output/"

#Read the data file in csv format

WR <- read.table(paste(WRPath, WRFile, sep = ""), sep = ";",
                 header = T)

#Add the column depth -D- to the data and attribute its value

WR["D"] <- 2000

#Compute peak period -Tp- based on peak frequency -fp- and
#add as a new column

WR["Tp"] <- 1 / WR$fp

#Compute the root mean square wave height -Hrms- based on Hs
#and add as a new column

WR["Hrms"] <- WR$Hs / 1.416

#Compute total energy per unit area -E- and add as a new column

WR["E"] <- (1 / 8) * 1025 * 9.81 * (WR$Hrms^2)

#Compute wave celerity -C- and add as a new column

WR["C"] <- (9.81 * WR$Tp) / (2 * pi)

#Compute wave number -k- and add as a new column

WR["k"] <- (2 * pi) / ((9.81 / (2 * pi)) * WR$Tp^2)

#Compute the ratio between wave group velocity and wave phase
#velocity -n- and add as a new column

WR["n"] <- (1 / 2) *
           (1 + ((2 * WR$k * WR$D) / (sinh(2 * WR$k * WR$D))))
```

```
#Compute energy flux (wave power) -P- and add to the dataset

WR["P"] <- WR$E * WR$C * WR$n

#Extract annual maxima from the dataset
#Create a column with the year of the records

WR["year"]<-as.numeric(substr(WR$Date, 1, 4))

#Create a factor classifying each record with the year

YearsC<-cut(WR$year, seq(1952, 2008, by=1), right=TRUE)

#Associate the years from the factor to all records

WR_Y<-cbind(WR, YearsC)
An_maxHs<-ddply(WR_Y,.(YearsC), summarise, Hs_max=max(Hs))
AM_Hs<-na.omit(An_maxHs)
AM_Hs["year"]<-seq(1953, 2008, by=1)
AM_Hs<-subset(AM_Hs, select = c(Hs_max, year))
An_maxTr<-ddply(WR_Y,.(YearsC), summarise, Tr_max=max(Tr))
AM_Tr<-na.omit(An_maxTr)
AM_Tr["year"]<-seq(1953, 2008, by=1)
AM_Tr<-subset(AM_Tr, select = c(Tr_max, year))
An_maxP<-ddply(WR_Y,.(YearsC), summarise, P_max=max(P))
AM_P<-na.omit(An_maxP)
AM_P["year"]<-seq(1953, 2008, by=1)
AM_P<-subset(AM_P, select = c(P_max, year))

#Fit GEV to yearly maxima of Hs, Tr and P

fevd_Hs<- fevd(AM_Hs$Hs, type = "GEV")
fevd_Tr<- fevd(AM_Tr$Tr, type = "GEV")
fevd_P<- fevd(AM_P$P, type = "GEV")

#Compute return levels and confidence bounds for return
#periods of 2,5,10,20,50,100 and 200 years and save as csv

ci_RL_Hs <- ci(fevd_Hs, alpha=0.05, type= "return.level",
               return.period= c(2,5,10,20,50,100,200))
write.table(ci_RL_Hs, paste(ExportDir, "RL_Hs.csv", sep=""),
            sep=";")
ci_RL_Tr <- ci(fevd_Tr, alpha=0.05, type= "return.level",
               return.period= c(2,5,10,20,50,100,200))
write.table(ci_RL_Tr, paste(ExportDir, "RL_Tr.csv", sep=""),
            sep=";")
ci_RL_P <- ci(fevd_P, alpha=0.05, type= "return.level",
               return.period= c(2,5,10,20,50,100,200))
write.table(ci_RL_P, paste(ExportDir, "RL_P.csv", sep=""),
            sep=";")
```

J. Mass density data

Table XXXII: Mass density data measured in the laboratory

LAYER	SAMPLE	VOLUME (cm^3)	MASS (g)	ρ_s ($g \cdot cm^{-3}$)	AVERAGE ρ_s ($kg \cdot m^{-3}$)
28	1	3.50	9.02	2.58	
	2	3.00	8.80	2.93	
	3	4.50	12.70	2.82	
	4	2.50	5.88	2.35	2671
26	1	7.50	19.88	2.65	
	2	7.50	20.22	2.70	
	3	6.00	14.35	2.39	2579
22-24	1	4.50	11.57	2.57	
	2	5.00	13.28	2.66	
	3	5.50	14.70	2.67	
	4	6.00	15.85	2.64	
	5	3.50	8.62	2.46	2601
21	1	5.50	13.52	2.46	
	2	7.00	17.36	2.48	
	3	7.00	17.39	2.48	
	4	6.00	15.07	2.51	2484
19	1	6.00	15.00	2.50	
	2	6.00	15.75	2.63	
	3	8.50	22.24	2.62	2580
18	1	6.00	16.43	2.74	
	2	4.00	9.74	2.44	
	3	4.50	12.52	2.78	2652
16	1	7.00	18.29	2.61	
	2	3.00	8.46	2.82	
	3	3.50	8.65	2.47	
	4	3.50	9.54	2.73	
	5	6.00	13.83	2.31	2587
15	1	6.00	16.03	2.67	
	2	4.00	9.49	2.37	
	3	2.50	6.43	2.57	
	4	4.50	11.13	2.47	2522

K. Boulder monitoring data

Table XXXIII: Observed boulder movement during January and February 2014 storms

BOULDER	MASS (kg)	DIRECTION OF MOVEMENT	zi (m)	zf (m)	Δz (m)	Δx (m)	DATE
B1654	3611	SE	9.20	9.24	0.04	1.18	Jan & Feb 2014
B1615	421	SE	12.06	12.18	0.12	2	Feb 2014
B1624	276	Unknown	?	12.44	?	>9	Feb 2014
B0006	98	S	12.01	11.58	-0.43	18	Jan/Feb 2014
B0005	337	SSW	12.16	12.16	0	0.7	Jan 2014
B0004	1478	S	11.65	11.75	0.1	1	Jan 2014
		S	11.75	11.76	0.01	2	Feb 2014
B0003	755	E	12.45	12.8	0.35	1	Jan 2014
B0009	598	SSW	11.54	11.19	-0.35	7.6	Jan 2014
		SSE	11.19	11.57	0.38	1.27	Feb 2014
B0010	161	Unknown	11.9	?	?	?	Jan 2014
B0011	86	Unknown	11.84	?	?	?	Jan 2014
B0012	95	Rotation	11.75	11.62	-0.13	-	Jan 2014
B0014	73	SSE	12.42	12.49	0.07	1	Jan 2014
B0016	1144	Rotation	11.55	11.54	-0.01	-	Jan 2014
		SE	11.54	11.54	0	1.8	Feb 2014
B0017	80	SSW	11.54	11.45	-0.09	2	Jan 2014
B0018	467	SW	11.15	9.06	-2.09	5	Jan 2014
B0033	1510	Rotation	11.02	11	-0.02	-	Jan 2014
B0028	95	S	11.22	11.63	0.41	6.5	Jan 2014
B1619	769	SE	~10.54	10.73	0.19	2	Jan 2014
B1620	587	E	~10.54	10.84	0.3	1	Jan 2014
B1621	478	SE	~10.54	10.7	0.16	2.3	Jan 2014
B0030	62	SW	11.65	11.48	-0.17	2	Jan 2014
B0041	150	SW	11.38	11.06	-0.32	2.4	Jan 2014
B0044	646	ESE	11.01	11.1	0.09	1	Jan 2014
B0060	199	SSW	10.98	10.92	-0.06	1	Jan 2014
		SSW	10.92	11.06	0.14	0.9	Feb 2014
B1623	373	Unknown	?	10.89	?	>4	Jan 2014
B1623	373	SSE	10.89	10.95	0.06	8.4	Feb 2014
B0082	384	ESE	10.67	11.27	0.6	1.7	Jan/Feb 2014
B0083	536	Rotation	10.73	10.61	-0.12	-	Jan/Feb 2014
B0090	165	SSE	11.18	11.16	-0.02	0.5	Jan/Feb 2014
B0092	1621	S	10.58	10.65	0.07	0.5	Jan/Feb 2014
B0103	1807	S	10.67	10.69	0.02	0.6	Jan/Feb 2014
B0102	535	SSE	10.66	10.68	0.02	0.6	Jan/Feb 2014
B0110	762	SE	10.74	10.72	-0.02	1	Feb 2014
B0112	1791	ESE	10.41	10.67	0.26	2.6	Feb 2014

BOULDER	MASS (kg)	DIRECTION OF MOVEMENT	zi (m)	zf (m)	Δz (m)	Δx (m)	DATE
B1625	305	Unknown	?	10.87	?	>8	Jan/Feb 2014
B0123	121	WSW	10.97	10.77	-0.2	1.3	Jan/Feb 2014
B0125	1784	S	10.54	10.32	-0.22	2.4	Jan/Feb 2014
B0185[39]	2999	E	10.18	10.16	-0.02	4.3	Jan/Feb 2014
	1446	SE	10.18	9.97	-0.21	5.3	Jan/Feb 2014
B0137	325	SE	10.67	10.23	-0.44	0.4	Jan/Feb 2014
B0655	2452	Rotation	8.68	9.24	0.56	-	Jan 2014
B1628	11087	SE	7.58	7.58	0	1	Feb 2014
B1651	271	Unknown	?	7.77	?	?	Feb 2014
B1629	4785	SE	7.58	8.46	0.88	7	Feb 2014
B0913	6250	ESE	8.19	8.26	0.07	3	Feb 2014
B1650	609	SSE	7.58	8.45	0.87	6.5	Feb 2014
B0921	69	S	8.34	7.59	-0.75	23	Jan/Feb 2014
B1649	252	Unknown	?	8.53	?	?	Jan/Feb 2014
B1630	13889	SE	3.4	6.55	3.15	5.6	Feb 2014
B1652	851	SE	7.4	9.09	1.69	17.5	Feb 2014
B1653	547	SE	7.4	9.39	1.99	19	Feb 2014
B1134	381	SSE	8.12	7.52	-0.6	14	Jan/Feb 2014
B1030	813	S	9.46	7.98	-1.48	7	Jan/Feb 2014
B1043	111	SSE	9.21	8.21	-1	9	Jan/Feb 2014
B1004	203	SSW	9.43	9.01	-0.42	5	Jan/Feb 2014
B1118	137	SSE	7.82	7.89	0.07	11	Jan/Feb 2014
B1121	756	SE	8.06	7.61	-0.45	10	Jan/Feb 2014
B1087	221	S	8.61	7.84	-0.77	6	Jan/Feb 2014
B1088	1222	S	7.91	7.83	-0.08	2.3	Jan 2014
B1165	16	SSW	9.23	8.47	-0.76	7	Jan/Feb 2014
B1648	295	Unknown	?	7.74	?	?	Jan/Feb 2014
B1645	150	Unknown	?	7.81	?	?	Jan/Feb 2014
B1182	178	SW	9.14	8.34	-0.8	6.3	Jan/Feb 2014
B1228	712	Rotation	7.38	7.32	-0.06	-	Jan/Feb 2014
B1643	879	Unknown	?	7.85	?	?	Jan/Feb 2014
B1316	129	SW	9.12	8.9	-0.22	0.5	Jan/Feb 2014
B1320	301	Rotation	8.78	9.06	0.28	-	Jan/Feb 2014
B1306	502	SW	8	8.47	0.47	0.7	Jan/Feb 2014
B1335	32	NNW	8.4	8.84	0.44	0.7	Jan/Feb 2014
B1234	830	S	7.62	7.36	-0.26	2	Jan/Feb 2014
B1236	1493	SW	7.3	7.35	0.05	0.8	Jan 2014
		SSE	7.35	7.06	-0.29	4.7	Feb 2014

[39] Boulder originally measured as one particle, split in two, and both particles suffered differential transport later on.

BOULDER	MASS (kg)	DIRECTION OF MOVEMENT	zi (m)	zf (m)	Δz (m)	Δx (m)	DATE
B1238	1841	S	7.45	7.09	-0.36	3	Jan/Feb 2014
B1340	55	SW	8.32	8.29	-0.03	0.3	Jan/Feb 2014
B1242	72	SSW	7.82	7.12	-0.7	4	Jan/Feb 2014
B1343	504	SE	7.88	8.05	0.17	2	Jan/Feb 2014
B1253	365	SSW	7.36	7.21	-0.15	0.6	Jan/Feb 2014
B1638	219	Unknown	?	7.55	?	?	Jan/Feb 2014
B1639	83	Unknown	?	7.43	?	?	Jan/Feb 2014
B1637	84	Unknown	?	7.56	?	?	Jan/Feb 2014
B1416	120	N	7.64	7.61	-0.03	0.3	Jan/Feb 2014
B1631	24	Unknown	?	7.46	?	?	Jan/Feb 2014
B1632	91	Unknown	?	7.28	?	?	Jan/Feb 2014
B1634	433	Unknown	?	7.21	?	?	Jan/Feb 2014
B1635	135	Unknown	?	7.28	?	?	Jan/Feb 2014
B1591	910	Unknown	?	6.52	?	?	Jan/Feb 2014
B1522[40]	2814	S	7.07	6.9	-0.17	11	Jan/Feb 2014
	~3380	Disappeared	7.07	?	?	?	Jan/Feb 2014
B1636	272	Unknown	?	7.33	?	?	Jan/Feb 2014
B1451	2798	NW	7.22	7.06	-0.16	0.3	Jan/Feb 2014
B1446	237	SW	7.29	7.41	0.12	0.4	Jan/Feb 2014
B1590	262	Unknown	?	6.96	?	?	Jan/Feb 2014
B1469	474	S	7.44	7.47	0.03	5.6	Jan/Feb 2014
B1477	250	SSE	7.15	7.31	0.16	4.6	Jan/Feb 2014
B1478	47	SSE	7.28	7.22	-0.06	5	Jan/Feb 2014
B1475	1247	SSE	8.44	8.13	-0.31	2	Jan/Feb 2014
B1627	4044	Unknown	?	6.84	?	?	Jan/Feb 2014
B1497	1105	SSW	7.37	7.47	0.1	1	Jan/Feb 2014
B1501	2264	Rotation	7.3	7.3	0	-	Jan/Feb 2014
B1502	3174	Rotation	6.98	7.20	0.22	-	Jan 2014
		SE	7.20	7.17	-0.03	0.3	Feb 2014
B1560	10008	SE	3.28	2.88	-0.4	110	Jan/Feb 2014

[40] Boulder, already split in two, was originally measured as one particle, and both particles suffered differential transport later on

L. Description of control points used in the construction of the lichen growth curve

Near Nazaré there is an ancient fort named S. Miguel de Arcanjo (location in the Portuguese coast depicted in Figure 105). The construction of this structure started around 1577 to protect the bay and port from pirates and pillages (Almeida, 1946; Machado, 2009). The earlier and unfinished version revealed inadequate defensive capabilities and was later rebuilt, remodelled and expanded, until finally reaching its current configuration in 1645 (Almeida, 1946; Machado, 2009).

Lichen size and cover data were collected on 13-11-2015, in the corner-stones of the N facing wall of the fort (Figure 129a and b). The 5 largest thalli covering the corner-stones presented an average diameter of 38.8 mm and a lichen cover, considering a 100x100 mm area, of 100% (Figure 129c and d).

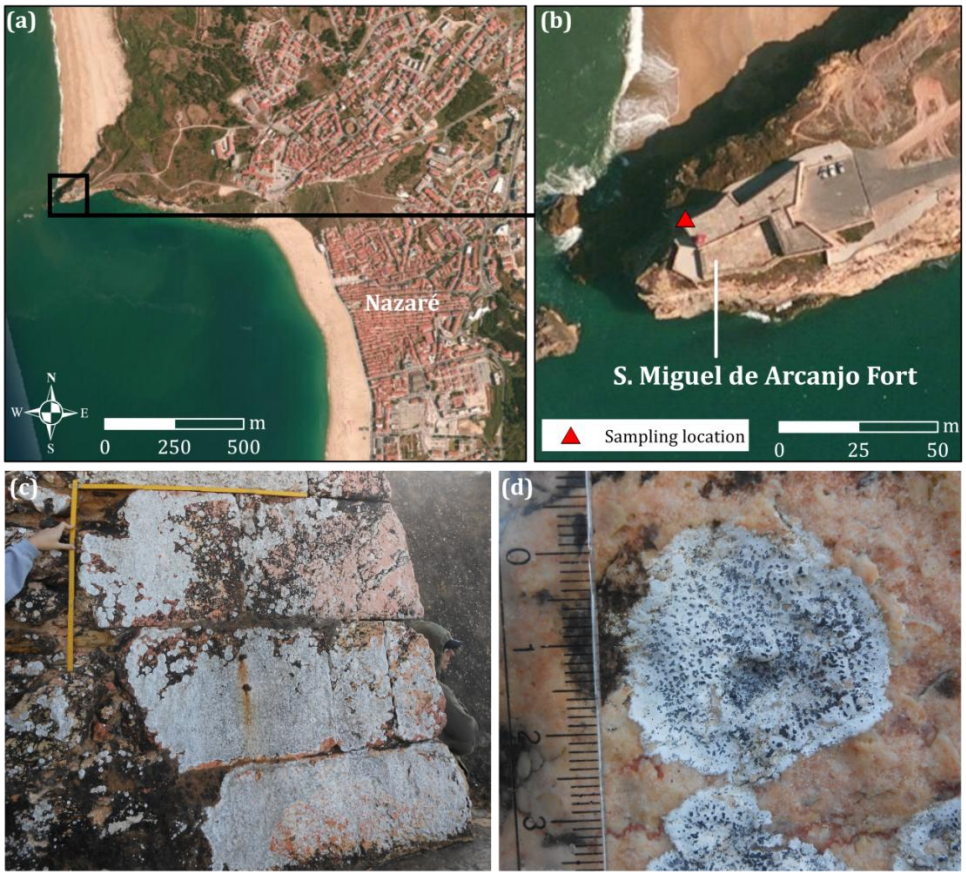

Figure 129: (a and b) Location of the control point in S. Miguel de Arcanjo Fort over a satellite image (source of the satellite image: Esri, Digital Globe, GeoEye, i-cubed, USDA, USGS, AEX, Getmapping, Aerogrid, IGN, IGP, swisstopo, and the GIS User Community). (c) Corner-stones used in lichen cover measurements; vertical scale corresponds to 0.6 m and horizontal scale to 0.8 m. (d) Detail of a lichen thallus over the corner-stone

Berlengas corresponds to a small archipelago offshore Peniche (Figure 105). São João Baptista Fort is in the SW facing coast of the largest island, Berlenga Grande (Figure 130a and b). This fort was built around 1520, functioning as a convent, it was abandoned around 1570 and later, in 1640, rebuilt and turned into a fort (Direção Geral dos Edifícios e Monumentos Nacionais, 1953). Since then, São João Baptista Fort suffered a severe attack and was rebuilt in 1678, as stated in an inscription located over the main door (*cf.* Direção Geral dos Edifícios e Monumentos Nacionais, 1953). Today, this fort is mainly made of granite, except for the limestone main door frame, inscription stone and coat of arms (Figure 130c).

Figure 130: São João Baptista Fort control point. (a) Berlenga Grande Island and general location of the São João Baptista Fort, over a satellite image (image source: "Berlenga Grande Islands." 455993 m E and 4362855 m N Universal Transverse Mercator WGS 84, Google Earth, Image from October 30, 2006, Accessed on August 8, 2016). (b) São João Baptista Fort and sampling location over a satellite image (source of the satellite image: Esri, Digital Globe, GeoEye, i-cubed, USDA, USGS, AEX, Getmapping, Aerogrid, IGN, IGP, swisstopo, and the GIS User Community. (c) Front door of São João Baptista Fort and sampling location in the upper-left door-frame. (d) Detail of the lichen covering the surface of the stones; vertical scale corresponds to ~0.42 m and horizontal scale to ~0.19 m

The northern part of the limestone door frame, completed in 1678, was covered with lichens of the species *Opegrapha durieui*. Lichen size and cover data were collected on 31-07-2016, and measured along the limestone stones limiting the upper left side of the door (Figure 130d). The average diameter of the 5 largest thalli covering these stones was of 33.0 mm and the lichen cover, considering a 100x100 mm area, was 94.89%.

Baluarte Redondo is a small round fort located in Peniche, corresponding to the oldest defensive structure in the area (Mateus, 1999) and in the dataset (Figure 131a and b). As stated in an inscription over the main door, construction of this structure ended in 1558 (Mateus, 1999). Later, in 1567, some of the walls that comprise Peniche fort were built around Baluarte Redondo (Mateus, 1999), which has become a small fort within a larger and younger fort (Figure 131b).

Figure 131: Peniche Fort control point. (a) Satellite image with the location of Peniche Fort. (b) Satellite image with the location of Baluarte Redondo fort within Peniche Fort and sampling location of the control point (source of the satellite images: Esri, Digital Globe, GeoEye, i-cubed, USDA, USGS, AEX, Getmapping, Aerogrid, IGN, IGP, swisstopo, and the GIS User Community). (c) Stones limiting the main door in Baluarte Redondo, where lichen size and cover data were acquired; vertical scale corresponds to 1 m. (d) Detail of the lichen covering the surface of the stones; vertical scale corresponds to 1.2 m and horizontal scale to 0.2 m

Lichen cover data was collected on 17-06-2015 in the limestone stones limiting the left side of the main door (Figure 131c and d). Lichen size, however, was measured on 05-08-2016 and all limestone stones were considered. The fort has been subject to improvements, such as cleaning, plastering and painting, resulting in dead lichen thalli and stone discoloration due to lichen removal, were observed. The dates of reconstruction and cleaning are unknown, so time of exposure considered in this control point can be overestimated. The 5 largest thalli in the limestone stones presented an average diameter of 37.6 mm and lichen cover, considering a 100x100 mm area, was of 98.07%.

A large block associated with a rock-fall and scar (L05) was detected in the cliffs limiting S. Lourenço beach to the S (Figure 132a). The mass movement was not present in a field campaign undertaken by Sónia Queiroz during September of 2011 (in the scope of the Project "Creation and implementation of a Costal Monitoring System for the jurisdiction area of Administração da Região Hidrográfica do Tejo IP"), and the block is visible in online photographs (www.panoramio.com) from 30-05-2012 onwards (Figure 132b), thus constricting its movement between those dates. Direct observation of the scar was undertaken in 20-09-2013. There were no visible lichens covering the fresh surface exposed after the rock-fall, contrasting with older surfaces of the cliff covered with patina and presenting small lichen thalli (Figure 132c and d).

Further west, still in the cliffs limiting S. Lourenço beach to the S, another rock-fall was identified (L01) (Figure 132a). Movement of a boulder was detected on photographs kindly made available by Paulo Henriques, geologist in the Autoridade Nacional de Protecção Cívil (Portuguese National Authority for Civil Protection) (Figure 132b). Detailed observations of changes occurring in this location, also made by Paulo Henriques, lead to the time constriction of the rock-fall between 1-11-2005 and 10-06-2006. Direct observation of the fresh surface was undertaken in 20-09-2013. This surface showed lichens with an average diameter of the 5 largest thalli of 5 mm and lichen cover, considering a 100x100 mm area, was of 2.68%. Lichen size and cover observed in the fresh surface contrasted with older surfaces of the cliff covered with patina and presenting larger lichen thalli (Figure 132c and d).

Figure 132: Santa Susana Fort, L01 and L05 control points. (a) Location of control points near S. Lourenço beach, over digital orthophotos of the year 2010 (IGEO, 2010). (b) Photograph of the southern view of S. Lourenço beach in which the fresh surface L01 resulting from rock-fall, is circled in red; photo by P. Henriques. (c) Photograph of the southern view of S. Lourenço beach taken in 30-05-2012 in which the block and fresh surface L05 resulting from rock-fall are circled in red (available at http://www.panoramio.com/photo/73430010). (d) Surface L01; vertical scale corresponds to 1 m; photo by P. Henriques. (e) Detail of the lichen cover in L01 surface; vertical scale is 0.2 m and horizontal scale is 0.4 m. (f) Part of the surface L05 surface. (g) Detail of the contrast of lichen cover between the L05 fresh and older surfaces; vertical scale corresponds to 1 m

Santa Susana Fort is located over the southern cliffs of S. Lourenço beach (Figure 132a) and was built in 1657 to protect the land from pirate attacks (Costa, 1997). By 1777 the Fort was reported to be missing plaster and doors (Costa, 1997). However, only around 1831 did any reconstruction for military use occurred (Costa, 1997). A part of the fort was demolished between 1944 and 1949 and a new building was built in its place (Costa, 1997). The comparison of the original architectural plant, available in Costa (1997), with the current plant sows that the northern wall of the fort maintained its configuration. Field observation confirmed the existence of an

older and preserved section of the fort, facing N, and missing plaster. The remaining part of the fort is younger, and dated from 1944-1949 (Costa, 1997).

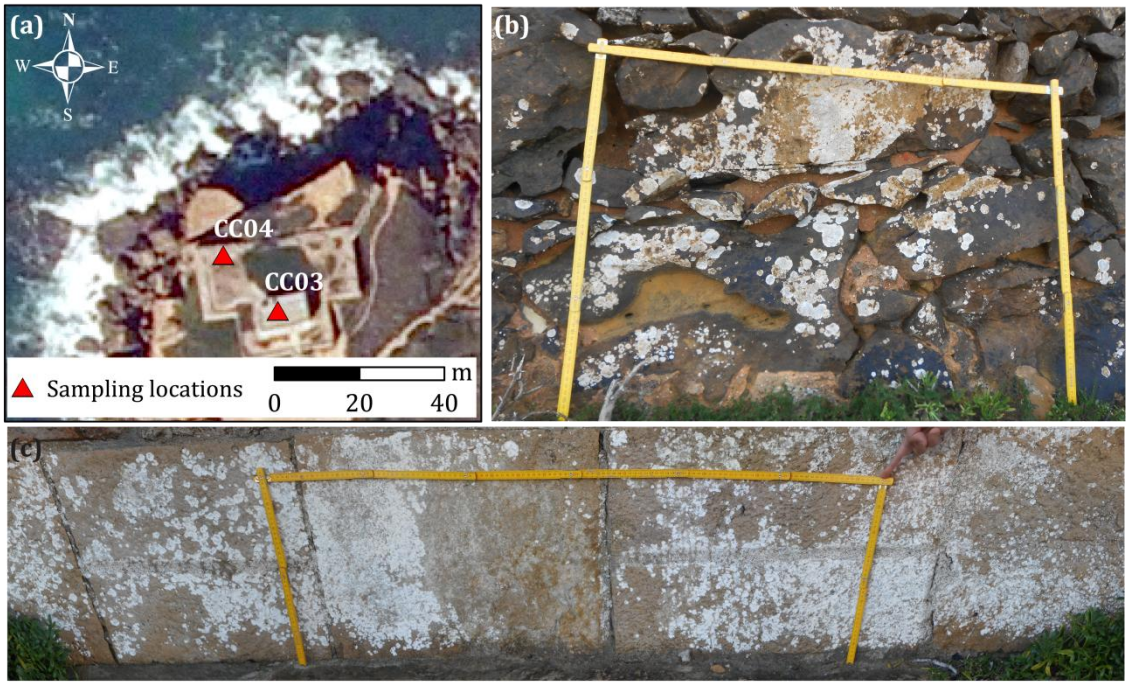

Figure 133: CC04 and CC03 control points. (a) Approximate sampling locations in Santa Susana Fort, over digital orthophotos dated from 2010 (IGEO, 2010). (b) Detail of lichens covering surface CC04; vertical scale corresponds to 0.6 m and horizontal scale to 0.8 m. (c) Detail of lichens covering surface CC03; vertical scale corresponds to 0.4 m and horizontal scale to 1.2 m

Lichen size and cover measurements were undertaken on 26-12-2013 in two distinct locations (Figure 133a): (1) one in the stones missing plaster, which comprise the northern wall, with date of exposure between 1657 and 1777 (CC04); (2) a second location in the N-facing part of the new building, dated from 1944-1949 (CC03). The average diameter of the 5 largest thalli covering the oldest surface (CC04) was 31.4 mm and lichen cover, considering a 100x100 mm area, was 82.36% (Figure 133b). The more recently exposed surface presented an average diameter of the 5 largest thalli of 24.4 mm and a lichen cover, considering a 100x100 mm area, of 93.47% (Figure 133c).

Further S, in the cliffs limiting Ribeira de Ilhas beach, a large rock-fall (L12) was detected by Sónia Queiroz when comparing aerial photographs from 1980 and 2010 (Figure 134a) (in the scope of the Project "Creation and implementation of a Costal Monitoring System for the jurisdiction area of Administração da Região Hidrográfica do Tejo IP"). This movement was further time-constricted to 1980-1989 by observation of aerial photographs from 1989 (Figure 134b and c). Direct

observation of the scar was undertaken in 07-11-2013. The average diameter of the 5 largest thalli was 11 mm and lichen cover, considering a 100x100 mm area, was of 6.15% (Figure 134d and e).

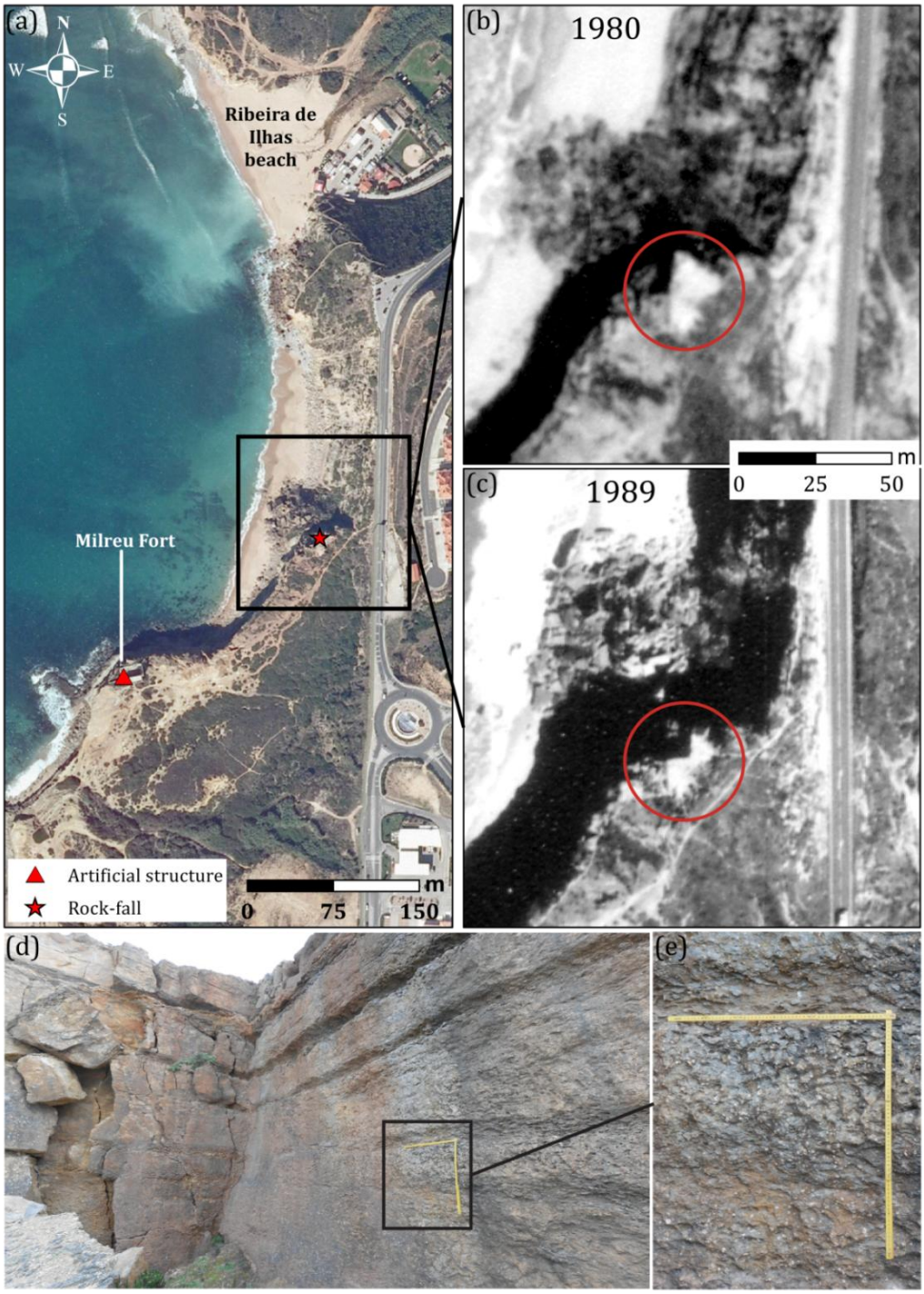

Figure 134: Milreu Fort and L12 control point. (a) Location of control points, near Ribeira de Ilhas beach, over digital orthophotos dated from 2010 (IGEO, 2010). (b) Aerial photograph from 24-05-1980 with a red circle limiting the general area of the L12 rock-fall. (c) Aerial photograph from 18-04-1989 with a red circle limiting the general area of the L12 rock-fall. (d) Part of the L12 fresh surface. (e) Detail of the lichens covering surface L12; vertical and horizontal scales correspond to 0.6 m

Milreu Fort was built over a cliff edge, N of Ericeira, and S of Ribeira de Ilhas beach (Figure 134a) with the propose to protect the land from piracy attacks (Costa, 1997). Costa (1997) suggests a probable age for this fort identical to S. Susana's Fort (from around 1657) but mentions the possibility of it being older, prior to 1589. This Fort was also reported to be missing plaster in 1777, and reconstruction also occurred in 1831 (*cf.* Costa, 1997). Even though the Fort is in ruins, differences in building materials used during reconstruction can be observed, such as distinct types of plaster and the use of bricks instead of stones.

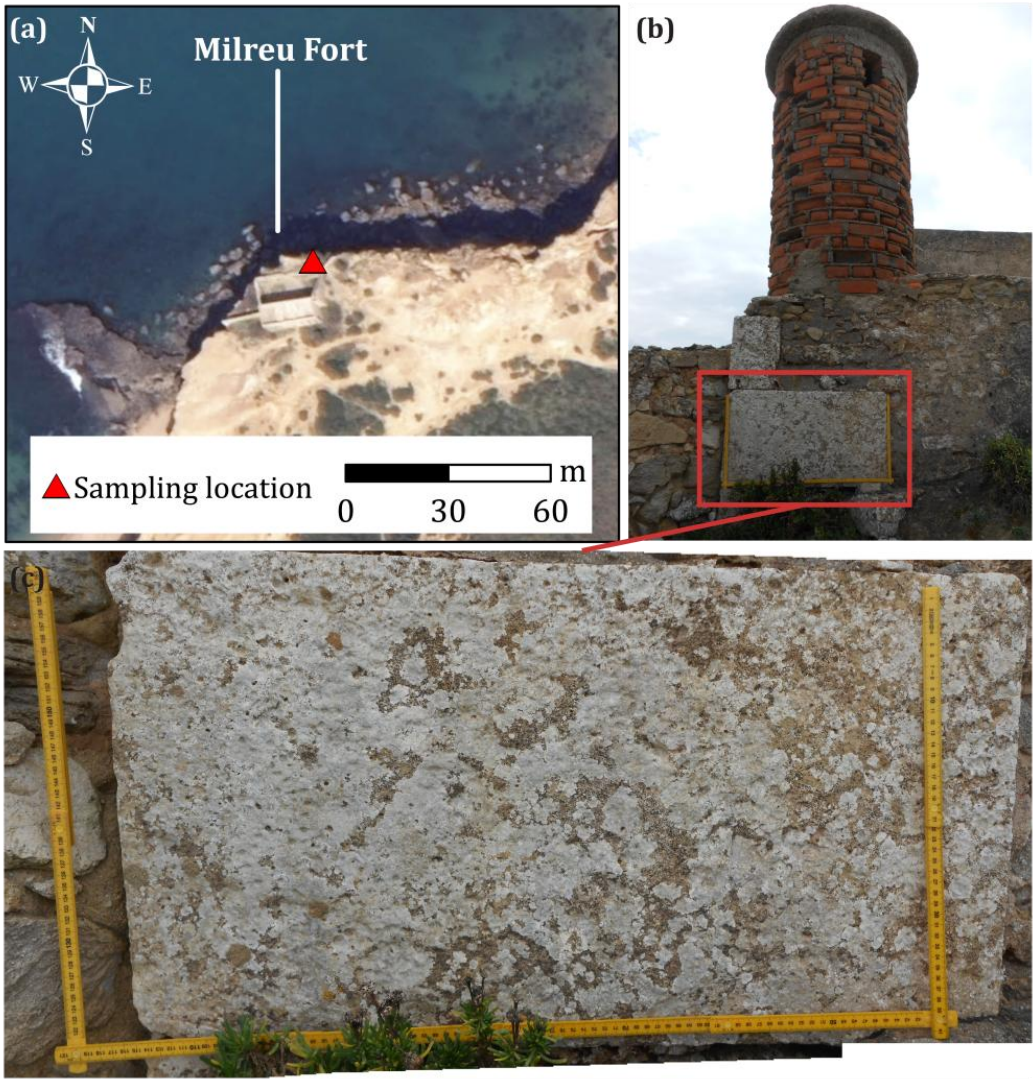

Figure 135: Milreu Fort control point. (a) Approximate location of S. Pedro de Milreu Fort, over digital orthophotos dated from 2010 (IGEO, 2010). (b) General view of the cornerstone used in lichen cover measurements; vertical scale corresponds to 0.2 m and horizontal scale to 0.8 m. (c) Detail of the lichens covering the surface of the cornerstone; vertical scales correspond to 0.2 m and horizontal scale to 0.8 m

An effort was made to assure the use of surfaces with known age. For this purpose, lichen size was measured in unplastered stones that comprise the N-facing wall,

which have become exposed sometime between 1657 (date of construction) and 1777. Lichen cover was measured in a cornerstone at the base of the same wall, which was never covered with plaster and exposed since the date of construction (Figure 135a, b and c). Direct observation of these surfaces firstly occurred on 07-11-2013, when lichen cover data was collected. Lichen size, however, was only measured on 30-01-2014. The average diameter of the 5 largest thalli was 34.8 mm and lichen cover, considering a 100x100 mm area, was of 93.68%.

Changes in the configuration of an artificial wall constructed on the top of the cliff along the coastline of Ericeira were detected while comparing aerial photographs (Figure 136a and b).

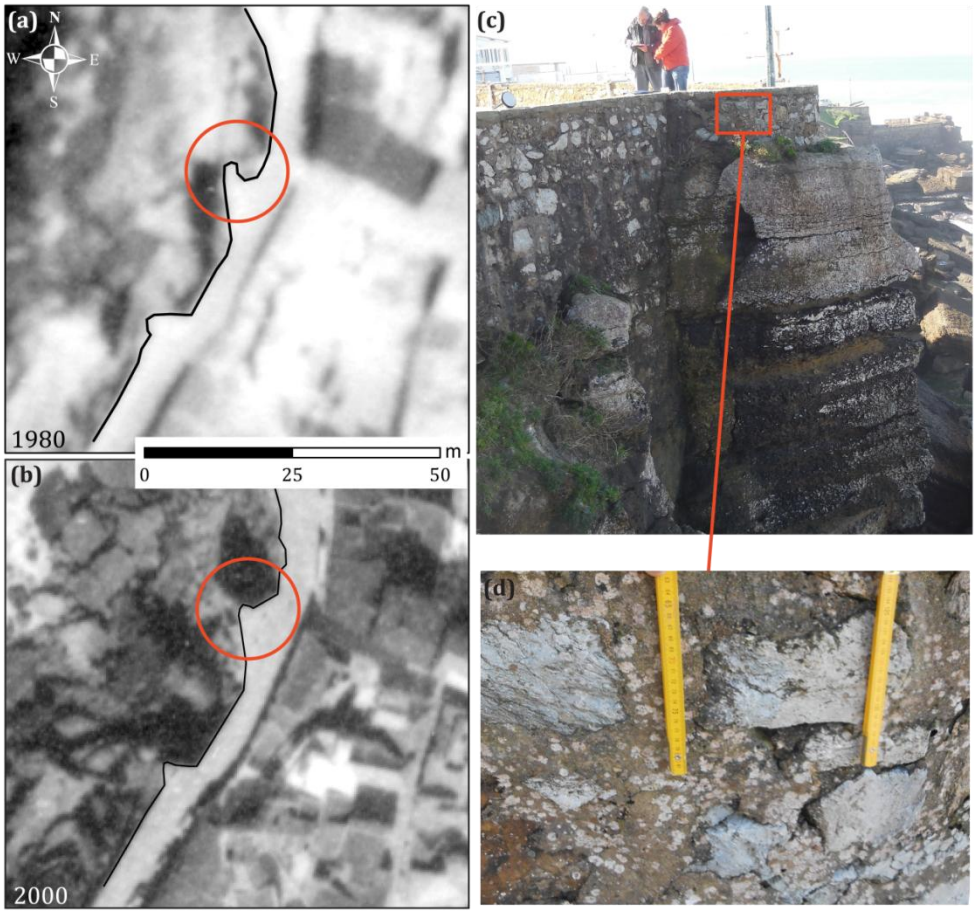

Figure 136: Ericeira wall control point. (a) Aerial photograph from 24-05-1980; red circle is limiting the general area of the artificial wall at the top of the cliff in Ericeira, represented by the black line (b) Aerial photograph from 24-02-2000; red circle is limiting the general area of the artificial wall in Ericeira, represented by the black line, which showed changes when compared to the general configuration observed in 1980. (c) Photograph of the southern view of the artificial wall in Ericeira (photo by S. Queiroz). (d) Detail of the lichens covering the surface of the wall; vertical scales correspond to 0.2 m

These changes occurred between the dates of the aerial photographs: 24-05-1980 and 24-02-2000. Lichen size and cover measurements were undertaken on 18-02-

2014, in the N-facing part of the wall, showing the highest lichen cover. The average diameter of the 5 largest thalli was of 13.2 mm and lichen cover, considering a 100x100 mm area, was of 22.11% (Figure 136b and c).

Pessegueiro Fort, was originally part of a major coastal port and defensive structure located between Pessegueiro Island and the beach (Figure 137a and b), which started in 1588 (Quaresma, 2007). This project was repeatedly interrupted and resumed under the direction of several engineers, being abandoned in 1608 (*cf.* Guedes, 1989; Quaresma, 2007). Before being abandoned, construction of Pessegueiro Fort based on the original plan was limited to the defensive trenches (*cf.* Quaresma, 2007). Construction with its current configuration started in 1680 and was completed in 1690 (Quaresma, 2007; Severino, 2014).

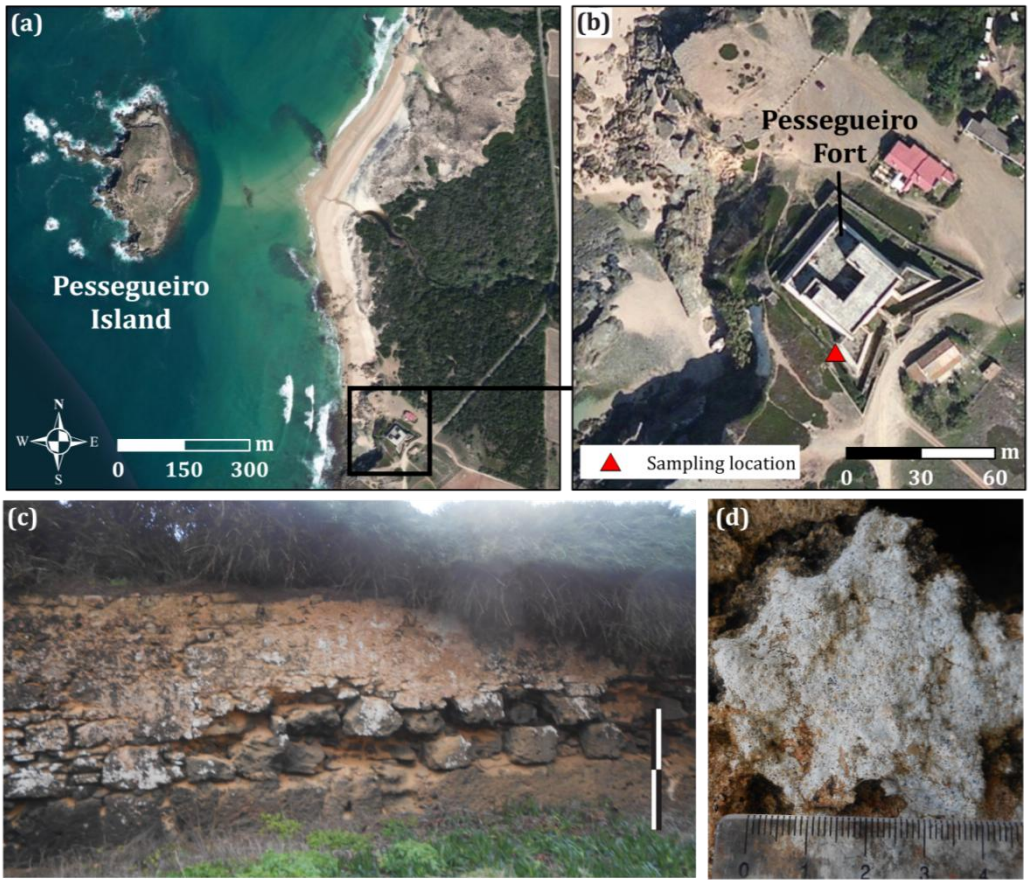

Figure 137: Pessegueiro Fort control point. (a) Location of the control point in Pessegueiro Fort in front the island, over a satellite image. (b) Sampling location used in the construction of the growth curve of lichen size and cover over a satellite image (source of the satellite images: Esri, Digital Globe, GeoEye, i-cubed, USDA, USGS, AEX, Getmapping, Aerogrid, IGN, IGP, swisstopo, and the GIS User Community). (c) Wall of the southern trench used in lichen cover measurements; vertical scale corresponds to 1 m. (d) Detail of a lichen observed in the trench wall

Lichen cover data was collected on 09-02-2014 in the walls of the southern trench, facing NE (Figure 137b, c and d). There were several lichen species covering the wall. The specific location chosen for lichen cover measurements mainly contained *Opegrapha durieui* thalli. Lichen size data were collected in the same wall on 03-08-2016. The time of exposure of the trench walls considered for lichen cover and size was of 324 and 326, respectively. Average diameter of the 5 largest thalli was 31.6 mm and lichen cover, considering a 100x100 mm area, was of 72.73%.

Belixe Fort, located in the SW tip of mainland Portugal (Figure 105), was originally built during the XV-XVI centuries, destroyed by pirate Francis Drake in 1587, and later rebuilt in 1632 (Direção Geral dos Edifícios e Monumentos Nacionais, 1960; Severino, 2014). The *AD* 1755 earthquake caused some damages to the fortress, which was reconstructed by Direção Geral dos Edifícios e Monumentos Nacionais (General Directorate of National Buildings and Monuments) between 1940 and 1960 (Direção Geral dos Edifícios e Monumentos Nacionais, 1960).

Figure 138: Belixe Fort control point. (a) Location of Belixe Fortress, E of cape S. Vicente, over a satellite image. (b) Sampling location in Belixe Fortress, over a satellite image (source of the satellite images: Esri, Digital Globe, GeoEye, i-cubed, USDA, USGS, AEX, Getmapping, Aerogrid, IGN, IGP, swisstopo, and the GIS User Community) (c) Eastern part of Belixe Fortress bulwark; vertical scale corresponds to 1 m. (d) Area of the bulwark used in lichen cover measurements; vertical scale corresponds to ~0.2 m and horizontal scale to~0.8 m

Photographs taken before and after the reconstruction, available in Direção Geral dos Edifícios e Monumentos Nacionais (1960), show that the lower eastern part of the fortress bulwark was mostly unharmed and left untouched (Figure 138a).

Sagres Fort, also located in the SW tip of mainland Portugal, S of Sagres village (Figure 105 and Figure 139a), is dated from the XV century, evidenced by archaeological remains found in this place (Silva, 2013) and by extensive historical documents which mention the existence of a village attributed to this location by several historians (*cf*. Direção Geral dos Edifícios e Monumentos Nacionais, 1960). However, the current configuration of the bulwark is different from the one portrayed in historical documents (Direção Geral dos Edifícios e Monumentos Nacionais, 1960; Mesquita, 2000). The original bulwark and gateway was destroyed by pirate Francis Drake in 1587 and by two earthquakes (27-12-1722 and 1-11-1755) (Direção Geral dos Edifícios e Monumentos Nacionais, 1960; Mesquita, 2000; Silva, 2013). Reconstruction with the current configuration finished in 1793, as stated in an inscription located over the gateway (Direção Geral dos Edifícios e Monumentos Nacionais, 1960; Mesquita, 2000; Silva, 2013). Since then, improvement works were carried out by Direção Geral dos Edifícios e Monumentos Nacionais, including the extension of the gateway, during 1940-1960 (Direção Geral dos Edifícios e Monumentos Nacionais, 1960; Mesquita, 2000). Gateway stones removed and later re-used, maintained at least part of the lichen cover visible in photographs taken immediately after improvement works and available in Direção Geral dos Edifícios e Monumentos Nacionais (1960). However, where the stones were located and if they were cleaned during that time is unknown.

Lichen sampling for species identification and measurement of lichen cover were undertaken on 26-01-2014. Initial observations indicated that many thalli were dead, which is probably related to stone cleaning during reconstruction. The absence of lichens and the presence of stone discoloration in other limestone stones throughout the fort wall confirms that they were in fact cleaned. Lichen size and cover was measured in limestone stones with preserved thalli, located in the right side of the gateway of Sagres Fortress, (Figure 139c). Species identification was only possible for two of the 5 largest thalli measured in this location, given the absence of preserved reproductive structures. Lichen size measurements were undertaken on

03-08-2016 and, assuming that all lichens belonged to the species *Opegrapha durieui*, they averaged in size 29.6 mm. Percentage cover measurements possibly correspond to an underestimation due to lichen removal during stone cleaning procedures. Nevertheless, undertaken measurements showed percentage cover of 90.01%, considering a 100x100 mm area (Figure 139d). Given that most individuals were dead possibly due to reconstruction during 1940-1960, it is assumed that lichens stopped growing in ~1950.

Figure 139: Sagres Fort control point. (a) Location of Sagres Fort over a satellite image. (b) Sampling location in Sagres Fortress, over a satellite image (source of the satellite images: Esri, Digital Globe, GeoEye, i-cubed, USDA, USGS, AEX, Getmapping, Aerogrid, IGN, IGP, swisstopo, and the GIS User Community) (c) Sagres Fortress door; vertical scale corresponds to 1 m. (d) Area selected for measurements of lichen cover; vertical scale corresponds to 1 m and horizontal scale to 0.2 m

S. Luís de Almádena Fort is in the S-facing coast of Portugal (Figure 105) and in ruins, although it is possible to identify most of the original architecture (Severino,

2014). The fort was built in 1632 to defend the coastline, particularly the fishing settlements frequently attacked by pirates (Coutinho, 1997).

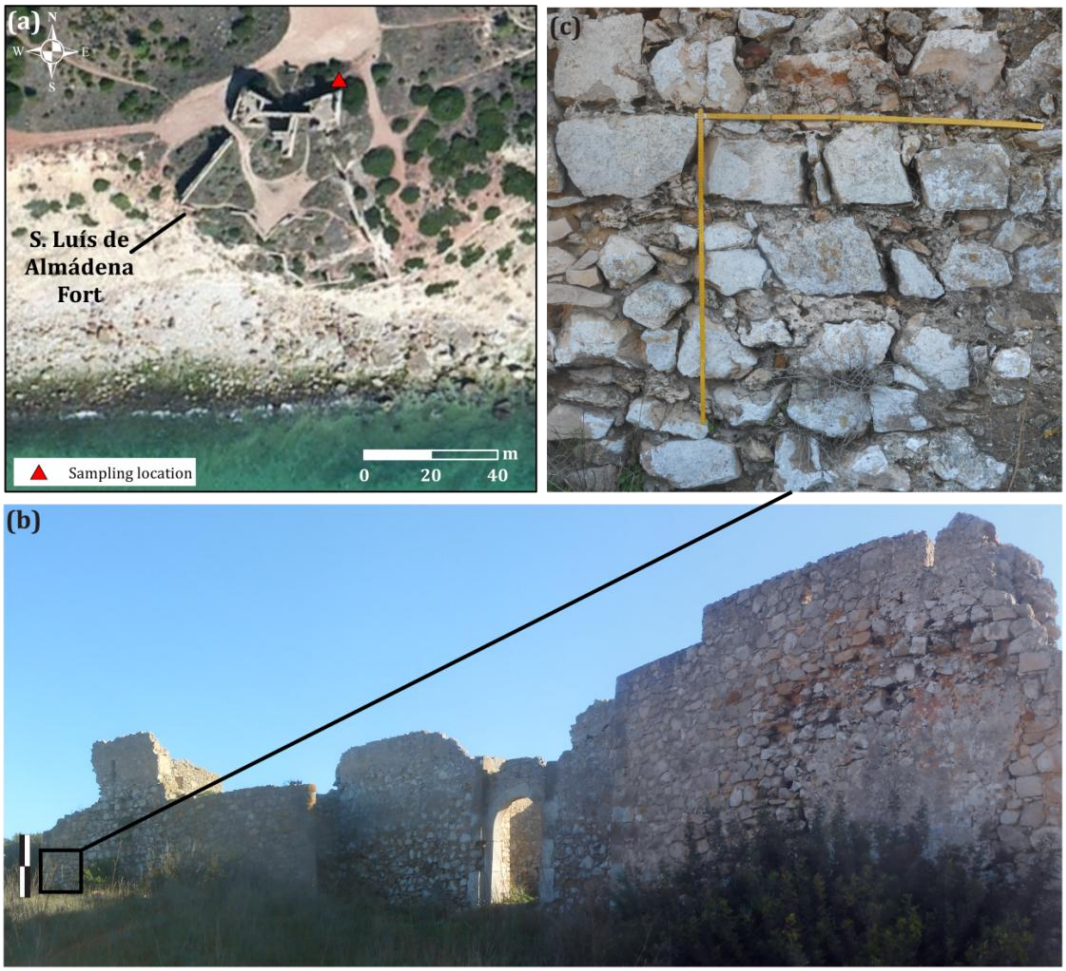

Figure 140: S. Luís de Almádena Fort control point. (a) Satellite image showing S. Luís de Almádena Fort (source of the satellite images: Esri, Digital Globe, GeoEye, i-cubed, USDA, USGS, AEX, Getmapping, Aerogrid, IGN, IGP, swisstopo, and the GIS User Community). (b) View of the northern wall of the Fort; vertical scale corresponds to ~2 m. (c) Detail of the wall surface used in lichen cover measurements; vertical and horizontal scales correspond to 1 m

Lichen cover measurements were undertaken in the N-facing walls of the fort on 26-01-2014 (Figure 140a and b). Although other lichen species were present, measurements were focused in an area where the species *Opegrapha durieui* showed maximum development (Figure 140c). Lichen size data was collected on 03-08-2016. Average diameter of the 5 largest thalli was of 37.2 mm and lichen cover, considering a 100x100 mm area, of 96.80%.

M. Script used in lichenometry to find the best fit to the control points and to infer age of lichen growth in boulders

```
#Load the packages that contain the necessary functions

library(xlsx)

#Define the path for the data files and the export directory

FileDir <- "G:/Lichenometry/Growth curves/"
ExportDir <- "G:/Lichenometry/R/Export/"

#Read the files containing the growth curve data

diameter = read.xlsx(paste(FileDir,
                           "Growth_curves.xlsx",
                           sep=""),
                     sheetName = "R_diameter")
area = read.xlsx(paste(FileDir,
                       "Growth_curves.xlsx",
                        sep=""),
                 sheetName = "R_area")

#Attach objects to the database

attach(diameter)
attach(area)
attach(cover)

#Fit linear models to the growth data

diameter.lm = lm(log(time_d)~diameter_d)
area.lm = lm(time_a~area_a)

#Generate confidence and prediction intervals

newx_d <- seq(min(diameter_d), 100, 1)
newx_a <- seq(min(area_a), 1400, 10)
pred.int.diameter<- exp(predict(diameter.lm,
                                data.frame(diameter_d=newx_d),
                                interval="prediction"))
conf.int.diameter<- exp(predict(diameter.lm,
                                data.frame(diameter_d=newx_d),
                                interval="confidence"))
pred.int.area <- predict(area.lm,
                         data.frame(area_a=newx_a),
                         interval="prediction")
conf.int.area <- predict(area.lm,
                         data.frame(area_a=newx_a),
                         interval="confidence")

#Plot the data, models and intervals and save as a pdf file

pdf(file=paste(ExportDir,"diameter_lm.pdf",sep=""))
```

```
plot(diameter_d,
     log(time_d),
     xlab = "Lichen diameter (mm)",
     ylab = "Log(Time) (years)")
abline(diameter.lm)
lines(newx_d, log(pred.int.diameter [,2]), lty=2)
lines(newx_d, log(pred.int.diameter [,3]), lty=2)
lines(newx_d, log(conf.int.diameter [,2]), lty=3)
lines(newx_d, log(conf.int.diameter [,3]), lty=3)
dev.off()

pdf(file=paste(ExportDir,"area_lm.pdf",sep=""))
plot(area_a,
     time_a,
     xlab = "Area, A (mm^2)",
     ylab = "Time (years)")
abline(area.lm)
lines(newx_a, pred.int.area [,2], lty=2)
lines(newx_a, pred.int.area [,3], lty=2)
lines(newx_a, conf.int.area [,2], lty=3)
lines(newx_a, conf.int.area [,3], lty=3)
dev.off()

#Read the files containing lichen data covering the boulders

boulders = read.xlsx(paste(FileDir,
                           "Growth_curves.xlsx",
                           sep=""),
                     sheetName = "R_boulders")

#Attach objects to the database

attach(boulders)

#Estimate age prediction intervals for boulder lichen data

boulders.diameter <- exp(predict(diameter.lm,
                         data.frame(diameter_d=diameter_b),
                         interval="prediction"))
boulders.area <- predict(area.lm,
                         data.frame(area_a=area_b),
                         interval="prediction")

#Save the results in csv tables

write.table(boulders.diameter,
            paste(ExportDir, "boulders.diam.csv", sep=""),
            sep=";",
            row.names=FALSE)
write.table(boulders.area,
            paste(ExportDir, "boulders.area.csv", sep=""),
            sep=";",
            row.names=FALSE)
```

N. Age estimation of lichens measured in the Coxos boulder accumulation

Table XXXIV: Age estimation results obtained with the application of the growth models. * corresponds to data from the combination of dead and living lichen populations

Boulder	Sector	Age before sampling (years)			Age (Calendar Years)	
		Fit	Prediction Interval		Fit	Prediction Interval
			Lower	Upper		
B1532	N	39	16	91	1977	1925 – 2000
B1533	N	8	3	21	2007	1994 – 2012
B1533*	N	50	21	117	1965	1898 – 1994
B1536	N	435	311	559	1580	1454 – 1704
B1540	N	617	477	758	1398	1257 – 1538
B1556	N	276	158	394	1739	1621 – 1857
B1542	N	124	53	289	1891	1726 – 1962
B1544	N	95	41	222	1920	1793 – 1974
B1543	N	372	251	493	1644	1523 – 1765
B1614	S	667	521	814	1348	1201 – 1494
B1144	S	8	3	19	2004	1993 – 2009
B1140	S	25	10	59	1987	1953 – 2002
B1143	S	18	8	44	1994	1968 – 2004
B1306	S	103	44	240	1913	1776 – 1972
B1333	S	10	4	25	2006	1991 – 2012
B1333*	S	51	22	119	1965	1897 – 1994
B1280	S	19	8	47	1997	1969 – 2008
B1264	S	6	2	14	2006	1998 – 2010
B1406	S	11	5	27	2001	1985 – 2007
B1451	S	18	7	42	1994	1970 – 2005
B1452	S	11	5	27	2001	1985 – 2007
B1362	S	44	19	104	1968	1908 – 1993
B1473	S	77	33	179	1935	1833 – 1979
B1481	S	19	8	47	1993	1965 – 2004
B1492	S	53	23	124	1959	1888 – 1989
B1493	S	32	14	76	1980	1936 – 1998
B1367	S	30	13	70	1982	1942 – 1999
B1496	S	33	14	78	1979	1934 – 1998
B1504	S	30	13	70	1982	1942 – 1999
B1504*	S	124	53	289	1888	1723 – 1957
B1502	S	10	4	24	2002	1988 – 2008
B1509	S	34	14	80	1978	1932 – 1998
B1509*	S	352	232	472	1660	1540 – 1780
B1512	S	18	7	43	1994	1969 – 2005
B1515	S	8	3	20	2004	1992 – 2009
B1517	S	39	16	91	1973	1921 – 1996

O. Micro-erosion-meter measurements

Table XXXV: Average of the measurements and standard deviation in station CX-01

Time (days)	Position 1		Position 2		Position 3	
	Average (mm)	Standard deviation (mm)	Average (mm)	Standard deviation (mm)	Average (mm)	Standard deviation (mm)
0	15.685	0.049	16.473	0.202	11.433	0.159
3	15.636	0.078	16.588	0.029	11.495	0.037
210	15.480	0.000	16.277	0.309	11.835	0.311
472	15.425	0.042	16.430	0.014	10.908	0.030
836	15.459	0.018	16.411	0.084	10.654	0.035
997	15.404	0.036	16.342	0.097	10.679	0.169
1233	15.392	0.003	16.292	0.106	10.818	0.018

Table XXXVI: Average of the measurements and standard deviation in station CX-02

Time (days)	Position 2	
	Average (mm)	Standard deviation (mm)
0	17.552	0.233
207	17.550	0.141
469	17.210	0.129
833	16.943	0.222
994	16.830	0.239
1230	16.518	0.140

Table XXXVII: Average of the measurements and standard deviation in station CX-03

Time (days)	Position 1		Position 3	
	Average (mm)	Standard deviation (mm)	Average (mm)	Standard deviation (mm)
0	15.509	0.103	16.059	0.035
207	16.248	0.004	16.460	0.014
469	14.658	0.062	14.691	0.023
833	14.436	0.015	14.391	0.053
994	14.355	0.063	14.401	0.032
1230	14.217	0.012	14.165	0.009

P. Optically stimulated luminescence results

UNL #	Field #	Burial Depth (m)	H_2O (%)[a]	K_2O (%)	±	U (ppm)	±	Th (ppm)	±	Cosmic (Gy)	Dose Rate (Gy/ka)	D_e (Gy)	No. of Aliquots	Age (ka)
UNL4003	Q20 CxS	0.35	7.5	1.57	0.05	1.99	0.12	12.55	0.47	0.20	2.66±0.10	3.86±0.36	75	1.45±0.14
								Minimum Age Model (Galbraith et al., 1999) =				0.60±0.06		0.23±0.02
UNL4004	Q21 CxS	0.35	9.6	1.90	0.05	1.83	0.10	9.62	0.38	0.20	2.63±0.10	3.95±0.47	72	1.50±0.19
								Minimum Age Model (Galbraith et al., 1999) =				0.77±0.13		0.29±0.05

[a] In-situ Moisture Content
Error on De is 1 standard error
Error on age includes random and systematic errors calculated in quadrature

Dose Recovery Test on UNL4003:

Preheat Temp (ºC)	De (Gy)	±	
180	4.75	0.02	
200	4.74	0.03	
220	4.78	0.05	
240	4.80	0.02	
260	4.83	0.01	
280	4.96	0.03	
Applied Dose =		4.77	Gy
Recovered Dose =		4.81 ±	0.08 Gy

Thermal Transfer Test on UNL4003:

Preheat Temp (ºC)	De (Gy)	±	
180	0.01	0.01	
200	-0.01	0.00	
220	0.01	0.01	
240	0.02	0.01	
260	0.03	0.01	
280	0.07	0.01	
Thermal Transfer =		0.02 ±	0.02 Gy

Preheat Plateau on UNL4003:

Preheat Temp (ºC)	De (Gy)	±
180	4.35	0.75
200	4.21	0.73
220	4.07	0.52
240	3.76	0.46
260	6.22	2.19
280	4.56	0.80

Preheat of 240C used for analyses!

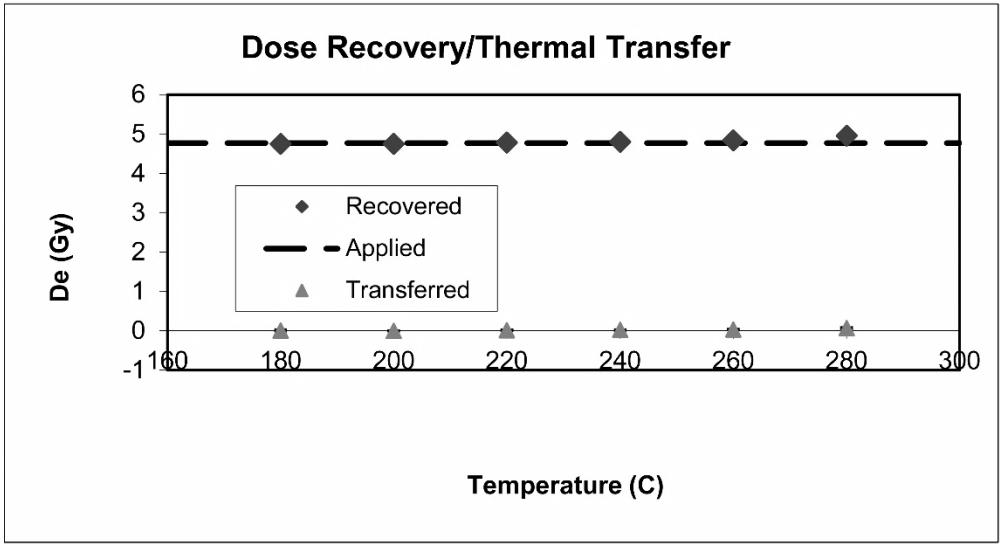

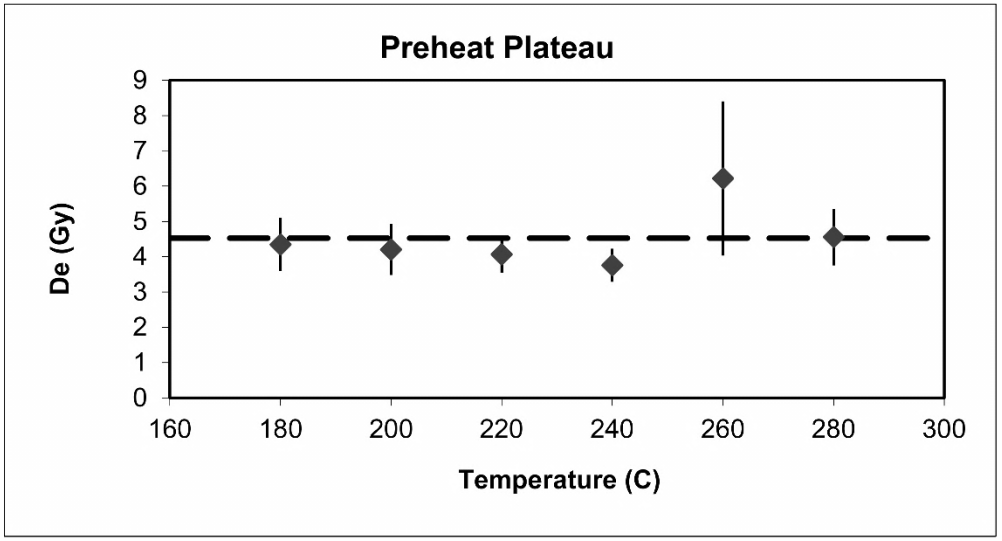

UNL #	Dose Recovery		Skew/$2\sigma_c$[b]	Kurt/$2\sigma_k$[b]	c/c_{crit}[b]	k/k_{crit}[b]	Overdisp (%)[c]	CAM/Med[d]	CAM/PDF Fit[e]	CAM/Mode[f]	CAM/Mean[g]
	Rec/Appl	±									
UNL4003	1.01	0.00	3.78	5.70	0.31	3.13	80	1.04	1.10	1.05	0.71
UNL4004	1.02	0.01	3.27	2.78	0.28	1.56	99	1.14	1.68	2.95	0.59

[b] Bailey & Arnold (2006)
[c] Galbraith (2005)
[d] Central Age Model/Median
[e] Central Age Model/Probability Density Function Fit
[f] Central Age Model/Mode
[g] Central Age Model/Unweighted Mean